Proceedings

Sono convinto che mai come oggi, pur vivendo in contesti sempre più dilatati, nei quali i contatti sono velocissimi, per resistere non dobbiamo mai abbandonare le nostre radici. Per diventare internazionali, dobbiamo appartenere a un Paese. Quel Paese, per me, è il Mediterraneo, che è sterminato patrimonio di culture e di visioni.

Mimmo Palladino

The organizing committee wishes to dedicate Medyna2020 conference and this book of proceedings to Dr. Paolo Russo.

Paolo was our PhD student, spending good part of his working days in the lab located closeby, within this very conference venue.

In February Paolo was unable to join us at the conference as he was fighting against a vital disease.

In April, Paolo passed to better life.

Conference Objectives

This Euro-Mediterranean conference brought together researchers from the worldwide scientific community**,** to discuss about the major advances in the field of Vibrations, Acoustics and Vibroacoustics. It addressed both theoretical (analytical and numerical) and experimental methods in these topics by gathering applied mathematicians, mechanicians and acousticians. This edition was organised with the support of AIDAA, Italian Association of Aeronautics and Astronautics (www.aidaa.it) and it was inserted in the series of events to celebrate its centenary **(**1920-2020).

The 3rd edition of MEDYNA brought together 136 attendants in Naples from 15 countries and 4 continents.

Conference topics

Stochastic Dynamics and Uncertain systems

Periodic structures and metamaterial

Vibro-acoustics

Machine Learning in Vibroacoustics

Mid-high frequency range

Impact

Damage detection and Structural Health monitoring

Active vibration control

Structural acoustic and noise control

Experimental techniques

Smart materials & structures for vibroacoustics

Computational techniques & reduced order modeling

Similitudes in Vibroacoustics

H2020 projects

CASTLE Project

VIPER Project

Organising Committee

Chair / Sergio De Rosa

Co-Chairs /

- Michele Guida
- Francesco Franco
- Francesco Marulo
- Giuseppe Petrone

with the support of /

- Ernesto Monaco
- Fabrizio Ricci
- Massimo Viscardi

Scientific Committee

- Makrem Arfaoui / Applied Mechanics and Engineering Laboratory, National School of Engineering of Tunis, University of Tunis El Manar, Tunisia
- Olivier Bareille / LTDS, Ecole Centrale Lyon, France
- Joachim Bös / System Reliability, Adaptive Structures, and Machine Acoustics SAM, Technische Universität Darmstadt, Germany /
- Noureddine Bouhaddi / UBFC, Université Bourgogne Franche-Comté, Institut Femto-ST, Département Mécanique Appliquée, Besançon, France
- Antonio Carcaterra / Dipartimento di Ingegneria Meccanica e Aerospaziale, Università di Roma La Sapienza, Italy
- Wim Desmet / Department of Mechanical Engineering, PMA Section, KU Leuven, Belgium
- Jean-François Deü / Conservatoire national des arts et métiers (Cnam); Laboratoire de Mécanique des Structures et des Systèmes Couplés (LMSSC) Paris, France
- Lorenzo Dozio / Department of Aerospace Science and Technology, Politecnico di Milano, Italy
- Mohamed Ichchou / LTDS, Ecole Centrale Lyon, France
- Leif Kari / KTH Royal Institute of Technology, Stochkolm, Sweden
- Alain Le Bot / LTDS, Ecole Centrale Lyon, France
- Laurent Maxit / Laboratoire Vibrations Acoustique, INSA-Lyon, France
- Jarir Mahfoud / Laboratoire de Mécanique des Contacts et des Structures, INSA-Lyon, France
- Alberto Milazzo / Università di Palermo, Italy
- Tobias Melz / Fraunhofer Institute for Structural Durability and System Reliability LBF, Darmstadt, Germany
- Viviana Meruane N. / Department of Mechanical Engineering, Universidad de Chile
- Roger Ohayon / Chair of Mechanics (Emeritus), Conservatoire National des Arts et Metiers, Paris, France
- Ramzi Othman / Mechanical Engineering Department, College of Engineering King Abdulaziz University, Saudi Arabia
- Morvan Ouisse / ENSMM, Université Bourgogne Franche-Comté, École Nationale Supérieure de Mécanique et des Microtechniques de Besançon, Institut FEMTO-ST, Département Mécanique Appliquée, Besançon, France
- Nicolas Totaro / Laboratoire Vibrations Acoustique, INSA-Lyon, France
- Daniel G. Vallejo / Escuela Técnica Superior de Ingeniería, Universidad de Sevilla, Spain

Program		Main Room / T3	Room T1	Room T2	Room I4	Room I5
Monday, February 17						
08:00 - 09:00	Registration (welcome and reception desk always open during the conference days)					
08:30 - 08:45	Welcome address	Prof. Sergio De Rosa & Prof. Rita Mastrullo				
08:45 - 09:15	Opening Lecture	Prof. Francesco Marulo				
09:20 - 11:00	Technical sessions 1		CASTLE	GEAR NOISE	VIBROACOUSTICS & FSI I	
11:00 - 11:20	Coffee Break					
11:20 - 12:40	Technical sessions 2		IMPACT DYNAMICS	AEROELASTICITY & GVT	NUMERICAL METHODS I	
12:40 - 14:00	Lunch					
14:00 - 15:00	Keynotes	Prof. Ines Artega Lopez & Dr. Elena Ciappi				
15:00 - 16:40	Technical sessions 3		ACOUSTICS I	T-WING	METAMATERIALS	
16:40 - 17:00	Coffee Break					
17:00 - 18:00	Technical sessions 4		ACOUSTICS II	STRUCTURAL DYNAMICS I		
Tuesday, February 18						
09:00 - 11:00	Technical sessions 5		DEVISU	MACHINE LEARNING & SHM	VIBROACOUSTICS & FSI II	NON-LINEAR DYNAMICS
11:00 - 11:30	Coffee Break					
11:30 - 13:00	Special Session	Talented Researchers				
13:00 - 14:00	Lunch					
14:00 - 15:00	Keynotes	Prof. Erasmo Carrera & Prof. Stefan Rinderknecht				
15:00 - 16:40	Technical sessions 6		VIPER I	WAVES	NUMERICAL METHODS II	
18:00 - 20:00	Social event: Tour in Napoli					
20:30 - 23:00	Pizza dinner					
Wednesday, February 19						
09:00 - 10:00	Keynotes	Prof. Weidong Zhu & Dr. Alain Le Bot				
10:00 - 12:00	Technical sessions 7		VIPER II	MATERIALS & DAMPING	STRUCTURAL DYNAMICS II	
12:00 - 13:00	Arrivederci (Lunch Cocktail)					

February 17th, 2020 **Monday**	
Welcome	
08:30 – 08:45	*S. De Rosa, R. Mastrullo*
Opening Lecture	
08:45 – 09:15	LIFE (**LI**FE, SA**F**E, QUI**E**T) FOR AERONAUTICS *F. Marulo*
Keynotes	
14:15 – 14:45	APPLICATIONS OF MICROPHONE ARRAYS AND MACHINE LEARNING TO FAULT DETECTION *I. A. Lopez*
14:45 – 15:15	OPEN CHALLENGES FOR STRUCTURAL DYNAMICS IN MARINE ENGINEERING *E. Ciappi*
February 18th, 2020 **Tuesday**	
Special Session: Talented Researchers	
11:30 – 12:00	PADÉ APPROXIMANTS FOR MULTIVARIATE REDUCED ORDER MODELS *R. Rumpler*
12:00 – 12:30	GENERAL BLOCH MODELING OF PIECEWISE PERIODIC STRUCTURES *C. Droz, E. Deckers, W. Desmet*
12:30 – 13:00	TOWARDS NONLINEAR MULTIMODAL APPROACHES FOR VIBRATION ENERGY HARVESTING *N. Kacem and N. Bouhaddi*
Keynotes	
14:00 – 14:30	ASSESSMENT OF COMPUTATIONAL MODELS FOR THE DYNAMIC RESPONSE OF ROTATING COMPOSITE TURBINE BLADES *E. Carrera*, M. Filippi, D. Giusa, A. Pagani, E. Zappino*
14:30 – 15:00	SYSTEM DYNAMICS IMPROVEMENT WITH STATE-OF-THE-ART MECHATRONICS – POTENTIALS AND CHALLENGES *S. Rinderknecht*
February 19th, 2020 **Wednesday**	
Keynotes	
09:00 – 09:30	VIBRATION-BASED DAMAGE DETECTION AND NONLINEAR DYNAMIC ANALYSIS *W. Zhu*
09:30 – 10:00	STATISTICAL ENERGY ANALYSIS, THEORETICAL FOUNDATIONS AND RANGE OF APPLICABILITY *A. Le Bot*

Technical sessions

February 17th, 2020
Monday

Technical sessions 1		
CASTLE		
09:20 – 09:40	301055	ELIGIBILITY OF ELECTROSPUN NANOFIBERS FOR AERONAUTICAL THERMOACOUSTIC INSULATION BLANKETS *B. Vitolo, M. Guida, T. Polito, F. Marulo, F. Branda*
09:40 – 10:00	300730	OPTIMIZATION OF PASSIVE AND ACTIVE SOUNDPROOFING FOR AN ADVANCED TURBO-PROP AIRCRAFT CABIN *R. Lombardi, P. Vitiello, I. Dimino, G. Petrone, M. Barbarino*
10:00 – 10:20	305157	INNOVATIVE SOUNDPROOFING MATERIALS THROUGH ELECTROSPINNING *F. Branda*
10:20 – 10:40	301743	ACOUSTIC CHARACTERISTICS OF INNOVATIVE MATERIALS THROUGH ELECTROSPINNING *G. Iannace*
10:40 – 11:00	303627	PASSIVE NOISE CONTROL ORIENTED DESIGN OF AIRCRAFT HEADRESTS *V. Giannella, R. Citarella, M. Barbarino, P. Vitiello, D. Bianco, G. Petrone*
GEAR NOISE		
09:20 – 09:40	298653	DYNAMIC POWER LOSS MODEL INCLUDING FRICTIONAL EFFECTS FOR SPUR GEARS *M. Hammami, N. Feki, O. Ksentini, M. S. Abbes, M. Haddar*
09:40 – 10:00	299758	VIBROACOUSTIC SIMULATION FE METHODOLOGIES: EXTERNAL GEAR PUMP CASE STUDY *G. Miccoli, K. Hamiche*
10:00 – 10:20	298500	SOME RESULTS OF VIBROACOUSTIC OPTIMIZATION OF A RAILWAY GEARBOX *K. Landet, J. Perret-Liaudet, E. Rigaud, M. Fraces*
10:20 – 10:40	400003	INFLUENCE OF TOOTH PROFILE MODIFICATIONS ON THE DYNAMIC BEHAVIOR OF A PLANETARY GEAR SET: EXPERIMENTAL INVESTIGATION AND NUMERICAL VALIDATION FOR DIFFERENT AMPLITUDES OF TOOTH PROFILE MODIFICATIONS *J. Neufond, E. Rigaud, J. Perret-Liaudet, A. Carbonelli*
VIBROACOUSTICS & FSI I		
09:20 – 09:40	300094	VIBRO-ACOUSTIC CHARACTERIZATION OF A MILITARY SHELTER SYSTEM *M. Viscardi, M. Lomasto, R. Molitierno*
09:40 – 10:00	300180	VIBRO-ACOUSTIC PERFORMANCE ANALYSIS OF A TURBOPROP INSULATION PACKAGE *M. Viscardi, G. Bizzarro, V. M. Porpora, G. Di Paola*
10:00 – 10:20	300557	TOWARDS A COUPLED FLUID-STRUCTURE MODEL FOR SLUG FLOW IN A FLEXIBLE RISER *A. Elliott, G. Hunt, A. Cammarano, G. Falcone*
10:20 – 10:40	299972	TOWARDS FULL-FIELD MODAL ANALYSIS: COMBINING OPTICAL TECHNIQUES WITH STRUCTURAL DYNAMICS TESTING *E. Di Lorenzo, D. Mastrodicasa, L. Wittevrongel, P. Lava, B. Peeters*
10:40 – 11:00	297188	COMPARISON OF THE PERFORMANCE OF VIBROACOUSTIC SIMILITUDE METHODS *C. Adams, J. Bös, T. Melz*
Technical sessions 2		
IMPACT DYNAMICS		
11:20 – 11:40	301291	DYNAMIC BUCKLING INVESTIGATION OF AIRCRAFT COMPOSITE STANCHIONS SUBJECTED TO CYCLIC LOADING CONDITIONS *F. Di Caprio, A. Sellitto, S. Saputo, M. Guida, A. Riccio*
11:40 – 12:00	298860	A SENSITIVITY ANALYSIS ON THE DAMAGE BEHAVIOR OF A LEADING EDGE SUBJECT TO BIRD STRIKE *F. Di Caprio, A. Sellitto, S. Saputo, M. Guida, A. Riccio*
12:00 – 12:20	293644	EFFECT OF COLD SPRAY DEPOSITION ON THERMOSETTING COMPOSITE SUBSTRATES UNDER DYNAMIC LOADS *I. Papa, A. Viscusi, A. S. Perna, A. Astarita, V. Lopresto, L. Carrino, V. Antonucci, M. R. Ricciardi*
12:20 – 12:40	400001	A SIMPLIFIED FINITE ELEMENT MODELLING OF A FULL-SCALE FUSELAGE SECTION FOR CRASHWORTHINESS DESIGN *M. Manzo, A. De Luca, D. Perfetto, L. Di Palma, M. Waimer, P. Schatrow*

AEROELASTICITY & GVT		
11:20 – 11:40	293198	AEROELASTICITY OF BISTABLE COMPOSITE PLATES *F. Nicassio, G. Scarselli*
11:40 – 12:00	300156	FLUTTER ANALYSIS OF A LARGE CIVIL AIRPLANE EQUIPPED WITH MORPHING WING FLAPS *R. Pecora, M. C. Noviello*
12:00 – 12:20	300665	ACTIVE OPTIMAL CONTROL FOR FLUTTER IN SUSPENSION BRIDGES *E. Paifelman, G. Pepe, A. Carcaterra*
12:20 – 12:40	293110	AIRCRAFT MODEL UPDATING ACCORDING RESULTS OF GROUND VIBRATION TEST *J. Cecrdle*
NUMERICAL METHODS I		
11:20 – 11:40	300506	INTELLIGENT SLIDING MODE REFERENCE CONDITIONING CONTROLLER *M. Haddar, R. Chaari, S. C. Baslimisli, F. Chaari, M. Haddar*
11:40 – 12:00	292502	ENERGY FLOW IN 2D ORTHOTROPIC MEDIA BY THE RADIATIVE ENERGY TRANSFER THEORY *Q. Zhong, H. Chen, A. Le Bot*
12:00 – 12:20	298072	PROGRESSIVE FAILURE ANALYSIS OF LAMINATED COMPOSITE BEAMS USING THE WAVE FINITE ELEMENT METHOD *M. Mallouli, M. Ben Souf, O. Bareille, M. Ichchou, T. Fakhfakh, M. Haddar*
12:20 – 12:40	300726	ENHANCEMENTS IN STRUCTURAL OPTIMIZATION OF AUTOMOTIVE UNDERBODY PANELS SUBJECTED TO WATER WADING LOAD *A. Daving*
Technical sessions 3		
ACOUSTICS I		
15:00 – 15:20	298401	INVESTIGATION ON AN ADAPTIVE HELMHOLTZ RESONATOR CONCEPT *A. Benouhiba, M. Ouisse, K. Rebenorosoa, N. Andreff*
15:20 – 15:40	296866	NON-LOCAL BOUNDARY CONTROL FOR BROADBAND NON-RECIPROCAL PROPAGATION: ANALYTICAL DEMONSTRATION AND EXPERIMENTAL VALIDATION *E. De Bono, M. Collet, S. Karkar, G. Matten, M. Ouisse*
15:40 – 16:00	292729	NUMERICAL SIMULATION OF SOUND TRANSMISSION THROUGH PORO-ELASTIC SHELL STRUCTURES *M. Gfrerer, M. Schanz*
16:00 – 16:20	293444	NUMERICAL ANALYSES OF THE SOUND TRANSMISSION THROUGH DOUBLE-GLAZING SYSTEM AT LOW FREQUENCIES *C. Soussi, W. Larbi, M. Aucejo, JF. Deü*
16:20 – 16:40	297506	SOUND TRANSMISSION ANALYTICAL SOLUTION OF COMPOSITE SHELL STRUCTURES EMBEDDING VISCOELASTIC LAYERS *A. Alaimo, C. Orlando, S. Valvano*
T-WING		
15:00 – 15:20	400006	NUMERICAL INVESTIGATION ON A TILTROTOR WING UNDER BIRD IMPACT CONDITION *F. Di Caprio, F. Ciardiello*
15:20 – 15:40	400005	COMPARISON OF NUMERICAL MODELS FOR THE PREDICTION OF BLADDER TANK CRASHWORTHINESS *D. Cristillo, F. Di Caprio, C. Pezzella, C. Paciello*
15:40 – 16:00	400009	TILTROTOR STRUCTURAL-ACOUSTIC DATA ACQUISITION AND ANALYSIS *A. D. Marano, T. Polito, M. Guida, F. Marulo, M. Belardo, M. Barbarino, A. Perazzolo*
16:00 – 16:20	400007	DESIGN STRATEGY OF THE WING OF THE NEXT GENERSTION CIVIL TITL ROTOR TECHNOLOGY DEMONSTRATOR. *M. Belardo, j. Beretta, A.D. Marano, G. Diodati, N. Paletta, M. Graziano, M. Capasso, L. Di Palma*
METAMATERIALS		
15:00 – 15:20	300817	ATTENUATION PERFORMANCE DUE TO CORRELATED DISORDER IN RAINBOW METAMATERIALS *A. T. Fabro, H. Meng, D. Chronopoulos*
15:20 – 15:40	299110	OPTIMAL DESIGN OF RAINBOW METAMATERIALS *H. Meng, D. Chronopoulos, A. T. Fabro, W. Elmadih, R. Leach*
15:40 – 16:00	300228	DYNAMIC PROPERTIES OF METAMATERIALS WITH DIFFERENT RESONATOR CONNECTION METHODS *H. Meng, D. Chronopoulos*

16:00 – 16:20	297107	DYNAMIC ANALYSIS OF METASTRUCTURE BEAM WITH LOW FREQUENCY MULTI-MODE RESONATORS *Q. C. Wu, C. Droz, M. Ichchou, S. I. Xie*
16:20 – 16:40	300738	PERIODIC AND RANDOM LONG-RANGE INTERACTIONS IN METAMATERIALS *F. Mezzani, A. S. Rezaei, A. Carcaterra*
Technical sessions 4		
ACOUSTICS II		
17:00 – 17:20	300175	MULTIMODAL CONTROL OF INTERIOR RANDOM SOUND PRESSURE USING OPTIMIZED TUNED MASS DAMPERS *E. Mrabet, M. Ichchou, N. Bouhaddi*
17:20 – 17:40	300947	FIRST MODELS FOR STRUCTURAL ENERGY TRANSMISSION DECOUPLING *G. Mazzeo, M. Ichchou, G. Petrone, O. Bareille, F. Franco, S. De Rosa*
17:40 – 18:00	297363	ANALYSIS OF SOUND RADIATION FROM COMPLEX TIMOSHENKO BEAM BASED ON SECOND STRAIN GRADIENT THEORY *G. Zhu, M. Ichchou, AM. Zine*
STRUCTURAL DYNAMICS I		
17:00 – 17:20	300689	UTILIZING A LUMPED PARAMETER MODEL FOR ANALYZING THE SOUND RADIATION OF A SPINNING PLATE *M. Maeder, R. D'Auria, E. Grasso, G. Petrone, S. De Rosa, M. Klaerner, L. Kroll, S. Marburg*
17:20 – 17:40	303234	RELIABILITY AND OPTIMIZATION OF EMBEDDED MECHATRONIC SYSTEMS: WHAT APPLICATION FOR THE AUTOMOTIVE AND AERONAUTICS INDUSTRY *A. El Hami*
17:40 – 18:00	300602	TORSIONAL ENERGY FLOW THROUGH A TOUGH HYDROGEL VIBRATION ISOLATOR *L. Kari*

February 18th, 2020 **Tuesday**		
Technical sessions 5		
DEVISU		
09:00 – 09:20	300447	TUNING OF SHUNTED ELECTRO-MAGNETIC ABSORBERS BASED ON ELECTRICAL POWER DISSIPATED *E. Turco, L. Dal Bo, P. Gardonio*
09:20 – 09:40	296200	REFINED BEAM MODELS FOR THE COMPUTATION OF DISPERSION RELATIONS AND TRANSMISSION IN PERIODIC METAMATERIALS *A. De Miguel, A. Pagani, M. Filippi, M. Cinefra, E. Carrera*
09:40 – 10:00	292266	NONLINEAR FREE VIBRATIONS OF COMPOSITE STRUCTURES VIA THE X-RITZ METHOD *A. Milazzo*
10:00 – 10:20	400000	NONLINEAR VIBRATIONS OF VARIABLE-STIFFNESS PLATES USING DIFFERENT SEMI-ANALYTICAL MODELS *A. Y. Cheng, R. Vescovini, E. L. Jansen*
10:20 – 10:40	300439	INVESTIGATION OF THE ARTIFICIAL NEURAL NETWORK PREDICTION CAPABILITIES APPLIED TO VIBRATING PLATES IN SIMILITUDE *A. Casaburo, G. Petrone, V. Meruane, F. Franco, S. De Rosa*
10:40 – 11:00	304883	IMPROVED WAVE DISPERSION PROPERTIES IN A PERIDYNAMIC BAR M. Zaccariotto
MACHINE LEARNING AND SHM		
09:00 – 09:20	299247	MACHINE HEALTH DIAGNOSTICS USING ACOUSTIC IMAGING AND ALGORITHMS FOR MACHINE LEARNING *A. Aulitto, I. Lopez Arteaga, D. Kostić, F. Boughorbel, S. De Rosa, G. Petrone*
09:20 – 09:40	300577	UNSUPERVISED LEARNING ALGORITHM AND A SENSOR SWARM FOR STRUCTURAL HEALTH MONITORING OF A BRIDGE *N. Roveri, S. Milana, A. Culla, P. Conte, A. Carcaterra*
09:40 – 10:00	297507	COMBINING IMPORTANCE SAMPLING WITH MACHINE LEARNING TO ACCELERATE STRUCTURAL RELIABILITY ANALYSIS *W. You, A. Saidi, AM. Zine, M. Ichchou*
10:00 – 10:20	297333	SIMULATION-BASED HEALTH MONITORING OF A COMPOSITE SANDWICH STRUCTURE USING CONVOLUTIONAL NEURAL NETWORK *Z. Liu, M. Ardabilian, M. Ichchou, AM. Zine*
10:20 – 10:40	300772	RELIABILITY ASSESSMENT OF DAMAGE DETECTION TECHNIQUES BASED ON GUIDED ULTRASONIC WAVES *F. Ricci, V. Memmolo, L. Maio, N. D. Boffa, E. Monaco*
10:40 – 11:00	300973	IMPROVED STRUCTURAL HEALTH MONITORING FEATURES ON 3D PRINTED STRUCTURES BY PIEZOELECTRIC IMPLANTS *X. Cui, O. Bareille, M. Salvia*
VIBROACOUSTICS & FSI II		
09:00 – 09:20	302787	VIBROACOUSTIC PERFORMANCES OF AN ACOUSTIC BOX THROUGH HYBRID FE-SEA METHOD *G. Piccirillo Sibiano, G. Petrone, G. Bizzarro*
09:20 – 09:40	296932	FULLY-COUPLED VIBRO-ACOUSTIC ANALYSIS OF MULTI-LAYERED PLATES BY CUF FINITE ELEMENTS *M. Cinefra, E. Zappino, E. Carrera, S. De Rosa*
09:40 – 10:00	293432	SOUND TRANSMISSION THROUGH BAFFLED SEMI-CYLINDRICAL SHELLS USINF TRANSFER MATRIX METHOD *A. Parrinello, N. Atalla*
10:00 – 10:20	298135	RESPONSE OF A SUBMERGED FLUID-FILLED CYLINDRICAL SHELL TO TRANSIENT ACOUSTIC PULSES AND WEAK SHOCK WAVES *S. Iakovlev, H. A. F. A. Santos*
10:20 – 10:40	298772	VIBRATION OF PRESTRESSED STRUCTURES COUPLED WITH AN INCOMPRESSIBLE FLUID *C. Hoareau, JF. Deü, R. Ohayon*

NON-LINEAR DYNAMICS		
09:00 – 09:20	301098	ON THE PERFORMANCE OF A FLOW ENERGY HARVESTER USING TIME DELAY *Z. Ghouli, M. Belhaq, M. Hamdi*
09:20 – 09:40	300846	NON-LINEAR FREE VIBRATIONS OF FUNCTIONALLY GRADED NON-UNIFORM BEAMS WITH DISCONTINUITIES *M. Chajdi, A. Adri, K. El Bikri, R. Benamar*
09:40 – 10:00	304167	GEOMETRICALLY LINEAR FREE VIBRATION OF RECTANGULAR PLATES SIMPLY SUPPORTED AT TWO OPPOSITE EDGES AND CONNECTED BY DISTRIBUTED TRANSLATIONAL AND ROTATIONAL SPRINGS AT THE TWO OTHER EDGES *A. Babahammou, R. Banamar*
10:00 – 10:20	301649	A NEW FRICTION MODEL TO DESCRIBE THE FREE DYNAMIC RESPONSE OF A SLIDING OSCILLATING SYSTEM UNDER LUBRICATION *J. Perret-Liaudet, A. Hriouech, M. Belin, MI. De Barros-Bouchet*
10:20 – 10:40	300529	INVESTIGATING THE APPROXIMATION OF HIGHER-ORDER NONLINEAR BEHAVIOUR INTO NON-INTRUSIVE REDUCED-ORDER MODELS *A. Elliott, A. Cammarano*
10:40 – 11:00	302732	THE DYNAMICS OF DELAYED BIRHYTHMICITY OSCILLATOR WITH MODULATED DELAY AMPLITUDE *M. Hamdi, M. Belhaq, Z. Ghouli*
Technical sessions 6		
VIPER I		
15:00 – 15:20	293149	K-SPACE ANALYSIS OF COMPOSITE SANDWICH SHELL WITH SMALL-SCALE RESONATORS *G. Tufano, M. Ichchou, W. Desmet, N. Atalla*
15:20 – 15:40	299671	UNCERTAINTIES IN WAVE CHARACTERISTIC OF TWO-DIMENSIONAL PERIODIC MEDIA USING THE FUZZY WAVE FINITE ELEMENT METHOD *R. P. Singh, S. De Rosa, F. Franco, O. Bareille, M. Ichchou, G. Petrone*
15:40 – 16:00	298707	WAVE AND FINITE ELEMENT ANALYSIS OF QUASI PERIODIC 2D PHONONIC SUPER-CELL CRYSTALS *S. Timorian, S. De Rosa, F. Franco, M. Ouisse, N. Bouhaddi*
16:00 – 16:20	296962	ON THE MULTI-MODAL BEHAVIOR AND INNER RESONANCE OF STIFFENED SHELLS *M. Ichchou, G. Tufano, O. Bareille, B. Pluymers, A. Zine, W. Desmet*
16:20 – 16:40	300004	INVESTIGATION OF THE SOUND TRANSMISSION LOSS WITH THE USE OF THE INNER-RESONANCE AND THE VEERING EFFECT OF A MULTI-LAYER CORE TOPOLOGY SYSTEM *N. Guenfoud, C. Droz, M. Ichchou, O. Bareille, E. Deckers, W. Desmet*
WAVES		
15:00 – 15:20	297025	WAVE FINITE ELEMENT METHOD BASED ON SECOND STRAIN GRADIENT ELASTICITY THEORY FOR ONE-DIMENSIONAL NANO-SIZED PERIODIC STRUCTURES *B. Yang, M. Ichchou, A. Zine*
15:20 – 15:40	300585	WAVE PROPAGATION IN AN AIRCRAFT WING SLAT FOR DE-ICING PURPOSES *D. Raffaele, T. P. Waters and E. Rustighi*
15:40 – 16:00	297352	WAVE REFLECTION AND TRANSMISSION ANALYSIS THROUGH COMPLEX ROD BASED ON SECOND STRAIN GRADIENT THEORY *G. Zhu, M. Ichchou, A. Zine*
16:00 – 16:20	297006	ATYPICAL DISPERSION FEATURES IN CONTRASTED RESONANT CELLULAR PANELS: ANALYTICAL HOMOGENIZED MODEL AND EXPERIMENTAL MEASUREMENTS *P. Fossat, C. Boutin, M. Ichchou*
16:20 – 16:40	300480	BAND GAP OPTIMIZATION OF PERIODIC BEAMS USING FOURIER SHAPE COEFFICIENTS *V. De Lima, J. R. Arruda*
NUMERICAL METHODS II		
15:00 – 15:20	300263	BEST PRACTICES FOR SPACECRAFTS ACOUSTIC ANALYSIS AND ASSESSMENTS *M. Cordaro*
15:20 – 15:40	300342	IDENTIFICATION OF FORCES IN EULER-BERNOULLI BEAMS : BAYESIAN UPDATING *A. Zine, A. Kawano*
15:40 – 16:00	301178	SIMULATION OF THE TBL INDUCED VIBRATIONS OF A PLATE USING VIRTUAL SOURCES *A. Pouye*
16:00 – 16:20	303237	THERMAL MODELING OF HIGH POWER TRANSISTOR HEMT *A. Amar, A. El Hami, B. Radi*

February 19th, 2020 **Wednesday**		
Technical sessions 7		
VIPER II		
10:00 – 10:20	299928	BANDGAP INVESTIGATION OF HIERARCHICAL ISOVOLUMETRIC PERIODIC CORES WITH NEGATIVE POISSON RATIO *S. Del Broccolo, M. Ouisse, E. Foltête, F. Scarpa*
10:20 – 10:40	300678	RESONANT STOP BAND ANALYSIS USING AN INHOMOGENEOUS RE-ENTRANT HONEYCOMB CORE STRUCTURE *MA. Campana*
10:40 – 11:00	296766	A CONVOLUTION BASED WAVENUMBER EXTRACTION METHOD *R. F. Boukadia, E. Deckers, C. Claeys, W. Desmet, M. Ichchou*
11:00 – 11:20	298639	DESIGN GUIDELINES FOR THE ACOUSTIC PERFORMANCE IMPROVEMENT OF A PERIODIC POROUS MATERIAL *D. Magliacano, M. Ouisse, S. De Rosa, F. Franco, A. Khelif*
11:20 – 11:40	293147	EXPERIMENTAL INVESTIGATION OF REDUCED SOUND TRANSMISSION OF SANDWICH PANELS USING 3D-PRINTED MODELS *F. Errico, M. Ichchou, F. Franco, S. De Rosa, P. Giuseppe, O. Bareille*
MATERIALS AND DAMPING		
10:00 – 10:20	300748	SYNTHESIS AND CHARACTERIZATION OF NATURAL FIBERS REINFORCED EPOXY COMPOSITE *M. Zhang, M. Salvia, O. Bareille*
10:20 – 10:40	293710	EXPERIMENTAL IDENTIFICATION OF VISCOELASTIC PROPERTIES OF VIBRATING PLATES *P. Grosso, A. De Felice, S. Sorrentino*
10:40 – 11:00	300728	MANUFACTURING TOLERANCE IMPACT ON STATIC CHARACTERISITICS FOR A TILTING PAD JOURNAL BEARING *M. Lou, O. Bareille, W. Chai, M. Ichchou, W. Chen*
11:00 – 11:20	300793	COMPARISON OF DAMPING PERFORMANCES OF CONSTRAINED VISCOELASTIC LAYERS AND PASSIVE PIEZOELECTRIC NETWORKS *L. Rouleau, B. Lossouarn, R. Darleux, JF. Deü*
11:20 – 11:40	400002	EXPERIMENTAL STUDY OF GRAPHENE AND CARBON NANOTUBES THERMAL SENSING PROPERTIES *D. Passato, M. Akermo, P. Hallander, S. De Rosa, G. Petrone*
11:40 – 12:00	297421	REAL-TIME TUNING OF STIFFNESS AND DAMPING PROPERTIES OF LAMINATE COMPOSITES *M. Ouisse, P. Butaud, D. Renault, B. Verdin, G. Chevallier*
STRUCTURAL DYNAMICS II		
10:00 – 10:20	296852	PASSIVE VIBRATION CONTROL OF TYRES USING EMBEDDED MECHANICAL RESONATORS *F. Errico, G. Petrone, F. Franco, S. De Rosa, M. Ichchou*
10:20 – 10:40	300853	SIMPLIFIED 3D TIRE MODEL INFRASTRUCTURE FOR DYNAMIC AND FREQUENCY ANALYSIS *V. M. Arricale, A. Sakhnevych, F. Farroni, F. Timpone*
10:40 – 11:00	298852	FRICTION POWER LOSSES PREDICTION OF SPUR GEAR PAIRS WITH CONSIDERING DYNAMIC EFFECTS *N. Feki, M. Hammami, O. Ksentini, M. S. Abbes, M. Haddar*
11:00 – 11:20	430000	DYNAMIC CHARACTERIZATION OF POLYMERIC VIBRATION DAMPERS *M. Barbieri, A. De Felice, F. Pellicano, S. Sorrentino, A. Zippo*

Table of contents

Keynotes
and
Special Sessions

Keynote Speakers

Francesco Marulo

Professor, Department of Industrial Engineering, University of Naples Federico II, Italy

Born on January 1, 1955, Francesco was graduated Magna cum laude in Aeronautical Engineering at the University of Naples “Federico II”; assistant professor since 1984. On November 1992 is appointed Associate Professor and on November 2001 Full Professor of Aerospace Structures. To date Francesco is in charge of the Advanced Aerospace Structures and Aeroelasticity courses. In 1986 he was visiting scientist at NASA Langley Research Center in Hampton, Va (USA) and in 1997 Fulbright visiting professor at the Center for Acoustics and Vibration of the Pennsylvania State University, University Park, Pa, USA. His scientific work has been presented at several National and International congresses and published by National and International journals. Invited professor at the Second University of Naples, from 2007 to 2012 has served as Head of the Department of Aerospace Engineering of the University of Naples Federico II. Francesco has been coordinator of several National and International research programs and scientific responsible of contracts and research grants from aerospace industries and research centers. Francesco has been scientific consultant for aircraft accident investigation, consultant for aeronautical industries and EASA Noise CVE.

Ines Lopez Arteaga

Professor, Mechanical Engineering Department, Eindhoven University of Technology, Netherlands

Ines is a Full Professor at the Dynamics and Control group of the Mechanical Engineering Department and Chair of Acoustic and Noise Control at Eindhoven University of Technology (TU/e). Ines’ research focuses on optimal vibro-acoustic design of complex systems. Excessive noise levels affect the economic and technological development of Western countries in many ways. In 2020, noise pollution will be the main environmental problem in the Netherlands, surpassing air pollution as the main cause of environment-related health problems. Overexposure to noise can lead to, for example, heart attacks, high blood pressure or poor learning performance. Acoustic disturbances can cause failure of complex systems such as turbines and limit the performance of high-tech precision machinery. Optimal vibro-acoustic design of complex systems implies three main steps, which are covered in Ines’ research: characterization of vibro-acoustic sources, vibro-acoustic modeling and developing noise and vibration reduction measures.

Elena Ciappi

Senior Researcher –National Research Council of Italy, Institute of Marine Engineering (CNR-INM)

Elena received a B.S. in Mechanical Engineering from the University of Rome "La Sapienza" in 1996 and in 1999 the Ph.D. in Theoretical and Applied Mechanics from the same University. In 1999 she joined as researcher the Marine Technology Research Institute (INSEAN), later become the Institute of Marine Engineering (INM) of the National Research Council of Italy. Since 2010 she is senior researcher at INM. She has been doing research activity in the field of experimental and theoretical modeling of Fluid-Structure Interaction problems with particular reference to ship hydro-elasticity, to the characterization and control of aero/hydrodynamic noise sources and of the vibro-acoustic response of structures to turbulent flow. She has been principal investigator of research projects and testing activities founded by the European Community, the European Defense Agency, the Italian and US Navy, as well as by maritime and aeronautical industries. In recent years she has been involved in the management of projects and initiatives related to the Blue Growth Strategy for the Mediterranean sea. She has been Chairman of the Specialist Committee on *Hydrodynamic Noise* and member (for two terms) of the Specialist Committee on *Vortex Induced Vibrations* of the International Towing Tank Conference (ITTC). She is also one of the founders of the *flinovia* group (www.flinovia.org).

Erasmo Carrera / Professor, Aerospace Engineering Department, Politecnico di Torino, Italy /

After earning two degrees (Aeronautics, 1986, and Aerospace Engineering, 1988) at the Politecnico di Torino, Erasmo received his PhD degree in Aerospace Engineering jointly at the Politecnico di Milano, Politecnico di Torino, and Università di Pisa in 1991. He began working as a Researcher in the Department of Aerospace Engineering for the Politecnico di Torino in 1992 where he held courses on Missiles and Aerospace Structure Design, Plates and Shells, and the Finite Element Method. He became Associate Professor of Aerospace Structures and Computational Aeroelasticity in 2000, and Full Professor at the Politecnico di Torino in 2011. He has visited the University of Stuttgart twice, the first time as a PhD student (six months in 1991) and then as Visiting Scientist under a GKKS Grant (18 months in 1995–1996). In the summers of 1996, 2003 and 2009, he was Visiting Professor at the ESM Department of Virginia Tech, at SUPMECA in Paris (France) and at the CRP TUDOR in Luxembourg, respectively. His main research topics are: composite materials, finite elements, plates and shells, postbuckling and stability, smart structures, thermal stress, aeroelasticity, multibody dynamics, and the design and analysis of non-classical lifting systems. He is author of more than 350 articles on these topics, many of which have been published in international journals. He serves as referee for international journals and as a contributing editor for Mechanics of Advanced Materials and Structures, Composite Structures, Journal of Thermal Stress, Computer and Structures and International

Journal of Aeronautical and Space Sciences. From 2017 he is President of AIDAA.

Stephan Rinderknecht / Professor, Institute for Mechatronic Systems, Technische Universität Darmstadt, Germany /

Stephan is full Professor for Mechatronic Systems in Mechanical Engineering since 2009 at Technische Universität Darmstadt. His research focus is on mechatronic vehicle systems, energy storage systems, active vibration systems and recently also on robotic systems. On some of his research fields as for example innovative drivetrains and propulsion systems for e-mobility as well as highly integrated designs for kinetic energy storage systems he works in very close cooperation with industry. For others like active piezo electric systems to reduce bending vibrations of flexible rotors the projects approach more fundamental problems. Before becoming university professor, Stephan worked in the automotive transmission industry for more than 13 years and left in the position of senior vice president research and development. He graduated and received his doctoral degree at University of Stuttgart in the faculty of Aerospace Engineering.

Weidong Zhu / Professor, Department of Mechanical Engineering, University of Maryland, USA /

Weidong is a Professor in the Department of Mechanical Engineering at the University of Maryland, Baltimore County, and the founder and director of its Dynamic Systems and Vibrations Laboratory and Laser Vibrometry Laboratory. He received his double major BS degree in Mechanical Engineering and Computational Science from Shanghai Jiao Tong University in 1986, and his MS and PhD degrees in Mechanical Engineering from Arizona State University and the University of California at Berkeley in 1988 and 1994, respectively. He is a recipient of the 2004 National Science Foundation CAREER Award and has been an ASME Fellow since 2010. He was an Associate Editor of the ASME Journal of Vibration and Acoustics from 2007-2014 and is a Subject Editor of the Journal of Sound and Vibration. His research spans the fields of dynamics, vibration, control, applied mechanics, structural health monitoring, wind energy, and metamaterial, and involves analytical development, numerical simulation, experimental validation, and industrial application. He has published over 170 archival journal papers in these areas, and has five US patents and five ASME best paper awards.

Alain le Bot / Senior researcher, CNRS, Ecole Centrale de Lyon, France /

Alain is graduated in Engineering, holds a Master of Mathematics, is Doctor in Acoustics and is accredited to supervise research. He started his career as Assistant Professor in Mathematics at Institut national polytechnique Félix Houphouët-Boigny (INP-HB) in Yamoussoukro, Ivory Coast. Back in France, he joined EDF as research engineer in the Department of Acoustics and Vibratory Mechanics. During the nineties, he started an academic career in CNRS. Alain Le Bot is currently Senior Researcher at the French CNRS in the Tribology and System Dynamics Laboratory (UMR CNRS 5513) in École Centrale de Lyon. His researches concern statistical theories in tribology, sound and vibration. Being an internationally recognized specialist in statistical energy analysis and high frequency theories in sound and vibration, he published a book in vibroacoustics edited by Oxford University Press and more than a hundred publications in various scientific journals. A second book entitled Introduction aux vibrations aléatoires by Dunod, Paris, has been released since 2019. Alain Le Bot is responsible of the course Random vibration in Ecole centrale de Lyon, member of the Executive Committee of labex Celya, officier in Agence française de développement and deputy director of Ecole doctorale MEGA.

LIFE (LIght, saFe, quiEt) for Aeronautics

Francesco Marulo

Department of Industrial Engineering
University of Napoli Federico II
Via Claudio, 21 – 80125 Napoli - ITALY
Email: francesco.marulo@unina.it

ABSTRACT

An opportunity is caught with this paper to collect and to summarize the research activities performed in more than three decades by a group of researchers, professors and students in the field of structural dynamics, both linear and nonlinear, aeroelasticity, vibroacoustics and community noise. For sake of synthesis many associated activities are just mentioned, or sometimes disregarded. Few aspects are considered important and highlighted throughout the paper, and they refer to the persuasion in always trying to create a link among theory, simulation and test, the suggestion to check procedures with known results and to progress through small increasing complexities. These basic approaches to solve new problems and to pass new difficulties are considered a good tip for keeping confidence with models, numerical results and experimental measurements, and for avoiding to lose contact with real evidence.

1 INTRODUCTION

The title of this paper might create a bit of confusion. LIFE is the acronym of the laboratory we have established at the new site of University of Napoli Federico II. It came in our mind with the wish for good health and well-being for anybody interacting with the laboratory and the persons doing research in it.
The main focus of LIFE lab is on linear and nonlinear dynamics applied mainly to aeronautics, collecting the work of many persons for several years. The opportunity offered by the Federico II San Giovanni campus has been the main driver for LIFE lab, allowing the necessary room for hosting full scale examples of fuselages, both commercial and general aviation airplanes.
The research on interior vibroacoustic behavior of fuselages has quite a long tradition in our research group. It can be dated back in the mid 80's, as an evolution of the activities in the field of aeroelasticity,

enlarging the interests to the wider sector of the fluid-structure interaction, including, time by time, the nonlinear aspects of the crashworthiness, impact dynamics and bird-strike analysis of aircraft structures.

Simple and basic pillars have always been the roots of the activities developed since the beginning of the experimental research converged now in LIFE lab. They can be summarized in a constant effort to correlate theory, simulation and measurement driven by realistic engineering problems, also called, in the group, the "3-curve" approach.

This paper has the main focus to collect some of the experiences and lessons learnt by the research group in these years, sometime jointly with other academic institutions and companies.

The LIFE research group has been involved, and still is, in several research projects and industrial programs in the field of fuselage comfort, aircraft exterior noise assessment, simulation and certification, aeroelasticity, crashworthiness and passive safety, full-scale fatigue and flight testing, and now opening to the image analysis and correlation.

The backbone of these activities has been the field of aeroelasticity which was the starting point for the flutter clearance of general aviation airplanes [1]-[2], and the beginning of the applications for fluid-structure interaction problems, [3]-[4], based on both, deterministic and statistical approach.

Struggling for modeling the real world and analyzing data coming from measurements has become, with the time, a confident approach for understanding the behavior of aircraft structures when exposed to different environments.

Joking, but not so much, we have come up with the definition of "Tom Tom approach". Repeated experience coming from both simulation and testing tells us that it is always very important and usually time saving, to add a verification step to make sure that the measurement (or the result, in case of numerical simulation) is correct. And this is what could be called "Navigator Principle". Nowadays, when facing with a new GPS-based navigator system or App, it is well known, and suggested by the manuals, that to become fully confident on how the navigation information are delivered, the new system should be initially used during very well-known routes and conditions. This basic use allows the user to correctly understand and interpret the different information available and where they are located on the screen, much better and quicker than just reading a flat but perfect user's manual. Such exercises will generate a subjective strong confidence between the user and the measurement system which is the basis for an unstressful driving when the route is unknown.

Exactly the same approach is generally followed by our research group when starting with lab or field testing. First measure something, which is well known. The result of such measurement will confirm the reliability of the measurement chain, the ability of the user in performing the test and, eventually, the tolerance to be adopted.

This procedure appears so straightforward that, very often, is neglected. During a test campaign started rapidly for several reasons, it may happen that doubts and uncertainties become too many, and a check appears as the only system to put things in order. If the check fails, all the previous measurements are useless and one understands why the "Navigator Principle" is time-saving.

This paper will go through several activities performed at LIFE Lab which range from classical modal analysis where [5]-[7] are just few examples often related to both research projects and steps of industrial programs, as requested measurements for aeroelastic clearance. Another consolidated topic of the research group refers to non-linear dynamics and impact analysis, [8]-[17], with applications, as always in the backbone of the laboratory, to research activities and to real aeronautical programs (seat and bird-strike certification, for example).

Regarding the vibroacoustic applications, which has been the first follow-up of long-time ago aeroelastic studies [18]-[19], numerous activities are summarized herein, from a dedicated research on soundproofing materials obtained using electrospinning technique, [20]-[21], acoustic properties of bare and furnished fuselages, dynamics vibration absorbers design and applications, measurements of in-flight acoustic loads and interior noise levels [22].

Community noise [23]-[26] is another long tradition activity of LIFE Lab, passing through the certification of numerous general aviation and commercial airplanes and contribution to research projects for the simulation, prediction and mitigation of the noise emitted by aircraft, and recently drones. The paper ends with a small description of some on-going activities on structural dynamics, [27]-[28], and a first example of a full scale aircraft fatigue testing relative to the wing of the P2012 airplane. Another example of the technological transfer attitude of our research group.

2 GROUND VIBRATION AND FLIGHT FLUTTER TESTING OF AIRPLANES

The motivation for performing a ground vibration test on a structure, and specifically on an airplane, comes from the need of determining the modal parameters (frequencies, damping factors, modal vectors and modal scaling) to be used as part of the input for the aeroelastic calculations which needs to be performed in order to make sure that the airplane flight envelope is free from any aeroelastic instability.

The process of determining the modal parameters may follow several approaches which may affect both the excitation system and the modal identification algorithms. Usually the test setup, the data acquisition and analysis are performed using standard approved procedure employing both commercial and in-house developed software. Regarding airplanes, we split the ground vibration tests in two parts:

1. Measurements of the elastic mode-shapes fixing the aerodynamic control surfaces;
2. Measurements of the control surfaces mode-shapes ensuring the structure fixed to the ground.

The tests pertaining to the first part are performed by measuring the frequency response functions between each single point of the structure, with reference to a fixed position of the excitation point. Then the position of the excitation point is changed and the frequency response functions are measured again at the same positions. This approach should lower the possibility of missing mode-shapes.

For an airplane as in fig. 1a, more than 200 frequency response functions, fig. 1b and c, are measured in an about two-day session, post processed for obtaining a good correlation with a numerical model, fig. 1d.

(a)

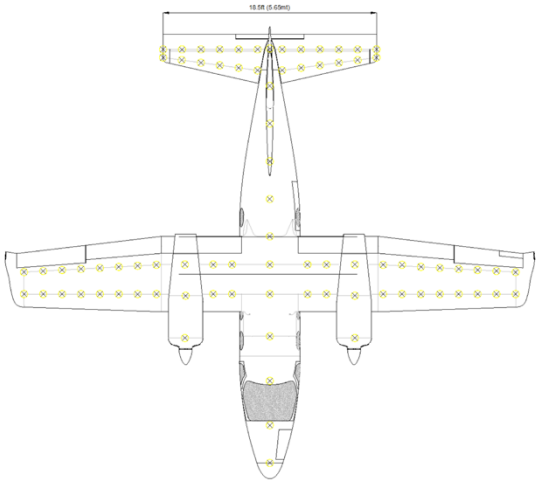

(b)

(c) (d)

Fig. 1 – GVT on a Small Commuter Airplane (a); measuring points (b); electrodynamic shaker excitation (c) and example of mode-shape (d)

Frequency and damping analysis, including operational modal analysis, has been employed for several applications and particularly for flight flutter testing, which are required for confirming the safe aeroelastic behavior of aircraft. The main objective of these flight tests is firstly to make sure that no unwanted vibration result from the pilot excitation and that no significant variation of the damping characteristics of the airplane arise versus the flight speed. When dealing with small airplanes, an accepted test procedure is fully accomplished based on the pilot abrupt input to the main control surfaces. It is well known that this input usually is not able to excite the high order natural frequencies and mode-shapes of the airplane, but it gives the necessary feedback for clearing any unwanted onset of vibration amplitude and damping decrease with the airplane speed.

Usually the airplane is equipped with sensors, typically accelerometers, on the tips of the main aerodynamic control surfaces, as shown in fig. 2, measuring the vibration of the aerodynamic surfaces after the pilot input, which is measured by potentiometer installed along the command line. These channels are simultaneously acquired during the flight, at several speeds, with the airplane in trim condition. Post-flight data processing is requested for assessing the aeroelastic stability of the airplane. Fig. 3 and 4 give an example of the time and frequency analysis results, respectively, where accelerations are in [g] unit.

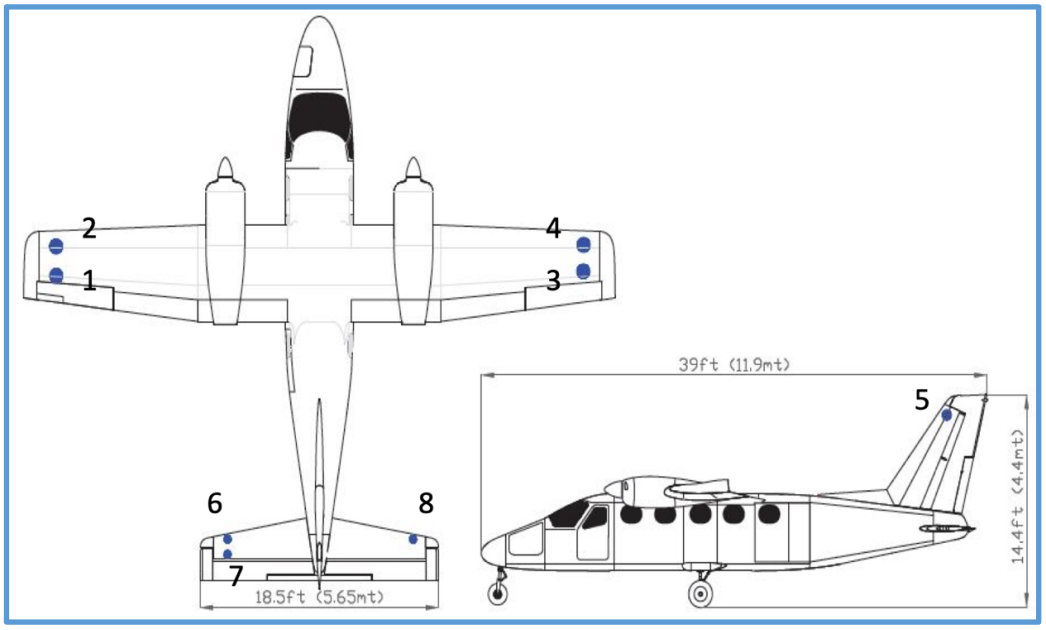

Fig. 2 – Positions of the accelerometers on the aerodynamic surfaces

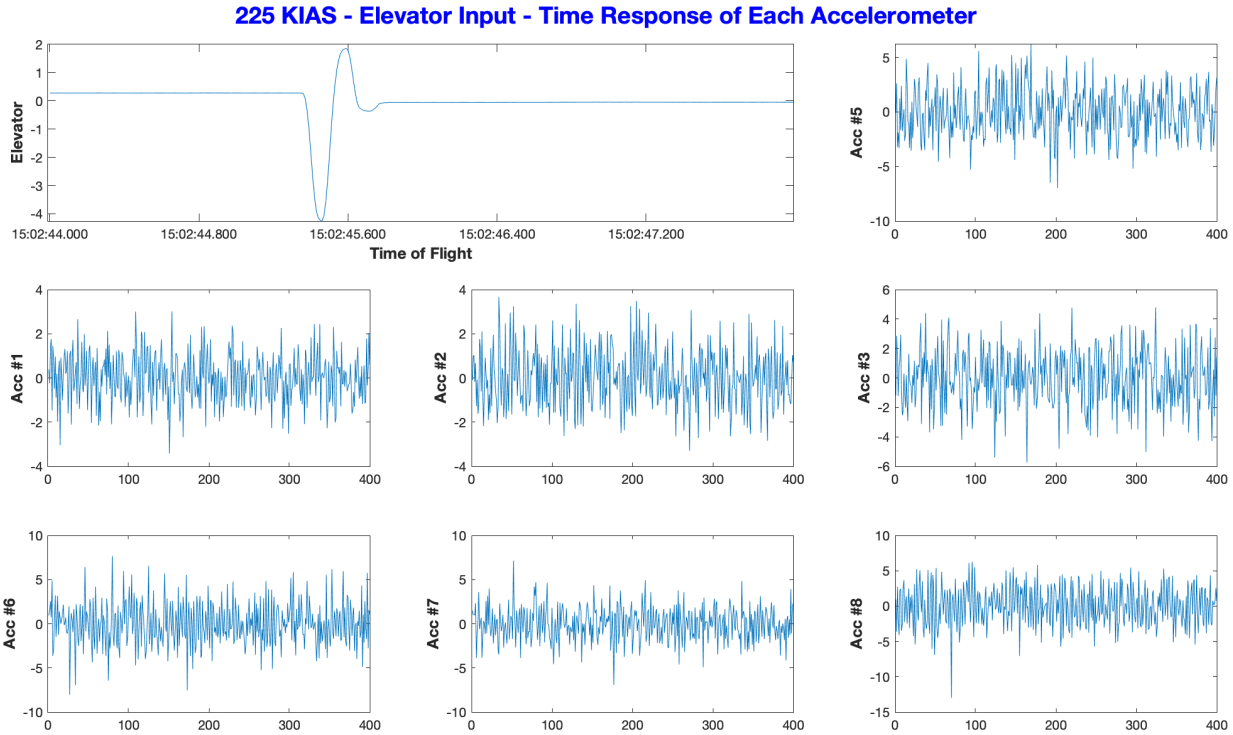

Fig. 3 – Time response after an elevator input of the pilot (top left diagram)

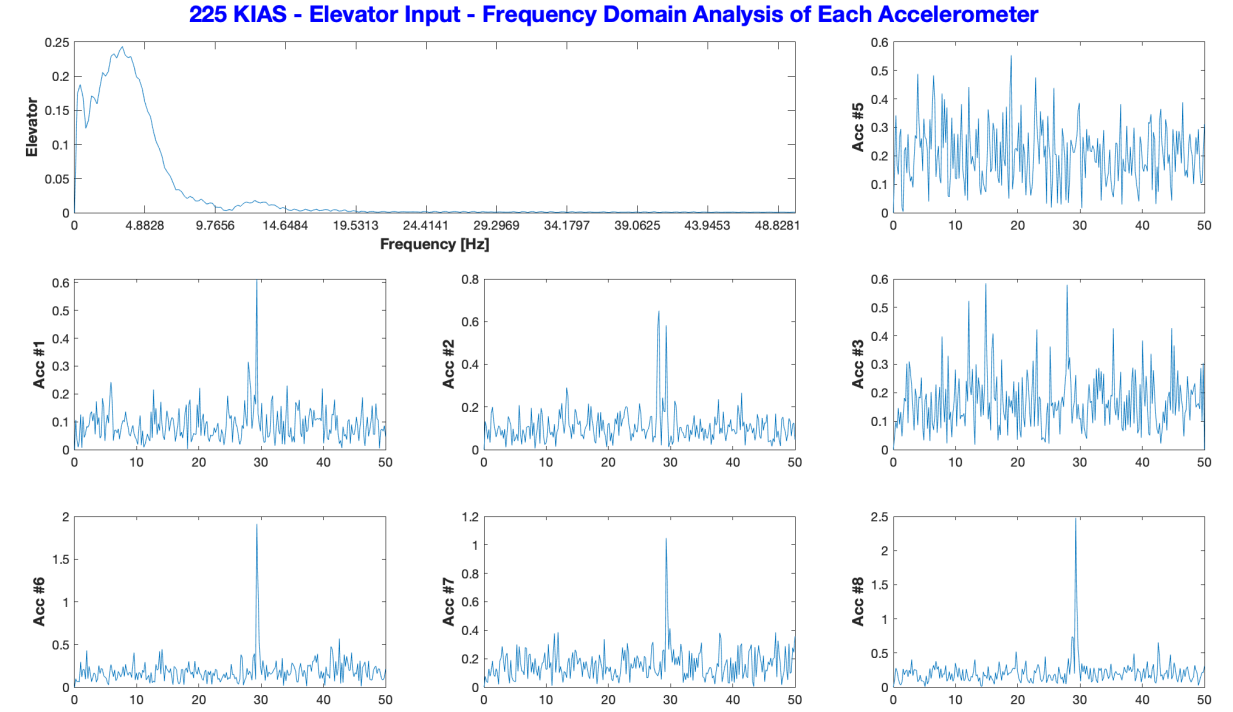

Fig. 4 – Frequency response as result of an elevator input of the pilot (top left diagram)

3 VIBROACOUSTIC AND INTERIOR NOISE

The improvement of the passenger comfort level has become, with the years, a strong requirement in many design problems. Noise and vibration inside an aircraft cabin may cause increasing risks in health and performance of flight and cabin crews besides the discomfort to the passengers. Many aircraft industries are therefore striving hard in achieving a higher comfortable level. Aircraft noise contains the following main components: engine noise, propeller noise, airframe noise (turbulent

boundary layer) and structure borne noise. Depending on the frequency range, different theoretical and numerical approaches are used. With reference to low frequency region, where modal approach is expected to give its best performance, the finite element method is employed for the analysis of the interaction of the structural vibrations and the acoustic volume. Dedicated tools have been created, for simplifying the generation of the FEM model, including exterior dynamic loading, and results' analysis.

The following figure 5 gives an example of the procedure used for vibroacoustic FEM analysis.
After having prepared and validated the structural and the acoustical model separately, they are coupled, then the loading pressure is added and the interior noise level is computed. As an example of these calculations, Table 1 shows the averaged SPL computed along several section of the fuselage, at 1.2 m from the floor, due to the first engine-propeller tonal loads (100 Hz).
As expected, the maximum averaged SPL values result to be close to the propeller-engine position. The baseline configuration provides an averaged SPL of 90.85 dBA and a maximum SPL of 99.8 dBA.

x-dist. [m]	SPL [dB(A)]
0.75	82.8
1.50	83.5
2.25	89.3
3.00	92.4
3.75	92.6
4.50	91.3
5.25	92.0
6.00	93.2
6.75	93.1
7.50	90.3
8.25	83.8

Tab. 1 – Interior Noise Results

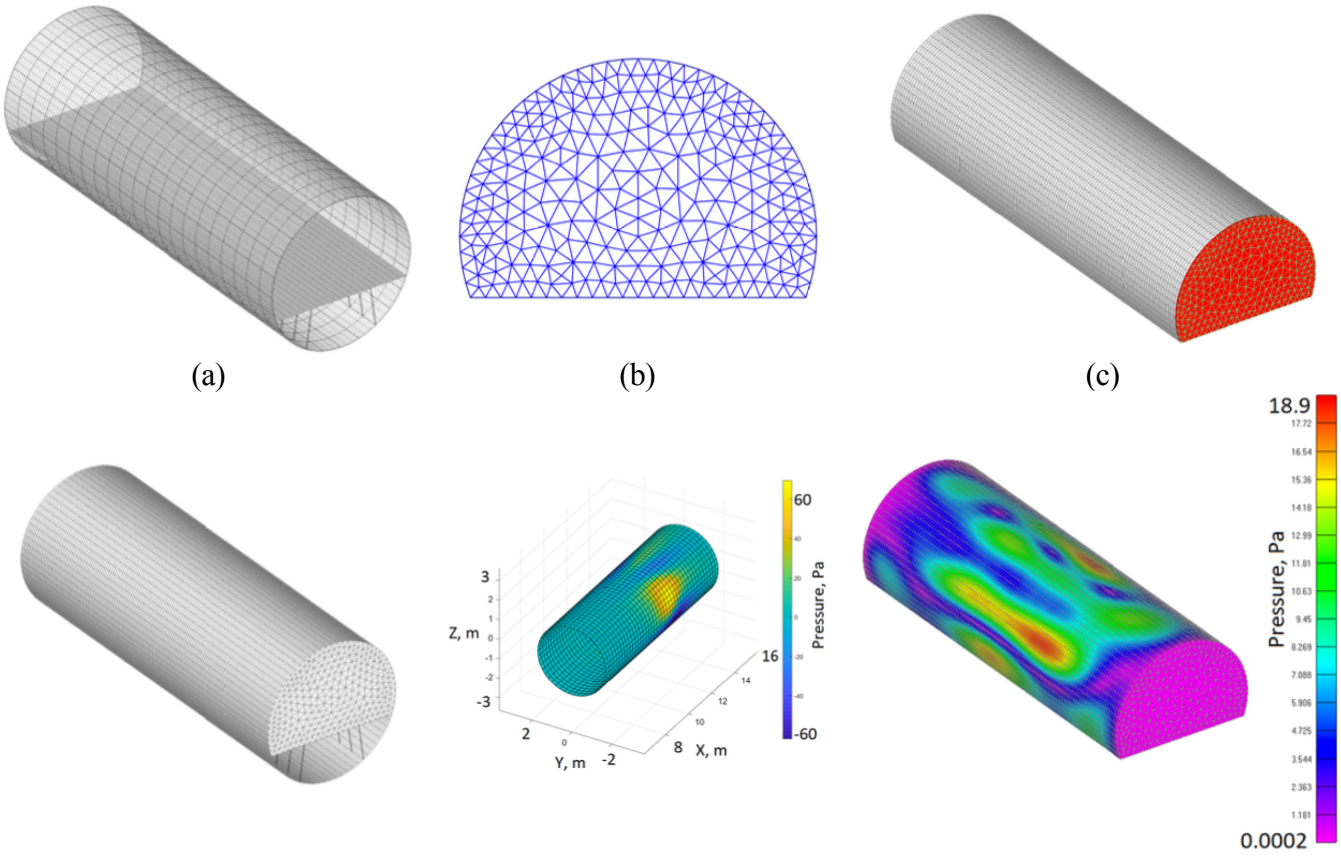

Fig. 5 - Main steps for Fluid-Structure Finite Element simulation
Structural model (a) – 2-D Acoustic Surface (b) – 3-D Acoustic Volume (c)
Structural-Acoustic Coupling (d) – Exterior Pressure (e) – Interior Noise (f)

Passive technology has been implemented for mitigating noise and vibration at BPF. Typical examples are dynamic vibration absorbers (DVA) which are designed to resonate close to propeller

tonal loads. An optimization process of the number and the position of each DVA can be addressed for identifying the most promising solution. Additionally, the design of each DVA may be addressed considering not only the resonant frequency, but including the associated vibration energy.
Another example of passive solution for noise reduction is a doublewall system. The term "doublewall system" is used to identify a system composed by external skin, acoustic insulation and interior trim. A simplified model is presented here which includes fuselage skin, stringer, frames, interior trim and airgap, but it neglects the complicating effects of windows and doors, fig. 6.

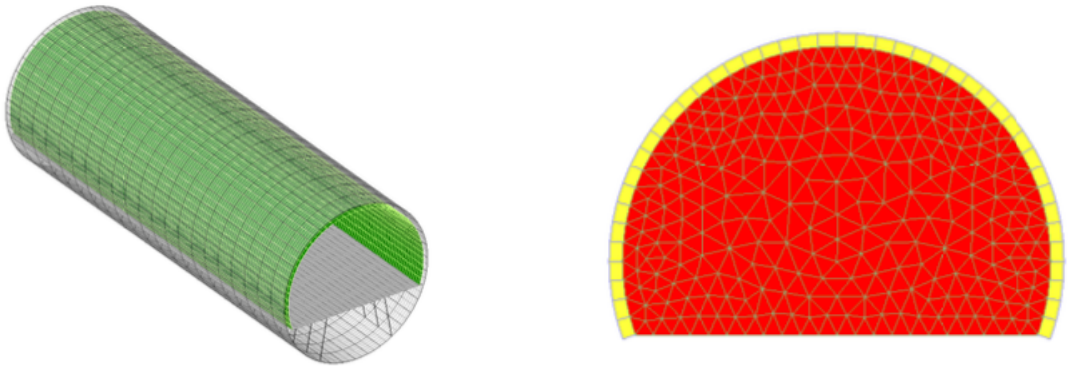

(a) (b)

Fig. 6 - Fuselage FE model with trim panel (a); Acoustics cavities (b) – cabin (red) airgap (yellow)

The research on the vibroacoustic behavior of fuselages has generated interesting side activities especially in the field of soundproofing materials, which are again a passive system for noise control. The efficiency of passive noise control is greatest at higher frequencies; however, they are still capable of providing noise reduction at low frequency. Based on this consideration an interesting research has demonstrated that soundproofing blankets could be produced through electrospinning, possessing sound absorption coefficient near unity at very low frequencies that can be tuned by changing the sample mass. Several specimens were manufactured by electrospinning specific PVP solution in ethanol under an applied electrical potential of 20 kV. Fig. 7 is a simple sketch of the experimental electrospinning setup, while fig. 8 shows an example of the specimens prepared for the acoustical impedance tube.

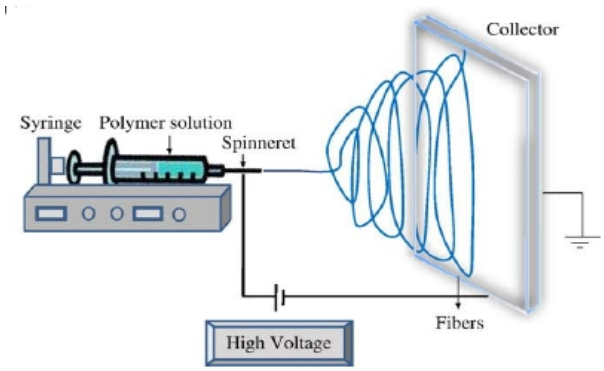

Fig. 7 – Sketch of the electrospinning process

Fig. 8 – Specimens for the impedace tube

Electrospun nanocomposite fibres are lightweight, dimensionally stable, porous, flexible, and can absorb sound waves at high, medium, and low frequencies. The resulting specimens have been further treated by heat and with silica particles for being airworthy and compliant with the stringer rules on the materials which can be installed inside the aircraft, and now the lab-based process is moving toward a more industrial definition.

The interior noise activity has addressed measurements on real aircraft fuselages, both in the lab and in-flight.
Global difference, measured in terms of reverberation time and average absorption, between a bare and a furnished fuselage has been carried out in the lab and reported in fig. 9.
An interesting comparison is given in fig.10, where a comparison in terms of overall acoustic properties is proposed among different classes of airplanes. It turns out that the acoustic volume is "damped" similarly for each class of airplane and, therefore, what makes the difference are the external pressure loads.
Acoustic measurements have been done in flight conditions to compare cabin treatments and layouts on-board of general aviation and business aircraft.

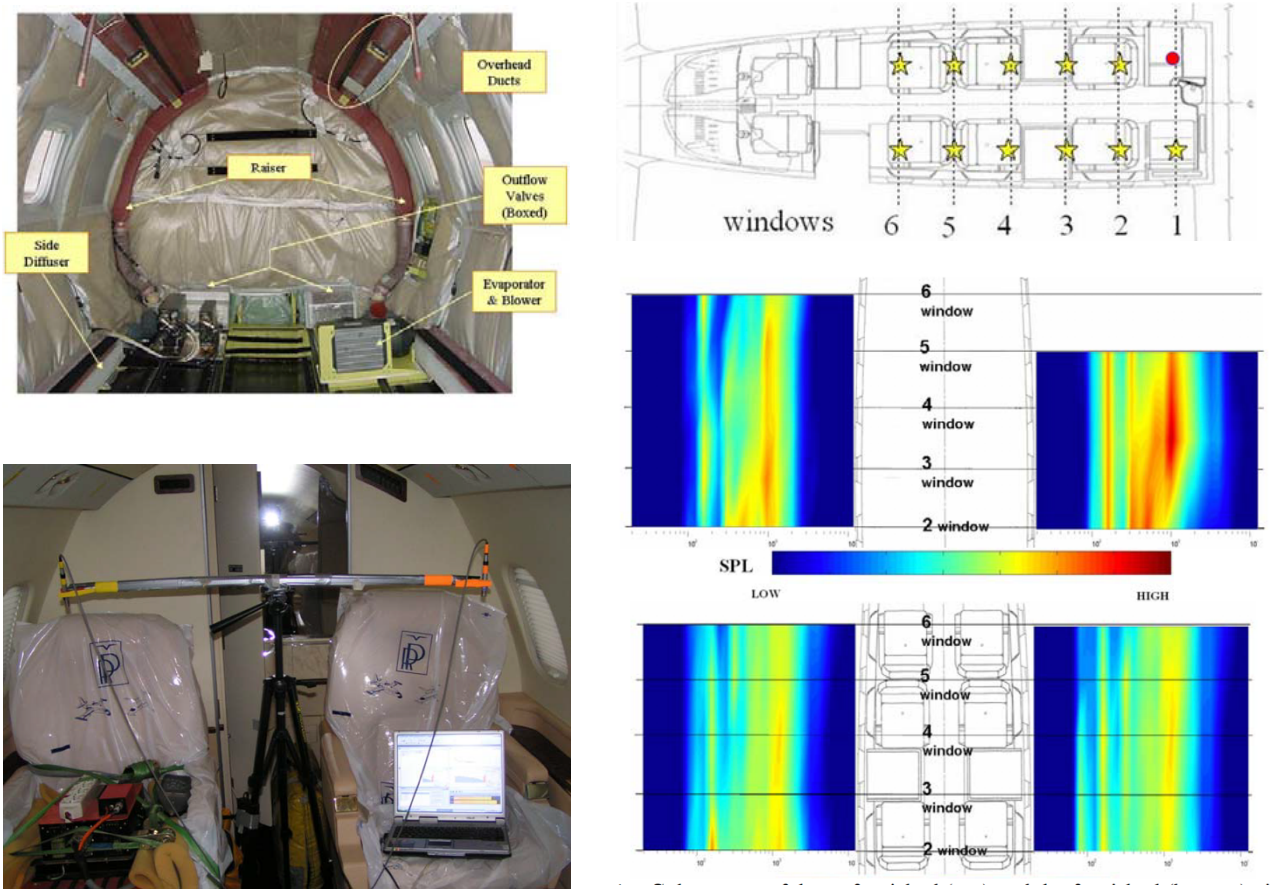

Fig. 9 - Cabin noise measurements on a business aircraft

Local acoustical measurements may result very useful for understanding specific transmission path, at specific frequencies. With the help of an acoustic antenna, Life Lab have performed some measurements of the window installation on the mock-up of the full-scale fuselage. An overview of such measurements is presented in fig. 11. A speaker excites the fuselage window with a specific noise "color" (white, pink, blue, and so on). On the back, behind the window, inside the fuselage, the acoustic antenna measures what is transferred, at which frequency and magnitude.
These measurements help in improving the design and checking the efficiency of the installation effects.
As outlined previously, the identification of the pressure loading is a fundamental aspect in assessing the vibroacoustic environment of a fuselage, therefore a correct simulation is extremely important. In order to check the confidence of aeroacoustic codes, in-flight measurements have been carried out. In

the framework of a European funded project, these measurements have been performed on a Tilt Rotor, for several flight conditions. Flush-mounted microphones have been installed at selected locations on the external skin of the fuselage and recorded in flight. Fig. 12 shows some of installed microphones and the preliminary results obtained from the data analysis.

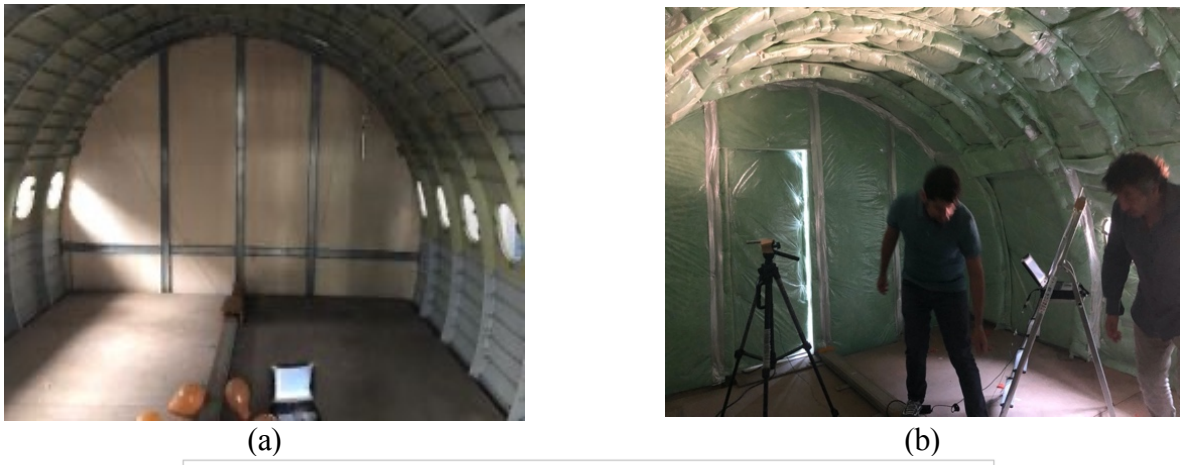

(a) (b)

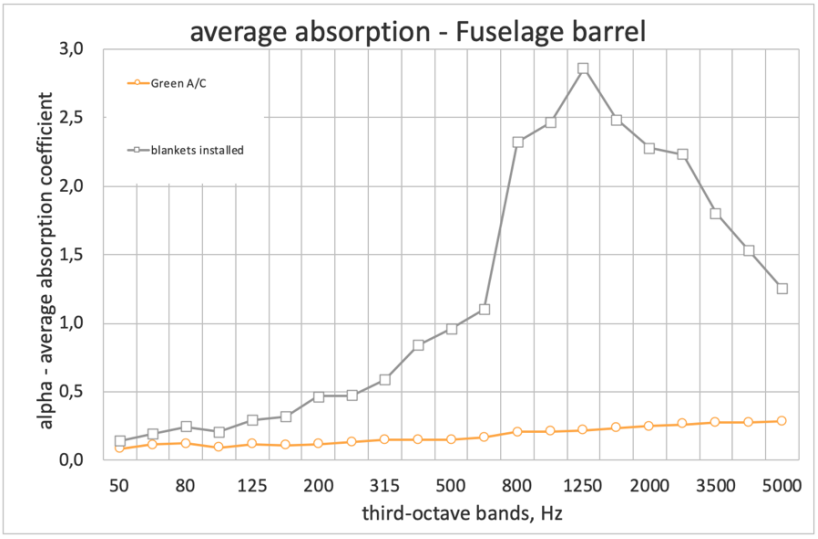

Fig. 10 - Acoustic absorption difference between a bare (a) and furnished (b) fuselage

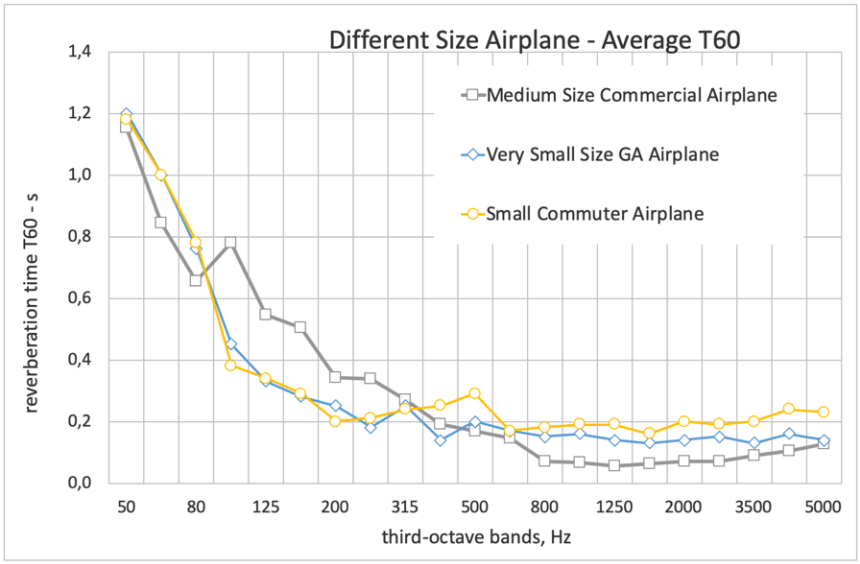

Fig. 11 - Reverberation time (T60) measured inside different airplanes

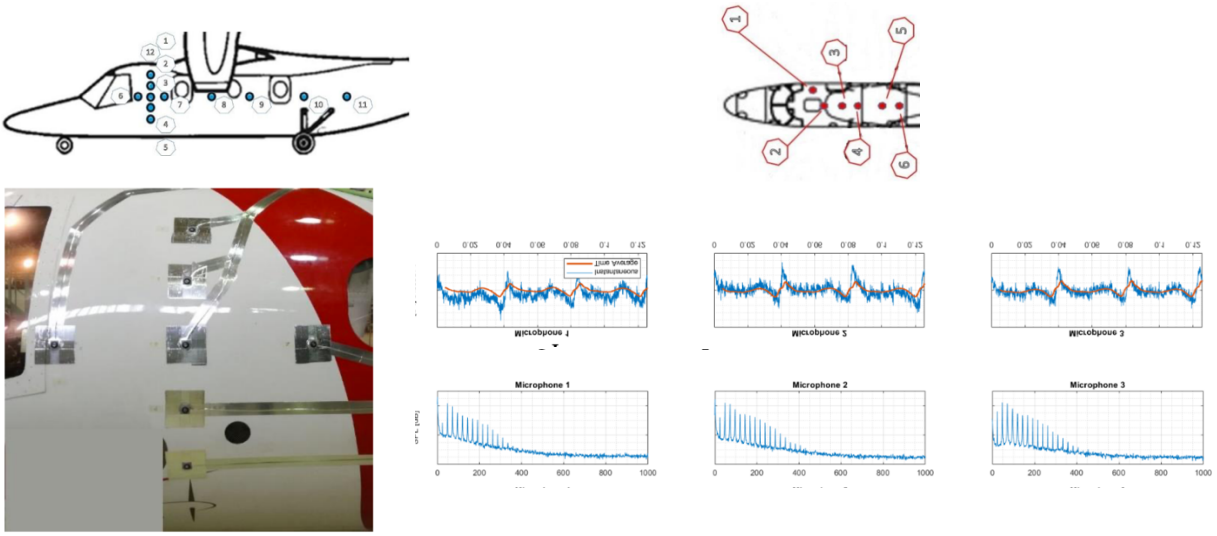

Fig. 12 - Location of the exterior (top left) and interior microphone (top right). Picture of the real installation (bottom left) and example of data analysis (bottom right)

4 COMMUNITY NOISE

Noise has been sometimes used as a technology progress indicator. Modern times are considered an expression of very high technological environment and, undoubtedly, we are all subjected to higher noise level than our predecessors of few centuries ago. The price to be paid to the technological progress. The incredible high level of efficiency and safety attained by modern airplanes, together with an increased interest of the world population toward "greener" economy, has raised a lot of attention toward the aircraft community noise, pushing the scientific community to reconsider the importance of this disturbing parameter and to force the compliance with noise regulation which have been resulted always more stringent, grounding in some cases airplanes which had noise figures higher than acceptable.

The LIFE Lab activity in the field of community noise is dated back in the 90's and went through the actual noise certification of numerous general aviation airplanes, the noise sources analysis, the simulation and the prediction, including both flight path analysis and component noise generation.

Several activities have been carried out during the development of international research project, like HiSAC for the prediction of the sonic boom of supersonic commercial airplanes, or more recently, ADORNO which refers more to popular high subsonic airplanes. Fig. 13 presents the measuring locations requested by the certification procedure of a subsonic jet airplane and the prediction obtained by an in-house developed computer program. The list of the airplanes which have been noise certified includes most of the Partenavia (now Vulcanair) general aviation airplanes, all the Tecnam airplanes and their derived versions, the Piaggio P180, whose history for mitigating the emitted noise is reported in ref. [26], and several other small general aviation airplanes.

According to the simplified noise certification procedure applicable to this class of propeller airplanes, the microphone is set at 2500m from brake release and measures noise emission throughout take off phase at maximum continuous power. Fig. 14 shows the reference flight path for computing the reference height based on the airplane performances, and the measurement setup typically employed for such tests.

Further measurements and analyses have been performed on the possibility to introduce a simplification of the test procedure for a monitoring of the noise behaviour with the life of the airplane, Fig. 15.

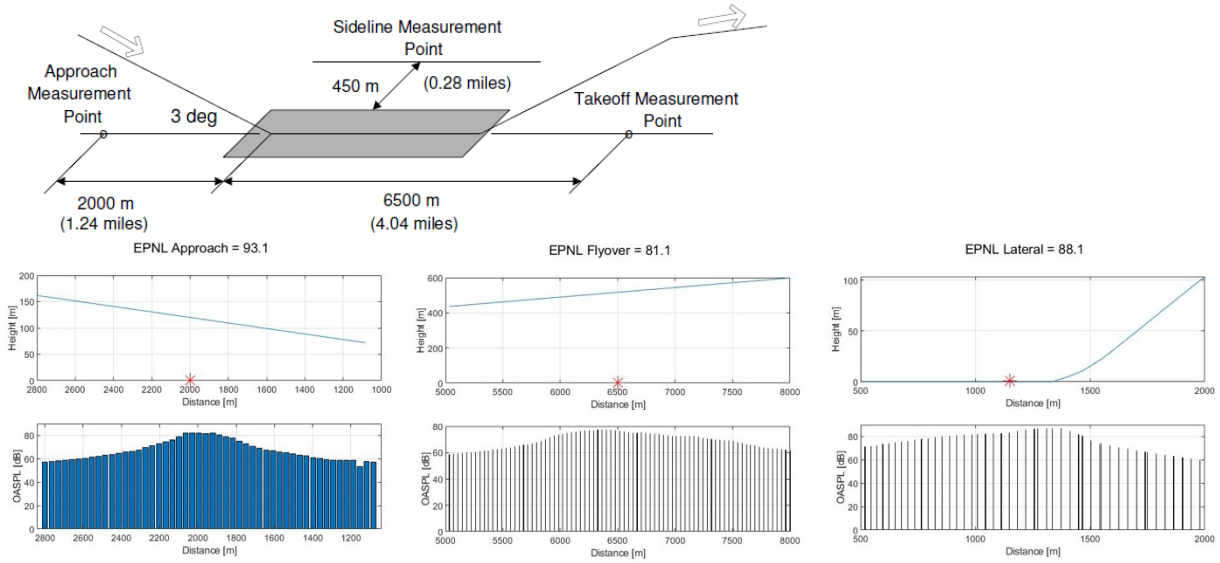

Fig. 13 - ICAO Annex 16 measuring locations (top) and simulation output (bottom)

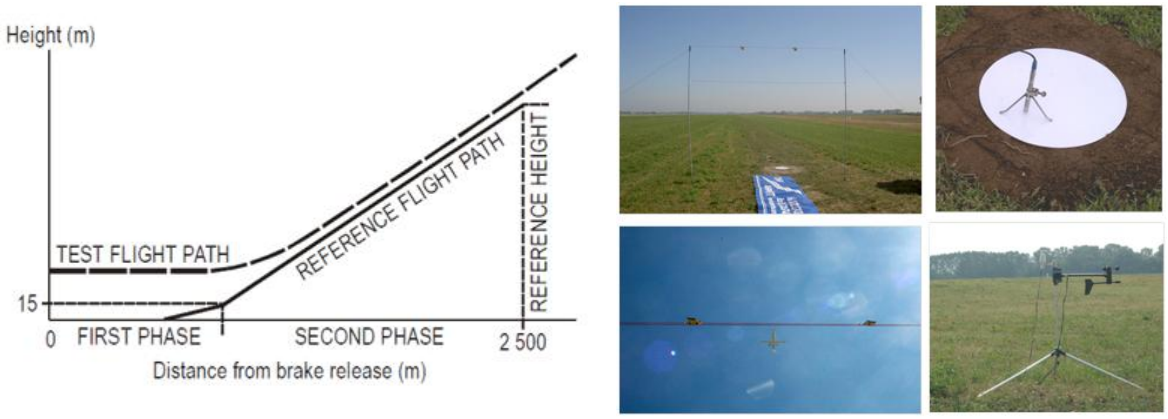

Fig. 14 - Reference flight path for exterior noise certification and measurement set up

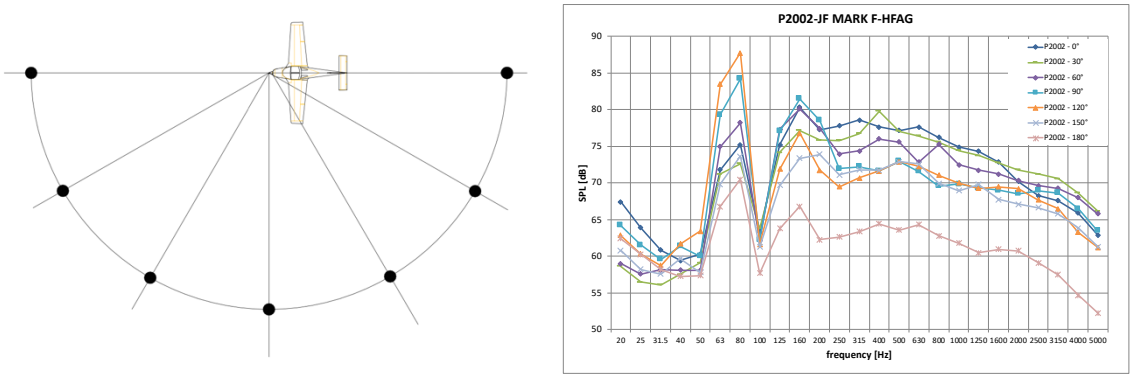

Fig. 15 - Ground noise measurements of a single engine piston aircraft

5 IMPACT DYNAMICS

The study of the impact dynamics is another important topic which involves teaching and research at LIFE Lab. The first applications to nonlinear dynamic problems are dated back almost two decades, when it became clear the need of correlating several experimental tests, both for bird strike and seat crashworthiness certification, with numerical models.

The bird strike is a collision between aircraft and birds. Such collision, apparently inoffensive to the aircraft, can produce considerable damages and consequences, not only to the structure, but also to the

electronic systems, mechanical systems, visual systems and guidance and control systems. So, it can even affect the flight safety and the proper functioning of the whole system.
Crashworthiness refers more to passive safety and it is the ability of an aircraft structure and its internal systems to protect occupants from injury in an event of crash.
As usual in LIFE Lab, a new research topic comes from real life, when a positive interaction between academia and industry turns out and they run together and parallelly for approaching new problems or looking for improved design solutions.
Further activities in the framework of impact dynamics have been, for example, materials' characterization for low, medium and high-speed impacts. This is a very important aspect of the impact simulation, since materials can change, sometimes substantially, their physical properties versus the impact velocity, affecting the result of long computation.
With regard to the numerical point of view, algorithms implementing multi-body dynamics have shown their strong validity, both during the design phase of new structural component, and for the analysis of the results, highlighting with proper modeling the main parameters involved in the process.
These activities have been always supported by experimental tests, partially using an in-house built drop tower, or test equipment made available by industry and research center. One example is shown in fig. 16, where the design of a composite crash absorber device went through the process of designing, building, material characterization, static and dynamic drop testing, installation on a real landing gear and testing its efficiency.

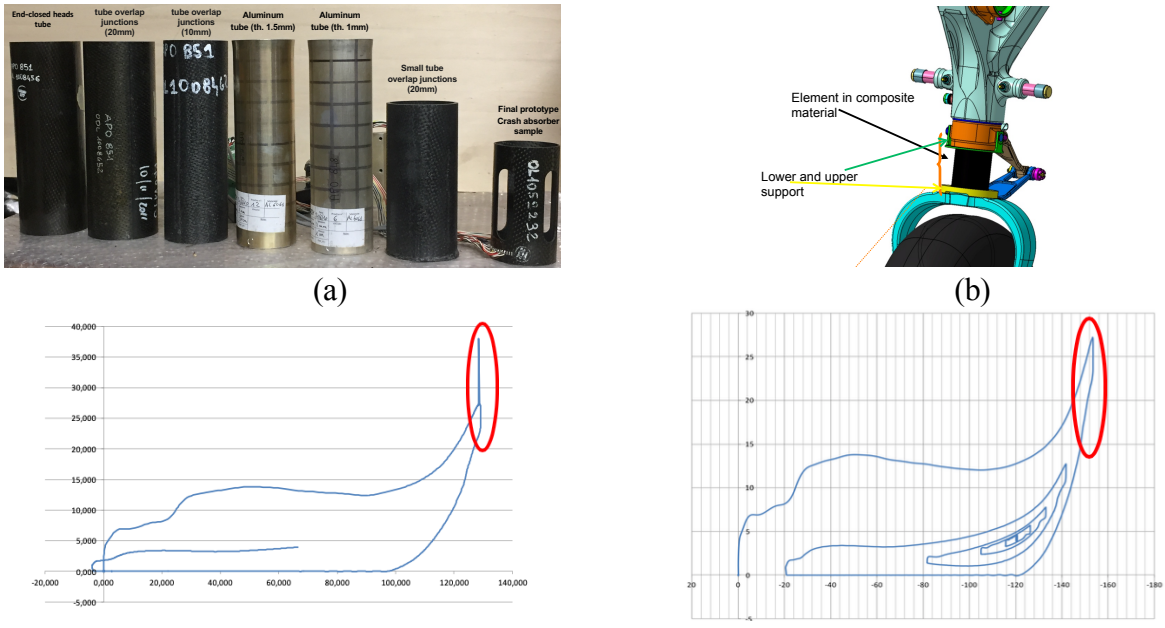

Fig. 16 - Example of design of a composite crash absorber device, (a); its installation on a landing gear, (b); and test results (no device (c), and with the device installed (d))

The studies performed during this design process formed the basis for the definition of the bird strike assessment and optimization for inboard and outboard wing flap of a commercial airplane. Similarly, for the approach in designing solutions for bird strike clearance for cockpit. Fig. 17 reports several studies performed on a wide cockpit of a general aviation airplane, which involved the definition of the boundary conditions and the material characterization of glass compound.
In the field of passenger passive safety, an incredible amount of activities has been performed, ranging from testing, numerical simulation, static and fatigue testing, multibody simulation, assessment of passenger comfort, DoE (Design of Experiments) procedure for most sensitive parameters' identification, fig 18. These activities have been mostly funded by research projects on a competitive basis and, leaded by LIFE Lab, have given the opportunity for training on real, complex structural problems, some generations of young engineers.

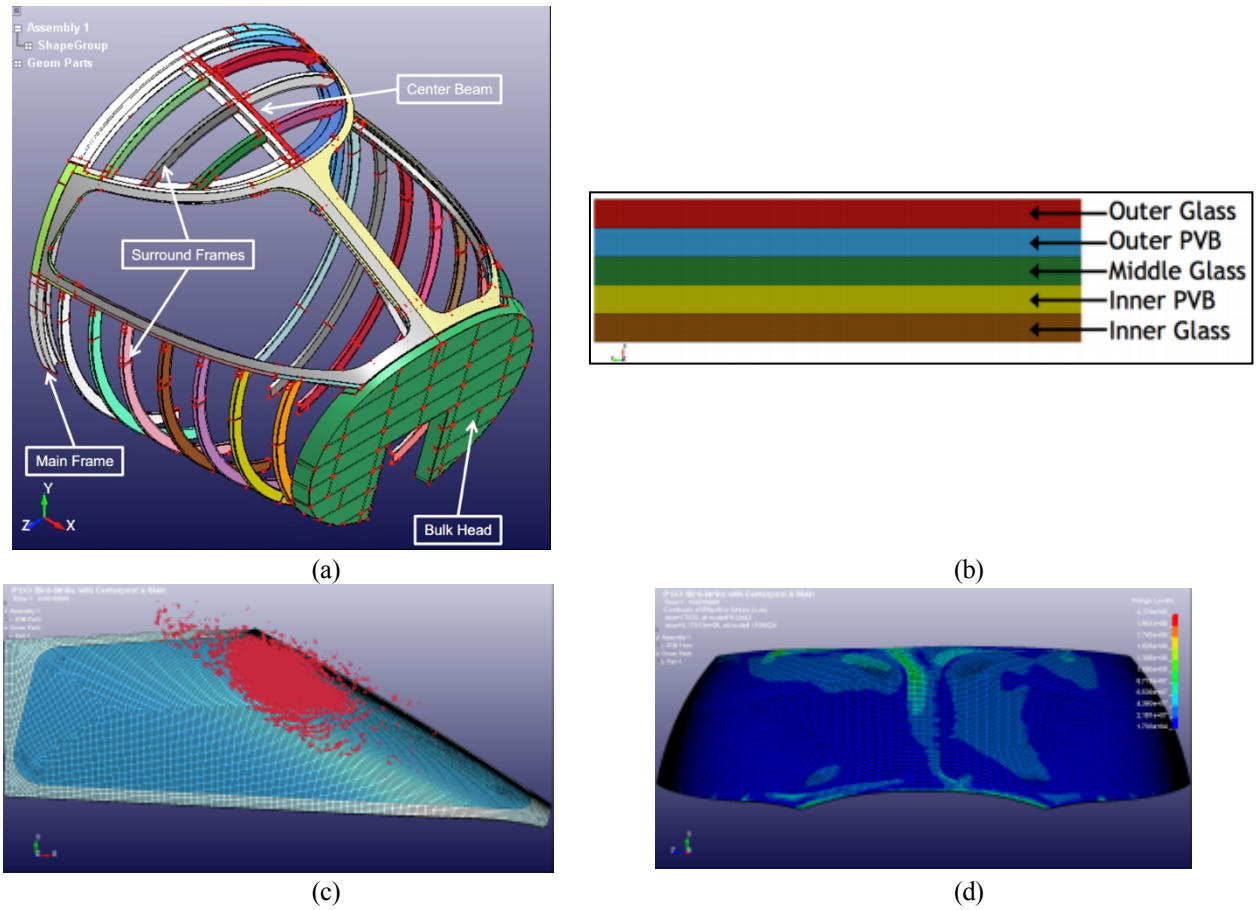

(a) (b)

(c) (d)

Fig. 17 - Design of the cockpit structure, (a); windshield lay-up configuration, (b); and numerical results (lateral view (c), front view (d))

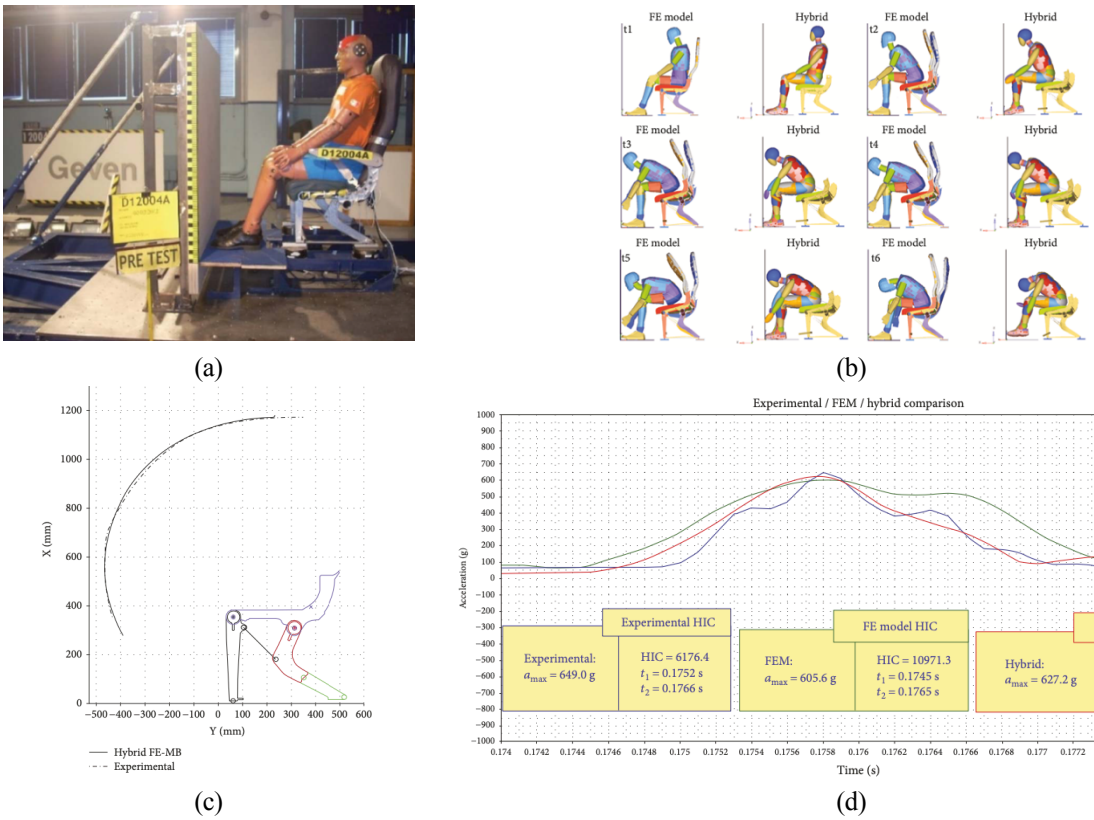

(a) (b)

(c) (d)

Fig. 18 - Typical seat-sled experimental setup, (a); results of numerical simulation with different modeling, (b); head path analysis, (c); accelerations' comparison, (d)

6 CONCLUSIONS

Several activities are on-going and they refer mainly to international research projects. A new system for full scale acoustic excitation of fuselage has to be designed and tested, the dynamic testing of the proposed new wing of next generation tilt rotor, the improvement of the community noise prediction software, and so on. Another milestone reached by this research group is the participation to the setup and execution of the full-scale fatigue testing of the wing of the P2012 aircraft, fig. 19.

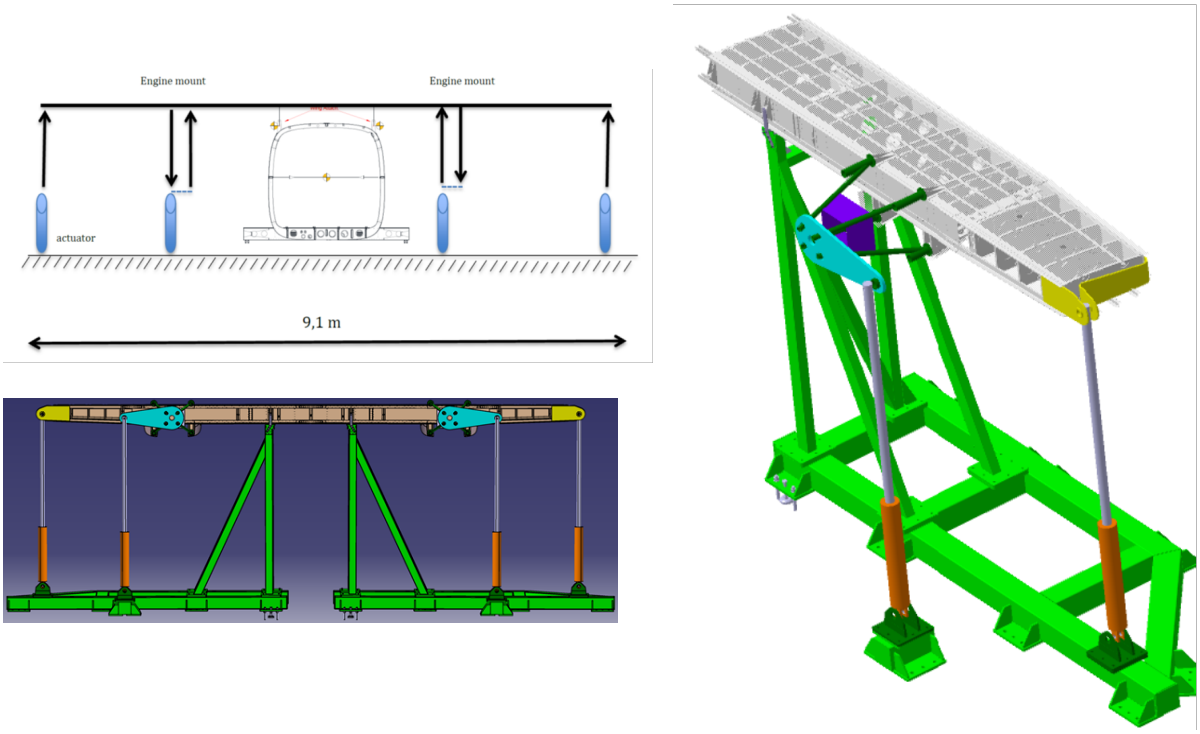

Fig. 19 - General view of the experimental fatigue set-up (semi-test article on the top) and detail of the test rig on the bottom (front view on the left and 3D view on the right

This final, partial list of activities, concludes the overview of the research activities performed and on-going at LIFE Lab, a laboratory of the Department of Industrial Engineering based in San Giovanni, a new campus of the University of Napoli Federico II. The backbone of all the activities is identifying and maintaining a track able to put together theory, simulation and test. The paper has summarized the research developed in the field of aeroelasticity, vibroacoustics, community noise and impact dynamics. These main topics have generated a continuous interest in the scientific community and industrial partners, offering opportunities for preparing research projects, both nationally and internationally funded, presenting papers at conferences and publishing on journals, participating to industrial programs ending with certified approval from worldwide aeronautical agencies (ENAC, EASA and FAA, just to name a few). An important follow up of all these activities has been a big number of master thesis and PhD programs with former students able to satisfy the requirements of the worldwide aerospace community in different fields. LIFE Lab has created the basis for future developments, always using the principle of development through small increasing complexities.

7 ACKNOWLEDGEMENTS

The author is indebted with many Colleagues, Students and Technicians who, with their help, dedication, strong support and infinite patience, have continuously contributed to the activities synthesized in this paper and to many others. A list of these friends goes widely outside any acceptable limit and therefore only a few of them are here recalled. It was an honour to share some of these results

with Prof. Luigi Pascale, unsurpassed reference and mentor in aircraft design. My most lucky opportunity is working with PhD's Michele Guida and Tiziano Polito who have corrected all my mistakes becoming my lifetime reference. My friends, top talented aeronautical engineers, Michele Oliva and Antonio Sollo, who are still acting as convinced drivers for continuous research and industrial projects, with great human comprehension and outstanding technical and scientific competence, hiding all my deficiencies. Many other Professors and Engineers have concurred to the success of the activities summarized in this paper. To all of them goes an indebted thankful thought. As for any aeronautical commitment, a successful first flight is the expected unvaluable prize, just to underline the dedication, enthusiasm and passion, a sincere gratitude goes to the flight test pilots Enzo De Blasio, Marcello Vitale, Marco Locatelli, Alessandro Scaburri and Lorenzo De Stefano for the unbelievable confidence they deserved in my calculations.

8 REFERENCES

[1] Marulo F., Lecce L., Pecora M., "Flight flutter test of a military transport aircraft ", International Forum on Aeroelasticity and Structural Dynamics, June 3-6, 1991, Aachen, Germany

[2] Pecora M., Lecce L., Marulo F., Coiro D.P., "Aeroelastic behavior of long span bridges with "multibox" type deck sections ", Journal of Wind Engineering and Industrial Aerodynamics, 48 (1993) pp. 343-358

[3] Marulo F., Beyer T.B., "Nastran application for the prediction of aircraft interior noise", NASA CP-2481, Proceedings of a Colloquium held in Kansas City, Missouri, May 4-8, 1987, pagg. 266-285

[4] Grosveld F.W., Sullivan B.M., Marulo F., "Aircraft interior noise using a structural-acoustic analogy in Nastran modal synthesis", 6th International Modal Analysis Conference, 1-4 February 1988, Orlando, Florida, pp. 1191-1198

[5] Marulo F., Lecce L., Scaramuzzino F., Bifulco A., "Identification of dynamical data using eigensystem realization algorithm (ERA) ", Proceedings of the 17th Int'l Seminar on Modal Analysis, Leuven Belgium, 21-25 Sep.,1992

[6] Clemente P., Marulo F., Lecce L., Bifulco A., "Experimental modal analysis of the Garigliano cable-stayed bridge", "Soil Dynamics and Earthquake Engineering", Vol. 17, 1998, pp. 485-493

[7] Marano A.D., "ModLab: A New MatLab Toolbox for Modal Parameters Identification", Pegasus Student Conference, Glasgow, 2019

[8] Grimaldi A., Benson D.J., Marulo F., Guida M., "Steel structure impacting onto water: FE/SPH numerical modeling". Journal of Aircraft, vol. 48, n. 4, pp 1299-1308 DOI: 10.2514/1.C031258

[9] Marulo F., Guida M., Maio L., Ricci F., "Numerical simulations and experimental experiences of impact on composite structures", (Book Chapter), Editor(s): Valentina Lopresto, Antonio Langella, Serge Abrate, Dynamic Response and Failure of Composite Materials and Structures, Woodhead Publishing, 2017, ISBN 9780081008874, https://doi.org/10.1016/B978-0-08-100887-4.09992-3.

[10] Orlando S., Marulo F., Guida M., Timbrato F., "Bird strike assessment for a composite wing flap", International Journal of Crashworthiness, Vol. 23, 2018, Issue 2, Pages 219-235, https://doi.org/10.1080/13588265.2017.1342521

[11] Guida M., Manzoni A., Caputo F., Marulo, F., De Luca, A., "Development of a multibody system for crashworthiness certification of aircraft seat", Multibody System Dynamics, Volume 44, Issue 2, 2018, Pages 191-221, ISSN: 13845640, DOI: 10.1007/s11044-018-9612-0

[12] Guida M., Marulo F., Abrate S., "Advances in crash dynamics for aircraft safety", Progress in Aerospace Sciences, Volume 98, 2018, Pages 106-123, ISSN 0376-0421, https://doi.org/10.1016/j.paerosci.2018.03.008.

[13] Guida M., Marulo F., Russo, S., "NiTi SMA Wires Coupled with Kevlar Fabric: a Real Application of an Innovative Aircraft LE Slat System in SMAHC Material", Applied Composite Materials (2018) 25: 269, https://doi.org/10.1007/s10443-017-9618-4

[14] Guida M., Marulo F., Bruno M., Montesarchio B., Orlando S., "Design validation of a composite crash absorber energy to an emergency landing", Advances in Aircraft and Spacecraft Science, Vol. 5, Number 3, May 2018, pages 319-334, DOI: 10.12989/aas.2018.5.3.319

[15] Di Napoli F., De Luca A., Caputo F., Marulo F., Guida M., Vitolo B., "Mixed FE–MB methodology for the evaluation of passive safety performances of aeronautical seats", International Journal of Crashworthiness Published online: 02 Apr 2018, https://doi.org/10.1080/13588265.2018.1441616

[16] Caputo F., De Luca A., Marulo F., Guida M., and Vitolo B., "Numerical-Experimental Assessment of a Hybrid FE-MB Model of an Aircraft Seat Sled Test," International Journal of Aerospace Engineering, vol. 2018, Article ID 8943826, 7 pages, 2018. https://doi.org/10.1155/2018/8943826.

[17] Guida M., Sellitto A., Marulo F., Riccio A., "Analysis of the impact dynamics of shape memory alloy hybrid composites for advanced applications", (2019) Materials, Volume 12, Issue 1, Article number 153, ISSN: 19961944, doi: 10.3390/ma12010153

[18] Carducci G., Carducci S., "Numerical Vibroacoustic Analysis of a Fuselage Section: Low-Frequency Noise Reduction", Pegasus Student Conference, Glasgow, 2019

[19] Marulo F. and Polito T. (2017), Probabilistic analysis and experimental results of sound transmission loss of composite panels. Polym Eng Sci, 57: 722-730. doi:10.1002/pen.24619

[20] Del Sorbo G.R., Truda G., Bifulco A., Passaro J., Petrone G., Vitolo B., Ausanio G., Vergara A., Marulo F., Branda F.,"Non monotonous effects of noncovalently functionalized graphene addition on the structure and sound absorption properties of Polyvinylpyrrolidone (1300 kDa) electrospun mats", (2018) Materials, Volume 12, Issue 1, Article number 108, ISSN: 19961944, doi: 10.3390/ma12010108

[21] Avossa J., Branda F., Marulo F., Petrone G., Guido S., Tomaiuolo G., Costantini A., "Light Electrospun Polyvinylpyrrolidone Blanket for Low Frequencies Sound Absorption, Chinese Journal of Polymer Science, Vol. 36, Issue 12, Dec. 2018, Pages 1368-1374, ISSN: 02567679, DOI: 10.1007/s10118-018-2154-3

[22] Marulo F., Sollo A., Aversano M., Russo G. and Polito T., "Interior noise sources identifications, in-flight measurements and numerical correlations of an advanced business aircraft", Proceedings of the 12th AIAA/CEAS Aeroacoustics Conference, Cambridge, MA, USA, May 2006, AIAA 2006-2491

[23] Marulo F., Sollo A., Aversano M., Polimeno U., Perna F., "Measurements and predictions of community noise of a pusher-propeller general aviation aircraft", Proceedings of the 11th AIAA/CEAS Aeroacoustics Conference, Monterey, Ca, May 2005

[24] Scarselli G., Marulo F., "Sonic Boom Minimization through a simplified approach for the preliminary design of a civil supersonic aircraft", 16th AIAA/CEAS Aeroacoustics Conference (31st AIAA Aeroacoustics Conference), 2010, Stockolm, Sweden

[25] Marulo F., Polito T., Oliva M., "Experiences in noise testing of light general aviation airplanes. proposal for a new certification approach", 21th SFTE (EC) Symposium, Vergiate (VA), Italy, October 2010.

[26] Marulo F., "Aircraft Community Noise. The Revenge of a Neglected Problem", L'Aerotecnica Missili & Spazio, Vol. 94, No. 3 (2015), pp. 184-194

[27] Di Lorenzo E., Manzato S., Peeters B., Marulo F., Desmet W., "Structural Health Monitoring strategies based on the estimation of modal parameters", December 2017, Procedia Engineering 199:3182-3187, DOI:10.1016/j.proeng.2017.09.521

[28] Musella U., D'Elia G., Carrella A., Peeters B., Mucchi E., Marulo F., Guillaume P.,"A minimum drives automatic target definition procedure for multi-axis random control testing", Mechanical Systems and Signal Processing, Volume 107, July 2018, Pages 452-468, ISSN: 08883270, DOI: 10.1016/j.ymssp.2018.01.039

APPLICATIONS OF MICROPHONE ARRAYS AND MACHINE LEARNING TO FAULT DETECTION: ADDED VALUE OF SPATIAL INFORMATION

Ines Lopez Arteaga[1,2] , Lars Janssen[1] and Julian Korver[1]

[1]Department of Mechanical Engineering
Eindhoven University of Technology, Eindhoven, The Netherlands
Email: i.lopez@tue.nl, l.a.l.janssen@student.tue.nl, a.aulitto@tue.nl,
k.anginthaya@student.tue.nl, j.n.korver@student.tue.nl

[2]Marcus Wallenberg Laboratory for Sound and Vibration Research (MWL)
KTH Royal Institute of Technology, Stockholm, Sweden
Email: inesla@kth.se

ABSTRACT

This paper discusses the application of microphone arrays in combination with machine learning to fault detection and, specifically, the potential added value of spatial information to enhance the detection capabilities of the machine learning algorithms. Acoustic signals from single microphones are extensively used in combination with machine learning for condition monitoring and fault detection in many applications. This is often done based on spectrograms (time-frequency images) and requires a priori knowledge of the location of the sources of faults to be detected in order to place the microphones in their vicinity. On the other hand, microphone arrays are a well-known tool to localize sources of sound and provide information about the spatial distribution of sources without a priori information about the system being observed. The question discussed in this paper is whether spatial information obtained with microphone arrays could potentially improve the fault detection capabilities of machine learning algorithms.

1 INTRODUCTION

Single microphone signals are applied in the literature for fault detection based on time-frequency information and machine learning when non-intrusive sensing is required or convenient to use [1]. However, the location of the microphone with respect to the source(s) to be observed determines the information contained in the signal and the use of a single microphone might lead to loss of information in complex systems with spatially distributed sources of errors. Therefore it seems natural to consider the potential of microphone arrays (acoustic cameras) for condition monitoring in combination wiht machine learning. Microphone arrays in combination with Machine Learning (ML) are already used for, for example, source localization based on beam forming techniques [2].

In this paper the application of microphone arrays for fault detection is considered, which implies discriminating between healthy and faulty conditions based on changes on the spatial distribution of the data. The results presented here are based on the unprocessed microphone array data, no beamforming nor other acoustic holography processing methods are applied on the data. It is expected that applying holography processing would enhance the information included in the images and, hence, improve the results. The main question addressed here is whether spatial information obtained with microphone arrays could potentially improve the fault detection capabilities of machine learning algorithms.

2 FAULT DETECTION BASED ON MULTI-DIMENSIONAL DATA

Information about the spatial distribution of sound and vibration sources has the potential to improve the fault detection accuracy of monitoring systems for complex systems and microphone arrays are a promising tool to provide this information. However, in general, deep learning models perform well if enough training samples are provided for the model to be able to generalize the input. If the size of the input increases, as is the case when microphone arrays are used, a larger number of training samples is required. In [3, 4] two data processing methods and a data augmentation method are proposed that allow microphone arrays to be used as a fault detection and potential condition monitoring tool using deep learning models. To reduce the size of the input, the proposed data processing methods condense the microphone array data to an amount of data that is better suited for deep learning models, while retaining the relevant information. They are based on Fourier transforms to create spatial- and frequency-domain images of the sound. Furthermore, to increase the amount of training data without the need of extra experimental data, the proposed data augmentation method generates new data by applying random windows to the microphone data in the time-domain, before they are transformed to the frequency domain. Consequently, the need for an extensive amount of experimental data in order to prevent over-fitting is reduced. The data processing and augmentation methods are applied to two classification cases: detecting the position of added mass on a plate and estimating the amount of unbalance mass in a rotating disc. A simple and robust neural network is trained to predict the location of the mass and the amount of unbalance respectively.

3 DETECTION OF ADDED MASS ON A PLATE

3.1 Multi-dimensional dataprocessing method

In [4] toe multi-dimensional dataprocessing methods are proposed: a peak finding method and three-dimensional (3D) image method. A schematic representation of the two methods and the corresponding neural network structure is provided in Figure 1.

In the peak finding method, a number of frequency peaks in the sound pressure spectrum measured with the microphone array are selected and images for each peak are generated. These images are feeded to separate neural networks and the outputs are combined to provide the input to the neural network that provides the classification outputs (see Figure 1). In this method, the acoustic images are treated as independent (unrelated) images. The 3D image method proposes a different approach alltogether and consideres the complete frequency information, split in equally distributed windows, leading to interrelated sequence of images, [space, space, frequency], that is comparable to video information and can be analysed applying video recognitions methods [5]. The 3D image method and corresponding neural network are represented in Figure 1. Both methods are discussed in detail in [4] and it is concluded that the 3D image method leads to significantly more accurate classification than the peak finding method. Therefore, only the results for the 3D image

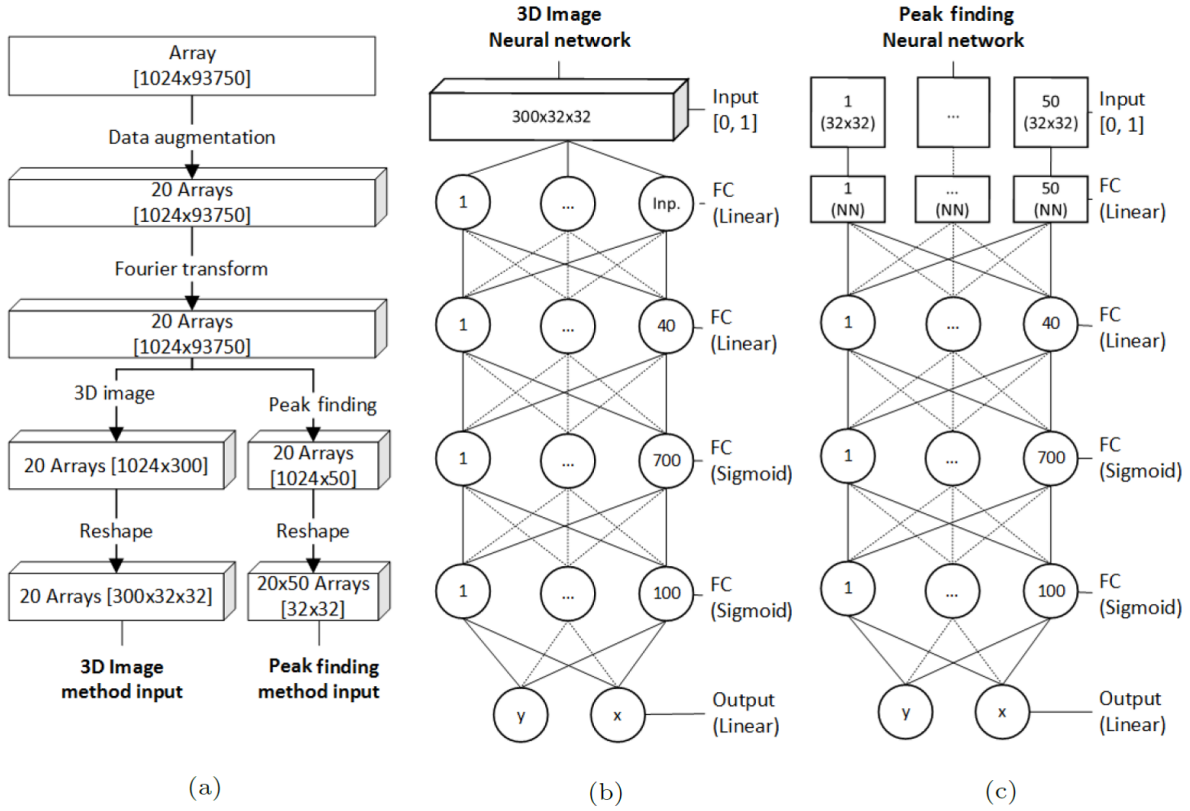

Figure 1: Data processing steps per measurement based on method and neural network structures per method. (a) Data processing steps, (b) Neural network for the 3D Image method, (c) Neural network for the Peak Finding method.

method are discussed in the remaining sections.

3.2 Experimental set-up

In order to validate the 3D image method described above an experiment is designed to train a deep learning algorithm to predict the location of a mass located on a vibrating plate using the data gathered by this acoustic array. The response of the vibrating plate is altered by adding extra mass to a specific location of this plate, which the microphone array should be able to measure when the data is properly handled using the proposed methods. The experiment resembles a situation similar to many fault detection applications where change in the response of the system is caused by a location specific fault.

An schematic drawing and a photograph of the experimental set-up is provided in Figure **??**. This set up includes a 32x32 miucrophone array (Sorama®CAM1K), a brass plate (401x401x2.05mm), a disturbance mass of 35g consisting of two magnets on each side of the plate and a mechanical shaker on double leaf-springs to avoid vibration tranmission to the frame.

The input voltage as function of time of the mechanical shaker is given as a chirp noise

$$f(t) = 10 \cdot \cos(10000\pi |\cos(\pi \frac{t}{2})|) \tag{1}$$

in the frequency range from 0Hz to 5000Hz and with a full chirp duration of 2 seconds.

The mesurement distance for the array is set to 300mm ro create a challenging realistic data-set. In general, measuring the system from a relatively close distance would result in better results, however, the goal of the experimental setup is to validate and compare the proposed methods in a setting that is translatable to industrial applications.

In order to create a data set that is manageable, the disturbance mass is only placed in a quarter of the available space. Note that the system is symmetric, so the results can in theory be

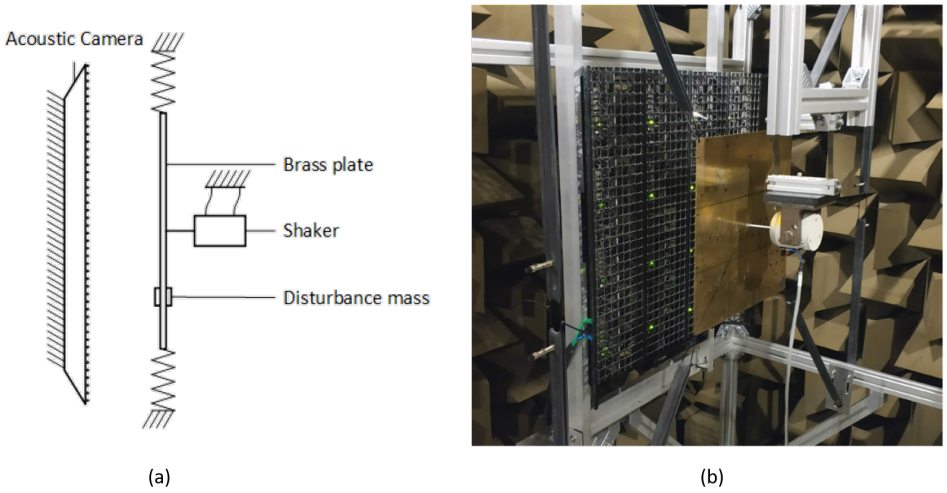

Figure 2: Experimental set-up. (a) Schematic drawing, (b) Photograph showing the Sorama®CAM1K, plate and shaker.

extrapolated to other quadrants of the plate. The data set is based on 42(6 by 7) locations for the disturbance mass, measured 5 times 2 seconds per location each. Thus, resulting in a total of 210 data samples in the complete data set. Note that this low number of samples is intentional, since it is unlikely for most applications that much training data is available.

3.3 Mass localization results

In Figure 3 the localization results are summarized for augmented training data with 4 training samples, which is the most accurate case found in [3].

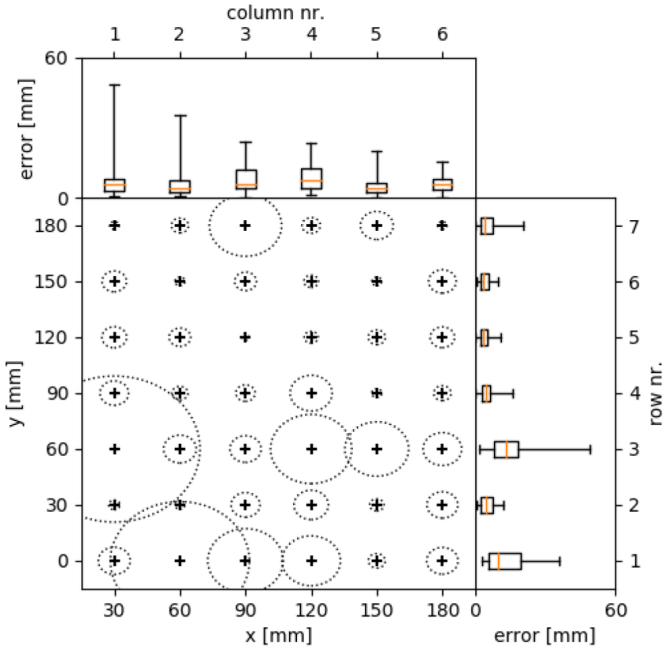

Figure 3: Test errors e of disturbance localization per position on the brass plate. The dotted circles specify the mean accuracy of the test data output for their respective position. The box plots show the error distribution of test output for the respective row/column of disturbance locations.

The main conclusion that can be derived from Figure 3 is that the majority of test locations of the disturbance mass is predicted accurately. However, in some cases the trained network is not able to accurately localize the position of the mass. In general, the large errors seem to occur

more frequently towards the center of the plate (bottom left of the figure), which can perhaps be explained by the fact that the shaker has more influence over the movement of the plate towards the center, while the outer edge of the plate is relatively more affected by the mass and thus easier to detect.

To assess whether the spatial information increases the accuracy of the fault detection, the number of microphones used in the training of the neural network is reduced. The results of this experiment are given in Figure 4. Note that the number of microphones is reduced by ”cropping” the images, i.e. removal of the outer edges of the microphone array. For uneven number of microphones, the rows and columns of microphones are removed from the top and left of the array respectively.

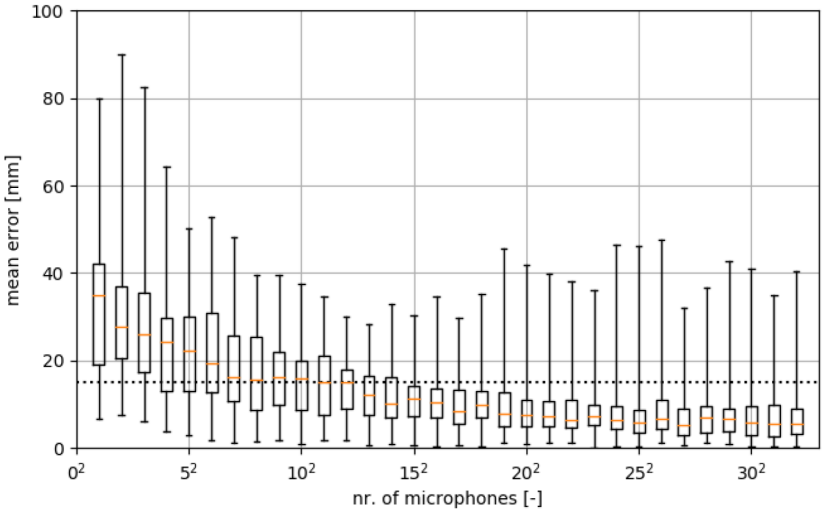

Figure 4: Box plots of test error e in millimeter for varying number of microphones as input. All samples that have an error below the dotted line are predicted at the correct location. Note that for box plots, 75% of the results are in or below the boxes.

As can be seen in this figure, when at least a 16 by 16 microphone array is used to train the model, the model is able to predict a location closest to the correct location in at least 75% of the cases. For smaller arrays, the error exponentially increases. Since the height and width of the plate are around half of the size of the microphone array, reducing the effective microphone array to an array smaller than the plate affects the performance negatively. These results indicate that in situations where the faulty components are distributed in space, multi-dimensional data including spatial information would potentially provide a better detection accuracy.

4 ROTOR UNBALANCE DETECTION

The approach proposed in the previous section is applied to detecting the amount of unbalance in a rotor [6]. To this end an experimental set-up is build where an aluminium disc of 0.15m diameter and 0.03m thicknes is mounted on the output shaft of an ABB M2aa 090L three-phase induction motor mounted on a cast iron table as shown in Figure 5. The disc has threaded perforation where bolts can be mounted to created a controlled unbalance. A MEMs microphone array with 32x32 microphones (Sorama CAM1K) is mounted on a rack at a distance of 39 cm from the edge of the table. After some preliminary tests the array is moved back to a distance of 82cm to recreate more realistic conditions. The rotational velocity of the motor is set to a constant value of 30Hz.

A controlled unbalance in the range 30-50g is created by combining of an M8 bolt (30g) and M8 nuts (4g) leading to seven different configurations, as indicated in Table 1. Each configuration is measured 16 times, leading to a data-set with 112 different mesurements.

The array measurements provide sound pressure levels in the frequency range 0-20kHz. A pre-study is carried out to identify the most suitable frequency range for the detection task at hand and the frequency range 0-300Hz is selected. The average normalized sound pressure in the frequency range 0 to 300 Hz is given in Figure 6 for the balanced case and the case with an unbalance mass of 50g. The average is taken over all 1024 microphones.

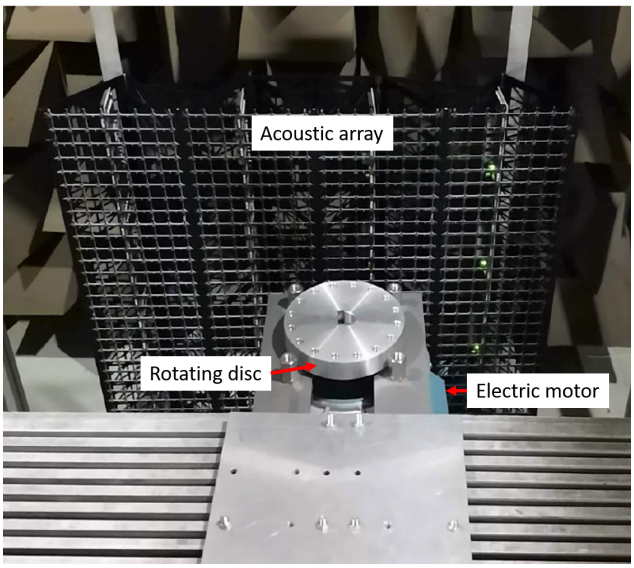

Figure 5: Photograph of the experimental set-up. The disc has threaded holes where bolts can be placed to create a controlled unbalance. All tests are performed for a rotating speed of 30Hz and measurement distance of 82cm.

Configuration	Structure	Weight [gram]
1	none	0
2	M8 bolt	30
3	M8 bolt, 1 x M8 nut	34
4	M8 bolt, 2 x M8 nut	38
5	M8 bolt, 3 x M8 nut	42
6	M8 bolt, 4 x M8 nut	46
7	M8 bolt, 5 x M8 nut	50

Table 1. Rotor imbalance configurations.

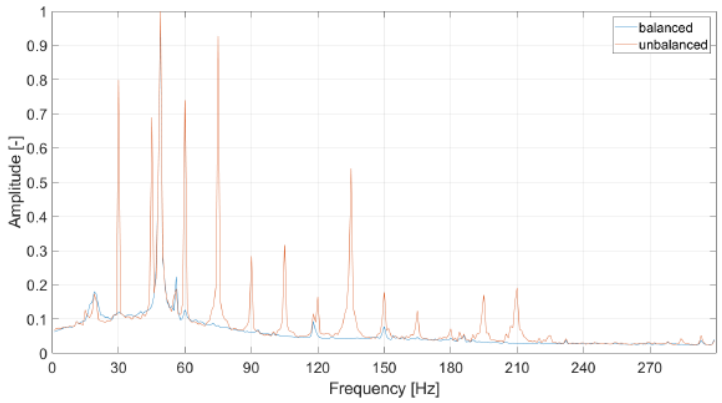

Figure 6: Average normalized sound pressure in the frequency range 0 to 300 Hz for the balanced and unbalanced (50g) disc. The average is taken over 1024 microphones.

The rotational speed of the motor (30Hz) and its harmonics can be clearly seen in the sound pressure spectrum corresponding to the unbalanced rotor while most of them are hardly visible for the balanced rotor. Therefore it is expected that the data proccesing approach and neural network proposed in the previous section 1 will lead to satisfactory classification results.

There are 105 different data-sets used to train the neural network. Each data-set contains an array with dimensions 300 by 32 by 32. The data-sets are used as input which is flattened to

change the input dimensions to a single row. After this layer, additional layers follow: 10 nodes with a linear activation, 700 nodes with a sigmoid activation, 100 nodes with a sigmoid activation activation and finally the last layer resulting in the output with a linear activation. The network has a single number as output which indicated the added mass to the electric motor. It has no loops within the network itself, making it a feedforward network. It can also be described as an multilayer perceptron (MLP) as it uses only feedforward in combination with activation functions [7].

The neural network is trained with 105 data sets and tested with one random data set per configuration. This procedure is repeated 20 times per configuration.The classification results obtained with the full array are summarized in 8(a), where the average unbalance mass over 20 training iteratioins detected for each of the seven cases is plotted. The 95% confidence interval is indicated as well. It can be seen that for all but for the smallest unbalance mass the right unbalance is detected within a margin of less than 1.5g. The errors are larger for the lowest unbalance of 30g and the balanced case. This is likely due to the fact that there is no learning data between 0 and 30g.

In order to assess the potential benefit of 3D-data for the detection of the unbalance mass, the analysis is repeated for different sizes of the microphone array from full (32x32) to 1 microphone with four intermidate sizes as indicated in Figure 7. The red square indicate active microphones. The arrays of size 8x8, 4x4 and 2x2 are centered with respect to the position of the disc-motor system position. An overview of the mean classification errors with corresponding 95% confidence intervals for all array sizes considered (including the full array and the single microphone case) is provided in Figure 8.

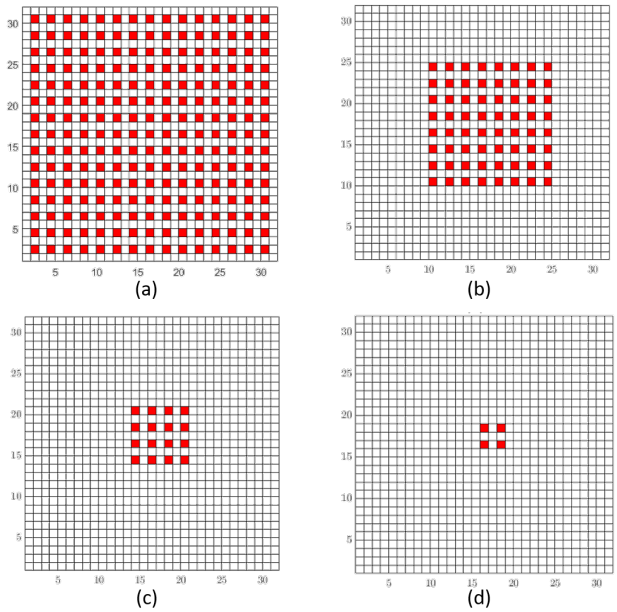

Figure 7: Microphone positions included in the data for the array size analysis with red squares indicating active microphones. The smaller arrays are centered with respect to the disc-motor system position. (a) 16x16, (b) 8x8, (c) 4x4, (d) 2x2.

It can be seen that the mean classification errors tend to be larger when the array size is reduced to 8x8 or less, although no clear trend of increasing errors for decreasing array sizes is seen. On the contrary, the 2x2 array data leads to smaller errors than the 8x8 array data. Overall, the 16x16 array data-set provides the smallest classification errors, except for the balanced case. This may be seen as an indication of the potential added value of 3D-data (2D space + frequency) for failt detection. However, in this case, the improvement in detection accuracy with respect to the 2x2 and even the single microphone does not seem to justify the much larger data-set required for the 16x16 array.

5 CONCLUDING REMARKS

In this paper fault detection methods based on acoustic cameras and machine learning are discussed and, in particular, the added values of the spatial information provided by by acoustic images for a more accurate fault detection. The results of the two test cases discussed indicate that spatial

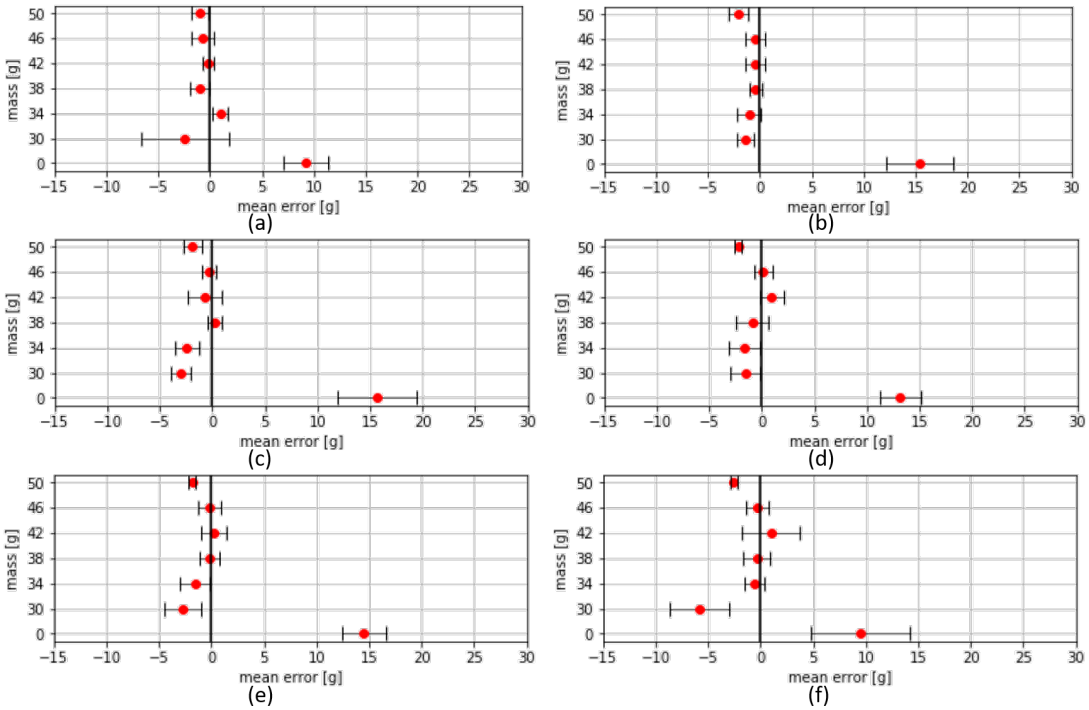

Figure 8: Mean classification errors with 95% confidence interval for 20 training iterations and different array sizes. (a) full array, (b) 16x16, (c) 8x8, (d) 4x4, (e) 2x2, (1) one microphone.

information might potentially lead to better fault detection in complex systems with many spatially distributed fault sources.

REFERENCES

[1] S. Delvecchio, P. Bonfiglio, and F. Pompoli. Vibro-acoustic condition monitoring of Internal Combustion Engines: A critical review of existing techniques. *Mechanical Systems and Signal Processing*, 99:661–683, 2018.

[2] Michael J Bianco, Peter Gerstoft, James Traer, Emma Ozanich, Marie A Roch, Sharon Gannot, and Charles-Alban Deledalle. Machine learning in acoustics: Theory and applications. *The Journal of the Acoustical Society of America*, 146(5):3590–3628, 2019.

[3] Lars Janssen. *Data processing and augmentation of microphone array data for fault detection with machine learning . Master thesis*. PhD thesis, TU/e, 2019.

[4] Lars Janssen and Ines Lopez Arteaga. Data processing and augmentation of acoustic array signals for fault detection with machine learning. *submitted for review*, 2020.

[5] Shuiwang Ji, Wei Xu, Ming Yang, and Kai Yu. 3D Convolutional neural networks for human action recognition. *IEEE Transactions on Pattern Analysis and Machine Intelligence*, 35(1):221–231, 2013.

[6] Julian Korver. *Detecting imbalance in an electric motor usingmicrophone data in a deep learning network. Bachelor thesis*. PhD thesis, TU/e, 2020.

[7] Ian Goodfellow. *Deep Learning*. 2016.

OPEN CHALLENGES FOR STRUCTURAL DYNAMICS IN MARINE ENGINEERING

E. Ciappi [1]

[1]National Research Council of Italy, Institute of Marine Engineering
Via di Vallerano 139, Rome, ITALY
Email: elena.ciappi@cnr.it

ABSTRACT

Short- and long-term strategies to address climate change together with the rapid growth of some new technologies and sectors have brought significant modifications in the field of marine engineering. In this respect, a traditional and well consolidated sector such as maritime transportation is experiencing a sudden increase of innovation to deal with new requirements in terms of environmental impact but maintaining the necessary level of safety. On the other side, emerging sectors such as marine robotics and new challenges for the offshore engineering, including the deep-sea mining and the exploitation of marine renewable energies, have introduced new issues which cannot be translated into a simple knowledge and technology transfer. Most of the structural dynamics related problems in marine engineering involve hydroelastic interaction therefore, the analysis of the coupling characteristics is fundamental for a correct verification of the structural resistance and for the development of ad hoc mitigation strategies. Innovative materials, active control and advanced methodologies for the design are the main features of this transformation. In this paper some new trends for structural dynamics related problems in the field of maritime transport, offshore structures and underwater robotics are analyzed and discussed.

1 INTRODUCTION

Marine engineering is facing a significant transformation due to the fast achievement of the maturity level of some technologies and to respond to climate change by reducing the environmental impact and preventing catastrophic accidents caused by increasingly frequent extreme events. In fact, the use of innovative technologies to reduce the impact on the environment and to increase the safety of shipping has increased significantly in recent years. On the other side, offshore structures

must respond to new challenges arising from the occurrence of extreme loads linked to climate change, the need to exploit marine renewable energies and the new frontiers of deep-sea activities. Among the emerging sectors, marine robotics is probably the most advanced and innovative one and offers several topics for structural dynamics. Beside the large use of Information and Communication Technologies (ICT), new smart and lightweight materials, sensor development, advanced mathematical models for the design, innovative control strategies are the key elements of this process.

Almost all structural dynamics problems in the marine and maritime engineering sector involve hydroelastic phenomena. Therefore, the study of the characteristics of the structure-fluid coupling should represent the fundamental element of the analysis. In the past and somehow still nowadays, most marine structures were considered as rigid bodies to simplify the design and the analysis phase even when the rigid body approximation was not properly verified. However, also when the deformation of the body can be considered small thus, not producing modification of the hydrodynamic field, the dynamic response of structures including heavy fluid effects, must be considered at least for the correct verification of structural integrity and fatigue life. It is important to underline that frequently the correct understanding of the dynamic behaviour of structures can lead to simplification in the calculation of the hydrodynamic loads since structures respond selectively, allowing to neglect some features of the hydrodynamic field. In recent years, it has been demonstrated that structural deformation can play a significant role in modifying the physics of several phenomena related to marine and maritime engineering. Apart for hydroelastic stability problems *i.e.* vortex induced vibrations of risers and mooring cables and flutter of control surfaces, it is worth citing impact problems (slamming, sloshing), large ships and offshore structure dynamics, flexible propellers, turbines for energy conversion and biomimetic propulsion. Moreover, in many cases the control strategy adopted to reduce the undesirable effects or to improve the performances are based on the physics underneath fluid-structure interaction coupling and on the use of deformable elastic materials. In this paper most of the marine engineering applications involving new challenges and trends for structural dynamics and noise are presented. Three sectors have been analysed: maritime transport, offshore structures and marine robotics with emphasis to bioinspired underwater autonomous vehicles.

2 SHIP STRUCTURES

2.1 Reducing the impact on the environment and increase the comfort level on board

The reduction of chemical and physical emissions is the main issue to support the economic development of maritime transportation while reducing the impact on the environment. Alternative fuels, innovative power generation from renewable sources and high levels of connectivity and automation with the large use of ICT to optimize operations on board and at sea are fundamental topics towards the zero-emission target set for 2050. Anyway, reducing greenhouse gases deals also with many practical improvements in ship efficiency as the use of lightweight materials and of hull coatings to reduce frictional drag but also the improvement of propeller efficiency. On the other side, one of the most severe anthropogenic impact for the marine life is the underwater radiated noise from commercial shipping. Its reduction implies the analysis of machinery, auxiliary engines and propulsive system which are, at the same time, the main sources of vibration and noise radiated on-board. Among noise sources, although relevant for military applications only, it is worth mentioning the hydrodynamic noise. In the following subsections the attention is devoted to a short description of the state of the art in the analysis of radiated noise on-board ships and to give a focus on new trends in propeller design.

2.1.1 Radiated noise on board

The analysis of noise generation and transmission is an important issue to guarantee an adequate level of comfort on board and, for military applications, to ensure the correct functioning of the on-board sensor arrays. For what concern noise radiated on-board commercial ships, several regulations already exist and state of the art methodologies, mainly based on finite element or SEA analyses, are available [1].

Hydroynamic noise includes vortex shedding from appendages and control surfaces as well as breaking waves at the ship bow and turbulent boundary layer (TBL) attached to the hull. The response of elastic structures to random TBL excitation has been studied to reduce the self-noise of military ships [2]. Most of the control strategies in the naval field deal with boundary layer control instead of structural or acoustic control. From the early 60ies different passive control devices have been applied, among them of concern are blowing and suction, the use compliant surfaces, micro-bubbles and polymer and, more recently, the development and application of water repellent bio inspired coatings [3]. However, given the broadband nature of TBL excitation, an effective mitigation approach must necessarily involve hybrid control strategies.

2.1.2 Reducing vibration and underwater radiated noise: the deformable composite propeller

Over the last century marine propellers have designed as rigid and with fixed geometry. This approach can lead to significant performance decay when operating in off-design conditions. In fact, the propeller is optimized for a single design condition corresponding to a specific advance ratio J and thus to a specific angle of attack of the incident flow. If the advance ratio changes as in the case of a propeller operating in off-design condition and if the pitch remains unchanged, the suboptimal angle of attack gives lesser hydrodynamic efficiency and can produce high vibrations that are transmitted to the hub and to the ship structures. Moreover, the rigid assumption precludes the possibility of exploiting the deformability of the material to control the hydrodynamic loads, the vibrational response and the noise radiated on board ships or at sea.

Address all these issues became mandatory since reducing the impact on the environment by reducing fuel consumption according to the long term strategy for a Climate Neutral EU by 2050, and reducing underwater radiated noise according to the Marine Strategy Framework Directive (GES 11) are major challenges for shipping. Propeller efficiency can be improved with controllable pitch devices that adapt blades to different loading conditions. However, these devices are complex, expensive both for operational and maintenance issues and large thus limiting the propeller size. A new perspective is given by the recent advances in material technology; the idea is to have self-adaptive structures *i.e.* able to modify their shape by adapting to different loading conditions.

For instance, considering laminated fiber reinforced composite materials, the material anisotropy can be used to generate twist in the propeller blade from its bending under the action of hydrodynamic loading. This twist alters the effective pitch of the propeller which may be used to improve the hydrodynamic performance at off-design conditions.

Moreover, composite laminates (mostly glass and carbon fiber) have many other advantages over traditional metallic materials such as aluminum and nickel aluminum bronze (NAB), including higher strength-to-weight ratios, improved vibration damping properties, reduced magnetic/electric signatures, better fatigue characteristics, higher durability, resistance to corrosion (salt water and other chemical agents) and to biological growth, lower life-cycle costs, and reduced manufacturing cost for complex shapes if compared with manual pitch orientation devices.

In [4] the effects of stacking sequence on the hydroelastic performance of composite propeller blades is analysed for the first time. More recently and over the last ten years several papers have been published by Young and its co-authors [5-8] to address different issues regarding

numerical as well experimental analyses of flexible propellers and hydrofoil. For a comprehensive review on this topic see [9]

When using deformable materials, a two-way structural-hydrodynamic coupling must be considered and therefore fluid-structure interaction (FSI) models must be developed. The most common way to numerically analyse the problem is to couple Boundary Element with Finite Element, but it is demonstrated that to correctly model the complex fluid conditions around a propeller *i.e.* the turbulent ship wake, the boundary layer and the rudder propeller interaction it is necessary to consider fluid viscosity [5-10] .

Moreover, a propeller of a surface ship when rotates at high speed is affected by cavitation, the instability of the cavitation bubble consisting in the periodic growth and collapse generates high hydrodynamic load fluctuations, strong vibrations, fatigue, noise and erosion. Therefore, flexible composite propeller blade should be designed to reduce or avoid cavitation. The description of the complex phenomena associated with different kind of cavitation and their generation is outside the scope of this paper nevertheless, what has been observed numerically and experimentally is that, for a deformable propeller, cavitation inception is delayed and that the size of the cavitation bubble is smaller than for a rigid propeller operating at the same conditions [11].

However, the interaction between blade vibrations and cavitation bubbles should be studied in deep since instability effects such as those reported for hydrofoils could arise.

Experimental tests both at model and full scale have been performed to evaluate the performances of flexible composite propellers. Few model scale tests can be found in literature (for a comprehensive review see [9]), many are dedicated to the comparison between the performance of rigid and flexible propellers these last characterized by different construction solutions in terms of geometries and materials. Tests have been performed also in off-design conditions and in manoeuvres as for instance during cashback [9]. However, improvement in performance compared to the rigid model has not always been verified, the comparison with the reference rigid model does not always exist, the experimental results do not always confirm the numerical ones. Moreover, there is a total lack of structural experimental data, in fact tests are limited to measure hydrodynamic quantities.

It is important to underline that model scale tests have been performed on small size propeller ($D< 2$ m) therefore it is not clear if the results can be extended to full scale size propellers that typically have diameters up to 5-6 m. An attempt to provide scaling laws for the composite flexible blade including hydrodynamic, structural dynamic and cavitation can be found in [12]. Neglecting the effect of surface waves, yaw and shaft inclination angle, 12 structural and hydrodynamic variables affects the propeller performances therefore, 9 dimensionless parameters governing the phenomenon can be found. Among them the Froude, Reynolds and Mach similarities cannot be verified simultaneously unless the scale λ is equal to 1. The results of the comparison between different numerical simulations performed considering separately the above three similarities suggested that the Mach scaling is the most practical since it allows to use the same material for the model and the prototype which will make simpler the construction of a geometrically similar model that will have the same normalized 3D distribution of the structural mass, bending rigidity, torsional rigidity, and bending–torsional coupling rigidity. The use of Mach similarity implies also that the axial model scale velocity must be the same as that at full scale. The Mach similarity can be applied only if gravitational forces are negligible compared to hydrodynamic inertial force, rotor elastic force, rotor inertial force and if the speed is sufficiently high so that the flow is fully turbulent. Moreover, it is important to keep in mind that although the 3D load-deformation responses will be similar between the Mach-scaled model and the prototype, the detailed stresses and strains distributions, and potential material failure mechanisms, may be different because of differences in manufacturing which is an hard task especially at the root and at

the tip. It should be clear from the above that the trend is to develop numerical models for design and to use experimental model scale data for code validation only.

Some full-scale data exist but most of them being related to warships or submarines are classified.

For what concern structural modelling, Abrate [13] presented the mathematical and theoretical background necessary to understand the issues involved in the analysis of flexible composite marine propeller and a detailed analysis of the state of the art focusing on material design and modelling. He also pointed out a number of key issues concerning the structural design: *i)* as already stated, model scale experiments could not provide valuable information for full scale design, *ii)* for large propeller it would be better to use sandwich structures with core and spars, *iii)* the results of numerical simulations shown that better performances are achieved by considering a single anisotropic layer that provides the maximum elastic bending-twist coupling however, in this way, it is not possible to have a multidirectional stiffness that would be necessary to resist to hydrodynamic load, iv) as a consequence of the previous point, the strength analysis should be considered also during the preliminary design and *v)* the interlaminar stress concentrations due to the reduction of the number of plies necessary to achieve the desired variation of the thickness from the root to the tip of the blades can lead to delamination that shall be studied.

Another way to address this topic is to use smart materials to generate twist considering an adequate structural strength, among them shape memory alloys (SMAs) seem to be very effective for structural shape control due to the large strain (~6–8%) they can produce with the change in temperature. An application to marine propeller can be found in [14], the authors considered a full-scale propeller 4.2 m diameter, made of graphite-epoxy composite integrated with SMA actuators. They numerically evaluated the performances using a viscous flow model the results shown that the maximum hydrodynamic performance is achieved for a specific J when the twist is maxima. Finally, for what concern composite material damping, Hong et al. [15] proposed a hybrid methodology to investigate the effect of lamination parameters on the structural damping and the dynamic responses of the composite blade providing some suggestions about the possibility to reduce the vibrational response.

2.2 Ship response to extreme events

2.2.1 Global dynamic behavior: springing and whipping response

The dynamic response of ships to waves is indicated as linear springing when the natural frequencies of the ship (2-nodes bending mode) are close to the encounter wave frequency (around 0.1-0.3 Hz) leading to a resonance response. This phenomenon is particularly important for long and flexible ships, typically ultra-large containerships (ULCS), for which the first resonance frequencies are low and, consequently, of the order of the encounter frequency. Nonlinear springing occurs when the ship response is forced by multiples of the (encounter) peak wave excitation frequency. On the contrary, the structural response to transient excitations, such as those related to impulsive forces typically of severe sea states (slamming or green water) or to underwater explosions (UNDEX), is called whipping. The evaluation of the whipping and springing responses are important for the correct estimation of the fatigue life.

Both problems are dealt numerically and experimentally, with tests mainly used to provide validation of the numerical predictions than to give further insights into the physical phenomena, with few exceptions (multihulls, UNDEX, ULCS in oblique and following seas). Potential codes for the fluid loads coupled to FE or higher-order beam-like theories are still robust and efficient approaches compared to CFD-CSD massive approaches. Segmented models with elastic backspline scaling a significant subset of the structural properties, typically according to a modal description,

have reached the capability to catch the vibratory bending/torsional response of ships under different relative wave directions [16].

Over the last years, the need of increasing the fidelity of simulations for whipping and springing problems has prompt researchers to a particular attention regarding the evaluation of structural and hydrodynamic damping. This concern, along with a growing use of monitoring systems on-board, has motivated a full-scale analysis of ship damping. This implies the use of damping estimation techniques based on output-only measurements, or operational modal analysis (EFDD, BP-POD, SSI, TDIM etc). The high modal density and other issues still pose limits to identify uniquely the coefficients to be inserted in hydroelastic codes. To get a better insight into the problem, a combined use of full-scale and segmented model tests has been recently proposed. Model tests are performed in dry and wet conditions to evaluate the structural and global (hydrodynamic plus structural) modal damping [17]. The difference between the two values gives the added fluid damping. Assuming a linear behaviour, the Froude scaling allows the determination of the full scale added damping value that can be subtracted from full-scale damping measurements to finally identify the structural one.

2.2.2 Local dynamic response: impact problems

Slamming is the impulsive and randomly occurring load which usually involves the ship bow in head sea and, for some hull forms like cruise ships or some cargos, the aft part of the ship, due to the particular geometry of the stern, might occur. As previously discussed, due to its short-period duration and the high local pressures slamming excites the low-order global ship modes but, at the same time, is responsible for overloading the ship hull plating, frequently causing plastic deformations and visible damage. Numerical approaches have to address the two-phase fluid description (air entrapment between the hull panel the water affects the loads) and the coupling with the elastic structure, typically stiffened plates or composites. CFD-CSD simulations with partitioned approaches have received an increased attention, setting the coupling strategy between fluid and solid at the mid-point between accuracy and computational efficiency. Experimentally, much effort has been dedicated to the development of testing set-ups and measurement techniques where reproducibility of the test and material conditions in the codes is guaranteed. This has often implied structural assessment of the impact facilities.

The violent impact of liquid masses inside ship tanks is named sloshing, this phenomenon can be responsible for large deformations and serious structural damage. In the last decades sloshing has become a critical issue because of the increase number and size of LNG ships. The phenomenon is extremely complex from a physical point of view since it involves air cushion, liquid compressibility, hydroelasticity, aeration, thermal exchange [1,18]. All these phenomena are randomly combined so that experimental data obtained in nominal identical conditions show big scatter.

For a complete understanding of the phenomenon it would be necessary to solve the coupled liquid-gas and structural problem at the same time. However, most of the numerical and experimental effort is devoted to the evaluation of the extreme pressure on a rigid flat surface. This approach has several shortcomings since impact pressure is very localized both in space and in time therefore, its extreme value is not easy to be captured. Moreover, pressure peak does not provide the maximum structural response that highly depends on the fluid structure interaction characteristics.

The major limitation to a correct estimation of the structural damage is the lack of reference data [18]. Typical experimental tests involve laboratory experiments at small scale using the exapode to infer the desired motion. These tests can give a correct estimation with a high degree of repeatability of global quantities such as the hydrodynamic force but are not so significance for the

calculation of the pressure field since the Froude scaling does not apply when other physical phenomena occur (gas cushion, compressibility etc.). Moreover, as already stated, the repeatability of these tests is very low. The lack of scaling laws seems to be at the moment the most important problem to be solved. In [19] the scaling of the air cushion is addressed by considering not only the Froude similarity but also the Euler number similarity by decreasing pressure inside the test tank. In [20] the hydroelastic coupling for 2D flow is analysed by measuring impact pressure and strains over a flexible beam. As a final remark it is important to underline that, in laboratory experiments the side of the tank are represented by flat beams or plates while ship tanks present several geometrical discontinuities such as corrugation and raised edge to alleviate impact loads.

Full scale tests are extremely complex and expensive, the available data regards pressure measurements inside a container tank. As reported in [18] the quality of data is poor due to the inherent difficulties at measuring impact pressure moreover, the exact test conditions are uncertain. Data can be used just to provide information about the rate of occurrence of impacts. Large scale laboratory tests have been performed by drop tests or wave flume impacts. Results obtained within a EU project shown that quasi full scale tests are the best way to provide data for validation of the numerical models.

Concerning numerical methods, a preliminary seakeeping analysis is necessary to set the impact conditions. However, the definition of the simulation scenario is not an easy task implying multiple combinations of environmental and navigation condition calling for a non-deterministic analysis of the full problem. For the local analysis, CFD or potential flow theory is employed but till date only simplified analytical models have the possibility to incorporate hydroelastic effects. FEM is usually used to calculate the structural response. Numerical models are not yet at the state of the art and are not able to correctly simulate the nonlinear fluid-structural coupling.

3 UNDERWATER ROBOTICS

3.1 Biomimetic propulsion: the robotic fish

Over the last years underwater robotics has become an attractive topic for the scientific community due to the large number of applications in the field of marine engineering. Unmanned Underwater Vehicles (AUV) are used for both civilian and military purposes to perform missions that cannot be easily done by other marine vehicles or by humans because of the harsh environment (chemical pollution, possible underwater explosion etc.) or because they involve risky operations such as the monitoring and maintenance of submerged structures, inspection inside pipes or other narrow mechanical components. Moreover, if designed to mimicking biological systems, AUVs can offer stealth (invisibility and silence) in maritime surveillance operations. AUVs are frequently used also for scientific purposes such as environmental and biological monitoring and observations. Since each mission requires specific capabilities, ad hoc design is needed to meet the precise requirements. The development and the construction of bioinspired AUVs takes advantages from the recent fast development in soft and cooperative robotics, actuation, control and new materials [21,22].

With the intention of mimicking their swimming mode, fish locomotion has been deeply studied to understand their unique capacity at moving at high speed with low energy and at easily manoeuvring. Of the 30.000 known species of fish, most use undulatory swimming as the main mode of locomotion. Among them we can distinguish between those characterized by an aspect ratio of 10 or more with a cross section that vary moderately along the length (eel-like swimmers) and the salmon-like or tuna-like swimmers that have typically an aspect ratio of 5, a large and streamlined anterior region which accounts for the most part of the mass and are separated by a caudal fin from a caudal peduncle of reduced cross section. The former generated thrust by the bending of the whole body, the latter by propagating a bending wave through the caudal fin [23,24].

For a comprehensive analysis of hydromechanics of different fish propulsion one can refer to Lighthill work [24].

Notwithstanding the large number of scientific papers devoted to the modelling of kinematics, dynamics, hydrodynamic, actuation, control and material design, these robotic fishes still do not compete with their biological counterparts in terms of swimming abilities. As reported in [22], the maximum velocity reached till date with a robotic fish is 3.7 m/s whereas the maximum speed of a swordfish is 27 m/s. Anyhow, robotic fishes usually move with speeds lower than 1 m/s and their manoeuvring capability is very low.

Most of the engineering applications regard the salmon/tuna-like swimmers because, as highlighted in [4], are more efficient and can swim at high speed (20 m/s or more depending on their morphological characteristics). In line with the above considerations, the body is assumed rigid and the caudal fin that oscillates laterally with respect to the horizontal fish axis is partially rigid and partially flexible.

The hydrodynamic field are solved either by analytical or numerical CFD models being the former preferred because they can give real time responses. Starting from the papers of Lighthill [23, 25, 26, 27] who first provided mathematical models for the definition of the inertia force and thrust in the case of small and large oscillations, and of Wu [28,29] with its *waving plate* theory, little has been done. These models are based on inviscid 2D flow theory valid for enough high Reynolds number value. Lighthill models are based on the slender body theory, thrust is obtained by simple energetic considerations as a result of the reactive force generated by the fast acceleration of the virtual fluid mass produced by the lateral fish motion. Wu translated the aeroelastic models for flexible oscillating wings to the fish propulsion. In both cases the wake is considered frozen thus, translating with a constant velocity. More recently in [30, 31], the Morison equation and experimental tests are used to derive the inertia and the drag force generated by the oscillation of the fish tail modelled as a Euler Bernoulli beam with different cross sections. The model provides the deflection of the tail end that is used to calculate thrust through Lighthill analytical expressions. Results are validated by experimental data relative to static thrust measurements performed varying the tail oscillation frequency. Static thrust can be considered a good approximation of the dynamic one for small velocity. Validation of the tail displacement amplitude is performed with data obtained by free running experiments once added mass and damping coefficients have been corrected by the results of static experimental data. This semi-empirical model considers viscous effects but neglects the vortex generation. Numerical simulations and flow visualization [32] have shown the importance of an accurate modelling of the vortex wake which is nonstationary and 3D. In [32] vortex control is presented as a fruitful way to optimize the efficiency of robotic fishes.

Fish structure is modelled by lumped parameter models or by continuous models, the Euler-Bernoulli beam is used in [30,31] but some attempts at considering more complex models such as the Timoshenko beam have been made [33].

Passive flexible materials have shown limitation at mimicking the exact fish motion therefore one of the ways to improve the efficiency of the robots is to use actively actuated flexible materials [22]. Moreover, some first attempts at evaluating the optimum shape of the robotic fish based on simple hydrodynamic considerations have been made by Lighthill [26]. More recently Eloy [24] using evolutionary algorithms performed the optimization of the whole fish body maximizing speed and efficiency. Finally, in [34] multi objective optimization is applied to identify the best design for the caudal fin considering the material stiffness and using the Lighthill large displacement elongated theory.

From this picture it is evident that improving robotic fish performances is still an open challenge. The first bottleneck regards hydrodynamic and fluid structure interaction modelling that should consider more sophisticated models able to include correctly the vortex shedding process, viscous effects and nonlinearities. CFD can provide useful information that must be used to enhance

the predictivity of simplified, low time-consuming models necessary to perform optimization and control. The role of innovative smart material is a key issue for this kind of applications.

4 OFFSHORE STRUCTURES

4.1 Dynamic response of marine risers

A marine riser is used in the subsea oil and gas industry as a conductor between the seabed and the offshore platform or vessel. The analysis of its fatigue life and its response to particularly severe sea and wind conditions represents a major issue for marine engineering to avoid sudden failure that can be catastrophic for the marine environment.

A marine riser operates in a severe environment due to the continuous loading generated by currents and waves. Currents affect directly the riser dynamics whereas waves excite the support platform/vessel that transmits forces to the riser. Another important issue to be considered, even if rarely included in the analyses, is the internal fluid effect affecting the riser tension.

Depending on the assumptions made on sea state and current conditions, hydrodynamic loads can be treated as deterministic or random. Anyhow, one of the major issues in the most recent technical literature is to consider the stochastic nature of the problem due to several inherent hydrodynamic [35] and structural [36] uncertainties (flow velocity and profile along the span, riser configuration/position, fouling altering the mass of the risers, corrosion altering the stiffness, inhomogeneity of material, manufacturing, connection joints, surface finish etc.).

The fundamental physics beneath currents and riser interaction which generates one of the most relevant and popular hydroelastic coupled problem in ocean engineering, arises from the fact that a bluff body – in this case a cylinder- placed in a current, generates a vortex wake that is unstable due to flow instabilities and riser movement. Insights into the characteristic of the vortex shedding process that depends upon the Reynolds number $Re = UD/\nu$ where U is the current velocity , D is the riser diameter and ν is the kinematic viscosity of the fluid, can be found in the early review of Govhardan [37] and Bearman [38]. The shed vortices exert periodic forces in in-line and crossflow directions which cause the riser to vibrate. The amplitude and characteristics of the vibrational response depend on many factors, including the level of structural damping, the relative mass of the body to the displaced water mass (the so-called “mass ratio”), the aspect ratio, the magnitude of the fluid forces, and the proximity of the vortex shedding frequency to the natural frequencies of vibration of the body [39]. In particular, when the vortex shedding frequency $f=StU/D$, where St is the Strouhal number, is close to a natural frequency of the riser the lock-in can occurs characterized by large amplitude resonance response. To note that due to the vortex shedding process the added mass can change in time therefore, the lock-in can occur at frequencies that are different to those predicted in calm water condition. Moreover, added damping increases with increasing amplitude of oscillation moderating VIV amplitude [39].

After more than fifty years of research on this topic conducted theoretically, numerically and experimentally by means of laboratory and field tests [35,40], much is known about Vortex Induced Vibration (VIV) of short risers for which prediction methods are quite consolidated. On the contrary, the features of VIV in long flexible and slender risers remains not fully understood [41].

The main difference between risers characterized by a low aspect ratio compared to long risers is the possibility for the latter to exhibit multimodal response. In fact, long slender cylinders are exposed to shear or other non-uniform flows across the length, so that different modes can be simultaneously excited at different locations in three dimensions. Thus, under a non-uniform flow, different modes can be involved in the lock-in response. As reported in [41], experimental tests shown that, for long slender cylinders in a shear flow, the response during the lock-in is not stationary, often presents non-lock-in behaviour or can alternate from the lock-in to the non-lock-in

form. In the case of non-lock-in response the spectrum exhibits a peak at the shedding frequency but with a broader bandwidth encompassing the nearest natural frequencies. The total root mean square (RMS) responses in the non-lock-in case were remarkably lower than those in single mode lock-in cases.

Another peculiarity of long slender cylinder is the coexistence of standing and travelling waves and the combination of the two. For short riser the standing wave behaviour is the dominant mode. On the contrary, when a travelling wave reaches the riser ends the reflection generates a standing wave which however attenuate very quickly with the distance from the end. Therefore, a mixed standing-travelling mode is simultaneously observed but since standing wave quickly disappears the response of very long risers is generally characterized by travelling waves only. Strain measurements shown that the peak is in the travelling wave region instead of close to the riser ends i.e. in the standing wave region.

Moreover, when the ratio between the natural frequencies of the IL and CF excited modes is equal to the excitation frequency ratio *i.e.* the ratio of the IL excitation frequency to the CF, the IL and CF motions resonate simultaneously. Some experiments have shown that dual resonance is characterized by highly repeatable orbits, a steady phase difference between IL and CF vibrations, and a high to third harmonic in the lift force.

Model scale tests are a valuable tool to understand the physics of the problem even if suffer of some limitations related to the complexity of the experimental setup, to the relatively small aspect ratio with respect to the full scale problem and to the impossibility to reproduce the real flow conditions (Reynolds number and current profile). On the other side, full scale tests are expensive extremely complex and test condition cannot be under control as a consequence, full scale data are almost absent.

The hydrodynamic loads are modelled using:

- Semi empirical methods based on simplified expression and hydrodynamic coefficient (lift, drag added mass and damping etc.) databases collected from many experimental tests generally performed on rigid cylinders;
- low order methods such as the powerful wake oscillator model that represents the time varying forces generated by the wake using the nonlinear Van der pol oscillator [42,43]. A general characteristic common to all wake oscillator models is the choice of a representative wake quantity. However, differences exist in the assumed mechanisms through which this variable is coupled with the body motion [44]. The original Kernel of the Van der pol oscillator has been reinterpreted to represent the 3D wake effect. In this case oscillators are distributed along the spanwise extent of the structures. These models can capture at least qualitatively the main features of VIV [45].
- CFD simulations based on Direct Numerical Simulations (DNS), Reynolds Averaged Navier Stokes (RANS), Large Eddy Simulations (LES), Detached Eddy Simulations (DES) and Discrete Vortex Method (DVM). The obvious limitation is related to the computational time needed at high Re.

These models are coupled with structural models that , depending on the simplifications made, can be simply spring-mass systems or a continuous system usually modelled as an Euler Bernoulli beam which response is calculated by FEM most likely in the time domain to account for nonlinearities.

In 2005 Chaplin et al. [46] proposed a benchmark study to test the validity of different codes and methods (5 semiempirical codes, 5 CFD codes and 1 wake oscillator model) at evaluating the IL and CF response of a 13 m riser in a stepped current, comparing the results to strain measurements performed in a flume. The analysis shown that CF motion is better predicted by semiempirical codes than by CFD whereas the wake oscillator model gives very conservative results. None of the

semiempirical codes were able to calculate the IL curvature and CFD results are affected by a large error.

VIV control is traditionally performed by passive methods such as fairings and strakes and more recently by active strategies by controlling the displacement of the riser ends. Both methods have large shortcomings, strakes to be efficacy should cover a large part of the riser surface, which is a very expensive operation on the contrary, active control is not efficacy as far as depth increases. A hybrid control with active systems at different locations, reducing the density of strakes could be the best strategy.

5 CONCLUDING REMARKS

In this paper some open challenges for structural dynamics in the field of maritime transportation, offshore engineering and marine robotics have been presented. All the analysed problems involve a strong fluid structural coupling that is usually nonlinear. Some common numerical and experimental modelling gaps can be identified:

- the characteristics of the structure-fluid interaction are not completely understood;
- the analysis of the hydroelastic interaction using full numerical approaches (CFD-CSD) is still unfeasible or not enough robust and efficient: there is a strong need for mathematical models;
- model scale tests are not always able to provide useful information for the full-scale problem because it is not possible to replicate the real conditions with the related uncertainty and/or because scaling laws are not available;
- full scale tests are extremely complex and expensive and test conditions are not controllable.

On the other side, some common research trends emerged:

- the development and application of multidisciplinary optimization algorithms that are fundamental to provide innovative and enhanced design solutions;
- the implementation of nondeterministic analyses to account for flow and structural uncertainties;
- the use of the characteristics of the structural-fluid coupling to develop different and nonstandard control strategies based on flow, structural or hybrid control;
- the use of innovative smart materials;
- the design of new research facilities, innovative model scale experimental setup and full-scale experimental campaigns.

REFERENCES

[1] Final Report of the Dynamic Response Committee. Proceedings of the 20th Internal Ships and Offshore Structures Congress-ISSC 2018.

[2] E. Ciappi, F. Magionesi, S. De Rosa and F. Franco. Hydrodynamic and hydroelastic analyses of a plate excited by the turbulent boundary layer. Journal of Fluids and Structures. 25(2): 321-342, 2009.

[3] F. Veronesi, M. Raimondo, G. Boveri, E. Ciappi, C. Nicolai, F. La Gala, A. Conforti, and F. Sajeva. Attenuation of turbulent boundary layer induced vibration using water-repellent coatings. NOVEM 2018. Ibiza, Spain, 2018.

[4] H. Lin, and J. Lin. Effect of Stacking Sequence on the Hydroelastic Behavior of Composite Propeller Blades. 11th International Conference on Composite Materials, Australian Composite Structures Society. Gold Coast, Australia, 1997.

[5] Y.L. Young. Fluid-Structure Interaction Analysis of Flexible Composite Marine Propellers. Journal of Fluids and Structures. 24: 799-818, 2008.

[6] M.R. Motley, Z. Liu and Y.L. Young. Utilizing Fluid–Structure Interactions to Improve Energy Efficiency of Composite Marine Propellers in Spatially Varying Wake. Composite Structures. 90: 304-313, 2009.

[7] Z. Liu and Y.L. Young. Utilization of Bending-Twisting Coupling Effects for Performance Enhancement of Composite Marine Propellers. Journal Fluids and Structure. 25(6): 1102–1116, 2009.

[8] Y.L. Young, J.W. Baker and M.R. Motley. Reliability-Based Design and Optimization of Adaptive Marine Structures. Composite Structures. 92: 244-253, 2010.

[9] Y. L. Young, M. R. Motley, R. Barber, E. J. Chae and N. Garg. Adaptive Composite Marine Propulsors and Turbines: Progress and Challenges. ASME. Appl. Mech. Rev. 68(6): 1-34, 2016

[10] P. J. Maljaars, M. L. Kaminski. Hydro-elastic Analysis of Flexible Propellers: An Overview. Fourth International Symposium on Marine Propulsors smp'15, Austin, Texas, USA, 2015

[11] Z. Huang, Y. Xiong and G. Yang. Fluid-structure Hydroelastic Analysis and Hydrodynamic Cavitation Experiments of Composite Propeller. Proceedings of the Twenty-sixth (2016) International Ocean and Polar Engineering Conference. Rhodes, Greece, 2016

[12] Y.L. Young. Dynamic hydroelastic scaling of self-adaptive composite marine rotors. Composite Structures 92: 97-106, 2010.

[13] S. Abrate. Dynamic behavior of composite marine propeller blades. Editor(s): Valentina Lopresto, Antonio Langella, Serge Abrate, Dynamic Response and Failure of Composite Materials and Structures, Woodhead Publishing, 2017.

[14] S. Kapuria, H.N. Das. Improving hydrodynamic efficiency of composite marine propellers in off-design conditions using shape memory alloy composite actuators. Ocean Engineering. 168: 185-203, 2018.

[15] Y. Hong, X.D. He, R.G. Wang. Vibration and damping analysis of a composite blade. Materials and Design. 34, 98–105, 2012.

[16] D. Dessi, E. Faiella, J. Geiser, E. Alley and J. Dukes. Design and structural testing of a physical model for wetdeck slamming analysis. 6th International Conference on Marine Structures. Lisbon, Portugal, 2017.

[17] D. Dessi, E. Faiella and F. Riccioli. A Procedure for the Identification of Hydrodynamic Damping Associated to Elastic Modes. 14th International Symposium on Practical Design for Ships and other Floating StructuresYokohama, Japan, 2019.

[18] S. Malenica, L. Diebold, S. H. Kwon and D. Cho. Sloshing assessment of the LNG floating units with membrane type containment system where we are? Marine Structures.56: 99-116, 2017.

[19] C Lugni, A Bardazzi, OM Faltinsen and G Graziani. Hydroelastic slamming response in the evolution of a flip-through event during shallow-liquid sloshing. Physics of Fluids.26 (3), 2014.

[20] C Lugni, M Miozzi, M Brocchini, OM Faltinsen. Evolution of the air cavity during a depressurized wave impact. I. The kinematic flow field. Physics of Fluids. 22 (5), 2010.

[21] D. Rus and M. Tolley. Design, fabrication and control of soft robots. Nature. 521:467–475, 2015.

[22] P. Duraisamy, R. Kumar Sidharthan and M. Nagarajan Santhanakrishnan. Design, Modeling, and Control of Biomimetic Fish Robot: A Review. J Bionic Engineering. 16: 967–993, 2019.

[23] J. Lighthill. Hydromecanics of aquatic animal propulsion. Annual Review of Fluid Mechanics.1:413–45, 1969.

[24] C. Eloy. On the best design for undulatory swimming. J. Fluid Mechanics. 717: 48–89, 2013.

[25] M. Lighthill. Note on the swimming of slender fish. Journal of Fluid Mechanics. 9(2): 305-317, 1960.

[26] M. Lighthill. Aquatic animal propulsion of high hydromechanical efficiency. Journal of Fluid Mechanics. 44(2): 265-301, 1970.

[27] M. Lighthill. Large-amplitude elongated-body theory of fish locomotion. Proc. R. Soc. London B. 179:125–38, 1971.

[28] T. Wu. Swimming of a waving plate. Journal of Fluid Mechanics. 10: 321–44, 1961.

[29] T. Wu. Hydromechanics of swimming propulsion. Part 1. Swimming of a two-dimensional flexible plate at variable forward speeds in an inviscid fluid. Journal of Fluid Mechanics. 46: 337–55, 1971.

[30] V. Kopman and M. Porfiri. Design, modeling, and characterization of a miniature robotic fish for research and education in biomimetics and bioinspiration. ASME Transaction on Mechatronics. 18 : 471-483, 2013.

[31] V. Kopman, J. Launt, M. Porfiri, F. Acquaviva and A. Rizzo. Dynamic Modeling of a Robotic Fish Propelled by a Compliant Tail. IEEE Journal of Oceanic Engineering.40:209-221, 2015.

[32] M.S. Triantafyllou, G. S. Triantafyllou and D. K. P. Triantafyllou. Hydrodynamics of Fishlike Swimming. Annual Review of Fluid Mechanics. 32:33-53, 2000.

[33] Ganesh Govindarajan, R. Sharma and P. Ananthakrishnan. Development of a numerical approach for the prediction of thrust generated by a biomimetic propulsion system. Ships and Offshore Structures. 14(8): 804-817, 2019.

[34] A. J. Clark, X. Tan and P.K. McKinley. Evolutionary multiobjective design of a flexible caudal fin for robotic fish. Bioinspiration and Biomimetics. 10:1-17, 2015.

[35] K. Hong and U. H. Shah. Vortex-induced vibrations and control of marine risers: A review. Ocean Engineering. 152: 300-315, 2018.

[36] P. Ni, J. Li, H. Hao and Y. Xia. Stochastic dynamic analysis of marine risers considering Gaussian system uncertainties. Journal of Sound and Vibration. 416: 224-243, 2018.

[37] C.H.K.Williamson and R. Govardhan. Vortex-induced vibrations. Annu. Rev. Fluid Mech. 36:413–55, 2004.

[38] P. W. Bearman. Vortex shedding from oscillating bluff bodies. Ann. Rev. Fluid Mech. 16: 195-222, 1984.

[39] H. Lie, E. Ciappi et al. Report of the Specialist Committee of Vortex Induced Vibration of the 25th Towing Tank Conference. Fukuoka , Japan, 2008.

[40] G. Liu, H. Li, Z. Qiu, D. Leng, Z. Li and W. Li. A mini review of recent progress on vortex-induced vibrations of marine risers. Ocean Engineering, 2019 (in press).

[41] Z. Chen and S. H. Rhee. Effect of traveling wave on the vortex-induced vibration of a long flexible pipe. Applied Ocean Research. 84:122-132, 2019.

[42] G. Birkoff and E.H. Zarantanello. Jets, wakes and cavities. Academic Press, NewYork, 1957.

[43] R. Bishop and A.Y. Hassan. The lift and the drag forces on a circular cylinder oscillating in a flowing fluid. Proc Roy Soc London – Series A. 277:51–75,1964.

[44] M.L. Facchinetti, E. de Langre and F. Biolley. Coupling of structure and wake oscillators in vortex induced vibrations. J Fluids and Structures. 19: 123–40, 2004.

[45] V. Kurushina and E. Pavlovskaia. Wake oscillator equations in modelling vortex-induced vibrations at low mass ratios. OCEANS 2017-Aberdeen, 2017.

[46] J.R. Chaplin, P.W. Bearman, Y. Cheng, E. Fontaine, J.M.R. Graham, K. Herfjord, F.J. Huera Huarte, M. Isherwood, M., K. Lambrakos, C.M. Larsen, J.R. Meneghini, G. Moe, R.J. Pattenden, M.S. Triantafyllou and R.H.J. Willden. Blind Predictions of Laboratory Measurements of Vortex-Induced Vibrations of a Tension Riser. Journal of Fluids and Structures. 21:25-40, 2005.

ASSESSMENT OF COMPUTATIONAL MODELS FOR THE DYNAMIC RESPONSE OF ROTATING COMPOSITE TURBINE BLADES

E. Carrera[1] , M. Filippi[1], D. Giusa[1], A. Pagani[1] and E. Zappino[1]

[1]Mul[2] Group, Department of Mechanical and Aerospace Engineering
Politecnico di Torino, Turin, ITALY
Email: erasmo.carrera@polito.it, matteo.filippi@polito.it, daniel.giusa@studenti.polito.it,
alfonso.pagani@polito.it, enrico.zappino@polito.it

ABSTRACT

The comparison between different structural models for the analyses of a composite rotating plate is discussed in this work. The mathematical methodology, that is based on the one-dimensional (1D) Carrera Unified Formulation, enables to express the governing equations and related finite element arrays as independent of the theory approximation order. The main objective is to demonstrate that CUF-based models, although they are 1D, can provide efficient and accurate results, both in terms of vibration analysis and 3D stress states characterization. Particular attention is focused on composite laminated materials, which are well combined with the proposed formulation to study the effect of the stacking sequence on mode aberration of rotating plates and shells.

1 INTRODUCTION

Composite materials are replacing titanium in the manufacture of fan blades due their higher strength and stiffness, at the same density, which leads to an important weight reduction. Moreover composite blades are subjected to lower centrifugal loads and stresses due to less mass translation. For this reason the interest in this types of blades is growing, making necessary new studies about their static and dynamic behavior in different conditions. Representing thin walled blades as a beam in highly inaccurate because the classical beam models cannot foresee many 3D effects which occur due to rotation. Leissa et al. [1, 2] overcome this problem analyzing thin blades by means of shell formulations and they were the first to analyze the vibrations characteristics of rotating structures by the same method. The present work, which makes use of the Carrera Unified Formulation (CUF), which is a hierarchical formulation of theories of structures, wants to highlight the effect of the theory approximation order on the vibration characteristics of composite rotating plates and shells.
CUF for one-dimensional elements (1D) expresses the displacement field $\mathbf{u}^T = [u_x\, u_y\, u_z]$ as an arbitrary expansions of cross-sectional functions $F_\tau(x, z)$ and the generalized displacements $u_\tau(y, t)$, which lay along the beam axis y. If the finite element method is adopted, the generalized displacements are approximated using the shape functions, $N_i(y)$, and the vector of nodal displacement $\mathbf{q}_{\tau i}(t)$. Therefore the displacement field is being approximated as:

$$\mathbf{u} = F_\tau(x, z) N_i \mathbf{q}_{\tau i}(t) \quad \tau = 1, ..., M \quad i = 1, ..., N_{nodes} \tag{1}$$

the number of elements nodes are N_{nodes}, τ is related to the expansion used for defining the cross-sectional kinematics and its maximum value, M, is an input parameter of the analysis. Moreover the parameter M defines the polynomial order for the Taylor-type models, named TEM. In case of Lagrange-type CUF models (LE) the beam kinematics is obtained as combination of Lagrange polynomials that are defined within sub-regions (or elements) delimited by arbitrary numbers of points (or nodes).
In the case of rotating structures, the virtual work done by the inertial forces, $\mathbf{F}_I$, is:

$$\delta L_{ine} = \int_V \delta \mathbf{u}^T \mathbf{F}_I \, dV \tag{2}$$

Velocities $\dot{\mathbf{u}}$ and accelerations $\ddot{\mathbf{u}}$ are expressed with respect to a coordinate reference frame attached to the blade that rotates at constant speed Ω. Accordingly, the inertial forces are:

$$\mathbf{F}_I = -\rho \begin{pmatrix} \ddot{u}_x \\ \ddot{u}_y \\ \ddot{u}_z \end{pmatrix} - 2\rho\Omega \begin{pmatrix} -\dot{u}_y \\ \dot{u}_x \\ 0 \end{pmatrix} + \rho\Omega^2 \begin{pmatrix} u_x \\ u_y \\ 0 \end{pmatrix} + \rho\Omega^2 \begin{pmatrix} x_e \\ y_e \\ 0 \end{pmatrix} \tag{3}$$

The vector $\mathbf{r} = [x_e, y_e, 0]$ defines the distance of a generic point with respect to the rotational axis. By substituting Equation (3) into Equation (2), the fundamental nuclei of the mass $\mathbf{M}^{ij\tau s}$, Coriolis $\mathbf{G}^{ij\tau s}$, centrifugal $\mathbf{K}^{ij\tau s}$ matrices, and the centrifugal forces vector $\mathbf{F}_\Omega^{js}$ can be obtained with ease [1]. The natural frequencies (ω) and eigenvectors ($\bar{\mathbf{u}}$) associated with small-amplitude vibrations are obtained by assuming an harmonic solutions ($\mathbf{u} = \bar{\mathbf{u}} e^{\sqrt{-1}\omega t}$) for the following homogeneous equation that is solved through the state-space transformation technique:

$$\mathbf{M}\ddot{\mathbf{u}} + \mathbf{G}\dot{\mathbf{u}} + (\mathbf{K}_0 + \Omega^2 \mathbf{K}_\sigma + \mathbf{K}_\Omega)\mathbf{u} = 0 \tag{4}$$

where $\mathbf{K_0}$ and $\mathbf{K}_\sigma$ are respectively the stiffness and the geometric stiffness matrices. is CUF has been widely employed in the recent literature for the analysis of composite structures [2]; Filippi et al. [1] studied natural frequencies an isotropic cantilever fan blades, via CUF formulation, with a linear and nonlinear approach. In this work, a number of representative examples are studied, including two- and three-layer composite rotating shells. Free vibration analysis are performed and the influence of the rotation speed on the modal characteristics are highlited.

2 NUMERICAL RESULTS

For the purposes of determining the difference between the TEM models with different polynomial orders, M, and LE models, a curved shell was considered. The geometrical features are described in Figure 1, where $L = b = 30{,}5\,\mathrm{cm}$, $t = L/100$ and $R_x = 2b$. Different lamination configurations were analyzed to show the effect of the structure anisotropy (material properties are shown in Table 1).

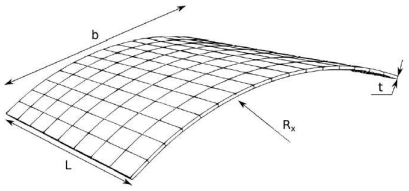

Figure 1. Sketch of fan blades

Graphite/epoxy					
E_L	E_z	G_{Lz}	ν_{Lz}	ν_{xz}	ρ
GPa	GPa	GPa	a	a	Kg/m^3
181	10.3	7.17	0.28	0.33	1600

Table 1. Material properties

2.1 Natural frequencies and modal shapes

Histograms in Figure 2 show difference in terms of natural frequencies between the various models, considering the same modal shapes among the first six modes of the structure (modes with out-of-scale frequencies are not completely displayed in the histograms). Comparing the results with the reference case LE9, only TE5 and TE6 models provide similar frequencies and comparable modal shapes. Frequencies for TE4 models are slightly different and in some cases there are no modal shapes to compare. For TE3, a satisfactory degree of accuracy is found only for the first computed frequency, which is always the first torsional one, but comparing the modes at higher frequencies shows a greater discrepancy between the values of the frequencies. The poor accuracy of models TE1 and TE2 is evident, even for low frequency modes. Furthermore, the computed modes similar to those of more refined models are lower in number, highlighting the poor ability of these models to describe the correct behavior of the structure. Finally, EULE and FSDT models are able to compute natural frequencies of only bending modes with an acceptable accuracy.
Differences between configurations with various fibers lamination angles have been studied through

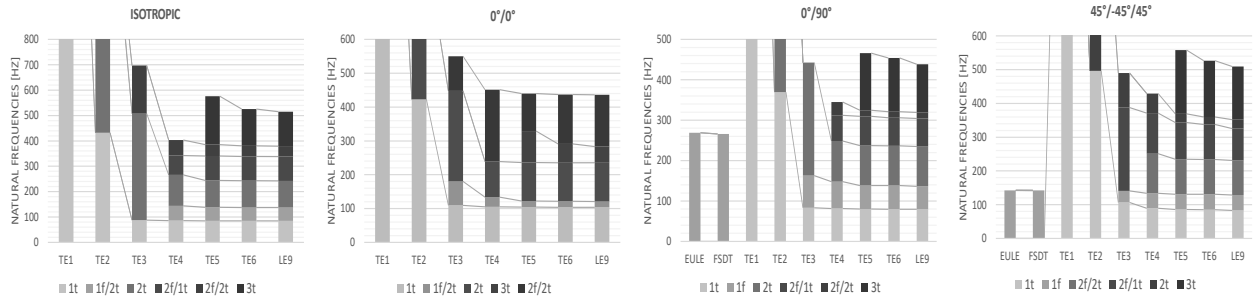

Figure 2: Comparison of the frequencies between Taylor-type and Lagrange-type models at different fibers lamination angles

the MAC analysis. MAC values have been plotted in graphic matrices shown in Figure 3. They show a low similarity between the various modal shapes for the different configurations, in most cases the MAC value is very different from the unit. Figure 4 show the six frequencies as functions of the rotational speed computed using Lagrange model. To enable the comparison with the results presented in Reference [1], the circular frequencies (ω) and the speed have been reported in nondimensional forms such that $\omega_n^* = \omega_n(\sqrt{12\rho L^4(1-\nu^2)/Et^2})$ and $\Omega^* = \Omega/\omega_1$, where ω_1 is the natural frequency.

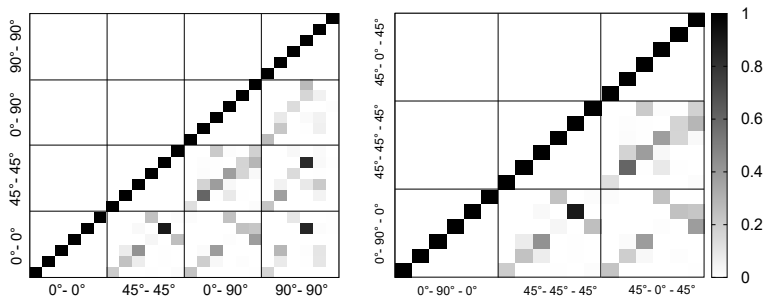

Figure 3. MAC between different configurations - Models LE9

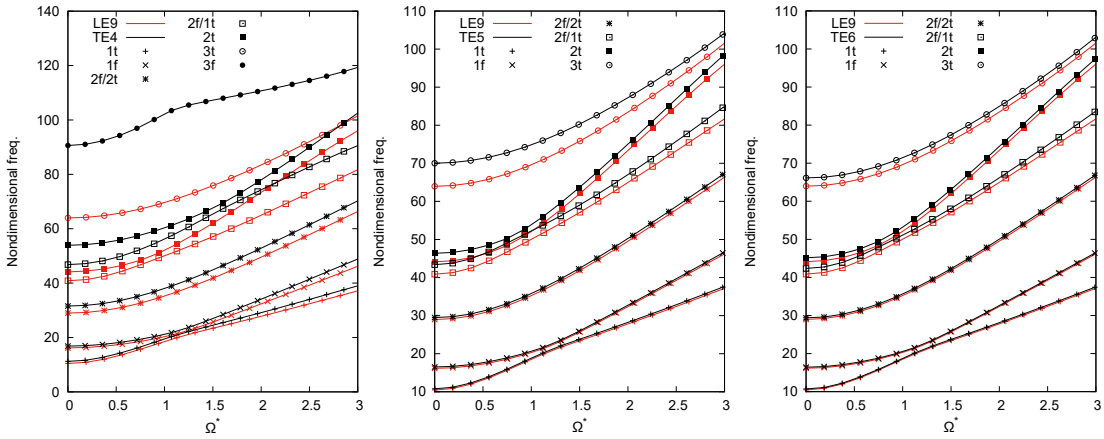

Figure 4. Frequency evolutions versus the rotational speed for $[45°/-45°/45°]$ configuration

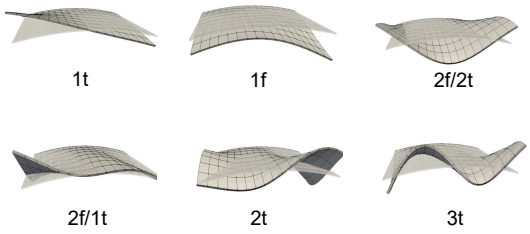

Figure 5. Modal shapes for LE9 model for $[45°/-45°/45°]$ configuration

3 CONCLUSIONS

Vibration analysis and mode aberration of a rotating composite shell have been discussed in this paper. For this purpose, the 1D Carrera Unified Formulation (CUF) has been used succesfully. According to CUF, the governing equations can be tuned opportunely according to the problem complexity and the available computer power. We have demonstrated that fundamental modes can be foreseen by simple lower-order CUF models. Instead, shell-like and higher-frequancy modes request for a more refined analysis, e.g. LE, especially when high anisotropic lamination sequences are employed.

REFERENCES

[1] M. Filippi, A. Pagani, and E. Carrera. Accurate nonlinear dynamics and mode aberration of rotating blades. *Journal of Applied Mechanics*, 85(11):111004, 2018.

[2] A. Pagani, AG De Miguel, M. Petrolo, and E. Carrera. Analysis of laminated beams via unified formulation and legendre polynomial expansions. *Composite Structures*, 156:78–92, 2016.

SYSTEM DYNAMICS IMPROVEMENT WITH STATE-OF-THE-ART MECHATRONICS – POTENTIALS AND CHALLENGES

J. Jungblut, A. Viehmann, P. Jardin and S. Rinderknecht

Mechatronic Systems in Mechanical Engineering
Technische Universität Darmstadt, Darmstadt, GERMANY
Email: rinderknecht@ims.tu-darmstadt.de

ABSTRACT

Throughout the increasing ambition to optimize a mechanical system in respect to its weight and efficiency to match environmental requirements, the systems tend to be more sensitive to vibrations. These cause undesired audible noise, which can be countered by implementing passive components such as dampers. These on the other hand lead to a decrease in efficiency and an increase in mass. Mechatronic systems open up a new design space, which have the potential to partially resolve the compromise between efficiency, weight and the noise-vibration-harshness (NVH) behaviour. However, this potential also comprises several challenges, which have to be mastered. Three different topics will be addressed in this talk.

The first one is the active vibration control of narrow banded vibrations, where two systems are discussed. The first system is an active piezoelectric bearing where the actuators are placed in the load path. Piezoelectric actuators are well suited for this task because of their high stiffness. Classic control algorithms can be applied to achieve a decent vibration reduction. However, under consideration of system knowledge, control algorithms can be designed which show a better performance than the classic approaches without requiring a model. The second system is a planetary gearbox where piezoelectric inertial mass actuators are used to reduce vibrations. A model free control is implemented which can only be implemented with the knowledge of the excitation behaviour.

The second challenge focuses on jerking in powertrains of pure electric and hybrid electric vehicles with two electric motors. The use of two electric motors offers a broad variety of operational modes, which allows an efficient operation of each motor. For high comfort gear shifts without interruption of traction force, torque blending between the two electric motors is necessary. If the torque at the driveshaft is not kept constant, jerking occurs which is uncomfortable for the vehicle passengers. The minimization of unpleasant jerking throughout control of the electric motors is the second topic to be addressed.

Third, new arising methods throughout digitalization, which may lead to a transformation of classic mechatronics, are discussed. That is done with the example application of hybrid dynamic system modelling approach where traditional physical modelling is used in combination with machine learning algorithms. From our perspective, the additional usage of available system knowledge in these hybrid models will outerperform models which are solely based on big data approaches. That is because synergies between both worlds are used in such way, that the overall system performance is improved.

1 INTRODUCTION

Industrial applications offer a broad variety of mechanical structures and requirements. Lightweight structures move more and more in the focus because of rising CO_2 requirements. The reduction of mass yields a more efficient system but worsens the noise-vibration-harshness (NVH) behaviour because the structures become more sensitive to vibrations. Passive measures might be taken to improve the NVH behaviour, but they will also increase the mass and reduce the efficiency. Mechatronic systems open a new design space and offer a big potential. They can reduce vibrations efficiently and improve the system dynamics. However, these systems are associated with higher overall costs. Thus there is always a conflict between efficiency, costs and the NVH behaviour. Several challenges have to be mastered in order to obtain a well designed mechatronic system. Standard approaches can yield good results for a broad range of applications but take much effort to be implemented. Whereas, system specific solutions might require less effort and still score better results than the standard approaches. This paper presents a short summary of the research results of the Institute for Mechatronic Systems in Mechanical Engineering of the TU Darmstadt. The focus of this paper lies on the use of system knowledge to design an efficient system which might not be obtained by standard approaches. The paper is organised as followed. First, the active control of rotors with piezoelectric bearings and of planetary gearboxes with piezoelectric inertial mass actuators will be presented. Afterwards, the control of jerking in drivetrains will be discussed. Last, a hybrid modelling approach comprising machine learning is discussed.

2 ACTIVE VIBRATION CONTROL OF NARROW-BAND VIBRATION

Many technical applications comprise rotary machinery, where vibrations are often caused by gear meshing and unbalance excitation. The resulting noise can be attenuated by the application of a passive system or the use of an active system. Actuators in combination with a suited control algorithm are implemented in the latter case. In most cases, standard control algorithms like robust H_∞ and optimal LQR control are used for controller design, which requires a model of the system. Thus, the application of the control system often presuppose expert knowledge in the modelling of systems and control theory.

Two examples will be shown where a complex modelling and control design process is prevented by the consideration of system knowledge. The first step of applying an active control system is the placement of the actuator, where two general options are available. The actuators can be either placed within the load path or outside of it. One application for each approach is given in the following two sections.

2.1 Active bearings for rotors

Active bearings are one example for a placement of the actuator within the load path. These aim to reduce vibrations directly at the source by, for example, active balancing of the rotor. The two most common implementations of active bearings are active magnetic bearing and piezoelectric bearings, where the first one is the most popular one. Piezoelectric bearings can bear higher loads than magnetic bearings and show a good fail save behaviour because of their high passive stiffness. Figure 1 shows two different active piezoelectric bearings. The piezos are linked to a ball bearing and are preloaded by prestressing springs. Force sensors are located directly under the piezo actuators to achieve an approximately collocated force measurement.

Many different control algorithms have been implemented on these two test-rigs. First, model free approaches such as PD-feedback [1], PDT1-feedback [2] and integral force feedback (IFF) [3], which is equal to a PT1-feedback, have been implemented for vibration reduction and isolation. All these controllers use the advantage of the collocation of the actuators and force sensor, which results in a stable system because of the maximum phase lag of $180°$. To further increase the vibration attenuation, model-based approaches have been implemented. Using finite element models of the rotor systems, standard control algorithms such as LQR/LQG [4, 5], μ-synthesis [6] and gain scheduled H_∞ [7], see Figure 2, have been implemented in order to reduce the bearing forces for vibration isolation. Those algorithms show a good performance but need high effort to be implemented.

The consideration of the system excitation and collocation of actuator and sensor can be used to implement a controller which shows a better performance than the standard algorithms. The main excitation of the rotor is caused by its unbalance. Thus, if the rotor speed is known, the

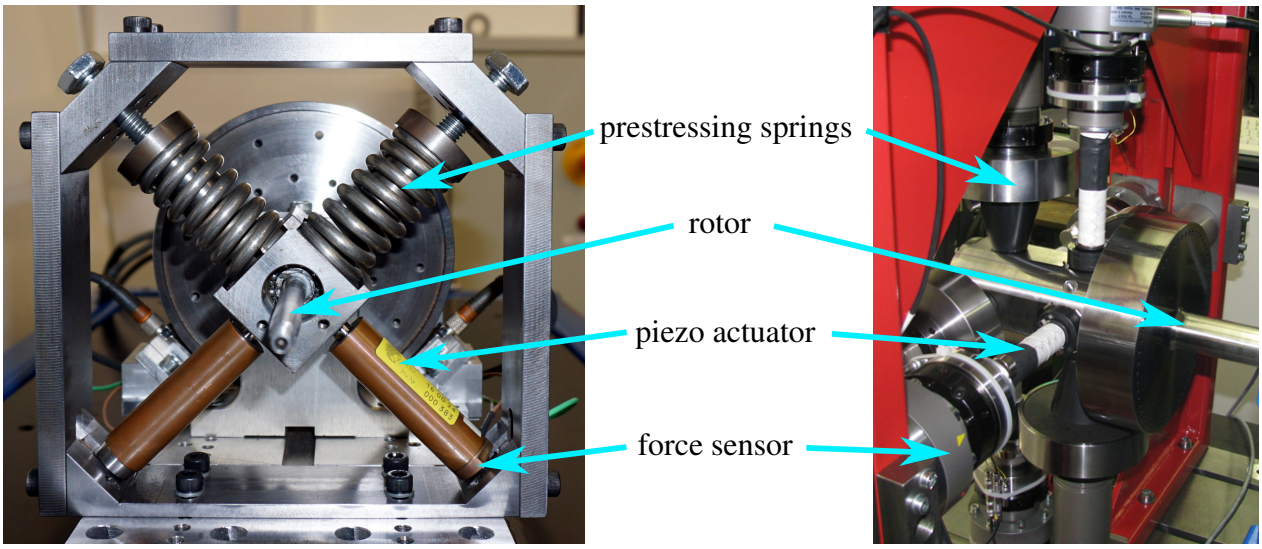

Figure 1: Picture of a active piezoelectric bearing for a scaled jet trubine engine (right) with two active planes and one of an elastic rotor test-rig (left). The active bearing is comprised of a ball bearing, piezoelectric actuators, prestressing springs and force sensors.

frequency of the excitation is given as well. Instead of designing a controller for a broad frequency range, a controller which focuses on the unbalance excitation can be implemented. The most popular algorithm in this category is the filtered-x least mean squares (FxLMS) algorithm. This one is an adaptive feedforward algorithm which uses a reference oscillator to achieve a theoretically perfect vibration reduction. In addition, a broadband feedback control for the remaining transient vibrations is needed. Lindeborn [8] combines the FxLMS and IFF to reduce the displacement and bearing force individually in different time periods.

However, the FxLMS still requires a simple non-parametric model of the frequency response function between actuator and sensor, which can be discarded in case of a collocated system. Heindel [9, 10] developed an algorithm which is a combination of an adaptive feedforward control and integral force feedback and does not require a model of the system. He proofed that the algorithm is always stable in the time continuous domain. Figure 3 shows the bearing forces of a run-up with the algorithm of Heindel [9]. It can be seen that the model-free approach achieves better results than the standard model-based controller from Becker, see Figure 2. Thus, the system knowledge, which in this case is the collocation of actuator and sensor as well as the rotor speed, can be used to implement a more efficient controller in comparison to standard approaches.

The active bearing system takes full advantage of the collocation property of force sensor and actuator. In case of systems where this is not possible, other approaches have to be used. The following section presents such a system, whereas the actuators are no longer placed in the load path.

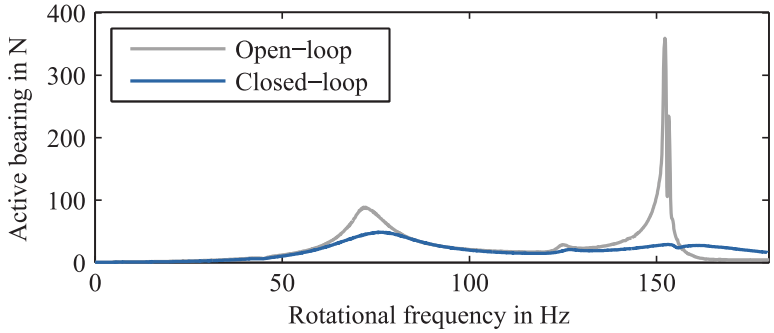

Figure 2: Results of Beckers gain-scheduled H_∞ controller [7] during a rotor run-up. Shown are the bearing forces of the active bearing.

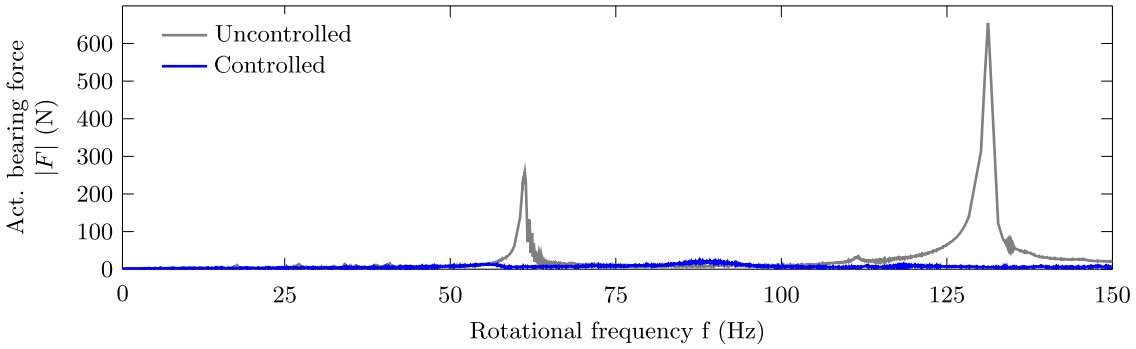

Figure 3: Results of Heindels controller [9] during a rotor run-up. Shown are the bearing forces of the active bearing.

2.2 Active control for planetary gearboxes

Planetary gearboxes, which for example can be found in drivetrains, excite the surrounding structure, causing vibrations. The resulting noise can for example be reduced with helical gears, which on the other hand reduces the overall efficiency of the system, or by increasing the mass of the gears, which leads to higher material costs and a less efficient design. Thus, there is always a conflict between NVH behaviour, efficiency and the system costs. The application of a active vibration system has the potential to partially resolve this conflict because it is able to reduce the vibration efficiently. The challenge of the implementation in case of the presented system lies within the complex excitation of the planetary gearbox, which causes vibrations at high frequencies, here 4 kHz, and distributed over a broad range of frequencies.

Figure 4 (left) shows the used active vibration system which uses piezoelectric inertial mass actuators. These are especially suited for high frequencies, whereas they perform badly at low frequencies. They can be mounted anywhere outside of the load path and thus offer a high flexibility. The design is simpler in comparison to the one of active bearings. However, the excitation spectrum of planetary gearboxes is more sophisticated. The spectrum comprises multiple frequencies distributed over a broad range instead of a single frequency. The analysation of the excitation is the first crucial step towards the design of an efficient controller without using the standard approaches. Even though the frequencies are distributed over a broad range, they still show a dependency to the gearbox output rotor speed. Plöger [12] describes the distribution an determines that the frequencies are always natural multiples of the output rotor speed, see Figure 4 (right). Furthermore, the

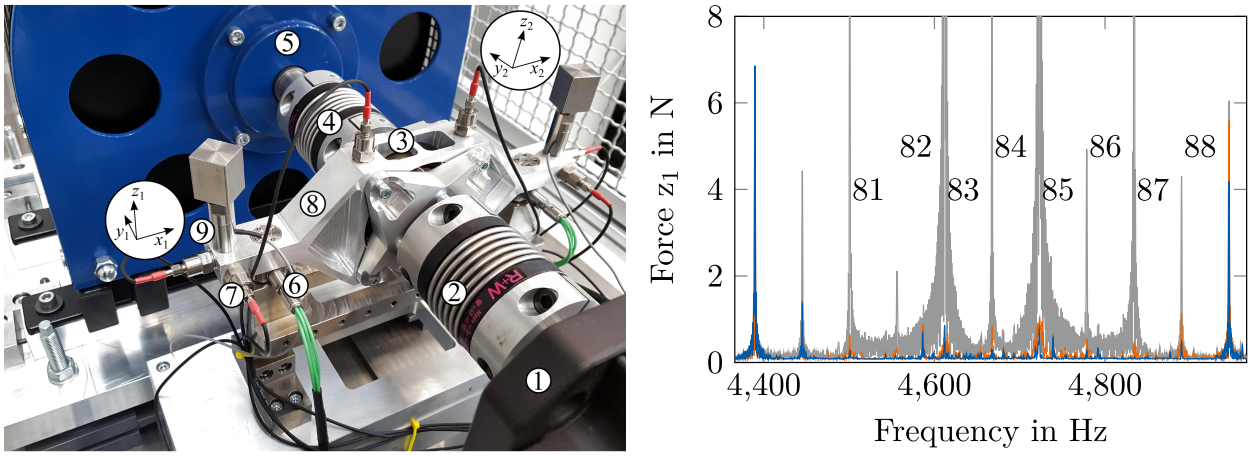

Figure 4: ***Left:*** Active vibration system with asynchronous motor (1), metal bellow couplings (2,4), planetary gearbox (3), eddy current break (5), triaxial force sensors (6), accelerometers (7), gearbox mount (8) and piezoelectric inertial mass actuators (9).
Right: Vibration reduction results by Zech [11]. The numbers indicate the multiple of the ring gear speed, the grey line the passive system, the blue line the amplitudes after using the FxLMS with a model and the orange line after applying the simultaneous equation algorithm.

largest amplitudes are measured close by the nominal gear meshing frequency, which is equal to the output rotor speed times the number of teeth on the ring gear, which is 84 for the planetary gearbox depicted in Figure 4.

Thus, the excitation frequencies are known if the output speed of the gearbox is known and an adaptive feedforward control which focuses on the narrow banded spectrum can be implemented. A feedback control is not necessary because the system shows relative high damping. The implementation of a model-free feedback control would not be possible anyway since the sensor and actuator are not collocated and phase lags greater than 180° occur. The FxLMS requires a model of the system in this case and thus is not suited for this task if a model free approach is desired. The simultaneous equation algorithm on the other hand is well suited for this task. It uses a combination of a test signal and order tracking to estimate the frequency transfer function between actuator and sensor. This approach is analogous to passive balancing of rotors where test masses are placed on the rotor to determine the actual unbalance of the rotor. The performance of the active vibration system from Zech [11] is depicted in Figure 4 (right) along with the results of a model based FxLMS control. The model-free algorithm shows a comparable performance as the FxLMS. Throughout the consideration of the excitation properties it was possible to implement a model-free controller which shows a good performance.

3 ACTIVE CONTROL FOR DRIVETRAINS

The electrification of vehicle propulsion systems is an important approach towards meeting the increasing legal requirements for reducing energy consumption and CO2 emissions. Therefore, a large number of electrified drives are developed with the aim of achieving high efficiency and high comfort at low costs. Thereby, investigations indicate that multi-speed electric powertrains show potential for increasing efficiency and thus for reducing electrical energy consumption [13]. The Institute for Mechatronic Systems in Mechanical Engineering at TU Darmstadt pursues the idea of modular electric and hybrid multi-speed powertrains with two electric motors (EM) and a transmission consisting of two subtransmissions (e.g. [14]), which, amongst others, are investigated in the publicly funded projects called Doppel-E-Antrieb (e.g. [15]), Speed2E (e.g. [16]), Speed4E (e.g.[17]) and DE-REX (e.g. [18, 19]). Instead of developing each component of the powertrain and its functions separately, the approach of a consequent functional integration of the mechatronic system is applied: for example, the electric motors provide transmissions functionality like synchronization of speeds, typically performed by friction-based synchronizer rings, or torque blending for gear shifts, usually done with friction clutches.

Basic requirements for the acceptance of electric multi-speed transmissions are comfort and fast gear shifts. For a high shift comfort, oscillations of the drive shaft torque should be avoided, since these oscillations lead to unpleasant low-frequency longitudinal vibrations of the vehicle acceleration called jerk. In order to model the dynamic behavior of the powertrain regarding jerking, typically a two-mass-oscillator is used. As shown in Figure 5, the inertia of the powertrain consisting of the electric motors and the transmission is reduced to a single rotating mass Θ_{PT}. The second mass Θ_{V} represents the mass of the vehicle. The flexible drive shaft is modelled as a spring-damper combination and connects the two masses [20].

In case of driving with two electric motors, the torque of the powertrain T_{PT} can be expressed as the sum of the torques of each electric motor times the respective gear ratio of the subtransmission. Since the shifting elements in the subtransmissions are form-locking dog clutches,

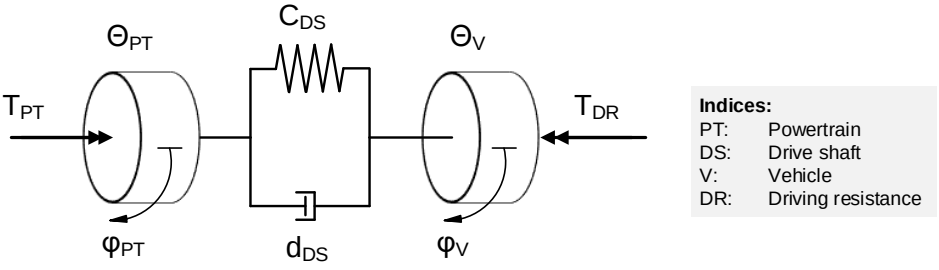

Figure 5: Two-mass-oscillator for modeling the powertrain dynamics with regard to vehicle jerk [20].

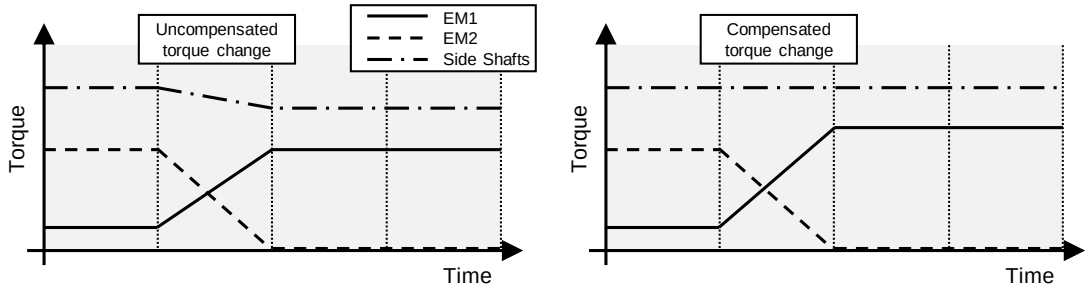

Figure 6: Schematic diagram illustrating the difference between uncompensated and compensated torque blending phases (based on [20]).

the dog clutches have to be load-free while (dis-)engaging during gear shifts. Therefore, the torque of one electric motor has to be ramped to zero and the second electric motor has to compensate the torque reduction in order to maintain a continuous powertrain torque. With regard to the gear shift comfort, it is of great importance that no drive shaft oscillations are induced as far as possible by changes in the powertrain torque which would directly lead to unpleasant jerking.

With regard to the control of the powertrain, this poses, among others, the challenge of optimum torque blending between the electric motors. Thereby, a distinction can be made between compensated and uncompensated torque changes like schematically shown in Figure 6 [20]. In case of perfect blending of a compensated torque change, the blending phase can be performed very fast, since the drive shaft torque remains constant and no oscillations are excited. In real applications, even in case of fully compensated torque changes, the shortening of blending time is limited by the dynamic behaviour of the electric motors and furthermore, oscillations can occur due to inaccuracy of the control of the electric motors.

Fully compensated torque blending can be realized, for example, while upshifting at partial vehicle load. If the torque blending is applied in an optimum manner, the gear shift is not noticeable for the driver and the duration of the torque blending phase and of the total gear shift is of minor importance. Investigations with test persons as part of driving tests confirmed the high shifting comfort in the DE-REX demonstrator vehicle [19].

For upshifts at high power acceleration maneuver, the powertrain torque cannot be maintained constant, because of the limitation of the maximum torque of the remaining electric motor. Therefore, the drive shaft torque is uncompensated in some extend. The change in the drive shaft torque induces oscillations resulting in vehicle jerking. Thus, the torque-blending phase in uncompensated gear shifts is of high relevance for the shift comfort. On the one hand, it is desirable, for example for performance reasons, that the duration of the gear shift is as short as possible. On the other hand, a sudden change of the powertrain torque would excite intense oscillations of the drive shaft torque, which in turn would lead to vehicle jerk. In the course of [21] different approaches for torque blending were investigated. For example, the shape of torque blending can be implemented as a ramp or can be filtered with a PT1 transfer function. If the dynamic behavior of the powertrain model is known, the excitation of oscillations can be lowered by tuning the gradient of the ramp according to the eigenfrequency of the two-mass-oscillator (note: the reduced mass of the powertrain depends on the selected mode and therefore, the gradient of the ramp has to be adjusted based on the actual driving mode) [20]. This enables the vibration behavior of the powertrain to be improved by knowing and taking into account the dynamic behavior of the mechatronic system. The second variant of the shaping the torque blending is implemented with a PT1 filtering of the torque of the electric motors. Figure 7 shows the results for an entire high power upshift with torque blending in PT1 matter measured in the DE-REX demonstrator vehicle. As introduced before, the torque reduction of EM1 in the torque-blending phase (highlighted in grey) cannot by fully compensated by EM2, since the torque limit of EM2 is reached (100 Nm). Therefore, the resulting vehicle acceleration decreases. Due to the uncompensated torque blending, oscillations in the vehicle acceleration are excited. Even if the vehicle acceleration oscillations indicate a possibly uncomfortable gear shift, the objective evaluation of the gear shift is in the same range than for conventional automatic or dual-clutch transmissions [19]. Furthermore, the gear shift comfort can be further improved by different approaches like active control of the drive shaft torque (so called “Anti-Jerk-Control”) or a short time high overloading of the electric motors. With the high overloading of the electric motor during the gear shift, it would be possible to fully compensate the torque reduction. Therefore, it is

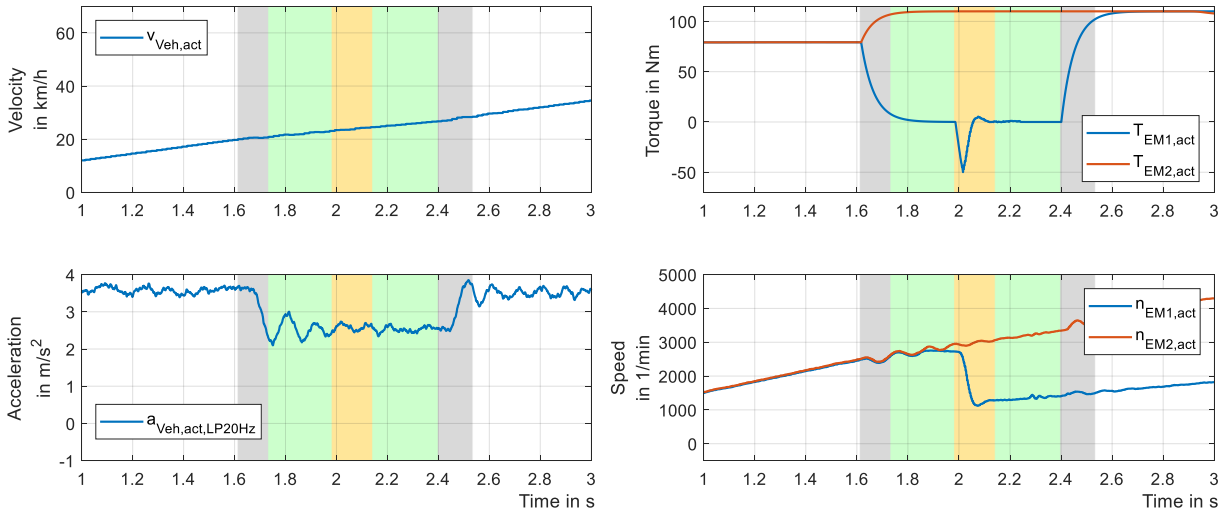

Figure 7: High power upshift in the DE-REX demonstrator vehicle with umcompensated torque blending [22].

possible to optimize both the gear shift comfort and the gear shift time.

The investigations concerning the gear shift comfort with simplified electrified multi-speed transmission in the DE-REX vehicle show that the mechatronic approach of functional integration helps to reduce the mechanical complexity (and at the same time the costs) (e.g. [19]) and increases the efficiency by smart control of future electrified powertrain systems.

4 NEW METHODS THROUGH ARTIFICIAL INTELLIGENCE IN MECHATRONICS

Classically, the development process of mechatronic systems incorporates building a dynamic simulation model, mapping the system inputs to the outputs. These models are generally based on first principles which are describing the physical system behaviour. Grey-box approaches are often used in vehicle modelling which combine theoretical knowledge in form of differential equations and experimental data to identify the free model parameters [23], see Figure 8. However, the performance of these approaches relies on a correct description of non-linear physical phenomena which is often complex or even impossible. Halfmann [24] introduced the so-called Hybrid Modelling approach where the basic physical phenomena are described throughout grey-box modelling and the complex system behaviour, which is not covered by differential equations, is for example described by a neural network. Despite the promising benefits of such an approach in mechatronic system modelling, it has not been thoroughly used until today. Whereas, it has recently been applied in other domains, especially chemical engineering [25–27].

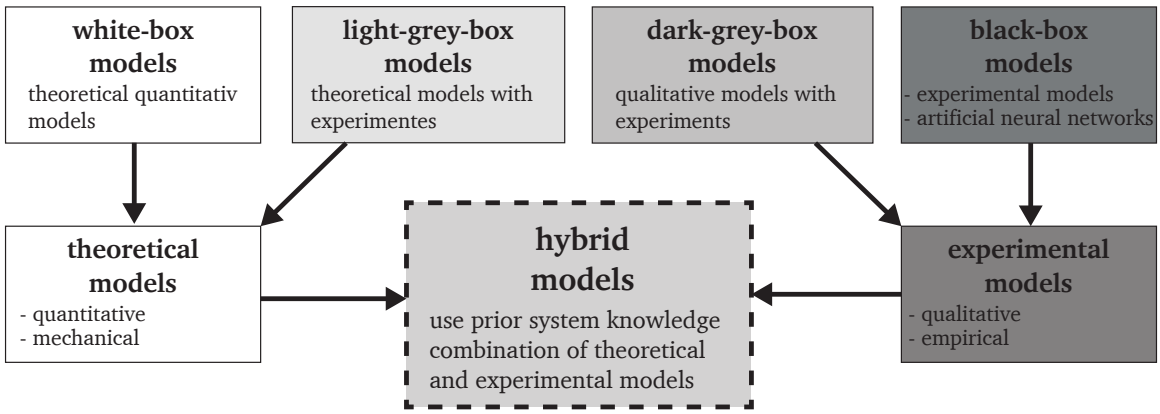

Figure 8: Whilst grey-box models combine theoretical and experimental models in one modelling approach, hybrid models form as a combination of theoretical and experimental models. Here both modelling approaches coexist. [24]

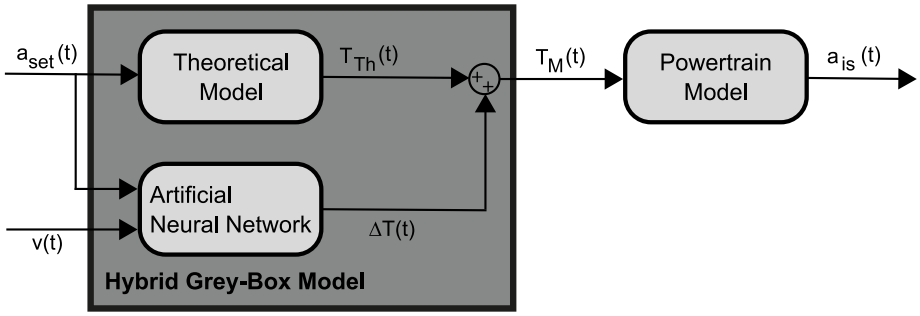

Figure 9: The parallel hybrid grey-box model contains both, a theoretical model containing prior system knowledge and an artificial neural network for learning complex and non-linear phenomena.

Within this paper we show a possible application for such modelling in an inverse vehicle longitudinal model. In our case, the appropriate traction force to realise a given trajectory for feed-forward control shall be derived. Here, a parallel architecture is applied where physical equations are used in parallel to a neural network as depicted in Figure 9. Thus, the output of the theoretical model in form of inverse differential equations is corrected by an Artificial Neural Network (ANN). Whilst the classic modelling approach cannot cover arbitrary non-linearities from complex physical phenomena, the neural network is capable of learning these in a supervised learning setting. In a wider context that property also facilitates the application of model-based approaches in conjunction with controllers or observers showing high potential for further system dynamics improvement. Today, a detailed knowledge about the physical system phenomena in form of first principles is necessary to apply these approaches which is often not available or expensive. Through the application of Artificial Intelligence (e.g ANN) data-based system knowledge can be used to achieve highly capable models in these domains.

For that, the implemented learning algorithm must be able to learn from temporal information. That can be done through different approaches. The most basic idea is a Time Delay Network (TDN) where the network input will not only use the current time step, but also gets n prior time steps [28]. More recently developed applications often use Long Short Term Memory (LSTM) networks which belong to the class of recurrent neural networks [29]. With the help of an internal cell state and numerous gates for information flow control, this approach is capable of learning long term dependencies within datasets.

To train the neural network in order to correct a theoretical model, training data has to be generated. Basically, this can easily be done throughout running the theoretical model without any corrective feedback and then using the resulting data pairs from input torque and output state of the powertrain for training. Here, a typical but significant problem arises. For training a neural network in supervised learning, the training examples must span across the entire latter input space to learn the correct behaviour. However, this is generally not the case if the data is solely generated in the described way. Therefore, an exploration strategy shall be developed to explore the entire state space while generating data. That could be done throughout random exploration, in analogy to reinforcement learning, or theoretical system knowledge, for example by solving an optimal control problem offline.

We think, that using prior system knowledge in machine learning enhanced modelling processes is the key for the success of machine learning in mechatronics. By that, the overall system level performance and the robustness of training will be improved. In further steps, the neural network may not only be trained within the development process but also later during operation of the system. In that way, an adaptive system is created which is able to react on changes in the system properties without sacrificing system level performance.

5 SUMMARY AND CONCLUSION

This paper has given an rough overview on some of the research topics of the Institute for Mechatronic Systems in Mechanical Engineering at TU Darmstadt. All four different presented mechatronic systems are united by the approach of embedding system knowledge into the design. This approach offers the possibility of a better performing system and may require even less effort to

be implemented in comparison to standard design approaches. From our perspective it is essential to incorporate the system knowledge into the design process to establish an efficient mechatronic application which can improve the system dynamics and partially overcome the conflict between costs, efficiency and NVH behaviour.

REFERENCES

[1] Matthias Borsdorf, R. Sebastian Schittenhelm, and Stephan Rinderknecht. Vibration reduction of a turbofan engine high pressure rotor with piezoelectric stack actuators. In *Proceedings of the International Symposium on Air Breathing Engines 2013 (ISABE 2013)*, Busan, 2013.

[2] Robert Köhler, Christian Kaletsch, Markus Marszolek, and Stephan Rinderknecht. Active vibration damping of engine rotor considering piezo electric self heating effects. In *International Symposium on Air Breathing Engines 2011 (ISABE 2011)*, Gothenburg, September 2011.

[3] Matthias Borsdorf, R. Sebastian Schittenhelm, Zhentao Wang, Johannes Bos, and Stephan Rinderknecht. Active damping of aircraft engine shafts using integral force feedback and piezoelectric stack actuators. In *2013 IEEE/ASME International Conference on Advanced Intelligent Mechatronics*, pages 1731–1736, Wollongong, July 2013.

[4] R. Sebastian Schittenhelm, Zhentao Wang, Bernd Riemann, and Stephan Rinderknecht. State feedback in the context of a gyroscopic rotor using a disturbance observer. *Engineering Letters*, 21(1):44–51, 2013.

[5] Filip Lebo, Stephan Rinderknecht, and Mahmut Özel. Model-based control of an elastic aircraft engine rotor with piezo stack actuators. In *2010 IEEE 17th International Conference on Industrial Engineering and Engineering Management*, pages 537–541, October 2010.

[6] Bernd Riemann, Martin A. Sehr, R. Sebastian Schittenhelm, and Stephan Rinderknecht. Real gyroscopic uncertainties in robust control of flexible rotors. In *52nd IEEE Conference on Decision and Control*, pages 3762–3769, Florence, December 2013.

[7] Fabian B. Becker, Martin A. Sehr, and Stephan Rinderknecht. Vibration isolation for parameter-varying rotor systems using piezoelectric actuators and gain-scheduled control. *Journal of Intelligent Material Systems and Structures*, 28(16):2286–2297, September 2017.

[8] Otto Lindenborn, Bernd Hasch, Daniel Peters, and Rainer Nordmann. Vibration reduction and isolation of a rotor in an actively supported bearing using piezoelectric actuators and the FXLMS algorithm. In *9th International Conference on Vibrations in Rotating Machinery*, Exeter, September 2008.

[9] Stefan Heindel, Peter C. Müller, and Stephan Rinderknecht. Unbalance and resonance elimination with active bearings on general rotors. *Journal of Sound and Vibration*, 431:422–440, September 2018.

[10] Stefan Heindel, Fabian Becker, and Stephan Rinderknecht. Unbalance and resonance elimination with active bearings on a jeffcott rotor. *Mechanical Systems and Signal Processing*, 85:339–353, February 2017.

[11] Philipp Zech, Daniel Fritz Plöger, and Stephan Rinderknecht. Active control of planetary gearbox vibration using phase-exact and narrowband simultaneous equations adaptation without explicitly identified secondary path models. *Mechanical Systems and Signal Processing*, 120:234–251, April 2019.

[12] Daniel Fritz Plöger, Philipp Zech, and Stephan Rinderknecht. Vibration signature analysis of commodity planetary gearboxes. *Mechanical Systems and Signal Processing*, 119:255–265, March 2019.

[13] Andreas Viehmann, Jean-Eric Schleiffer, and Stephan Rinderknecht. Evaluation of the dedicated range-extender transmission powertrain concept DE-REX regarding efficiency, costs and complexity. In VDI, editor, *VDI-Berichte 2354*, 2019.

[14] Stephan Rinderknecht, Ruben König, and Jean-Eric Schleiffer. Modularity aspects for hybrid electric powertrains on the example of the two-drive-transmission. In VDI, editor, *VDI-Berichte 2218*, 2014.

[15] Ruben König and Stephan Rinderknecht. Multi-objective optimization of the two-drive-transmission for a hybrid electric vehicle. In *FISITA World Automotive Congress 2014*, 2014.

[16] Ruben König, Andreas Viehmann, and Stephan Rinderknecht. Development of the transmission control for a high-speed multi-gear powertrain concept for electric vehicles. In VDI, editor, *VDI-Berichte 2276*, 2016.

[17] Daniel Schöneberger, Marco Mileti, Karsten Stahl, and Stephan Rinderknecht. Development of an innovative shift actuator for electrified multispeed transmissions. In *International Conference on Advanced Vehicle Powertrains*, 2019.

[18] Stephan Rinderknecht, Andreas Viehmann, and Ruben König. Two-drive-transmission with range-extender (DE-REX). In CTI - Car Training Institute, editor, *14th International CTI Symposium*, 2015.

[19] Andreas Viehmann, Jean-Eric Schleiffer, Ruben König, and Stephan Rinderknecht. Innovative powertrain concept for the smart vehicle of the future. *ATZ worldwide*, 121(10):70–75, 2019.

[20] Ruben König, Stephan Rinderknecht, and Andreas Viehmann. Investigation of gear shifts and hybrid mode changes in an innovative parallel-series hybrid powertrain with dog clutches. In *FISITA World Automotive Congress*, 2016.

[21] Ruben König. *Gang- und Moduswechsel in elektrischen und hybrid-elektrischen Antriebssträngen mit aktiv synchronisierten Klauenkupplungen*. Forschungsberichte Mechatronische Systeme im Maschinenbau. Shaker, Dissertation. Düren, 2019.

[22] Andreas Viehmann, Ruben König, and Stephan Rinderknecht. Investigation in gear shifts in a parallel-series hybrid powertrain with dog clutches in a demonstrator vehicle. In VDI, editor, *VDI-Berichte 2328*, 2018.

[23] Dieter Schramm, Manfred Hiller, and Roberto Bardini. *Vehicle Dynamics: Modeling and Simulation*. Springer, 2014.

[24] Christoph Halfmann and Henning Holzmann. *Adaptive Modelle für die Kraftfahrzeugdynamik*. Engineering online library. Springer, 2003.

[25] Angelo Basile, Marjan Alavi, and Stefano Curcio. *Artificial Neural Networks in Chemical Engineering*. Chemical Engineering Methods and Technology. Nova Science Publishers Incorporated, Hauppauge, 2017.

[26] Donovan Chaffart and Luis A. Ricardez-Sandoval. Optimization and control of a thin film growth process: A hybrid first principles/artificial neural network based multiscale modelling approach. *Computers & Chemical Engineering*, 119:465–479, 2018.

[27] Zaher Mundher Yaseen, Minglei Fu, Chen Wang, Wan Hanna Melini Wan Mohtar, Ravinesh C. Deo, and Ahmed El-shafie. Application of the hybrid artificial neural network coupled with rolling mechanism and grey model algorithms for streamflow forecasting over multiple time horizons. *Water Resources Management*, 32(5):1883–1899, 2018.

[28] Alexander Waibel, Toshiyuki Hanazawa, Geoffry Hinton, Kiyohiro Shikano, and Kevin J. Lang. Phoneme recognition using time-delay neural networks. *IEEE Transactions on Acoustics, Speech, and Signal Processing*, 37(3):328–339, 1989.

[29] Felix. A. Gers, Jürgen Schmidhuber, and Fred Cummis. Learning to forget: continual prediction with lstm. In *ICANN99*, Conference publication, pages 850–855, London, 1999.

STATISTICAL ENERGY ANALYSIS, THEORETICAL ANALYSIS AND RANGE OF APPLICABILITY

A. Le Bot[1]

[1]Laboratory of tribology and dynamics of systems UMR CNRS 5513
École centrale de Lyon, Ecully, FRANCE
Email: alain.le-bot@ec-lyon.fr

ABSTRACT

This paper presents an overview of the physical assumptions of the theory of statistical energy analysis. We discuss the concepts of high frequency, random excitation, diffuse field, weak coupling, and energy transfer within the framework of thermodynamics. We show that only few conditions are absolutely required in statistical energy analysis. These are diffuse field in all subsystems and weak coupling between any pair of subsystems. Example and counter-examples are presented.

1 INTRODUCTION

Statistical energy analysis [1] is a statistical theory of sound and vibration in the same way that it exists a statistical mechanics, statistical electromagnetism, statistical physics. The basic idea is quite simple. If a mechanical system submitted to sound and vibration is sufficiently disordered, the vibrational energy behaves like heat and thus, follows the law of classical thermodynamics [2]. This includes the second law of thermodynamics [3–5].

But the large number of assumptions mentioned in the literature may sometimes puzzle those who discover the theory [6, 7].

In this paper, we review some of the assumptions of statistical energy analysis. And with examples and counter-examples, we show that the only requirements are the a diffuse field is established in all subsystems and that all couplings between subsystems are weak.

2 THERMODYNAMICS OF SOUND AND VIBRATION

In statistical energy analysis, the vibration is supposed to be random. So, the vibrational energy E_i of subsystem i and the power P_{ij} exchanged between subsystems i and j must be understood as mathematical expectations of the actual quantities. When sources are ergodic, we may replace the word expectation by time-averages. Remark that ergodicity of stochastic processes is not strictly speaking a required assumption but just a condition favourable in practice.

The main result of statistical energy analysis is the so-called coupling power proportionality. The power exchanged between subsystems is proportional to the difference of modal energies

$$P_{ij} = \beta_{ij} \left(\frac{E_i}{N_i} - \frac{E_j}{N_j} \right) \tag{1}$$

where N_i is the number of resonant modes of subsystem i (modes whose natural frequency is within the frequency band of excitation). The proportionality coefficient β_{ij} depends only on the mechanical properties of adjacent subsystems but not on their levels of energy. It is analogous to a heat conduction factor [8].

This law of exchange of energy is exactly Clausius' law in thermodynamics. Its validity is easy to understand. 1) Each subsystem must be in thermal equilibrium, the temperature being the same at all points of the subsystem. This justifies the assumption of vibrational diffuse field (equivalent to uniform temperature). 2) The exchange of heat must be light in order to not disturb the local equilibrium. We speak of linear non-equilibrium thermodynamics. This justifies the condition of weak coupling.

3 DIFFUSE FIELD

A diffuse field is a vibrational field which is random, homogeneous and isotropic. In particular the vibrational energy is uniformly distributed in the subsystem. The easiest way to get a diffuse field is to apply a so-called rain-on-the-roof excitation on the system. The system is uniformly excited with random sources which are δ-correlated in space and time. With a rain-on-the-roof excitation, the vibrational field is *always* diffuse irrespective of its geometry or level of damping.

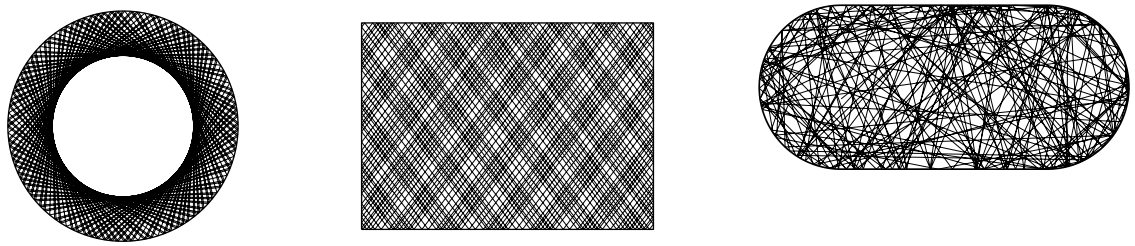

Figure 1. Ray propagation in various billards.

When the source is a point force, the situation is more delicate. It depends on the geometrical properties of the subsystem. In figure 1 is shown the path of a unique ray in various billiards. We can see that rays propagating in a circle do not explore the entire billiard. In a rectangle they pass through all points but do not take all directions. And in a Bunimovich stadium, they explore the entire phase space. Ergodicity of billiard is therefore a favourable condition to ensure a diffuse field and therefore a good application of statistical energy analysis [9].

4 WEAK COUPLING

Weak coupling may easily be introduced as the ratio of exchanged energy and dissipated energy. This ratio, called Smith's criterion [10], must be low. In figure 2, we see the transition from weak

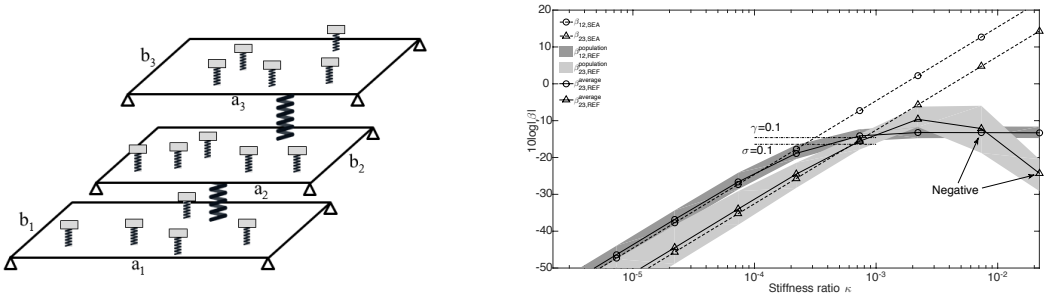

Figure 2: Comparison of the heat conduction factor β predicted by SEA with that observed by a direct numerical simulation versus coupling strength.

to strong coupling in a system made of three coupled plates with additional mass-spring resonators. We observe that when the coupling strength is low, we have a fine agreement between statistical energy analysis and result of the direct numerical simulation. But when the coupling is strong, the disagreement may become very important and can even lead to an inversion of the flow of energy in the worst case [11].

5 VALIDITY DIAGRAM

The range of application of statistical energy analysis is a subdomain of the space of parameters. For a plate in bending vibration, we have six parameters, length, width, thickness, Young's modulus, Poisson's ratio, damping loss factor. A dimensional analysis by application of Vaschy-Buckingham theorem shows that it exists only 4 dimensionless parameters and mainly two if we discard Poisson's ratio and the shape factor. We may propose the damping loss factor η and a dimensionless wavenumber κ (or equivalently a dimensionless frequency). It is therefore possible to plot the domain of validity of statistical energy analysis in the η, κ-plane [12].

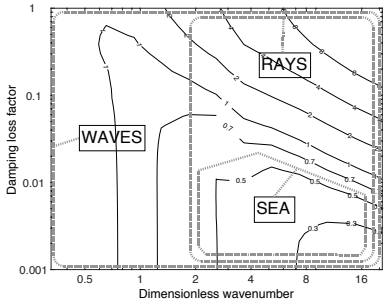

Figure 3: Validity diagram of statistical energy analysis in the η, κ-plane [13]. Lines of isovalue of spatial fluctuations of vibrational energy (0.5 means a standard deviation of 50%).

Figure 3 has been plotted by solving the governing a thin rectangular plates excited by a random transverse force and checking the diffuseness of the obtained vibrational field. Of course the domain of validity of the wave approach is the entire plate (if we ignore the quantum limit at very high frequency). The domain of application of geometrical acoustics is simply the domain of short

wavelengths. And finally, we observe that the domain of application of statistical energy analysis is a subdomain of geometrical acoustics for which the wavelength is short AND the damping is light.

We thus observe the importance of the damping loss factor. A strong damping implies a rapid decreasing of the energy of rays during their propagation. Therefore, they cannot mix efficiently the vibrational energy with a large number of reflections [14].

6 CONCLUDING REMARKS

In conclusion, if statistical energy analysis is sometimes criticized for its difficulty to be applied in practice, this is largely to a lack of understanding of its basic assumptions. Statistical is a true theory of physics which provides reliable prediction provided that it is applied within its range of application.

REFERENCES

[1] A. Le Bot, Foundation of statistical energy analysis in vibroacoustics, Oxford University Press, Oxford, 2015.

[2] A. Le Bot, A. Carcaterra, D. Mazuyer, Statistical vibroacoustics and entropy concept, Entropy **12** (2010) 2418-2435.

[3] A. Carcaterra, An entropy formulation for the analysis of energy flow between mechanical resonators. Mech. Syst. Sign. Process. 2002, 16, 905?920.

[4] A. Le Bot, Entropy in Statistical Energy Analysis, J. Acoust. Soc. Am. **125** (2009) 1473-1478.

[5] D.A. Tufano, Z. Sotoudeh, Entropy in strongly coupled oscillators, J. Vib. Acoust. **140** (2017) 011003.

[6] F.J. Fahy, Statistical energy analysis: A critical overview. In Statistical energy analysis an overview with applications in structural dynamics Edited by A.J. Keane and W.G. Price, Cambridge University Press, Cambridge, 1994.

[7] T. Lafont, N. Totaro, A. Le Bot, Review of statistical energy analysis hypotheses in vibroacoustics, Proc. R. Soc. A **470** (2013) 20130515.

[8] B.R. Mace, L. Ji, The statistical energy analysis of coupled sets of oscillators, Proceedings of the royal society A **463** (2007) 1359-1377.

[9] H. Li, N. Totaro, L. Maxit, A. Le Bot, Ergodic billiard and statistical energy analysis, Wave Motion **87** (2019) 166–178.

[10] P.W. Smith, Statistical models of coupled dynamical systems and the transition from weak to strong coupling, J. Acoust. Soc. Am. **65** (1979) 695-698.

[11] T. Lafont, N. Totaro, A. Le Bot, Coupling strength assumption in statistical energy analysis, Proc. R. Soc. A **473** (2017) 20160927.

[12] A. Le Bot, V. Cotoni, Validity diagrams of statistical energy analysis, J. Sound Vib. **329** (2010) 221-235.

[13] A. Le Bot, Entropy in sound and vibration: towards a new paradigm, Proc. R. Soc. A **473** (2017) 20160602.

[14] A. Le Bot, Derivation of statistical energy analysis from radiative exchanges, J. Sound Vib. **300** (2007) 763-779.

PADÉ APPROXIMANTS FOR MULTIVARIATE REDUCED ORDER MODELS

R. Rumpler

MWL/Centre for ECO2 Vehicle Design, Department of Aeronautical and Vehicle Engineering,
KTH Royal Institute of Technology, Stockholm, Sweden
Email: rumpler@kth.se, pege@kth.se

ABSTRACT

Most engineering applications involving solutions by numerical methods are dependent on several parameters, whose impact on the solution may significantly vary from one to the other. At times, an evaluation of these multivariate solutions may be required at the expense of a prohibitively high computational cost. In the present work, a multivariate finite element approach is proposed, allowing for a fast evaluation of parametric responses. It is based on the construction of a reduced basis spanning a subspace able to capture rough variations of the response. The method consists in an extension of the Well-Conditioned Asymptotic Waveform Evaluation (WCAWE) to multivariate problems, by an appropriate choice of derivative sequences, and a selection of the most relevant basis components. It is validated and demonstrated for its potential on a semi-industrial sized 3D application involving coupled poroelastic and internal acoustic domains.

1 INTRODUCTION

In order to limit the high computational burden associated with the evaluation of multivariate Finite Element (FE) solutions, an approach based on a Reduced-Order-Model (ROM), derived after a univariate moment-matching method, is proposed. This univariate method, namely the Well-Conditioned Asymptotic Waveform Evaluation (WCAWE) method, proposed by Slone *et al*. [1], is shown to allow for a robust generation of basis components with good convergence properties of the associated reduced systems [1–3]. It relies on a sequence of successive derivatives of the system of interest, leading to multiple Right-Hand-Side (RHS) problems to be solved sequentially, with intermediate orthonormalization steps and correction terms ensuring the robustness of the procedure and the good conditioning of the resulting transformation matrix. This univariate basis generation procedure may be extended to a multivariate procedure. However, the cost associated with the orthonormalization and correction steps, may lead to a computationally prohibitive cost, particularly as the dimension of the variable space increases [3]. Additionally, not all cross-derivative terms may contribute significantly to the convergence of the ROM, and it may be critical to be able to reduce them to a minimum. In this contribution, an effort is made to bring the WCAWE to multivariate problems, starting with a bivariate illustration, and attempting to limit the transformation bases to a minimum in view of higher dimensionality applications. The foundation for a multi-interval strategy is also presented in view of the reconstruction of wide parametric ranges. The approach is shown to benefit from the superior robustness of the WCAWE compared to the so-called component-wise Padé approximants [3–6], previously used to derive the Nested Padé approximant method [7, 8].

2 THE WCAWE, A MOMENT-MATCHING, PROJECTION-BASED ROM

2.1 Generic multivariate problem and associated transformation

The starting point of the WCAWE-based parametric sweep is given by a linear system of the following form,

$$\mathbf{Z}(\mathbf{x})\mathbf{U}(\mathbf{x}) = \mathbf{F}(\mathbf{x}), \tag{1}$$

where $\mathbf{x}$ may be a vector of N_x independent variables corresponding to the parametric problem of interest, e.g. including the angular frequency ω, material parameters, ... For the original univariate case [1], the vector reduces to a scalar such that $\mathbf{x} = [x]$. In an FE problem, $\mathbf{Z}(\mathbf{x})$, $\mathbf{U}(\mathbf{x})$, and $\mathbf{F}(\mathbf{x})$ respectively represent the system matrix of the discretized problem, the solution vector and the vector of externally applied loads.

The projection-based approach relies on the construction of a transformation basis emerging from successive derivatives of the solution vector in Eq. (1) at a specific point $\mathbf{x}_0$ in the parameter space. The WCAWE algorithm provides a robust generation of this sequence of successive derivatives. The resulting well-conditioned transformation matrix $\mathbf{V}_\mathrm{N}$, consisting of N orthonormalized basis vectors, allows for a robust, non-stagnating convergence upon increasing the size of the subspace spanned. The associated approximation of the solution in Eq. (1), to the order N, and the associated reduced system corresponding to Eq. (1), are such that

$$\widehat{\mathbf{U}}_\mathrm{N}(\mathbf{x}) = \mathbf{V}_\mathrm{N}\,\boldsymbol{\alpha}(\mathbf{x}) \approx \mathbf{U}(\mathbf{x}), \quad \text{and} \quad {\mathbf{V}_\mathrm{N}}^T\mathbf{Z}(\mathbf{x})\mathbf{V}_\mathrm{N}\boldsymbol{\alpha}(\mathbf{x}) = {\mathbf{V}_\mathrm{N}}^T\mathbf{F}(\mathbf{x}), \tag{2}$$

$\boldsymbol{\alpha}$ being a vector of N generalized coordinates.

2.2 A multivariate WCAWE basis generation procedure

Adapting the WCAWE algorithm from univariate problems to multivariate ones lies in the generation of sequences of RHS vectors, emerging from sequences of iteratively differentiated matrices $\mathbf{Z}^{(k)}$, the exponent k standing here for the total order of differentiation regardless of the associated differentiation variables. The choice adopted here is to generate such sequences independently, thus generating a set of $\mathrm{N_V}$ bases $\left\{\mathbf{V}_\mathrm{N}^1, \cdots, \mathbf{V}_\mathrm{N}^{\mathrm{N_V}}\right\}$ associated with $\mathrm{N_V}$ sequences of iteratively differentiated matrices $\mathbf{Z}^{(k)}$. These bases, in principle all of the same size N, each consist of orthonormalized basis vectors, but these are naturally not mutually orthonormalized from one to the next basis. A simple way to ensure this, as well as to reduce the basis to a minimum number of basis vectors is to proceed to a compression, or a component selection, via a Singular Value Decomposition (SVD)

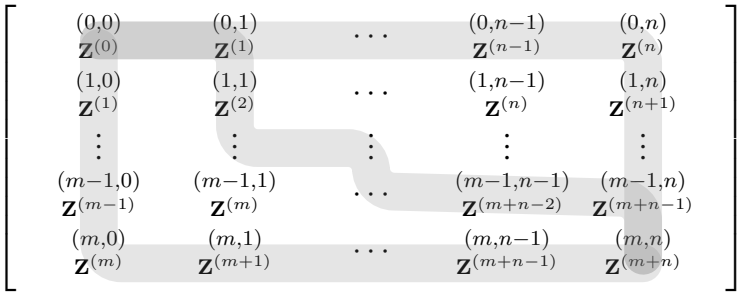

Figure 1: Illustration of three possible bivariate derivation paths for the system matrix $\mathbf{Z}$ up to the "cumulated order" $k = (m + n)$.

of the merged set of bases. Either way, the initial step consists in an SVD of the merged basis after concatenation, $\mathbf{V}_{\mathrm{N}}^{\mathrm{mer}} = \left[\mathbf{V}_{\mathrm{N}}^{1} \cdots \mathbf{V}_{\mathrm{N}}^{\mathrm{N_V}}\right]$, resulting in $\mathbf{V}_{\mathrm{N}}^{\mathrm{mer}} = \sum_{i=1}^{\mathrm{N_{mer}}} \sigma_i \mathbf{w}_i^{\mathrm{l}} \mathbf{w}_i^{\mathrm{r}T}$, where $\mathrm{N_{mer}}$ corresponds to the total number of basis vectors in $\mathbf{V}_{\mathrm{N}}^{\mathrm{mer}}$, *i.e.* $\mathrm{N_{mer}} = \mathrm{N} \cdot \mathrm{N_V}$; σ_i, $\mathbf{w}_i^{\mathrm{l}}$, and $\mathbf{w}_i^{\mathrm{r}}$ correspond to the singular values, left and right singular vectors respectively.

Assuming a descending-ordered sequence of singular values $(\sigma_1 \cdots \sigma_{\mathrm{N_{mer}}})$, the reduced, merged basis $\mathbf{V}^*$ is subsequently obtained such that $\mathbf{V}^* = \left\{\mathbf{w}_i^{\mathrm{l}} \mid i \in (1, \mathrm{N_{mer}}) \wedge \sigma_i \geq \sigma_{\mathrm{thresh}}\right\}$, where σ_{thresh} corresponds to the empirically chosen threshold value for the selection of the singular values resulting from the decomposition.

The resulting reduced basis $\mathbf{V}^*$, consisting of $\mathrm{N_{V^*}}$ vectors, is then used in place of the univariate transformations corresponding to Eq. (2), in order to solve a reduced set of equations at most involving $\mathrm{N_{mer}}$ DOFs.

2.3 Sequences of multivariate differentiation, and multi-interval strategy

The sequential WCAWE procedure above depends on the generation of sequences of differentiated system matrices to successive "cumulated multivariate orders" k, i.e. $\mathbf{Z}^{(k)}$. For the bivariate case, these differentiation paths may be represented in a matrix form, see Fig. 1.

The matrix sequences obtained from these differentiation paths of the system matrix subsequently feed the WCAWE algorithm [1, 10]. The rationale behind choosing a limited number of derivation paths is connected to the potential inefficiency resulting from the attempt to calculate all multivariate derivatives for a given set of maximum orders. In practice, it is estimated that a number of sequences of the order of the dimensionality of the multivariate problem may be sufficient in order to provide good convergence properties of the ROM. For instance, 2 sequences may be sufficient for a bivariate problem, which addresses in part the issue of dimensionality and the associated efficiency of the approach: the number of successive derivatives necessary may grow linearly with the dimensionality as opposed to an exponential growth if all cross-derivatives are calculated in a fully multivariate approach.

When the solution over a large parametric space is to be approximated, several smaller bases associated with their interval of approximation may become more efficient than building a large basis leading to larger, fully-populated reduced system. This multi-interval strategy is implemented using a combination of error-estimation, contour following algorithm in order to determine the bounds of convergence for each interval, and a sequential multi-interval reconstruction over the full parametric space.

3 APPLICATION TO A BIVARIATE PROBLEM

The proposed multivariate approach is tested on an average-sized problem consisting of the interior cavity of a passenger train (around 300000 acoustic pressure DOFs), treated with a 15-cm layer of sound absorbing porous material on the top surface, and excited by a time-harmonic point source at a corner of the cavity. The porous boundary is modelled by an equivalent fluid formulation, such that the resulting FE problem has the general form

$$\left(\mathbf{K_a} - \frac{\omega^2}{c_0^2}\mathbf{M_a} + \mathbf{K_p} - \frac{\omega^2}{\tilde{c_{\mathrm{p}}}^2}\mathbf{M_p}\right)\tilde{\mathbf{U}} = \mathbf{F}, \quad \text{with } \tilde{c_{\mathrm{p}}} = \frac{c_0}{\sqrt{\dfrac{1 - i\Phi}{\rho_0 \omega}}} \tag{3}$$

where $\square_{\mathbf{a}}$ correspond to air cavity global matrices, and $\square_{\mathbf{p}}$ to porous global matrices. $\tilde{\mathbf{U}}$ is the vector of nodal unknowns (acoustic pressure fluctuation here). The problem thus depends on two

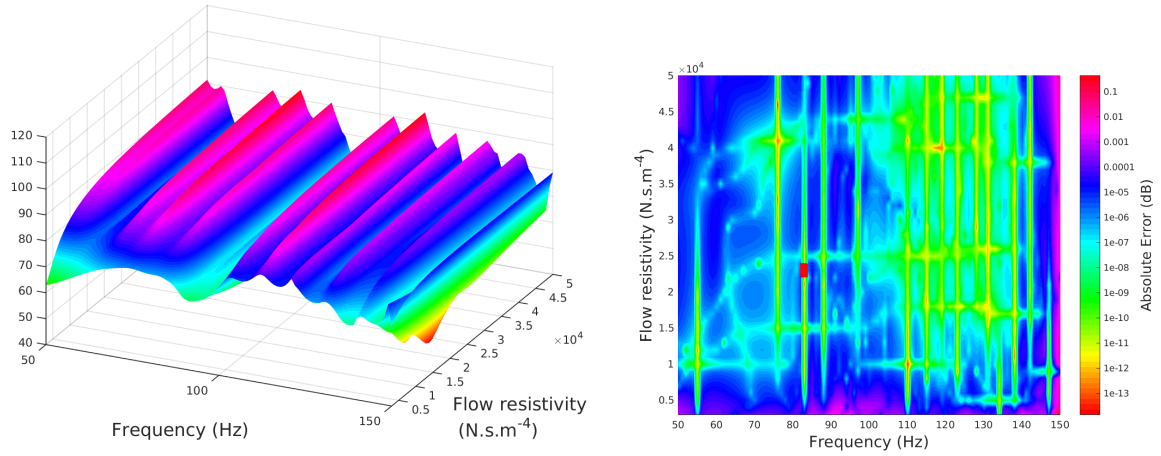

(a) (b)

Figure 2: Solution approximation by the multi-interval, bivariate WCAWE. SPL at a single point, in dB. (a) Solution approximation; (b) Approximation error (dB difference to reference solution).

chosen parameters of interest: the angular frequency ω and the static flow resistivity in the porous material Φ.

Fig. 2 the approximation of the reference solution together with the associated difference between the two solutions. As may be seen for this conservative approximation based on 15 intervals associated with very small bases (below 20 components), the approximation is excellent (well below 0.1 dB difference) for a fraction of the cost associated with the reference problem.

ACKNOWLEDGEMENTS

The financial support from the Swedish Research Council (VR Grant 2015-04925) and the Centre for ECO2 Vehicle Design (VINNOVA Grant 2016-05195) are gratefully acknowledged.

REFERENCES

[1] R. D. Slone, R. Lee, and J.-F. Lee. Well-conditioned asymptotic waveform evaluation for finite elements. *IEEE Transactions on Antennas and Propagation*, 51(9):2442–2447, 2003.

[2] M. S. Lenzi, S. Lefteriu, H. Beriot, and W. Desmet. A fast frequency sweep approach using Padé approximations for solving Helmholtz finite element models. *Journal of Sound and Vibration*, 332(8):1897–1917, 2013.

[3] R. Rumpler, and P. Göransson. An assessment of two popular Padé-based approaches for fast frequency sweeps of time-harmonic finite element problems. *Proceedings of Meetings on Acoustics*, 30(1):022003, 2017. DOI: 10.1121/2.0000649

[4] G.A. Baker and P.R. Graves-Morris. *Padé approximants*, vol. 59. Cambridge Univ. Press, 1996.

[5] R. Djellouli, C. Farhat, and R. Tezaur. A fast method for solving acoustic scattering problems in frequency bands. *Journal of Computational Physics*, 168(2):412–432, 2001.

[6] R. Rumpler, P. Göransson, and J.-F. Deü. A finite element approach combining a reduced-order system, padé approximants, and an adaptive frequency windowing for fast multi-frequency solution of poro-acoustic problems. *Int. J. Numer. Meth. Eng.*, 97(10):759–784, 2014.

[7] P. Guillaume. Nested multivariate padé approximants. *Journal of computational and applied mathematics*, 82(1):149–158, 1997.

[8] R. Rumpler, P. Göransson, and H.J. Rice. An adaptive strategy for the bivariate solution of finite element problems using multivariate nested Padé approximants. *International Journal for Numerical Methods in Engineering*, 100(9):689–710, 2014.

[9] R. Rumpler. Padé approximants and the modal connection: towards increased robustness for fast parametric sweeps. *Int. J. Numer. Meth. Eng.*, 113(1):65–81, 2018.

[10] R. Rumpler, R. Rodriguez Sánchez, and P. Göransson Multivariate Padé approximants for finite element solutions with complex parametric dependence. *COMPDYN 2019*, Crete, Greece, 24-26 June 2019.

GENERAL BLOCH MODELING OF PIECEWISE PERIODIC STRUCTURES

C. Droz[1a,2*], E. Deckers[1b,2] and W. Desmet[1a,2]

[1a]KU Leuven, Mechanical Engineering Department, Heverlee, BELGIUM
Email: christophe.droz@kuleuven.be

[1b] KU Leuven, Diepenbeek Campus, Mechanical Engineering Technology TC, Diepenbeek, BELGIUM

[2]DMMS Lab, Flanders Make, BELGIUM

ABSTRACT

Bloch theory is broadly used to determine local wave dispersion characteristics of periodic media, which are key vibroacoustic indicators in a number of research fields such as metamaterials. Nonetheless, numerical frameworks based on Bloch theory, such as the Wave Finite Element method, can also be used to compute the dynamic response of large-scaled waveguides' assemblies. This formalism was used to tackle a variety of problems such as damage localization, material identification or vibroacoustic optimization of periodic media. The focus of this work is therefore to review and generalize the wave-finite element framework, as a tool for exploring wave dispersion, scattering or dynamic response in piecewise periodic structures.

1 INTRODUCTION

The need to de-carbonize our economy has led to an urgent strive for lightweight alternatives to various structural components used in the transportation industry. Combined with increasingly challenging acoustic comfort and safety EU regulations, the compromise between enhanced vibroacoustic performances and lightweight design is often achieved at the cost of an increased topological and material complexity. In the mid-frequency range (generally the low-medium audible bandwidth), this complexity involves a variety dynamic behaviors which may co-exist at different scales (e.g. see. [1]) In terms of modeling, this can be tackled by using refined finite element descriptions of these structures. Therefore, tremendous progresses had to be made on the acoustic modeling and optimization of complex metamaterials and meta-structures, which are generally relying on model order reduction schemes or the introduction of relevant yet simple vibroacoustic indicators. Noteworthy, most of these indicators (e.g. transmission loss, dispersion curves, scattering coefficients) have the remarkable advantage of being retrieved from a single unit-cell model by exploiting multi-scale or periodic structure theories (see [2, 3]). For acoustic applications, one can mention the succession of works [4–8] only to cite a few dedicated to retrieve the sound transmission loss of periodic waveguides. Although it is now possible to design and produce meta-structures with desirable vibroacoustic performances within targeted bandwidths, these components still rarely appear among the most critical parts of a structure. Most metamaterials are therefore considered as "add-ons" to an existing structure whose integrity is guaranteed or monitored using state-of-the-art inspection techniques. A further embedding of lightweight meta-structures in the design process of critical transportation components will undeniably raise the following question: can we achieve the structural health monitoring of such complex structures?

In the presence of variable or uncertain boundary conditions, wave-based inspection techniques can prove efficient to perform damage inspection on specific regions of a waveguide. Periodic structure theory can also help to compute the dynamic response, hence provides an efficient numerical framework for modeling large-scaled slender structures such as pipes, ducts, blades, etc. The so-called "Wave Finite Element" method have been used in a variety of contexts relevant to SHM/NDE applications. Kessentini et al. [9] used the diffusion matrix method along with the WFE framework to study the transmission and reflection of acoustic waves in ducts. Mitrou et al. [10] investigated the scattering produced by infinite plates' junctions using the same method. Gras et al. [11] extended a formulation for railways with periodic supports and several applications were proposed to compute the forced response and scattering matrices of two waveguides connected by a junction, an external load or a damage/delamination [12]. An overview of the Bloch modeling framework is therefore proposed in this work.

2 METHOD AND RESULTS

The above formalism was implemented in many ways, including various edges or boundary conditions, the coupling of two waveguides with a middle junction or external loads. First, we propose an overview of Bloch modeling framework for 1D structures with recent developments on resolution techniques. Our aim is then to present a simple formalism addressing a wide range of possible waveguide configurations, where Bloch theory can be used to reduce considerably the modeling and computational efforts. Note that in many cases, a structure can be decomposed into a combination of periodic parts, separated by joints, coupling and loading regions, so that it can eventually be described as a piecewise periodic structure. The displacement $\mathbf{u}$ at any unit-cell position p of a N-cell waveguide section can be expressed using the following Bloch

expansion:

$$\mathbf{u}_p = \sum_{i=1}^{n} \lambda_i^p \Psi_i^+ \mathbf{Q}_i^+ + \lambda_i^{N-p} \Psi_i^- \mathbf{Q}_i^-, \tag{1}$$

where $\mathbf{Q}_i^+$ and $\mathbf{Q}_i^-$ are the respective wave amplitudes while the n positive Ψ_i^+ and negative Ψ_i^- eigenvectors and the propagation constants λ_i are solution of the quadratic eigenvalue problem Eq.(2), which is function of the unit-cell's dynamic stiffness sub-matrices $\mathbb{D}_{ab}$:

$$\left(\frac{1}{\lambda_i} \mathbb{D}_{RL} + (\mathbb{D}_{LL} + \mathbb{D}_{RR}) + \lambda_i \mathbb{D}_{RL} \right) \Psi_i = 0. \tag{2}$$

A simple validation is shown in Figure 1. The structure is made of four different regions name 'A', 'B', 'C', and 'D', while four loads are applied, including a load splitting the region 'B' in two. The framework provides good results although some numerical issues have to be discussed.

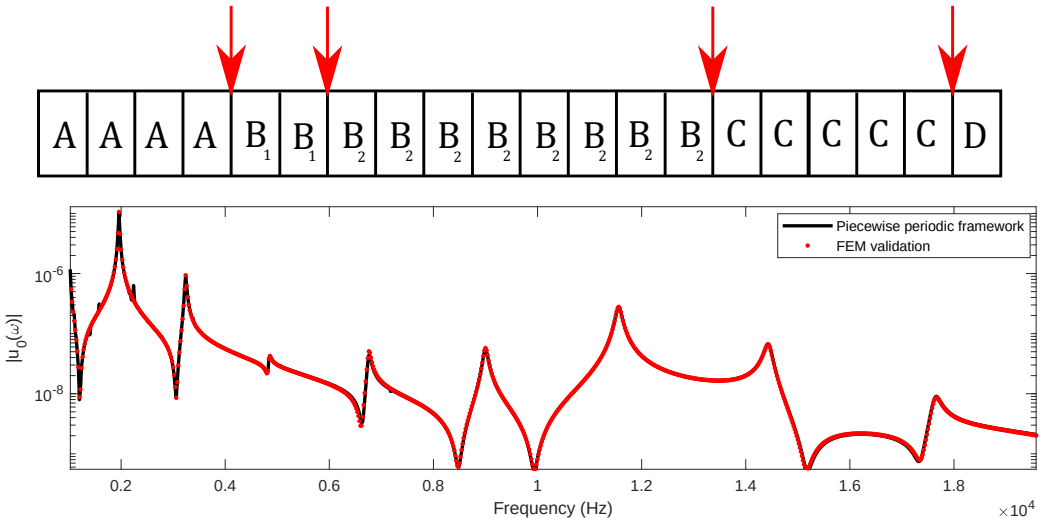

Figure 1. Forced response of a piece-wise periodic structure with irregular punctual loads

3 PERSPECTIVES

The framework is generalized and applied to various examples relevant to SHM and in a context damage scattering analysis.

A typical case scenario is shown in Figure 2, where different FE models of structural damages can be considered in a large-scaled duct whose periodicity is of equivalent or higher dimension that those considered damages or defects. Note that this reduced models can be efficiently used for sub-structuring purposes, while different 'damages' can be analyzed with remarkable computational efficiency (i.e. 2-4 orders of magnitude compared with FEM).

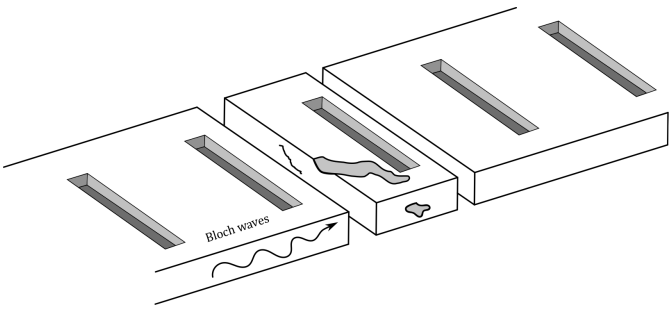

Figure 2. Scattering of Bloch waves in a periodic waveguide.

ACKNOWLEDGMENTS

C. Droz is an individual Marie Skłodowska-Curie fellow funded by the European Union's Horizon 2020 research and innovation programme under the grant agreement No. 797034 (WIDEA). The research of E. Deckers is funded by a grant from the Research Foundation - Flanders (FWO). The Research Fund KU Leuven is gratefully acknowledged for its support (IOF).

REFERENCES

[1] Pascal Fossat, Claude Boutin, and Mohamed Ichchou. Dynamics of periodic ribbed plates with inner resonance: Analytical homogenized model and dispersion features. *Int. J. Solids Struct.*, 152:85–103, 2018.

[2] D.J. Mead. A general theory of harmonic wave propagation in linear periodic systems with multiple coupling. *J. Sound Vib.*, 27(2):235–260, 1973.

[3] Y.L.Y.K. Yong and Y.K. Lin. Propagation of decaying waves in periodic and piecewise periodic structures of finite length. *J. Sound Vib.*, 129(1):99–118, 1989.

[4] A. Parrinello and G.L. Ghiringhelli. Transfer matrix representation for periodic planar media. *J. Sound Vib.*, 371:196–209, 2016.

[5] J.-L. Christen, M. Ichchou, A. Zine, and B. Troclet. Wave finite element formulation of the acoustic transmission through complex infinite plates. *Act. Acust Ac*, 102(6):984–991, 2016.

[6] E. Deckers, S. Jonckheere, L. Van Belle, C. Claeys, and W. Desmet. Prediction of transmission, reflection and absorption coefficients of periodic structures using a hybrid wave based–finite element unit cell method. *J. Comp. Phys.*, 356:282–302, 2018.

[7] Y. Yang, B.R. Mace, and M.J. Kingan. Vibroacoustic analysis of periodic structures using a wave and finite element method. *J. Sound Vib.*, 457:333–353, 2019.

[8] F. Errico, M. Ichchou, F. Franco, S. De Rosa, O. Bareille, and C. Droz. Schemes for the sound transmission of flat, curved and axisymmetric structures excited by aerodynamic and acoustic sources. *J. Sound Vib.*, 456:221 – 238, 2019.

[9] A. Kessentini, M. Taktak, M.A.B. Souf, O. Bareille, M.N. Ichchou, and M. Haddar. Computation of the scattering matrix of guided acoustical propagation by the wave finite element approach. *App. Ac.*, 108:92–100, 2016.

[10] G. Mitrou, N. Ferguson, and J. Renno. Wave transmission through two-dimensional structures by the hybrid fe/wfe approach. *J. Sound Vib.*, 389:484–501, 2017.

[11] T. Gras, M.-A. Hamdi, M.B. Tahar, O. Tanneau, and L. Beaubatie. On a coupling between the finite element (fe) and the wave finite element (wfe) method to study the effect of a local heterogeneity within a railway track. *J. Sound Vib.*, 429:45–62, 2018.

[12] C. Droz, O. Bareille, J.-P. Lainé, and M.N. Ichchou. Wave-based shm of sandwich structures using cross-sectional waves. *Struct. Contr. Health Monit.*, 25(2):e2085, 2018.

TOWARDS NONLINEAR MULTIMODAL APPROACHES FOR VIBRATION ENERGY HARVESTING

N. Kacem and N. Bouhaddi

Univ. Bourgogne Franche-Comté, FEMTO-ST Institute, CNRS/UFC/ENSMM/UTBM,
Department of Applied Mechanics, 24 rue de l'Epitaphe, 25000 Besançon, France
Email: najib.kacem@univ-fcomte.fr, noureddine.bouhaddi@univ-fcomte.fr

ABSTRACT

The mechanical structures are subjected to ambient and internal vibrations, which could be exploited to produce energy by using suitable transducers, enabling the conversion of mechanical energy into electrical energy. The energy produced in these cases can be stored and used in low-energy consuming applications for which autonomy is a priority regardless of the external conditions in which these structures are located. This energy harvesting approach is suitable to small-scale smart systems such as wireless sensor networks or portable embedded systems for various applications such as monitoring, diagnosis and control in the fields of urban transport, aeronautics, biomedical, environment and so on. Vibration Energy Harvesters (VEHs) are generally designed and optimized for frequencies that correspond to those of the excitation. These resonators possess low damping, which causes a great loss of the harvested electrical power as soon as a slight deviation of the excitation frequency from the resonant one occurs. To overcome this issue, it has been shown that nonlinearities or modal interactions significantly improve the frequency bandwidth or the harvested power. We will here focus on how these properties have opened the way towards nonlinear multimodal approaches for vibration energy harvesting and more specifically on the functionalization of nonlinearities and structural quasiperiodicity in order to take advantage of both mode localization and multistability. Interestingly, these phenomena induce a substantial widening of the useful frequency bandwidth and increase the harvested power, which has been highlighted thanks to the design and experimental characterization of a nonlinear electromagnetic VEH based on nearly identical coupled resonators.

Technical sessions

NONLINEAR FREE VIBRATIONS OF COMPOSITE STRUCTURES VIA THE X-RITZ METHOD

A. Milazzo[1]

[1]Department of Engineering
University of Palermo, Palermo, ITALY
Email: alberto.milazzo@unipa.it

ABSTRACT

The analysis of large amplitude vibrations of thin-walled cracked structures build as plate assembly is considered in this study. The problem is addressed via a Ritz approach, called X-Ritz, based on the first order shear deformation theory and von Kármán's geometric nonlinearity assumptions. The trial functions are expressed as series of regular orthogonal polynomial products supplemented with special functions able to represent the crack behaviour; boundary functions are used to guarantee the fulfillment of the kinematic boundary conditions. Results are presented, which illustrate the influence of cracks on the stiffening effect due to large amplitude vibrations.

1 INTRODUCTION

Analysis tools able to predict the effects of cracks on the plate dynamics may help prevent undesired effect and improve structural design towards enhanced safety. Many studies focused on the linear vibration analysis of both isotropic and composite structures, providing for a comprehensive knowledge of the plate dynamic behaviour and design guidelines. However, for an accurate appraisal of structural dynamics, in some applications the nonlinear free vibration problem needs to be investigated, which for cracked configurations has been poorly addressed especially for composite structures. In the present paper, the large amplitude free vibrations of cracked composite structures are studied based on an eXtended Ritz approach, dubbed as X-Ritz, recently proposed by the author and his co-workers [1–3].

2 FORMULATION

Let us consider a thin-walled structure consisting of the assembly of composite, multilayered, quadrilateral plates joined along their edges, see Fig. 1(a). Each constituent plate can present an embedded through-the-thickness crack. The k-th plate of such a structure is modeled by the first-order shear deformation theory [4]. Assuming that the von Kármán's strain-displacements

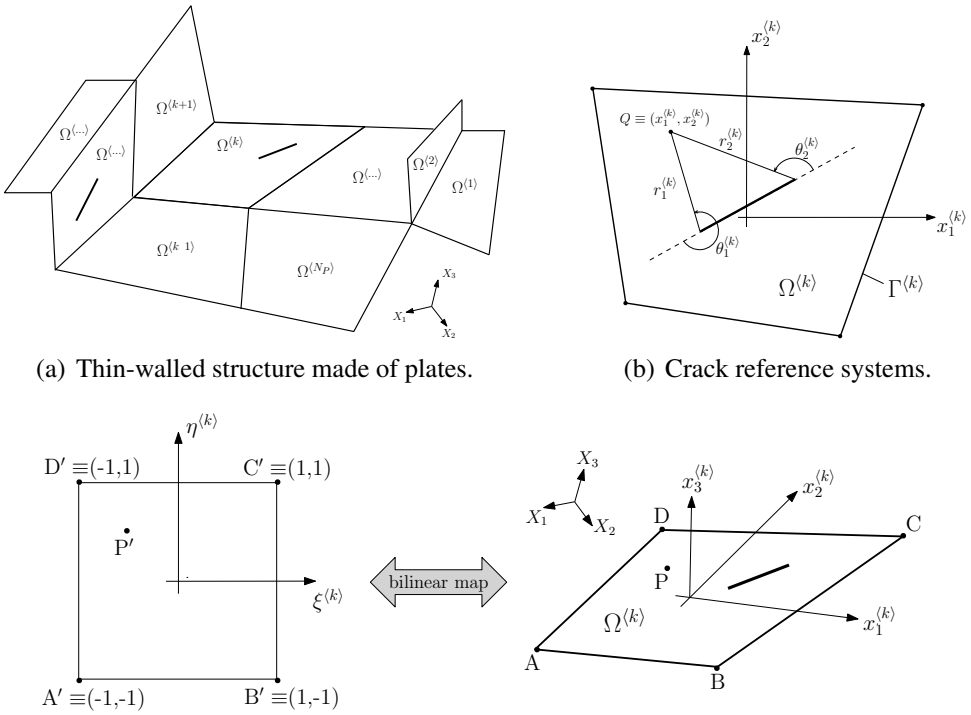

(a) Thin-walled structure made of plates.

(b) Crack reference systems.

(c) Plate reference coordinates.

Figure 1. Thin-walled structure configuration and reference systems

equations, the constitutive equations and the kinematical boundary conditions are verified, the free vibrations governing equations can be deduced from the stationarity of the total energy (potential and kinetic) providing that the joining conditions along the contiguous plates edges are fulfilled. In the framework of variational calculus, this statement can be implemented by augmenting the expression of the total energy of the structure with the plates joining equations via the penalty technique, obtaining a functional Π whose free stationarity with respect to the generalized displacements provides the problem governing equations. Details on the functional definition and expression can be found in Ref. [3].

The solution of the non linear vibration problem of cracked plates is obtained by a Ritz approach, called X–Ritz, that approximates the generalized displacements via suitable defined enriched trial functions able to describe the crack opening and the crack tip fields [1, 3]. With reference to Figs. 1(b) and 1(c), the plate generalized displacement component χ is expressed as

$$
\begin{aligned}
\chi = f_\chi(\xi,\eta) \sum_{m=0}^{M_\chi}\sum_{n=0}^{N_\chi} \mathscr{L}_m(\xi)\mathscr{L}_n(\eta) C_{\chi mn}^{\langle 0\rangle} + \\
g_\chi(\xi,\eta) \sum_{m=\overline{m}_\chi}^{\overline{N}_\chi^{\langle 1\rangle}} \sum_{n=0}^{m} r_1^{\frac{2m-1}{2}} \cos\left(\frac{2n+1}{2}\theta_1\right) C_{\chi mn}^{\langle 1\rangle} + \\
g_\chi(\xi,\eta) \sum_{m=\overline{m}_\chi}^{\overline{N}_\chi^{\langle 2\rangle}} \sum_{n=0}^{m} r_2^{\frac{2m-1}{2}} \cos\left(\frac{2n+1}{2}\theta_2\right) C_{\chi mn}^{\langle 2\rangle} + \\
g_\chi(\xi,\eta) \sum_{m=\overline{m}_\chi}^{\overline{N}_\chi^{\langle 3\rangle}} \sum_{n=0}^{m} \sqrt{r_2{}^3}\sin^2(\theta_2/2) r_1^{\frac{2m-1}{2}} \sin\left(\frac{2n+1}{2}\theta_1\right) C_{\chi mn}^{\langle 3\rangle} + \\
g_\chi(\xi,\eta) \sum_{m=\overline{m}_\chi}^{\overline{N}_\chi^{\langle 4\rangle}} \sum_{n=0}^{m} \sqrt{r_1{}^3}\sin^2(\theta_1/2) r_2^{\frac{2m-1}{2}} \sin\left(\frac{2n+1}{2}\theta_2\right) C_{\chi mn}^{\langle 4\rangle}
\end{aligned}
\tag{1}
$$

where $\mathscr{L}_j(\zeta)$ is the j–th order Legendre polynomial of the coordinate ζ and the $C_{\chi mn}^{\langle i\rangle}$ are the unknown coefficients. The functions $f_\chi(\xi,\eta)$ and $g_\chi(\xi,\eta)$ are suitably defined to guarantee the fulfillment of the kinematical boundary conditions [5]. Details on the characteristics of these trial functions can be found in Refs. [1, 6]. Here, it is remarked that: (i) the first series in Eq. (1) considers regular functions able to describe the global plate behaviour; (ii) the other series consist of terms able to describe the crack opening and the singular fields at the crack tips. Their starting index $\overline{m}_\chi$ governs the asymptotic behaviour at the crack tips, and it is chosen assuming that the strain energy density asymptotically behaves as r^{-1} when $r \to 0$ [7]; (iii) the trial function defined in Eq. (1) holds also for uncracked plates when only the first series is retained.

By using the above discussed generalized displacements, the discretized form of the functional Π is obtained. Applying the standard calculus of variations and assuming harmonic motion the nonlinear free vibration governing equations are deduced as [1, 3]

$$
\left[\boldsymbol{K} + \boldsymbol{K}_{NL}\left(\boldsymbol{X}\right) - \omega^2 \boldsymbol{M}\right] \boldsymbol{X} = \boldsymbol{0} \tag{2}
$$

where ω is the natural frequency, $\boldsymbol{X}$ is the vector collecting the unknown Ritz coefficients. The definition of the matrices involved in Eq. (2) can be recovered from Refs. [2, 3]. The Eq. (2) identifies a nonlinear eigenvalue problem, whose solution can be achieved iteratively for a fixed amplitude of the eigenvectors.

3 RESULTS

To show the effectiveness of the method for composite structures nonlinear free vibration analysis, representative results are presented for the rectangular simply-supported blade stiffened composite panel shown in Fig. 2. The following geometrical parameters have been set: $b = 0.70$ m, $\ell = 0.28$ m, $h = 0.02$ m, $a = 0.14$ m and $\beta = 0°$. Layups for the skin and blades are $[0/45/-45/0]_S$ and $[(0/45/-45/0)_S]_3$, respectively, with 0.15 mm thick layers whose material properties are $E_1 = 113$ GPa, $E_2 = 9$ GPa, $\nu_{12} = 0.302$, $G_{12} = G_{13} = G_{23} = 3.82$ GPa. Analyses were performed by considering the panel composed by 7 plates: one plate for each bay skin and one plate for each blade stringer. The employed approximation scheme uses polynomials with order up to the eighth and enrichment contributions with $\overline{N}_\chi^{\langle j\rangle} = 4$. Fig. 3 shows the backbone curves of the nonlinear to linear frequency ratio of the first mode versus the vibration amplitude for both the uncracked and cracked configurations. The stiffening effect of large amplitude on free vibrations is clearly observed with a tendency to a saturation effect, which is more pronounced for the uncracked panel.

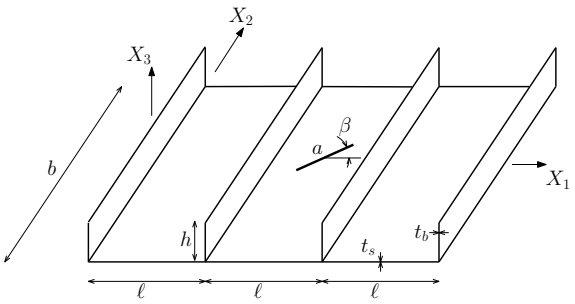

Figure 2. Blade stiffened composite panel geometry.

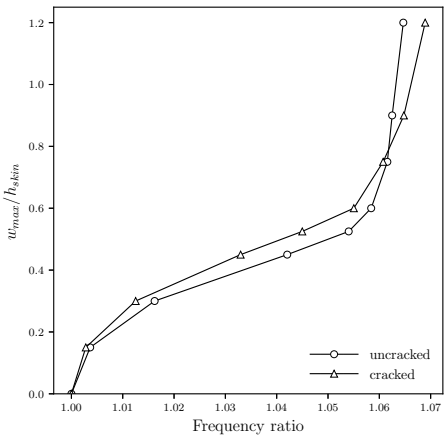

Figure 3. First mode nonlinear to linear frequency ratio with respect to the vibration amplitude.

4 CONCLUDING REMARKS

The X-Ritz method has been proposed for the analysis of nonlinear free vibrations of cracked composite structures. The presented results show the capacity of the approach to describe the effects of large amplitude on the natural frequency, confirming the potentiality of the method.

REFERENCES

[1] A. Milazzo, I. Benedetti, and V. Gulizzi. An extended ritz formulation for buckling and post-buckling analysis of cracked multilayered plates. *Composite Structures*, 201:980–994, 2018.

[2] Ivano Benedetti, Vincenzo Gulizzi, and Alberto Milazzo. X-ritz solution for nonlinear free vibrations of plates with embedded cracks. *Aerotecnica Missili & Spazio*, 98(1):75–83.

[3] V. Gulizzi, V. Oliveri, and A. Milazzo. Buckling and post-buckling analysis of cracked stiffened panels via an X-Ritz method. *Aerospace Science and Technology*, 86:268–282, 2019.

[4] J.N. Reddy. *Mechanics of Laminated Composite Plates and Shells. Theory and analysis*. CRC Press, 2004.

[5] A. Milazzo and V. Oliveri. Post-buckling analysis of cracked multilayered composite plates by pb-2 rayleigh-ritz method. *Composite Structures*, 132:75–86, 2015.

[6] CS Huang, AW Leissa, and RS Li. Accurate vibration analysis of thick, cracked rectangular plates. *Journal of Sound and Vibration*, 330(9):2079–2093, 2011.

[7] Alan T. Zehnder and Mark J. Viz. Fracture mechanics of thin plates and shells under combined membrane, bending, and twisting loads. *Applied Mechanics Reviews*, 58(1):37–48, 2005.

ENERGY FLOW IN 2D ORTHOTROPIC MEDIA BY THE RADIATIVE ENERGY TRANSFER THEORY

Qiang Zhong[1,2] , Haibo Chen[2], Alain Le Bot[1*]

[1]Laboratoire de tribologie et dynamique des systèmes
École centrale de Lyon, Lyon, FRANCE
Email: qzhong@mail.ustc.edu.cn, alian.le-bot@ec-lyon.fr

[2]CAS Key Laboratory of Mechanical Behavior and Design of Materials
University of Science and Technology of China, Hefei, CHINA
Email: qzhong@mail.ustc.edu.cn

ABSTRACT

In this study, we develop the high-frequency energy method called the radiative energy transfer method (RETM) for orthotropic media. For homogeneous orthotropic media, the energy velocity vector has an amplitude which depends on the ray direction. First, the kernel functions of energy density and energy flow vector are given. The derivation shows that the kernel functions not only depend on the distance but also the angle from source to receiver. Second, a boundary integral equation is set for energy inside the domain. For a finite orthotropic media, the fictitious sources on the boundary are determined by the energy balance. Simulations are performed for a high frequency vibrating rectangular orthotropic plate. Results of energy density distribution and energy flow field show the correctness of the model by comparing with the traditional modal superposition solution.

1 INTRODUCTION

In the past few decades, various energetic methods have been developed to alternate Statistical Energy Analysis (SEA)[1] beyond its limits of application. One of them called Energy Finite Element Method (EFEM) or Power Flow Analysis (PFA) [2] uses the same variables as in SEA: energy and energy flow and is based on an equation similar to the heat conduction equation. However, for 2D system, the solution of EFEM indicates that the energy density decreases like $W \propto \exp(-\eta\omega r)/\sqrt{r}$ in opposition with $W \propto \exp(-\eta\omega r)/r$ for the exact result where r is the source-receiver distance, η the damping loss factor and ω the circular frequency [3]. To solve this problem, Alain Le Bot [4, 5] proposed a high-frequency energy theory called radiosity method [6, 7] or the radiative energy transfer method (RETM) which provides the exact energy density distribution.

Considering the widely application of the composite materials, the energy methods have been developed for anisotropic composites in recent years except for RETM. For instance, Renjin [8] and Park[9] have respectively extended SEA and PFA to composites. This paper proposes to develop RETM for homogeneous orthotropic media aiming application to anisotropic composites. Finally, we perform a numerical illustration which provides the energy density distribution and the energy flow field of a typical orthotropic plate.

2 THEORETICAL FORMULATION

This formulation involves two energy variables which are the energy density W and the energy flow vector $\mathbf{I}$. The group velocity $\mathbf{c}_g(\varphi)$ is a vector which depends on the ray direction angle φ from source to receiver. In homogeneous and anisotropic media, rays follows straight lines as it can be verified by Fermat's principle[10]. To establish the energy model, four basic assumptions are required: (H1) linear, homogeneous system in steady-state conditions under broadband excitation centered on ω, (H2) evanescent waves and near-field are neglected, (H3) interferences between propagative waves are ignored, (H4) the directivity of fictitious reflection sources on the boundary obeys Lambert's law.

Let us start with the local power balance for an unloaded region,

$$\nabla \cdot \mathbf{H}(r,\ \varphi) + \eta\omega G(r,\ \varphi) = 0 \tag{1}$$

where $r = |M - S|$ the distance from source S to receiver M, $G(r,\ \varphi)$ the kernel function of energy density, $\mathbf{H}(r,\ \varphi)$ the kernel function of energy flow vector and $m(\varphi) = \eta\omega/c_g(\varphi)$ the wave attenuation coefficient. For pure propagating waves

$$\mathbf{H}(r,\ \varphi) = \mathbf{c}_g(\varphi) G(r,\ \varphi) \tag{2}$$

Substituting (2) into (1), we obtain the kernel functions

$$G(r,\ \varphi) = \frac{c_g(\varphi)}{C}\frac{e^{-m(\varphi)r}}{r}, \quad \mathbf{H}(r,\ \varphi) = \frac{c_g^2(\varphi)}{C}\frac{e^{-m(\varphi)r}}{r}\mathbf{u}(\varphi), \quad \text{and } C = \int_0^{2\pi} c_g^2(\varphi)\mathrm{d}\varphi \tag{3}$$

where $\mathbf{u}(\varphi) = (\cos\varphi,\ \sin\varphi)$ is the unit vector from source to receiver.

To establish the fields W and $\mathbf{I}$ for a system which contains multiple traveling waves submitted to reflection on boundaries, two principle must be applied. Firstly, the interferences between propagative waves are neglected. Therefore, the total energy density at a receiver obeys the linear superposition principle. Secondly, according to Huygens principle, the wave field is determined by superposition of the direct fields created by the real sources inside Ω and fictitious sources on the boundary $\partial\Omega$. This reads

$$W(M) = \int_\Omega \rho(S) G(r,\varphi)\mathrm{d}S + \int_{\partial\Omega} \sigma(P)\cos(\mathbf{u},\ \mathbf{n}) G(r,\varphi)\mathrm{d}P \tag{4}$$

$$\mathbf{I}(M) = \int_\Omega \rho(S) \mathbf{H}(r,\varphi)\mathrm{d}S + \int_{\partial\Omega} \sigma(P)\cos(\mathbf{u},\ \mathbf{n}) \mathbf{H}(r,\varphi)\mathrm{d}P \tag{5}$$

where ρ and σ are respectively the magnitudes of the real and the fictitious sources and $\mathbf{n}$ is the unit outward normal at point P on boundary $\partial\Omega$. The presence of $\cos(\mathbf{u},\ \mathbf{n})$, cosine of emission angle at P is justified by Lambert's law.

To determine the fictitious sources, the power balance at the boundary $\partial\Omega$ is considered. Assuming that no power is absorbed by the boundary, the power reflects by the boundary obeys Lambert's law. Then, the balance equation is

$$\frac{\sigma(P)}{C_\beta} = \left[\int_\Omega \rho(S)\mathbf{H}(r,\varphi)\mathrm{d}\Omega + \int_\Gamma \sigma(P')\cos(\mathbf{u},\ \mathbf{n}')\mathbf{H}(r,\varphi)\mathrm{d}P'\right]\mathbf{n} \quad (P' \neq P) \tag{6}$$

where $\mathbf{n}'$ is the unit outward normal at point P', $C_\beta = \int_{-\pi/2}^{\pi/2} c_g^2(\beta+\theta)cos\theta\mathrm{d}\theta$, β is defined the angle between the outward normal and the principal axes and θ is the angle between the emitted ray and the outward normal.

Table 1. Parameter numerical values of the orthotropic plate.

Parameter	a	b	M_m	D_x	D_y	ν_x	ν_y
Units	m	m	kg/m^2	$N\cdot m$	$N\cdot m$	-	-
Value	1	1	12.4	8	160	0.4	0.02

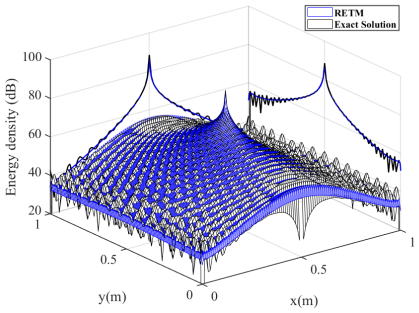

Figure 1: Energy response level of a rectangular orthotropic plate under a harmonic excitation (f = 8000Hz, η=0.1, ref=$1\times10^{12}\mathrm{J/m^2}$).

Eq. (6) is a Fredholm equation of second type. Solving it by classical numerical methods gives the magnitude of the fictitious sources $\sigma(P)$. With Eqs. (4) and (5), the energy density $W(M)$ and energy flow $\mathbf{I}(M)$ are then obtained.

3 SIMULATION RESULTS AND DISCUSSION

The simulations are performed on an orthotropic plate under a high-frequency harmonic point load with the unit force amplitude located at the center of the plate. The exact energy density and energy flow field calculated here are based on the formulas shown in [9]. physical properties of the plate are shown in Table 1 where a and b are the length and width, M_m the mass per unit area, ν_x and ν_y Poisson's ratios, D_x and D_y the principal bending stiffnesses of the material. We assume that the principal axes of the orthotropic material are co-linear with the global Cartesian coordinates.

The group velocity is $c_g(\varphi) = 2\omega/[\kappa\Phi(\varphi)]$ where $\Phi(\varphi) = (\sqrt[4]{\frac{D_y}{D_x}}\cos^2\varphi + \sqrt[4]{\frac{D_x}{D_y}}\sin^2\varphi)^{0.5}$ and $\kappa = (M_m\omega^2/\sqrt{D_xD_y})^{0.25}$. The energy density level simulated by RETM well matches with the modal superposition solution [11] as shown in Figure 1 when the excitation is centred on 8 kHz and the damping loss factor is $\eta = 0.1$. As shown in Figure 2 (b), the energy flow vector (the blue line) and the wave front curve (the black dashed line) predicted by RETM ignored the small oscillations visible on the reference solution. Compared with the exact solution, RETM approximately evaluate the wave front curve and energy flow field of the high-frequency vibration orthotropic plate.

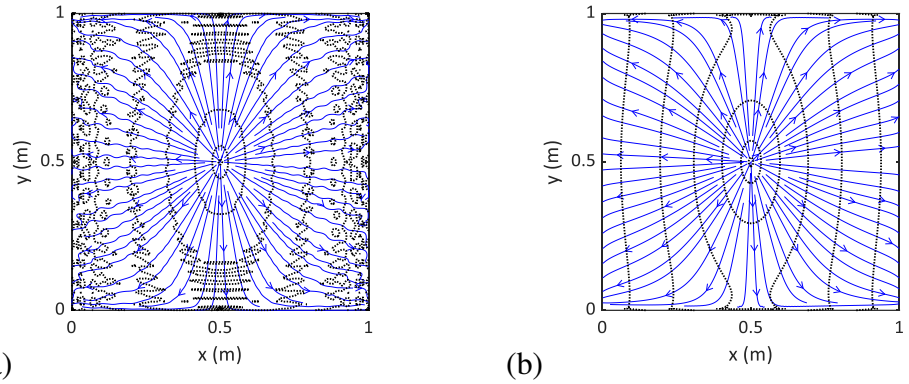

Figure 2: Energy flow field $\mathbf{I}$ and corresponding group wave front curve ($f = 8000$Hz, η=0.1): (a) Modal superposition solution; (b) RETM.

3.1 Conclusion

This study extended the RETM to 2D homogeneous orthotropic media. Firstly, basic assumptions for building the wave field are established. Secondly, the formulas of the RETM are derived by taking all the assumptions. Finally, a series of simulations on a typical orthotropic plate show the correction of the model. In general, the energy model presented in this paper ignores the small oscillations of the local particles and predicts a smooth energy response of the high-frequency vibrational 2D orthotropic media.

REFERENCES

[1] A. Le Bot. *Foundation of statistical energy analysis in vibroacoustics*. OUP Oxford, 2015.

[2] DJ Nefske and SH Sung. Power flow finite element analysis of dynamic systems: basic theory and application to beams. *Journal of Vibration, Acoustics, Stress, and Reliability in Design*, 111(1):94–100, 1989.

[3] A. Le Bot. Geometric diffusion of vibrational energy and comparison with the vibrational conductivity approach. *Journal of Sound and Vibration*, 212(4):203–224, 1998.

[4] A. Le Bot. A vibroacoustic model for high frequency analysis. *Journal of sound and vibration*, 211(4):537–554, 1998.

[5] A. Le Bot. Energy transfer for high frequencies in built-up structures. *Journal of Sound and Vibration*, 250(2):247–275, 2002.

[6] A. Le Bot. A functional equation for the specular reflection of rays. *The Journal of the Acoustical Society of America*, 112(4):1276–1287, 2002.

[7] A. Le Bot and E. Sadoulet-Reboul. High frequency vibroacoustics: A radiative transfer equation and radiosity based approach. *Wave Motion*, 51(4):598–605, 2014.

[8] K Renji and S Josephine Kelvina Florence. Estimation of strains/stresses in composite panels using statistical energy analysis. *Journal of Sound and Vibration*, 408:400–410, 2017.

[9] D-H Park, S-Y Hong, and H-G Kil. Power flow model of flexural waves in finite orthotropic plates. *Journal of sound and vibration*, 264(1):203–224, 2003.

[10] A. Le Bot. Geometrical theory of diffraction for sound radiation and structural response. *Wave Motion*, 87:179–192, 2019.

[11] A. Le Bot, Z. Bazari, P. Klein, and J. Lelong. Statistical analysis of vibration in tyres. *Journal of Sound and Vibration*, 392:187–199, 2017.

NUMERICAL SIMULATION OF SOUND TRANSMISSION THROUGH PORO-ELASTIC SHELL STRUCTURES

M.H. Gfrerer[1,2*] and M. Schanz[1]

[1]Institute for Applied Mechanics
Graz University of Technology, Graz, AUSTRIA
Email: m.gfrerer@tugraz.at, m.schanz@tugraz.at

[2]Felix-Klein-Center for Mathematics
University of Kaiserslautern, Kaiserslautern, GERMANY

ABSTRACT

A new simulation framework for the vibro-acoustic simulation of poro-elastic shells is presented. The proposed methods can be used to investigate arbitrary curved layered panels, as well as their interaction with the surrounding air. We employ a high order finite element method (FEM) for the discretization of the shell structure. In order to discretize the fluid surrounding the structure, a variational variant of the method of fundamental solutions (MFS) is developed. Thus, the meshing of the fluid domain can be avoided and in the case of unbounded domains and the Sommerfeld radiation condition is fulfilled. In order to simulate coupled fluid-structure interaction problems, the FEM and the MFS are combined to a coupled method. In order to show the potential of the method sound transmission from a cavity to an exterior half-spaces is simulated.

1 INTRODUCTION

In order to reduce noise levels which are harmful for the human health, lightweight poro-elastic materials are often used in a wide range of applications. In the present paper, we develop a numerical method for the simulation of the situation illustrated in Figure 1. We assume that the upper half-space has a sound hard ground and is divided into an bounded interior domain and an unbounded exterior domain by a laminated shell structure made of elastic and poro-elastic materials. Our main focus is to develop a simulation method in order to calculate the sound transmission from the interior to the exterior domain. We describe poro-elastic materials with the dynamic Biot theory [1, 2].

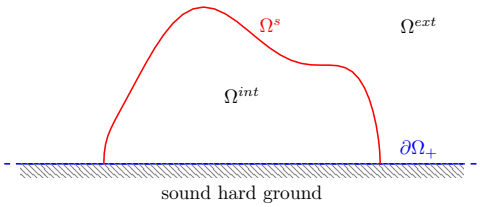

Figure 1: Problem setting: Sound hard ground surface $\partial\Omega_+$, interior fluid domain Ω^{int}, exterior fluid domain Ω^{ext}, shell structure Ω^s

One main part of our work is the extension of the poro-elastic plate theory presented in [3], to the present situation of poro-elastic layer-wise shells. The second contribution is the discretization and numerical solution of the problem. We use the finite element method for the discretization of the shell structure and a variational variant of the method of fundamental solutions for the discretization of fluid domains. Both methods are coupled to achieve a monolithic simulation.

2 PORO-ELASTIC SHELL STRUCTURE

In this section, we describe a layer-wise theory for laminated poro-elastic shells. We consider shell reference surfaces $\bar{\Omega}$ which are given parametrically by $\bar{\mathfrak{g}} : \bar{U} \subset \mathbb{R}^2 \to \bar{\Omega}$ with given parameter domain $\bar{U}$. The tangent plane is spanned by the two covariant base vectors $\overline{\mathbf{G}}_\alpha := \frac{\partial \bar{\mathfrak{g}}}{\partial \theta^\alpha}$. With the base vectors we can compute the unit normal vector $\mathbf{n}$. The parametrization of the three-dimensional shell volume Ω is given by

$$\begin{aligned} \mathfrak{g} : \ & (\bar{U} \times T) \subset \mathbb{R}^3 \to \Omega \subset \mathbb{R}^3 \\ & (\theta^1, \theta^2) \times \theta^3 \mapsto \mathfrak{g}(\theta^1, \theta^2, \theta^3) = \bar{\mathfrak{g}}(\theta^1, \theta^2) + \theta^3 \, \mathbf{n}, \end{aligned} \tag{1}$$

with the one-dimensional thickness interval T. We consider a layered shell structure with a layup as depicted in Figure 2. The total number of layers is L. Each layer has a thickness t_i, $i = 1 \dots L$

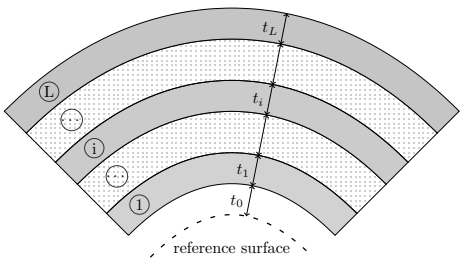

Figure 2: Layup of the shell

and is classified as elastic or poro-elastic. The distance from the reference surface to the bottom of the shell is denoted by t_0. Furthermore, we define the individual layer thickness intervals $T_i = \left[\sum_{j=0}^{i-1} t_j \ , \ \sum_{j=0}^{i} t_j\right]$. Thus, $T = \bigcup_{i=1}^{L} T_i$. The relations between the local thickness coordinate $\tau_i \in [0, 1]$ of layer i and the global thickness coordinate $\theta^3 \in T_i$ are

$$\tau_i(\theta^3) = \frac{1}{t_i}\left(\theta^3 - \sum_{j=0}^{i-1} t_j\right), \quad \text{and} \quad \theta^3(\tau_i) = \sum_{j=0}^{i-1} t_j + t_i \, \tau_i \, . \tag{2}$$

The present layer-wise theory is based on the assumed seven-parameter displacement field for layer $\ell \in \{1, \dots, L\}$ of the form

$$\mathbf{u}^\ell(\theta^1, \theta^2, \theta^3) = \overset{(1)}{V}(\tau_\ell(\theta^3)) \overset{(1,\ell)}{u_i}\, \mathbf{e}^i + \overset{(2)}{V}(\tau_\ell(\theta^3)) \overset{(2,\ell)}{u_i}\, \mathbf{e}^i + \overset{(n)}{V}(\tau_\ell(\theta^3)) \overset{(n,\ell)}{u}\, \mathbf{n}. \tag{3}$$

The through-the-thickness functions are $\overset{(1)}{V}(\tau) = 1 - \tau$, $\overset{(2)}{V}(\tau) = \tau$, $\overset{(n)}{V}(\tau) = \tau^2 - \tau$. Furthermore, $\overset{(1,\ell)}{u}_i$, $\overset{2,\ell}{u}_i$, $\overset{(n,\ell)}{u}$ are seven local displacement parameters and $\mathbf{e}^i$ are the base vectors of a Cartesian coordinate system. Thus, the parameters $\overset{(1,\ell)}{u_i} = \overset{(1,\ell)}{u_i}(\theta^1, \theta^2)$ and $\overset{(2,\ell)}{u_i} = \overset{(2,\ell)}{u_i}(\theta^1, \theta^2)$ describe the displacement of the bottom ($\tau = 0$) and the top ($\tau = 1$) of layer ℓ, respectively. This is enhanced with the parameter $\overset{(n,\ell)}{u_i} = \overset{(n,\ell)}{u_i}(\theta^1, \theta^2)$. Following [3], the fluid pressure field in poro-elastic layers is approximated by a quadratic expansion through-the-thickness. The pressure field for layer ℓ is assumed to be of the form

$$p^\ell(\theta^1, \theta^2, \theta^3) = \overset{(1)}{V}(\tau_\ell(\theta^3)) \overset{(1,\ell)}{p} + \overset{(2)}{V}(\tau_\ell(\theta^3)) \overset{(2,\ell)}{p} + \overset{(n)}{V}(\tau_\ell(\theta^3)) \overset{(n,\ell)}{p}, \tag{4}$$

where $\overset{(1,\ell)}{p} = \overset{(1,\ell)}{p}(\theta^1, \theta^2)$, $\overset{(2,\ell)}{p} = \overset{(2,\ell)}{p}(\theta^1, \theta^2)$, and $\overset{(n,\ell)}{p} = \overset{(n,\ell)}{p}(\theta^1, \theta^2)$ are three local parameters.

3 NUMERICAL METHODS

We use the finite element method to discretize the poro-elastic shell structure. Here, our implementation allows for hierarchical shape functions of arbitrary order. Fluid domains are discretized by the method of fundamental solutions. This allows us to circumvent a volume parametrization of the fluid domains and the Sommerfeld radiation condition is fulfilled identically. For further details we refer to [4–6].

4 NUMERICAL EXAMPLE - DEFORMED SWEEP

We consider the problem geometry depicted in Figure 3. The shell structure is composed of an

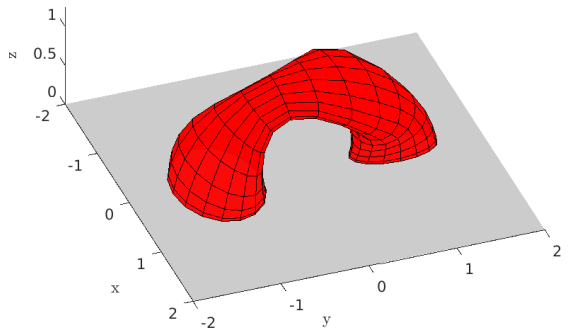

Figure 3: Geometry of the deformed sweep problem

elastic aluminum layer (0.01 m) and a poro-elastic polyurethane layer ($0.03\,\mathrm{m}$). The poro-elastic layer is in contact with the interior fluid. For the study of sound transmission from the interior to the exterior, we use a 64-element mesh for the FEM and 372 MFS source points for the interior, as well as for the exterior fluid. A source with unit strength for the excitation of the system is placed at $[0\,\mathrm{m}, -1\,\mathrm{m}, 0.5\,\mathrm{m}]$. We consider an interior evaluation point $[0\,\mathrm{m}, 1\,\mathrm{m}, 0.5\,\mathrm{m}]$ and an exterior evaluation point $[0\,\mathrm{m}, 0\,\mathrm{m}, 1.5\,\mathrm{m}]$. The results are given in Figure 4. We compare the cases *uncoupled MFS*, *aluminum shell* and *poro-elastic shell*. The results for the cases *uncoupled MFS* and *aluminum shell* virtually agree. In the case of the *uncoupled MFS*, no dissipation occurs in the system and the solution is infinite at the eigenfrequencies. In the case of *aluminum shell* a small structural dissipation effect is present. This can be seen in Figure 4a, where the eigenfrequencies are damped. However, we conclude that the compliance of the aluminum structure has only little influence on the interior sound pressure field. Nevertheless, the effects of the dissipation introduced by virtue of the

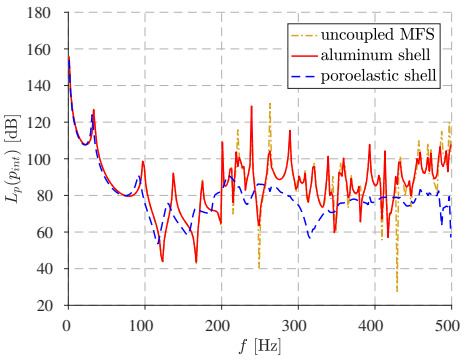

(a) interior evaluation point

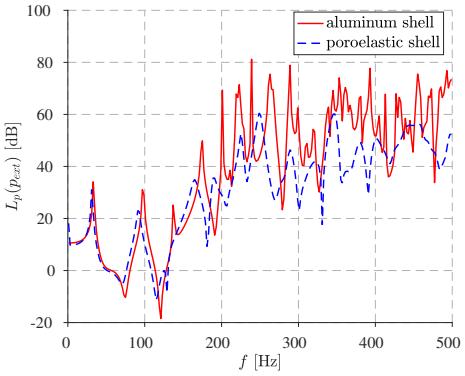

(b) exterior evaluation point

Figure 4: Comparison of the sound pressure levels

poro-elastic polyurethane layer are clearly visible, in particular for frequencies above $f = 200\,\mathrm{Hz}$. The same conclusion is valid for the results at the exterior evaluation point $[0\,\mathrm{m}, 0\,\mathrm{m}, 1.5\,\mathrm{m}]$. The sound pressure level determined at the exterior evaluation point $[0\,\mathrm{m}, 0\,\mathrm{m}, 1.5\,\mathrm{m}]$ is plotted over the frequency in Figure 4b. In the case of an rigid structure no transmission can occur. Therefore, this case is not considered in Figure 4b. Again, the sound pressure level is significantly reduced in the case *poro-elastic shell* compared to the case *aluminum shell*.

5 CONCLUSION

We have presented a new simulation framework for vibro-acoustic analysis. In particular, we have treated the simulation of laminated poro-elastic shell structures and their interaction with the surrounding fluid. In order to face this complicated situation, a layer-wise shell model has been developed. The through-the-thickness variation of the displacement field is described by a seven-parameter model, which is assumed in each layer. The pressure field occurring only in the poro-elastic layers is described with a quadratic expansion through-the-thickness.

The numerical model consist of a FEM formulation for the shell and the MFS for the acoustic domains. Hence, the radiation condition is implicitly fulfilled by the MFS due to the usage of the acoustic fundamental solutions. Contrary to most MFS solutions, here, the strength of the sources for the field approximation are determined by a variational formulation. This has the advantage that the need of collocation points is circumvented. The calculation of the sound transmission through geometrically complicated layered shells structure has shown the suitability of the proposed approach.

REFERENCES

[1] M. Biot. Theory of propagation of elastic waves in a fluid-saturated porous solid. I. Low-frequency range. *J. Acoust. Soc. Am.*, 28(2):168–178, 1956.

[2] J. Allard and N. Atalla. *Propagation of sound in porous media*. John Wiley & Sons, 2nd edition, 2009.

[3] J. Sladek, V. Sladek, M. Gfrerer, and M. Schanz. Mindlin theory for the bending of porous plates. *Acta Mechanica*, 226(6):1909–1928, 2015.

[4] M. Gfrerer and M. Schanz. A high-order fem with exact geometry description for the laplacian on implicitly defined surfaces. *Int. J. Numer. Methods. Eng.*, 114(11):1163–1178, 2018.

[5] M. Gfrerer and M. Schanz. High order exact geometry finite elements for seven-parameter shells with parametric and implicit reference surfaces. *Comp. Mech.*, 64(1):133–145, 2019.

[6] M. Gfrerer. *Vibro-acoustic simulation of poroelastic shells*. Monographic Series TU Graz, Computation in Engineering and Science, 2018.

AIRCRAFT MODEL UPDATING ACCORDING RESULTS OF GROUND VIBRATION TEST

J. Cecrdle[1]

[1]Czech Aerospace Research Centre
Beranovych 130, Prague, CZECH REPUBLIC
Email: cecrdle@vzlu.cz

ABSTRACT

This paper is focused on the updating of aircraft structure computational model according to the results of ground vibration test. Subjected model is used for aeroelastic analyses, in particular for flutter analyses. First, the applicable approaches of flutter analyses are outlined. Next, the theoretical background of commonly used Bayesian parameter estimation technique of model updating is provided. After that, the methodology of model updating adjusted for aircraft structures is described. Finally, the methodology is demonstrated on the example of the twin-engine turboprop commuter aircraft for 19 passengers. Selected results are shown, evaluated and the conclusions are formulated.

1 INTRODUCTION

Computational models must be validated according to experimental data. For aircraft aeroelastic model validation, the data of ground vibration test (GVT) are used. Stiffness parameters of structural models are adjusted in order to match FE-based modal parameters with the GVT-based modal parameters. Various applications of model updating are documented in references [1-3]. The approach using updating allows further modifications of the model and parametric studies; therefore, it is applied mainly to more complex certification process of larger aircraft. Contrary to that, for general aviation aircraft, the approach of the direct usage of the GVT results for flutter analysis is usually employed [4].

2 THEORETICAL BACKGROUND

Model updating may be simply characterized as the problem of the structural optimization. For standard applications, the Bayesian Least Squares Method is commonly used. The objective function is defined as

$$OBJ = \{\Delta R\}^T [W_R]\{\Delta R\} + \{\Delta P\}^T [W_P]\{\Delta P\} \tag{1}$$

This function can be described as the weighted sum of error in response modal parameters. Basic matrix equation of the iterative solution can be expressed as

$$\{P_u\} = \{P_0\} + [G]\{-\Delta R\} \tag{2}$$

where $\{P_u\}$ is the final vector of design variables, $\{P_0\}$ is the initial vector of design variables, $\{\Delta R\}$ is design response change vector and $[G]$ is gain matrix. Gain matrix is calculated using one of these expressions (based on the number of design variables and design responses).

$$[G] = ([W_P] + [S]^T [W_R][S])^{-1}[S]^T [W_R] \tag{3}$$

$$[G] = [W_P]^{-1}[S]^T([W_R]^{-1} + [S][W_P]^{-1}[S]^T)^{-1} \tag{4}$$

where $[W_P]$ and $[W_R]$ are diagonal weight matrices for parameters and responses, respectively, and $[S]$ is a sensitivity matrix expressed as

$$[S] = \left[\frac{\partial R_i}{\partial P_j}\right] \tag{5}$$

where design responses are modal parameters, i.e. natural frequencies and mode shapes. Correlation in natural frequencies is given as relative error in natural frequency expressed as

$$\{\varepsilon_f\} = \left[\frac{f_{FEM} - f_{GVT}}{f_{GVT}}\right] \tag{6}$$

and correlation in mode shapes is expressed using Modal Assurance Criterion.

$$MAC(\Psi_{FEM}, \Psi_{GVT}) = \frac{|(\{\Psi_{FEM}\}^T\{\Psi_{GVT}\})|^2}{((\{\Psi_{FEM}\}^T\{\Psi_{FEM}\})(\{\Psi_{GVT}\}^T\{\Psi_{GVT}\}))} \tag{7}$$

Design variables are stiffness characteristics including bending and torsional stiffness of beam-like elements and spring constants of spring-like elements. The reason of this selection is the fact, that the stiffness data are less accurate and reliable, compare to the inertia data.

3 MODELS AND METHODOLOGY

Updating of an aircraft model is very complex problem as an aircraft structure is dynamically complicated system. The key issue is the appropriate selection of design parameters and design

responses and the appropriate strategy of updating. Therefore, good knowledge regarding the structure dynamic behaviour, reliability and accuracy of the data and possible error sources is important.

FE model has a character of a stick model as shown in figure 1(a). In general, stick models are suitable for updating as the design space is not so large compare to detailed models and the relation between design variables and design responses is more direct. The model includes a single side only and appropriate (symmetric or antisymmetric) boundary condition at the plane of symmetry. Such models are ordinarily used for flutter analyses.

GVT measurement points grid is reduced as shown in figure 1(b). It is important to use only the appropriate points for pairing and for calculation of MAC values.

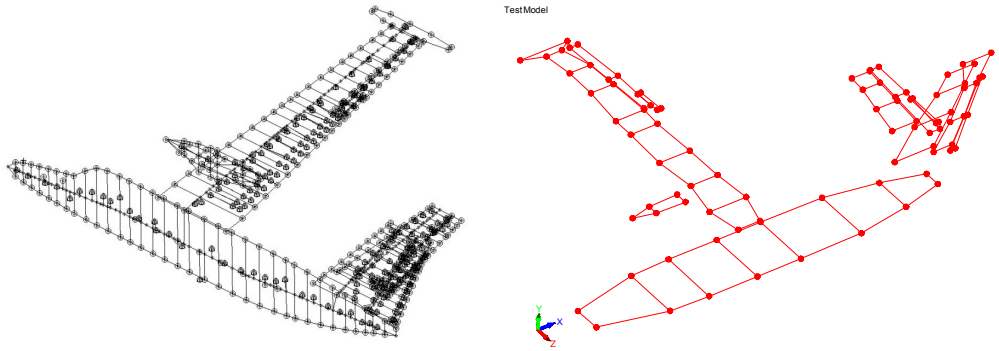

Figure 1. (a) structural (FEM) model, (b) grid of experimental points.

In the preparatory phase, mass of controls, tabs and of the complete aircraft are adjusted according to weighing. Effective stiffness of tabs actuation is adjusted according to the static stiffness measurements. Finally, adjustment of node points of the engine pitch and yaw attachment according to the appropriate GVT modes is performed.

#	Mode title	f (Hz)
01	1st symmetric wing bending	3.759
02	Symmetric elevator flapping (fixed stick)	5.809
03	1st symmetric engine pitch	8.672
04	2nd symmetric wing bending	9.463
05	1st symmetric engine yaw	10.126
06	1st symmetric wing in-plane bending	11.678
07	1st symmetric tailplane bending	13.504
08	1st fuselage vertical bending	16.527
09	1st symmetric wing torsion	18.310
12	Symmetric aileron flapping	28.227
16	1st symmetric tailplane in-plane bending	42.990
19	1st symmetric tailplane torsion	59.289

Table 1. Selected GVT symmetric modes, baseline configuration.

GVT data usually include a single mass configuration (baseline) for which a complete measurement is performed. In addition, mass configurations varying in the fuel load, for which just wing modes are measured, are performed. For a conventional aircraft, one additional configuration is usually sufficient. For the unconventional concepts (e.g., wing with wing-tip tank, external pods, etc.), the number of additional configurations may be much higher. First, updating of the baseline mass configuration is performed. Next, the correlation of the updated model for other mass configurations with the corresponding GVT data is checked. In practice, the agreement

of updated model is found satisfactory in the most cases; provided not, further updating to the modes of the appropriate mass configuration is performed. Optionally, the updating considering a subset of major modes, contributing to specific flutter instability, is also applicable.

4 APPLICATION EXAMPLE

As the example, updating of the symmetric model, baseline configuration, is presented here. GVT results included 21 symmetric modes applicable for updating from which 12 modes were selected. The list of selected modes is shown in table 1.

Comparison of the initial and final pairing of modes is shown in figure 2. Figure 2(a) demonstrates relative error in natural frequencies with the excellent result (the final errors are less than 3.3%). Figure 2(b) shows MAC values, also with the good result (all MAC values increased).

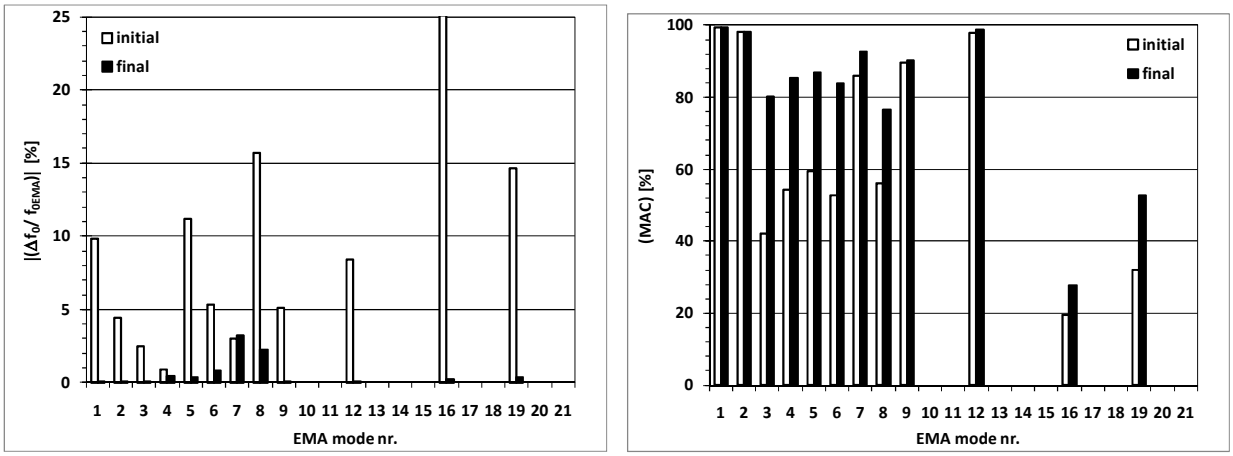

Figure 2. Comparison of initial and final state (a) frequency eror, (b) MAC values.

5 CONCLUDING REMARKS

This paper describes the updating of structural parameters of the aircraft structure FE model according to the results of the GVT. Methodology is demonstrated on the example of a twin-engine turboprop commuter aircraft for 19 passengers. After updating, modal parameters got much closer to the target GVT data, and therefore the updated models are prepared to the final phase of flutter calculations of the subjected aircraft.

REFERENCES

[1] K.D. Blakely, M.W. Dobbs. Modifications and Refinement of Large Dynamic Structural Models, Efficient Algorithms and Computer Applications. In: Proceedings of the 1st International Modal Analysis Conference, Orlando, FL, USA, 1982.

[2] K.D. Blakely, W.B. Walton. Selection of Measurement and Parameter Uncertainties for Finite Element Model Revision. In: Proceedings of the 2nd International Modal Analysis Conference, Orlando, FL, USA, 1984.

[3] K.D. Blakely. Updating MSC/NASTRAN Models to Match Test Data. In: Proceedings of the MSC World Users' Conference, Long Beach, CA, USA, 1991.

[4] J. Cecrdle, V. Hlavaty. Aeroelastic Analysis of Light Sport Aircraft Using Ground Vibration Test Data. *Proceedings of the Institution of Mechanical Engineers, Part G: Journal of Aerospace Engineering*. 229(12): 2282-2296, 2015.

EXPERIMENTAL INVESTIGATION OF REDUCED SOUND TRANSMISSION OF SANDWICH PANELS USING 3D-PRINTED MODELS

F. Errico[1,2*] , M. Ichchou[1], F. Franco[2], S. De Rosa[2], G. Petrone[2] and O. Bareille[1]

[1]Laboratoire de Tribologie et Dynamique des Systems, Ecole Centrale de Lyon
36 Avenue Guy de Collongue, 69134, Ecully, France
Email: fabrizio.errico@ec-lyon.fr; mohamed.ichchou@ec-lyon.fr; olivier.bareille@ec-lyon.fr

[2]Department of Industrial Engineering, University of Naples Federico II
Via Claudio 21, 80125, Napoli, Italy
Email: francesco.franco@unina.it; sergio.derosa@unina.it; giuseppe.petrone@unina.it

ABSTRACT

An investigation is carried out on alternative periodic designs of sandwich panels, for vibroacoustic purposes; a mechanically-linked double-wall panel and a rectangular core sandwich panel are considered. The elastic bending waves' propagation versus the acoustic wavenumbers is trimmed using folded and corrugated core walls, trying to keep the same mass and compression stiffness of the original configurations. Standard and proposed configurations are 3D-printed and the sound transmission loss measurements carried out. The experimental evidence of reduced acoustic radiation of the panels, in a large frequency band, is achieved with measurements on the printed solutions.

1 INTRODUCTION

In transport industry, the requirements for light and stiff structures often lead to sandwich structural solutions. On the other hand, while a reduced mass is an advantage for fixed structural resistance, it generally induces lower vibroacoustic performance. Therefore, the design of sandwich panels for reduced acoustic radiation, has received more and more attention in the last decades [1–3].

Some authors tried to design the core geometry in order to optimize the sound transmission. Palumbo et al. [4] proved experimentally the increase of vibroacoustic performance of honeycomb-cored sandwich plates when periodical voids and recesses are included in the original geometry. Hambric et al. [5] also proposed a design rule for honeycomb panels targeting a different bending wave speed versus the acoustic one. Random truss-like core shapes where proposed in [6].

Within the present paper, two common configurations of sandwich panels are modified using the periodic structure theory. The aim is to induce alterations of the bending wave propagation of the panels versus frequency, keeping the same mass and, optionally, the same compression stiffness as the original designs. The frequency band targeted is 600 Hz to 10 kHz, corresponding to the measurements frequency range available for the facility used within this work.

2 CORRUGATED WALLS DESIGN

A standard mechanically-linked double-wall panel is investigated (Fig. 1a). It is 1.06 cm thick (total thickness) and has a 1.0 cm spacing between consecutive stiffeners, in the periodicity direction (axis x in Fig. 1). The thickness of the skins and core walls is 0.6 mm. A unit cell is illustrated in Fig. 1a.

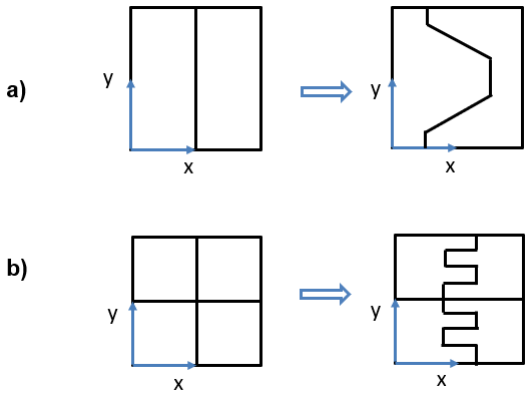

Figure 1: Cell models extracted from: a) Double-Wall Panel with Mechanical link; b) Sandwich Panel with rectangular core.

The modified design is characterised by a trapezoidal (top-view) shape of the stiffer (Fig. 1a). The same global thickness and stiffeners' spacing as the classic double-wall panel is used; the skins are 0.6 mm-thick and the core walls are 0.45 mm-thick, in order to keep the same mass of the system. The idea of using such a geometrical shape comes from the usually low bending and shear stiffness of this kind of panels in the direction normal to the stiffener envelope (axis x).

For the rectangular-cored panel, the initial design (Fig. 1b) has a total thickness of 1.06 cm and a 1.0 cm spacing between consecutive stiffeners, in both directions (Fig. 1b). Both skins and core-walls are 0.6 mm-thick. Similarly to the previous case, the modified design proposed here is characterised by a trapezoidal (top-view) shape of the stiffener in one direction (axis y in Fig. 1b), while the rectilinear geometry is kept in the other direction. To keep the same mass, global thickness and stiffeners spacing of the original system, the skins are 0.6 mm-thick and the core walls are 0.36 mm-thick.

3 EXPERIMENTAL SET-UP

Using the method described in [7], the numerical dispersion curves and transmission loss are computed and compared to chose the right design. Then, a CAD model is developed and the panels 3D- printed using a Stratasys Fortus 450mc. The material used is the ABS-M30 (Acrylonitrile butadiene styrene): E = 1.8 GPa; ρ = 988 kg/m^2; ν = 0.32.

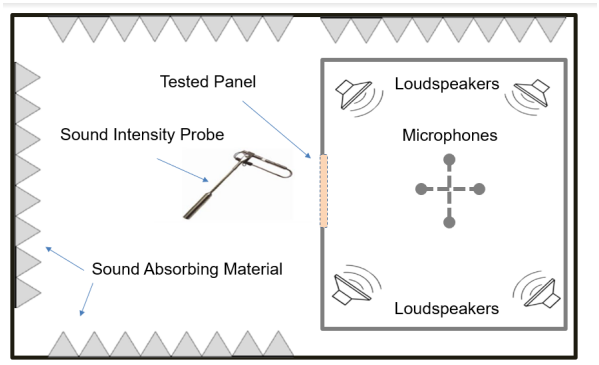

Figure 2: Illustration of the test facility with un-coupled reverberant-anechoic rooms for transmission loss measurements.

The sound transmission measurements were performed in an un-coupled reverberant-anechoic room as in Fig. 2. The reverberant room has volume of 2.50 x 1.40 x 1.75 m^3 and reflective surfaces are installed inside to increase the diffusiveness of the reverberant room; the calculated Schroeder frequency (see [8]) is $\approx$ 600 kHz. The acoustic excitation is generated using four speakers installed at the four top corners of the reverberant room, with an uncorrelated white noise input from 50 to 10 kHz.

The transmitted sound power is measured using a Bruel & Kjaer sound intensity probe with two half-inch microphones and a 6.0 mm spacer. The incident sound power is obtained by the sound pressure level measurements in the cabin room, averaged among four half-inch microphones disposed as in Fig. 2. The anechoic conditions of the receiving room are simulated by covering the room walls with absorbing layers, whose distance from the tested panel is larger than 2 m. The sound transmission loss (TL) is finally calculated, assuming that the excited and radiating surfaces are the same, as $\mathrm{TL} = L_p - L_i - 6.18$.; where L_p is the average pressure level measured in the reverberant room, L_i the average sound intensity level over the surface of the test-panels in the semi-anechoic room, while the -6.18 factor arises from reference values in dB conversion [9].

3.1 Sound Transmission Loss Measurements

The 3D-printed panels are installed and clamped in the TL facility, as in Fig. 2. The expected and real weights of the printed panels differ slightly and the measured transmission loss curves are scaled to compare mass-normalised results.

In Fig. 3a, the measured sound transmission losses (mass-normalised) are compared for the double-wall panel with mechanical link. While the total surface of the plates is 0.40 x 0.35 m^2, the exposed panel surface is 0.34 x 0.29 m^2. The increase of sound transmission loss starts from 1.5 kHz and continues up to the end of the frequency band of interest.

Similarly, in Fig. 3b, the same trends are experimentally observed for the rectagular-cored panel. The increase of sound transmission loss, as in the previous case, appears in a very large frequency band that goes from 1 kHz to 10 kHz, at least, for a fixed mass of the panel.

4 CONCLUDING REMARKS

Two designs of two types of sandwich panels are analysed in terms of sound transmission loss. A double-wall panel with mechanical links and a sandwich panel with rectangular core are considered. A new core design using corrugated core walls is proposed targeting the structural waves' propagation versus the acoustic wavenumbers, for fixed mass of the system. The different configurations are 3D-printed and sound transmission loss measurements are carried out using a facility with uncoupled reverberant and semi-anechoic configuration.

The experimental tests evidence an increased vibro-acoustic performance of the new designs. Even keeping the same total mass of the panels, the sound transmission loss is increased in a large frequency band that goes from $\approx$ 1.5 kHz to 10 kHz.

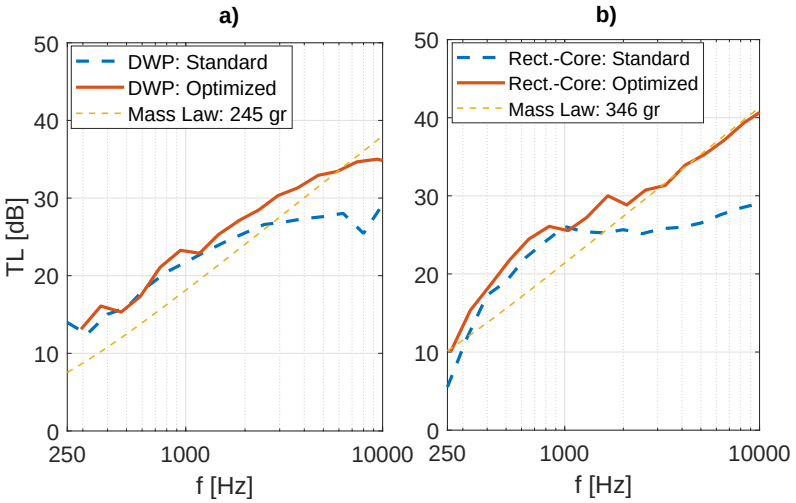

Figure 3: Measured Transmission Loss (mass-normalised) for the 3D-printed panels. Total panel surface: 0.40x0.35 m^2. Exposed panel surface: 0.34x0.29 m^2. a) Mechanically-linked double-wall panels designs; b) Rectangular-cored sandwich panel designs.

Acknowledgments

This project has received funding from the European Unions Horizon 2020 research and innovation programme under the Marie Sklodowska-Curie grant agreement No. 675441. N. Guenfoud, B. Minard and S. Lemahieu, are acknowledged for their contribution to the set-ups.

REFERENCES

[1] Mark A. Lang and Clive L. Dym. Optimal acoustic design of sandwich panels. *The Journal of the Acoustical Society of America*, 57(6):1481–1487, 1975.

[2] J. A. Moore and R. H. Lyon. Sound transmission loss characteristics of sandwich panel constructions. *The Journal of the Acoustical Society of America*, 89(2):777–791, 1991.

[3] Clive L. Dym, C. Samuel Ventres, and Mark A. Lang. Transmission of sound through sandwich panels: A reconsideration. *The Journal of the Acoustical Society of America*, 59(2):364–367, 1976.

[4] Daniel L Palumbo and Jacob Klos. Development of quiet honeycomb panels, Virginia, Langley Research Center; NASA/TM-2009-215954, 2009.

[5] Stephen Hambric, Micah Shepherd, Kevin Koudela, Denis Wess, Royce Snider, Carl May, Phil Kendrick, Edward Lee, and Liang-Wu Cai. Acoustically tailored composite rotorcraft fuselage panels, Virginia, Langley Research Center; NASA/CR2015-218769, 2015.

[6] Francesco Franco, Ken A. Cunefare, and Massimo Ruzzene. Structural-acoustic optimization of sandwich panels. *ASME J. Vib. Acoust*, 129 (3):330–340, 2006.

[7] Fabrizio Errico, Mohamed Ichchou, Francesco Franco, S. De Rosa, Olivier Bareille, and C. Droz. Schemes for the sound transmission of flat, curved and axisymmetric structures excited by aerodynamic and acoustic sources. *Journal of Sound and Vibration*, 476:221–238, 2019.

[8] Manfred R. Schroeder. The Schroeder frequency revisited. *The Journal of the Acoustical Society of America*, 99(5):3240–3241, 1996.

[9] Albert London. *Transmission of Reverberant Sound Through Single Walls, Department of Commerce National Bureau of Standard,* Part of the Journal of Research of the National Bureau of Standards *42*, volume 42. 1949.

K-SPACE ANALYSIS OF COMPOSITE SANDWICH SHELL WITH SMALL-SCALE RESONATORS

G. Tufano[1,2*], M. Ichchou[1], W. Desmet[2,3] and N. Atalla[4]

[1]Vibroacoustics & Complex Media Research Group, LTDS-CNRS UMR 5513
École Centrale de Lyon, Écully, 69134, FRANCE
Email: giovanni.tufano@ec-lyon.fr, mohamed.ichchou@ec-lyon.fr

[2]Noise and Vibration Research Group, Dept. Mechanical Engineering, section LMSD
KU Leuven, Heverlee, BELGIUM
Email: giovanni.tufano@kuleuven.be, wim.desmet@kuleuven.be

[3]DMMS core lab
Flanders Make, BELGIUM

[4]GAUS, Group d'Acoustique de l'Université de Sherbrooke
Université de Sherbrooke, Sherbrooke, QC, J1K 2R1, CANADA
Email: Noureddine.Atalla@USherbrooke.ca

ABSTRACT

An inverse wavenumber identification tool is used to characterize the vibration behavior of a curved thick composite sandwich shell. The bare structure is firstly studied and then equipped with spatially distributed small-scale resonators, leading to a meta-structure. Experimental tests are conducted under diffuse acoustic field and point mechanical excitations.
For each studied case, the effect of the industrially-oriented small-scale resonators is highlighted using frequency and wavenumber analysis, showing general attenuation of the vibration level and even band gaps occurrence. The complex wavenumber identification allows also estimating the structural loss factor.

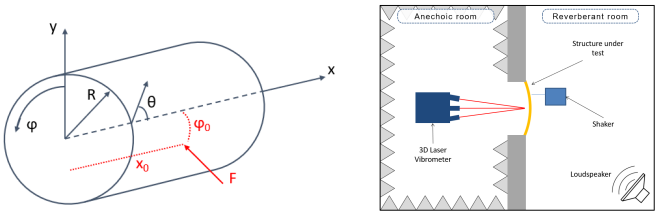

(a) (b)

Figure 1: Curved structure coordinates system (a) and illustration of the coupled rooms (b)

1 INTRODUCTION

In the aerospace sector, curved shells and axial-symmetric structures are widely used. The identification of the energy propagation, of the waves attenuation, with the related damping informations, and of the waves dispersions characteristics are relevant aspects to fully describe the vibro-acoustic behavior of a system [1]. In a wave propagation framework, for parameters identification a method based on the wavenumber domain (k-space) analysis is introduced: the Inhomogeneous Wave Correlation (IWC) method [2, 3]. This method allows the identification of the complex wavenumber and of the damping loss factor in the broadband frequency range. In order to increase the waves attenuation in certain frequency bands or to generate some band gaps, periodic adds-on and locally resonant devices are widely used. Nateghi et al. [4] have discussed and experimentally validated that by adding locally resonating structures to cylindrically curved panels and pipes, improved noise and vibration behavior can be obtained in a targeted and tunable frequency band. This concept was applied on an aircraft sidewall panel by Droz et al. [5] , improving the acoustic properties of the panel in the ring frequency region. This work is fully devoted to the experimental identification of the dispersion characteristics of a complex meta-structure, subjected to either a diffuse acoustic field or a point mechanical excitations. The structure is firstly tested alone, and then with the addition of spatially-distributed small-scale resonators. The method used in this work is an extended version of the IWC method [6].

2 IWC METHOD FORMULATION FOR CURVED STRUCTURES

The IWC method is here proposed in an extended version to complex curved structures, in presence of periodic elements and small-scale resonators. This method makes a correlation between the energy carried on by an inhomogeneous traveling wave and the total energy of the vibrational field. From the notations and the coordinates system shown in Figure 1a, identifying with R the curvature radius of the structure and with φ the angular coordinate, the following relationships can be derived: $y = R\sin\varphi \approx R\varphi$ and $k_\varphi = Rk_y$, where a small value of the angle φ is assumed (this value is strictly depended from the discretization resolution). The expression of the inhomogeneous wave in this coordinate system is given by:

$$\tilde{w}_{k_\mathbb{C},\theta}(x,\varphi) = e^{-ik_\mathbb{C}(\theta)((x-x_0)\cos\theta+(\varphi-\varphi_0)\sin\theta)}, \tag{1}$$

where θ is the angle of propagation and $k_\mathbb{C} = k_\Re + ik_\Im$ is the complex wavenumber, which contains both propagation and attenuation informations and (x_0,φ_0) is the location of the excitation point. At each frequency f and for a given direction θ, the unknown complex wavenumber $k_\mathbb{C}$ can be identified as the location of the maximum of the normalized correlation function, denoting the point where the measured signal $\hat{w}$ correlates best with the inhomogeneous wave $\tilde{w}_{k_\mathbb{C},\theta}(x,\varphi)$:

$$\mathcal{I}(k_\mathbb{C},\theta) = \frac{\left|\sum_{j=1}^{N}\hat{w}(x_j,\varphi_j)\cdot\tilde{w}^*_{k_\mathbb{C},\theta}(x_j,\varphi_j)h_j\Omega_j\right|}{\sqrt{\sum_{j=1}^{N}|\hat{w}(x_j,\varphi_j)|^2h_j\Omega_j\cdot\sum_{j=1}^{N}|\tilde{w}_{k_\mathbb{C},\theta}(x_j,\varphi_j)|^2h_j\Omega_j}}, \tag{2}$$

where N is the total number of points, h_j is the coherence of the measured signal and Ω_j is the estimation of the punctual surface. The location of the maximum of the correlation function $\mathcal{I}(k_\mathbb{C},\theta)$ gives the identified complex wavenumber in the specified direction.

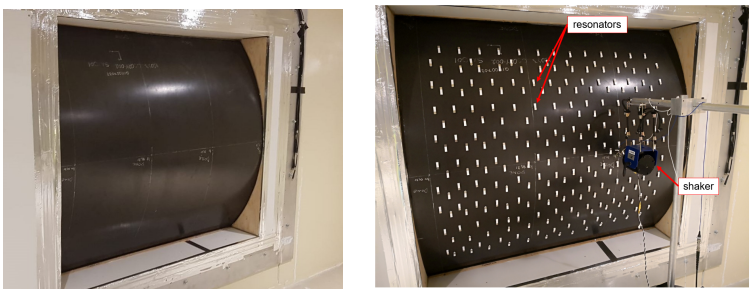

(a) (b)

Figure 2: Composite panel: bare (a) and distributed resonators (b) configurations.

3 EXPERIMENTAL SET-UP AND RESULTS DISCUSSION

The composite panel dimensions are $1.54\,\mathrm{m}$ x $1.62\,\mathrm{m}$, with a curvature radius approximatively of $0.97\,\mathrm{m}$ and thickness equal to $27.5\,\mathrm{mm}$. The panel was installed in the aperture between the coupled reverberant-anechoic rooms of the GAUS (*Groupe d'Acoustique de l'Université de Sherbrooke*) laboratory, at Université de Sherbrooke. The representative scheme of the coupled rooms is shown in Figure 1b. The acoustic excitation was generated by a loudspeaker placed close to a corner of the room, with a white noise signal input from $100\,\mathrm{Hz}$ to $3000\,\mathrm{Hz}$. Concerning the mechanical excitation, a Modal Shop Model 2025E shaker was installed in the reverberant room and attached to the test structure using an impedance head, as shown in Figure2b; the excitation was generated using a white noise signal from $100\,\mathrm{Hz}$ to $3000\,\mathrm{Hz}$. The full vibrational field was measured using a Polytec 3D Scanning Vibrometer (PSV-3D), installed in the anechoic room. The acquisition window was approximatively of $1.2\,\mathrm{m}$ x $1.0\,\mathrm{m}$, with a total number of 3111 measured points (mesh grid of 61 x 51). A distributed pattern of 3D-printed small-scale resonators was then attached to the panel and compared to the bare test case; the tuning frequency was chosen at $1000\,\mathrm{Hz}$, resulting an added mass around the 4%, for a total number of 246 resonators.
The bending dispersion curves for both configurations, with and without resonators, are shown in Figure 3; they are computed in the two orthogonal directions, axial and circumferential. From the estimation of the complex wavenumbers, a calculation of the damping loss factor is performed, using the relationship between the real and the imaginary part: $\eta = |k_{\Im}^4/k_{\Re}^4|$. The damping loss factor is then compared to the one estimated with the Power Input Method (PIM, [1]), as shown in Figure 4; the damping loss factor is expressed as follows: $\eta_f = P_f/\omega E_f$, where P_f is the input power and the E_f is the total energy, averaged in the frequency band.

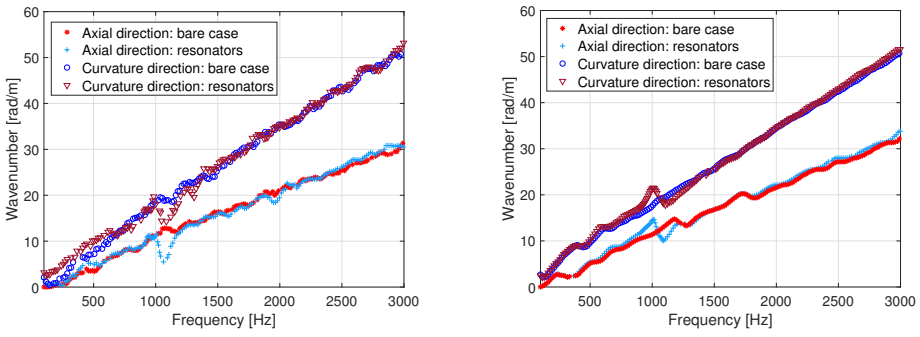

(a) (b)

Figure 3: Dispersion curves under DAF (a) and shaker excitation(b)

4 CONCLUDING REMARKS

The feasibility of the Inhomogeneous Wave Correlation method on complex structures, in presence of a local dynamics effect and under diffuse acoustic field excitation have been demonstrated, giving

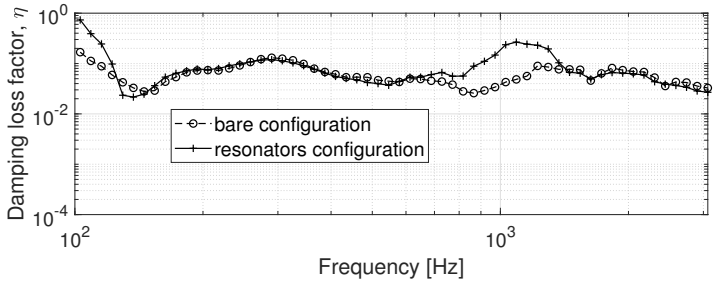

(a)

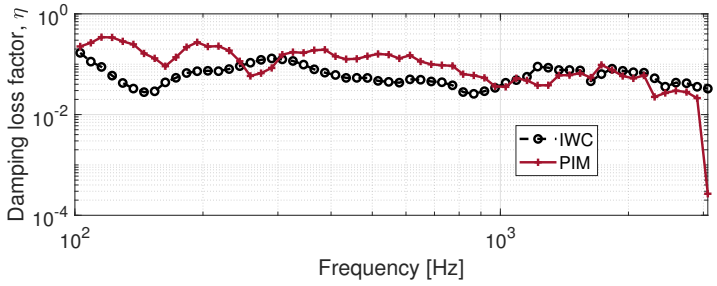

(b)

Figure 4: Damping Loss Factor: complex wavenumber estimation (a) and PIM (b)

a good estimation of the dispersion curves for all tested configurations. The efficiency of this 3D-printed small-scale resonators is also demonstrated, obtaining a reduction of the vibrational field of the panel. For all tested configuration, in the frequency band the resonators were tuned to work in, a drop in the dispersion curves is observed.

ACKNOWLEDGMENT

This project has received funding from the European Union's Horizon 2020 research and innovation program under the Marie Sklodowska-Curie grant agreement No. 675441. The authors would like to acknowledge Fabrizio Errico, Olivier Robin and Christophe Droz.

REFERENCES

[1] R. Cherif, J.-D. Chazot, and N. Atalla. Damping loss factor estimation of two-dimensional orthotropic structures from a displacement field measurement. *Journal of Sound and Vibration*, 356:61–71, 2015.

[2] J. Berthaut, M. N. Ichchou, and L. Jezequel. *K*-space identification of apparent structural behavior. *Journal of Sound and Vibration*, 280:1125–1131, 2005.

[3] M. N. Ichchou, J. Berthaut, and M. Collet. Multi-mode wave propagation in ribbed plates: Part I, wavenumber-space characteristics. *International Journal of Solids and Structures*, 45:1179–1195, 2008.

[4] A. Nateghi, L. Van Belle, C. Claeys, E. Deckers, B. Pluymers, and W. Desmet. Wave propagation in locally resonant cylindrically curved metamaterial panels. *International Journal of Mechanical Sciences*, 127:73–90, 2017.

[5] C. Droz, O. Robin, M. Ichchou, and N. Atalla. Improving sound transmission loss at ring frequency of a curved panel using tunable 3D-printed small-scale resonators. *Journal of Acoustical Society of America*, 145(1):72–78, 2019.

[6] G. Tufano, F. Errico, O. Robin, C. Droz, M. Ichchou, B. Pluymers, W. Desmet, and N. Atalla. K-space analysis of large-scale complex meta-structures using the inhomogeneous wave correlation method. *Mechanical Systems and Signal Processing*, 135:106407, 2020.

AEROELASTICITY OF BISTABLE COMPOSITE PLATES

F. Nicassio[1*] and G. Scarselli[1]

[1]Department of Engineering for Innovation, University of Salento,
Via per Monteroni, Lecce, 73100, ITALY
Email: francesco.nicassio@unisalento.it, gennaro.scarselli@unisalento.it

ABSTRACT

In this paper, the commercial code MSC PATRAN–NASTRAN is used to simulate the fluid-structure interaction on a cantilever composite bistable plate. Bistable laminates have two stable mechanical shapes that, when properly loaded, snap-through from one stable configuration to another, causing large plate strains. Several aeronautical applications of this kind of structures as morphing devices or power harvesters are taken into account in the technical literature. The aim of this work is to explore the dynamic behavior of this bistable structure, in terms of divergence and flutter characteristics to be used for future works. Experimental and Finite Element (FE) modal analysis of the two stable states of the plate are performed to obtain natural frequencies and corresponding mode shapes, which is used as an input for aeroelastic analysis. The structure and the aerodynamic grids are used to create lifting surfaces by assuming the plates as infinite uniform plates. The MK pair set is created to calculate the unsteady aerodynamic forces to perform the dynamic stability analysis. Frequency and damping estimates are obtained at several velocities in order to predict divergence and flutter speeds.

1 INTRODUCTION

Aeroelastic phenomena must be considered in the early phase of the aircraft structural design [1],[2]. Flutter and divergence are two of them, characterized by dynamic and static instability, respectively [3]. The energy transfer between aerodynamic structure and airflow can be exploited by bistable structures for morphing [4]-[6] or power harvesting scopes [7],[8]. The bistable laminates have two stable states that are receiving interest in several aeronautic applications such as shape changing applications without the need of servo-activated control systems [9]. Therefore, the dynamic investigation of the bistables performance is needed due to the lack of information in the technical literature, to the best of the authors' knowledge. Accordingly, frequency and damping curves of a bistable plate are estimated by using MSC/PATRAN&NASTRAN [10]. In this paper, the analysis of natural modes, static divergence and flutter instability of a rectangular bistable plate are numerically performed. The main purpose

is to show the velocities and the predominant eigenmodes when the aeroelastic instability occurs for each stable shape of the bistable plate.

2 BISTABLE COMPOSITE PLATES

Asymmetrical $[0_2/90_2]$ laminates (120 mm × 240 mm) were fabricated laying up 4 unidirectional prepreg plies made of T800/M21 (prepreg mechanical and physical properties in [11]). The rectangular shape of the laminates was chosen in order to enhance the asymmetry between the 0° and 90° oriented plies, thus increasing the maximum curvature after curing and cooling at room temperature. Sample was cured in autoclave using the recommended cure cycle for the T800/M21 prepreg. In order to increase the thermal residual stresses and to obtain a higher level of curvature in the sample, the batch was removed from the autoclave immediately after the curing reaction and rapidly cooled down in open air, not adopting the recommended cool rate of 2–5 °C/min. Upon cooling to room-temperature, each laminate was observed to have the two expected stable states (see Figure 1).

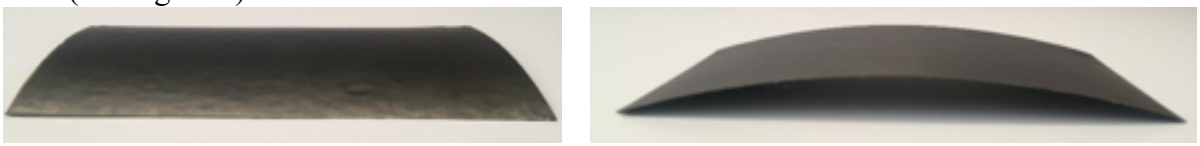

Figure 1. Stable states (LEFT first stable state, RIGHT second stable state) post cooling down.

3 AEROELASTICITY: NATURAL FREQUENCIES AND FE RESULTS

The initial step in performing the aeroelastic testing was to determine the natural frequencies and mode shapes of the structure. The FE bistable models (previously developed and validated in [8], [9]) were used to perform modal analyses (MSC/PATRAN&NASTRAN – Modal analysis – SOL 103 [10]) in order to obtain the first natural frequencies and the first mode shapes in both stable configurations. Subsequently, experimental investigations were conducted in order to validate the FE first natural frequencies and mode shapes of the bistable plate in the two stable states. The free oscillations were recorded after an imposed displacement at the free end of the cantilever plate. The vibrational amplitude acquired by an accelerometer located close to the clamped edge of the sample (to avoid saturation of the electrical signal) is reported in the following Figure 2. The FFT applied to these signals reveals the relative first two natural frequencies (see Table 1).

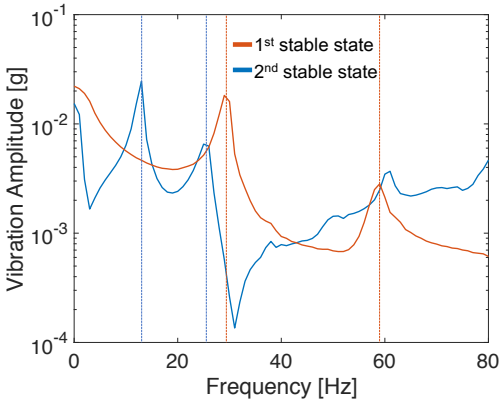

Figure 2. Experimental natural frequencies of cantilever bistable plate.

The close agreement between the experimental and numerical values of the first two natural frequencies (with the exception of the first natural frequency related to the second stable state in Table 1) is due to a proper description of the boundary conditions and of the material properties.

Natural Frequencies [Hz]		FE values	Experimental data
First stable state	Torsional mode	28.9	29.3
	Bending mode	62.4	58.7
Second stable state	Bending mode	17.3	13.2
	Torsional mode	28.5	25.3

Table 1. Mode shapes and natural frequencies comparison (FE results vs experimental data).

These results characterize the basic dynamic behavior of the structure and indicate how the structure respond to dynamic loading. The aeroelastic FE analyses (FlightLoads and Dynamics MSC Module [10]) were performed under the assumption of simple harmonic oscillations and the modal damping values were calculated by the MK–method in MSC/NASTRAN analysis solver (SOL 145). An Aerodynamic Model was made up of a collection of lifting surfaces (each of stable configuration); then a Flat Lifting Surface was defined to provide the primary lifting capability for the surfaces; after that Global Data was set (i.e. reference span and chord, flow density and direction in Figure 4) and eventually Aeroelastic Module was used to couple the aerodynamic and structural models and perform aeroelastic analyses.

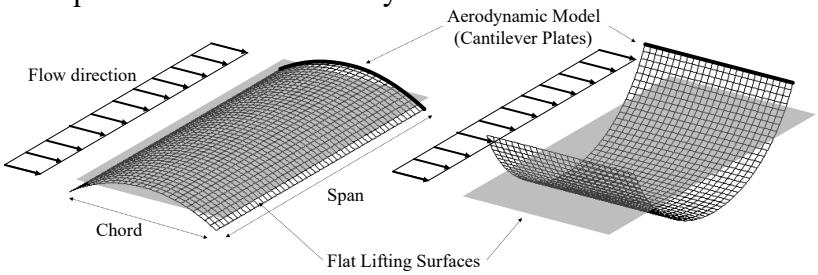

Figure 3. Aeroelastic FE features.

By using the natural frequencies as an input to the aeroelastic analyses, the velocity vs damping and velocity vs frequency curves were obtained for the corresponding natural modes.

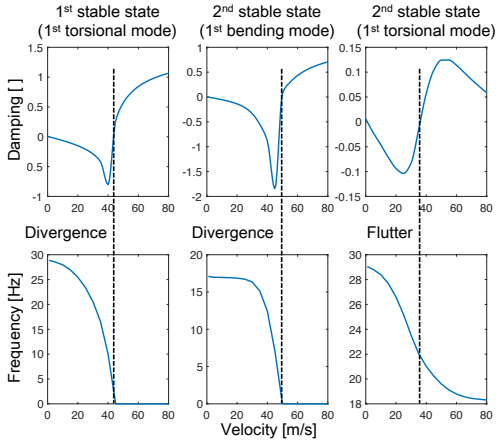

Figure 4. V-damping and V-frequency curves for first and second bistable shapes.

The flutter and divergence features of the bistable plate are shown in Figure 4. It is known that the flutter velocity (36 m/s for the second stable state) is lower than the divergence velocity (43 m/s for the first stable state and 50 m/s for the second one) for rectangular plates [12]:

- flutter velocity equals to 36 m/s for the second stable state (1st torsional mode);
- divergence velocities equal to 43 m/s for the first stable state (1st torsional mode) and 50 m/s for the second one (1st bending mode).

Moreover, the flutter mode occurs at lowest frequency torsion mode (for the second stable state) because of shortness of the plate (AR equal 2) as elucidated by Howell et al. in [13].

4 CONCLUSIONS

In this paper, a rectangular bistable plate was FE modeled to investigate its divergence behavior and to perform flutter analysis. By using MSC/PATRAN&NASTRAN, the modal modes and frequencies of the plate (in the two stable states) were evaluated. The results numerically found were in a good agreement with the experimental modal analysis demonstrating the consistence of the FE model. The FE aeroelastic study was performed considering the MK–method in MSC/NASTRAN. The plate becomes unstable at speed of 43 m/s for the first stable state (divergence) and 36 m/s for the second one (flutter). As the technical literature suggests, the shortness of the plate gives rise to the flutter at lowest frequency torsion mode. The target of future works will be to use the dynamical FE data to design and perform aeroelastic experimental campaign with bistable plates.

REFERENCES

[1] R.L. Bisplinghoff, H. Ashley. *Principles of aeroelasticity*. Courier Corporation, 2013.

[2] J.R. Wright, J.E. Cooper. *Introduction to aircraft aeroelasticity and loads*. John Wiley & Sons, 2008.

[3] I. Lottati. Flutter and divergence aeroelastic characteristics for composite forward swept cantilevered wing. *Journal of Aircraft*. 22(11):1001-7, 1985.

[4] Z. Zhang, Y. Li, X. Yu, X. Li, H. Wu, S. Jiang, G. Chai. Bistable morphing composite structures: A review. *Thin-Walled Structures*. 142:74-97, 2019.

[5] F. Nicassio, G. Scarselli, G. Avanzini, G. Del Core. Numerical and experimental study of bistable plates for morphing structures. *Active and Passive Smart Structures and Integrated Systems*. 10164:101640K, 2017.

[6] G. Scarselli, F. Nicassio, A. Maffezzoli. Mechanical characterization of bistable laminates for very small aircraft morphing applications. *Health Monitoring of Structural and Biological Systems.* 10600:106001Q, 2018.

[7] A. Abdelkefi. Aeroelastic energy harvesting: A review. *International Journal of Engineering Science*. 100:112-35, 2016.

[8] G. Scarselli, F. Nicassio, F. Pinto, F. Ciampa, O. Iervolino, M. Meo. A novel bistable energy harvesting concept. *Smart Materials and Structures*. 25(5):055001, 2016.

[9] F. Nicassio, G. Scarselli, F. Pinto, F. Ciampa, O. Iervolino, M. Meo. Low energy actuation technique of bistable composites for aircraft morphing. *Aerospace Science and Technology*. 75:35-46, 2018.

[10] MSC.NASTRAN, *Basic Dynamic Analysis User's Guide*, 2006.

[11] Hexcel Corporation, *Data Sheet Composite T800/M21 Unidirectional Prepreg.*

[12] D. Hodges, G. Pierce and M. Cutchins. Introduction to structural dynamics and aeroelasticity. *Cambridge Aerospace Series*. B35, 2002

[13] R.M. Howell, A.D. Lucey, P.W. Carpenter and M.W. Pitman. Interaction between a cantilevered-free flexible plate and ideal flow. *Journal of Fluids and Structures*. 25(3):544-66, 2009.

SOUND TRANSMISSION THROUGH BAFFLED SEMI-CYLINDRICAL SHELLS USING A TRANSFER MATRIX METHOD

A. Parrinello* and N. Atalla

Université de Sherbrooke
2500 Boulevard de l'Université J1K 2R1, Sherbrooke, Canada
Email: andrea.parrinello@usherbrooke.ca, noureddine.atalla@usherbrooke.ca

ABSTRACT

This paper discusses the use of a transfer matrix method for predicting the acoustic behavior of baffled semi-cylindrical shells consisting of a generic arrangement of homogeneous and heterogeneous periodic layers of various nature (fluid, solid, poroelastic). The through-radius transfer matrix of a layer characterized by cylindrical periodicity is derived by manipulating the dynamic stiffness matrix related to a finite element model of a unit cell. The proposed technique is equally appealing for homogeneous layers since few elements are needed in this case. In such a framework, different layers can be combined to form multilayered shells and the related acoustic radiation or transmission due to a plane wave or a diffuse acoustic field can be assessed. The blocked pressure field due to an incident plane wave is defined by taking into account the infinite baffle. Analytical expressions for the cylindrical acoustic impedances are exploited to define the coupling with the bounding fluid media. A one-dimensional windowing technique is also adopted, making it possible to account for the finite length of the shells. The proposed approach is validated in case of a baffled semi-cylindrical shell consisting of homogeneous layers by comparison with a full finite-boundary element model.

1 INTRODUCTION

The Transfer Matrix Method (TMM) is an efficient approach to model the sound propagation in stratified structures. Analytical expressions for the transfer matrices are only available for homogeneous media [1]. The transfer matrix of a periodic planar layer is obtained in [2] and a TMM for the sound transmission through infinite heterogeneous cylinders is presented in [3]. An extension of the method presented in [3] for finite heterogeneous semi-cylindrical shells is here presented. The present work differs from [3] in the calculation of the blocked pressure due to a plane wave excitation and accounting for an infinite planar baffle and in a one-dimensional (1D) windowing technique accounting for the finite length of the shell. Other details can be found in [3].

2 THEORY

A multilayered cylinder of length L whose longitudinal axis lies along the x-axis is cut by the $x-y$ plane ($z=0$) thus obtaining a baffled semi-cylindrical shell in the half space $z \geq 0$. The inner and outer surfaces of the shell are respectively located at $r=r_i$ and $r=r_o$. Subscripts i and o indicate values at the inner and outer surfaces. The two bulkheads at the ends of the shell are assumed rigid. A time-harmonic motion of the form $\exp(\mathrm{j}\omega t)$ is assumed.

2.1 Acoustic excitation and impedances

The shell is excited by an oblique plane wave traveling in $z>0$ with incident angle, θ, with respect to the z-axis and heading angle, Ψ, with respect to the x-axis. The incident pressure field can be expressed in cylindrical harmonics using the Jacobi-Anger expansion as

$$P_I = p_0 e^{\mathrm{j}(\omega t - k_x x - k_y y - k_z z)} = p_0 e^{\mathrm{j}(\omega t - k_x x)} \sum_{n=0}^{\infty} \varepsilon_n (-\mathrm{j})^n J_n(k_+ r) \cos(n\phi - n\beta) \,, \tag{1}$$

where p_0 is the incident wave amplitude, $k_x = \omega/c_+ \sin\theta\cos\Psi$ and $k_+ = \sqrt{\omega^2/c_+^2 - k_x^2}$ are the wavenumber components, c_+ is the speed of sound of the fluid in $z>0$, the auxiliary angle β is defined as $\tan\beta = \tan\theta \sin\Psi$ [4], n is the circumferential mode number, ε_n is the Neumann factor ($\varepsilon_n = 1$ if $n=0$, $\varepsilon_n = 2$ if $n>0$) and J_n is the Bessel function of order n. The *blocked-wall* pressure field is obtained by assuming a Neumann boundary at $r=r_o$ [5]:

$$P_B(\beta) = p_0 e^{\mathrm{j}(\omega t - k_x x)} \sum_{n=0}^{\infty} \varepsilon_n (-\mathrm{j})^n \left[J_n(k_+ r) - \frac{J_n'(k_+ r_o)}{H_n^{2\prime}(k_+ r_o)} H_n^2(k_+ r) \right] \cos(n\phi - n\beta) \,, \tag{2}$$

where $f'(x) = \mathrm{d}f/\mathrm{d}x$ and H_n^m is the Hankel function of m-th kind of order n. In order to obtain a zero normal velocity at the baffle ($z=0$), the blocked pressure must be modified as

$$\hat{P_B} = P_B(\beta) + P_B(\pi - \beta) = \sum_{n=0}^{\infty} \left[P_{Bn}(\beta) + (-1)^n P_{Bn}(-\beta) \right] \,. \tag{3}$$

Assuming non-resonant interior, the acoustic normal impedance at the inner (outer) surface is [3]

$$Z_{i(o),n} = (-) \frac{\mathrm{j}\omega\rho_{-(+)}}{k_{-(+)}} \frac{H_n^{1(2)}(k_{-(+)} r_{i(o)})}{H_n^{1(2)\prime}(k_{-(+)} r_{i(o)})} \tag{4}$$

where ρ_- and c_- are the density and the speed of sound of the z_- fluid and $k_- = \sqrt{(\omega^2/c_-^2 - k_x^2}$.

2.2 Windowing along the cylinder's axis

A wave of wavenumber k_p is assumed to propagate on an infinite 1D structure. The velocity field in the spatial domain can be written as $\hat{v}(x) = ve^{-\mathrm{j}k_p x}$. If only a part of length L contributes to the sound radiation, the velocity field in the wavenumber domain is defined as

$$\tilde{v}(k) = \int_{-L/2}^{L/2} ve^{-\mathrm{j}k_p x} e^{\mathrm{j}kx} \mathrm{d}x = 2v \frac{\sin\left[(k-k_p)L/2\right]}{k-k_p} \,. \tag{5}$$

The radiated power calculated from the wavenumber spectrum of the velocity field is [6]

$$\Pi(k_p) = \frac{\rho_o c_o}{4\pi} \int_0^{k_o} \frac{|\tilde{v}|^2 k_o}{\sqrt{k_o^2 - k^2}} \mathrm{d}k = \frac{\rho_o c_o k_o |v|^2}{2\pi} \int_0^{k_o} \frac{1 - \cos\left[(k-k_p)L\right]}{(k-k_p)^2 \sqrt{k_o^2 - k^2}} \mathrm{d}k \,. \tag{6}$$

Finally, the radiation efficiency can be calculated as [6]

$$\sigma(k_p) = \frac{2\Pi}{\rho_o c_o L |v|^2} = \frac{k_o}{\pi L} \int_0^{k_o} \frac{1 - \cos\left[(k-k_p)L\right]}{(k-k_p)^2 \sqrt{k_o^2 - k^2}} \mathrm{d}k \,. \tag{7}$$

2.3 Transmission loss

The incident acoustic power per unit length on the outer surface of the cylinder is given by [5]

$$W_I(\omega, \theta, \Psi) = \frac{r_o p_0^2 \cos\theta}{\rho_+ c_+ \cos\beta} \,. \tag{8}$$

The transmitted sound power per unit length of the inner surface ($r = r_i$) can be evaluated as

$$W_T(\omega, \theta, \Psi) = \frac{r_i}{2} \sum_{n=0}^{\infty} \Re\left[p_{i,n} (v_{i,n}^f)^H\right] \int_0^{\pi} \left[\cos(n\phi - n\beta) + (-1)^n \cos(n\phi + n\beta)\right]^2 \mathrm{d}\phi \,. \tag{9}$$

Thus, the transmission loss can be defined as

$$\mathrm{TL}(\omega, \theta, \Psi) = -10 \log_{10} \left(\sigma(k_x) \frac{r_i \rho_+ c_+}{r_o p_0^2} \sum_{n=0}^{\infty} \frac{\cos^2(n\beta + n\pi/2)}{\varepsilon_n} \Re(Z_{i,n}) |v_{i,n}^f|^2 \right) \,. \tag{10}$$

3 VALIDATION

A baffled semi-cylindrical shell of length $L = 0.6$ m, internal radius $r_i = 0.478$ m and external radius $r_o = 0.5$ m is considered. The shell consists of an external 2 mm thick steel layer ($E = 210$ GPa, $\nu = 0.3$, $\mu = 0.1$ %, $\rho = 7800$ kgm^{-3}), an intermediate 19 mm thick melamine layer ($\Phi = 0.99$, $\sigma = 10900$ Nsm^{-4}, $\alpha_\infty = 1.02$, $\Lambda = 100$ μm, $\Lambda' = 130$ μm, $E = 80$ kPa, $\nu = 0.4$, $\mu = 17$ %, $\rho = 8.8$ kgm^{-3}) and an internal 1 mm thick mass layer ($E = 1$ MPa, $\nu = 0.3$, $\mu = 50$ %, $\rho = 1500$ kgm^{-3}). The melamine is modeled as an equivalent fluid according to a limp model [1]. The fluids have properties $c_+ = c_- = 343$ ms^{-1} and $\rho_+ = \rho_- = 1.21$ kgm^{-3}. Figure 1 compares the TL at oblique incidence ($\theta = 45°$, $\Psi = 0°$) predicted by the proposed approach with the result produced by a coupled FEM-BEM. The solution for an infinite cylinder [3] with the same properties of the shell is also presented. The solution of the half cylinder is in better agreement to the reference solution over the whole frequency range with respect to the solution of the complete cylinder. The reason for such a difference must be ascribed to the blocked pressure. It should be noted, for example, that in case of $\beta = 0$ ($\Psi = 0$) only the even circumferential modes of the half cylinder are excited by the incident acoustic field. In general, the excitation seen by a baffled semi-cylindrical shell is different from the excitation seen by a complete cylinder because of the different pressure fields produced by an incident plane wave. On the other hand, the adopted 1D windowing technique improves the agreement to the reference solution in the low frequency range.

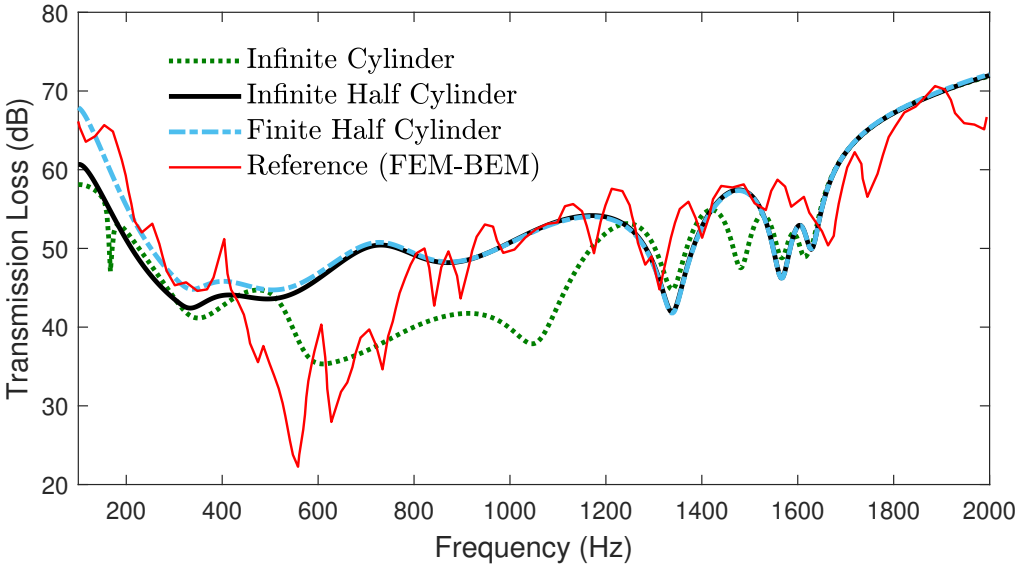

Figure 1. TL at oblique incidence ($\theta = 45°$, $\Psi = 0°$) of a baffled half cylinder.

4 CONCLUDING REMARKS

A model for the sound transmission through baffled semi-cylindrical shells is described. The proposed procedure allows to exploit the versatility of the TMM and makes it easy to deal with anisotropic, poroelastic and heterogeneous shells, avoiding the need for analytical formulations or homogeneous equivalent models. The accuracy of the method has been verified by showing agreement with the result produced by a FE-BE model in case of a shell consisting of homogeneous layers. The adopted 1D windowing technique makes it possible to properly account for the finite length of the shells. The presented TMM ensures a lower computational cost compared to other periodic approaches since each layer can be modeled per se and homogeneous layers may be modeled efficiently with a few finite elements. Ultimately, the proposed approach could represent an effective acoustic tool for cylindrical shells, due to its versatility and efficiency.

REFERENCES

[1] J. Allard and N. Atalla. *Propagation of sound in porous media : modelling sound absorbing materials 2nd edition*. John Wiley & Sons, 2009.

[2] A. Parrinello and G. L. Ghiringhelli. Transfer matrix representation for periodic planar media. *Journal of Sound and Vibration*, 371:196–209, 2016.

[3] A. Parrinello and N. Atalla. Sound transmission through multilayered cylinders using a transfer matrix method. *NoiseCon19*, 2019.

[4] A. Blaise and C. Lesueur. Acoustic transmission through a 2-d orthotropic multi-layered infinite cylindrical shell. *Journal of Sound and Vibration*, 155(1):95–109, 1992.

[5] Y Liu and C. He. Diffuse field sound transmission through sandwich composite cylindrical shells with poroelastic core and external mean flow. *Compos. Struct.*, 135:383 – 396, 2016.

[6] F. Fahy and P. Gordonio. *Sound and Structural Vibration: Radiation, Transmission and Response - Second Edition*. Academic Press, 2007.

NUMERICAL ANALYSES OF THE SOUND TRANSMISSION THROUGH DOUBLE-GLAZING SYSTEM AT LOW FREQUENCIES

Chaima SOUSSI[1] , Mathieu AUCEJO[1], Walid LARBI[1*] and Jean-François DEÜ[1]

[1] Laboratoire de Mécanique des Structures et des Systèmes Couplés
Conservatoire national des arts et métiers, Paris, France
Email: chaima.soussi@lecnam.net, mathieu.aucejo@lecnam.net, walid.larbi@lecnam.net, jean-francois.deu@cnam.fr

ABSTRACT

The acoustic performances of building elements such as windows are performed in laboratory according to standards. In addition to the high cost of the experimental tests, the measurements at low frequencies, face some difficulties such as the lack of reproducibility, the diffuseness of the acoustic field and the effect of the modal behaviour of the rooms. To overcome this, a numerical analysis of the transmission loss of a double-glazing structure is developed in this work. To this end, four numerical configurations, based on experimental conditions, are proposed. The differences concern the modeling of the emitting and receiving rooms. The numerical model used for the double-glazing was calibrated through the Experimental Model Analysis. Results show that there is a significant effect of the rooms on the transmission loss at low frequencies and so of its properties such as the acoustic absorption. A comparison with experimental results is also established to validate the chosen configuration with which parametric analyses are carried out, however, results are not presented in this paper.

Keywords: Double-glazing, Transmission Loss, Experimental Modal Analysis, Numerical analysis.

1 INTRODUCTION

Double-glazing is often used in noise reduction since a relatively high transmission loss is achieved by the introduction of an acoustic gap between the panels. Due to various effects of fluid-structure interaction, boundary conditions and the modal behaviour in low frequencies, the prediction of the acoustic performance of the double wall remains complicated. In the literature, Antònio et al studied experimentally the transmission loss through single, double and triple glazing [1], while, in Ref [2], the effect of boundary conditions on this acoustic indicator of double panels was investigated. A comparison of different type of glass can also be found in Ref [3]. Regarding the numerical prediction approaches, several methods are available. The choice of the method depends on the computational cost and the considered frequency band. The Finite Element Method (FEM) is suitable to treat problems in low frequencies. For example, Larbi et al used it to develop a model of a sandwich plate with viscoelastic core [4]. Another example can be found in Ref [5] which studied the prediction of sound transmission through double-wall with elastic porous lining.

In this paper, a numerical analysis based on an experimentally calibrated FEM model is proposed to predict the vibroacoustic behaviour of double-glazing.

2 NUMERICAL CALIBRATION OF THE DOUBLE-GLAZING FROM EMA

In this section, we are interested in the calibration of a numerical model of the double-glazing through the Experimental Modal Analysis (EMA) . The studied structure presented by Figure 1 is an Insulting Glass Unit. It consists of two glass and a separating edge which forms an air or gas gap. The complexity is located along the edge. In fact, the stainless hollow steel spacer is filled at least half by molecular sieve in the form of beads called the desiccant and used to dry out the cavity. In addition, a dual seal combination has a primary seal of polyisobutylene between the spacer and the panes, and a secondary seal of silicone around the outside edge is used to glue all the parts. So, to calibrate a model of the group "spacer + desiccant + seal", an EMA is carried out for the full system in order to determine the mechanical properties (E, ν and ρ) for an equivalent homogeneous isotropic material for this group.

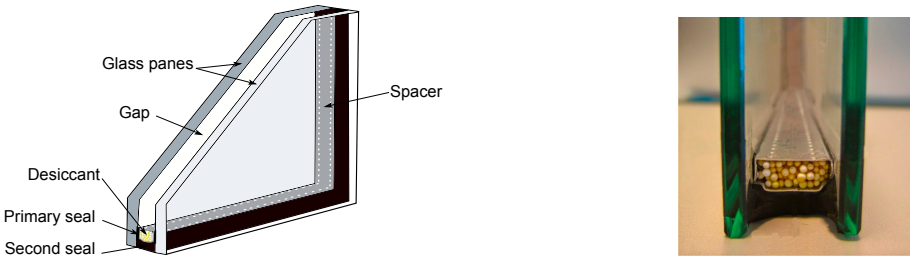

Figure 1. Details of the Insulting Double Unit

2.1 Experimental Modal Analysis

For performing the EMA, a home-made Matlab toolbox has been developed and includes several approachs like LSCF and its polyreference version. The suspended double-glazing (see Figure 2), composed of two glass of 6 mm and 4 mm separeted by 18 mm of argon, is meshed into 153 nodes in order to obtain a good visualisation of the mode shapes. The application of the method implemented in the toolbox requires the measurement of the Frequency Response Function (FRF) at different points of the structure after its excitement. In this work, the roving hammer test is used with an impact hammer and three reference accelerometers.

2.2 Numerical calibrated model

The double-glazing experimentally tested is calibrated numerically with the finite element method. The numerical model consists of two 2D shells representing the two panels separated by a 3D cavity filled with argon. An equivalent solid for the group "spacer + desiccant+ seal" (see Figure 2) is defined. Quadrilateral elements for the glass panels and hexahedral ones for the fluid and the

equivalent spacer are used for the finite element discretization, and their sizes are controlled by the wavelength of each subdomain.

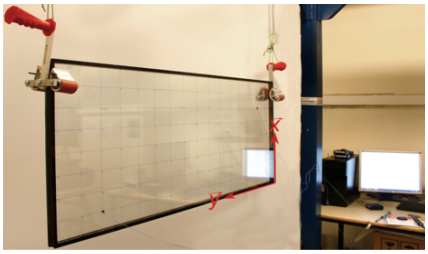

Figure 2. Suspended double-glazing

2.3 Results and discussion

Table 1 shows the comparison of the first ten natural frequencies of the structure obtained from the experimental and numerical analysis after calibration of the numerical model on the first natural frequency. For a such complex structure, results are considered satisfying since the maximum difference of natural frequency is 6.8 %, observed for Mode 8. Therefore, this calibrated model is used to evaluate numerically the transmission loss.

Mode	**1**	**2**	**3**	**4**	**5**	**6**	**7**	**8**	**9**	**10**
Experimental	29.9	37.7	41.2	56.4	60	75.5	93.9	94	98.4	117.6
Numerical	29.8	36.6	38.6	56.4	63.8	72.9	98.9	100.4	102.7	113.9
Gap (%)	0.4	2.9	6.3	0.1	6.4	3.4	5.4	6.8	4.4	3.1

Table 1. Experimental and numerical eigenfrequencies of the double-glazing

3 DETERMINATION OF THE SOUND TRANSMISSION LOSS

The airborne sound insulation of building elements is evaluated in laboratory according to standards ISO 10140. Measurement are done between two adjacent reverberation rooms. In low frequencies, tests face some difficulties such as the lack of reproducibility, the diffuseness of the acoustic field and the effect of the modal behaviour of the rooms. To study these different problems, four numerical configurations have been carried out. In the first one (Figure 3.a), a realistic laboratory configuration is considered. It consists in two reverberant rooms modelled with a spherical acoustic source in the emitting one. In fact, standards assume that the acoustic excitation is a diffuse field for the entire frequency band of measurement. However, this condition is respected only beyond the ”Schroeder frequency” which marks the limit between the modal and the diffuse field behaviour. So, a second configuration (Figure 3.b) considering the source side as a diffuse field even for the very low frequencies while modelling the receiving room is considered. Numerically, this condition is ensured from the superposition of set of plane waves with random phase. For the third configuration (Figure 3.c), to avoid the modal behaviour of the receiving room, an acoustic radiation in a half-space while modelling the emissive room is considered. The Rayleigh condition, which references to a vibrating structure in the plane of a rigid baffle, is used. Finally, the fourth configuration (Figure 3.d) combines the diffuse field in the source side and the Rayleigh radiation in the receiving one. The advantages of this model is a significant reduction in the model size, but considers perfect experimental conditions in both sides of the structure under test.

4 RESULTS

A comparison of the results in narrow band and third octave band is established and presented in Figure 4. As expected, in very low frequencies (below 100 Hz), the TL is sensitive to the presence of the acoustic rooms due to their modal behaviour. Of course, this observation is not observed for the results of the fourth configuration which presents only the modal behaviour of the double-glazing. From 125 Hz, TL has the same trend regardless which configuration is used whith a difference of 3 dB at 500 Hz.

5 CONCLUDING REMARKS

The double-glazing is calibrated numerically with the Experimentally Modal Analysis. The established model is used to carry out numerical acoustic analyses. The results show that the presence of the acoustic rooms has a significant influence on the TL at very low frequencies. However, above 125 Hz, all TL converge. The fourth configuration is thus preferred since it is the less expensive configuration in terms of computational cost. Finally, it can be noted that in addition to the experimental results presented in this paper, parametric analyses have been performed but are not presented here.

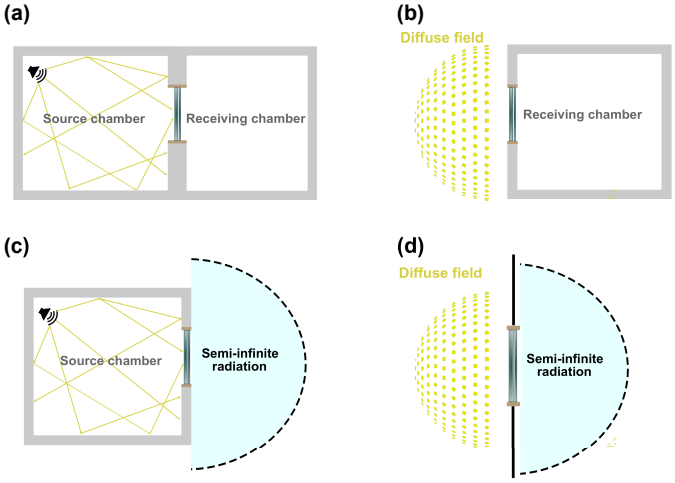

Figure 3. Numerical configurations considered for the prediction of the TL

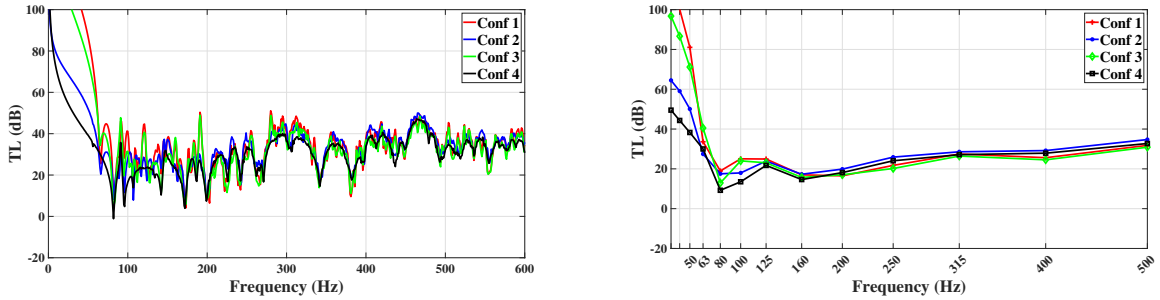

Figure 4. TL from the four numerical configurations

REFERENCES

[1] A.J.B. Tadeu and D.M.R. Mateus. Sound transmission through single, double and triple glazing. Experimental evaluation. *Applied Acoustics*, 62(3):307–325, March 2001.

[2] F. X. Xin and T. J. Lu. Analytical modeling of sound transmission through clamped triple-panel partition separated by enclosed air cavities. *European Journal of Mechanics - A/Solids*, 30(6):770–782, November 2011.

[3] K. Miskinis, V. Dikavicius, R. Bliudzius, and K. Banionis. Comparison of sound insulation of windows with double glass units. *Applied Acoustics*, 92(Supplement C):42–46, May 2015.

[4] W. Larbi, J.F. Deü, and R. Ohayon. Vibroacoustic analysis of double-wall sandwich panels with viscoelastic core. *Computers & Structures*, 174:92–103, October 2016.

[5] F. C. Sgard, N. Atalla, and J. Nicolas. A numerical model for the low frequency diffuse field sound transmission loss of double-wall sound barriers with elastic porous linings. *The Journal of the Acoustical Society of America*, 108(6):2865–2872, December 2000.

EFFECT OF COLD SPRAY DEPOSITION ON THERMOSETTING COMPOSITE SUBSTRATES UNDER DYNAMIC LOADS

Ilaria Papa[1], AntonioViscusi[1], Alessia Serena Perna[1,2], Antonello Astarita[1], Valentina Lopresto[1], Luigi Carrino[1], Vincenza Antonucci[3], Maria Rosaria Ricciardi[3]

[1] Department of Chemical, Materials and Industrial Production Engineering, University of Naples Federico II, Naples, Italy
Email: ilaria.papa@unina.it, antonio.viscusi@unina.it,antonello.astarita@unina.it, lopresto@unina.it, luigi.carrino@unina.it
[2]University of Bergamo, Italy
alessiaserena@icloud.com
[1]Institute for Polymer, Composites and biomaterials, National Research Council, Portici, Italy
Email: mariarosaria.ricciardi@cnr.it, vinanton@unina.it

ABSTRACT

In this study, the effects of aluminium cold spray deposition on basalt/epoxy composites under dynamic loads were investigated. Before the characterisation, the impact surface was treated with a commercial Polylactic acid (PLA) surface to allow better adhesion of the aluminium particles on the thermosetting composite. After the cold spray deposition, the neat and coated composite laminates have been experimentally characterized by performing low-velocity impact tests. The results have shown a good deposition of the aluminium coating on thermosetting composite and the effect of the coating on the latter is evaluated in terms of low-velocity impact parameters and damage mechanism. Even if the impact response of the coated composite is lower in terms of maximum load, the aluminium deposition seems to influence the damage mechanism propagation positively as confirmed by the measuring of the plastic deformation.

1 INTRODUCTION

Composite materials are increasing a lot their applications in structures and constituents due to their low density, high specific strength and stiffness and their lighter. They have been developed as mechanical components to substitute parts of metallic materials for aircraft structures. Among the

composite structures, Basalt fiber-reinforced plastic (BFRP) is becoming increasingly established in the world of composites as a good substitute for traditional composite materials made of fiberglass and carbon [1]: due to the particular mechanism of damage formation during low-velocity impact, their dynamic properties are receiving attention [2-5]. However, composite materials are in general non-homogenous and anisotropic, allowing failure through a variety of damage modes; this damage is not always visible but may lead to a complete structural collapse, without showing any prior external evidence [6-7]. For safety reasons, it is crucial to know the behaviour of composite laminates under low-velocity impact conditions at different increasing impact energies, as the latter can cause different more or less critical damages [8-9]. Moreover, panels mounted on aircraft bodies could be subject to damage due the lightning and electricity. As a consequence, the application of composite materials on an aircraft body needs a superficial conductive skin to reduce the damages mentioned above.

Therefore, the surface metallization is considered to be an effective technique to enhance the surface properties of the composite materials, to make the low-speed impact damage more visible to the naked eye and then to expand their engineering application fields. In this scenario, the Cold Gas-Dynamic Spray (CGDS) technology appears to be a suitable technique to make a metallic coating on temperature-sensitive materials, such as the composite ones [10]. In fact, compared to the traditional thermal spray techniques, in a cold spray process the particles stay completely in a solide state upon impact the target surface, making it possible to create metallic coatings on polymeric or FRPs, without inducing any damage or failure of the substrates [11-12].

According to their reaction, when they are subjected to heat, polymers are classified, in thermoplastics and thermosets. The bonding mechanisms of polymeric materials are strongly dependent on the type of matrix chosen: while the thermoplastics, being more ductile, are more suitable to be coated by the impact process, the thermosets are subject to breakages during impact due to their fragile behaviour. However, still nothing has been done on thermosets composite materials that are widely used in aerospace and automotive fields respect to the thermoplastic ones. The classic bonding mechanisms are not directly applicable during the deposition on thermosetting polymers [13].

So, in this paper it will be provided an innovative technique to facilitate the deposition of metallic coatings on thermosetting FRPs substrates through cold spray. In particular the impact surface was treated using a commercial Polylactic acid (PLA) to improve the anchoring of the aluminium particles on the thermosetting composite substrate. The effects of this treatment on the impact properties of basalt fiber composites are discussed.

2 MATERIALS

2.1 Laminates preparation

Basalt fibre reinforced plastic square laminates, 400 mm inside, were realised by resin vacuum infusion technology using basalt plain-woven fabrics, 200 g/m2 (Basaltex NV) and an epoxy infusion system by Gurit (Prime 20LV). 16 fabric layers were stacked to obtain a thickness of 2.50 mm.
To allow a better adhesion with the aluminium particles the impact surface was treated using a commercial Polylactic acid (PLA) film with a thickness of 30 μm. Once the film has been positioned, a heated plate press of the Collin model P 200 E is used to favour the PLA-composite coupling. Since the melting temperature of the polylactic acid is between 180 ° C and 220 ° C, the dishes were brought to a temperature of 200 ° C, and then a pressure of 5 bar was applied for about 5 min.
Dymet 423low-pressure equipment with nitrogen as a carrier gas was used for the cold spray depositions. Micron-sized powders of aluminium alloy Al-Si12 (particle mean size of 40 μm) were used for the spraying process to produce the metallic coating on the PLA substrate. First, different coating tracks 40 mm long and 5 mm width with a travel speed of the spraying gun of 8 mm/s were preliminary produced by varying the process parameters in a wide range (inlet gas temperature: 150 – 600 °C, inlet gas pressure: 4 – 8 bar, stand-off distance: 10 – 80 mm).

3 METHODS

Low-velocity impact tests (impact velocity, V_i=3m/s) were carried out by a falling weight machine, Ceast Instron, at energy level U=30J to avoid the penetration and to measure the indentation depth. The rectangular specimens, 100x150 mm, cut by a diamond saw from the original panels, were supported by the clamping device suggested by the ASTM D7137 Standard and were centrally loaded by an instrumented cylindrical impactor with a hemispherical nose, 19.8 mm in diameter. Tests were conducted using an impactor with a mass equal to 3.640 kg that combined with the drop heights allowed to obtain the selected impact energy. After the impact tests on both the original material and the aluminium cold sprayed substrate, the specimens were observed by visual inspection to investigate the damage, whereas a confocal microscope, Leica DCM3D, was used to measure the indentation depth with a magnification of 10x.

4 RESULTS AND DISCUSSION

The optimal process parameters adopted to produce the coated samples for the next phase of the experiments are 6 bar gas pressure, 600° C gas temperature, 35 mm stand-off distance (which is the distance between the CS exit-nozzle and the substrate). These parameters were chosen at the aim to obtain the best adhesion mechanism between the particle and the substrate. The thickness of the coating was approximately 100 μm.

In Figure 2, the comparison of the load-displacement curves obtained at U=30J for the basalt composite systems with the aluminium coating and without it are compared. The pictures clearly show that, for both conditions, closed type curves are obtained: the samples are not penetrated/perforated by the impactor that rebounds and the area enclosed in the loop of the loading/unloading part of the curve are the energy absorbed by the laminate to create damage or to bend.

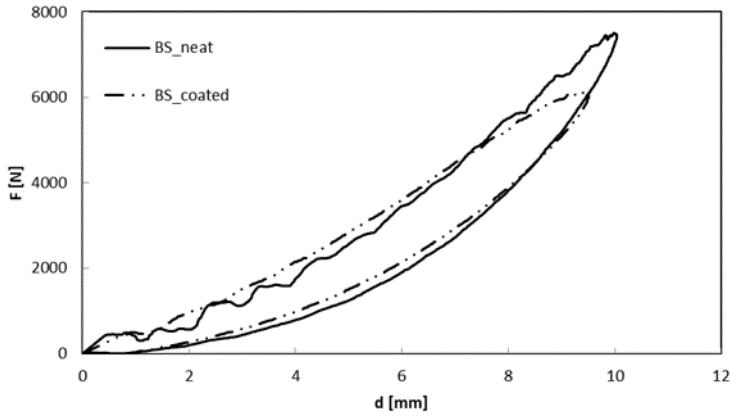

Figure 2. Load-displacement comparison between coated and neat composite at U=30J

In particular, the maximum load, F_{max}, seems to be affected by the cold spray deposition resulting higher in the case of BS_neat (Table 1). It is worth noting that, in the case of the coated materials (BS_coated), the first significant load drop occurs in correspondence of the maximum load, while, in the case of neat ones, several load drops, denoting matrix cracks and starting fibre failures, were observed on the increasing part of the curve. This means that the aluminium coating influences the damage mechanisms by protecting the fibres.

Condition	F_{max} [N]	U_{max} [J]	U_a [J]	d [mm]	I [μm]
TQ_30J	7504.33	30.55	10.50	10.02	191.93
CS_30J	6387.82	29.50	9.52	9.48	142.22

Table 1. Impact parameters at U=30J

The influence of the coating on the damage mechanism is also confirmed by the lower absorbed energy, U_a, and lower indentation depth, I, measured on the BS_coated composite. Recalling that the indentation depth, I, is the maximum depth of the plastic deformation left by the impactor on the impacted surface of the specimen, from Table 1 it is possible to note that the coated composite showed lower indentation respect to the composite neat.

REFERENCES

[1] V. Fiore , T. Scalici , G. Di Bella , A. Valenza , A review on basalt fibre and its composites. Composites Part B Engineering, 2015, 74, pp. 74-94.

[2] S. Liu, Z. Kutlu, and F. K. Chang, Matrix cracking and delamination propagation in laminated composites subjected to transverselyconcentrated loading. Journal of Composite Materials, 27 (5), (1993) 436-470.

[3] F.K. Chang, H.Y. Choi, and H.S. Wang, Damage of laminated composites due to low velocity impact, 31st AIAA/ASME/ASCE/AHS/ASC Structures, Struct. Dyn. and Mater. Conf., Long Beach, CA, April 2-4, 1990, pp. 930-940.

[4] M.G. Stout, D.A. Koss, C. Liu, J. Idasetima, Damage development in carbon/epoxy laminates under quasi-static and dynamic loading, Compos. Sci. and Technol., 59 (1999), pp. 2339-2350.

[5] G. Schoeppner, S. Abrate, Delamination threshold loads for low velocity impact on composite laminates, Composite Part A, 31 (2000) 903–915.

[6] C.F. Li, N Hu, J.G. Cheng, H. Fukunaga, H. Sekine, Low-velocity impact-induced damage of continuous fiber-reinforced composite laminates. Part II. Verification and numerical investigation, Composites Part A, 33, 2002, pp. 1063–1072.

[7] GAO Davies, R. Olsson, Impact on composite structures, Aeronaut. J., 108, 2004, pp. 541–563.

[8] S. Putić, M. Stamenović, B. Bajčeta, P. Stajčić, S. Bošnjak, The influence of high and low temperatures on the impact properties of glass–epoxy composites, J. Serb. Chem. Soc.; 72 (7), pp. 713–722, 2007.

[9] V. Lopresto, A. Langella, Composite Laminates Under Dynamic Extreme Conditions, Special Issue: International Symposium on Dynamic Response and Failure of Composite Materials, DRaF2014, Procedia Engineering, 88 (2014), pp. 173-179. Published by Elsevier Ltd.

[10] Zhou XL, Chen AF, Liu JC, Wu XK, Zhang JS (2015) Preparation of metallic coatings on polymer matrix composites by cold spray. Surf Coatings Technol 206(1):132-136.

[11] Archambault G, Jodoin B, Gaydos S, Yandouzi M (2016) Metallization of carbon fiber reinforced polymer composite by cold spray and lay-up molding processes. Surf Coatings Technol 300:78-86.

[12] Affi J, Okazaki H, Yamada M, Fukumoto M (2011) Fabrication of Aluminum Coating onto CFRP Substrate by Cold Spray. Mater Trans 52(9):1759-1763.

[13] Assadi H, Gärtner F, Stoltenhoff T, Kreye H (2003) Bonding mechanism in cold gas spraying. Acta Mater 51(15):4379-4394.

EXPERIMENTAL IDENTIFICATION OF VISCOELASTIC PROPERTIES OF VIBRATING PLATES

P. Grosso[1], A. De Felice[1] and S. Sorrentino[1*]

[1]Department of Engineering Enzo Ferrari
University of Modena and Reggio Emilia, Modena, ITALY
Email: {pasquale.grosso, alessandro.defelice, silvio.sorrentino}@unimore.it

ABSTRACT

Aim of the present study is the identification of equivalent viscoelastic models for layered thin walled structures, obtained from vibration measurement only, able to fit the experimental data on a wide frequency range by means of a minimum number of parameters. An identification method of general validity is proposed, based on the concept of equivalent modal damping ratio and on the classical circle-fit technique. It is applied to the analysis of both Aluminum plates coated by damping pads and plates made by Quiet Aluminum. To fit the experimentally found equivalent modal damping ratios, the linear Fractional Kelvin viscoelastic model is adopted, assessing the accuracy of the identified parameters by comparison of numerically simulated with experimentally measured frequency response functions.

1 INTRODUCTION

Accurate evaluation of damping properties of layered thin walled structures, as plates or shells, is a relevant problem for several industrial applications in the field of vibration control and noise reduction. The interest in the identification of equivalent viscoelastic models from vibration measurement only has therefore strong motivations, but direct identification from time or frequency domain data is generally a difficult task.

In this study an indirect approach is adopted, based on the concept of modal damping ratio (ζ_n), focusing the attention on its behaviour as a function of the related natural frequency (ω_n). It is well known under which assumptions ζ_n can be analytically defined and experimentally estimated, by considering a linear viscous dissipative model (integer order Kelvin model, based on a single Newton element). However this theoretical parameter shows a dependency on the related natural frequency that in most cases dramatically fails in fitting the experimental data; it was shown that a

better agreement between theory and experiments can be achieved by means of non–integer order differential models, obtained by replacing the first derivative (Newton element) with a fractional derivative (Scott–Blair element) [1]. Extensive literature exists on the application of fractional calculus to viscoelasticity, since it yields to physically consistent stress–strain constitutive relations with a few parameters, good curve fitting properties and causal behaviour [2,3,4].

To overcome the difficulty of finding analytical expressions for ζ_n in case of non–elementary dissipative models, a method of general validity has been developed, introducing the concept of equivalent modal damping ratio applied to the circle–fit technique [5]. This identification method is based on the assumption that the Nyquist plot of the mobility for any mode n can be approximated by a circumference, which is still acceptable when considering fractional derivative models [6]. The Fractional Kelvin model [1] is then considered, applied to the analysis of vibrating Aluminum plates coated by damping pads (ADP) or made of Quiet Aluminum (QA).

2 IDENTIFICATION METHOD

According to the circle–fit technique [5], (almost) circular experimental Nyquist plots of the Mobility allows the estimate of the related modal damping ratios ζ_n (Figure 1, left), which according to the integer order Kelvin model are given by:

$$\zeta_n = \frac{1}{2\omega_n}\left[\frac{\Omega_2^2 - \Omega_1^2}{\Omega_2 \tan(\gamma_2) + \Omega_1 \tan(\gamma_1)}\right] \tag{1}$$

where ω_n is the natural angular frequency and the other symbols refer to Figure1, right. Notice that $\omega_n = \Omega_0$ only for the integer order Kelvin model, but more in general it is $\omega_n \neq \Omega_0$, as in Figure 1.

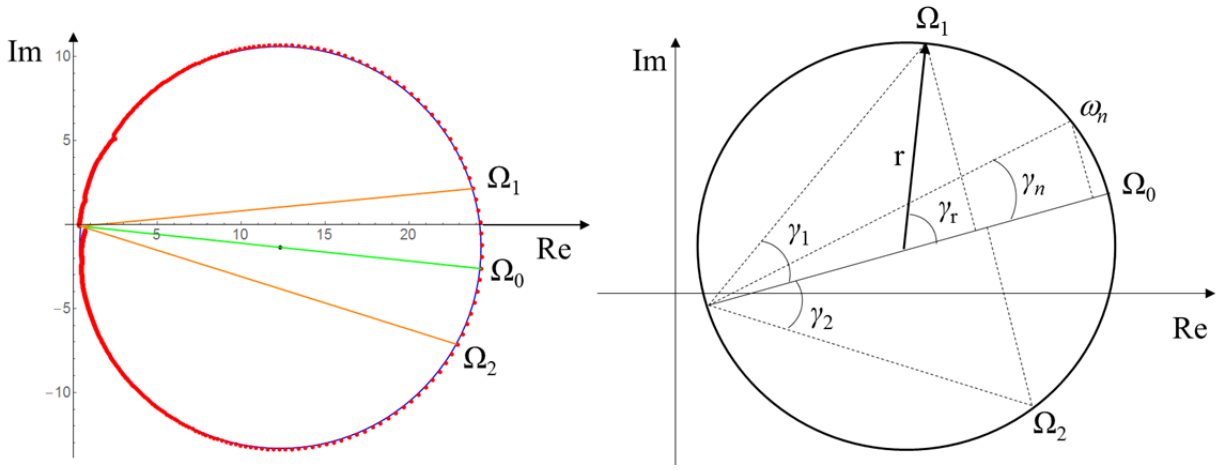

Figure 1. Nyquist plots of Mobility.
Experimental plot (left; mode at 150 Hz, ADP) and general scheme for mode n (right).

The experimental estimates of ζ_n as function of the natural frequencies ω_n usually show a behaviour which is very far from the linear one (straight increasing line passing through the origin) predicted by the integer order Kelvin model [6]. As a consequence, in order to fit such experimental curves, more refined models are needed; the Fractional Kelvin model is here adopted, with analytical expressions in the frequency and in the Laplace domains given by:

$$E(\omega) = E_0\left[1 + (\mathrm{i}\tau\omega)^\alpha\right], \quad E(s) = E_0 R(s) = E_0\left[1 + (\tau s)^\alpha\right] \tag{2}$$

where E_0 is the equivalent static Young's modulus, α is a non–integer or fractional derivative order (values between 0 and 1) and τ is a characteristic time.

At this stage a definition of general validity is needed for ζ_n, in order to create a link between

the experimental damping estimates of Equation 1 and the viscoelastic parameters of the selected model. For this purpose a homogeneous Kirchhoff plate is considered. By applying the elastic–viscoelastic correspondence principle [4] and separating the variables, the plate equation in the Laplace domain yields the characteristic equation associated with the *n*-th mode:

$$\frac{E_0 h^3}{12(1-\nu^2)\rho_h}\cdot\frac{\nabla^4 W(\mathbf{x})}{W(\mathbf{x})} = -\frac{s^2}{R(s)} = \omega_n^2 \quad \Rightarrow \quad s^2 + \omega_n^2 R(s) = 0 \tag{3}$$

where **x** denotes the spatial coordinates, ρ_h the mass per unit area of the plate, h its thickness, ν the Poisson's ratio and ω_n the n-th natural frequency. Since the real negative part of the complex conjugate roots is responsible for the oscillation decay, it can be proven that under certain conditions a general definition for an equivalent modal damping ratio ζ_n is given by:

$$\zeta_n \triangleq \frac{|\mathrm{Re}(s)|}{\omega_n} \cong \frac{1}{2}\omega_n \frac{\mathrm{Im}[R(\mathrm{i}\Omega_0)]}{\Omega_0} \tag{4}$$

which constitutes a link between a selected viscoelastic model (represented by the function R in both Equations 3 and 4) and the evaluation of ζ_n via circle–fit technique. Through Equation 4 it is then possible to fit the parameters of a viscoelastic model (as in Equation 2) with the experimental estimates of ζ_n.

3 EXPERIMENTAL RESULTS

Two square plates has been tested, with side length $l = 300$ mm, thickness $h = 2$ mm (QA) and $h = 3$ mm (ADP), total weight $P = 0.52$ kg (QA) and $P = 1.06$ kg (ADP). The experimental estimates of ζ_n are displayed vs the natural frequencies ω_n in Figure 2, for both QA (*a*) and ADP (*b*). On the experimental data (dots) are superimposed the curves $\zeta_n(\omega_n)$, plotted using the following identified parameters in the Fractional Kelvin model:

QA	$E_0 / E_{0\mathrm{Al}} = 0.825$	$\alpha = 0.219$	$\tau = 4.829\times10^{-8}$ s	($\rho = 2889$ kg/m^3, $\nu = 0.33$)
ADP	$E_0 / E_{0\mathrm{Al}} = 0.551$	$\alpha = 0.229$	$\tau = 5.097\times10^{-5}$ s	($\rho = 3926$ kg/m^3, $\nu = 0.33$)

where $E_{0\mathrm{Al}} = 7.1\times10^{10}$ [N m^{-2}] is the standard Young's modulus of Aluminum.

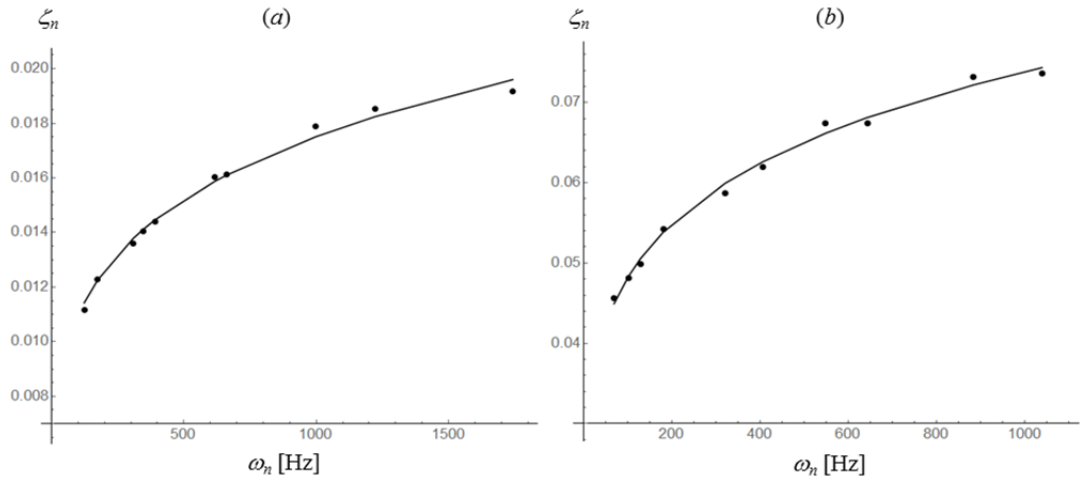

Figure 2. Modal damping ratios (ζ_n) vs natural frequencies (ω_n) [Hz]; QA (*a*) and ADP (*b*). Experimental identified data (dots) and Fractional Kelvin model interpolations (continuous).

The accuracy of the identified parameters has been assessed by comparison of numerical with experimental FRFs (modulus of Mobility), as shown in Figure 3 for both QA (*a*) and ADP (*b*).

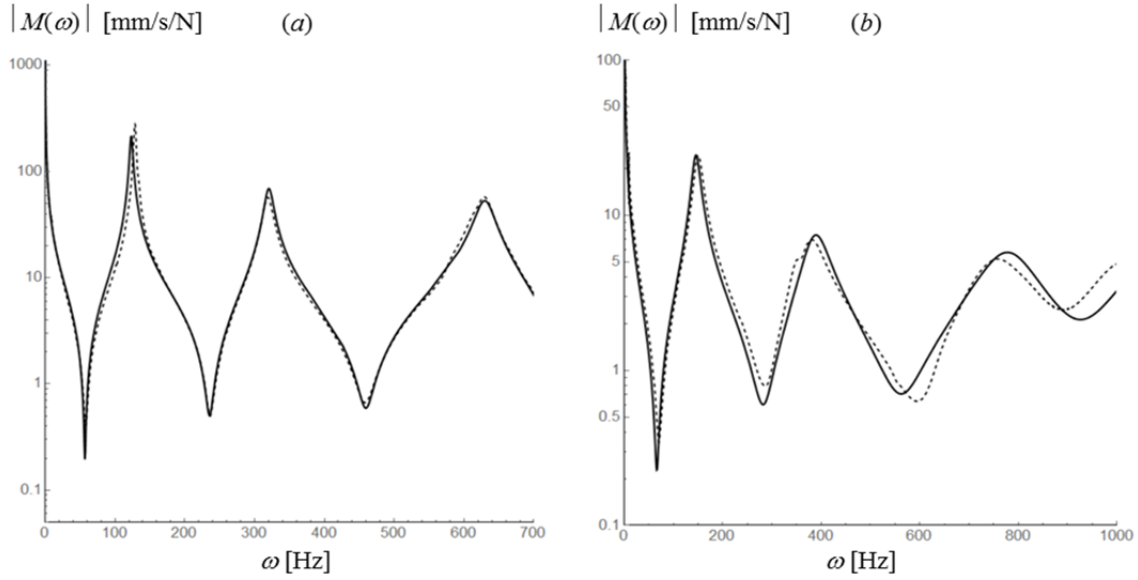

Figure 3. Experimental (continuous) and numerical (dotted)
Mobility modulus [mm $s^{-1} N^{-1}$] vs frequency [Hz]; QA (*a*) and ADP (*b*).

4 CONCLUDING REMARKS

The circle–fit technique has been applied to the experimental evaluation of equivalent modal damping ratios, developing a procedure valid for any linear viscoelastic model, thus overcoming the difficulty of direct identification from time or frequency domain data.

Plane flexural vibrations of free–free layered Aluminum plates have been considered (viscoelastic pads and Quiet Aluminum). The linear Fractional Kelvin model has been adopted fo fit the experimentally found equivalent modal damping ratios, and the accuracy of the identified parameters has been assessed by comparison of numerical with experimental frequency response functions.

The proposed identification procedure is suitable for application in the finite element method, for studying dissipative effects in thin walled structures of general shape.

REFERENCES

[1] F. Mainardi. *Fractional calculus: some basic problems in continuum and statistical mechanics*, in: *Fractals and fractional calculus in continuum mechanics*, Springer, Wien, 1997.

[2] P.G. Nutting. A new general law of deformation. *Journal of the Franklin Institute* 191, 679–685, 1921.

[3] A.D. Nashif, D.I.G. Jones, J.P. Henderson. *Vibration Damping*, John Wiley, New York, 1985.

[4] L. Gaul. The influence of damping on waves and vibrations. *Mechanical Systems and Signal Processing* 13, 1–30, 1999.

[5] D.J. Ewins. *Modal Testing: theory, practice and application*, 2nd ed., Research Studies Press, Baldock, 2000.

[6] G. Catania, S. Sorrentino. Experimental evaluation of the damping properties of beams and thin–walled structures made of polymeric materials. Proceedings of IMAC XXVII, Orlando, Florida (USA), 2009.

REFINED BEAM MODELS FOR THE COMPUTATION OF DISPERSION RELATIONS AND TRANSMISSION IN PERIODIC METAMATERIALS

A.G. de Miguel[1] , A. Pagani[1*], M. Filippi[1*], M. Cinefra[1*] and E. Carrera[1]

[1]Mul2 Research Group
Politecnico di Torino, Turin, ITALY
Email: alberto.garcia@polito.it, alfonso.pagani@polito.it, matteo.filippi@polito.it,
maria.cinefra@polito.it, erasmo.carrera@polito.it

ABSTRACT

The present research introduces a novel modeling approach for the numerical computation of the dispersion relations in periodic structures. A refined beam model is generated on the basis of the Carrera unified formulation (CUF), which allows the user to define any structural theory for the expansion unknowns over the cross-section. As a consequence, a beam theory with only displacement unknowns is generated for the unit cell model. Classical 1D elements are employed to interpolate the transverse direction of the model. The proposed class of beam elements are then suitable for the application of the Bloch's boundary conditions over the periodic interfaces. The model is applied to the computation of the dispersion relations in an infinite periodic structure and the transmission coefficient in a finite array of unit cells. The benchmark results show good agreement with the literature.

1 INTRODUCTION

In the past years there has been a growing interest in the study of the effects of acoustic and elastic waves in the human and structural well-being. Much attention is nowadays focused in the introduction of systems which are able to dump, and eventually eliminate, actively or passively, the sound transmission and structural vibrations. In air-borne lightweight structures, for instance, material insulators such as foams and rubbers are already being used to reduce the sound and structural noise radiation due to the engines, the air flowing around the cabin and the air-conditioning system, among others. Although these material solutions have proven its value to mitigate medium to high frequency excitations, they are not effective in the low frequency range due to the ratio between the structural dimensions, e.g. the thickness of the wall, and the long wavelengths of these frequencies.

Design materials, a.k.a. metamaterials, serve for this purpose. They can be defined as heterogeneous artificial materials that exhibit unusual responses to different physical excitations or constraints. A common application of metamaterials are the phononic crystals, which are formed by a periodic repetition of a certain geometry or material system. The main purpose of this design is to open band gaps in certain frequency ranges in which a given excitation does not propagate. This property is physically achieved via two different dynamic effects: the Bragg scattering, which exploits the periodicity to block passing waves through destructive interference, and local resonances, which are based on local oscillators that modify the propagation in the vicinity of their resonance frequency.

The accurate simulation of the dynamic problem is of paramount importance for the efficient design of such metamaterials. The classical approach is based on two main concepts: the *unit cell* and the *dispersion relations*. The former, also denoted to as repetitive volume element (RVE), defines the irreducible geometrical entity which is repeated in the space to create the macro-scale material. The latter represents the relation between the wave properties of the metamaterial, e.g. the frequency vs the wave number. It contains valuable information about the wavelength and speed of a certain excitation, as well as the frequencies in which the propagation is not allowed. The Floquet-Bloch [1] principle is usually recalled to compute these relations in metamaterials. For this purpose, especial periodic conditions are imposed to the unit cell and the eigenvalue problem is computed as a function of the frequency and the wavenumber. Classical methods to solve this problem are the transfer matrix method [2] and the finite element method [3], among others.

The present paper proposes the use of a especial formulation of the finite element method which presents certain advantages for multiscale problems: the Carrera unified formulation [4] (CUF). Based on this approach, the unit cell is modeled via refined beam models with non-local expansion unknowns which allow for the imposition of the Bloch's conditions. The model is applied to the evaluation of the dispersion curves in periodic elastic metamaterials. The assessment of the method is carried out through the well-known example of Wu et al. [5], which consist of a stubbed aluminum plate for dumping of Lamb waves. The evidence of band gaps is further supported here with the analysis of the transmission in a finite strip of the studied metamaterial.

2 REFINED BEAM MODELS

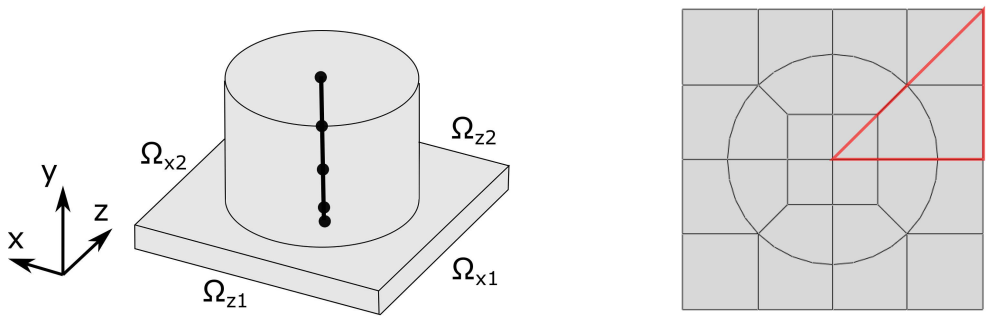

(a) Unit cell (b) Cross-section of the base

Figure 1: Model of the unit cell and detail of the cross-section discretization of the aluminum plate. The first Brillouin zone is marked in red in (b).

According to CUF, any refined beam model can be generated as a kinematic expansion over

the section plane. In this manner, higher-order effects, such as warping, in-plane deformations or zig-zag responses, can be captured by conveniently selecting the theory of structure. For the purposes of the present study, the cross-section unknowns are represented via standard 2D interpolating domains in the *xz*-plane, as follows

$$\boldsymbol{u}(x,y,z,t) = F_\tau(x,z)\,\boldsymbol{u}_\tau(y,t) \quad \tau = 1,2,...,M \tag{1}$$

where $\boldsymbol{u}$ is the displacement vector, F_τ are the expansion functions and $\boldsymbol{u}_\tau$ is the vector of the generalized unknowns. The repeated subscript τ denotes summation and M is the total number of expansion terms assumed for the kinematic field.

Recalling the finite element method, the thickness direction is discretized by means of standard 1D elements, as shown in Fig. 1 (a). Accordingly, the generalized unknowns, $\boldsymbol{u}_\tau$, are interpolated over *y* via Lagrange polynomials:

$$\boldsymbol{u}_\tau(y) = N_i(y)\,\boldsymbol{u}_{\tau i}(t) \quad i = 1,2,...,n \tag{2}$$

where $\boldsymbol{u}_{\tau i}(t)$ is the nodal unknown vector and n is the total number of beam nodes.

3 DISPERSION RELATIONS

In the current modeling framework, the application of the Bloch's boundary conditions is performed over the section degrees of freedom located at the edges of the plate, Ω_{xi} and Ω_{zi} (see Fig. 1). In this manner:

$$\boldsymbol{u}_{\tau i}^{\Omega_{x1}} = \boldsymbol{u}_{\tau i}^{\Omega_{x2}}\, e^{-j\boldsymbol{k}} \tag{3}$$

$$\boldsymbol{u}_{\tau i}^{\Omega_{z1}} = \boldsymbol{u}_{\tau i}^{\Omega_{z2}}\, e^{-j\boldsymbol{k}} \tag{4}$$

where j is the complex operator and $\boldsymbol{k}$ is the reduced wave vector. Grouping all the slave unknowns into a single global vector $\boldsymbol{v}$, one can write:

$$\boldsymbol{u} = \mathbf{W}\boldsymbol{v} \tag{5}$$

where the $\mathbf{W}$ matrix contains all the Bloch relations. Finally, the eigenvalue problem can be defined as:

$$(-\omega\mathbf{W}^H\mathbf{M}\mathbf{W} + \mathbf{W}^H\mathbf{K}\mathbf{W})\boldsymbol{v} = \mathbf{0} \tag{6}$$

where $\mathbf{M}$ and $\mathbf{K}$ are the global mass and stiffness matrices, respectively. The upper-script H denotes Hermitian transpose. Note that the wave vector variation is imposed though the matrix operator $\mathbf{W}$.

4 RESULTS

The benchmark example of the periodic stubbed surface [5] is used here for the assessment of the model. The structure under study is composed of a 1 mm thick aluminum plate with a periodical array of cylinders on the top. The height of the cylinder is taken here as 5 mm. The in-plane dimensions of the unit cell are 10 mm $\times$ 10 mm. Figure 2 shows the dispersion curves over the first Brillouin zone, which is marked in red in Fig. 1 (b). It can be observed that several complete band gaps open in the range between 0 and 250 kHz. The widest one is located around 170 kHz, which is in good agreement with the literature. A second study is carried out to confirm numerically these findings, which consists on the frequency response analysis of a finite strip of the metasurface, see Fig. 3. Reasonable similarity is found. The local resonance nature of the wide band gap is demonstrated by observing the modes in that frequency range.

5 CONCLUDING REMARKS

The present paper proposes the use of refined beam elements for the computation of the dispersion relations and transmission coefficient in periodic metamaterials. The Carrera unified formulation is employed to generate non-local beam models which can accurately simulate the Bloch's boundary conditions. The model presents certain advantages in terms of modeling time and computational costs in comparison to 3D finite elements, which are traditionally employed for this application. The results show a good agreement with the solutions found in the literature for the benchmark problem under study.

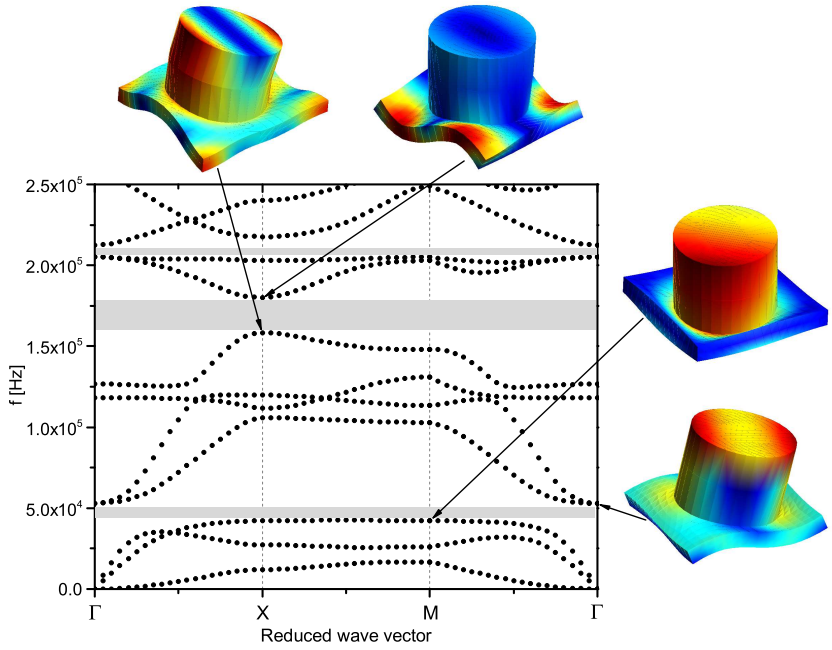

Figure 2: Dispersion curves of the periodic structure. The grey areas correspond to complete band gaps. The modes calculated at the edge frequencies of the first and second band gaps are shown.

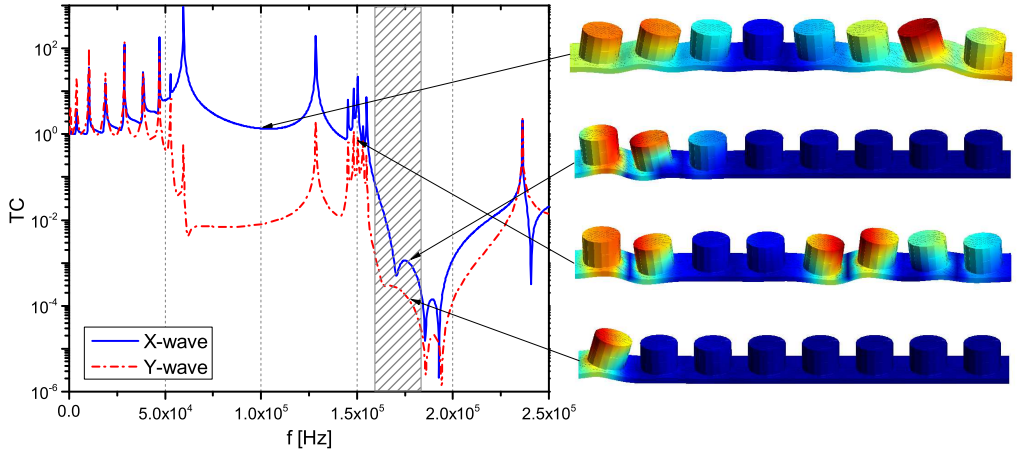

Figure 3: Transmission coefficient computed in a finite strip the stubbed plate for X and Z-polarized waves. The shaded area corresponds to the main band gap found in the dispersion curves. The images on the right-hand side show various relevant modes computed at different frequencies.

REFERENCES

[1] L. Brillouin. *Wave propagation in periodic structures*. Dover, second edition, 1953.

[2] M. I. Hussein, M. J. Leamy, and M. Ruzzene. Dynamics of Phononic Materials and Structures: Historical Origins, Recent Progress, and Future Outlook. *Applied Mechanics Reviews*, 66(4), 05 2014. 040802.

[3] P. Langlet, A.-C. Hladky-Hennion, and J.-N. Decarpigny. Analysis of the propagation of plane acoustic waves in passive periodic materials using the finite element method. *The Journal of the Acoustical Society of America*, 98(5):2792–2800, 1995.

[4] E. Carrera, M. Cinefra, M. Petrolo, and E. Zappino. *Finite Element Analysis of Structures through Unified Formulation*. John Wiley & Sons, Chichester, West Sussex, UK, 2014.

[5] T.-T. Wu, Z.-G. Huang, T.-C. Tsai, and T.-C. Wu. Evidence of complete band gap and resonances in a plate with periodic stubbed surface. *Applied Physics Letters*, 93(11):111902, 2008.

A CONVOLUTION BASED WAVENUMBER EXTRACTION METHOD

R.F. Boukadia[1,3,4] , E. Deckers [2,3] , C. Claeys[1,3] , M. Ichchou[4] and W. Desmet[1,3]

[1]KU Leuven, Department of Mechanical Engineering, Division LMSD
Celestijnenlaan 300 - box 2420, Heverlee, Belgium
Email: regis.boukadia@kuleuven.be, wim.desmet@kuleuven.be

[2]KU Leuven, Diepenbeek Campus, Mechanical Engineering Technology TC
Wetenschapspark 27, 3590 Diepenbeek, Belgium
Email: elke.deckers@kuleuven.be

[3]DMMS lab, Flanders Make

[4]Ecole Centrale de Lyon
36 Avenue Guy de Collongue, 69134 Ecully Cedex, France
Email: mohamed.ichchou@ec-lyon.fr

ABSTRACT

This paper presents a wavenumber extraction method for 1D and 2D wave propagation in periodic structures. In its simplest form, the method can be considered an inverse WFEM as it leverages spatially periodic measurements of the displacement field to build a convolution kernel that zeroes it out. This kernel is obtained by solving an inverse problem that encodes wavenumbers and K-Space information. The proposed class of algorithms achieves state of the art accuracy in the 1D case and extends what was feasible in the 2D case. Experimental results are presented for the 1D case while 2D propagation is only studied numerically.

1 INTRODUCTION

Structural identification and characterisation have become crucial issues at the core of engineering applications such as non-destructive testing, damage detection and structural health monitoring. Currently, many methods are able to tackle these problems in the low frequency domain. FRF based model updating [1, 2] schemes, and modal identification methods [3, 4] are some of the most successful. However, these methods become inappropriate in the mid and high frequency domains as uncertainty on boundary conditions and spacial variability of material properties have large effects on the displacement field. To tackle these issues, inverse methods assessing local wave propagation properties have been developed. In 2000, McDaniel et al. developed a method [5] based on non linear least-square optimization that enables wavenumber retrieval in 1D homogeneous structures. The method was subsequently applied to the identification of frequency dependent material properties by assuming an Euler-Bernoulli wave propagation model [6]. In 2005, The Inhomogeneous Wave Correlation (IWC) was developed by Berthaut et al. [7] enabling wavenumber identification in the 2D case. However, because it is based on the plane wave approximation, the method is only exact when that approximation is valid. In 2011, the Inverse Wave Decomposition (IWD) was developed by Chardon et al. [8]. It goes beyond the plane wave approximation by considering the displacement field as a superposition of plane waves with different propagation angles. The method is theoretically exact in the absence of sources but involves solving high dimensional non linear least square problems. As the dimension of the problem is proportional to the number of propagation angles needed to reconstruct the wavefield, the method become impractical in the targeted frequency range. This paper presents a convolution based wavenumber extraction methodology that achieves comparable performance to the IWD but only requires linear least square optimization with few parameters. This is achieved by placing a periodicity constraint on the array of measurements of the displacement field.

2 METHOD

The roots of the method can be understood starting from the equations of the direct form of the 1D Wave Finite Element Method [9] recalled in equation (1):

$$\left(\lambda D_{LR} + (D_{LL} + D_{RR}) + \frac{1}{\lambda} D_{RL}\right) \psi = 0 \tag{1}$$

Equation (1), once developed, can be understood as a convolution product between a geometric sequence of vectors and a three-term long sequence of matrix coefficients resulting in a null sequence of vectors. Usually, the matrix coefficients are known and the propagation constants λ_i and waveshapes ψ_i are determined using an eigenvalue solver. In the proposed method, the problem is reversed and the measured displacement field is used to partially reconstruct the matrix coefficients D_{LR}, $(D_{LL} + D_{RR})$ and D_{RL} via a linear least square problem. Once this is done, equation (1) can be solved again yielding the propagation constants λ_i. The same reasoning is straightforwardly applied to 2D wave propagation starting from the equations of the 2D WFEM.

3 RESULTS

First, the 1D version of the method is compared to McDaniel's method [5] on an experimental case. An aluminum beam treated with a constrained viscoelastic layer is considered. It is exited with a shaker and the displacement field is measured by a laser vibrometer. The set up is presented in Figure 1 and the experimental dispersion curves in Figure 2. The method successfully captures the real part of the wavenumber and even outperforms McDaniel's method at low frequency. The evaluation of the imaginary part comes with more variance compared to McDaniel's method though it is similar for both methods. This is to be expected as the former evaluates each frequency independently while the latter uses numerical continuation to ensure local minima obtained for adjacent frequencies are as close as possible. Lastly, the 2D version of the proposed method is applied to 2D wave propagation on a plate modeled using a FEM package with the aim of testing its ability to deal with directivty in a 2D wave propagation scenario. The results obtained, presented in Figure 3, show that the method can indeed recover all wave propagation features (including K-Space) in this noiseless case.

Figure 1: Experimental setup.

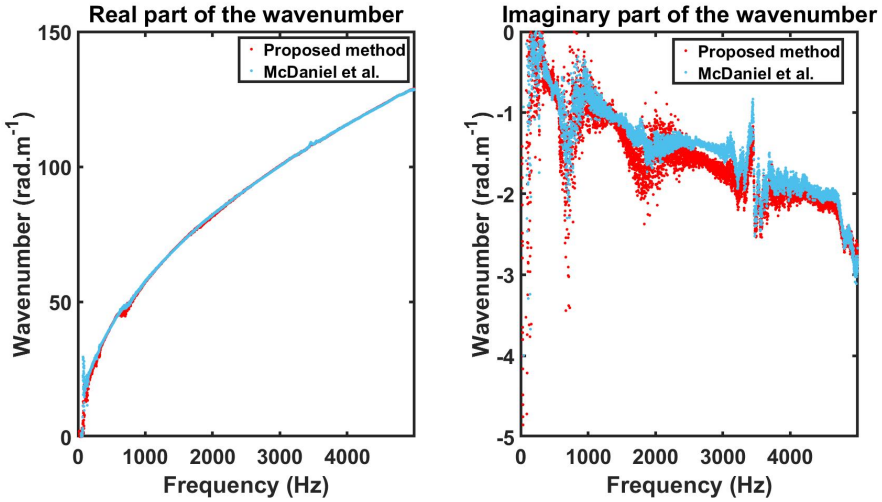

Figure 2: Experimental dispersion curves obtained with the proposed method (red dots) and McDaniel's method (light blue dots)

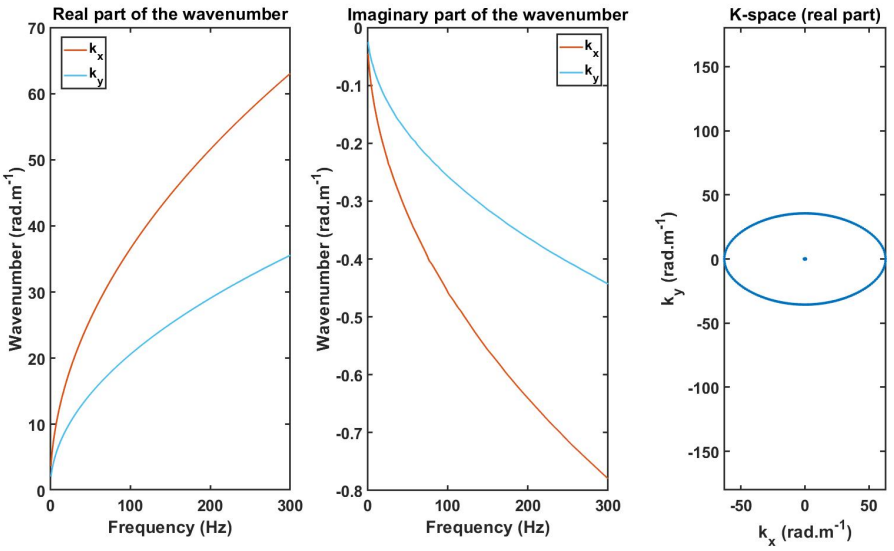

Figure 3: Dispersion curve and K-Space obtained using the proposed methodology on a numerical model.

4 CONCLUSION

A methodology for 1D and 2D wavenumber extraction was presented. Good experimental results were obtained in the 1D case while those obtained in the 2D case are promising. The method has yet to be applied experimentally in the 2D case. Also, its sensitivity to noise remains to be studied and tested.

ACKNOWLEDGEMENTS

The research of R. F. Boukadia is funded by an Early Stage Researcher grant within the European Project VIPER Marie Curie Initial Training Network (GA 675441). The research of E. Deckers is funded by a grant from the Research Foundation - Flanders (FWO). This research was partially supported by the ICON project DETECT-ION, which fits in the MacroModelMat(M3) research program, coordinated by Siemens (Siemens PLM software, Belgium) and funded by SIM (Strategic Initiative Materials in Flanders) and VLAIO (Flanders Innovation & Entrepreneurship Agency).

REFERENCES

[1] Axel van de Walle, Lucie Rouleau, Elke Deckers, and Wim Desmet. Parametric model-order reduction for viscoelastic finite element models: an application to material parameter identification. In *Proceedings of the 22nd International Congress on Sound and Vibration*. INT INST ACOUSTICS & VIBRATION, 2015.

[2] Sjoerd van Ophem, Axel van de Walle, Elke Deckers, and Wim Desmet. Efficient vibro-acoustic model updating of localized properties using low-rank parametric model order reduction schemes, 2017.

[3] Wilson Torres, Jos Luis Almazn, Cristin Sandoval, and Rubn Boroschek. Operational modal analysis and fe model updating of the metropolitan cathedral of santiago, chile. *Engineering Structures*, 143:169 – 188, 2017.

[4] Jess N. Eiras, Cdric Payan, Sandrine Rakotonarivo, and Vincent Garnier. Experimental modal analysis and finite element model updating for structural health monitoring of reinforced concrete radioactive waste packages. *Construction and Building Materials*, 180:531 – 543, 2018.

[5] J. G. McDaniel, P. Dupont, and L. Salvino. A wave approach to estimating frequency-dependent damping under transient loading. *Journal of Sound and Vibration*, 231(2):433–449, 2000.

[6] J. Gregory McDaniel and W. Steve Shepard. Estimation of structural wave numbers from spatially sparse response measurements. *The Journal of the Acoustical Society of America*, 108(4):1674–1682, 2002.

[7] J. Berthaut, M. N. Ichchou, and L. Jezequel. K-space identification of apparent structural behaviour. *Journal of Sound and Vibration*, 280(3-5):1125–1131, 2005.

[8] G. Chardon, A. Leblanc, and L. Daudet. Plate impulse response spatial interpolation with sub-Nyquist sampling. *Journal of Sound and Vibration*, 330(23):5678–5689, 2011.

[9] D.J. Mead. A general theory of harmonic wave propagation in linear periodic systems with multiple coupling. *Journal of Sound and Vibration*, 27(2):235 – 260, 1973.

PASSIVE VIBRATION CONTROL OF TYRES USING EMBEDDED MECHANICAL RESONATORS

F. Errico[1,2*], G. Petrone[2], F. Franco[2], S. De Rosa[2] and M. Ichchou[1]

[1]Laboratoire de Tribologie et Dynamique des Systems, Ecole Centrale de Lyon
36 Avenue Guy de Collongue, 69134, Ecully, France
Email: fabrizio.errico@ec-lyon.fr; mohamed.ichchou@ec-lyon.fr; olivier.bareille@ec-lyon.fr

[2]Department of Industrial Engineering, University of Naples Federico II
Via Claudio 21, 80125, Napoli, Italy
Email: francesco.franco@unina.it; sergio.derosa@unina.it; giuseppe.petrone@unina.it

ABSTRACT

An investigation is carried out on structure-borne vibration and noise propagation of tyres' models at low frequencies. The idea is to use embedded resonant meta-materials to damp the tyres' vibrations and thus reduce the transferred energy to the main attached structures. A simplified tyre model is used, being the investigation of the effects of the embedded substructures the main target of the work; internal pressure and tyre rotation effects are neglected at this stage. Different configurations are tested targeting different natural modes of the tyre, while mechanical excitation is assumed on one section of the tyres. The results show how the proposed designs are a feasible solution for vibration control.

1 INTRODUCTION

Tyre noise and vibrations are becoming some key comfort parameters in the automotive industry, even before 40 km/h [1, 2], because of the advent of hybrid and electric power-units [3]. In fact, the broadband noise distribution coming from an ICE (Internal Combustion Engine) is replaced by a generally high-frequency tonal whistling, which allows other noise sources, as tyre/road noise, to become dominant in other frequency ranges. Among these, the tyre noise, is dominant both in terms of structure-borne and air-borne propagations, respectively before and after 500Hz [4–6]. The structure-borne contributions derive mainly from the first natural modes of the tyre while the air-bone ones are mainly due to higher frequency circumferential modes of the tyre [6–9]. Modelling techniques based on finite elements (FEM) are often limited to low frequencies due to a high computational cost [6, 7]; wave-based approaches are also efficient to investigate the wave propagation in the tyre [10].

2 PROPOSED DESIGN

To investigate the effect of embedded resonant substructures on tyre vibrations, the configuration in Fig. 1b is proposed.

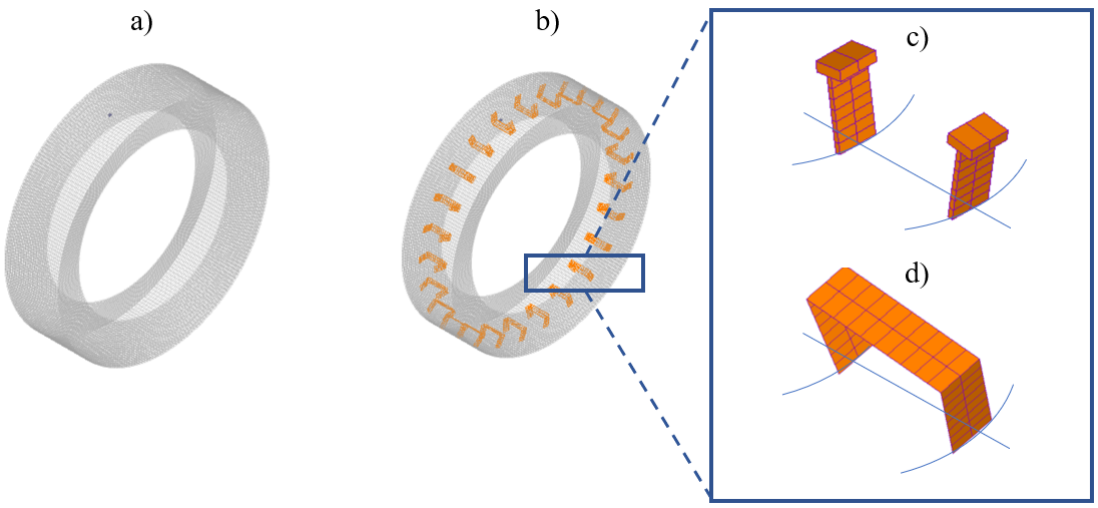

Figure 1: Simplified tyre model with shell elements. Tyre Configuration: a) Bare; b) Resonant. Target: c) Transversal Vibrations; d) Radial Vibrations.

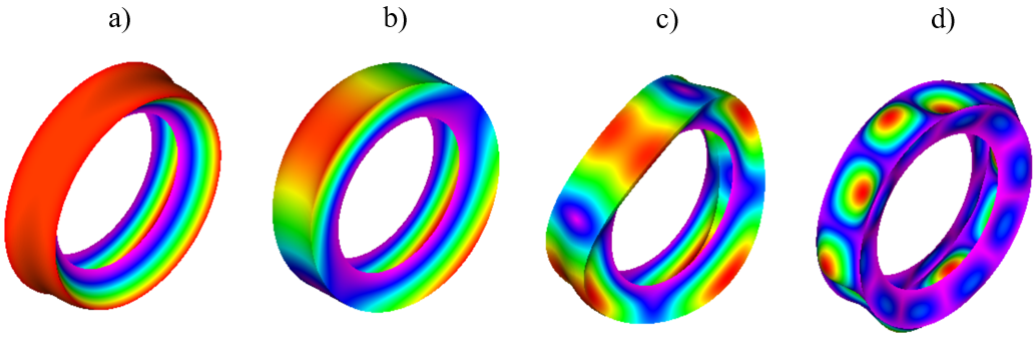

Figure 2: First four modes of the bare tyre. Transversal Modes: a) 243.6 Hz; b) 338.5 Hz; c) 610.6 Hz. Radial Mode: d) 702.4 Hz.

First, it is fundamental to know the frequencies or frequency bands to target with the embedded substructures. The transversal modes appear in lower band with respect to the mainly radial ones and thus the resonant configurations will be tuned depending on the needs. A modal analysis is conducted on the bare tyre configuration using NX NASTRAN shell elements (CQUAD4) and using more than 20 elements per wavelength at 2KHz. The first four modes of the structure at illustrated in Fig. 2. The material properties used are: E = 19.8 GPa, ν = 0.32 and ρ = 1850 Kg/m^3.

The targets of this work will be the first two modes in Fig. 2, for the transversal vibrations, and the fourth mode (and higher orders) in Fig. 2, for the radial vibrations. For this reason, when targeting the transversal motion of the tyre, the concept in Fig. 1c is used, while the one in Fig. 1d is employed when the radial motion of the tyre is targeted too. In the case of Fig. 1c, the first vibration modes of the embedded beams, which are classic cantilever-beam modes, are in the same direction of the transversal tyre motion. In the case of Fig. 1d, the resonator behanves as a bridge structure with two main vibration modes in the transversal direction (cantilever-beam modes of the pylon) and radial direction (simply-supported beam mode of the deck). The idea is to create resonance-induced band-gaps around the targeted tyre modes, in order to control vibrations in that region.

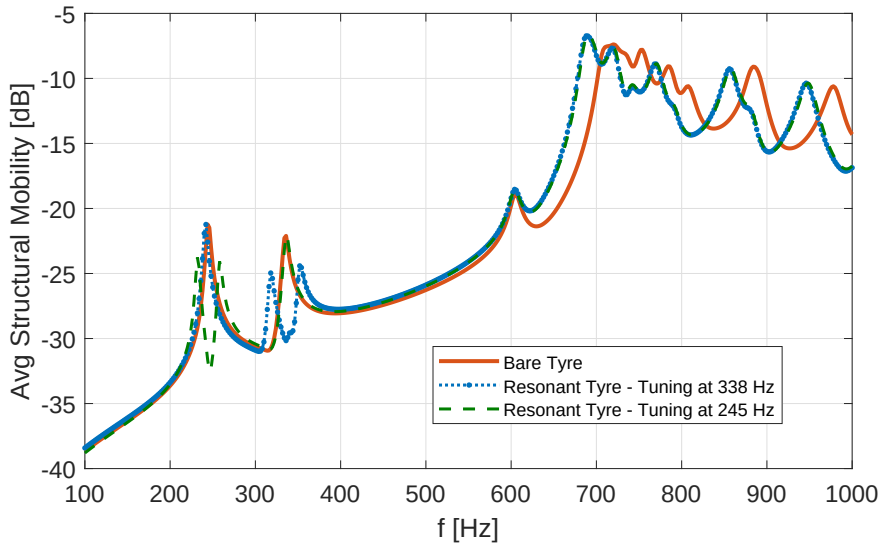

Figure 3: Average structural mobility of the tyre with and w/o mechanical resonators for transversal vibration control.

2.1 Force vibrations of resonant configurations

A set of forces normal to the tyres' plane, in order to simulate a mechanical road input, are used as white noise load. The response of the tyre is numerically calculated in a set of ten random point around the tyre and plotted in Figs. 3 and 4. Only structural damping is considered and the effect of pressure and tyre rotation is neglected.

In Fig. 3, the resonant configuration illustrated in Fig. 2c is tuned once on the first and once on the second transversal mode of the tyre. Two circumferential rows of 10 resonant elements are considered in both cases. The results show how the modal peaks in the response are strongly reduced, even if anti-resonances of the beams appear close to the modal frequencies, increasing the vibrations compared to the bare configuration. The effects, for both tuning conditions, are identical. No coupling between the tyre and the beam motion is observed and the resonators behave as classic TVAs (Tuned Vibration Absorbers) with avery narrow band effect.

In Fig. 4, the resonant configuration illustrated in Fig. 2d is tuned on the first purely radial mode of the tyre at $\approx$ 703 Hz and targets also the transversal vibration of the tyre at $\approx$ 330 Hz. A single circumferential row of 25 and then 5 resonant elements are considered, with added masses of $\approx$ 20% and $\approx$ 3% respectively. The average vibrations of the tyre in Fig. 4 show some main effects. First, the appearance of band-gaps around the targeted frequency bands with the second transversal mode of the tyre ($\approx$ 330 Hz) always well damped. In the configuration with five circumferential resonators, the band-gap opens also around the 600-750 Hz band, allowing a decrease of vibration levels of 15dBs. On the other hand, the same effect is not achieved when more resonators are added, since a strong coupling with the tyre dynamics is present, probably given by the excessive added mass. For this reason, there is a frequency shift to lower frequencies and vibrations are increased in the 400-500 Hz frequency band.

3 CONCLUDING REMARKS

The effects of embedded mechanical resonators in a tyre compound is analysed in terms of forced vibrations on a simplified tyre model. Two main configurations are analysed in order to target two main regions of tyre dynamics, strongly related to the structure-borne and air-borne issues respectively. Numerical simulations are carried out using a FEM approach and average vibrations on random tyre points are computed. The resonant substructures are observed to be very efficient when targeting the transversal motion of the tyre, while higher order coupling between the resonators and the tyre dynamics appears when targeting radial vibrations. The latter effect can be investigated with a detailed modelling of the tyre.

Further investigations could target the efficiency of the resonant configurations as a function of the resonators' shape and added mass.

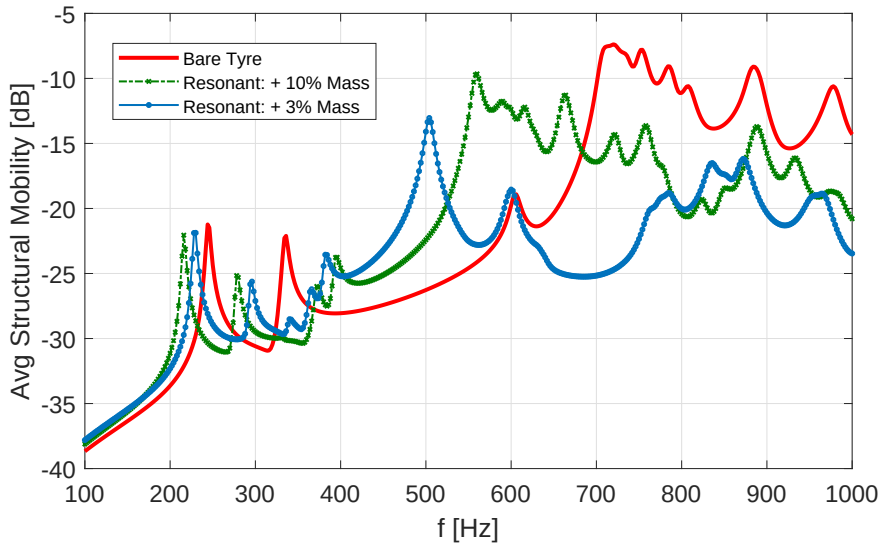

Figure 4: Average structural mobility of the tyre with and w/o mechanical resonators for radial vibration control.

Acknowledgments

This project has received funding from the European Unions Horizon 2020 research and innovation programme under the Marie Sklodowska-Curie grant agreement No. 675441.

REFERENCES

[1] Ulf Sandberg and Jerzy Ejsmont. Tyre/road noise. reference book. 2002.

[2] W. Kropp. Structure-borne sound on a smooth tyre. *Applied Acoustics*, 26(3):181 – 192, 1989.

[3] Martin Czuka, Marie Agns Pallas, Phil Morgan, and Marco Conter. Impact of potential and dedicated tyres of electric vehicles on the tyre-road noise and connection to the eu noise label. *Transportation Research Procedia*, 14:2678 – 2687, 2016. Transport Research Arena TRA2016.

[4] Y.-J Kim and J.S Bolton. Effects of rotation on the dynamics of a circular cylindrical shell with application to tire vibration. *Journal of Sound and Vibration*, 275(3):605 – 621, 2004.

[5] P. Kindt, P. Sas, and W. Desmet. Measurement and analysis of rolling tire vibrations. *Optics and Lasers in Engineering*, 47(3):443 – 453, 2009. Optical Measurements.

[6] Maik Brinkmeier, Udo Nackenhorst, Steffen Petersen, and Otto von Estorff. A finite element approach for the simulation of tire rolling noise. *Journal of Sound and Vibration*, 309(1):20 – 39, 2008.

[7] J.R. Cho, K.W. Kim, and H.S. Jeong. Numerical investigation of tire standing wave using 3-d patterned tire model. *Journal of Sound and Vibration*, 305(4):795 – 807, 2007.

[8] R.J. Pinnington. A wave model of a circular tyre. part 1: belt modelling. *Journal of Sound and Vibration*, 290(1):101 – 132, 2006.

[9] Michelin Grip. The tyre. 2001.

[10] Y. Waki, B.R. Mace, and M.J. Brennan. Free and forced vibrations of a tyre using a wave/finite element approach. *Journal of Sound and Vibration*, 323(3):737 – 756, 2009.

NON-LOCAL BOUNDARY CONTROL FOR BROADBAND NON-RECIPROCAL PROPAGATION: ANALYTICAL DEMONSTRATION AND EXPERIMENTAL VALIDATION

E. De Bono[1] , M. Collet[1*], S. Karkar[1*], G. Matten[2] and M. Ouisse[2]

[1]Laboratoire de tribologie et dynamique des systèmes (LTDS)
École Centrale de Lyon – CNRS UMR5513, 36 avenue Guy de Collongue, 69134 Ecully Cedex (France)
Email: emanuele.de-bono@ec-lyon.fr

[2]FEMTO-ST Institute, Department of Applied Mechanics, CNRS/UFC/ENSMM/UTBM
University of Bourgogne Franche-Comté, 24 Chemin de l'Épitaphe, 25000 Besançon, France

ABSTRACT

The semi-active impedance control techniques can offer new perspectives for acoustic treatment in the nacelle inlet of the new generation of Ultra-High-By-Pass-Ratio turbofan engines. In this contribution we present a non-local boundary condition capable of achieving broadband non-reciprocal propagation in a waveguide, envisaging the possibility of energy harvesting, other than acoustic transmission attenuation. The non-local boundary control concept is first illustrated analytically, and then it is implemented experimentally through a liner of electroacoustic devices.

1 INTRODUCTION

The new generation of ultra-high-by-pass-ratio (UHBPR) turbofan engines have a reduced number of blades with lower rotational speeds, this shifts the noise signature toward the lower frequencies. In addition, they present reduced space for the acoustic treatment of the internal walls of the nacelle. These new requirements and constraints must be accomplished by a new generation of liners. The main working principle of the classical Single/Multi Degree-of-Freedom liners is the quarter-wavelength resonance, which limits their performances to narrow frequency bandwidths and make them cumbersome for low-frequency targeting.
The Active Noise Cancellation (ANC) in the feedback configuration, from the "electronic sound absorber" of Olson and May [1] to the "active equivalent of the $\lambda/4$ resonator" of Guicking and Lorentz [2], further developed by Galland et al. [3], produced interesting results, but can hardly comply with the complexities of airflow noise cancellation in a UHBPR nacelle, and the problem of broadband attenuation was still unsolved. The quasi-colocation of pressure sensor and actuator has lead to another approach to the noise attenuation, that is the impedance control strategy. Boulandet et al. [4] analyzed numerically and experimentally the potentiality of the impedance control achieved through the adjustement of the loudspeaker membrane velocity, based upon the pressure measurement and a model of the loudspeaker mechanical dynamics. The main result was the possibility to tune, relatively easily, the resonance frequency of the loudspeaker and target lower frequencies. In 2009, Collet et al. [5] proposed a "generalized" impedance control approach, where the actuator velocity was function not only of the local pressure, but also of the pressure gradient along the longitudinal direction of the duct. In this contribution, we take up the same non-local boundary control as in [5] and analytically and experimentally show the non-reciprocal acoustic propagation effect. Apart from being a hot topic in metamaterials field of research, acoustic non-reciprocity can be highly attractive in view of acoustic energy harvesting and broadband noise mitigation.

2 ANALYTICAL ANALYSIS ON A 1D REDUCED MODEL

The non-local boundary condition proposed in [5] is:

$$\rho_0 \partial_t v_n = -\partial_n p = \frac{1}{c_a}\partial_t p - \partial_x p \tag{1}$$

where v_n is the velocity normal to the boundary and c_a is an advection celerity, used as a tunable parameter of the control. In order to analytically show how this boundary law is capable of producing non-reciprocal acoustic propagation, we reduce the waveguide problem to one dimension. Integrating the wave equation over the cross-section of the waveguide, and applying the divergence theorem to the integral of the y and z double derivatives (y and z being the dimensions along the cross section), we get:
$\forall t \in \mathbb{R}, \quad x \in \mathbb{R},$

$$\frac{1}{c_0^2}\partial_{tt}\tilde{p}(x,t) - \partial_{xx}\tilde{p}(x,t) = \frac{1}{S}\oint_{\partial\Omega} \partial_n p(x,s,t) ds \tag{2}$$

where $\tilde{p}(x,t)=\frac{1}{S}\iint_\Omega p(x,y,z,t)dydz$ is the mean acoustic pressure over the section Ω, s is a curvilinear coordinate along the boundary $\partial\Omega$, and ∂_n is the gradient along the outward direction.

Inserting the boundary control law, expressed in Equation (1), in the right-hand side in Equation (2), it reads:

$$\frac{1}{c_0^2}\partial_{tt}\tilde{p}(x,t) - \partial_{xx}\tilde{p}(x,t) = -\frac{1}{d}\left(\frac{1}{c_a}\partial_t p_b(x,t) - \partial_x p_b(x,t)\right). \tag{3}$$

Where $p_b(x,t)=\frac{1}{L_p}\oint_{\partial\Omega} p(x,s)ds$ is the mean acoustic pressure field along the boundary contour, and $d = S/L_p$ is the ratio between the cross-section area and perimeter of the waveguide.

2.1 Dispersion relation

We now suppose monomodal acoustic propagation in this waveguide, and drop the tilda above p and assimilate p_b and p. Assuming a time-harmonic wave propagation with angular frequency ω

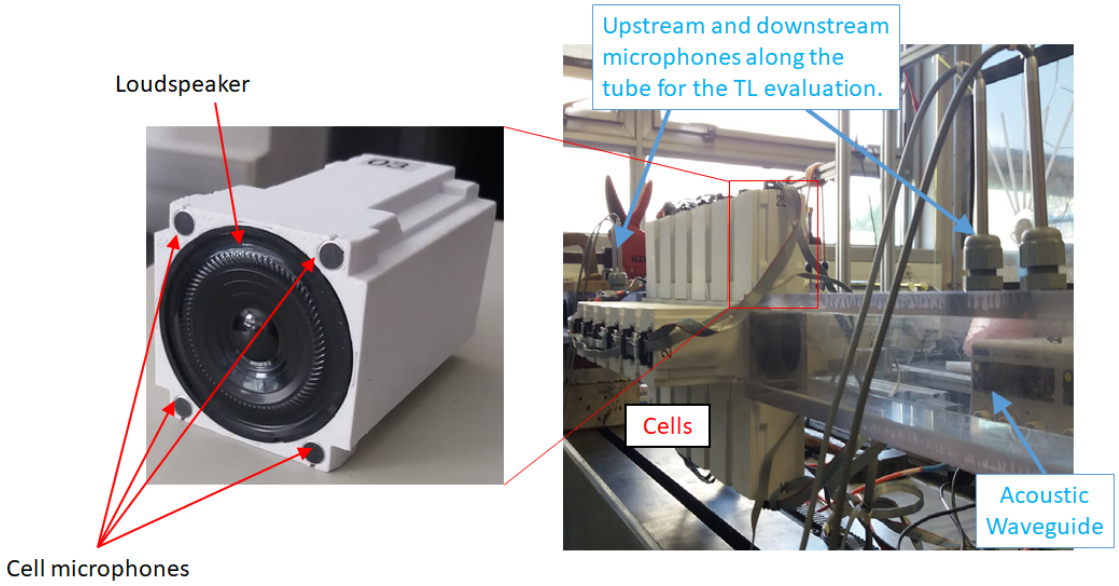

Figure 1: Left: Unit cell. Right: Prespective of the lined waveguide, with upstream and downstream microphones for the TL evaluation through the transfer matrix method.

and wavenumber k, we now seek solutions of the form:

$$p(x,t) = p_0 e^{j(\omega t - kx)}. \tag{4}$$

Inserting this ansatz in the propagation Equation (3), comes:

$$(j\omega/c_0)^2 - (jk)^2 = -\frac{1}{d}(j\omega/c_a + jk). \tag{5}$$

In the special case where $c_a = c_0 = c$ (that is the advection celerity is in tune with the sound speed), Equation (5) has two solutions: either $k^{(-)} = -\omega/c$, or $k^{(+)} = \omega/c - j/d$. The first solution corresponds to waves with purely real and negative wave numbers. The group velocity is negative, and equal to the phase velocity: this type of wave is propagating in the (-) direction (”backward waves”). Given the purely real wavenumber, they pass through the isolator without attenuation. The second solution corresponds to waves with $\mathcal{R}\mathrm{e}(k) > 0$ that propagate in the (+) direction (”forward waves”), given their positive group velocity, but with an exponential attenuation. It is equivalent to an evanescent guided mode, just like a waveguide higher mode under its cut-on frequency. Therefore, the 1D reduced model of the non-locally boundary controlled waveguide, shows the non-reciprocal relationship between forward and backward propagation.

3 EXPERIMENTAL IMPLEMENTATION

We now present the experimental results of an application of this boundary control strategy on a test-bench waveguide of square cross section of 5.5cm side (see Figure 1 on the right), lined with actively controlled devices which were capable of reproducing the boundary control law expressed in Equation (1). Evidently, the boundary control law has been discretized in order to be applied through units of electrodynamic devices. Each unit cell consisted of a loudspeaker (actuator) and four microphones (sensors) placed at the cell corners, see Figure 1 on the left. Six cells have been applied on each side of the duct, amounting to 24 cells in total.

3.1 Results

The insertion losses (IL) are plotted in Figure 2 (on the right), for incident waves coming from both directions. It has been evaluated according to the ASTM E2611-09 standard (single-load transfer matrix method). The synthesized algorithm for the implementation of the control law was able to invert the dynamics of the loudspeaker after its first resonance which is between 500 and 550

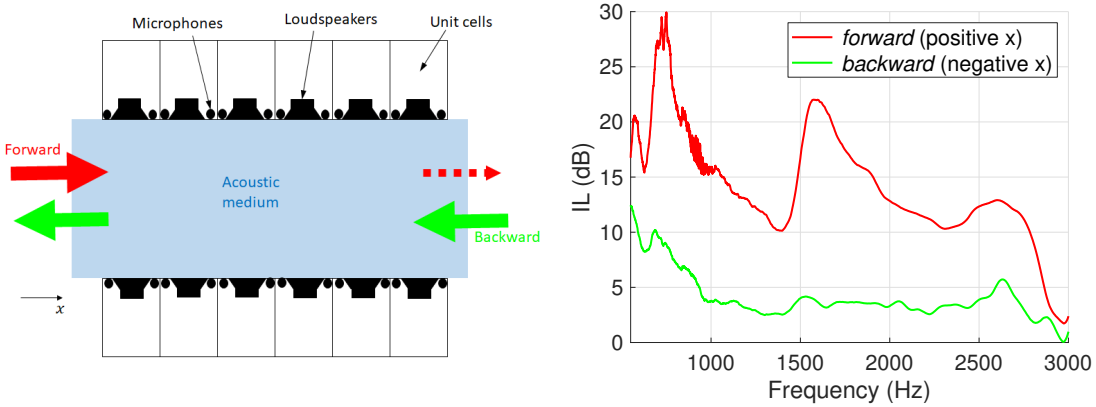

Figure 2: Left: 2D sketch of the lined waveguide. Right: Insertion Loss measurements relative to incident waves directed towards the positive x (*forward*), and towards the negative x (*backward*).

Hz for all loudspeakers, that is why the plot is limited to frequencies beyond 550 Hz. The higher frequency limit (3 kHz) corresponds to the cut-on of the first higher-order duct mode, beyond which the plane wave assumption for the TL evaluation is not valid anymore. Both the ILs relative to the *forward* and *backward* direction of propagation vary significantly with frequency. This is due to the modal behaviour of the speaker membrane and the limits of the synthesized control to invert the loudspeaker proper dynamics. As a consequence, the acoustic isolation (described by the Isolation Index, $IS = 20\log_{10}(|S_{12}/S_{21}|)$) is achieved with a variable amplitude: from maxima of 20 dB to minima of 8 dB, from 550 Hz up to 2800 Hz. The loss of efficiency above 2800 Hz is likely to be mainly caused by the spacing between the microphones, which is close to half the acoustic wavelength, thus causing aliasing effect in the pressure evaluation.

4 CONCLUSIONS

In this contribution we analyzed a non-local boundary condition. This boundary law has been implemented through semi-active electroacoustic prototypes, on a test-bench waveguide. Despite some limitations due to the practical implementation of the control strategy at its early stage design, it demonstrates the capability of achieving non-reciprocal acoustic propagation in a much broader sense with respect to all other present techniques.

REFERENCES

[1] Harry F Olson and Everett G May. Electronic sound absorber. *The Journal of the Acoustical Society of America*, 25(6):1130–1136, 1953.

[2] D Guicking and E Lorenz. An active sound absorber with porous plate. *Journal of vibration, acoustics, stress, and reliability in design*, 106(3):389–392, 1984.

[3] Marie-Annick Galland, Benoit Mazeaud, and Nadine Sellen. Hybrid passive/active absorbers for flow ducts. *Applied acoustics*, 66(6):691–708, 2005.

[4] R Boulandet, H Lissek, S Karkar, M Collet, G Matten, M Ouisse, and M Versaevel. Duct modes damping through an adjustable electroacoustic liner under grazing incidence. *Journal of Sound and Vibration*, 426:19–33, 2018.

[5] Manuel Collet, Petr David, and Marc Berthillier. Active acoustical impedance using distributed electrodynamical transducers. *The Journal of the Acoustical Society of America*, 125(2):882–894, 2009.

FULLY COUPLED VIBRO-ACOUSTIC ANALYSIS OF MULTI-LAYERED PLATES BY CUF FINITE ELEMENTS

M. Cinefra[1] , E. Zappino[1*] , E. Carrera[1*] and S. De Rosa[2]

[1]Department of Mechanical and Aerospace Engineering
Politecnico di Torino, Torino, ITALY
Email: maria.cinefra@polito.it, enrico.zappino@polito.it, erasmo.carrera@polito.it

[2]Department of Industrial Engineering
Università degli Studi di Napoli Federico II, Napoli, ITALY
Email: sergio.derosa@unina.it

ABSTRACT

The interaction between plate-like structures made of advanced materials (e.g. composite) and enclosed fluid-filled cavities represents a significant issue in automobile and aerospace design, where passengers comfort is an important issue. Over the last thirty years, a large amount of work has been published addressing the vibratory characteristic of structure-cavity systems and, thanks to this reaserch, the problems connected to the reduction of noise at low frequencies is well known. Neverthless, there is a lack of reliable and useful numerical models, valid for innovative materials, able to predict the structural response in low-frequency range. The objective of the present work is the development of accurate finite element models for the fully coupled vibro-acoustic analysis of structures made of advanced materials, coupled with enclosed acoustic cavities. In the framework of the axiomatic 2D theories, the structure is described according to the Carrera Unified Formulation (CUF). The powerful notation of this unified approach permits to obtain a wide class of refined 2D plate theories with a unique formulation, providing an optimal tool to arbitrarily describe the complicated effects arising from complex plate layouts at both low and higher frequency ranges. The resulting structural finite element model is coupled with a standard pressure-based finite element formulation of the acoustic field. Numerical results are presented for the case of plate backed by an air-filled and water-filled cavity. Different plate layouts are considered and the results are compared with the solutions obtained with Actran, a commercial software based on finite element method.

1 INTRODUCTION

The physics of a structural domain and of an acoustic domain are dependent on each other: the vibrations of the structure induce pressure waves in the fluid in contact with it and the pressure waves that propagate in the fluid cause structural vibrations. In this case, the coupling between the elastic structure and the enclosed acoustic cavity is total. Since the system is strongly coupled, its study must be carried out taking into account the natural frequencies and the dynamic response of the structure. Generally, this type of system is complex to study because of the complex shapes that the structure can assume. The availability of an efficient numerical tool is a fundamental need.
At present, numerical modeling techniques for coupled plate-cavity systems in the low-frequency range are based on deterministic approaches. All the system components are small compared to the wavelength over this range; for this reason, the Finite Element (FE) method is tipically used for computing the system response. An overview of models adopted to solve the problem in sandwich structures is provided in [1]. However, as the excitation frequency increases, it can be observed that the response becomes increasingly sensitive to minor structural modifications, such as material properties or boundary conditions. Such a behavior is associated with the shorter structural wavelengths, resulting in high complex mode shapes. In order to adequately capture the dynamic behavior over this range, an accurate structural model must be adopted.
Classical 2D models clearly reduce the computational effort, but can also introduce significant errors in the prediction of the dynamic response of multilayered composite structures. Then, more accurate 2-D plate theories must be accounted to correctly reproduce the complicated effects arising in these complex structures.

2 GOVERNING EQUATIONS

In this work, the gravity effects are neglected for both acoustic and structural domains. The structural domain Ω_s is represented by a flexible structure and it is in contact with an acoustic cavity that represents the fluid domain Ω_f (Figure 1). The motion of the structural component is described in terms of structural displacements u_i ($i = x, y, z$). The fluid is assumed to be inviscid, homogeneous and irrotational. Thereby, the governing equation of the acoustic fluid is represented by the wave equation, in absence of sound source, expressed in terms of acoustic pressure p.
In order to obtain the finite element formulation for the structural-acoustic problem, the weak form of the differential equations is derived. Let start with the equations related to the structure:

$$\int_{\Omega_s} \delta\epsilon_{ij}\sigma_{ij}\, dV + \int_{\Omega_s} \delta u_i \rho_s \ddot{u}_i dV = \int_{\Gamma_s} \delta u_i f_i ds + \int_{\Gamma_s} \delta u_i p\, n_i ds \tag{1}$$

where ρ_s is the density of the structure; σ_{ij} represents the stress tensor related to the linearized deformation tensor ϵ_{ij}; f_i are the external forces applied to the structure and n_i is the normal boundary vector to the contour Γ_s. This formula is equivalent to the Principal of Virtual Displacement for the mechanical variables including the coupling term with the acoustic field.
On the other side, the weak formulation of the acoustic problem is:

$$\int_{\Omega_f} \delta p_{,i} p_{,i}\, dV + \int_{\Omega_f} \frac{1}{c_f^2} \delta p\, \ddot{p} dV = \int_{\Gamma_f} \delta p \rho_f \ddot{u}_i n_i ds \tag{2}$$

where Γ_f is the boundary of the fluid volume and ρ_f, c_f are the density and the sound speed of the fluid, respectively. This formulation satisfies the Neumann boundary condition applied on the assumed rigid wall of the acoustic domain.
The primary variables of the vibro-acoustic problem are approximated by means of the Carrera Unified Formualtion. This formulation gives the opportunity to derive a class of several 2-D theories starting from the definition of a set of thickness functions F_τ in order to approximate the problem along the thickness z-axis. Assuming the summing convention with repeated index τ, the displacement vector $\boldsymbol{u}(x, y, z, t)$ can be expressed as follows:

$$\boldsymbol{u}(x, y, z, t) = F_\tau(z)\boldsymbol{u}_\tau(x, y, t) \qquad \tau = 0, ..., N. \tag{3}$$

Then applying the finite element method (FEM), it is possible to express the displacements $\boldsymbol{u}_\tau$ and the sound pressure p in terms of nodal displacements $\boldsymbol{U}_{\tau i}^k$ and pressure P_i through appropriate

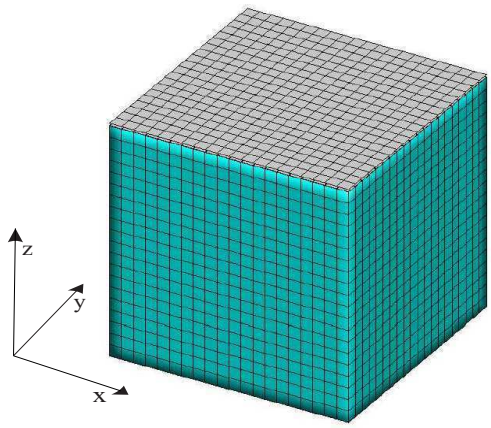

Figure 1: Plate-cavity system.

shape functions N. Thereby, the finite element formulation gives:

$$\boldsymbol{u}_\tau^k(x,y,t) = N_i^s(x,y)\boldsymbol{U}_{\tau i}^k(t), \qquad i = 0, ..., N_n^s \tag{4}$$

$$p(x,y,z,t) = N_i^f(x,y,z)P_i(t) \qquad i = 0, ..., N_n^f \tag{5}$$

with the index N_n^s number of nodes of structure, for structures variables, and N_n^f number of nodes of fluid, for the fluid variables. The apex k indicates the layer of the plate, since a layer-wise approach is adopted [2]. Therefore, the CUF theories are indicated with the acronym LWN, where N is the polynomial order of the Langrangian thickness functions.
Substituting the Equations (3), (4) and (5) in the variational statements (1) and (2), the following finite element formulation of the coupled vibro-acoustic problem is obtained:

$$\begin{bmatrix} \boldsymbol{M_s} & 0 \\ \rho_f \boldsymbol{S^T} & \boldsymbol{M_f} \end{bmatrix} \begin{bmatrix} \ddot{\mathbf{U}} \\ \ddot{\mathbf{P}} \end{bmatrix} + \begin{bmatrix} \boldsymbol{K_s} & \boldsymbol{S} \\ 0 & \boldsymbol{K_f} \end{bmatrix} \begin{bmatrix} \boldsymbol{U} \\ \boldsymbol{P} \end{bmatrix} = \begin{bmatrix} \boldsymbol{F} \\ 0 \end{bmatrix} \tag{6}$$

$\boldsymbol{M_s}$ and $\boldsymbol{K_s}$ are the mass and the stiffness matrices of the structure; $\boldsymbol{M_f}$ and $\boldsymbol{K_f}$ are representative of the mass and stiffness matrices of the fluid; $\boldsymbol{S}$ is the spatial coupling matrix and $\boldsymbol{F}$ is the mechanical force vector. $\boldsymbol{U}$ and $\boldsymbol{P}$ are the vectors and nodal displacements and pressure, respectively.

3 RESULTS

The test structure in Figure 1 is a square simply supported $1 \times 1\, m^2$ plate with thickness $t = 0.01m$, backed by a rigid walled cubic cavity of dimensions $1 \times 1 \times 1\, m^3$. The mechanical properties of the plate structure are: 1) Alluminium: Young's modulus $E = 70GPa$, mass density $\rho_s = 2700Kg/m^3$ and Poisson's ratio $\nu = 0.35$; 2) three-layered composite $[0°, 90°, 0°]$: $E_1 = 25\, GPa$, $E_2 = E_3 = 1\, GPa$, $G_{13} = G_{23} = 0.5\, GPa$, $G_{12} = 0.2\, GPa$ and $\nu_{13} = \nu_{23} = \nu_{12} = 0.25$. The cubic cavity is filled with air (speed of sound $c_f = 343\, m/s$ and density $\rho_f = 1.2Kg/m^3$) or water (speed of sound $c_f = 1500\, m/s$ and density $\rho_f = 1000Kg/m^3$). A constant amplitude mechanical excitation of $1\, N$ over the frequencies of $0 - 300\, Hz$, is applied on the FE structural node denoted by point A, with coordinates $(0.25\, m, 0.35\, m)$. The output is calculated in terms of sound pressure level (SPL) at point B of coordinates $(0.75\, m, 0.75\, m, 0.75\, m)$. A FE mesh of $10 \times 10 \times 10$ quadratic elements is used. The dynamic response analysis is performed with both Actran and the LW2 model of CUF. The comparison of the results is shown in Figure 2 for the alluminium plate with air-filled (a) and water-filled (b) cavity and in Figure 3 for the multi-layered composite plate with air-filled (a) and water-filled (b) cavity.

4 CONCLUDING REMARKS

The results obtained for the allunium-air system validate the model based on CUF that completely agrees with Actran solution. The same solution is also provided in literature [3]. Small differences with Actran are observed at higher frequencies for the allumium-water system. This demonstrates

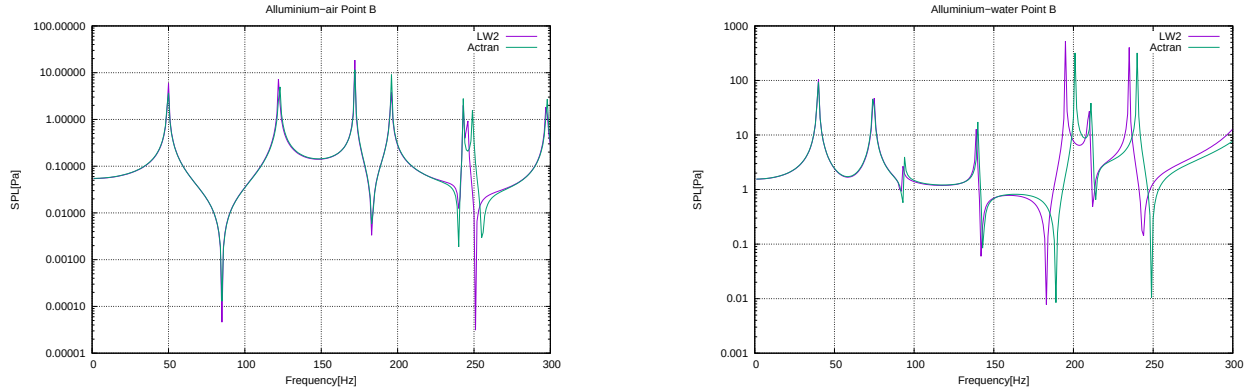

(a) (b)

Figure 2: Alluminium plate coupled with: (a) air-filled cavity (b) water-filled cavity.

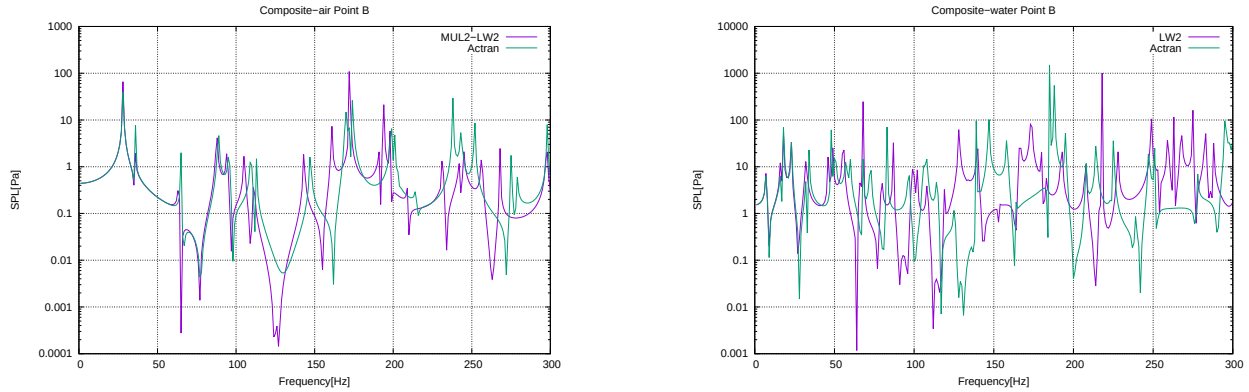

(a) (b)

Figure 3: Multi-layered composite plate coupled with: (a) air-filled cavity (b) water-filled cavity.

that the quadratic LW model can take into account thickness effects that are not covered by Actran 2D elements. The differences become larger in the case of composite plate, mainly for the water-filled cavity where the coupling effects are more pronounced. Indeed, the layer-wise model is able to capture the complex dynamic response of multi-layered structure better than classical 2D elements that produce some errors reflected in the sound pressure response of the fluid.
Further investigations on sandwich structures with soft core or structures with viscoelastic layers must be carried out to demonstrate the high potentialities of CUF models in the vibro-acoustic analysis.

REFERENCES

[1] V. D'Alessandro, G. Petrone, F. Franco, and S. De Rosa. A review of the vibroacoustics of sandwich panels: Models and experiments. *Journal of Sandwich Structures & Materials*, 15(5):541–582, 2013.

[2] G. Li, E. Carrera, M. Cinefra, G. A. De Miguel, A. Pagani, and E. Zappino. An adaptable refinement approach for shell finite element models based on node-dependent kinematics. *Composite Structures*, 210:1–19, 2019.

[3] R. Srinivasan Puri. Krylov subspace based direct projection techniques for low frequency, fully coupled, structural acoustic analysis and optimization. PhD thesis, Oxford Brookes University, 2008.

ON THE MULTI-MODAL BEHAVIOR AND INNER RESONANCE OF STIFFENED SHELLS

G. Tufano[1,2*], O. Bareille[1], B. Pluymers[2,3], A.-M. Zine[4], W. Desmet[2,3] and M. Ichchou[1]

[1]Vibroacoustics & Complex Media Research Group, LTDS-CNRS UMR 5513
École Centrale de Lyon, Écully, 69134, FRANCE
Email: giovanni.tufano@ec-lyon.fr, olivier.bareille@ec-lyon.fr, mohamed.ichchou@ec-lyon.fr

[2]Noise and Vibration Research Group, Dept. Mechanical Engineering, section LMSD
KU Leuven, Heverlee, BELGIUM
Email: giovanni.tufano@kuleuven.be, bert.pluymers@kuleuven.be, wim.desmet@kuleuven.be

[3]DMMS core lab
Flanders Make, BELGIUM

[4]Institut Camille Jordan, Département de Maths-Info
École Centrale de Lyon, Écully, 69134, FRANCE
Email: abdel-malek.zine@ec-lyon.fr

ABSTRACT

A numerical and experimental investigation on the effects of axial and circumferential periodically distributed stiffeners on shells is conducted in this work. The Inhomogeneous Wave Correlation (IWC) method is used to characterize the dynamic behavior and the wave propagation in the structures. The dispersion curves are calculated in two orthogonal directions (axial and circumferential), capturing the band-gaps related to the geometric periodicity and multi-modal behavior (in terms of uncoupled flexural stiffeners and skin motions).
The experimental tests are conducted on a stiffened aluminum aircraft sidewall panel under point mechanical excitations and laser doppler velocimeter acquisition; numerical simulations are computed using punctual harmonic excitation in a Finite Element framework.

1 INTRODUCTION

The presence of stringers and frames in the longitudinal and circumferential direction of aircraft fuselages lets assume a certain degree of structural periodicity which, if properly designed, can give some advantages in the vibroacoustic response. The identification of the dispersion curves associated to transverse displacements are of fundamental interest since they contain informations directly related to the vibroacoustic behavior of the structure. An algorithm for the identification of the complex flexural wavenumber in the broadband frequency range and of the damping loss factor, named Inhomogeneous Wave Correlation (IWC) method is presented in [1] to describe the wave propagation in ribbed plates; the method is also used to capture the multi-modal behavior, in terms of uncoupled plate and stringer flexural propagation. An application of the IWC method to identify the dispersion curves of a ribbed plate with inner resonance is presented in [2]. The effect of the internal frames on the vibroacoustic response of an aluminum cylinder is performed by Meyer et al. [3], providing a better understanding of frames' influence in the wavenumber domain and on the dispersion curves, mainly based on the numbers and the spatial distribution of the internal frames. In this work, numerical and experimental identification of both periodicity-related band-gaps and multi-modal behavior are obtained for stiffened shells.

2 IWC METHOD FORMULATION FOR CURVED STRUCTURES

The method used to identify the complex wavenumbers is the IWC method for curved structures [4]. This method makes a correlation between the energy carried on by an inhomogeneous traveling wave and the total energy of the vibrational field. The helical damped inhomogeneous wave can be expressed as follows:

$$\tilde{w}_{k_{\mathbb{C}},\theta}(x,\varphi) = e^{-ik_{\mathbb{C}}(\theta)((x-x_0)\cos\theta+(\varphi-\varphi_0)\sin\theta)}, \tag{1}$$

where θ is the angle of propagation, $k_{\mathbb{C}} = k_{\Re} + ik_{\Im}$ is the complex wavenumber, which contains both propagation and attenuation informations, and (x_0,φ_0) is the location of the excitation force. At each frequency f and for a given direction θ, the unknown complex wavenumber $k_{\mathbb{C}}$ can be identified as the location of the maximum of the normalized correlation function, denoting the point where the measured signal $\hat{w}$ correlates best with the inhomogeneous wave $\tilde{w}_{k_{\mathbb{C}},\theta}(x,\varphi)$:

$$\mathcal{I}(k_{\mathbb{C}},\theta) = \frac{\left|\sum_{j=1}^{N} \hat{w}(x_j,\varphi_j)\cdot\tilde{w}^*_{k_{\mathbb{C}},\theta}(x_j,\varphi_j)h_j\Omega_j\right|}{\sqrt{\sum_{j=1}^{N}|\hat{w}(x_j,\varphi_j)|^2h_j\Omega_j\cdot\sum_{j=1}^{N}|\tilde{w}_{k_{\mathbb{C}},\theta}(x_j,\varphi_j)|^2h_j\Omega_j}}, \tag{2}$$

where N is the total number of points, h_j is the coherence of the measured signal and Ω_j is the estimation of the punctual surface. The location of the maximum of the correlation function $\mathcal{I}(k_{\mathbb{C}},\theta)$ gives the identified complex wavenumber in the specified direction.

3 EXPERIMENTAL SET-UP, NUMERICAL MODELS AND RESULTS VALIDATION

The aluminum panel has dimensions $1.45\,\mathrm{m}$ x $1.70\,\mathrm{m}$, with a curvature radius approximatively of $1.30\,\mathrm{m}$ and a thickness of $1.2\,\mathrm{mm}$ (Fig. 1). The panel was installed in the GAUS (*Groupe d'Acoustique de l'Université de Sherbrooke*) laboratory, at Université de Sherbrooke; the structure was freely suspended to simulate free boundary condition; the shaker (a Modal Shop Model 2025E) was placed on an internal frame structure, as shown in Fig. 1a. The excitation was generated using a white noise signal from $100\,\mathrm{Hz}$ to $2000\,\mathrm{Hz}$ and the external surface was scanned using a Polytec 3D Scanning Vibrometer, with an acquisition window of approximatively of $0.85\,\mathrm{m}$ x $0.95\,\mathrm{m}$, with 5451 acquisition points (equivalent to a mesh grid of 69 x 79). The experimental results are validated using the finite element model of the panel, built using ANSYS SHELL181 structural elements (see Fig. 1b); the numerical displacement field is obtained by a full FE analysis, using a point harmonic excitation. The multi-modal behavior is well identified in the numerical simulation and experimental test, as shown in Fig. 3a. Two uncoupled wavenumber are identified at the same frequency: plate flexural and stringer flexural. Some discrepancy between the numerical and experimental dispersion curves are present in Fig. 3a, mainly due to the modeling choices.

To evaluate the band-gaps due to the periodic distribution of stiffeners, a bare test case panel is considered, then the stiffeners are applied in the axial and in the circumferential directions, separately (see Fig. 2). The panels have dimensions $0.60\,\mathrm{m}$ x $1.05\,\mathrm{m}$, with a curvature radius

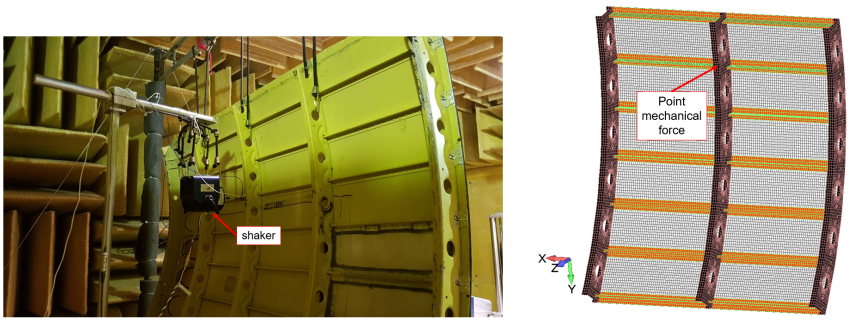

(a) (b)

Figure 1: Set-up and installation for shaker excitation (a) and FE model (b).

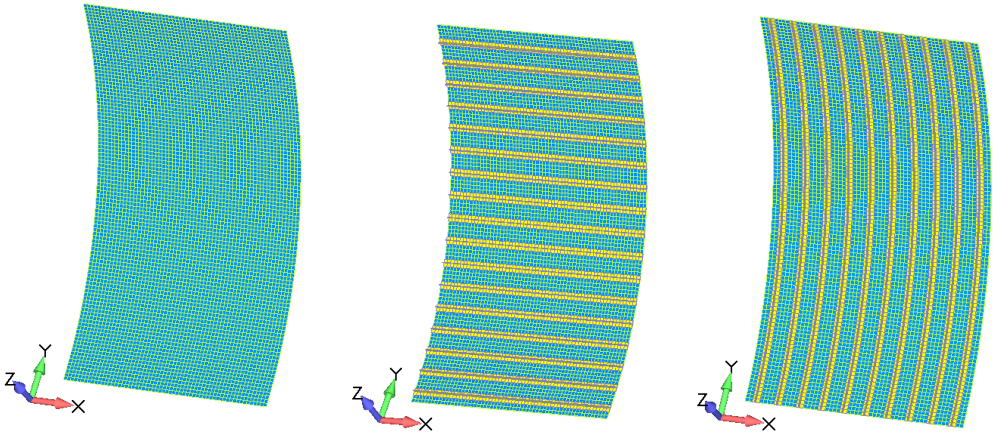

(a) (b) (c)

Figure 2: Bare configuration (a), axial (b) and circumferential (c) stiffeners.

$R = 1.0\,\mathrm{m}$ and thickness equal to $1.2\,\mathrm{mm}$ (Fig. 2a). The material properties are chosen similar to a standard aeronautical aluminum alloy. The stiffeners have *T* shaped cross-section, with $20\,\mathrm{mm}$ width, $10\,\mathrm{mm}$ height and $1.2\,\mathrm{mm}$ thickness, and with an inter-spacing of $6\,\mathrm{cm}$; they are modeled using ANSYS SHELL181 structural elements. For what concerns the axially stiffened panel, when evaluating the wave propagation in the axial direction (along the stiffeners direction) the behavior of the structure is dominated by the bending motion of the stiffeners, as shown in Fig. 4a. On the other hand, when the inhomogeneous wave travels in the circumferential direction it views the periodic distribution of stiffeners; the global behavior is dominated by the bending motion of the skin, but a band-gap is observed in the frequency range [$720\,\mathrm{Hz}$ - $920\,\mathrm{Hz}$] (Fig. 4b). The opposite behavior is observable for the circumferentially stiffened panel. The dispersion curve calculated in the orthogonal direction respect to the stiffeners main dimension presents a band-gap from $1030\,\mathrm{Hz}$ to $1380\,\mathrm{Hz}$; the presence of the stiffeners has an influence on the ring frequency, which is identified at $550\,\mathrm{Hz}$, as shown in Fig. 4a. The dispersion curve in the same direction of the stiffeners is shown in Fig. 4b; the structural behavior is dominated by the flexural motion of the stiffeners.

4 CONCLUDING REMARKS

In this paper, the Inhomogeneous Wave Correlation method is used to identify the multi-modal behavior of stiffened aircraft sidewall panel, identifying two dominant wavenumbers at the same frequency. The band-gaps associated to the periodic distributions of stiffeners are well captured, together with the global bending behavior of the curved panels. A reduction of the ring frequency is also observed for the stiffened panels compared to the bare test case.

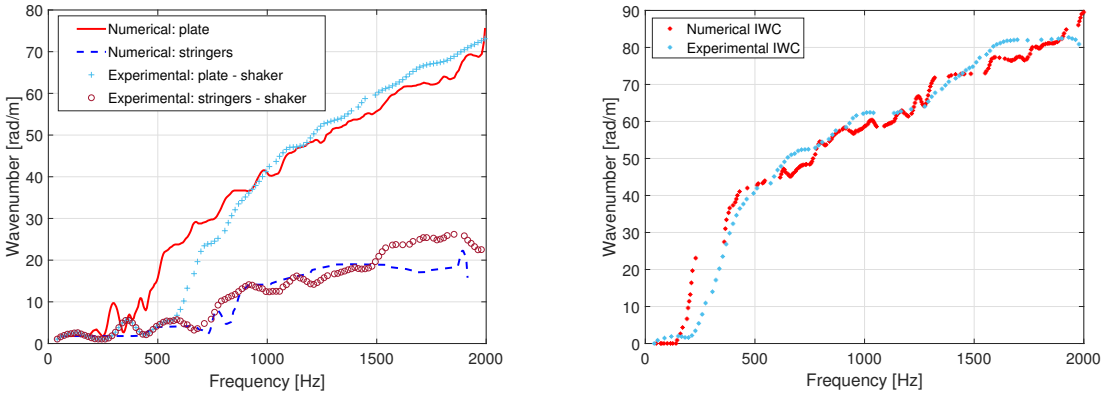

(a) (b)

Figure 3: Dispersion curves of the aircraft panel: axial (a) and circumferential (b) directions.

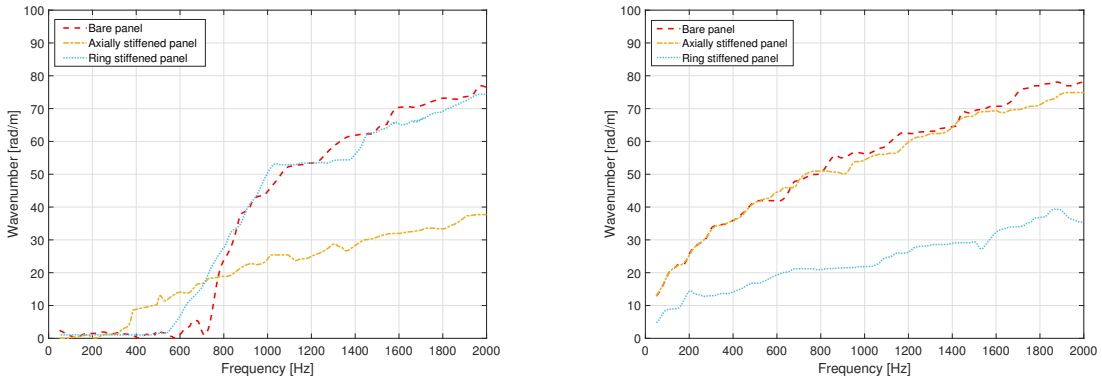

(a) (b)

Figure 4: Dispersion curves of the stiffened panels with *T* shaped stiffeners: axial direction (a) and circumferential direction (b).

ACKNOWLEDGMENT

This project has received funding from the European Union's Horizon 2020 research and innovation program under the Marie Sklodowska-Curie grant agreement No. 675441.

REFERENCES

[1] M. N. Ichchou, J. Berthaut, and M. Collet. Multi-mode wave propagation in ribbed plates: Part I, wavenumber-space characteristics. *International Journal of Solids and Structures*, 45:1179–1195, 2008.

[2] P. Fossat, C. Boutin, and M. Ichchou. Dynamics of periodic ribbed plates with inner resonance: Analytical homogenized model and dispersion features. *International Journal of Solids and Structures*, 152-153:85–103, 2018.

[3] V. Meyer, L. Maxit, Y. Renou, and C. Audoly. Experimental investigation of the influence of internal frames on the vibroacoustic behavior of a stiffened cylindrical shell using wavenumber analysis. *Mechanical Systems and Signal Processing*, 93:104–117, 2017.

[4] G. Tufano, F. Errico, O. Robin, C. Droz, M. Ichchou, B. Pluymers, W. Desmet, and N. Atalla. K-space analysis of large-scale complex meta-structures using the inhomogeneous wave correlation method. *Mechanical Systems and Signal Processing*, 135:106407, 2020.

ATYPICAL DISPERSION FEATURES IN CONTRASTED RESONANT CELLULAR PANELS : ANALYTICAL HOMOGENIZED MODEL AND EXPERIMENTAL MEASUREMENTS

P. Fossat[1*], C. Boutin [2] and M. Ichchou[1]

[1]Ecole Centrale de Lyon, LTDS, UMR-CNRS 5513,
36 Avenue Guy de Collongue 69134 Ecully, France
Email: pascal.fossat@ec-lyon.fr, mohamed.ichchou@ec-lyon.fr

[2]École Nationale des Travaux Publics de l'État, Université de Lyon
LTDS/LGCB UMR-CNRS 5513, Rue Maurice Audin, 69518, Vaulx-en-Velin, France
Email: claude.boutin@entpe.fr

ABSTRACT

This paper deals with the theoretical, numerical and experimental behavior of periodic orthogonally ribbed plates. Theoretical results describing the out-of-plane behavior of cellular plates involving inner resonance phenomena are derived using an asymptotic approach. In this aim, the out-of-plane model of beam grid accounting for local bending and torsion is first established through the method of asymptotic homogenization of periodic discrete media. Then, the coupling between the beam grid and the internal plates is taken into account. This leads to an explicit analytical formulation of the equivalent plate model whose effective parameters arise from the geometrical and mechanical properties of the unit cell. The unconventional features of the flexural wave dispersion are associated with the local resonances. These theoretical results are successfully compared to Wave Finite Element computations. Furthermore, experiments performed on a mock-up of cellular panel evidence the ability of the homogenized model to describe this complex dynamic behavior.

1 INTRODUCTION

The ribbed plates are widely used in structural and mechanical engineering. It is well known that they can present unconventional wave dispersion or atypical sound transmission and adsorption [1]. The understanding of such complex behaviors have motivated the development of numerical and theoretical approaches, that take advantage of the periodicity of the structure. Let us first recall a few references in statics, $i)$ the derivation by [2] of the equivalent orthotropic plates reinforced by stiffeners, $ii)$ the plate model describing the out-of-plane behavior of periodic beam grid established by [3], and $iii)$ the physical analysis of [4] that yields the effective torsional rigidities which incorporate the interaction between the plate and the stiffeners. In dynamics, numerical approaches such a WFEM (Wave Finite Element Method) has been used by [5] to determine the free-wave propagation in a plate stiffened by a grid of orthogonal beams. This method can be improved with modal reduction techniques as demonstrated by [6] in the case of orthogonally ribbed plates. Advanced numerical procedure have also been applied to the identification of propagation parameters in composite structures from experimental measurements. For example, the IWC (Inhomogeneous Wave Correlation) method introduced by [7] consists in a correlation index which allows extracting the wavenumber from the experimental data [8].These different numerical approaches provide accurate numerical results provided that he micro-structure is given, but fail to identify the underlying model that arises from the physics involved within the cell.

Among the theoretical approaches, the homogenization of periodic media [9, 10] is a rigorous asymptotic method for up-scaling the physics at micro-scale into a macroscopic model, in which the effective parameters are fully determined from the periodic cell. The method requires to consider domains made of a large number of periods, and phenomena evolving at a macroscopic length of characteristic dimension L significantly larger than the size ℓ of the cell. The asymptotic process consists in expanding the field's variables over the small scale parameter $\varepsilon = \ell/L \ll 1$. The macroscopic model results form the asymptotic process itself, without any assumption on the nature of the model to be found. This work extends the paper [11] in which a comprehensive homogenized model has been established for flexural and torsional motion of periodic 1D-ribbed plates. New theoretical results describing the transverse behavior of cellular plates involving inner resonance phenomena, are derived using an asymptotic approach, then compared with experimental measurements

2 DERIVATION OF THE HOMOGENIZED MODEL

The homogenization process is carried out according to the following steps : $i)$ the homogenization of periodic discrete media method enables to derive the dynamic model describing the transverse vibration of the beam grid only, $ii)$ the coupling between the beam grid and the internal plates is then introduced considering that the grid is loaded by efforts and moments exerted by the plates attached to it, $iii)$ the calculation of the dynamic contribution of the resonant internal plates driven by the motion of the grid. The explicit dispersion equation is finally obtained. This model is then enriched considering different internal boundary conditions and added mass.

The up-scaling process is performed through HPDM. The developments proceed into three steps, namely, the discretization of the dynamic balance, then the homogenization procedure itself through scale separation assumption and normalization, leading to the continuous model from the discrete pattern. The macroscopic description of the grid, valid at the dominant order, is the limit behavior reached for $\varepsilon \to 0$.

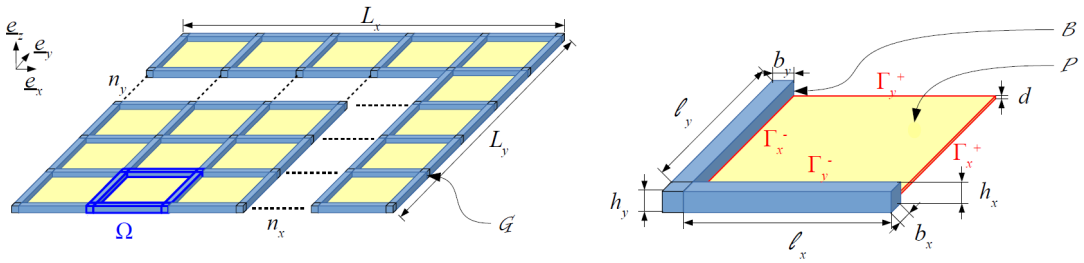

Figure 1: Orthogonally ribbed plate with with macro-beams constituting the beam grid $\mathcal{G}$, and focus on the unit cell Ω made of micro-beams $\mathcal{B}$ and internal micro-plate $\mathcal{P}$

In that case, the stiff ortho-grid conveys the large wavelength, while the soft internal plate experiences a local resonance. The action of internal plates is introduced in the beam grid model in the form an external loading constituted by a shear force $\mathcal{F}$ and a couple $\mathcal{C}$ resulting from the contact forces. Calculating analytically these terms yield the effective model of the 2-D ribbed plate that describes the grid behavior enriched by for the locally resonant internal plates.

$$\begin{cases} \mathrm{div}(\underline{T}^{\mathcal{G}}) + \omega^2(\Lambda^{\mathcal{G}} + \Lambda'_p\langle\phi^{bc}_\omega\rangle)U = 0 \quad ; \quad \Lambda^{\mathcal{G}} = \dfrac{\Lambda_x}{\ell_y} + \dfrac{\Lambda_y}{\ell_x} \\ \underline{\mathrm{div}}(\underline{\underline{M}}) - \underline{T}^{\mathcal{G}} - \omega^2\underline{\underline{J}}^{\mathcal{G}}.\underline{\mathrm{grad}}(U) + \underline{K}^{bc}_\omega U = 0 \\ \\ \underline{\underline{M}} = -\begin{pmatrix} \frac{E_xI_x}{\ell_y}\partial_x^2 U & \frac{G_yJ_y}{\ell_x}\partial_x\partial_y U \\ \frac{G_xJ_x}{\ell_y}\partial_y\partial_x U & \frac{E_yI_y}{\ell_x}\partial_y^2 U \end{pmatrix} \quad ; \quad \underline{\underline{J}} = \begin{pmatrix} \rho_y J_y & 0 \\ 0 & \rho_x J_x \end{pmatrix} \end{cases} \tag{1}$$

The inner resonance effect appears through the frequency dependent effective parameters $\langle\phi^{bc}_\omega\rangle$, and $\underline{K_\omega}^{bc}$ both associated with the dynamic motion of the internal plate. They results into a non conventional apparent mass and a unusual stiffness that links a specific torque to the deflection.

3 EXPERIMENTS ON 2D-RIBBED PLATE

The orthogonally ribbed plate with aluminium stiffeners and polycarbonate plate is depicted in Fig. 2(a). The velocity field is measured by a scanning vibrometer. The IWC method is used to extract the wavenumber from the experimental data, as shown in figure Fig. 2(b)

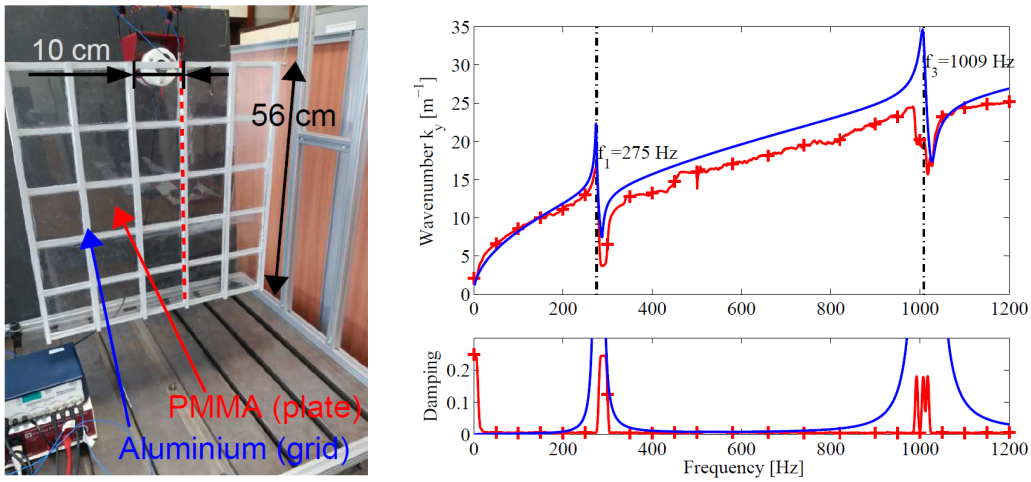

(a) (b)

Figure 2: (a) Orthogonally ribbed plate under study; (b) flexural wavenumber calculated with homogenized model (−) and estimated from experimental data (− + −)

The good agreement over the whole frequency range in terms of frequency and amplitude confirms that the inner resonance effect is accurately captured by the homogenized model.

4 CONCLUDING REMARKS

The homogenization method applied to periodic orthogonally ribbed plates with contrasted geometrical parameters and/or mechanical properties allowed to determine their unconventional macroscopic behavior. The model is established within the scale separation assumption, and its effective parameters are fully and explicitly determined from the geometry and mechanical properties of the plate and stiffeners. It encompasses the atypical flexural dispersion associated with the enriched local kinematics induced by the inner resonance. These outcomes are successfully compared with WFEM computations and with experiments performed on two prototypes in different configurations, with IWC post-processing of the data. This shows that the homogenized model correctly

captures the phenomena, that the study yields reliable design rules.

The present up-scaling method could be further applied on various cell geometries. The great amount of possible configurations enables tunable singularities of the panel behavior, and offer the possibility of broadband attenuation.

5 ACKNOWLEDGEMENTS

This work was supported by the LabEx CeLyA (Centre Lyonnais d'Acoustique, ANR-10-LABX-0060) of Université de Lyon, within the program "Investissements d'Avenir" (ANR-11-IDEX-0007) operated by the French National Research Agency (ANR). The authors are pleased to thank Dr. Christophe Droz for fruitful discussions, as well as Stéphane Lemahieu for his work on the experimental devices

REFERENCES

[1] Srinivas Varanasi, J. Stuart Bolton, Thomas H. Siegmund, and Raymond J. Cipra. The low frequency performance of metamaterial barriers based on cellular structures. *Applied Acoustics*, 74(4):485 – 495, 2013.

[2] S. Timoshenko and S. Woinowsky-Krieger. *Theory of plates and shells*. Engineering societies monographs. McGraw-Hill, 1959.

[3] J.D. Renton. A finite difference analysis of the flexural-torsional behaviour of grillages. *International Journal of Mechanical Sciences*, 6(3):209 – 224, 1964.

[4] Fumio Nishino, Ricardo P. Pama, and Seng-Lip Lee. Orthotropic plates with eccentric stiffeners. *IABSE publications*, 34 (1974), 1974.

[5] D.J. Mead, D.C. Zhu, and N.S. Bardell. Free vibration of an orthogonally stiffened flat plate. *Journal of Sound and Vibration*, 127(1):19 – 48, 1988.

[6] C. Droz, C. Zhou, M.N. Ichchou, and J.-P. Lainé. A hybrid wave-mode formulation for the vibro-acoustic analysis of 2d periodic structures. *Journal of Sound and Vibration*, 363:285 – 302, 2016.

[7] J. Berthaut, M.N. Ichchou, and L. Jezequel. K-space identification of apparent structural behaviour. *Journal of Sound and Vibration*, 280(3–5):1125 – 1131, 2005.

[8] M.N. Ichchou, J. Berthaut, and M. Collet. Multi-mode wave propagation in ribbed plates. part ii: Predictions and comparisons. *International Journal of Solids and Structures*, 45(5):1196 – 1216, 2008.

[9] Enrique Sanchez-Palencia. *Non-Homogeneous Media and Vibration Theory (Lecture Notes in Physics)*. Springer, spi edition, 6 1980.

[10] Jean-Louis Auriault, Claude Boutin, and Christian Geindreau. *Homogenization of Coupled Phenomena in Heterogenous Media (ISTE)*. Wiley-ISTE, 1 edition, 8 2009.

[11] P. Fossat, C. Boutin, and M. Ichchou. Dynamics of periodic ribbed plates with inner resonance: Analytical homogenized model and dispersion features. *International Journal of Solids and Structures*, 152-153:85 – 103, 2018.

WAVE FINITE ELEMENT METHOD BASED ON SECOND STRAIN GRADIENT ELASTICITY THEORY FOR ONE-DIMENSIONAL NANO-SIZED PERIODIC STRUCTURES

B. Yang[1], M. N. Ichchou[1*], A. M. Zine[2]

[1]Vibroacoustics and Complex Media Research Group, LTDS - CNRS UMR 5513, Ecole Centrale de Lyon, Ecully 69134, France
Email: bo.yang@ec-lyon.fr, mohamed.ichchou@ec-lyon.fr

[2]Institut Camille Jordan - CNRS UMR 5208, Ecole Centrale de Lyon, France
Email: abdel-malek.zine@ec-lyon.fr

ABSTRACT

In this paper, the dynamic behavior and wave propagation of 1D nano-sized periodic structures are studied. A numerical method called wave finite element method (WFEM) is utilized, which converting the whole periodic structure into a single unit cell or a small segment of the structure. Furthermore, the mechanical character of the structure is analyzed depending on second strain gradient elasticity theory (SSG), which considering the higher order material coefficients. The dynamic stiffness matrix of SSG model is established by transforming the lattice model with the nearest-neighbor, next-nearest-neighbor and next-next-nearest-neighbor masses interactions into SSG continuous model. Subsequently, longitudinal and bending waves in binary nano-sized periodic structures are calculated by WFEM. Dispersion relations for the longitudinal and bending waves with SSG, SG and CT methods are discussed.

1 INTRODUCTION

Periodic structures have been widely studied for their dynamic behaviors and wave propagation [1, 2]. Such as Nano-sized phononic crystals (PCs), which have been being widely investigated due to their excellent capacities of manipulating acoustic and elastic waves. The approach is based on Floquet's principle or the transfer matrix that the wave number is twice to degrees of freedom (DOFs) at coupling interfaces and can be disassembled into an equal number of positive and negative-going waves. The main purpose is to get dispersion relations utilizing finite element method (FEM) [3]. In periodic structures, the dispersion and attenuation characteristics of waves, known as Bloch waves [4], distinct from those in continuous structures. It is worth noting that the optimum design and parameter study of the stop band have aroused the extensive researches of scholars [5, 6].

But for the complex structure, FEM offering no other choice than meshing the whole structure requires excessive computational time. On the other hand, the mechanical behaviors of nano-sized structures are greatly different from their behaviors at the macro levels. The surface and interfaces properties with a very large surface-to-volume ratio have a non-negligible influence on the mechanical behaviors [7]. The microstructure is the most essential factor to determine the intrinsic properties of the material. It consists of the atomic structure of each element, the interaction between atoms and movement of atoms in space. Mechanical properties of materials are closely related to the microstructures of materials.

Converting the mentioned above study of the whole periodic structure into a single unit cell or a small segment of the structure called wave finite element method (WFEM) was developed and completed in various studies [8-10]. The resulting mass, stiffness matrices are then post-processed to give the dynamic stiffness matrix of the cell. Periodic structure theory is used to build the dynamic stiffness matrix of the whole structure.

2 METHOD AND RESULTS

This paper presents a method based on second strain gradient (SSG) theory [11, 12] and WFEM to analyse dynamic behaviors of nano-sized periodic structures. A lattice model that considered as a discrete nano-sized structural basis for gradient continuous model of the SSG theory is discussed. In order to obtain the SSG continuous model, the lattice model with the nearest-neighbor, next-nearest-neighbor and next-next-nearest-neighbor interactions with three different coupling constants is considered. The suggested lattice model gives unified description of the SSG model. And the sign in front each gradient is determined by the relation of the coupling constants of the nearest-neighbor, next-nearest-neighbor and next-next-nearest-neighbor interactions.

Subsequently, based on the relationship between coupling constants and higher order material coefficients, the element stiffness matrix is established utilizing the direct stiffness method. Then the global stiffness matrix $\mathbf{D}$ of a unit cell will be assembled by individual element stiffness matrices. Because of the cell coupling actions are supposed to be confined to its left and right boundaries only, a new global dynamic stiffness matrix $\tilde{\mathbf{D}}$ of a cell is obtained after eliminating the interior DOFs. The right boundary of a cell related to the left boundary can be expressed by a transfer matrix $\mathbf{S}$. Finally, the dynamic behaviors of the one-dimensional nano-sized periodic structures are discussed after solving the eigenvalue problem of transfer matrix $\mathbf{S}$.

The dynamic equation of SSG theory extended from SG theory [13] for one-dimensional nano-sized rod is given as:

$$\frac{\partial^2 u(x,t)}{\partial t^2} = G_2 \frac{\partial^2 u(x,t)}{\partial x^2} + G_4 \frac{\partial^4 u(x,t)}{\partial x^4} + G_6 \frac{\partial^6 u(x,t)}{\partial x^6} + \frac{1}{\rho} f(x), \tag{1}$$

where $G_2=\frac{(K_2+4K_4+9K_6)d^2}{m}$, $G_4=\frac{(K_2+16K_4+81K_6)}{12}\frac{d^4}{m}$, $G_6=\frac{(K_2+64K_4+729K_6)}{360}\frac{d^6}{m}$, ρ is density of rod.

The relationships between spring tension stiffness constants and higher order material coefficients are defined as:

$$K_2=\frac{\left(3Ed^4+13(B_2-B_4)d^2+30B_3\right)A}{2d^5},\ K_4=-\frac{\left(3Ed^4+40(B_2-B_4)d^2+120B_3\right)A}{20d^5},\ K_6=\frac{\left(Ed^4+15(B_2-B_4)d^2+90B_3\right)A}{90d^5},$$

where $B_2=2(a_1+a_2+a_3+a_4+a_5)$, $B_3=2(b_1+b_2+b_3+b_4+b_5+b_6+b_7)$, $B_4=2(c_1+c_2+c_3)$, E is the Young's modulus, A means cross sectional area of the rod, a_i, b_i, c_i represent the higher order material coefficients.

On the other hand, the dynamic equation of SSG theory for one-dimensional nano-sized Euler beam is given as:

$$\Lambda\frac{\partial^2 w(x,t)}{\partial t^2}=G_4'\frac{\partial^4 w(x,t)}{\partial x^4}+G_6'\frac{\partial^6 w(x,t)}{\partial x^6}+G_8'\frac{\partial^8 w(x,t)}{\partial x^8}+f(x)\ , \tag{2}$$

where $G_4'=K_4'+2K_6'+3K_8'$, $G_6'=\frac{(K_4'+8K_6'+27K_8')d^2}{6}$, $G_8'=\frac{(K_4'+32K_6'+243K_8')d^4}{80}$, Λ means linear mass of the beam.

The relationships between spring tension stiffness constants and higher order material coefficients are defined as:

$$K_4'=\frac{3I_1}{2}+\frac{13(I_2-I_4)}{4d^2}+\frac{10I_3}{3d^4},\ K_6'=-\frac{3I_1}{10}-\frac{2(I_2-I_4)}{d^2}-\frac{8I_3}{3d^4},\ K_8'=\frac{I_1}{30}+\frac{I_2-I_4}{4d^2}+\frac{2I_3}{3d^4},$$

where $I_1=EI+2A(a_1-a_2+a_3+3a_4-a_5)$, $I_2=2I(a_1+a_2+a_3+a_4+a_5)+4A(b_2-b_4+b_5+2b_6)$, $I_3=2I(b_1+b_2+b_3+b_4+b_5+b_6+b_7)$, $I_4=3I(c_1+c_2+c_3)$.

The dispersion relations of a rod and bending Euler beam for SSG, SG and CT are illustrated in Fig. 1 and Fig. 2.

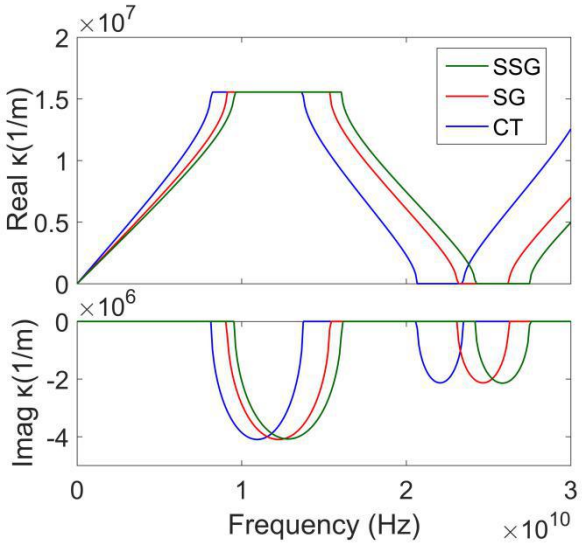

Fig. 1 Dispersion relation for longitudinal waves

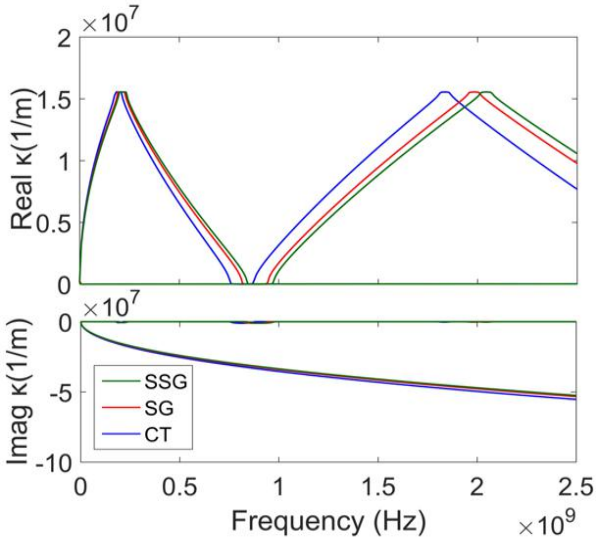

Fig. 2 Dispersion relation for bending waves

As shown in Fig. 1 and Fig. 2, the dispersion relation issued from SSG is compared to those calculated with SG and CT. The stop band frequencies range is bigger than SG and CT. SSG method taking into account higher order material coefficients more authentically reflects the mechanical properties of structures. Electrons or waves need more energy to transmit into the pass band from stop band.

3 PERSPECTIVES

Nano-sized periodic structures have been widely studied for their dynamic behaviors and wave propagation. Such as phononic crystals (PCs), which have been being widely investigated due to their excellent capacities of manipulating acoustic and elastic waves. Studies of PCs were mainly concentrated on the existence and applications of the band gaps (BGs), which are frequency ranges where wave propagation is prohibited.

ACKNOWLEDGMENTS

The research of B. Yang is funded by Chinese Scholarship Council (CSC).

REFERENCES

[1] Brillouin, L. Wave propagation in periodic structures, Dover, New York, 1953.

[2] Mead, D.J. Wave propagation in continuous periodic structures: Research contributions from southampton, 1964–1995, Journal of Sound and Vibration 190(3), 495–524, 1996.

[3] Houillon, L, Ichchou, M.N., Jezequel, L. Wave motion in thin-walled structures, Journal of Sound and Vibration 281, 483–507, 2005.

[4] Kittel, C.Introduction to solid state physics (Wiley, New York), 2004.

[5] Yu, D., Fang, J., Cai, L., Han, X. and Wen, J. Triply coupled vibrational band gap in a periodic and nonsymmetrical axially loaded thin-walled Bernoulli-Euler beam including the warping effect, Physics Letters A 373(38), 3464–3469, 2009.

[6] Olhoff, N., Niu, B. and Cheng, G. Optimum design of band-gap beam structures, International Journal of Solids and Structures 49(22), 3158–3169, 2012.

[7] Shodja, H.M. Calculation of the Additional Constants for fcc Materials in Second Strain Gradient Elasticity: Behavior of a Nano-Size Bernoulli-Euler Beam With Surface Effects, Journal of Applied Mechanics 79(2), 1–8, 2012.

[8] Droz, C., Lainé, J. P., Ichchou, M. N., and Inquiété, G. A reduced formulation for the free-wave propagation analysis in composite structures. Composite Structures, 113, 134-144, 2014.

[9] Mace, B. R., Duhamel, D., Brennan, M. J., and Hinke, L. Finite element prediction of wave motion in structural waveguides. The Journal of the Acoustical Society of America, 117(5), 2835-2843, 2005.

[10] Mencik, J.M., Ichchou, M.N. Wave finite elements in guided elastodynamics with internal fluid, International Journal of Solids and Structures 44, 2148–2167, 2007.

[11] Mindlin, R.D. Second gradient of strain and surface tension in linear elasticity, International Journal of Solids and Structures 1: 417–438, 1965.

[12] Zhu, G., Droz, C., Zine, A.M., and Ichchou, M.N. Wave propagation analysis for a second strain gradient rod theory. Chinese Journal of Aeronautics, 2019, in press, doi.org/10.1016/j.cja.2019.10.006.

[13] Tarasov, V.E. Lattice model with nearest-neighbor and next-nearest-neighbor interactions for gradient elasticity discontinuity. Nonlinearity, and Complexity 4(1), 11–23, 2015.

DYNAMIC ANALYSIS OF METASTRUCTURE BEAM WITH LOW FREQUENCY MULTI-MODE RESONATORS

Q.C. Wu[1,2*], C. Droz[1], M. Ichchou[1] and S.L. Xie[2]

[1]Ecole Centrale de Lyon, LTDS-CNRS UMR 5513, FRANCE
Email: wuqichen@stu.xjtu.edu.cn

[2]State Key Laboratory for Strength and Vibration of Mechanical Structures
Xi'an Jiaotong university, Xi'an, CHINA

[3a]KU Leuven, Mechanical Engineering Department, Heverlee, BELGIUM
[3b]DMMS-M Lab, Flanders Make, BELGIUM

ABSTRACT

Metastructures with resonators are effective in wave attenuating due to band gaps, but it is still a challenge to realize low frequency multi-mode vibration suppression. A new low frequency multi-mode (LFMM) resonator, which consists of two-stage high-static-low-dynamic stiffness oscillators is proposed in this paper. The theoretical model of metastructure beam with LFMM resonator is established and band structures are obtained by the Plane Wave Expansion Method (PWEM). Then, the Wave Finite (WFEM) is combined with Periodic Structure Theory (PST) to calculate the forced response of the metastructure beam. WFEM is a powerful numerical tool of structure dynamics, which converts the study of the whole periodic structure into a single unit cell or small segment of the structure. Numeric results show that multiple low frequency band gaps are generated, in which the forced response is suppressed obviously, which means analytical and numerical method validate each other. Furthermore, dynamic analysis of a simplified unit cell show that number and location of band gaps is determined by LFMM resonator, which can be adjusted by configuring the physical parameters of the oscillators based on needs. Finally, the influence of mass ratio and damping of LFMM resonator on band gaps is also analyzed.

1 INTRODUCTION

Recently, artificial periodic composites known as phononic crystals, metamaterial and metastructure have received amount of attention [1-2]. Such structures feature the capability of attenuating waves within some frequency ranges, called stop bands or band gaps. Local resonance mechanism [3] creates band gaps with lattice constant two orders of magnitude smaller than the relevant wavelength, which makes it applicable in vibration suppression. A large amount of work has been carried out and is documented in the comprehensive review article [2].

In some engineering fields, one frequently needs to suppress vibration of a structure in the low-frequency (even ultra-low-frequency) domain. It is a natural way to design resonator with low resonant frequency since the frequency range of the band gap of metastructure based on local resonance mechanism is determined by the resonant frequency of the resonators [3]. Traditionally, there are two measures to achieve this goal, they are reducing stiffness and increasing mass, respectively. Unfortunately, reducing stiffness weakens the bearing capacity of the structure and increasing mass may make the system too heavy. In recent years, the conception of negative stiffness has been introduced to realize low frequency vibration isolation of a structure. In classical negative stiffness mechanism, two oblique compressed springs, which can provide negative stiffness, are used to counteract the stiffness provided by a vertical spring so as to yield very low dynamic stiffness in the vibration state [4,5]. Zheng *et al* [6] designed a high-static-low-dynamic stiffness isolator by using a negative stiffness magnetic spring. Zhou *et al* [7] developed a metastructure beam based on local resonator with high-static-low-dynamic stiffness.

Aiming to suppress multiple low frequency modal vibrations of a structure, the low frequency multi-mode (LFMM) resonator based on two-stage high-static-low-dynamic (HSLD) stiffness oscillator is proposed in this work. With the beam as a considered host structure, the theoretical models for an infinite metastructure beam and finite metastructure beam equipped with LFMM resonators are deduced. Furthermore, the band gap structure and forced response are compared numerically and the parametric influence studies are also carried out to provide a basic guideline for optimal design of a metastructure beam.

2 LFMM RESONATOR

The configuration of an LFMM resonator is shown in Figure 1(a), which consists of two-stage HSLD stiffness oscillators. In addition, a classical negative stiffness mechanism, which is made up of two oblique compressed springs of identical stiffness is introduced to each oscillator. Two oblique compressed springs are adjusted to be horizontal at the static equilibrium position and can provide negative stiffness in the vertical direction when the mass vibrates around its equilibrium position. Since the mass block is supported by the vertical spring of relatively large stiffness in the static state, each oscillator features the HSLD stiffness. With this configuration, it can be anticipated that the LFMM resonator processes multiple low frequency modes by an elaborate design of physical parameters of each oscillator.

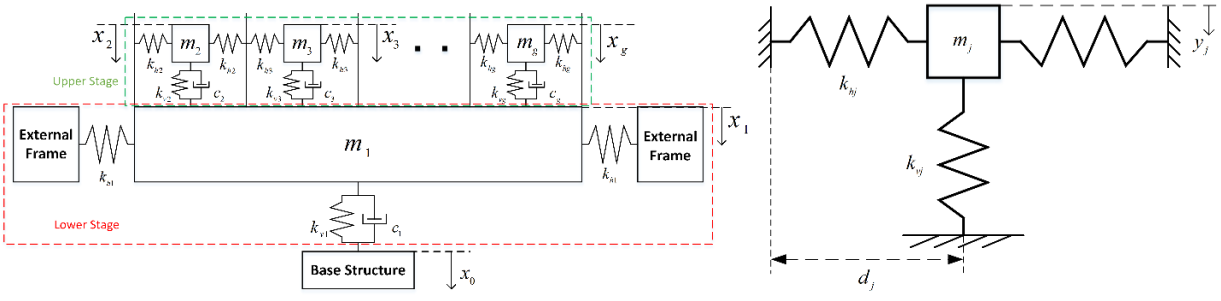

(a) (b)

Figure 1. Configuration of an LFMM resonator.

The dynamic characteristics of the LFMM resonator can be described with the help of a single HSLD oscillator, as shown in Figure 1(b).

In the author's previous works [8], the linearized dynamic stiffness of high-static-low-dynamic stiffness oscillator is deduced as

$$k_{dj} = \eta_j k_{vj}. \tag{1}$$

The constant coefficient η_j denotes the proportion of the residual stiffness of the oscillator in the vertical direction, which can be designed by adjusting synthetically the physical parameters of oscillators. Thus, the LFMM resonator is equivalent to a linear system.

Here, the physical structure of a LFMM resonator when number of oscillators i.e. g=3 is illustrated in Figure 3(a). The LFMM resonator is constructed of four main parts: supporting plates, mass block, negative stiffness mechanism and external frame.

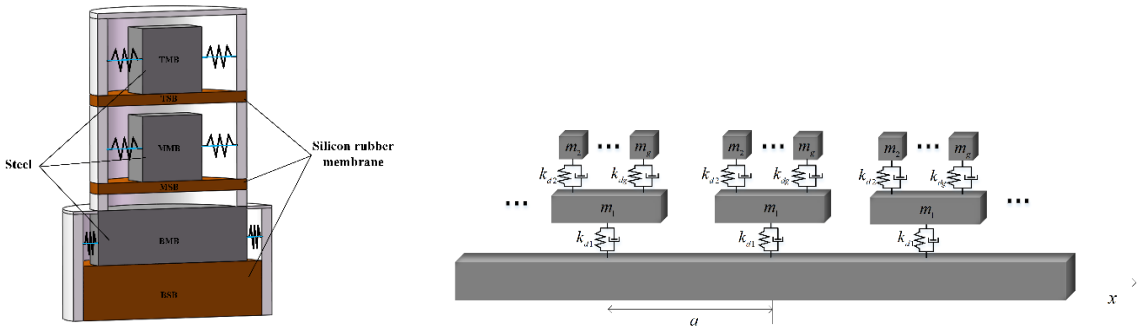

(a) (b)

Figure 3. Physical structure of LFMM resonator and metastructure beam

3 METASTRUCTURE BEAM WITH LFMM RESONATOR

A beam periodically equipped with LFMM resonators is shown in Figure 3(b).

3.1 Plane wave expansion method

Plane wave expansion (PWE) method is an analytic method for continuous systems, which is to expand the solution field and the material properties in a Fourier series, and then invoke orthogonality of the basis of the bases functions to solve individually the introduced solution coefficients [2]. In this case, PWE method is adopted to calculate band gap structure of metastructure with LFMM resonators.

3.2 Wave finite element method

The wave finite element method (WFEM) is a promising numerical tool of structural dynamics [9]. Based on periodic structures theory [10], WFEM converts the study of the whole periodic structure in to a single unit cell or a small segment of the structure. Conventional FE software packages can be used for modelling. WFEM can calculate the wave propagation properties and forced frequency response. In this case, the WFEM is also adopted and the results from analytic method and numerical method validate each other.

3.3 PARAMETRIC EFFECT STUDIES

Parametric effect studies can be carried out by the previous mentioned method. Mass ratio and damping are important physical parameters of LFMM resonators. The influence of the mass ratio and damping on band structure are studied.

4 CONCLUSION

Conceptual model and physical structure of a low frequency multi-mode resonator were proposed in this paper, which features by multiple low natural frequencies and can be adjusted according to the design objective. Theoretical models for metastructure beam with LFMM resonators are established, and the band gap structure and forced frequency response is calculated by plane wave extension method and wave finite element method, respectively. Besides, the influence of mass ratio and damping ratio on band gap structure are studied, providing a guideline for design of metastructure beam with LFMM resonators. Results show that multiple low-frequency modal resonances of the beam can be suppressed by periodically equipping it with LFMM resonators.

5 ACKNOWLEDGEMENT

This work is supported by China Scholarship Council (CSC) during a visit of Qichen Wu to Ecole Centrale de Lyon and the European Union's Horizon 2020 research and innovation programme under the grant agreement No. 797034 (WIDEA).

REFERENCES

[1] M. S. Kushwaha, P. Halevi, L. Dobrzynski, and B. Djafari-Rouhani. Acoustic band structure of periodic elastic composites. *Phys Rev Lett.*, 71.13: 2022.N, 1993.

[2] Hussein, Mahmoud I., Michael J. Leamy, and Massimo Ruzzene. Dynamics of phononic materials and structures: Historical origins, recent progress, and future outlook. *Appl. Mech. Rev.*, 66.4: 040802, 2014.

[3] Z.Y. Liu, X.X. Zhang, Y.W. Mao, Y.Y. Zhu, and Z.Y. Yang et al. "Locally resonant sonic materials." *Science.*, 289.5485: 1734-1736, 2000.

[4] Q.J. Cao, M. Wiercigroch, E. E. Pavlovskaia, C. Grebogi, and J.M T. Thompson. Archetypal oscillator for smooth and discontinuous dynamics. *Phys Rev E.*, 74.4: 046218, 2006.

[5] A. Carrella, M. J. Brennan, and T.P. Waters. Static analysis of a passive vibration isolator with quasi-zero-stiffness characteristic. *J. Sound. Vib.*, 301.3-5: 678-689, 2007.

[6] Y.S Zheng, X.N. Zhang, Y.J. Luo, B. Yan, and C.C. Ma. Design and experiment of a high-static–low-dynamic stiffness isolator using a negative stiffness magnetic spring. *J. Sound. Vib.*, 360: 31-52, 2016.

[7] J.X. Zhou, K. Wang, D.L. Xu, and H.J. Ouyang. Local resonator with high-static-low-dynamic stiffness for lowering band gaps of flexural wave in beams. *Jpn. J. Appl. Phys.*, 121.4: 044902, 2017.

[8] Q.C. Wu, G.T. Huang, C. Liu, S.L. Xie, and M.L. Xu. Low-frequency multi-mode vibration suppression of a metastructure beam with two-stage high-static-low-dynamic stiffness oscillators. *Ac. Ta. Mech.*, 1-16, 2019

[9] F. Yu, M. Collet, M. Ichchou, L. Lin, and O. Bareille et al. Enhanced wave and finite element method for wave propagation and forced response prediction in periodic piezoelectric structures. *Chinese. J. Aeronaut*., 30.1: 75-87, 2017.

[10] D.J. Mead. A general theory of harmonic wave propagation in linear periodic systems with multiple coupling. *J. Sound. Vib*., 27.2:235-260, 1973.

COMPARISON OF THE PERFORMANCE OF VIBROACOUSTIC SIMILITUDE METHODS

Christian Adams[1] , Joachim Bös[2,3], and Tobias Melz[1,4]

[1]Research Group System Reliability, Adaptive Structures, and Machine Acoustics SAM
Technische Universität Darmstadt, Darmstadt, GERMANY
Email: adams@sam.tu-darmstadt.de

[2]Fraunhofer Institute for Digital Media Technology IDMT
Ilmenau, GERMANY

[3]"Industrial Applications of Media Technologies" group, Department of Mechanical Engineering,
Technische Universität Ilmenau, Ilmenau, GERMANY

[4]Fraunhofer Institute for Structural Durability and System Reliability LBF
Darmstadt, GERMANY

ABSTRACT

Several similitude methods have been developed for vibroacoustic analyses in order to transfer the noise and vibration responses from a scaled structure to its original or from one machine size to another one. Current research enhances vibroacoustic similitude analysis methods towards distorted similitude, e.g., due to different scaling factors of the geometrical dimensions. However, the performance of different similitude analysis methods has not been analyzed yet, particularly, in case of distorted similitude. Thus, this paper is concerned with the analysis of the performance of two different similitude methods. The first one is called "similitude and asymptotic models for structural-acoustic research and applications" (SAMSARA), and the second one is called "similitude and sensitivity analysis for laboratory vibro-acoustics and basic investigations on model-scaling (SIMSALABIM). Two different measures are introduced in this paper that are used to assess the performance of these similitude methods in terms of accuracy. The performance is then analyzed for distorted rectangular plates. Numerical investigations show that SAMSARA and SIMSALABIM perform sufficiently well in case of distorted similitudes. However, further research is required to define the limits of application of the scaling laws obtained from SAMSARA and SIMSALABIM.

1 INTRODUCTION

Similitude analyses use scaling laws in order to scale up (or scale down) noise and vibration responses from a scaled structure to its original or to transfer the responses from one machine size to another one within a size range. Several similitude analysis methods have been introduced for structural engineering including vibroacoustics [1]. These methods perform well in case of complete similitude conditions, i.e., all geometrical dimensions are scaled by the same factor and the scaled structure and the original one have the same damping. However, distorted similitude conditions limit the use of scaling laws in practice since geometrical dimensions are usually scaled by different factors and the damping of the scaled structure differs from that of the original one [2, 3]. This causes the vibration responses replicated from the scaled structure to differ from the actual vibration responses of the original structure.

This paper aims at analyzing how different similitude analysis methods perform in case of distorted similitude conditions. The first similitude analysis method has been developed by DE ROSA and FRANCO [4]. It uses a generalized modal approach to derive scaling laws and is called *similitude and asymptotic models for structural-acoustic research and applications* (SAMSARA). The second one has been developed by ADAMS [3, 5]. It uses sensitivity analysis to derive scaling laws and is called *similitude and sensitivity analysis for laboratory vibro-acoustics and basic investigations on model-scaling* (SIMSALABIM[1]). Several measures are introduced in order to assess the performance of the similitude methods in terms of accuracy of the replicated vibration responses. Previous studies show that different accuracy measures lead to different conclusions on the accuracy of the replicated vibration responses [6]. This paper uses the HAUSDORFF distance [7] and the MAHALANOBIS distance [8] as accuracy measures. They have been introduced for similitude analyses in [2] and [3], respectively. The accuracy measures are analyzed for vibrating rectangular plates that are scaled by different factors in length, width, and thickness. The vibration responses are obtained from finite element (FE) analyses.

2 SCALING LAWS

The scaling laws are defined for a distorted similitude of rectangular plates using SAMSARA and SIMSALABIM. The original rectangular plate is referred to as *parent*, labeled (p), while the distorted scaled rectangular plates are referred to as avatars, labeled (a). Details on both methods can be found in [4] and [3, 5], respectively. This section presents the scaling laws for the surface-averaged squared RMS[2] vibration velocity $\overline{\tilde{v}^2}(f)$ of rectangular plates, which depends on the frequency f. The scaling factors of the plate's length, width, and thickness are

$$\phi_a = \frac{a^{(\mathrm{a})}}{a^{(\mathrm{p})}}, \phi_b = \frac{b^{(\mathrm{a})}}{b^{(\mathrm{p})}}, \text{ and } \phi_t = \frac{t^{(\mathrm{a})}}{t^{(\mathrm{p})}}, \tag{1}$$

respectively.

2.1 SAMSARA

Applying SAMSARA to vibrating rectangular plates yields

$$\frac{\overline{\tilde{v}^2}^{(\mathrm{a})}}{\overline{\tilde{v}^2}^{(\mathrm{p})}} = \phi_{\overline{v}} = \left(\phi_a \phi_b \phi_t \phi_f\right)^{-2}, \tag{2}$$

which is the scaling law for the magnitudes of the surface-averaged RMS vibration velocity. The scaling factor for the frequency reads

$$\phi_f = \frac{f^{(\mathrm{a})}}{f^{(\mathrm{p})}} = \phi_t \overline{\phi}_l^{\,-2}, \tag{3}$$

where

$$\overline{\phi}_l = \frac{1}{2}\left(\phi_a + \phi_b\right). \tag{4}$$

[1] also famous magic words: https://en.wikipedia.org/wiki/Magic_word

[2] RMS: root mean square

2.2 SIMSALABIM

Applying SIMSALABIM to vibrating rectangular plates yields

$$\frac{\overline{\tilde{v}^2}^{(\mathrm{a})}}{\overline{\tilde{v}^2}^{(\mathrm{p})}} = \phi_{\overline{v}} = \phi_t^{-4}. \tag{5}$$

The scaling law for the frequency obtained from SIMSALABIM equals Eq. (3), where $\overline{\phi}_l$ is calculated according to Eq. (4). Note that Eq. (2) equals Eq. (5) in case of complete similitude conditions ($\phi_a = \phi_b$).

3 NUMERICAL RESULTS

This paper exemplifies the results for a cantilever aluminum plate that has been investigated in [2]. The dimensions of the parent are $a = 570\,\mathrm{mm}$, $b = 400\,\mathrm{mm}$, and $t = 2\,\mathrm{mm}$. The material properties are: YOUNG'S modulus $E = 70.59 \cdot 10^9\,\mathrm{N\,m^{-2}}$, POISSON'S ratio $\mu = 0.33$, and mass density $\rho = 2\,676\,\mathrm{kg\,m^{-3}}$. An FE model is used to calculate the surface-averaged RMS vibration velocity. Two harmonic forces of $|F_1| = |F_2| = 1\,\mathrm{N}$ magnitude are applied to the FE model and cause the cantilever plate to vibrate. The forces act at the dimensionless coordinates $(0.885a, 0.161b)$ and $(0.885a, 0.839b)$, respectively. Three avatars a1 through a3 are investigated. The scaling factors ϕ_a and ϕ_b are 0.50 and 0.60 for avatar a1, 0.60 and 0.50 for avatar a2, and 0.62 and 0.65 for avatar a3. The scaling factor ϕ_t equals 1.0 for all avatars. The results are plotted in Fig. 1. The vibration velocities replicated by SAMSARA and SIMSALABIM are identical, although the scaling laws obtained from SAMSARA and SIMSALABIM differ, cf. Eqs. (2) and (5). The scaling factors $\overline{\phi}_l$ equal 0.55, 0.55, and 0.64 for the avatars a1, a2, and a3, respectively. Thus, they are close to the scaling factors ϕ_a and ϕ_b. Consequently, the length and the width of the avatars are weakly distorted only. However, the replicated vibration responses (obtained from SAMSARA and SIMSALABIM) somewhat differ from those of the FE calculation due to the distorted similitude. At some frequencies the replicated levels of the vibration velocity agree well with those of the FE calculation, e.g., at 58 Hz and 54 Hz of avatar a1 and a2, respectively, which can be seen in the top and the middle plot of Fig. 1. The replicated vibration velocity of avatar a3 agrees sufficiently well with that of the FE calculation since avatar a3 is distorted to a lesser extent than the avatars a1 and a2. Thus, it is closer to complete similitude conditions, where the replicated vibration responses usually agree well with the calculated ones. Table 1 shows the performance of SAMSARA and SIMSALABIM in terms of the HAUSDORFF distance and the MAHALANOBIS distance. Comparing the distance measures obtained for SAMSARA and SIMSALABIM shows that they are almost identical, which again confirms that SAMSARA and SIMSALABIM perform in the same manner. The distances calculated for avatar a3 are smaller than those of a1 and a2, which confirms that the vibration velocity of avatar a3 can be more accurately replicated than that of the avatars a1 and a2.

Table 1. distance measures of the replicated vibration velocities of the avatars

	HAUSDORFF distance		**MAHALANOBIS distance**	
avatar	SAMSARA	SIMSALABIM	SAMSARA	SIMSALABIM
a1	62.29	62.29	0.035	0.034
a2	243.40	243.40	0.032	0.033
a3	44.94	44.94	0.010	0.010

4 CONCLUSIONS

The similitude analysis methods SAMSARA and SIMSALABIM replicate the vibration velocities of the avatars a1 through a3 in the same manner. Future research will investigate the limits of application based on the HAUSDORFF distance and the MAHALANOBIS distance. This will require further FE analyses, where the rectangular plates are distorted to a higher extent than those in this paper. Furthermore, the limits of application also need to be validated by means of experimental investigations on distorted rectangular plates.

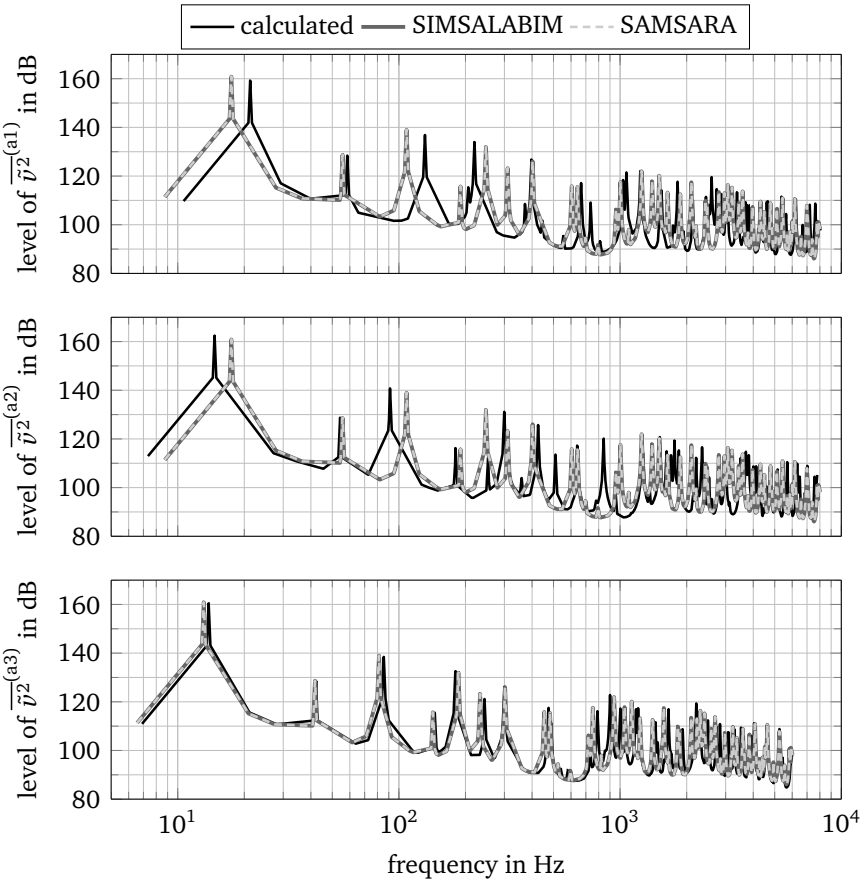

Figure 1. levels of the mean squared RMS velocity versus frequency (re $5 \cdot 10^{-8}\,\mathrm{m\,s^{-1}}$)

REFERENCES

[1] A. Casaburo, G. Petrone, F. Franco, and S. De Rosa. A review of similitude methods for structural engineering. *Applied Mechanics Reviews*, 71(3):030802 (32 pages), 2019.

[2] V. Meruane, S. De Rosa, and F. Franco. Numerical and experimental results for the frequency response of plates in similitude. *Proceedings of the Institution of Mechanical Engineers, Part C: Journal of Mechanical Engineering Science*, 230(18):3212–3221, 2016.

[3] C. Adams. *Similitudes and sensitivities as contributions to scaling laws in machine acoustics*. PhD thesis, Technische Universität Darmstadt, Darmstadt, Germany, 2019.

[4] S. De Rosa, F. Franco, and V. Meruane. Similitudes for the structural response of flexural plates. *Proceedings of the Institution of Mechanical Engineers, Part C: Journal of Mechanical Engineering Science*, 230(2):174–188, 2016.

[5] C. Adams, J. Bös, E.M. Slomski, and T. Melz. Scaling laws obtained from a sensitivity analysis and applied to thin vibrating structures. *Mechanical Systems and Signal Processing*, 110:590–610, 2018.

[6] C. Adams, J. Bös, and T. Melz. Assessing the similitude of vibrating plates. In *23rd International Congress on Acoustics ICA*, Aachen, Germany, September 09–13, 2019.

[7] D.P. Huttenlocher, G.A. Klanderman, and W.J. Rucklidge. Comparing images using the Hausdorff distance. *IEEE Transactions on Pattern Analysis and Machine Intelligence*, 15(9):850–863, 1993.

[8] P.C. Mahalanobis. On the generalized distance in statistics. *Proceedings of the National Institute of Sciences of India*, 2(1):49–55, 1936.

SIMULATION-BASED HEALTH MONITORING OF A COMPOSITE SANDWICH STRUCTURE USING CONVOLUTIONAL NEURAL NETWORK

Z. Liu[1*], M. Ardabilian[2], M. Ichchou[1] and A. Zine[3]

[1]Laboratory of Tribology and Systems Dynamics
École Centrale de Lyon, 36 Av. Guy de Collongue, Écully, FRANCE
Email: zeyu.liu@ec-lyon.fr, mohamed.ichchou@ec-lyon.fr

[2]Computer Science Laboratory for Image Processing and Information Systems
École Centrale de Lyon, 36 Av. Guy de Collongue, Écully, FRANCE
Email: mohsen.ardabilian@ec-lyon.fr

[3]Institut Camille Jordan
École Centrale de Lyon, 36 Av. Guy de Collongue, Écully, FRANCE
Email: abdel-malek.zine@ec-lyon.fr

ABSTRACT

Efficient and reliable Structural Health Monitoring (SHM) systems are required for structural damage detection of composite materials used in aeronautic and aerospace domains. In this work, a simulation-based health monitoring of a composite sandwich structure using convolutional neural networks (CNN) is reported. The goal of the study is to predict and localize crack-type damages in composite sandwich plates. A squared plate constituted of two thin composite faces in carbon/epoxy and a thick honeycomb core in Nomex is modelled by commercial software. Cracks are designed through the core and the top face sheet by disconnecting local nodes and the dimension of cracks is properly chosen so that the interaction of the propagated signal with the damage is detectable. Excitation pulse signals are applied on the actuator on one corner of the plate surface to stimulate vertical displacement. Raw vibration response signals are collected from three sensors located at other corners and are then transformed into 2D images by continuous wavelet transform, which are used as input to the CNN for training and test of the network. The proposed method is proven to be able to detect and localize crack damages in composite sandwich plates with an acceptable accuracy.

1 INTRODUCTION

Advanced composite materials have been widely used in different areas, including aerospace, medicine, machinery, construction and other industries due to the characteristics of light weight, good ductility, corrosion resistance, heat insulation, sound insulation, shock absorption and high (low) temperature resistance, etc. These features typically meet the material requirements in specific working environments. In civil aviation, aircraft weight reduction means less fuel is consumed and more cargo can be loaded, resulting in considerable profits and more environmentally friendly transport form. It is estimated that one ton of saved mass translates into a saving of 6,000 tons of kerosene over the lifetime of an aircraft [1]. Considering that under proper maintenance an aircraft can be used for more than 20 years. Even if the aircraft weight reduction is 1%, the profit can be considerable. However, due to the synthesis method of composite materials, they are susceptible to several structural damages, such as fiber fracture, matrix crack and delamination. These damages are usually caused by fatigue and impact events. In the early stage of the damages, they are very small and barely visible to visual inspections, but they could further lead to disasters, especially for aircrafts, causing huge loss of people lives and money. As a result, the development of *Structural Health Monitoring* (**SHM**) systems has been considerable concerns in the last 2 decades.

The definition of Structural Health Monitoring is given by D. Balageas et al. [2]: SHM aims to give, at every moment during the life of a structure, a diagnosis of the ”state” of the constituent materials, of different parts, and of the full assembly of these parts constituting the structure as a whole. A general process of SHM involves collecting relevant data, which is the structure response, from an array of sensors attached on the structure. Then necessary signal processing is carried out for the purpose of data reduction and key feature extraction from these measurements. Finally, the healthy state of the structure is determined by statistical analysis of these features.

In SHM, two of Nondestructive Testing (NDT) methods, vibration-based technique and guided wave-based technique have been developed for the extraction of damage-sensitive information about the health state of structures. They are the most commonly used among others. NDT methods have been successfully applied in SHM for honeycomb sandwich beams [3], composite sandwich plate [4], concrete plate and steel plate [5, 6], and railway bridges [7]. To have a higher accuracy in damage detection, combination of vibration-based and guided wave-based approaches was proposed by Maciej Radzienski et al. [8].

However, the limitations of these methods are obvious: firstly, they are time-consuming and labor-intensive. Secondly, there will be high requirements of expertise for practitioners, especially for complex structures, which is not always available. With the development of Artificial Intelligence (AI) in the last two decades, especially deep learning, the problems encountered in the traditional approaches have been solved. Deep learning approaches are increasingly applied in SHM in various engineering sections including bearings, rotating machines, bridges, steel frames, etc. To the authors' knowledge, although there are some related studies of SHM for composite materials, the research in this area is very scarce, and there is no attempt to apply deep learning in SHM for composite sandwich structures. In this work, a simulation-based health monitoring of a composite sandwich structure using convolutional neural networks (CNN) is reported. The goal of the study is to predict and localize crack-type damages in composite sandwich plates.

2 METHOD AND RESULTS

Convolutional Neural Networks (CNN) is a powerful deep learning algorithm in computer vision which is commonly used in image classification, face recognition, video analysis, etc. In

CNN-based SHM system, feature extraction and classification are combined in one computation body, which improves the efficiency and reliability of the learning process. A CNN interprets an input as hierarchical representations by learning features in a series of hidden layers. In CNN, there are basically three types of layers: Convolution layer, Pooling layer and Fully connected layer, as shown in Figure 1. The convolution layer is used to extract low-level and high-level features; the pooling layer is used to reduce size and speed up computation; the final fully connected layer is used for classification.

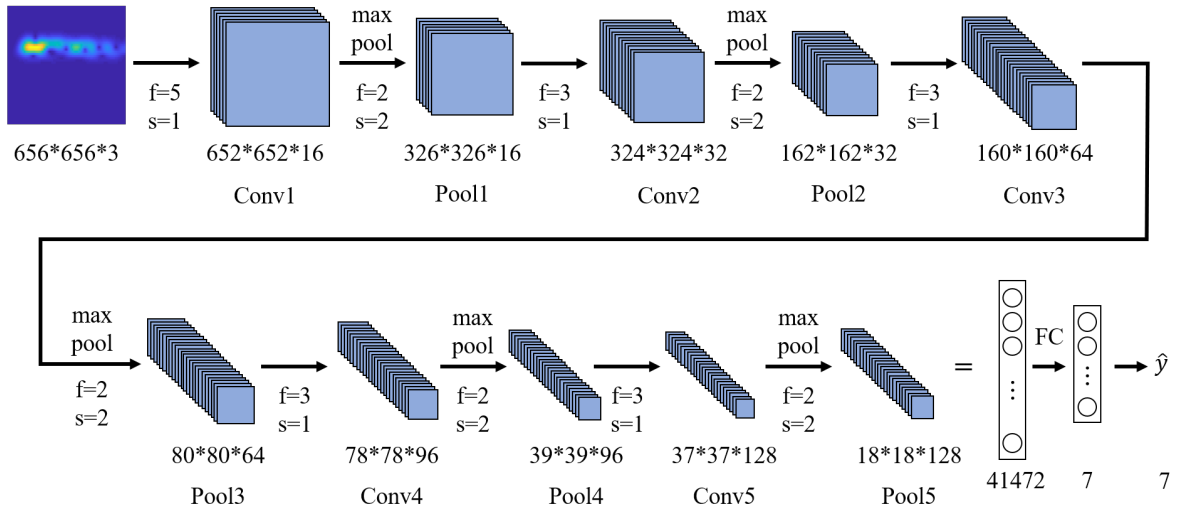

Figure 1. Architecture of the proposed CNN.

In the present study, a honeycomb sandwich plate consisting of a honeycomb core and two skin plates is constructed in commercial software ANSYS®. Crack damage is designed through the core and the top face sheet in the sandwich structure and investigation of the capability of detecting this kind of damage is conducted. 6 cracked models are constructed within each the damage locates at different positions. Random pulse excitation signals with 7 cycles are applied to the pristine and 6 cracked cases of composite sandwich plates to stimulate vertical displacement. Transient analysis is performed. Damping coefficients are set as follows: matrix multiplier is set as $\alpha = 0$ and stiffness matrix multiplier as $\beta = 6.37 \times 10^{-7}$. The calculation time is set as 0.01s, which is long enough for the wave to propagate through the whole plate. The sampling frequency f_s should be no less than 2 times the signal frequency f according to the Nyquist's rule. Raw 1 dimensional vibration response signals are collected and pre-processed by continuous wavelet transform (CWT) into 2 dimensional images containing both time and frequency information, which in turn are fed into CNN for training and test.

The filters and bias are randomly initialized. Stochastic gradient descent with momentum (SGDM) optimizer and Adam optimizer are adopted respectively. The models are trained with a mini-batch size of 32. The effect of initial learning rate, input size as well as training epochs on the classification accuracy are investigated. The architecture of the proposed CNN model is shown in Figure 1. Results show that the model with Adam optimizer, input size of 656*656*3, mini-batch size 32, initial learning rate $10^{-}5$, and training epochs 28 achieves a classification accuracy 95.47%, which is acceptable and is better than others.

3 PERSPECTIVES

The proposed CNN-based structural health monitoring approach achieves an acceptable classification accuracy for damage detection of a composite sandwich plate. The work could be further improved in these aspects:

- Interpretation of the inputs.
- Improvement of the CNN architecture:hidden layer numbers, filter numbers in each layer, filter size, etc.
- Determination of the sensitivity of the proposed method

ACKNOWLEDGEMENT

Z. Liu is a PhD student supported by China Scholarship Council.

REFERENCES

[1] R. Courteau. Sur les perspectives d'évolution de l'aviation civile à l'horizon 2040 : préserver l'avance de la france et de l'europe. `http://www.senat.fr/rap/r12-658/r12-65815.html#toc224`, 2013.

[2] D. Balageas, C.P. Fritzen, and A. Güemes. *Structural health monitoring*, volume 90. John Wiley & Sons, 2010.

[3] K. Zhu, M. Chen, Q. Lu, B. Wang, and D. Fang. Debonding detection of honeycomb sandwich structures using frequency response functions. *Journal of Sound and Vibration*, 333(21):5299 – 5311, 2014.

[4] A. Katunin. Vibration-based spatial damage identification in honeycomb-core sandwich composite structures using wavelet analysis. *Composite Structures*, 118:385 – 391, 2014.

[5] C.R. Farrar, S.W. Doebling, and D.A. Nix. Vibration-based structural damage identification. *Philosophical Transactions of the Royal Society of London A.*, 359(1778):131–149, 2001.

[6] W.L. Bayissa, N. Haritos, and S. Thelandersson. Vibration-based structural damage identification using wavelet transform. *Mechanical Systems and Signal Processing*, 22(5):1194 – 1215, 2008.

[7] E.K. Chalouhi, I. Gonzalez, C. Gentile, and R. Karoumi. Vibration-based shm of railway bridges using machine learning: The influence of temperature on the health prediction. In *International Conference on Experimental Vibration Analysis for Civil Engineering Structures*, pages 200–211. Springer, 2017.

[8] M. Radzienski, M Cao, X Wei, P Kudela, and W Ostachowicz. Combined vibration and guided wave-based approach for composite panels health assessment. In Tribikram Kundu, editor, *Health Monitoring of Structural and Biological Systems 2017*, volume 10170, pages 499 – 506. International Society for Optics and Photonics, SPIE, 2017.

WAVE REFLECTION AND TRANSMISSION ANALYSIS THROUGH COMPLEX ROD BASED ON SECOND STRAIN GRADIENT THEORY

G. Zhu[1], M.Ichchou[1*], A. Zine[2] and C. Droz[1]

[1]Vibroacoustics & Complex Media Research Group, LTDS - CNRS UMR 5513, Centre Lyonnais d'Acoustique CeLyA
École Centrale de Lyon, Université de Lyon, France
Email: guang.zhu@ec-lyon.fr, mohamed.ichchou@ec-lyon.fr

[2]Institute Camille Jordan – CNRS UMR 5208
École Centrale de Lyon, Université de Lyon, France
Email: abdel-malek.zine@ec-lyon.fr

ABSTRACT

Complex media is widely used in many industries. Typical examples include composite structure applied in aerospace, automotive industries and civil engineering. Co-dynamic behavior of multi-scale characters can be observed in complex media especially when the deformation wavelength is comparable with its internal characteristic size. In previous work of this research, multi-scale modelling of complex rod has been established with employing Mindlin's Second Strain Gradient theory. Wave propagation behavior in complex rod has been discovered to be significantly different. In the presented work, longitudinal wave transmission through a certain length of complex rod is investigated. Equilibrium on the interface between homogeneous rod and complex rod is developed based on force and higher order forces equilibrium as well as the continuity of displacement. According to the form of transfer matrix, transmission and reflection coefficients are highly dependent on all the material constants of the complex rod, wave propagation length and frequency. In the numerical calculation, transmission coefficient can approach to '0' or to '1' in some frequency range with some predefined material constants. The presented work is instructive in design of complex media and also in identify an equivalent model to classical homogeneous rod with ability of capturing the multi-scale behavior.

1 INTRODUCTION

Complex media consists of numerous small-sized heterogeneous components. In structural vibration, dynamic behavior will co-exist at both the macro-scale of the whole structure and the micro-scale of each heterogeneous components. Under some frequency, the co-dynamic behavior of multi-scale characters plays a major role in governing the material properties.

To capture local behavior of heterogeneity and describe the co-dynamics of multi-scale characters, one solution is enriching the classical theory with the micro-structure details explicitly included in the constitutive equation. This theory is know as 'generalized continuum theory'. Generalized continuum theory can be cataloged into 3 different branches namely the higher order theory, the higher gradient theory, and non-local elasticity theories. The basic idea of the generalized continuum theory is to establish a relationship between macroscopic mechanical quantities and microscope physical quantities within the framework of continuum mechanics by enriching the conventional elasticity theory with internal length, which can characterize the underlying microstructure from the constitutive equations.

Generalized continuum elasticity theory based modelling has been successfully applied by many researchers in complex media analysis. Among the others, Joseph et al. [1] established an enriched beam model based on strain gradient theory [1] to study the large deflections and fracture behavior of double cantilever beam. Tsiatas [2] and Thai [3] developed non-classical Kirchhoff plate model and Mindlin plate model based on Modified couple stress theory to investigate nonlinear deformation of bending, buckling, and vibration responses of micro-plates. Recent work by Suiker et al. [4] predicted dispersive body waves based on the proposed second-gradient micro-polar formulation. Wave propagation characteristics are also investigated by Gopalakrishnan [5] using the Erigen's stress gradient model and Mindlin's strain gradient model with atomistic length scale parameters brought into the continuum governing equations. These scale parameter are proven to significantly affect the wave propagation referring to the dispersion relation the escape frequency, phase speeds and group speeds in the structures. Placidi et al. [6] studied reflection and transmission of compression and shear wave in second-gradient continua. They noticed that the effect of the second-gradient parameter are important for the reflection and transmission coefficients at surfaces of discontinuity. Dell'Isola et al. [7] deduced the mechanical energy equilibrium for second gradient material, based on which they estimated that the reflection and transmission coefficients at plane displacement discontinuity surfaces are significantly frequency-dependent. Li et al.[8, 9] predicted that the reflection and transmission coefficients at the interface of two generalized medias are not only dependent of the micro-structure's parameters, but also of the incident angular frequency. This phenomenon only becomes pronounced when the incident wavelength is close to the characteristic length of the micro-structure.

The 'Second Strain Gradient theory' (SSG theory) is proposed by Mindlin [10] in 1965 with introducing the second and third derivatives of the displacement into the strain energy density along with the classical strain tensor. SSG theory based rod model has been developed to investigate its wave propagation features. In the presented work, reflection and transmission of longitudinal wave through a certain length of complex media analyzed with the SSG theory based on the rod model. Reflection of transmission coefficients are calculated. The influence of local behavior of heterogeneity is discussed with comparing the results from SSG theory model and classical theory model, some potential applications of complex media are introduced.

2 TRANSMISSION OF LONGITUDINAL WAVE THROUGH COMPLEX MEDIA

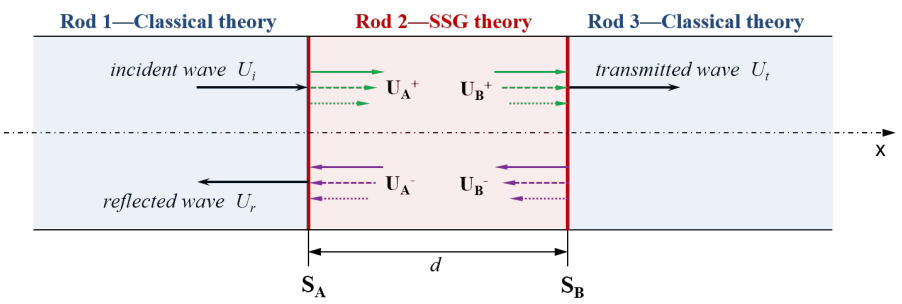

Figure 1: Reflection and transmission of longitudinal wave through SSG theory media

As shown in figure 1, longitudinal wave U_i normally inject on interface $\mathrm{S_A}$, part of the incident energy is reflected, and the remaining energy is transmitted to rod 2. Assuming the longitudinal wave in rod 1 and rod 3 is k_c, the incident wave with amplitude of "1" can be expressed as $U_i = e^{i(\omega t - k_c x)}$. Based on the previous research, 3 wave modes can be generated by the disturbance in SSG theory based rod: non-classical longitudinal wave k_1 and two evanescent waves k_2, k_3. State vector $\mathbf{X}$ is defined with including all the kinetic parameters and force components in SSG theory media. The state vector on the right hand of the studied interface $\mathrm{S_A}$ can be given as

$$\mathbf{X}_A{}^+ = \left[u_A{}^+, \frac{\partial u_A{}^+}{\partial x}, \frac{\partial^2 u_A{}^+}{\partial x^2}, P_0, P_1, P_2\right]^{\mathrm{T}}_{\mathrm{S=S_A}^+}.$$

All the components can be expressed in forms of wave superposition. Then we can achieve the state vector in form of

$$\mathbf{X}_A{}^+ = \mathbf{M}_A \cdot \mathbf{U}_A \tag{1}$$

in which $\mathbf{U}_A$ represents the vector consist of all modes, and $\mathbf{M}_A$ represents the coefficient matrix. Similarly, the state vector on the left hand of the studied interface $\mathrm{S_B}$ can be given as

$$\mathbf{X}_B{}^- = \mathbf{M}_B \cdot \mathbf{U}_B = \mathbf{M}_A \cdot \mathrm{diag}\left(e^{-ik_1 d}, e^{ik_1 d}, e^{-ik_2 d}, e^{ik_2 d}, e^{-ik_3 d}, e^{-ik_3 d}\right) \cdot \mathbf{U}_A \tag{2}$$

Comparing expression (1) and (2), we can have

$$\mathbf{X}_B^- = \mathbf{M} \cdot \mathbf{X}_A{}^+ \tag{3}$$

in which transfer matrix $\mathbf{M} = \mathbf{M}_A \cdot \mathrm{diag}\left(e^{-ik_1 d}, e^{ik_1 d}, e^{-ik_2 d}, e^{ik_2 d}, e^{-ik_3 d}, e^{-ik_3 d}\right) \cdot \mathbf{M}_A{}^{-1}$. For certain kinds of materials and propagation distance d, transfer matrix $\mathbf{M}$ can be determined.

Assuming the transmission coefficient is C_t and the reflection coefficient is C_r, the state vectors on the left hand of section $\mathrm{S_A}$ and right hand of section $\mathrm{S_B}$ in classical media can also be expressed out. If the interface does not dissipate energy, $\mathbf{X}_B^- = \mathbf{X}_B^+$ and $\mathbf{X}_A^+ = \mathbf{X}_A^-$. Then

$$\mathbf{X}_B^+ = \begin{bmatrix} C_t e^{-ik_c d} \\ u'^+_B \\ u''^+_B \\ -ik_c C_t E_1 A e^{-ik_c d} \\ 0 \\ 0 \end{bmatrix} = \mathbf{M} \cdot \begin{bmatrix} 1+C_r \\ u'^-_A \\ u''^-_A \\ -ik_c E_1 A + ik_c C_r E_1 A \\ 0 \\ 0 \end{bmatrix} = \mathbf{M} \cdot \mathbf{X}_A{}^-, \tag{4}$$

The six unknown variables including C_t and C_r can be achieved with the six equation in (4).

3 RESULTS AND DISCUSSION

Material of the rod 1 and rod 3 is classical aluminum. Material of rod 2 is set to be complex media with the different Young's modulus, mass density along with the higher order constants. Some cases with predefined material constants and and length d are implemented as follows

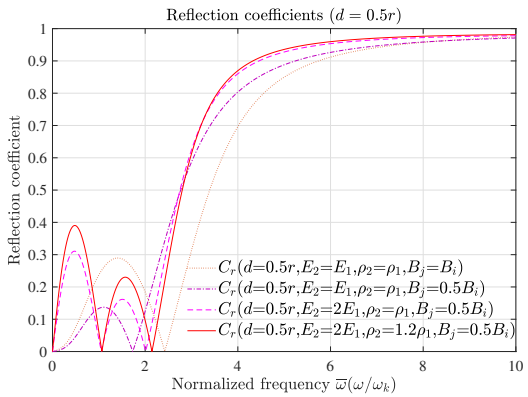

(a) Transmission coefficients

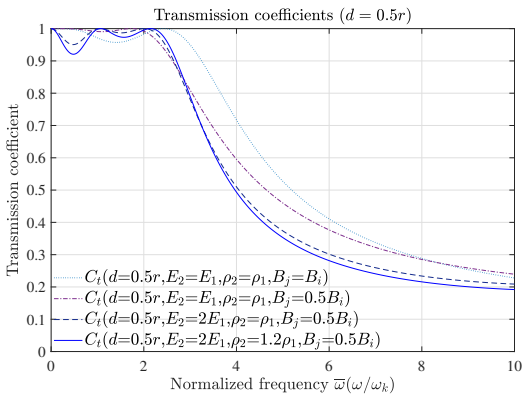

(b) Reflection coefficients

Figure 2: Transmission and reflection coefficients

Figure 2 displays the transmission and reflection coefficients changing with material constants when $d = 0.5r$. As we can see, reflection coefficient C_r can approach 0 extremely in some frequency range with some predefined Young's modulus, density and higher order material constants. In that frequency range, all the input energy will be reflected and the transmitted energy is close to zero.

4 CONCLUSIONS AND PERSPECTIVES

Wave reflection and transmission through SSG theory based rod is highly dependent on the properties and the length of SSG based media d. With some predefined Young's modulus, density and higher order material constants, all the input energy can be reflected while the transmitted energy is close to zero in some frequency range, thus the predefined SSG theory based media can show great seismic isolation performance. This research can be a start of optimizing structural performance in acoustics with enriching the internal micro-structures by generalized theory based modelling method.

ACKNOWLEDGEMENTS

This work was supported by the LabEx CeLyA (Centre Lyonnais d'Acoustique, ANR-10-LABX-0060) of Université de Lyon. Guang ZHU thanks a scholarship provided by the China Scholarship Council.

REFERENCES

[1] R. P. Joseph et al. Size effects on double cantilever beam fracture mechanics specimen based on strain gradient theory. *Engineering Fracture Mechanics*, 169:309 – 320, 2017.

[2] G.C. Tsiatas. A new kirchhoff plate model based on a modified couple stress theory. *International Journal of Solids and Structures*, 46(13):2757 – 2764, 2009.

[3] Huu Tai Thai and Dong Ho Choi. Size-dependent functionally graded kirchhoff and mindlin plate models based on a modified couple stress theory. *Composite Structures*, 95:142 – 153, 2013.

[4] A. S. J. Suiker et al. Micro-mechanical modelling of granular material. part 2: Plane wave propagation in infinite media. *Acta Mechanica*, 149(1):181–200, Mar 2001.

[5] S. Gopalakrishnan. Propagation of elastic waves in nanostructures. In *Nanosensors, Biosensors, and Info-Tech Sensors and Systems 2016*, volume 9802, page 98020N, 2016.

[6] Luca Placidi et al. Reflection and transmission of plane waves at surfaces carrying material properties and embedded in second-gradient materials. *Mathematics and Mechanics of Solids*, 19(5):555–578, 2014.

[7] Francesco Dell'Isola et al. Linear plane wave propagation and normal transmission and reflection at discontinuity surfaces in second gradient 3d continua. *Journal of Applied Mathematics and Mechanics / Zeitschrift für Angewandte Mathematik und Mechanik*, 92(1):52–71, January 2012.

[8] Y. Li and P. Wei. Reflection and transmission of thermo-elastic waves without energy dissipation at the interface of two dipolar gradient elastic solids. *Journal of the Acoustical Society of America*, 143(1):550–562, 2018.

[9] Y. Li et al. Reflection and transmission of elastic waves at the interface between two gradient-elastic solids with surface energy. *European Journal of Mechanics, A/Solids*, 52:54–71, 2015. cited By 7.

[10] R. D. Mindlin. Second gradient of strain and surface-tension in linear elasticity. *International Journal of Solids and Structures*, 1(4):417 – 438, 1965.

ANALYSIS OF SOUND RADIATION FROM COMPLEX TIMOSHENKO BEAM BASED ON SECOND STRAIN GRADIENT THEORY

G. Zhu[1] ,M. Ichchou[1*] and A. Zine[2]

[1]Vibroacoustics & Complex Media Research Group, LTDS - CNRS UMR 5513, Centre Lyonnais d'Acoustique CeLyA
École Centrale de Lyon, Université de Lyon, France
Email: guang.zhu@ec-lyon.fr, mohamed.ichchou@ec-lyon.fr

[2]Institute Camille Jordan – CNRS UMR 5208
École Centrale de Lyon, Université de Lyon, France
Email: abdel-malek.zine@ec-lyon.fr

ABSTRACT

Complex media is one kind of media in which local behavior and global behavior can be observed conjointly. Co-dynamic behavior of multi-scale characters is prominent in complex media especially when the external wavelength is comparable with its characteristic size of heterogeneous features. In previous work of this research, multi-scale modelling of complex Timoshenko has been established with employing Mindlin's Second Strain Gradient (SSG) theory. Dynamic behavior and wave propagation features of complex Timoshenko beam has been discovered to be significantly different. In the presented work, sound radiation from infinite complex Timoshenko beam is investigated with the established SSG theory model. The investigation is in terms of normal square velocity, radiation impedance and radiated pressure field. Then sound radiation from simple supported complex Timoshenko beam into an infinitely extended fluid domain is analyzed based on the principle of superposition and Kirchhoff–Helmholtz integral equation. The resulting radiation pressure field of complex Timoshenko beam are illustrated and well interpreted by comparing the SSG theory model result and classical theory result. Upon which, impact of local behavior in complex media to the structural radiation features is discussed.

1 INTRODUCTION

Complex media is defined as one kind of media with multi-scale characters in which local behavior and global behavior can be observed conjointly. Complex media are used in many industry field, typical examples include the steel prefabricated truss structures in construction engineering, the ribbed structure in automobiles and aircraft, advanced periodic composite in aerospace industry and nano-structures in MENS and NENS. Originating from its heterogeneous or periodic distributed components with contrast properties, these complex medias are lighter in weight, and acquire great performance in mechanics. In the meantime, the modelling of complex media becomes increasingly difficult with heterogeneous features between its micro-structures.

When the size of major heterogeneity is much smaller than the representative volume, this media can be treated as homogeneous media. Otherwise, the classical continuum theory does not apply anymore [1]. In this case, many other analyzing approaches have been developed, such as the experimental investigation, wave finite element method, homogenization method. They all has their own limitations and most importantly, these methods cannot include the the co-dynamic behavior of multi-scale characters in complex media, which becomes prominent when the external wavelength is comparable with its characteristic size of heterogeneous features.

Generalized continuum theory has been developed in recent years. In generalized continuum theory, the local behavior of heterogeneity caused by long-range interactions can by described by inserting length scale parameters. Generalized continuum elasticity theory based modelling has been applied by many researchers in complex media analysis in short wave limit. Among the others, Joseph et al. [2] established an enriched beam model based on strain gradient theory [2] to study the large deflections and fracture behavior of double cantilever beam. Nonlocal differential constitutive relation of Eringen has been employed by Reddy et al. [3, 4] to reformulate various beam theories and investigate the effect of the nonlocal behavior on deflections, buckling loads, and natural frequencies. Tsiatas [5] and Thai [6] developed non-classical Kirchhoff plate model and Mindlin plate model based on Modified couple stress theory to investigate nonlinear deformation of bending, buckling, and vibration responses of micro-plates. Second Strain Gradient (SSG) theory based Timoshenko beam model has been established by Asghari [7] to study its static and free-vibration behaviors, and to capturing the size effects in micro- and nano-scale structures. One can also cite the SSG theory based modelling by Momeni [8]) for functionally graded beam structures (FGMs).

The 'Second Strain Gradient theory' (SSG theory) is proposed by Mindlin [9] with introducing the second and third derivatives of the displacement along with the classical strain tensor into the strain energy density. Compared with other strain gradient theories, Mindlin's SSG theory is more general thus more effective in local behavior description. SSG theory based Timoshenko beam model has been developed to investigate its wave propagation and transmission features. In the presented work, sound radiation from an infinite complex beam is analyzed with the SSG theory based on the Timoshenko beam model. Radiation impedance and radiated pressure field from complex beam is calculated. The impact of local behavior of heterogeneity is discussed with comparing the results from SSG theory model and classical theory model.

2 SOUND RADIATION FROM INFINITE COMPLEX TIMOSHENKO BEAM

The studied structure-fluid system is illustrated as in Figure 1. The vibrating beam subject to a transverse harmonic force $F = \mathrm{Re}\left\{q_0 e^{i\omega t}\right\}$ at $x = 0$ is assumed to be infinitely extended along x direction, and the waves generated by the vibrating surface Ω_Σ in the fluid domain Ω_f will propagate away from the source at speed c_0.

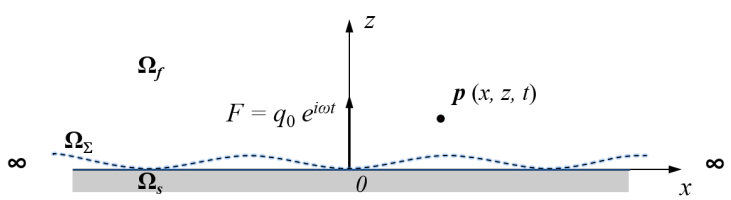

Figure 1: sound radiation from infinite Timoshenko beam

In studied system, the vibration is uniform along y direction, so will the acoustic pressure field. Then the two-dimensional acoustic wave motion equation governing the propagation of small acoustic disturbances through a homogeneous, inviscid, isotropic, compressible fluid can be written in terms of the variation of pressure about the equilibrium pressure as

$$\frac{\partial^2 p}{\partial x^2} + \frac{\partial^2 p}{\partial z^2} = -\left(\frac{\omega}{c_0}\right)^2 p = -k_0^2 p, \tag{1}$$

where p is the radiated acoustic pressure in the field. c_0 represents the frequency-independent speed of sound govern by fluid medium, $k_0 = \dfrac{\omega}{c_0}$. According to the SSG theory based formulation, the total transverse velocity of the vibrating surface in region $[0, +\infty)$ can be expressed in forms of the superposition of the contributions from all six positive wave modes as,

$$v_n(x,t) = i\omega \cdot w(x,t) = i\omega \cdot \left(\sum_{j=1}^{6} \mathcal{A}_j e^{-ik_j x}\right) \cdot e^{i\omega t} \tag{2}$$

Generated by the harmonic acceleration disturbance at the structure-fluid interface, the solution of the radiated acoustic pressure may also be expressed by the superposition of six acoustic pressure fields to physically represent the sound radiation from all the six wave modes generated by the source as,

$$p(x,z,t) = \left(\sum_{j=1}^{6} \mathcal{R}_j \cdot e^{-i\left(k_{x_j} x + k_{z_j} z\right)}\right) \cdot e^{i\omega t}, \tag{3}$$

in which k_{x_j} and k_{z_j} represent the component of wavevector $\mathbf{k}_j$ in x and z direction generated by elastic wave k_j in the solid. In deriving the wave equation, linearised form of Euler momentum equations are used as

$$\nabla \mathbf{p} + \rho_0 \frac{\partial \dot{\mathbf{u}}}{\partial t} = 0. \tag{4}$$

in which $\nabla \mathbf{p}$, $\dot{\mathbf{u}}$ respectively denote the pressure gradient and particle velocity vector, and ρ_0 is the mean density of fluid medium. With the above Eqs. (1), (2), (3) and (4), the radiated wave vectors and the corresponding amplitudes can be obtained.

3 RESULTS AND DISCUSSION

One numerical case is implemented in this section. The cross section of the studied beam is considered to be rectangular with width $b = 3h$ and height of the section $h = 10a_0$, with the lattice parameter $a_0 = 4.04$Å. The material is assumed to be aluminum with $\mu = 26\,\mathrm{GPa}$. The higher-order material constant values refers to the work by Shodja et al. (2012) [10] which are obtained with atomistic approach. The resulting acoustic pressure is shown as.

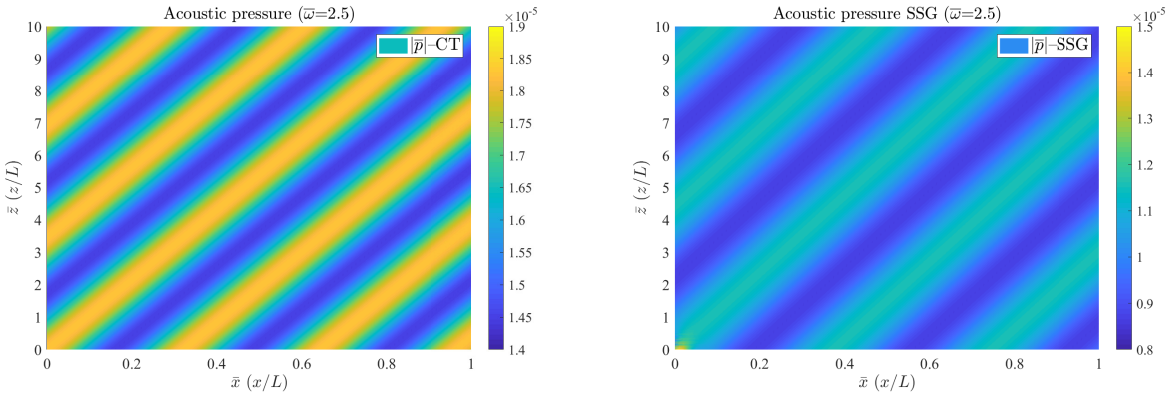

(a) Acoustic pressure of classical theory (b) Acoustic pressure of SSG theory

Figure 2: Acoustic pressure field in $x - z$ plane

Figure 2 illustrates the acoustic pressure field resulting from classical model and SSG theory-based mode on frequency ($\overline{\omega}$ = 2.5). Radiation pressure field of complex beam resulting from SSG theory model shows great differences with radiation of classical beam as the pressure variation amplitude resulting from SSG theory model is lower than the classical one. In higher frequency, wavelength is more comparable with the length of inner micro-structures, therefore the resulting influence is prominent. Moreover, the highest pressure can be observed near the force input source. Then the high pressure decrease rapidly with some slight fluctuation in the near field.

4 CONCLUSIONS AND PERSPECTIVES

Radiated pressure resulting from SSG theory model decrease distinctly in the far radiation field in high frequency. Another interesting phenomenon is that radiated pressure field decreases with fluctuation in the near field of force excitation. This phenomenon is caused by decay of short waves in fluid domain, which are generated by evanescent waves in complex structure. The underlying physics lies in the distinct local behavior of heterogeneity governed by both near range and long range interactions. For future investigation, radiation from finite complex structures can be developed.

ACKNOWLEDGEMENTS

This work was supported by the LabEx CeLyA (Centre Lyonnais d'Acoustique, ANR-10-LABX-0060) of Université de Lyon. Guang ZHU thanks a scholarship provided by the China Scholarship Council.

REFERENCES

[1] M. Jirásek. Nonlocal theories in continuum mechanics. *Acta Polytechnica*, 44(5):16 – 34, 2004.

[2] R. P. Joseph et al. Size effects on double cantilever beam fracture mechanics specimen based on strain gradient theory. *Engineering Fracture Mechanics*, 169:309 – 320, 2017.

[3] J.N. Reddy. Nonlocal theories for bending, buckling and vibration of beams. *International Journal of Engineering Science*, 45(2-8):288–307, 2007.

[4] J. N. Reddy and S. D. Pang. Nonlocal continuum theories of beams for the analysis of carbon nanotubes. *Journal of Applied Physics*, 103(2):023511, 2008.

[5] G.C. Tsiatas. A new kirchhoff plate model based on a modified couple stress theory. *International Journal of Solids and Structures*, 46(13):2757 – 2764, 2009.

[6] Huu Tai Thai and Dong Ho Choi. Size-dependent functionally graded kirchhoff and mindlin plate models based on a modified couple stress theory. *Composite Structures*, 95:142 – 153, 2013.

[7] M. Asghari et al. The second strain gradient theory-based timoshenko beam model. *Journal of Vibration and Control*, 23(13):2155–2166, 2017.

[8] S.A. Momeni and M. Asghari. The second strain gradient functionally graded beam formulation. *Composite Structures*, 188:15 – 24, 2018.

[9] R. D. Mindlin. Second gradient of strain and surface-tension in linear elasticity. *International Journal of Solids and Structures*, 1(4):417 – 438, 1965.

[10] M. Shodja et al. Calculation of the additional constants for fcc materials in second strain gradient elasticity: Behavior of a nano-size bernoulli-euler beam with surface effects. *Journal of Applied Mechanics*, 79(2):1008–1016, 3 2012.

REAL-TIME TUNING OF STIFFNESS AND DAMPING PROPERTIES OF LAMINATE COMPOSITES

M. Ouisse[1], P. Butaud[1], D. Renault[1], B. Verdin[1], G. Chevallier[1]

Univ. Bourgogne Franche-Comté, FEMTO-ST Institute, CNRS/UFC/ENSMM/UTBM,
Department of Applied Mechanics, 24 rue de l'épitaphe, 25000 Besançon, France

ABSTRACT

In this paper, a laminate composite structure is designed with real-time stiffness and damping tuning capabilities. It is composed of 3 layers: a base steal layer which provides the global stiffness, a viscoelastic core whose properties are tuned in real time through conductive tracks which are printed on the top glass-fibre composite skin. The temperature dependency of the viscoelastic core is used as physical mechanism to tune the global stiffness and damping properties of the composite structure. Moreover, in order to realize a compromise between static stiffness and dynamic damping, some zones are defined on the wing. This provides the ability to locally change the temperature to reach the expected compromise. In the talk, the design issues are addressed, and an experimental demonstration of the concept is presented on a complex structure.

1 INTRODUCTION

Viscoelastic materials [1, 2] are widely used to control the vibration levels in composite structures [3]. Many research papers on the optimization of the design of multilayered composites for vibration control can be found in open literature [4, 6–8]: the common objective lies in the reduction of the vibration levels by adjusting the shear effect in the core layer according to the geometry, materials, boundary conditions and external forces acting on the structure. In this work, shape memory polymers are used as viscoelastic materials as they exhibit high damping capabilities at glass transition [9, 10], and the concept takes advantage of the temperature and frequency dependency of the viscoelastic properties [1, 12] to provide the tuning ability to the composite structure. It is inspired by the works presented in [10, 13–15] so that specific stiffness and damping can be obtained in real time.

2 A SANDWICH CORE WITH TUNING CAPABILITIES

The structure which is presented here is a reduced-scale airplane whose wings are made of the composite sandwich structure. A stainless steel base layer is used to confer a global stiffness to the wing. Then, a tBA/PEGDMA is used as core material. This shape memory polymer has been characterized in [16] and a the model which is used here has been described in [10]. Finally, the top layer is a FR4 plate (glass-fibre epoxy composite) on which conductive tracks are printed and used as heating devices by Joule effect.

3 ZONING FOR LOCAL CONTROL OF STIFFNESS AND DAMPING

Global heating of the composite structure may be used to tune the damping or the stiffness [10, 14, 15], but it results in coupled effect since the glass transition of the polymer layer acts on both damping and stiffness of the material. The concept of zoning [13] is used here to locally act on the mechanical properties and provide a set of configurations corresponding to various stiffness/damping combinations that cannot be achieved by global effects. In the work presented here, 6 zones are defined on each wing, each being controlled independently, and an algorithm is used to build Pareto-optimal solutions for static stiffness and damping characteristics of the composite structure.

4 EXPERIMENTAL SETUP

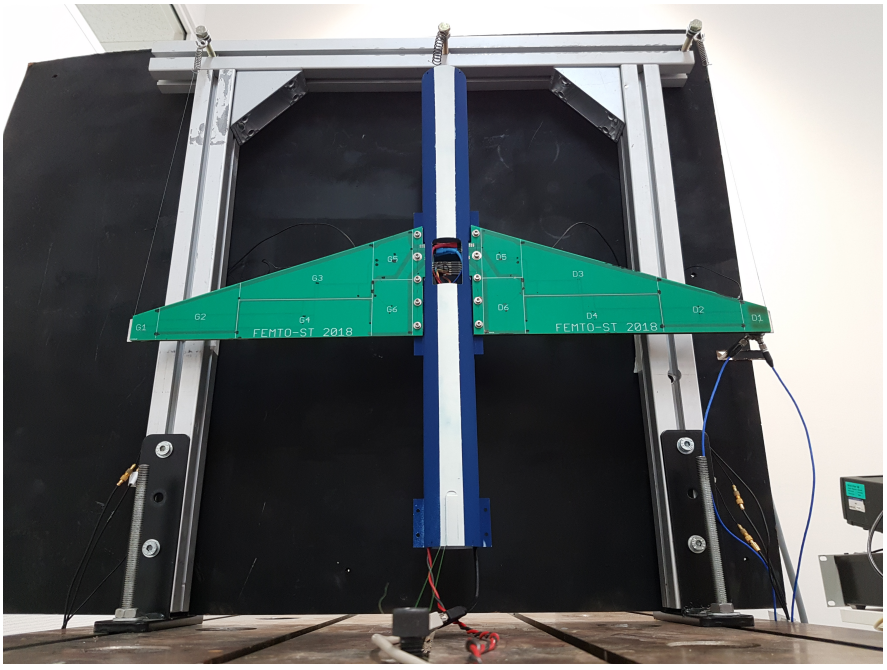

Figure 1. View of the structure on the experimental setup

The structure is shown in Figure 1, suspended under a rigid frame to obtain free-free boundary conditions. A point force is exciting the end of a wing, and the displacement field is measured using a scanning vibrometer. Each zone is controlled independently: the temperature is regulated on the zones according to some reference points of the Pareto front. A first set corresponds to high static stiffness (all the zones are heated with temperatures between 20 and 40°C), a second one to large damping with low static stiffness, and a third one corresponding to the compromise between static stiffness and dynamic damping. Practically speaking, the regulation is performed by an Arduino controller embedded in the fuselage.

5 EXPERIMENTAL RESULTS

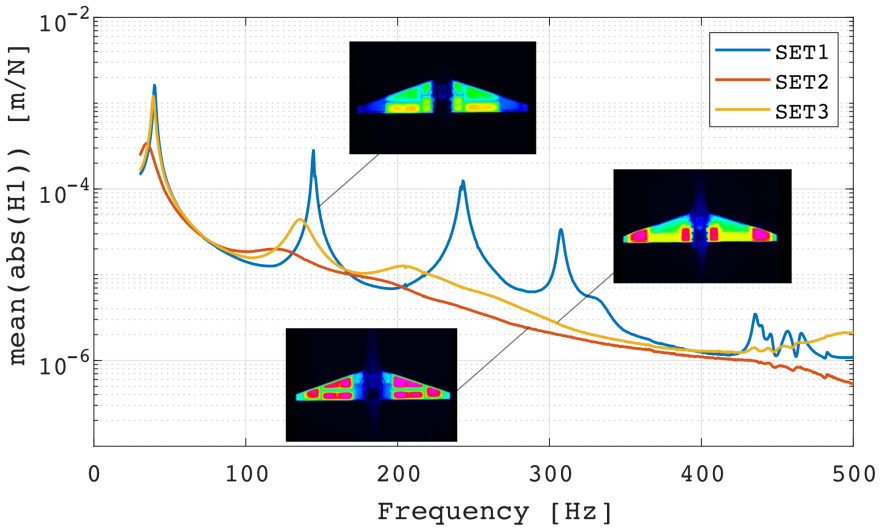

Figure 2: Experimental setup: FRFs of the three configurations, and associated temperature fields on the wings (blue: 20°C, pink: 80°C)

Figure 2 shows the results for the three chosen sets. For each configuration, the thermal field is measured on the wing by infra-red thermography. For each configuration, the averaged value of the displacement amplitude over the force is plotted versus frequency. The experimental results are in accordance with the simulations: set 1 provides a high static stiffness with low damping, set 2 is highly damped on the whole frequency range but has low static stiffness, while set 3 represents the compromise configuration. Passing from one configuration to another is possible through real-time change of the regulation loop, which is instantaneous, while changing the temperature field on the wing requires less than one minute for heating and around 10 minutes for cooling since no specific devices has been implemented to control temperature decrease.

ACKNOWLEDGEMENTS

This work has been funded by ANR (contract ANR-17-CE08-0035 ETNAA), in collaboration with EIPHI Graduate School (ANR-17-EURE-0002). The authors would like to acknowledge Eric Joseph and Thomas Jeannin for their contribution to the experimental part of the work.

REFERENCES

[1] John D Ferry and John Douglass Ferry. *Viscoelastic properties of polymers*. John Wiley & Sons, 1980.

[2] Mohan D. Rao. Recent applications of viscoelastic damping for noise control in automobiles and commercial airplanes. *Journal of Sound and Vibration*, 262(3):457 – 474, 2003.

[3] P Grootenhuis. The control of vibrations with viscoelastic materials. *Journal of Sound and Vibration*, 11(4):421–433, 1970.

[4] JM Lifshitz and M Leibowitz. Optimal sandwich beam design for maximum viscoelastic damping. *International Journal of Solids and Structures*, 23(7):1027–1034, 1987.

[5] Jinqiang Li and Yoshihiro Narita. The effect of aspect ratios and edge conditions on the optimal damping design of thin soft core sandwich plates and beams. *Journal of Vibration and Control*, page 1077546312463756, 2012.

[6] Jean-Marie Berthelot, Mustapha Assarar, Youssef Sefrani, and Abderrahim El Mahi. Damping analysis of composite materials and structures. *Composite Structures*, 85(3):189 – 204, 2008.

[7] Kerem Ege, NB Roozen, Quentin Leclere, and Renaud G Rinaldi. Assessment of the apparent bending stiffness and damping of multilayer plates; modelling and experiment. *Journal of Sound and Vibration*, 426:129–149, 2018.

[8] Fessal Kpeky, Komlan Akoussan, Farid Abed-Meraim, and El-Mostafa Daya. Influence of geometric and material parameters on the damping properties of multilayer structures. *Composite Structures*, 183:611–619, 2018.

[9] Yuhsin Tsai, Chia-hon Tai, Shih-Jung Tsai, and Fuu-Jen Tsai. Shape memory effects of poly (ethylene terephthalate-co-ethylene succinate) random copolymers. *European Polymer Journal*, 44(2):550–554, 2008.

[10] P. Butaud, E. Foltête, and M. Ouisse. Sandwich structures with tunable damping properties: on the use of shape memory polymer as viscoelastic core. *Composite Structures*, 153:401–408, 2016.

[11] M Caputo and F Mainardi. Linear models of dissipation in anelastic solids. *La Rivista del Nuovo Cimento (1971-1977)*, 1(2):161–198, 1971.

[12] Roderic S Lakes. *Viscoelastic solids*, volume 9. CRC press, 1998.

[13] David McCoul, Samuel Rosset, Nadine Besse, and Herbert Shea. Multifunctional shape memory electrodes for dielectric elastomer actuators enabling high holding force and low-voltage multisegment addressing. *Smart Materials and Structures*, 26(2):025015, 2016.

[14] K. Billon, M. Ouisse, E. Sadoulet-Reboul, M. Collet, P. Butaud, G. Chevallier, and A. Khelif. Design and experimental validation of a temperature-driven adaptive phononic crystal slab. *Smart Materials and Structures*, 2019.

[15] Morvan Ouisse, David Renault, Pauline Butaud, and Emeline Sadoulet-Reboul. Damping control for improvement of acoustic black hole effect. *Journal of Sound and Vibration*, 454:63–72, 2019.

[16] P. Butaud, M. Ouisse, V. Placet, F. Renaud, T. Travaillot, A. Maynadier, G. Chevallier, F. Amiot, P. Delobelle, E. Foltête, and C. Rogueda-Berriet. Identification of the viscoelastic properties of the tBA/PEGDMA polymer from multi-loading modes conducted over a wide frequency–temperature scale range. *Polymer Testing*, 69, 2018.

SOUND TRANSMISSION ANALYTICAL SOLUTION OF COMPOSITE SHELL STRUCTURES EMBEDDING VISCOELASTIC LAYERS

A. Alaimo[1] , C. Orlando[1] and S. Valvano[1*]

[1]Faculty of Engineering and Architecture
University of Enna Kore
Cittadella Universitaria, 94100 Enna, Italy
Email: andrea.alaimo@unikore.it, caloger.orlando@unikore.it, stefano.valvano@unikore.it

ABSTRACT

The noise transmission of aeronautical panels is an important phase of the design process of an airplane. In this work an analytical Navier-type solution, based on higher-order layer-wise shell models, is proposed for the analysis of the sound insulation of laminated panels. The considered multilayered structures are laminated with cross-ply composite layers embedded with interlaminar viscoelastic sheets. The use of the soft interlayers permits to have a passive insulation effect in the study of the sound transmission. In order to take into account the frequency depedent properties of a realistic viscoelastic layer, the damping behavior is modeled through a fractional derivative Zener model. The Rayleigh integral method is used to extrapolate the acoustic indicators for the sound transmission analysis. Some results are presented to validate and demonstrate the efficiency of the present approach, comparing the present solutions with others taken from the literature.

1 INTRODUCTION

The sound insulation of aeronautical panels is one of the major problem to be satisfied in the comfort study of an airplane. During the design process, the main issue is the correct modelization of the vibroacoustic characteristics of the analyzed structure. In literature an experimental campaign of sound transmission through single and multi-glazing are reported in [1] and a statistical analysis in [2] found a relation between the structural damping loss factor and the noise reduction level. A number of finite element models are developed to compute the sound insulation of double elastic panels in [3]. Multifunctional materials and new honeycomb core concepts have been investigated in [4] and [5] for a better acoustic insulation. In the framework of the multilayered structures, the use of interlayer viscoelastic sheets is able to give a better acoustic insulation [6]. A theoretical study with higher-order plate finite elements and with a design of some stacking parameters, through a particle decline swarm optimization process, of multi-layered viscoelastic flat panels is given [7]. The sound transmission FEM analysis of multi-layered composite viscoelastic shells is investigated in [8].
The novelty of this work is focused on the development of an advanced analytical shell formulation for the sound transmission analysis of viscoelastic composite shell structures taking into account a fractional derivative approach for the viscoelastic sheets. To the best authors knowledge, very few results on an analytical model based on Goldenveizer-Novozhilov thin shell theory is used for the active control of the sound transmission of a simplified aircraft fuselage [9] and sound transmission through composite shells using analytical model neglecting structural damping [10] are present in literature. For the reason stated above, an analytical advanced shell formulation for the sound transmission analysis of viscoelastic composite multi-layered structures has been developed here. The results are obtained with an in-house code, developed by Authors. The governing equations are derived from the Principle of Virtual Displacement (PVD) and are solved by the use of the Navier method. Orthotropic properties for composite materials and the frequency dependence of the viscoelastic material are taken into account.

2 SOUND RADIATION BY VIBRATING SHELLS

In order to evaluate the sound insulation property of the multilayered shell structures and their acoustic performances, some acoustic indicators have to be defined. For a shell embedded in an infinite rigid baffle and radiating in a semi infinite fluid, the emitted acoustic pressure p and the radiated or transmitted sound power Π_t, by the shell surface Ω can be obtained using the Rayleigh Integral [11]:

$$p\left(\alpha,\beta,z,\omega\right)=\frac{\rho_{air}j\omega}{2\pi}\int\limits_{\Omega}v_n\left(\alpha',\beta',0,\omega\right)\frac{e^{-j\omega R/c_{air}}}{R}\,d\Omega \qquad \Pi_t\left(\omega\right)=\frac{1}{2}\Re\left(\int\limits_{\Omega}p\left(\alpha,\beta,0,\omega\right)\overline{v}_n\left(\alpha,\beta,0,\omega\right)\,d\Omega\right) \quad (1)$$

where ρ_{air} and c_{air} are the mass density and the sound speed of the external acoustic domain, $v_n\left(\alpha',\beta',0,\omega\right)$ is the normal vibrating velocity of the external shell surface and $\overline{v}_n$ is its complex conjugate, and R is the distance between the point (α,β,z) where the sound pressure is estimated and the vibrating surface element at $(\alpha',\beta',0)$, moreover the Π_t is obtained taking into account only the real part $\Re$ of the surface integral.
The structural vibrating velocity can be easily obtained from the mechanical displacements results of the dynamic equation system as follows: $v_n\left(\alpha',\beta',0,\omega\right)=j\omega\,u_n\left(\alpha',\beta',0,\omega\right)$.
In order to introduce the displacement kinematic assumptions, in this work the generalized Galerkin method is employed, as well described in the book of Washizu [12], and the three-dimensional mechanical displacements $\boldsymbol{u}=(u,v,w)$ are expressed as: $\boldsymbol{u}(\alpha,\beta,z)^d=\sum_{d=0}^{N}\boldsymbol{u}^d(\alpha,\beta)\boldsymbol{g}^d(z)$, where the three-dimensional displacements can be approximated by a proper choice of the functions in the shell reference surface $\boldsymbol{u}^d(\alpha,\beta)$ and of the functions along the thickness $\boldsymbol{g}^d(z)$, moreover the accuracy depends also on the number of terms N. In this work the attention is focused on advanced shell kinematic models well-known in literature as Layer-Wise models (LW). In order to easily implement this modelization, the Legendre polynomial are used and, in particular, an higher-order cubic expansion LW 3 has taken into account: $\boldsymbol{u}^k(\alpha,\beta,z)=\left(\frac{1+\zeta}{2}\right)\boldsymbol{u}_0^k(\alpha,\beta)+\left(\frac{1-\zeta}{2}\right)\boldsymbol{u}_1^k(\alpha,\beta)+\left[\frac{3\left(\zeta^2-1\right)}{2}\right]\boldsymbol{u}_2^k(\alpha,\beta)+\left[\frac{5\zeta\left(\zeta^2-1\right)}{2}\right]\boldsymbol{u}_3^k(\alpha,\beta)$ in which the used polynomials are function of ζ, locally defined: $-1\leq\zeta\leq1$, for more details refers to [8]. To consider a lower kinematic model

LW^{ith} the higher-order terms $\boldsymbol{u}_{jth}$, with $j > i$, are set to zero.
In this work, the functions defined in the structure reference shell surface $\boldsymbol{u}^d(\alpha, \beta)$ are defined according to the Navier solution type, they are a double trigonometric (Fourier) expansion. Specially orthotropic laminates are considered here, it means that the orthotropic material properties coefficients are reduced ($C_{16} = C_{26} = C_{36} = C_{45} = 0$). Considering a simply-supported shell domain, the generalized displacement vector is defined with the following harmonic forms:

$$\boldsymbol{u}^d(\alpha, \beta) = \sum_{m=1}^{\infty} \sum_{n=1}^{\infty} \boldsymbol{U}^{mn} \boldsymbol{f}\,(\alpha)\, \boldsymbol{f}\,(\beta) \tag{2}$$

where $\boldsymbol{f}\,(\alpha) = \left[\cos\left(\frac{m\pi\alpha}{a}\right), \sin\left(\frac{m\pi\alpha}{a}\right), \sin\left(\frac{m\pi\alpha}{a}\right)\right]$ and $\boldsymbol{f}\,(\beta) = \left[\sin\left(\frac{n\pi\beta}{b}\right), \cos\left(\frac{n\pi\beta}{b}\right), \sin\left(\frac{n\pi\beta}{b}\right)\right]$ are the in-plane functions for the displacements $\boldsymbol{u} = (u, v, w)$, $\boldsymbol{U} = (U, V, W)$ are the displacements unknowns, m and n, a and b are the half-waves and the length dimensions defined on the whole shell domain in the α and β directions respectively. Even if it is demonstrated in the literature that it is possible to get an higher solution accuracy increasing the number of the trigonometric series, usually a truncated Fourier series is used for computational purpose. The generalized Galerkin method is used, in this work, in conjunction with the Principle of Virtual Displacements (PVD), which is defined as follows:

$$\int_{\Omega}\int_{A} \delta\boldsymbol{\epsilon}^T\, \boldsymbol{\sigma}\; d\Omega dz + \int_{\Omega}\int_{A} \rho\, \delta\boldsymbol{u}^T\, \ddot{\boldsymbol{u}}\, d\Omega dz = \int_{\Omega}\int_{A} \delta\boldsymbol{u}^T\, \bar{t}\; d\Omega dz \tag{3}$$

where the in-plane domain and the thickness direction domain are indicated as Ω and A respectively, $\ddot{\boldsymbol{u}}$ is the accelerations vector, ρ is the material density, $\bar{t}$ is the surface traction, the mechanical stresses $\boldsymbol{\sigma}$ and the mechanical strains $\boldsymbol{\epsilon}$. Taking into account the complex elastic material constitutive equations, see [8], the linear geometrical relations for shells, see [8], and using the mechanical displacement assumptions, the governing equations can be derived in a compact form as follows: $\delta\boldsymbol{u} : (\boldsymbol{K} - \omega^2\boldsymbol{M})\, \boldsymbol{u} = \boldsymbol{P}$, where $\boldsymbol{K}$ is the complex stiffness matrix, $\boldsymbol{M}$ is the mass matrix and $\boldsymbol{P}$ is the load vector.

In order to validate the present analytical approach, rectangular shell panels are considered. The geometry and the material data are taken from the work of Valvano et al. [8]. The shell edge dimensions are $a = 1.5\,m$; $b = 0.66\,m$; $R_\alpha = R_\beta = 3\,m$; $h_{total} = 0.05\,m$ where the total thickness is kept constant for all the considered analysis. The properties of the viscoelastic sheets are taken from the wrok of Valvano et al. [8]. The composite layers material properties are $E_1 = 130.8\,GPa$; $E_2 = E_3 = 10.6\,GPa$; $G_{12} = 5.6\,GPa$; $G_{13} = 4.2\,GPa$; $G_{23} = 3\,GPa$; $\nu_{12} = \nu_{13} = \nu_{23} = 0.36$; $\rho = 1543\,kg/m^3$. An incident wave, normal to the top shell surface, is defined as $P_z(\alpha, \beta, z) = P_0(\alpha, \beta, +h/2) = 1\,N/m^2$. The emitted sound power is evaluated at the bottom surface where the air has the following properties: $\rho_{air} = 1.21\,kg/m^3$; $c_{air} = 340\,m/s$. The results are given in terms of sound power levels (SPL) varying on the frequency, where $SPL = 10 \times \log_{10}(\Pi_t/10^{-12})$. The present results are obtained with an in-plane Fourier expansion up to $m = n = 7$ half-waves number, and a cubic layer-wise expansion LW^3. The viscoelastic interlamina position effect, see Figure 1a, on the SPL parameter is investigated for cylindrical and spherical panels with composite cross-ply layers embedding viscoelastic sheets. The considered lamination schemes are: $[0°/90°/visco]_S$, $[0°/visco/90°]_S$. Moreover the transmitted sound pressure field is depicted in Figure 1b through a three-dimensional representation at $f = 380\,Hz$.

3 CONCLUDING REMARKS

The present higher-order shell analytical formulation permits to include in the variational principle the effects of frequency-dependent viscoelastic materials through the use of fractional derivative models for the sound transmission analysis of multi-layered composite shell structures. A limited number of half-waves (m=n=7) and a cubic layer-wise expansion are necessary to correctly reproduce the radiated sound power engendered by a constant uniform incident pressure. The present analytical solution is in agreement with other FEM results present in literature.

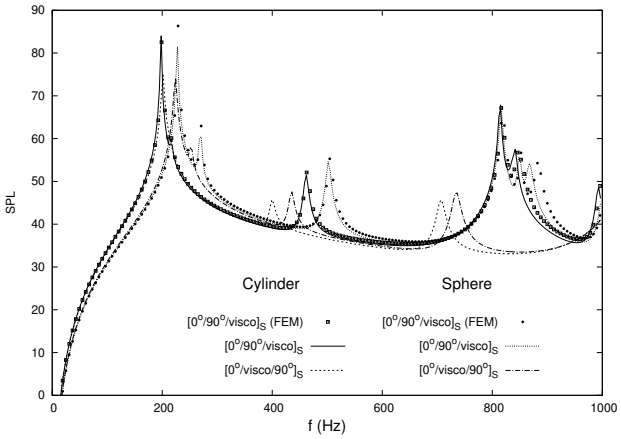

(a) *Viscoelastic sheets position effect*

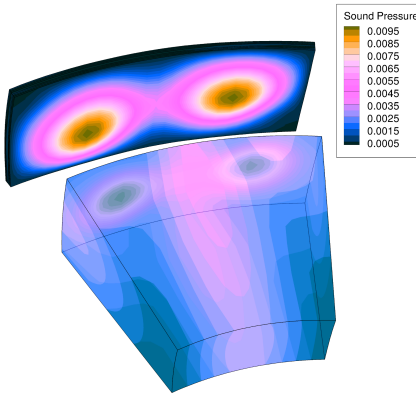

(b) *Transmitted sound pressure at* $f = 380\,Hz$

Figure 1: Study of the viscoelastic sheets position effect for composite cylindrical and spherical shells, and the transmitted sound pressure field for a cylindrical composite sandwich panel.

REFERENCES

[1] A.J.B. Tadeu and D.M.R. Mateus. Sound transmission through single, double and triple glazing. experimental evaluation. *Applied Acoustics*, 62:307–325, 2001.

[2] A. Parrinello and G.L. Ghiringhelli. Evaluation of damping loss factor of flat laminates by sound transmission. *Journal of Sound and Vibration*, 23:112–119, 2018.

[3] A. London. Transmission of reverberant sound through double walls. *Journal of the Acoustical Society of America*, 22:270–279, 1950.

[4] M. Arena, M. Viscardi, G. Barra, L. Vertuccio, and L. Guadagno. Multifunctional performance of a nano-modified fiber reinforced composite aeronautical panel. *Materials*, 12(6):869, 2019.

[5] C.F. Ng and C.K. Hui. Low frequency sound insulation using stiffness control with honeycomb panels. *Applied Acoustics*, 63(4):293–301, 2008.

[6] R.V. Foss, T.A. Dear, M.A. Hamdi, and S. Assaf. Facade noise control with glass and laminates. *Glass Process Days*, 13:424–431, 1999.

[7] S. Valvano, C. Orlando, and A. Alaimo. Design of a noise reduction passive control system based on viscoelastic multilayered plate using p$_d$so. *Mechanical Systems and Signal Processing*, 123:153–173, 2019.

[8] S. Valvano, A. Alaimo, and C. Orlando. Sound transmission analysis of viscoelastic composite multi-layered shells structures. *Aerospace*, 6:69, 2019.

[9] D.R. Thomas, P.A. Nelson, and S.J. Elliott. Active control of the transmission of sound through a thin cylindrical shell, part i: the minimization of vibrational energy. *Journal of Sound and Vibration*, 167(1):91–111, 1993.

[10] K. Daneshjou, A. Nouri, and R. Talebitooti. Sound transmission through laminated composite cylindrical shells using analytical model. *Archive of Applied mechanics*, 77:363–379, 2007.

[11] F. Fahy and P. Gardonio. *Sound and Structural Vibration, Radiation, Transmission and Response*. Academic Press, by Elsevier, Linacre House, Jordan Hill, Oxford OX2 8DP, UK, 2007.

[12] K. Wahsizu. *Variational methods in elasticity and plasticity*. Pergamon Press Ltd., Headington Hill Hall, Oxford OX3, UK, 1968.

COMBINING IMPORTANCE SAMPLING WITH MACHINE LEARNING TO ACCELERATE STRUCTURAL RELIABILITY ANALYSIS

Weizhen YOU[1] , Alexandre SAIDI[2], Abdel-malek ZINE[3] and Mohamed ICHCHOU[1*]

[1]Laboratoire de Tribologie et Dynamique des Systèmes (LTDS)
[2]Laboratoire d'Informatique en Image et Systèmes d'Information (LIRIS)
[3]Institut Camille Jordan (ICJ)
Ecole Centrale de Lyon, Écully, France
Email: weizhen.you@ec-lyon.fr, alexandre.saidi@ec-lyon.fr
abdel-malek.zine@ec-lyon.fr, mohamed.ichchou@ec-lyon.fr

ABSTRACT

In reliability analysis of linear systems subjected to random excitation, an important issue is to determine the first-excursion probability. When this probability is very small, general Monte Carlo simulations (MCS) are always computationally impractical. In deterministic case where the structural properties are constant, advanced MCS such as importance sampling (IS) can be employed to improve the calculation efficiency. This results in the so-called conditional failure probability (CFP). However, when the uncertainties in structural properties are high-dimension, the IS technique still demands a large number of analysis of CFPs. Recent studies show that, machine learning (ML) theories can be used to build effective surrogates that maps the structural uncertainties into CFPs. In this study, the structural reliability, denoted as first-excursion probability, is evaluated by a more efficient technique that combines IS with ML. Besides, Karhunen–Loève (K-L) expansion is implemented to denote the stochastic excitation. The structural responses are calculated by convolution integral with respect to impulse responses. Numerical simulations show that the proposed method can effectively accelerate the evaluation process, meanwhile achieving the accuracy close to general MCS.

1 INTRODUCTION

Reliability mechanical structures describes the probability that the object realizes its functions under given conditions for a specified time period [1]. For a mechanical structure subjected to stochastic excitation, an important task is to evaluate the structural failure probability. In fact, due to various factors (manufacture, environmental, fatigue...), the structural properties become uncertain. Hence, the assessment of failure probability involves a high-dimension problem considering the uncertainties in both structural parameters and the excitation. Direct MCS demand a huge number of samples to ensure a high accuracy of the estimated CFP, but this will be very time-consuming. In this aspect, surrogate models become a good alternative. Response surface method (RSM) [2] is among the most popular surrogate models. Support vector machine (SVM) has also gained much attention recently [3]. Other surrogate models such as metamodel, ANNs and Kriging have been proposed by other researchers [[4], [5], [6]]. The disadvantages in ANNs mainly include the complex architecture optimization, low robustness and enormous training time. SVM is time consuming for large-scale applications and sometimes shows large error in sensitivity calculation of reliability index. RSM has been popular however it may be time-consuming to use the polynomial function when the number of random variables is large.

In the authors' viewpoint, the evaluation of CFP can be seen as a regression problem that takes a realization of the structural uncertain properties as input and the CFP as output. To improve reliability assessment considering structural uncertainties, attention is paid to non-parametric statistical learning methods in this research. The rest of the paper is organized as follows. In Section 2, the theories pertaining to CFP and its estimation are presented. In Section 3, the framework of failure probability estimation based on ML models is introduced, and numerical simulations on different structures are applied and discussed.

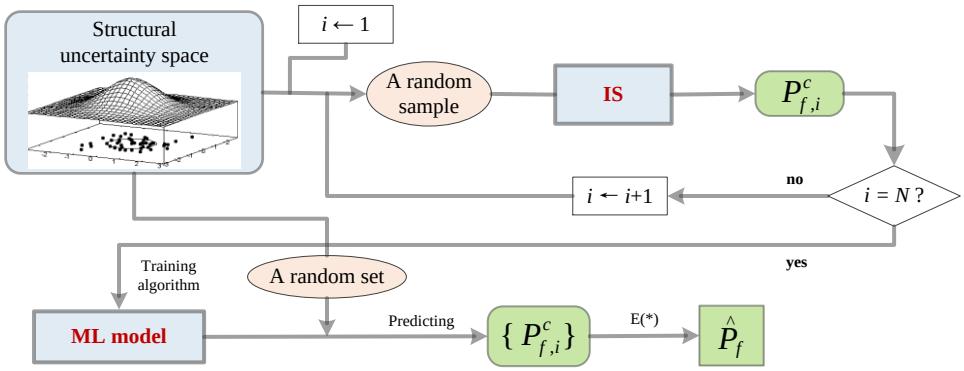

Figure 1. Theoretical framework to estimate failure probability by ML model

2 THEORETICAL FRAMEWORK

A basic assumption in this research is that the uncertainties of the structural properties and those of the excitation are relatively independent. Mathematically, the failure probability is determined by a multi-dimension integral over the joint distribution of all variables involved, *i.e.*

$$P_f = \int_{g(\mathbf{x},\mathbf{z})\leq 0} p_X(x)p_Z(z)\mathrm{d}\mathbf{x}\mathrm{d}\mathbf{z} = \int_{\mathbf{x}\in\Omega_X,\mathbf{z}\in\Omega_Z} I_f(\mathbf{x},\mathbf{z})p_X(x)p_Z(z)\mathrm{d}\mathbf{x}\mathrm{d}\mathbf{z} \tag{1}$$

where $I_f(\mathbf{x},\mathbf{z})$ is the indicator function which equals to 1 when the performance function $g(\mathbf{x},\mathbf{z}) \leq 0$ and 0 otherwise. It is noted that the calculation in Eq. (1) considers uncertainty in

both structural parameters and excitation. To construct the CFP, eq. (1) is rewritten as

$$P_f = \int_{\mathbf{x}\in\Omega_X} [\int_{\mathbf{z}\in\Omega_Z} I_f(\mathbf{z}|\mathbf{x}) p_Z(\mathbf{z}) \mathrm{d}\mathbf{z}] p_X(\mathbf{x}) \mathrm{d}\mathbf{x} = \int_{\mathbf{x}\in\Omega_X} P_f^c(\mathbf{x}) p_X(\mathbf{x}) \mathrm{d}\mathbf{x} = E_{\mathbf{x}\in\Omega_X}[P_f^c(\mathbf{x})] \quad (2)$$

$E[\cdot]$ denotes the mathematical expectation. By eq. (2), a ML model can be built that takes the random samples of structural properties as input and CFPs as outputs. Once the ML model is built, it is employed to make predictions on the samples outside the sample set used to train the ML model. The expectation of these predictions is seen as the structural failure probability considering both kinds of uncertainties. Figure 1 illustrates the theoretical framework.

As is known that the estimations by direct MCS can be treated as a standard reference. However, it is not computationally efficient for estimating very small failure probabilities (less than 1%) since the number of samples required to achieve a given accuracy is inversely proportional to the scale of P_f. In view of this, the IS method a good choice to compute small P_f values. In principle, an IS method tries to adjust the sampling density so that more samples are obtained from the failure region F. Figure 2 shows the procedures to apply IS [7] to estimate CFPs.

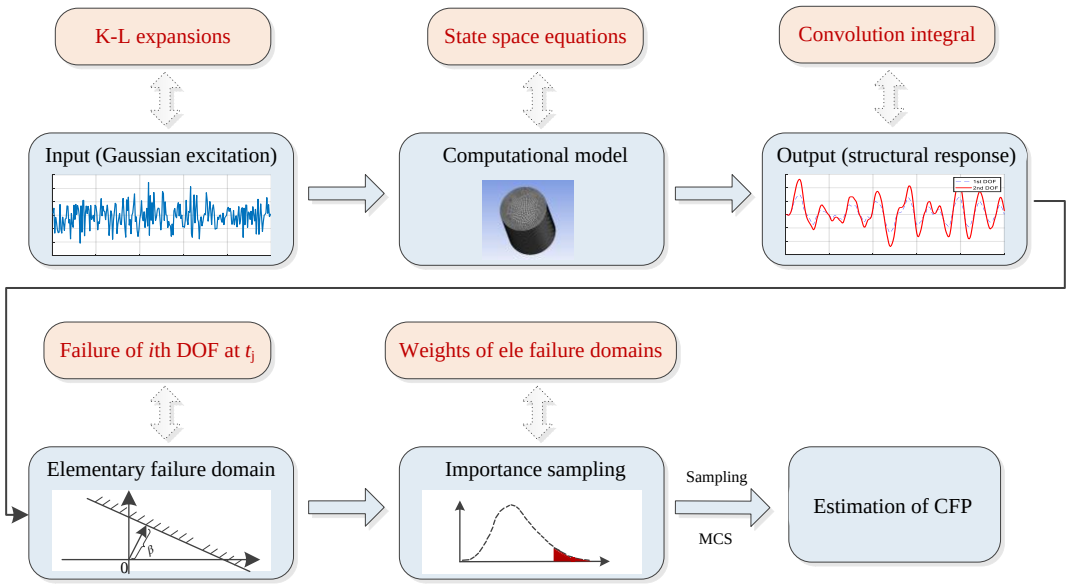

Figure 2. IS to estimate CFP

3 A BENCHMARK STUDY

As a benchmark problem introduced in G.I. Schueller [8], the ten-DOF Duffing type oscillator has been widely used by researchers in structural reliability domain. In this study, we focus on the linear random structures under stochastic excitation. The statistical properties of the structural parameters and their constraints are shown in [8]. In this simulation, the estimated failure probability values are very small (below 10^{-4}), therefore IS is used to estimate CFPs. Three ML models Random Forest (RF) [9], Gradient Boosting (GB) [10] and Extra-trees (ETs) [11] are employed to estimate the failure probability. The three methods are compared with standard MCS, see Table 1. In the simulations, it is found that the ensemble learning based methods all reach a convergence at the point $n\_sample = 500$. This benchmark study tells that

Table 1. Reliability estimatios by different ML-based methods

Method	1stDOF $0.057m$	1stDOF $0.073m$	10thDOF $0.013m$	10thDOF $0.017m$
Standard MCS	$1.06e^{-4}$	$8.07e^{-7}$	$4.88e^{-5}$	$2.52e^{-7}$
num of samples	$2.98e^{7}$	$2.98e^{7}$	$2.98e^{7}$	$2.98e^{7}$
RF-based	$7.6e^{-5}$	$1.0e^{-6}$	$4.2e^{-5}$	$1.1e^{-7}$
num of samples	500	500	500	500
GB-based	$8.48e^{-5}$	$9.15e^{-7}$	$4.24e^{-5}$	$1.06e^{-7}$
num of samples	500	500	500	500
ETs-based	$8.73e^{-5}$	$9.89e^{-7}$	$4.09e^{-5}$	$1.10e^{-7}$
num of samples	500	500	500	500

the combination of IS and ML models can largely improve the efficiency of failure probability estimations.

REFERENCES

[1] Bernd Bertsche. *Reliability in automotive and mechanical engineering: determination of component and system reliability*. Springer Science & Business Media, 2008.

[2] Sang Hoon Lee and Byung Man Kwak. Response surface augmented moment method for efficient reliability analysis. *Structural safety*, 28(3):261–272, 2006.

[3] Qiujing Pan and Daniel Dias. An efficient reliability method combining adaptive support vector machine and monte carlo simulation. *Structural Safety*, 67:85–95, 2017.

[4] Vincent Dubourg, Bruno Sudret, and Franois Deheeger. Metamodel-based importance sampling for structural reliability analysis. *Probabilistic Engineering Mechanics*, 33:47–57, 2013.

[5] João B Cardoso, João R de Almeida, José M Dias, and Pedro G Coelho. Structural reliability analysis using monte carlo simulation and neural networks. *Advances in Engineering Software*, 39(6):505–513, 2008.

[6] Guoshao Su, Lifeng Peng, and Lihua Hu. A gaussian process-based dynamic surrogate model for complex engineering structural reliability analysis. *Structural Safety*, 68:97–109, 2017.

[7] SK Au and James L Beck. First excursion probabilities for linear systems by very efficient importance sampling. *Probabilistic engineering mechanics*, 16(3):193–207, 2001.

[8] Gerhart I Schuëller and Helmuth J Pradlwarter. Benchmark study on reliability estimation in higher dimensions of structural systems–an overview. *Structural Safety*, 29(3):167–182, 2007.

[9] Leo Breiman. Random forests. *Machine learning*, 45(1):5–32, 2001.

[10] Jerome H Friedman. Greedy function approximation: a gradient boosting machine. *Annals of statistics*, pages 1189–1232, 2001.

[11] David H Wolpert. Stacked generalization. *Neural networks*, 5(2):241–259, 1992.

PROGRESSIVE FAILURE ANALYSIS OF LAMINATED COMPOSITE BEAMS USING THE WAVE FINITE ELEMENT METHOD

M. Mallouli[1,2*] , M. A. Ben Souf[1,2] ,O. Bareille[1], M. N. Ichchou[1], T. Fakhfakh[2] and M. Haddar[2]

[1]LTDS, École Centrale Lyon
36 Avenue Guy de Collongue, F-69134 Ecully Cedex, France

[2]LA2MP, École Nationale d'Ingénieurs de Sfax
Route de la Soukra km 4, 3038 sfax, Tunisie

ABSTRACT

In this study, progressive failure analysis has been developed for predicting the failure of laminated composite structures subjected to a transverse low velocity impact. The proposed strategy consist of a dynamic stress analysis using the hybrid method WFE/EF and a damage analysis which is performed using Hashin's failure criteria and the material property degradation rules.
The studied structure is made of E-glass/epoxy and it is decomposed in undamaged and damaged substructures. The material properties in the damaged substructure are modified according to sudden material property degradation rule. The damage describes the creation of micro-discontinuities in the structure during the loading.
The numerical method combines the Finite Element(FE) method to model the discontinuous regions, impact region and damaged region, and the wave finite element (WFE) to accurately model the periodic substructures (intact substructures). This hybrid method enables the calculation of the waves-damage interaction scattering coefficients and the response of the whole structure in both the frequency as well as in the time domain and it provides the reduction of the computational cost of analyses in space and time .
Several numerical simulations have been performed, first to validate the accuracy of the results predicted by the proposed formulation and second to investigate the damage propagation.

1 INTRODUCTION

For several years, composite materials are increasingly used in the realization of structures in different fields, such as aerospace and automotive, due to high strength to weight and stiffness to weight ratios.
Due to their anisotropic nature, composite structures may exhibit a various forms of damage, such as matrix cracks, delamination and fibre breakage, which can cause considerable degradation of the mechanical properties and consequently which can change, locally, its mechanical behavior. The ability to predict the initiation and propagation of such damage is essential for predicting the performance of composite laminated structures and developing safe designs which exploit the advantages offered by composite materials.

2 THE HYBRID FE/WFE METHOD [1]

In this paper, a FE/WFE hybrid method is developed to determine the waves-damage interaction scattering coefficients then the forced response of damaged laminated composite structures. A new Diffusion Matrix Formulation is proposed to analyse the scattering induced by discontinuities in structure. Let us consider three intact periodic waveguides connected by two coupling joints, on which impact zone and damage are described respectively. In order to evaluate the wave interaction coefficients, the WFE approach is used to calculate the wave propagation constants of each waveguide and is then coupled to the standard FE method described coupling joints.

Once the vectors of displacements q and forces F are written in terms of the wave amplitudes in the waveguides:

$$D^{c1*}\begin{bmatrix} \Phi_q^{inc(1)}Q^{inc(1)} + \Phi_q^{ref(1)}Q^{ref(1)} \\ \Phi_q^{inc(2)}Q^{inc(2)} + \Phi_q^{ref(2)}Q^{ref(2)} \end{bmatrix} = -\begin{bmatrix} \Phi_f^{inc(1)}Q^{inc(1)} + \Phi_f^{ref(1)}Q^{ref(1)} \\ \Phi_f^{inc(2)}Q^{inc(2)} + \Phi_f^{ref(2)}Q^{ref(2)} \end{bmatrix} - \begin{pmatrix} D_{1I}^{c1}(D_{II}^{c1})^{-1}F_I^{c1} \\ D_{2I}^{c1}(D_{II}^{c1})^{-1}F_I^{c1} \end{pmatrix} \tag{1}$$

$$D^{c2*}\begin{bmatrix} \Phi_q^{inc(2)}Q^{inc(2)} + \Phi_q^{ref(2)}Q^{ref(2)} \\ \Phi_q^{inc(3)}Q^{inc(3)} + \Phi_q^{ref(3)}Q^{ref(3)} \end{bmatrix} = -\begin{bmatrix} \Phi_f^{inc(2)}Q^{inc(2)} + \Phi_f^{ref(2)}Q^{ref(2)} \\ \Phi_f^{inc(3)}Q^{inc(3)} + \Phi_f^{ref(3)}Q^{ref(3)} \end{bmatrix} \tag{2}$$

By rearranging Eqs. (1) and (2), it can be proved that the reflection and transmission coefficients of the wave modes through the dynamical behavior of the two coupling elements can be related via diffusion matrices, namely C^1 and C^2 :

$$\begin{pmatrix} Q^{ref(1)} \\ Q^{ref(2)} \end{pmatrix} = C^1 \begin{pmatrix} Q^{inc(1)} \\ Q^{inc(2)} \end{pmatrix} + F \tag{3}$$

$$\begin{pmatrix} Q^{ref(2)} \\ Q^{ref(3)} \end{pmatrix} = C^2 \begin{pmatrix} Q^{inc(2)} \\ Q^{inc(3)} \end{pmatrix} \tag{4}$$

In order to obtain the forced response of the structure, the boundary conditions will be expressed in matrix form as:

$$\begin{bmatrix} I & (\Phi_f^{inc})_1^+(\Phi_f^{ref})_1 & 0 & 0 & 0 & 0 \\ -C_{11}^1\lambda_1^{N_1} & I & 0 & -C_{12}^1\lambda_1^{N_2} & 0 & 0 \\ -C_{21}^1\lambda_1^{N_1} & 0 & I & -C_{22}^1\lambda_2^{N_2} & 0 & 0 \\ 0 & 0 & -(C_{11}^2)^+\lambda_2^{N_2} & I & (C_{11}^2)^+C_{12}^2 & 0 \\ 0 & 0 & 0 & (C_{22}^2)^+C_{21}^2 & I & -(C_{22}^2)^+\lambda_3^{N_3} \\ 0 & 0 & 0 & 0 & (\Phi_Q^{ref})_1^+(\Phi_q^{inc})_3\lambda_3^{N_3} & I \end{bmatrix} \times \begin{bmatrix} I & 0 & 0 & 0 & 0 & 0 \\ 0 & \lambda_1^{-N_1} & 0 & 0 & 0 & 0 \\ 0 & 0 & \lambda_2^{-N_2} & 0 & 0 & 0 \\ 0 & 0 & 0 & I & 0 & 0 \\ 0 & 0 & 0 & 0 & I & 0 \\ 0 & 0 & 0 & 0 & 0 & \lambda_3^{-N_3} \end{bmatrix} \begin{pmatrix} Q_1^{inc(1)} \\ Q_1^{ref(1)} \\ Q_2^{ref(1)} \\ Q_2^{inc(1)} \\ Q_3^{inc(1)} \\ Q_3^{ref(1)} \end{pmatrix} = \begin{pmatrix} 0 \\ F_1 \\ F_2 \\ 0 \\ 0 \\ 0 \end{pmatrix} \tag{5}$$

This hybrid approach is formulated in the frequency domain and therefore the Inverse Discrete Fourier Transformation of the frequency response to describe the dynamics in time domain, is required.

3 FAILURE ANALYSIS

In this study, the impact damage analysis follows a two step process. First, Three-dimensional Hashin's [2] criteria are used to predict the layer failure in the laminated composite and to determine damage modes (critical matrix cracking, delamination). Once failure occurs in a ply, its material properties are changed by implementing a sudden degradation rule. These rules determine the mechanical parameters that are degraded when a failure occurs and are applied to characterize the post-damage material behaviour of each failed layer. The degradation is characterized by the reduction of the elastic parameters. In the present work, the degradation rules used have been taken from Shokrieh et al [3] due to their satisfactory physical and also to its simplicity of implementation. Therefore, for different failure modes, there exists an appropriate failure criteria and sudden material property degradation rule which are presented in the table 1.

	Hashin's failure criteria	The degradation rules
Matrix cracking	$(\frac{\sigma_{22}+\sigma_{33}}{Y_t})^2 + (\frac{\sigma_{12}^2+\sigma_{13}^2}{S_{12}^2}) + (\frac{\sigma_{23}^2-\sigma_{22}\sigma_{33}}{S_{23}^2})$	$E_{yy} = \upsilon_{xy} = 0$
Fibre failure	$(\frac{\sigma_{11}}{X_t})^2 + \frac{1}{S_{12}^2}(\sigma_{12}^2 + \sigma_{13}^2)$	$E_{xx} = E_{yy} = E_{zz} = G_{xy} = G_{yz} = G_{xz} = 0$
Delamination	$(\frac{\sigma_{33}}{Z_t})^2 + (\frac{\sigma_{23}}{S_{23}})^2 + (\frac{\sigma_{13}}{S_{13}})^2$	$E_{yy} = G_{yz} = G_{xz} = \upsilon_{yz} = \upsilon_{xz} = 0$

Table 1. Hashin's failure criteria and degradation rules

4 NUMERICAL RESULTS

The goal of this section is to to develop a progressive failure analysis methodology for laminated composite beam subjected to transverse impact. A cantilever laminated beam made of E-glass/epoxy is considered for this study. The beam with dimension: length L= 0.12 m, width b= 0.02 m and depth h= 0.004 mThe structure is made of four layers oriented as $[0/45/-45/0]$ degrees, it is clamped at x = L and free at x = 0 . The beam is subjected to an impulse load in transverse direction with $F = 50$ N as magnitude and $\tau = 15\ ms$ s as a duration. Each layer was modelled with four SOLID185 elements, which comprises a 3D displacement fields and is defined by eight nodes having three degrees of freedom at each node: translations in the nodal x, y and z directions.

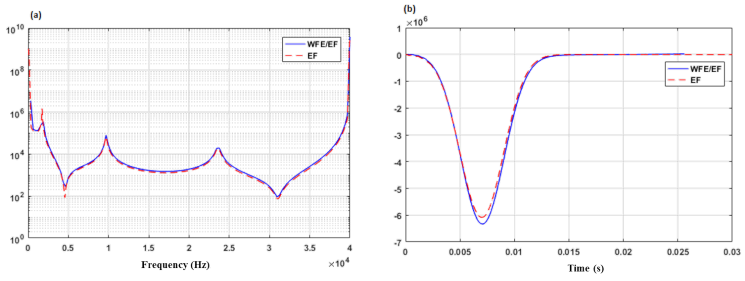

Figure 1: Stress distribution at the last lamina in the x-direction: a) frequency response, (b) time response

The stress distribution, in the x-direction on the top surface,in the frequency and time domain, are evaluated and compared with a reference solution provided by the FE model as shown respectively in Fig .1(a) and Fig .1(b). A good agreement between the two results can be observed. These comparisons with the reference solution highlights the validation of the proposed hybrid method to estimate the time response of composite structures subjected to transverse impact with much smaller system size and lower computational cost.

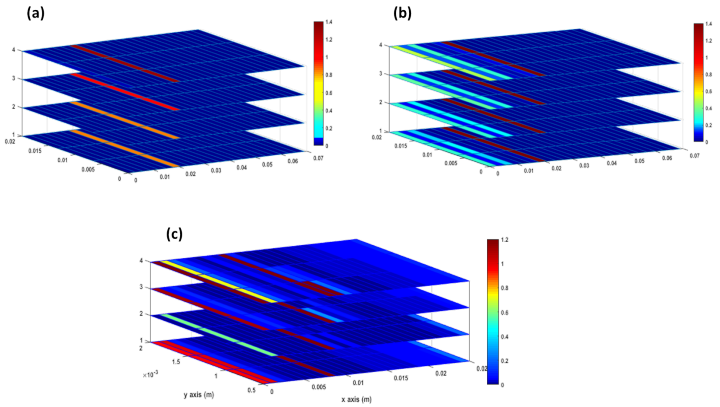

Figure 2: Propagation of maximum failure indices in the beam: (a) t=1.9 ms, (b) t=2.8 ms, , (b) t=4 ms

In order to investigate the propagation of the matrix damage in the laminated composite beam, the failure indices along the thickness in different time are presented in Fig. 2.
Fig. 2(a) shows the location of the first damage appearance in the beam. Fig. 2(b) and . 2(c) show the progressive failure when the damage occurred in both upper and bottom of the structure. The maximum damage area occurred at the top surface of the laminated, i.e. at the position of impact point.

5 CONCLUSION

In this paper, an hybrid FE/WFE approach is proposed to calculate the scattering coefficients of the wave interaction with the damage. The validation of this formulation is very important for the prediction of the impact damage propagation. Once the stress distribution in the global coordinate are computed, we proceed to calculate firstly the Hashin failure index to identify the impact damage of entire ply. Then, the modification of the material properties induced by damage has taken account using a sudden material property degradation rule.

REFERENCES

[1] M.Mallouli, M.A.ben souf, O.Bareille, M.Ichchou, T.Fakhfakh, and M.Haddar. Transient wave scattering and forced response analysis of damaged composite beams through a hybrid finite element-wave based method. *Finite Elements in Analysis and Design*, 147:1–9, 2018.

[2] Z. Hashin. Failure criteria for unidirectional fiber composites. *J Appl Mech*, 47:329–334, 1980.

[3] M.M. Shokrieh and L.B. Lessard. Progressive fatigue damage modeling of composite materials. *J Compos Mater*, 34:1056–1080, 2000.

RESPONSE OF A SUBMERGED FLUID-FILLED CYLINDRICAL SHELL TO TRANSIENT ACOUTSIC PULSES AND WEAK SHOCK WAVES

S. Iakovlev[1], H. A. F. A. Santos[2]

[1]Department of Engineering Mathematics and Internetworking
Dalhousie University, Halifax, CANADA
Email: serguei.iakovlev@dal.ca

[2]Instituto Superior de Engenharia de Lisboa
Instituto Politécnico de Lisboa, Lisbon, PORTUGAL
Email: hugo.santos@isel.pt

ABSTRACT

A circular cylindrical shell filled with and submerged into fluid is considered, and its response to an external acoustic pulse or weak shock wave is analyzed. The analysis is carried out using a semi-analytical model based on the use of the classical apparatus of mathematical physics. Both the fluid dynamics and the structural dynamics of the system are considered, with particular attention paid to the fluid-structure interaction effects. For the structural dynamics, the main outcome of the study is the understanding of how the peak structural stress observed in the shell, both compressive and tensile, evolves with the changing properties of the fluids. For the fluid dynamics, the most interesting result is the understanding of the structure and evolution of the complex radiated wave patterns observed in the fluids, with particular focus on the symmetric Lamb waves, the pseudo-Rayleigh waves and the Scholte-Stoneley waves.

1 INTRODUCTION

Thin-walled cylindrical structures that are both submerged into and filled with fluid are common in many applications, including, but not limited to, those in ocean engineering, naval architecture, aerospace, chemical and nuclear industries. Analysis of the acoustic response of such systems is essential for ensuring their optimal everyday performance, while understanding the response of these systems to shock waves is of critical importance when their reliability and survivability under

extreme conditions of operation is assessed. The model we discuss here is suitable to address both of these needs in a reliable and computationally efficient way, and the use of the model is illustrated by two most recent and most interesting results.

2 MATHEMATICAL MODEL

2.1 Problem formulation

We consider a circular cylindrical shell of radius r_0 and thickness h_0 filled with the fluid of density ρ_i and with the sound speed in it c_i and submerged into the fluid with the density ρ_e and sound speed c_e. The sound speed in and the density and Poisson's ratio of the shell material are c_s, ρ_s and ν, respectively. The following assumptions are made: (i) the shell is either thin or moderately thick, and the deflections of the shell surface are small compared to its thickness; (ii) either Kirchhoff-Love or Reissner-Mindlin hypothesis holds true (with the choice of one or the other depending on the particular variant of the formulation); (iii) the fluids are linearly compressible, irrotational and inviscid.

The fluids, therefore, are governed by the wave equations, and the shell is governed by the linear equations of either the Kirchhoff-Love or Reissner-Mindlin shell theory (the former was found to be most suitable when the shell is very thin and when the structural dynamics alone is of interest, while the latter is needed when the shell is thicker and/or when the fine structure of the hydrodynamic fields radiated by the shell is sought).

2.2 Solution

The adopted approach is based on the classical apparatus of mathematical physics. Specifically, the Laplace transform is applied to the wave equations with respect to time, and then the spatial variables are separated. This allows for the components of the resulting hydrodynamic fields to be obtained in the form of Fourier series (ordinary for the 2D formulation and double for the 3D one), with the time-dependent coefficients expressed as convolution integrals of either the normal velocity of the incident loading (scattered field) or the normal displacement of the shell surface (radiated field) and the two response functions, one for the internal fluid and one for the external fluid. The response functions represent all the essential physics of the system's behaviour as it responds to a transient loading, and their computation is far from trivial [1, 2]. Thus obtained, the hydrodynamic field components are then used to couple the fluid and structural dynamics by means of solving several (usually hundreds to ensure satisfactory convergence) systems of integro-differential equations for each set of the shell displacement harmonics, and this is accomplished by using an explicit one-dimensional finite-difference scheme. The model has been successfully validated using several independent experimental datasets.

3 RESULTS AND DISCUSSION

We consider a steel shell (c_s=5000 m/s, ρ_s=7800 kg/m^3, ν=0.30) of radius 1 m and of several different thicknesses in the range 0.01-0.06 m submerged in water, ρ_e=1000 kg/m^3 and c_e=1400 m/s, and filled with fluids of varying properties (ρ_i is always assumed the same as that of water [3], while c_i changes). The shell is subjected to a pressure pulse (interpreted, depending on the application, as either a weak shock wave or an acoustic pulse) with the pressure in the front at the instant of the first contact with the shell of 25 kPa and with the exponential decay constant of 0.1314 ms. As was established in [3], the single most important parameter that drives all the phenomenological changes in the system in question is the ratio, ζ, of the sound speed in the internal fluid to that in the external one, $\zeta=c_i/c_e$. It is, therefore, of the outmost importance to understand how the changes of ζ affect the structural and fluid dynamics of the system, and this is what the present study is focusing on.

3.1 Fluid dynamics/Hydroacoustics

The overall hydrodynamic pattern of the field radiated by the shell can be divided into two major components: the slower-propagating and higher-magnitude waves representing the direct response of the shell to the incident load (the scattered field in the external fluid and the field induced by the direct action of the incident wave on the shell in the internal fluid), and the faster-propagating, lower-magnitude waves that represent the radiation into the fluid of various elastic waves propagating in the shell, and that also include the interface Scholte-Stoneley wave.

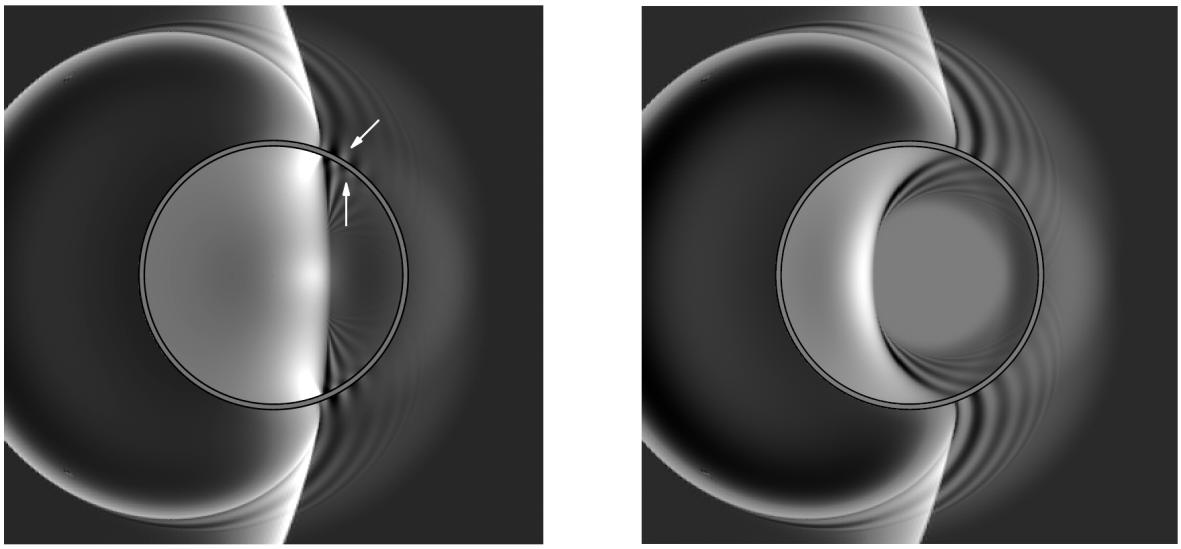

(a) (b)

Figure 1. Hydrodynamic field induced by the response of the shell with h_0/r_0=0.04 for the case of ζ=1.00, (a), and ζ=0.50, (b); the A waves are marked with arrows.

As ζ changes, the internal field undergoes the most dramatic changes: not only the geometry of the primary, high-magnitude wavefront changes from convex (Fig. 1, (a)) to concave (Fig. 1, (b)), the geometry of the wave patterns corresponding to the symmetric Lamb waves (S_0) and the pseudo-Rayleigh waves (A_0) is very significantly altered as well. Most notably, the Scholte-Stoneley wave (A) is present, for the exact same shell, for the case of ζ=1.00, but is absent when ζ=0.50: a novel, as far as we are aware, finding.

3.2 Structural dynamics

The dynamics of the stress state of the shell is driven by the two phenomenologically rather independent processes simultaneously occurring in the system: the propagation of the elastic waves in the shell and the propagation of the hydrodynamics waves in the internal fluid. The former produce the high compressive stress, Fig. 2 (a), while the latter are responsible for the tensile peaks, Fig. 2 (b). The interplay between these two phenomena is the chief reason behind the complexity of the dynamics of the stress state of the shell in question.

Specifically, as ζ decreases, the timing and location of the highest compressive stress undergo no essential changes since they are determined by the elastic properties of the shell, while the highest tensile stress occurs later and later in the interaction because its timing is determined by the properties of the internal fluid. The interaction of the compressive and tensile waves, therefore, occurs differently for different ζ, and extensive parametric studies are necessary in order to fully understand these changes. To that end, Fig. 3 shows the evolution of the tensile and compressive peaks as ζ changes: while the compressive peak exhibits an almost linear trend, the tensile peak is

highly sensitive to ζ. The latter is a rather far-reaching finding that certainly needs to be taken into account at the pre-design stage.

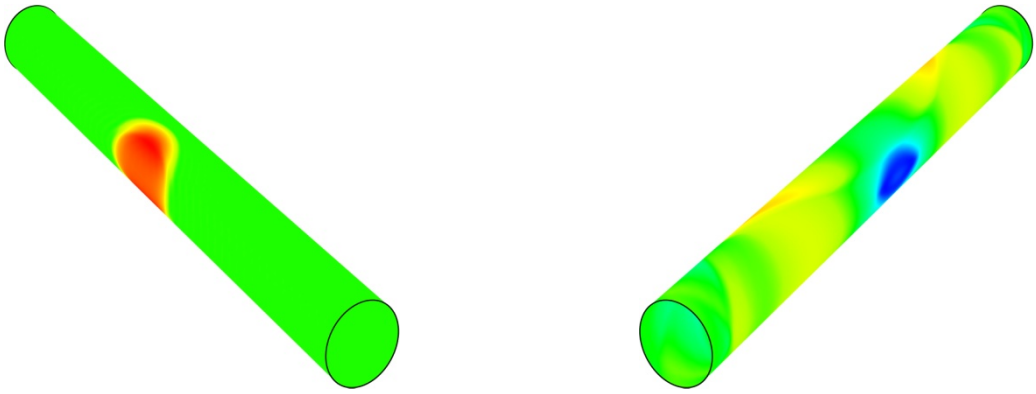

(a) (b)

Figure 2. Stress state of the shell with h_0/r_0=0.01 for ζ=0.50: high compressive stress, t=0.40, (a), and high tensile stress, t=4.20, (b).

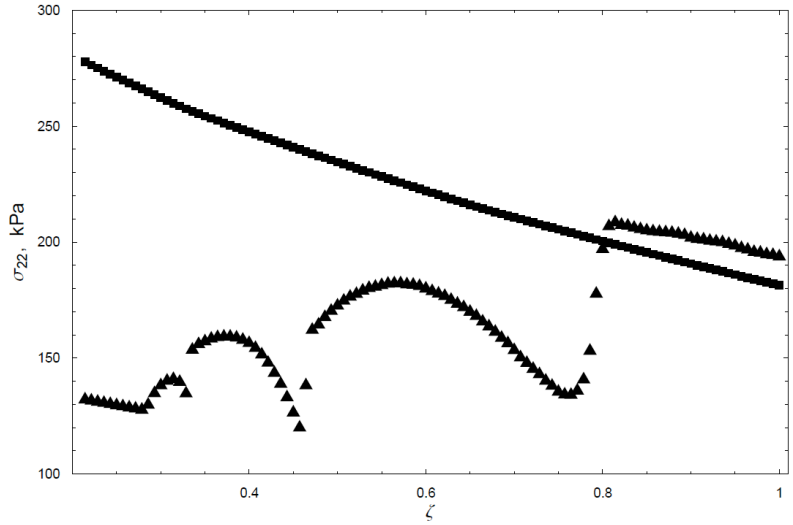

Figure 3. Evolution of the peak compressive (squares) and tensile (triangles) stress for the shell with h_0/r_0=0.01.

4 ACKNOWLEDGEMENTS

This study was carried out with the financial support of the Natural Sciences and Engineering Research Council (NSERC) of Canada (Discovery Grants Program), as well as of the Killam Trusts.

REFERENCES

[1] S. Iakovlev. External shock loading on a submerged fluid-filled cylindrical shell. *Journal of Fluids and Structures*. 22: 997-1028, 2006.

[2] S. Iakovlev. Interaction between a submerged evacuated cylindrical shell and a shock wave. Part II: Numerical aspects of the solution. *Journal of Fluids and Structures*. 24: 1098-1119, 2008.

[3] S. Iakovlev, G. Dooley, K. Williston, J. Gaudet. Evolution of the reflection and focusing patterns and stress states in two-fluid cylindrical shell systems subjected to an external shock wave. *Journal of Sound and Vibration*. 330: 6254-6276, 2011.

INVESTIGATIONS ON AN ADAPTIVE HELMHOLTZ RESONATOR CONCEPT

A. Benouhiba, M. Ouisse, K. Rabenorosoa, N. Andreff

Univ. Bourgogne Franche-Comté, FEMTO-ST Institute, CNRS/UFC/ENSMM/UTBM,
Department of Applied Mechanics, 24 rue de l'épitaphe, 25000 Besançon, France

ABSTRACT

Helmholtz resonators have been historically one of the first engineered concepts for acoustic control. They can be used either for increasing sound at a specific frequency, or create antiresonances depending on the way they are implemented. In terms of acoustic control for industrial applications, they constitute very efficient solutions for tonal excitations with a fixed frequency. The resonance frequency of the resonator has to be tuned on this frequency, meaning that if any change occurs in the excitation frequency, the control is no longer possible with the resonator. The concept proposed here to overcome this limitation consists in designing a Helmholtz resonator with a variable volume, that can be controlled in real-time. On the basis of waterbomb origami design, multiphysics simulations are performed to define the geometry of the adaptive cavity. After manufacturing, experimental tests are used to validate the models and illustrate the efficiency of the concept.

1 INTRODUCTION

Helmholtz resonance is the name given to the resonance phenomenon occurring in a cavity linked to the surrounding atmosphere (which is usually air) via a constricted neck or necks. Hermann L. F. von Helmholtz [1] established first its physical and mathematical principles. The most common example for Helmholtz resonators, are bottles and stringed instruments, especially bottles given the fact that they fit the description very well (small opening into a large chamber) [2]. As the frequency is controlled by the geometrical properties of the resonator [3–5], controlling the geometry of the device (such as the volume of the cavity), means controlling the frequency at which noise reduction is desired. Following this line of reasoning, creating an adaptive Helmholtz resonator is a valid option. There are several works in the literature that address the subject of tunable Helmholtz resonators and the most effective means of using them in order to control sound and thereby, achieve noise attenuation. De Dedout [6] proposed an adaptive-passive noise control with self-tuning Helmholtz resonators, where a varying cavity volume was achieved, by adding two rigid walls inside the cylindrical resonator cavity. Both walls were linked to each other at the center of the cavity, allowing easily the rotation of the movable wall through a DC motor. Rigid walls being difficult to use to obtain continuously varying volumes, polymers have been at the center of recent works to try to tune the frequency of acoustic resonators. Yu [7] proposed a tunable acoustic metamaterial with an array of (non-Helmholtz) resonators actuated by a dielectric elastomer. Abbad used a similar material to control an elastic resonance of a membraned Helmholtz resonator [8], but also its volume [9]. Following this strategy, relatively small volume variations can be obtained, hence in this work, a new concept is proposed: in order to obtain large volume variations, an origami-based design is investigated.

2 GEOMETRY OF THE ADAPTIVE HELMHOLTZ RESONATOR

Origami designs offer extreme reconfigurability and a wide range of deployability thanks to their hinges rotation and their facets deformation. This can be exploited to create lightweight devices with controlled characteristics and tunable properties [10]. The origami base chosen here, on the basis of the requirements and state of the art [11, 12] is the waterbomb (see fig. 1). The origami waterbomb base is a single-vertex origami mechanism with unique characteristics that may prove advantageous in a wide range of applications, one of which is vibro-acoustics. The base shows a high potential as a testbed for smart materials and integrated actuation systems thanks to its straightforward geometry and multiple phases of folding/unfolding motion, that ranges from simple (completely flat) to more complex (3D configurations) [13]. The cavity is closed with an end part, which was inspired by the mechanism of the umbrella. This last part keeps the cavity closed during the folding and unfolding of the resonator. On the opposite side, a cylinder is used as resonator neck.

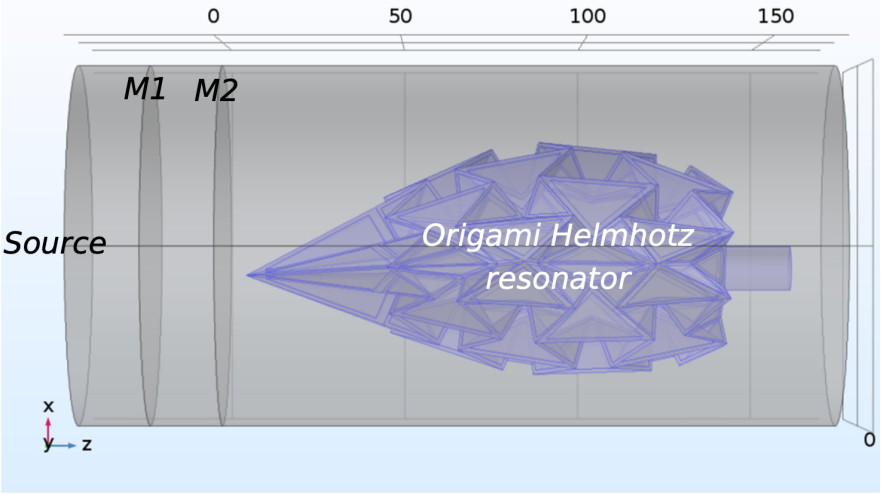

Figure 1: View of the waterbomb Helmholtz resonator in the computation configuration (impedance tube)

3 MULTIPHYSICS SIMULATIONS

In order to define the optimal design of the adaptive Helmholtz resonator, several multiphysics simulations are performed.

- Analytical expressions of resonance frequency are first used to define the macroscopic volume and neck characteristics to achieve the expected frequency shift;
- acoustic finite elements computations are then used by considering rigid walls on the origami structure, in order to check the effect of the complex geometry on the resonance frequency and absorption properties of the resonator (losses in the neck are included in these computations);
- vibro-acoustic coupled finite elements computations are performed to check the effect of walls resonances on the properties of the resonator (structural losses are considered here);
- PTMM [14] computations are used to understand the effect of losses in the constrictions of the origami;
- Nonlinear structural computations using hyperelastic models for the origami walls are finally used to check the foldability and required forces to tune the resonance frequency.

These computations are used to design the final geometry of the Helmholtz resonator, which is manufactured in the lab.

4 EXPERIMENTAL CHARACTERIZATION

Experiments are performed in an impedance tube, using the various folding states of the origami.

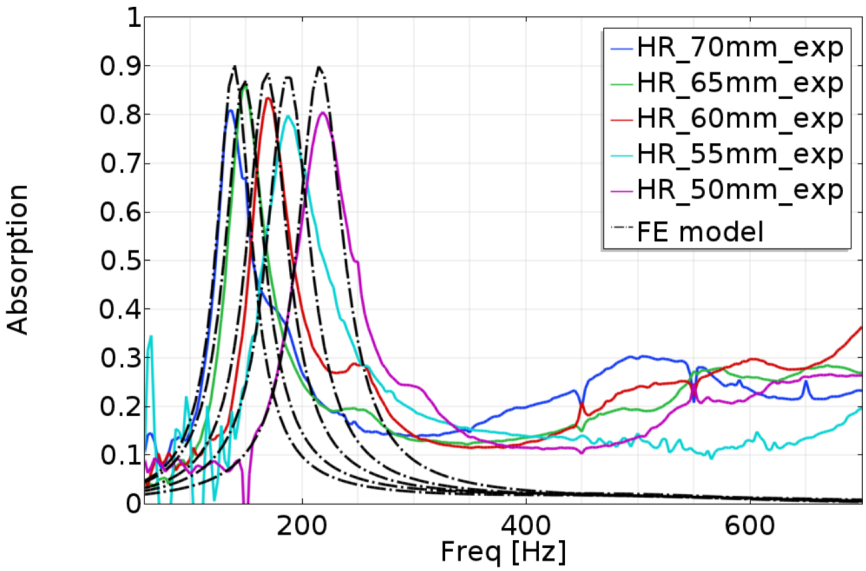

Figure 2. Comparison of experimental tests and simulation results

Results are presented in Figure 2, in terms of absorption coefficient, for several configurations expressed in terms of maximum external diameter of the origami resonator. As expected, the larger the volume, the lower the resonance frequency. A shift from 138 Hz to 219 Hz can be obtained by unfolding the resonator from 50 mm diameter to 70 mm diameter. The resonance frequency and the maximum absorption level are well captured by the model, however the slight increase of absorption coefficient above 400 Hz is not reproduced and may be due to unperfect gluing/manufacturing/geometry of the tested device. The efficiency of prediction of the frequency and levels around the resonance frequency, compared to experimental tests, illustrates the applicability of the adaptive origami-based Helmholtz resonator for practical applications.

ACKNOWLEDGEMENTS

This work has been funded by ANR (contract ANR-17-CE08-0035 ETNAA), in collaboration with EIPHI Graduate School (ANR-17-EURE-0002).

REFERENCES

[1] Hermann Von Helmholtz. *On the Sensations of Tone as a Physiological Basis for the Theory of Music*. Longmans, Green, 1912.

[2] Emile S Webster and Clive E Davies. The use of helmholtz resonance for measuring the volume of liquids and solids. *Sensors*, 10(12):10663–10672, 2010.

[3] Ronald L Panton and John M Miller. Resonant frequencies of cylindrical helmholtz resonators. *The Journal of the Acoustical Society of America*, 57(6):1533–1535, 1975.

[4] RC Chanaud. Effects of geometry on the resonance frequency of helmholtz resonators. *Journal of Sound and Vibration*, 178(3):337–348, 1994.

[5] Uno Ingard. On the theory and design of acoustic resonators. *The Journal of the acoustical society of America*, 25(6):1037–1061, 1953.

[6] Juan M de Bedout, Matthew A Franchek, Robert J Bernhard, and Luc Mongeau. Adaptive-passive noise control with self-tuning helmholtz resonators. *Journal of Sound and Vibration*, 202(1):109–123, 1997.

[7] Xiang Yu, Zhenbo Lu, Fangsen Cui, Li Cheng, and Yongdong Cui. Tunable acoustic metamaterial with an array of resonators actuated by dielectric elastomer. *Extreme Mechanics Letters*, 12:37–40, 2017.

[8] Ahmed Abbad, Noureddine Atalla, Morvan Ouisse, and Olivier Doutres. Numerical and experimental investigations on the acoustic performances of membraned helmholtz resonators embedded in a porous matrix. *Journal of Sound and Vibration*, 459:114873, 2019.

[9] Ahmed Abbad, Kanty Rabenorosoa, Morvan Ouisse, and Noureddine Atalla. Adaptive helmholtz resonator based on electroactive polymers: modeling, characterization, and control. *Smart Materials and Structures*, 27(10):105029, 2018.

[10] Soroush Kamrava, Davood Mousanezhad, Samuel M Felton, and Ashkan Vaziri. Programmable structures: Programmable origami strings (adv. mater. technol. 3/2018). *Advanced Materials Technologies*, 3(3):1870012, 2018.

[11] Kaori Kuribayashi, Koichi Tsuchiya, Zhong You, Dacian Tomus, Minoru Umemoto, Takahiro Ito, and Masahiro Sasaki. Self-deployable origami stent grafts as a biomedical application of ni-rich tini shape memory alloy foil. *Materials Science and Engineering: A*, 419(1-2):131–137, 2006.

[12] Dae-Young Lee, Ji-Suk Kim, Jae-Jun Park, Sa-Reum Kim, and Kyu-Jin Cho. Fabrication of origami wheel using pattern embedded fabric and its application to a deformable mobile robot. In *2014 IEEE International Conference on Robotics and Automation (ICRA)*, pages 2565–2565. IEEE, 2014.

[13] Brandon H Hanna, Jason M Lund, Robert J Lang, Spencer P Magleby, and Larry L Howell. Waterbomb base: a symmetric single-vertex bistable origami mechanism. *Smart Materials and Structures*, 23(9):094009, 2014.

[14] Kévin Verdière, Raymond Panneton, Saïd Elkoun, Thomas Dupont, and Philippe Leclaire. Transfer matrix method applied to the parallel assembly of sound absorbing materials. *The Journal of the Acoustical Society of America*, 134(6):4648–4658, 2013.

Some results of vibroacoustics optimization of a railway gearbox

K. Landet[1], J. Perret-Liaudet[1], E. Rigaud[1] and M. Fraces[2]

[1]Univ. Lyon, Ecole Centrale de Lyon, Laboratoire de Tribologie et Dynamique des Systèmes
LTDS, UMR 5513 CNRS, ECL, ENISE, ENTPE
36 Avenue de Guy Collongue, 69134 Ecully Cedex, France
Email: karl.landet@ec-lyon.fr, joel.perret-liaudet@ec-lyon.fr, emmanuel.rigaud@ec-lyon.fr,

[2]Alstom
105 Allée Albert Einstein, 71200 Le Creusot, France
Email: mathieu.fraces@alstomgroup.com

ABSTRACT

This paper presents the vibroacoustics optimization of a railway gearbox. This gearbox will fit SNCB (Société National des Chemin de fer Belge) trains. In the case of railway applications, the gearbox whining noise contributes significantly to the overall noise. The main excitation source of whining noise is generated by the meshing process. It is usually assumed that the well-known transmission error and the mesh stiffness fluctuations are responsible of this source [1]. Their characteristics result from local tooth and global gearbox deflections, tooth flank corrections and mounting and manufacturing errors. Under operating conditions, they generate dynamic fluctuation of mesh force which is transmitted to the housing through shafts and bearings. The whining noise radiated by the gearbox is closely related to the vibratory level of the housing [1,2].

1 INTRODUCTION

This paper presents the vibroacoustics optimization of a railway gearbox. This gearbox will fit SNCB (Société National des Chemin de fer Belge) trains. In the case of railway applications, the gearbox whining noise contributes significantly to the overall noise. The main excitation source of whining noise is generated by the meshing process. It is usually assumed that the well-known transmission error and the mesh stiffness fluctuations are responsible of this source [1]. Their characteristics result from local tooth and global gearbox deflections, tooth flank corrections and mounting and manufacturing errors. Under operating conditions, they generate dynamic fluctuation

of mesh force which is transmitted to the housing through shafts and bearings. The whining noise radiated by the gearbox is closely related to the vibratory level of the housing [1,2].

The studied gearbox has been designed by Alstom company**.** The maximum power transmitted is equal to 850 kW, for an input speed range from 0 to 4300 rpm. The maximum output torque is equal to 26 kNm. Its weight is approximately 500 kg including 220 kg for the housing. The housing's dimension is approximately 1100x800x400 mm^3 with a mean housing thickness equal to 12 mm. The input shaft is supported by 2 roller bearings and 1 ball bearing. The output shaft is supported by 2 tapered roller bearings. The first part of this work provides the modelling of the gearbox. The second part concerns the optimization parameters. Finally, some results are presented.

2 NUMERICAL MODEL DESCRIPTION

The numerical model is based on FEA (Finite Element Analysis) and presented Figure 1. In this model we discretised the housing (red and blue), an oil collector (grey), shafts, bearings, gears and the experimental bench support (blue and purple).

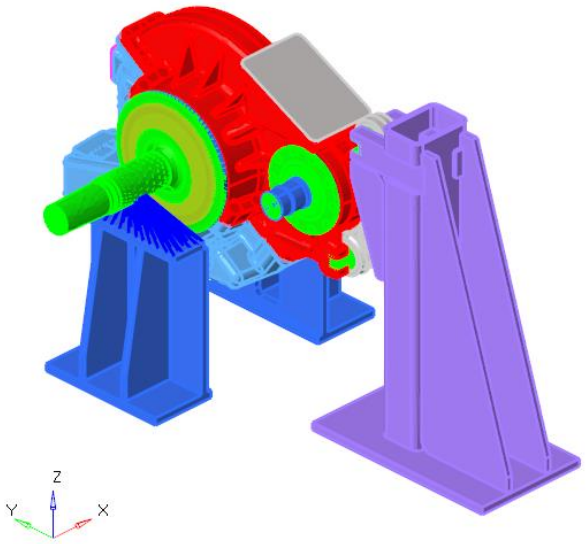

Figure 1: Numerical modelling of the gearbox

This model has 10 million degrees of freedom. With time consuming consideration, we have built a lighter numerical model based on this model for optimizations. We updated this numerical model regarding to ODS experimental data. This light model has 500 000 degree of freedom. All components are modelled with 3D linear tetrahedral element. The bench is clamped on the ground and the green axle is supported by two bearings on the blue bench. These bearings are modelled like pivot joints. The input shaft in blue is free and supported in the gearbox by its bearings. The contacts between the most gearbox's part are considered frozen. For the modelling, the shafts are modelled in 3D to take account their modal behaviour. The bearings inner and outer rings are considered rigid and modelled with RBE2 elements. These two rings are connected by a spring with a stiffness value are computed with the manufacturer data and linearize at the defined torque. The bearing mass is taking account by a punctual mass (CONM2) on the inner ring.

The two shafts are connected together by three springs in the gear action plan with a stiffness value equal to the mean mesh stiffness linearize around the desired work conditions. The excitatory source is the static transmission error (STE) and it is strongly impacted by the meshing frequency. The static transmission error has been computed using a software called Genom©, developed by Alstom company. The nonlinear contact equations to compute STE are solved with a procedure as describe in [3]. This model is confident on studied frequency range (0 to 3 kHz).

3 VIBROACOUSTICS TOPOLOGY OPTIMIZATION

3.1 Optimization parameters

In order to optimize the gearbox, we used a criterion associated to the radiated sound power. To do this we introduced Equivalent Radiated Power (ERP). This ERP is proportional to the time- and space-averaged mean squared vibrational normal velocity of the housing induced by a unique harmonic force applied in the action plan of gear. By assuming a radiation ration equal to the unity this ERP is written as follow:

$$ERP = \rho_0 c_0 \sum_{i}^{n} A_i \overline{V_i^2} \qquad (1)$$

In this equation, V_i^2 is the time-averaged squared normal velocity of each selected node on the housing multiplied by the associated area (A_i). The parameters are the speed of sound (c_0), fluid density (ρ_0). The ERP will usually overestimate the radiation but it will give a qualitatively good approximation [4]. The ERP is obtain from a classic FRF computations. Practically, we compute the ERP for different frequencies with a uniform repartition on the studied frequency range. The cost function to minimize corresponds to the average of ERP over the studied frequency range. We add some constraints in the optimization process: We set a constant mass constraint and constraint misalignment induced by static deformation of the gearbox.

We choose to optimize the housing by topology method. To do this it is necessary to mesh the design space around the housing. The optimization is based on a solid-void density defined for each element in the design space using a method as described in [5]. So the element densities are defined as design variables. A gradient method is used to do the optimization. Finally, we are used a stop criterion based on the relative difference of the cost function. When the difference is smaller than 0.5% for two consecutive step, we stop the optimization.

3.2 Optimization results

We perform the optimization on a uniform frequency range (0 to 3kHz). At the first step we deleted all ribs and oil carrying from the original gearbox. This represent 13kg of matter. Figure 2 shows a result of a topology optimization (in green). As we can see it try to stiffened the oil collector and the oil tank because these areas have high vibratory level.

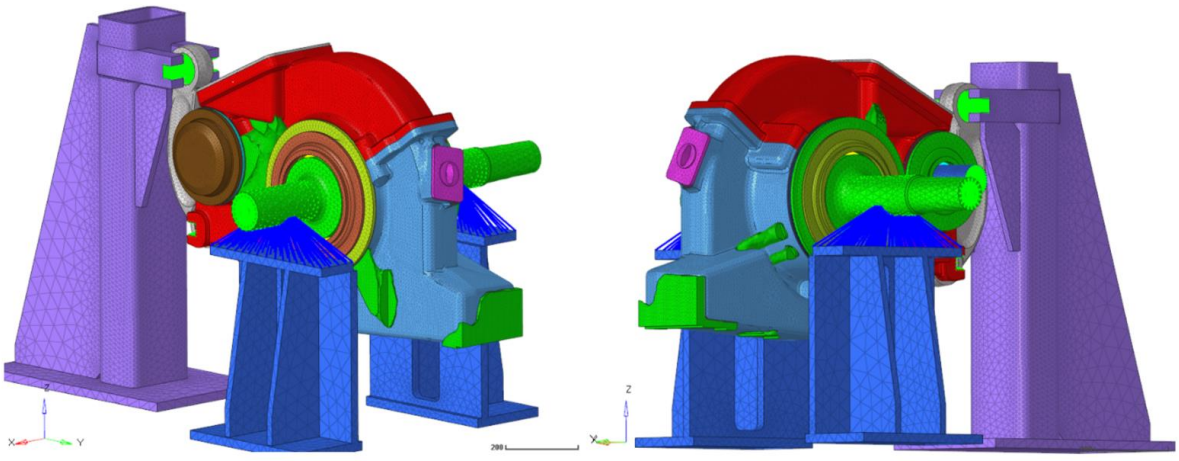

Figure 2: Optimized gearbox

After the optimization and the post treatment we checked the ERP in Figure 3. Between 0 to 3kHz, we computed the integral of the curves. We get 2.74 $\mu m^2.s^{-2}$ for the optimized gearbox instead of 3.54 $\mu m^2.s^{-2}$ for the original gearbox, so an important decrease of 22.5% of the vibratory power. As we can see Figure 3, this decrease is mainly correspond to decrease over the frequency range between 1.5 to 2.5 kHz (a mean decrease of 31%) in the ear sentivity.

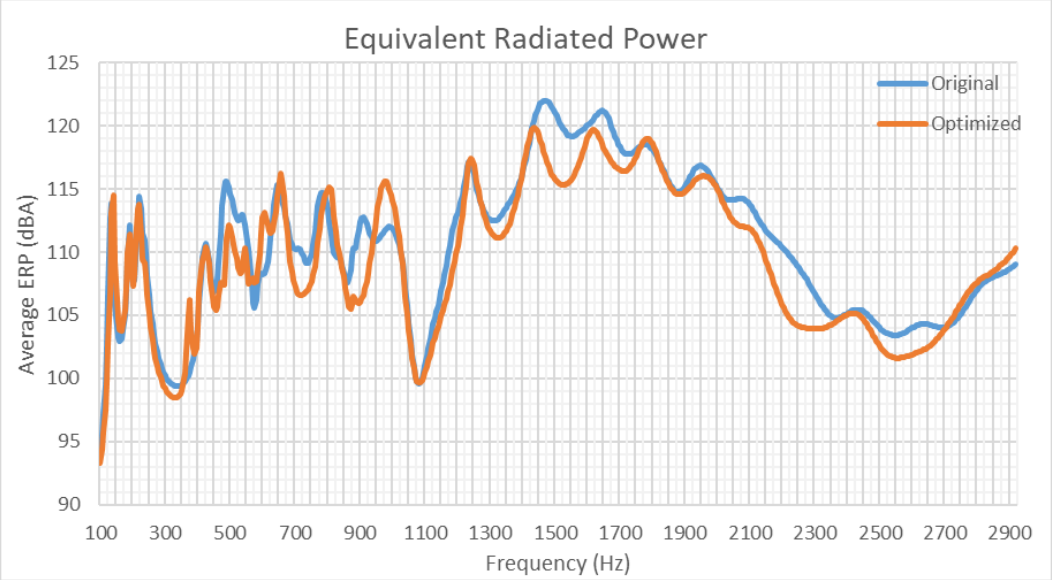

Figure 3: ERP with a dBA filter of the original gearbox and the optimized gearbox

4 CONCLUDING REMARKS

To conclude, we modelled a gearbox correlated on experimental data to do vibroacoustics optimization. We performed topological optimizations with the element densities of the design space as design variables. For building cost function, we used equivalent radiated power as criterion for the radiated sound power. The optimization gives exploitable results to manufacturing a prototype in the hope of get the same decrease of the ERP criterion of 22.5% on average. In point of view of the procedure the time consuming is small. One optimization is performed on 1-2 days on a computer with 32 cores and 192 Gb of RAM memory. Scratch RAM memory method are used to boost the computation during the generation of temporary files.

REFERENCES

[1] D. B. Welbourn, « Fundamental knowledge of gear noise: a survey », IMechE-C117/79, 1979.
[2] A. Carbonelli, E. Rigaud, et J. Perret-Liaudet, « Vibro-Acoustic Analysis of Geared Systems—Predicting and Controlling the Whining Noise », in *Automotive NVH Technology*, Springer, 2016, p. 63–79.
[3] E. Rigaud et D. Barday, « Modelling and analysis of static transmission error. Effect of wheel body deformation and interactions between adjacent loaded teeth », in *4th World Congress on Gearing and Power Transmission*, 1999, vol. 3, p. 1961–1972.
[4] D. Fritze, S. Marburg, et H.-J. Hardtke, « Estimation of radiated sound power: A case study on common approximation methods », *Acta Acustica united with Acustica*, vol. 95, n° 5, p. 833–842, 2009.
[5] D. Brackett, I. Ashcroft, et R. Hague, « Topology optimization for additive manufacturing », in *Proceedings of the solid freeform fabrication symposium, Austin, TX*, 2011, vol. 1, p. 348–362.

DESIGN GUIDELINES FOR THE ACOUSTIC PERFORMANCE IMPROVEMENT OF A PERIODIC POROUS MATERIAL

D. Magliacano[1,2], M. Ouisse[1], S. De Rosa[2], F. Franco[2] and A. Khelif[1]

[1] FEMTO-ST Institute, Univ. Bourgogne Franche-Comté, Besançon, FRANCE
Email: dario.magliacano@univ-fcomte.fr, morvan.ouisse@univ-fcomte.fr, abdelkrim.khelif@univ-fcomte.fr

[2]DII – Sez. Ing. Aerospaziale, Università degli Studi di Napoli "Federico II", Naples, ITALY
Email: sergio.derosa@unina.it, francesco.franco@unina.it

ABSTRACT

In this paper, some guidelines are provided in order to predict at which frequency the 1st performance peak (related to periodicity effects: half of the wavelength = periodicity dimension) appears, together with its amplitude, as functions of the unit cell dimensions. Conversely, also the link between the unit cell dimensions and the 1st performance peak amplitude as functions of the design frequency is shown. Furthermore, some additional guidelines are provided in order to predict at which frequency the 1st performance peak appears, together with its amplitude, as functions of the foam airflow resistivity.

1 INTRODUCTION

The design based on periodic elements is a powerful strategy for the achievement of lightweight sound packages and represents a convenient solution for manufacturing aspects [1]. An interesting research target is the inclusion of vibroacoustic treatments at early stage of product development through the use of porous media with periodic inclusions, which exhibit proper dynamic filtering effects [2]; this address different applications in transportation (aerospace, automotive, railway), energy and civil engineering sectors, where both weight and space, as well as vibroacoustic comfort, still remain as critical issues. Here we propose some design guidelines in order to tune the performances of a JCA-modeled foam [3], [4], which make possible to obtain a device whose frequency efficiency outperforms existing designs.

2 DESIGN GUIDELINES

Some guidelines are provided in order to predict at which frequency the 1st performance peak (related to periodicity effects: half of the wavelength = periodicity dimension) appears, together with its amplitude, as functions of the unit cell dimensions. Conversely, also the link between the unit cell dimensions and the 1st performance peak amplitude as functions of the design frequency is shown. The test campaign is carried out in the 0 – 18000 Hz frequency range, through the use of a repetition of five 3D unitary cells constituted by a 2 cm cube with a 0.5 cm radius perfectly rigid cylindrical inclusion, where the dimension of the inclusion changes accordingly to those of the unit cell (the ratio between the unit cell and the inclusion dimensions is kept constant).

Density [kg/m^3]	Prandtl number	Dynamic viscosity [kg/(m*s)]	Adiabatic bulk modulus [kg/(m*s^2)]	Specific heat ratio
1.205	0.713	$1.983*10^{-5}$	$1.42*10^5$	1.401

Table 1: Air properties.

Porosity	Tortuosity	Resistivity [Pa*s/m^2]	Viscous characteristic length [mm]	Thermal characteristic length [mm]
0.99	1.02	8430	0.138	0.154

Table 2: Acoustic parameters of the foam used for the numerical test campaign.

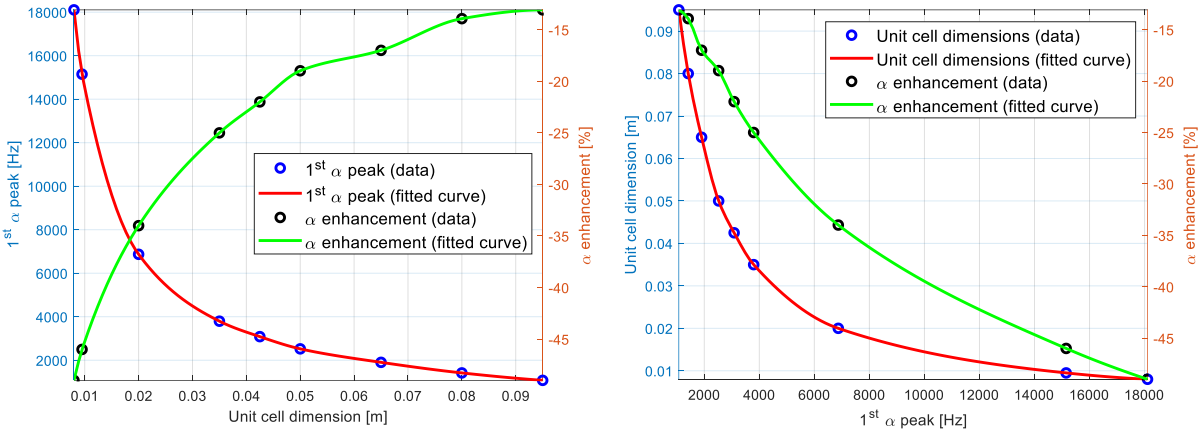

Figure 1: Absorption coefficient design curves as a function of the unit cell dimension (on the left) and the frequency of the 1st peak (on the right).

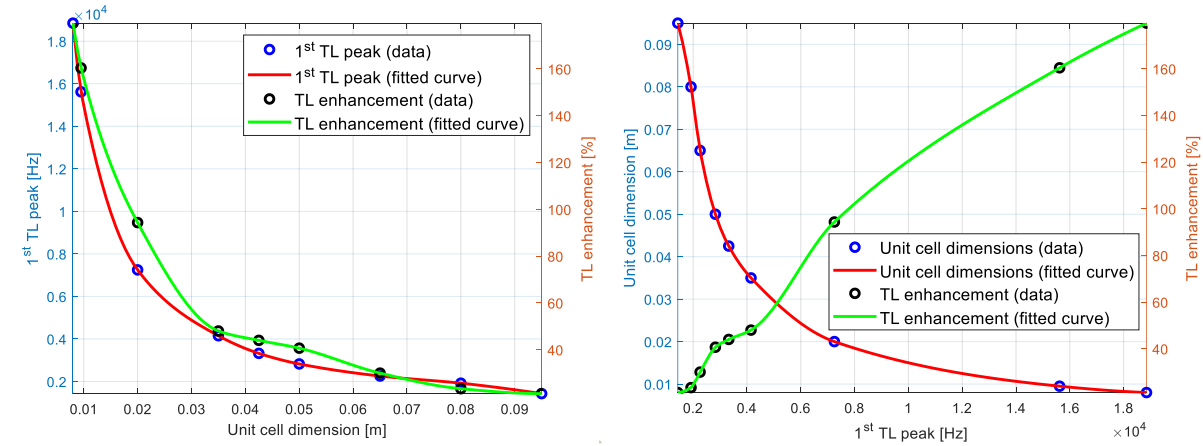

Figure 2: Transmission loss design curves as a function of the unit cell dimension (on the left) and the frequency of the 1st peak (on the right).

According to the results obtained in Figure 1 and Figure 2, and considering that a typical acoustic excitation in aeronautics lays in the range of 20 – 2000 Hz [5], one should choose a unit cell dimension between 0.065 m and 0.1 m in order to obtain a transmission loss improvement of averagely 25% respect to the use of a simple foam layer of the same thickness. Considering an automotive application, instead, the typical acoustic excitation lays in the range of 20 – 4000 Hz [6], and therefore one should choose a unit cell dimension between 0.035 m and 0.1 m in order to obtain a transmission loss improvement of averagely 35% respect to the use of a simple foam layer of the same thickness.

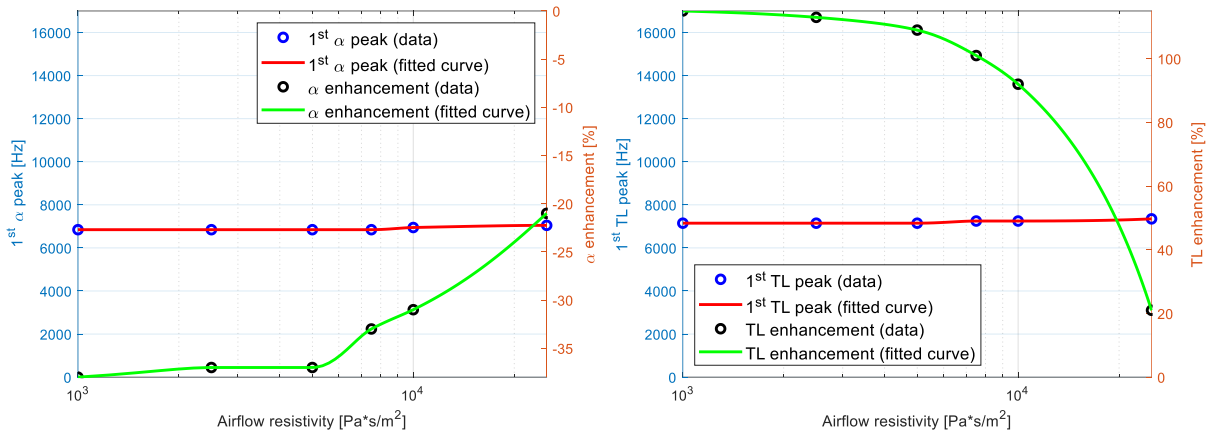

Figure 3: Absorption coefficient (on the left) and transmission loss (on the right) design curves as functions of the foam airflow resistivity value.

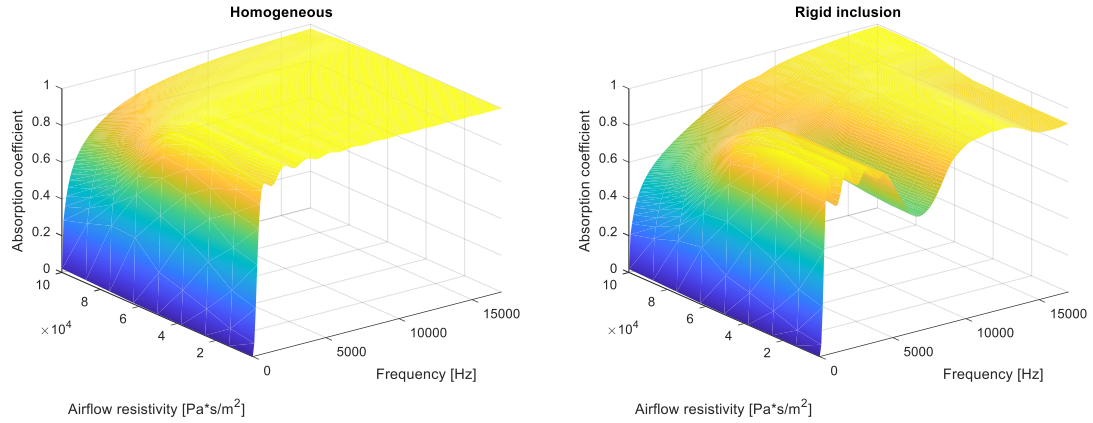

Figure 4: Absorption coefficient value as a function of frequency and foam airflow resistivity; homogeneous case (on the left) and case with a cylindrical perfectly rigid inclusion (on the right).

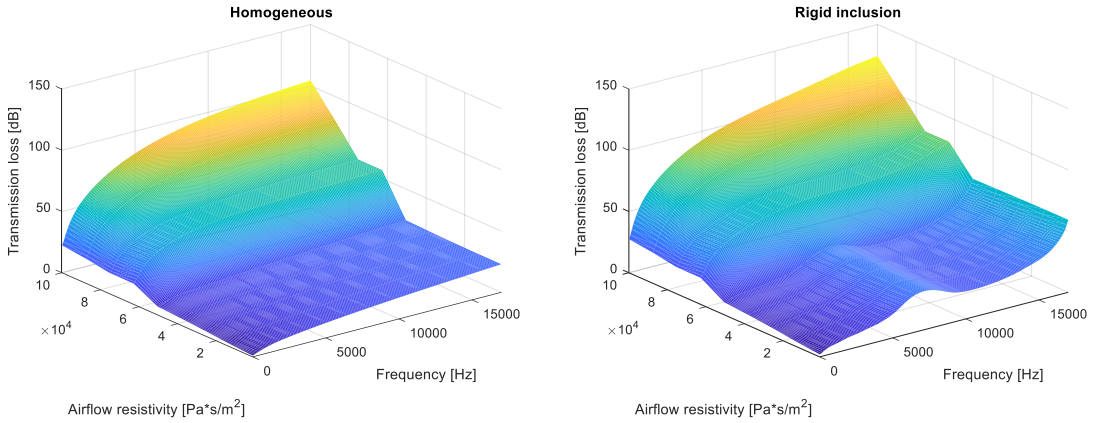

Figure 5: Transmission loss value as a function of frequency and foam airflow resistivity; homogeneous case (on the left) and case with a cylindrical perfectly rigid inclusion (on the right).

Furthermore, some guidelines are also provided in order to predict at which frequency the 1st performance peak appears, together with its amplitude, as functions of the airflow resistivity value of the foam. The test campaign is carried out in the 0 – 17000 Hz frequency range, by comparing a repetition of five melamine unit cells, where the airflow resistivity value is artificially changed. Looking at Figure 3, it is clear that the static airflow resistivity has no meaningful impact on the position of the periodicity peak in the frequency range. Instead, one may notice that σ has a non-negligible effect on the variation of the non-homogeneous values, compared to the homogeneous ones, in correspondence of the periodicity peak: in particular, this variation reduces its amplitude at increasing airflow resistivity values, both for absorption coefficient and transmission loss performances. This is probably due to the fact that, as shown in Figure 4 and, in an even more evident manner, in Figure 5, for a homogeneous layer of foam, when σ increases absorption coefficient performances decrease, while transmission loss ones gets better. This is an expected phenomenon, since the airflow resistivity parameter may be considered as an "acoustical hardness" indicator of a foam, in the sense that, the higher it is, the less air permeability there is. It is evident, then, that the general effect of the presence of any external inclusion in the foam reduces at increasing σ, and the non-homogeneous curves tends to assume the same behavior of the homogeneous one, still maintaining a bias difference in the average value (as it can be clearly seen from Figure 5). Indeed, already starting from $\sigma = 50000 \ \frac{\mathrm{Pa*s}}{\mathrm{m}^2}$, periodicity peaks are no more precisely identifiable.

3 CONCLUSIONS

In this paper, some guidelines are provided in order to predict at which frequency the 1st performance peak appears, together with its amplitude, as functions of the unit cell dimensions and of the airflow resistivity; conversely, also the link between the unit cell dimensions and the 1st performance peak amplitude as functions of the design frequency is shown. Results are very promising for aeronautic and automotive applications.

ACKNOWLEDGEMENTS

This project has received funding from the European Union's Horizon 2020 research and innovation program under the Marie Skłodowska-Curie grant agreement No. 675441 (ViPer project).

REFERENCES

[1] J. F. Allard and N. Atalla, *Propagation of Sound in Porous Media: Modelling Sound Absorbing Materials*, 2nd ed. Wiley, 2009.

[2] D. Magliacano *et al.*, "Computation of dispersion diagrams for periodic porous materials modeled as equivalent fluids," *Mech. Syst. Signal Process.*, vol. 130, pp. 692–706, 2019.

[3] D. L. Johnson, J. Koplik, and R. Dashen, "Theory of dynamic permeability and tortuosity in fluid-saturated porous media," *J. Fluid Mech.*, vol. 176, no. 1, p. 379, 1987.

[4] Y. Champoux and J. F. Allard, "Dynamic tortuosity and bulk modulus in air-saturated porous media," *J. Appl. Phys.*, vol. 70, no. 4, pp. 1975–1979, 1991.

[5] A. Peiffer, "Full frequency vibro-acoustic simulation in the aeronautics industry," in *Isma2016*, 2016.

[6] A. Mohanty and S. Fatima, "An overview of automobile noise and vibration control," *Noise Notes*, vol. 13, no. 1, pp. 43–56, 2014.

DYNAMIC POWER LOSS MODEL INCLUDING FRICTIONAL EFFECTS FOR SPUR GEARS

Maroua Hammami[1] , Nabih Feki[1,2] , Olfa Ksentini[1] , Mohamed Slim Abbes[1] and Mohamed Haddar[1]

[1]Laboratory of Mechanics, Modelling and Manufacturing (LA2MP), National Engineering School of Sfax, Ministry of Higher Education and Research of Tunisia, BP 1173, 3038 Sfax, Tunisia
Email: hammamimaroi@gmail.com, olfa.ing@gmail.com, slim.abbes@enis.tn, Mohamed.haddar@enis.rnu.tn

[2]University of Sousse, Higher Institute of Applied Science and Technology of Sousse, 4003, Sousse, Tunisia
Email: fekinabih@gmail.com

ABSTRACT

A twelve-degree-of-freedom gear dynamics model taking into account frictional effects, time varying mesh stiffness and damping was investigated. Fiction between meshing gear teeth are the most influential power loss sources in a gearbox under several operating conditions. Frictional losses in gears are deeply related to load, speed and coefficient of friction. The aim of this work is to introduce a gear dynamic model for spur gears and to evaluate the power loss at different operating conditions using an experimental coefficient of friction allowing to more refined the gear friction losses estimation.

1 INTRODUCTION

Optimizing gearbox efficiency under a static load conditions was studied in previous works [1, 2] as first step in this direction, but it is interesting also to understand the behaviour of a rotating gears since dynamic effects as a determining factor in the gearbox were considered.

In order to design a more reliable and efficient gearboxes, a detailed gearbox efficiency estimations in dynamic conditions were used, which can save resources not only during development, but also through the gearbox's expected life [2].

For many years, several authors have studied the problem of gear dynamics by modifying the details of their dynamic models like increasing degrees of freedom, varying mesh stiffness and frictional, gyroscopic and rocking effects in order to evaluate the dynamic overloads, critical speeds, transmission errors and gear noise [3, 4].

As previously cited, infrequent studies around gear efficiency including dynamic effects. In this work a twelve degree of freedom (DoF) model that takes into account time varying mesh stiffness, damping and frictional effects was used. The main focus of this work was the influence of gear tooth geometry and dynamics in gear power loss. A spur gears that were studied in previous works [1], were analysed under different operating conditions and a constant coefficient of friction.

2 MODEL FORMULATION

The model of four nodes with three DOFs per node, presented in Figure 1, contains two shafts simulated by two node Timoshenko beams, the pinion gear pair assimilated as two rigid-cylinders, the bearings inserted as lumped stiffness and damping elements, a motor and a load imposing by the FZG machine.

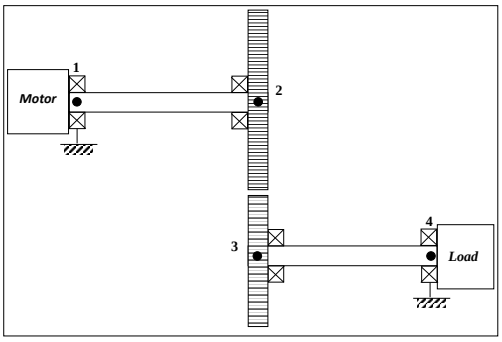

Figure 1: The nodes of the dynamic gear model (12 DOFs).

By using the Lagrange equation and neglecting centrifugal and gyroscopic effects, the equations of motion of the system is detailed as follow:

$$[M]\,\ddot{X} + [C]\,\dot{X} + [K(t,X)]\,X = F_1(f,t) + F_f(t,X) \tag{1}$$

where $[X] = [v_1, w_1, \theta_1, v_g, w_g, \theta_g, v_p, w_p, \theta_p, v_2, w_2, \theta_2]^T$ is the DOF's vector including only translational (v_j,w_j) and torsion (θ_j) degrees; $[M]$, $[K(t,X)]$, and $[C]$ are the global mass, stiffness, and damping matrices; $F_1(f,t)$ is the external load vector and $F_f(t,X)$ is tooth friction excitation vector.

$$F_1(t,X,f) = [0, 0, C_m(t,X,f), 0, 0, 0, 0, 0, 0, 0, 0, C_r(t,X,f)]^T \tag{2}$$

$$F_f(t,X) = -f\frac{1}{\epsilon_\alpha} S(t,X) Km(t) W V_G^T \tag{3}$$

3 RESULTS

The Newmark's integration method is used to solve the equations and obtain the dynamic responses.

Table 1 shows the geometric parameters of the spur gear geometries. Table 2 presents the average coefficient of friction and operating conditions for each simulation performed in previous

experimental work [1, 2]. The simulations were carried out at FZG lod stages K5 ($C_m = 70Nm$) and K11 ($C_m = 319Nm$) for both 500 and 1750 rpm. The 75W90-A oil was selected and the operating temperatures was maintained at 80 °C.

Table 1: C40 FZG gears properties.

Gears	Parameters										
		z [/]	m[mm]	a[mm]	α [°]	β[°]	b[mm]	x[/]	d_a[mm]	ϵ_γ [/]	$R_a[\mu m]$
C40	pinion	16	4.5	91.5	20	0	40	+0.1817	82.46	1.44	0.5
	wheel	24						+0.1715	118.54		

Table 2: Experimental Coefficient of friction (COF) (75W90-A axle gear oil [2]).

Speed [rpm]	FZG load stage	Gear geometry and COF
		C40
500	K5	0.029
	K11	0.039
1750	K5	0.023
	K11	0.031

Figures 2 and 3 show the dynamic coefficient and the power loss at the selected period.

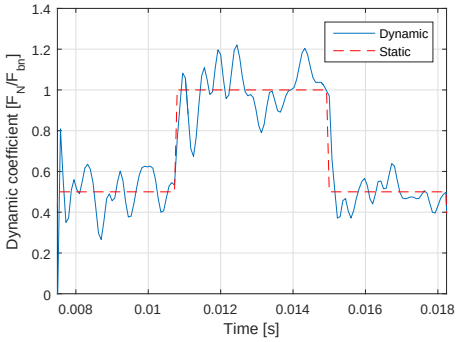

(a) Dynamic coefficient-500 rpm

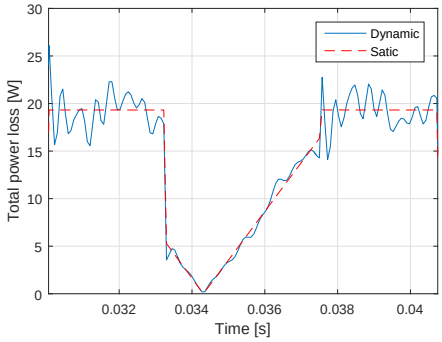

(b) Total power loss-500 rpm

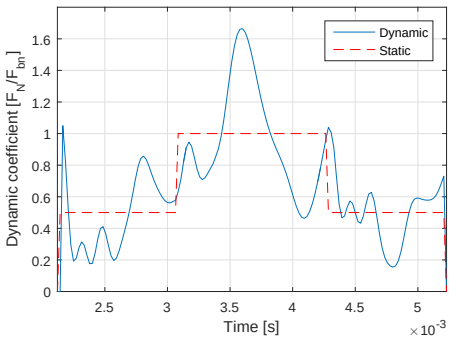

(c) Dynamic coefficient-1750 rpm

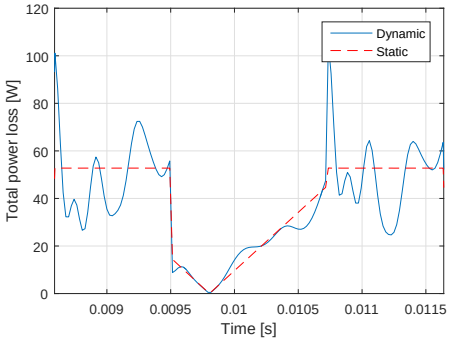

(d) Total power loss-1750 rpm

Figure 2: Dynamic coefficient and total power simulations for C40 spur gears at K5.

The dash lines represent the quasi-static simulations and the continuous lines are the dynamic simulations.

It is observed that the results obtained when including frictional effects were clearly different from the ones considered in quasi-static simulations.

Both load stage K5 and K11 results show that spur gears promote higher dynamic overloads when increasing speed from 500 rpm to 1750 rpm. The dynamic coefficient (F_N/F_{bn}) was 1.2 at 200 rpm and about 1.67 at 1750 rpm.

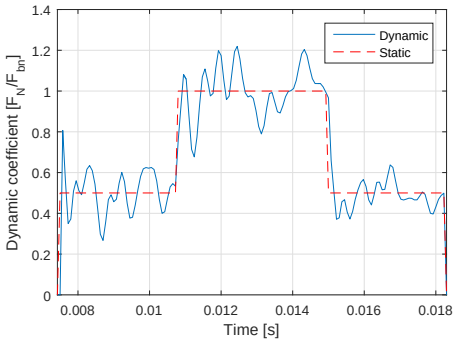

(a) Dynamic coefficient-500 rpm

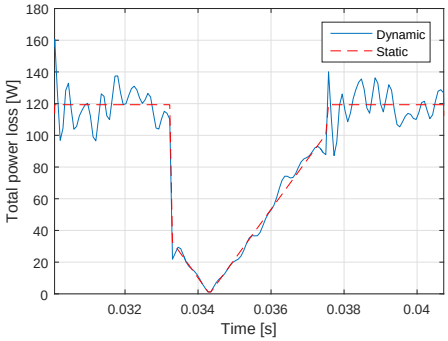

(b) Total power loss-500 rpm

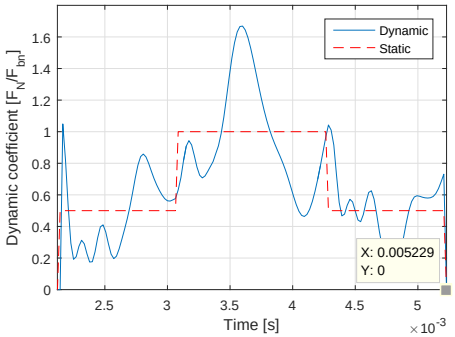

(c) Dynamic coefficient-1750 rpm

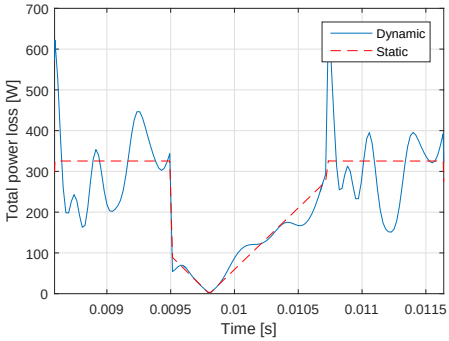

(d) Total power loss-1750 rpm

Figure 3: Dynamic coefficient and total power simulations for C40 spur gears at K11.

The power loss results show that the power loss (P_{VZP}) increases with both load and speed in quasi-static conditions where P_{VZP} at k11 increased from 119.3 W to 325.4 W when the speed increases from 500 rpm to 1750 rpm. The results presented show that the average power loss at stable dynamic conditions with a constant COF are higher than the one calculated in quasi-static conditions.

4 CONCLUSIONS

A twelve degree of freedom gear dynamic model considered frictional effects (constant COF) was used. The effects of gear dynamics and gear geometry in the power loss were evaluated. Friction has show a significant effect in the dynamic behaviour of spur gears. The results show the differences between the average power loss calculations under dynamic and quasi-static conditions proving the coefficient of friction dependency.

REFERENCES

[1] Maroua Hammami, Carlos MCG Fernandes, Ramiro Martins, Mohamed Slim Abbes, Mohamed Haddar, and Jorge Seabra. Torque loss in FZG - A10 gears lubricated with axle oils. *Tribology International*, 131:112–127, 2019.

[2] Maroua Hammami. *Efficiency and wear in automotive gear transmissions*. PhD thesis, National School of Engineers of Sfax (ENIS), Tunisia and Faculdade de Engenharia da Universidade do Porto (FEUP), Portugal, 2017.

[3] H Nevzat Özgüven and Donald Russell Houser. Mathematical models used in gear dynamics −a review. *Journal of sound and vibration*, 121(3):383–411, 1988.

[4] Jianjun Wang, Runfang Li, and Xianghe Peng. Survey of nonlinear vibration of gear transmission systems. *Applied Mechanics Reviews*, 56(3):309–329, 2003.

WAVE AND FINITE ELEMENT ANALYSIS OF QUASI PERIODIC 2D PHONONIC SUPER-CELL CRYSTALS

S. Timorian[1,2], S. De Rosa[1], F. Franco[1], M. Ouisse[2], N. Bouhaddi[2]

[1]Laboratory for Promoting experience in Aeronautics Structures
Department of Industrial Engineering —Aerospace Section
University of Naples Federico II, Napoli
via Claudio 21, 80125, Naples, Italy.
Email: safiullah.timorian@gmail.com, safiullah.timorian@unina.it

[2]Femto-ST Institute
Department of Applied Mechanics
Univ Bourgogne Franche-Comté, Besancon, 25000, France
Email: safiullah.timorian@femto-st.fr

ABSTRACT

Phononic Crystals (PCs) are artificial materials with extensive application in the aerospace and aeronautical industries since they introduce frequency stop-bands (frequency ranges where wave cannot freely propagates). In this investigation 2D periodic and quasi-periodic pattern: instead of strictly repeating a pattern, a certain degree of irregularity is introduced. Quasi-periodic PCs in this paper are defined as assemblies of two different elements in two direction by using Thue-Morse and semi-Sierpinski carpet which results in asymmetry in both directions. Numerical studies on periodic and quasi-periodic lattices are performed. The spectral analysis in periodic waveguide is validated with the dispersion diagram of a reference model and vibration transmission of the lattices are studied. The wave characteristics in quasi-periodic super-cell configuration increases the wide of band-gaps about 22% compared to the reference model. Nevertheless, the associated level of vibration in the forced response of quasi-periodic lattices are predicted.

1 INTRODUCTION

The very first findings of PCs dates back to Sir Lord Isaac Newton who imagined that sound waves propagated through air in the same way that an elastic wave would propagate along a lattice of point masses connected by springs with an elastic force constant. Recent literature study shows theoretical, numerical and experimental works based on vibration reduction and acoustic transmission loss of small and large scale elastic structures using 2D PCs. The existence of band-gaps in PCs was predicted theoretically by [1]. There are two types of band-gap mechanism: the first one is Bragg scattering, this type of band-gaps can be shaped by the elastic wave reflection during the incidence with the scatterer of the neighbouring element which operates as a perfect non-absorbing mirror. The second one is local resonances mechanism that can provide a low frequency band-gap due to the coupling of two oscillators, say, the frequency is not dictated by the spacing of the periodic arrays but by the frequency of the local oscillator. This property could be an asset in plenty

of applications, from vibration filtering to acoustic shielding and from seismology to the dynamic behaviour of space stations. In this investigation quasi-periodic 2D PCs is considered for passive broad band-gaps analysis. The PCs which is embedded in a super-cell is composed of a periodic combination proposed by [2]. The model is optimised by introducing a small degree of irregularity by using Thue-Morse and semi-Sierpinski carpet. The proposed model has same mass as in the reference [2], but with different filling rates of resonator and different cylindrical radius. Dispersion analysis of infinite PCs and forced response of finite panels are analysed. The content of this paper is structured as follows: in section 2 quasi-periodic lexicon is presented. Section 3 introduces results of the infinite super-cells and finite forced response. Closing section brings the conclusion of this study.

2 QUASI-PERIODIC LEXICON

The quasi-periodic model is defined by a small degree of irregularity in the PCs super-cells and finite panels [3]. Two unit cells are modelled for wave finite element analysis, beside that two finite periodic and one quasi-periodic panels are modelled for forced response analysis shown in Fig. 1

2.1 Thue-morse sequence

The Thue-Morse sequence is based on binary arrays. Starting from a 1D example, the sequence can be derived by a function s from the set of binary sequences to itself by replacing every A in a 1D sequence with AB and every B with BA [4]:

$$s(x, y) = s(x)s(y) \tag{1}$$

Eq.1 defines a map s for all strings x, y. Defining the Thue-Morse morphism s(A) = AB, leads to the relations for increasing the quasi-periodicity pattern in one direction. The associated sequence starts with A then AB, ABBA, ABBABAAB, and so on, [5].

2.2 Semi-Sierpinski carpet PCs

Sierpinski carpet has a technique of subdividing a shape into 9 smaller copies of itself by removing one copy from the middle, and continuing recursively for the rest of copies [6]. In the present model Semi-Sierpinski carpet is used to create PCs with local resonators.

2.3 Super-cell

The super-cell is made of 25 cells including square matrices with circular scatters, in which 9 of the circles of these square unit cells are filled with metal scatters and the rest are hollow air holes all around the super-cell. Cell-A and cell-B are designed in two different cases. In case 1 (quasi-periodic 1) the Thue-Morse sequence is applied by considering cell-A ($r = 5$ mm), cell-B ($r = 3$ mm), cell-C ($r = 5.5$ mm), and cell-D ($r = 2.5$ mm). The 9 middle cells are associated to Semi-Sierpinski carpet model and the other circles with the air holes follows Thue-Morse sequence (Fig. 1). The semi-Sierpinski carpet model is adapted to the variation of volume fraction of resonance material by reducing the inclusion (45 steel) of cell-A and at the same time increasing the inclusion (45 steel) of cell-B, using different circular radius in order to keep the same mass as the reference model. On the contrary, case 2 (quasi-periodic 2) deals with a super-lattice of cell-A and cell-B ($r = 4$ mm) as in the reference model but the position of coordinate of the circles in the entire lattice is changed with only two combined elements, using Thue-Morse sequence. For instance the coordinate of the constant cell-B is at base position $p(\vec{\mathbf{i}}, \vec{\mathbf{j}})$, in this method unit cell-A is displaced to $\rho(2\vec{\mathbf{i}}, -2\vec{\mathbf{j}})$. In this case cell-A and B is replicated by Thue-morse sequence in two directions (Fig. 1). Material properties are introduced in the Tab. 1

3 RESULTS OF THE INFINITE SUPER-CELLS AND FINITE FORCED RESPONSE

The dispersion diagram of the super cell quasi-periodic 1 in Fig. 2 shows a complete stop-band effects in the ranges of $139 - 208$ Hz compared to the reference model $153 - 196$ Hz [2], which is 22% larger than the reference model shown in the Fig. 2. On the contrary, the quasi-periodic 2

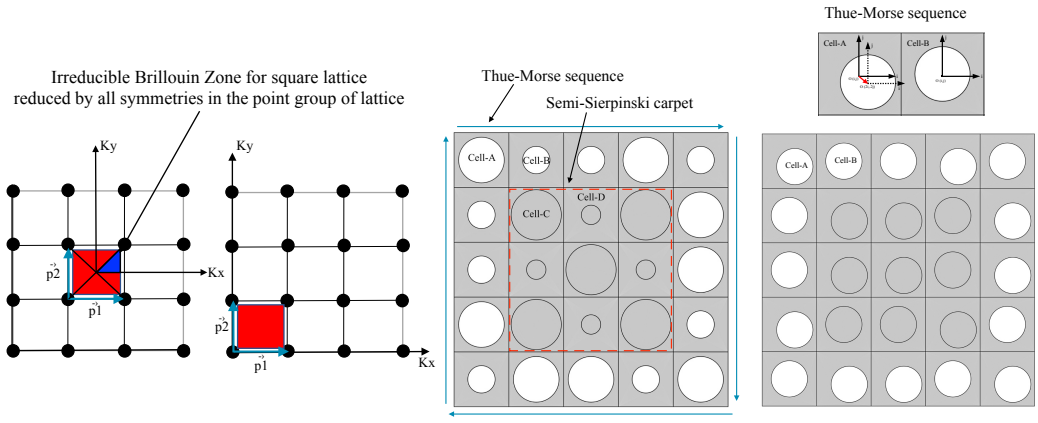

Figure 1: From the right, quasi-periodic 1 and quasi-periodic 2 configurations are graphically presented, in the left, first Brillouin zone reduced by all symmetries in the point group of the lattice

Material type	Modulus of elasticity (Pa)	Poissons Ratio	Density ($kg \cdot m^{-3}$)
Matrix (vulcanized rubber)	21.06×10^{10}	0.26	7780
Scatter (45 steel)	1×10^{6}	0.47	1300

Table 1. Physical parameters

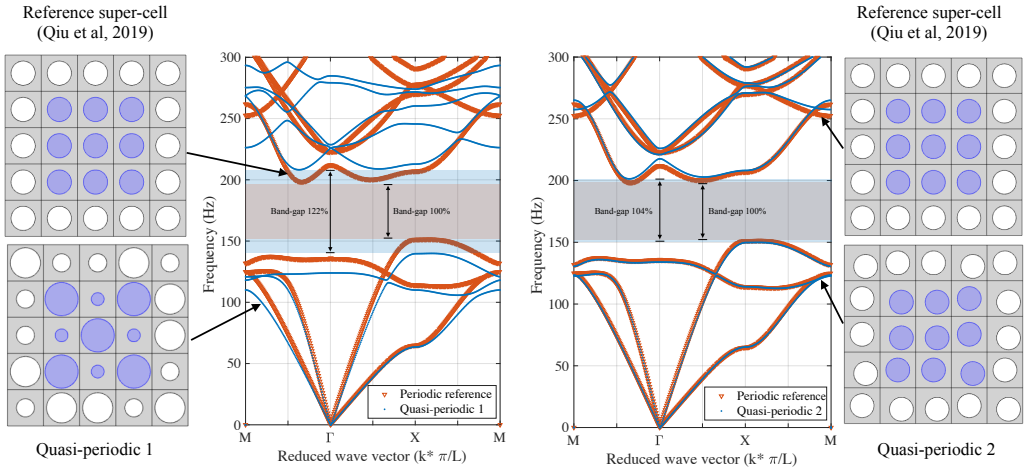

Figure 2. Dispersion diagram of periodic and quasi-periodic PCs

has less effects at around 4% increment compared to the strictly periodic model. The finite panels are made of 2×2 super-cells. In periodic pattern a total of four super-cells exist, whereas for the quasi-periodic panel 2 periodic super cells and 2 quasi-periodic super cells are combined (Fig. 3). Forced response of the panels are computed by applying fixed constraint boundary conditions in the upper and lower sides of the panels (Fig. 3) and a unit boundary load is applied with the frequency range of $0-300$ Hz with a bandwidth of 1 Hz. The vibration transmission is observed as $TL = 20log(a_1/a_2)$. The response of finite panels give four types of band-gaps (BG1, BG2, BG3, and BG4), in the BG1 the response is the same almost for periodic B and quasi-periodic cases. It is the largest one for both cases but possesses a localised mode in the last part of the attenuation level. In BG2 the band-gap is very narrow, and it is only in periodic 2, while BG3 is narrower compared to BG2 and it is in periodic 2 and quasi-periodic case. BG4 is almost two times of BG3 and it is in quasi-periodic with a great fall and partially it could be seen in periodic 2 too. In conclusion periodic B has more band-gaps following quasi-periodic case.

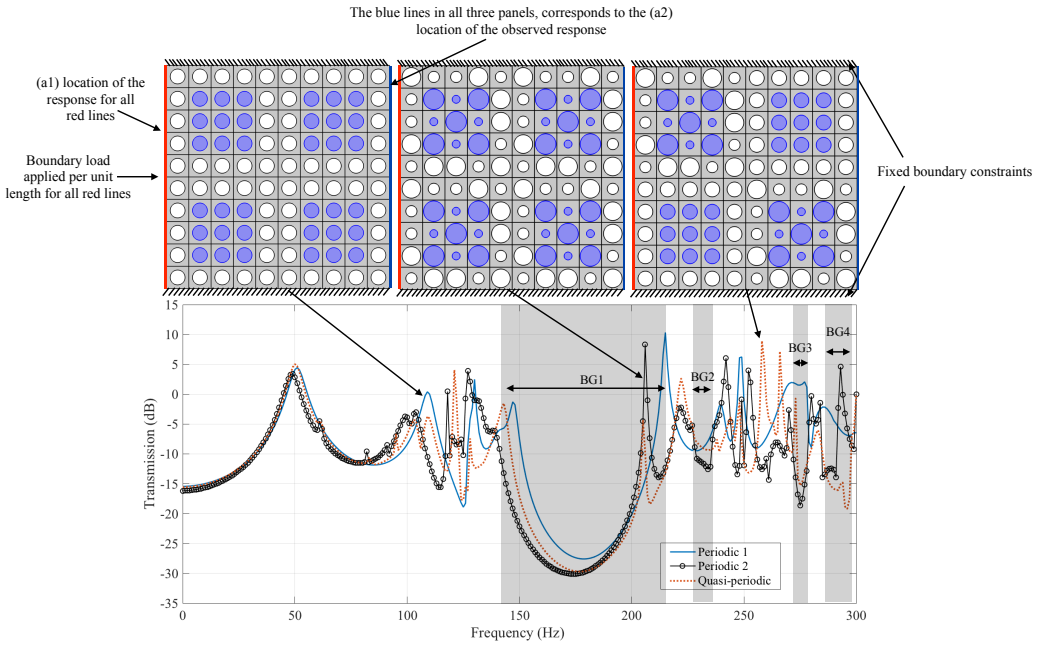

Figure 3. Vibration transmission of two types of periodic and one quasi-periodic panel

4 CONCLUSION

Dispersion diagram of quasi-periodic super-cell enlarges the wide of band-gap more than 22% in lower frequency range $0-300$ Hz compared to the reference model. Quasi-periodic 2 configuration has less effects. Despite its low effects, it gives a good prediction of the associated level of vibration. Finite panels verify the predicted band-gaps for quasi-periodic cases. Good dynamic behaviour is seen in periodic 2 and quasi-periodic with wider band-gaps and extra stop bands above 250 Hz.

ACKNOWLEDGEMENTS

The work is carried out in the framework of the VIPER project (VIbroacoustic of PERiodic media). The project has received funding from the European Union's Horizon 2020 research and innovation program under Marie Curie grant agreement No 675441 and EUR EIPHI (ANR 17-EURE-0002) project.

REFERENCES

[1] Manvir S Kushwaha, Peter Halevi, Leonard Dobrzynski, and Bahram Djafari-Rouhani. Acoustic band structure of periodic elastic composites. *Physical review letters*, 71(13):2022, 1993.

[2] Yingjian Sun, Yingjie Yu, Yayu Zuo, Lili Qiu, Mingming Dong, Jiatong Ye, and Jun Yang. Band gap and experimental study in phononic crystals with super-cell structure. *Results in Physics*, 13:102200, 2019.

[3] S. Timorian, G. Petrone, S. De Rosa, F. Franco, M. Ouisse, and N. Bouhaddi. Spectral analysis and structural response of periodic and quasi-periodic beams. *Journal of Mechanical Engineering Science*, "accepted-in press", 2019.

[4] Jean Berstel. *Combinatorics on words: Christoffel words and repetitions in words*, volume 27. American Mathematical Soc., 2009.

[5] Jean-Paul Allouche and Jeffrey Shallit. The ubiquitous prouhet-thue-morse sequence. In *Sequences and their applications*, pages 1–16. Springer, 1999.

[6] Martin T Barlow. Analysis on the sierpinski carpet. *Analysis and geometry of metric measure spaces*, 56:27–53, 2011.

VIBRATIONS OF PRESTRESSED STRUCTURES COUPLED WITH AN INCOMPRESSIBLE FLUID

C. Hoareau[1], J.-F. Deü[1] and R. Ohayon[1]

[1]Laboratoire de Mécanique des Structures et des Systèmes Couplés
Conservatoire national des arts et métiers (Cnam)
292 rue Saint-Martin, 75003 Paris, France
Email: jean-francois.deu@cnam.fr

ABSTRACT

This paper deals with the computation of vibrations of prestressed elastic tanks partially filled with inviscid incompressible liquids, neglecting sloshing/surface-tension effects. Usually, the prestressed effects due to the liquid load are not taken into account. From experimental point of view, it is shown in [1] that these effects can be significant and influence the vibrations of the system. Indeed, the geometrical nonlinearities may lead to important shift in frequencies due to quasi-static follower loads. In reference [2], the static equilibrium state was supposed given. In particular, in the case of pressured vessel, only the usual geometric stiffness due to the pressure above the liquid (in the case of closed tanks) were taken into account through a linear static analysis. In reference [3], a complete nonlinear analysis has been derived through an original level-set methodology. In reference [4], comparison between experimental and 3D finite element results showed very promising results concerning a rigid cylinder with a flat elastic bottom. The purpose of this work is to present new numerical results on a more complex coupled system and to use a specific modal reduction method in order to reduce the numerical costs related to the added mass effect computation.

Keyword : Fluid-structure interaction, Hydroelasticity, Prestressed effect, Reduced order model.

1 INTRODUCTION

The problem consists in computing the hydroelastic vibrations of a prestressed elastic tank partially filled with liquid (see Fig. 1). Each equilibrium states are obtained by resolution of a nonlinear problem involving hydrostatic follower forces [3]. In the following, we proposed in the first place to express the linearized harmonic three dimensional problem by considering a coupled weak (variational) formulation [2]. The state variables are the structural displacement $\mathbf{u}$ and the fluctuation of pressure p. We recall that the linearization is expressed around a nonlinear equilibrium state. Then, the hydroelastic vibration modes are computed by projection of the fluid-structure problem on the dry modes and a linear combination of induced pressure fields. Usually, the liquid field unknown (here the pressure field) is eliminated as a function of the structural displacement field via an added mass operator which is a symmetric, positive definite and full matrix. The computation of such matrix is obtaned by the Schur complement (or Gauss elimination) analysis and it is known that such a computation - specially for 3D analysis of complex coupled systems - may be very costly. The computational methodology presented here has the advantage to lead to reasonable computational costs, specially for situations in which the wet liquid-structure interface coincides with the elastic structure. The application case envisaged is a rigid cylindrical tank with an elastic hemi-ellipsoidal bottom containing a liquid, for different levels of liquid in the cylinder part. Shift of the hydroelastic frequencies are clearly put into evidence.

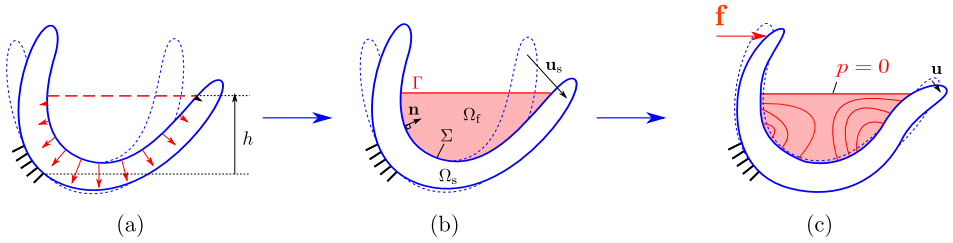

Figure 1: (a) Prestress equilibrium; (b) Fluid-structure domains at rest; (c) Hydroelastic vibrations around the prestressed state.

The hypotheses are the following: the structure is supposed to be elastic and the quasi-static displacement field $\mathbf{u}_s(h)$ is supposed to be known from a nonlinear simulation. Harmonic vibrations are now considered around this static equilibrium state and the corresponding displacement field is denoted $\mathbf{u}$. The liquid is homogeneous, inviscid, incompressible and the potential energy of the free surface due to gravity (or surface tension) is supposed to be negligible with respect to the kinetic energy of the liquid and the potential and kinetic energies of the structure (those hypotheses come from experimental observations). Therefore the liquid pressure is zero on the free surface.

2 COUPLED (U-P) FORMULATION

The coupled non-symmetric problem can be written such that $(\mathbf{u}, p)$ satisfy the following equations:

$$\mathcal{K}_{\text{tan}}(\mathbf{u}_s, \mathbf{u}, \delta\mathbf{u}) + \mathcal{C}(p, \delta\mathbf{u}) - \omega^2 \mathcal{M}(\mathbf{u}, \delta\mathbf{u}) = \mathcal{F}(\delta\mathbf{u}), \qquad \forall\, \delta\mathbf{u} \in \mathcal{C}_u \tag{1}$$

$$\mathcal{H}(p, \delta p) + \omega^2 \rho_f \mathcal{C}(\mathbf{u}, \delta p) = 0, \qquad \forall\, \delta p \in \mathcal{C}_u \tag{2}$$

where $\mathbf{u}_s$ is known. All the forms in the previous equations are express as follow:

$$\mathcal{C}(p, \delta\mathbf{u}) = \int_\Sigma p\mathbf{n} \cdot \delta\mathbf{u}\, ds \;\; ; \;\; \mathcal{M}(\mathbf{u}, \delta\mathbf{u}) = \int_{\Omega_s} \rho_f \mathbf{u} \cdot \delta\mathbf{u}\, dv \;\; ; \;\; \mathcal{F}(\delta\mathbf{u}) = \int_{\partial_t\Omega_f} \mathbf{f} \cdot \delta\mathbf{u}\, ds \tag{3}$$

$$\mathcal{C}(\mathbf{u}, \delta p) = \int_\Sigma \delta p\, \mathbf{n} \cdot \mathbf{u}\, ds \;\; ; \;\; \mathcal{H}(p, \delta p) = \int_{\Omega_f} \mathbf{grad} p \cdot \mathbf{grad} \delta p\, dv \tag{4}$$

where $\mathbf{n}$ is the outward unit normal vector to the structure at the interface Σ, $\mathcal{C}(\bullet, \bullet)$ is a coupling operator at the fluid-structure interface, $\mathcal{F}(\bullet)$ comes from the external fluctuation load, $\mathcal{M}(\bullet, \bullet)$ and $\mathcal{H}(\bullet, \bullet)$ are respectively the kinetic energy forms of the structure and the fluid. The tangent stiffness operator $\mathcal{K}_{\text{tan}}(\bullet, \bullet)$ is the sum of the geometrical, material and the follower force contributions [3]:

$$\mathcal{K}_{\text{tan}}(\mathbf{u}_s, \mathbf{u}, \delta\mathbf{u}) = \mathcal{K}_{\text{geo}}(\mathbf{u}_s, \mathbf{u}, \delta\mathbf{u}) + \mathcal{K}_{\text{mat}}(\mathbf{u}_s, \mathbf{u}, \delta\mathbf{u}) + \mathcal{K}_{\text{fol}}(\mathbf{u}_s, \mathbf{u}, \delta\mathbf{u}) \tag{5}$$

The associated eigenvalue problem is non-symmetric. The projection of this problem on prestressed dry modes are proposed in the following.

3 PROJECTION ON PRESTRESSED DRY MODES

First, we consider the eigenvalue problem associated with the prestressed dry problem (i.e. structure *in vacuo*) such that:

$$\mathcal{K}_{\text{tan}}(\mathbf{u}_\text{s}, \mathbf{u}, \delta\mathbf{u}) - \omega^2 \mathcal{M}(\mathbf{u}, \delta\mathbf{u}) = 0, \quad \forall\, \delta\mathbf{u} \in \mathcal{C}_\text{u} \tag{6}$$

The K first dry modes and the associated circular frequencies are noted $\{\mathbf{u}_\beta, \omega_\beta\}_{\beta=1\ldots K}$. Then, as the liquid motion is irrotationnal in linear vibrations, the fluid displacement potential φ can be used instead of the liquid displacement field. It verifies, for each prescribed modal displacement of the fluid-structure interface $\mathbf{u}_\beta$, the following equations:

$$\Delta\varphi_\beta = 0 \qquad \in \Omega_\text{f} \tag{7}$$

$$\mathbf{grad}\varphi_\beta \cdot \mathbf{n} = \mathbf{u}_\beta \cdot \mathbf{n} \qquad \in \Sigma \tag{8}$$

$$\varphi_\beta = 0 \qquad \in \Gamma \tag{9}$$

We shall highlight that this stage only involve linear system of equations. We now make the assumption that the displacement and the induced pressure are expressed as linear combination of the K dry modes and potential of displacements such that:

$$\mathbf{u} \simeq \sum_{\beta=1}^{K} \mathbf{u}_\beta \kappa_\beta \quad \text{and} \quad p \simeq \sum_{\beta=1}^{K} \rho_\text{f} \omega^2 \varphi_\beta \kappa_\beta \tag{10}$$

where κ_β are the generalized coordinates. The new problem can be expressed by considering the induced pressure as an external load as:

$$\mathcal{K}_{\text{tan}}(\mathbf{u}_\text{s}, \mathbf{u}, \delta\mathbf{u}) - \omega^2 \mathcal{M}(\mathbf{u}, \delta\mathbf{u}) = -\rho_\text{f}\omega^2 \sum_{\beta=1}^{K} \mathcal{C}(p, \delta\mathbf{u})\kappa_\beta, \quad \forall\, \delta\mathbf{u} \in \mathcal{C}_\text{u} \tag{11}$$

By taking successively $\delta\mathbf{u} = \mathbf{u}_\beta$, for each dry modes, the reduced hydroelastic problem becomes:

$$\sum_{\beta=1}^{K} \left\{ \omega_\beta^2 - \omega^2 \left(1 + \sum_{\gamma=1}^{K} m_{\beta\gamma} \right) \right\} \kappa_\beta = 0 \quad \text{where} \quad m_{\beta\gamma} = -\rho_\text{f} \mathcal{C}(\varphi_\beta, \mathbf{u}_\gamma) \tag{12}$$

We can show numerically that if the number of modes K is high enough, the first natural frequencies of Equation (12) converge toward the hydroelastic natural frequencies of the fluid-structure system.

4 RIGID CYLINDRICAL TANK WITH AN HEMI-ELLIPSOID ELASTIC BOTTOM

The vibration problem of a rigid cylindrical tank with an hemi-ellipsoid elastic bottom and partially filled with liquid is solved here by the finite element method (see Fig. 2 for the geometry and mesh).

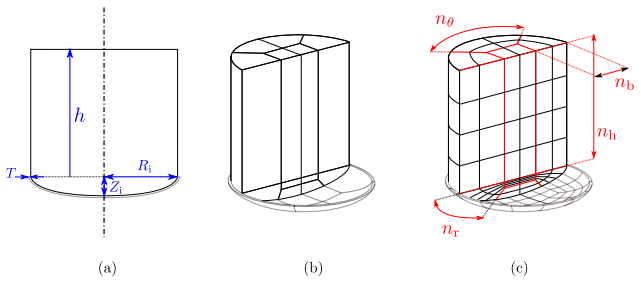

Figure 2: (a) $R_i = 0.144$ m, $Z_i = 0.25R_i$, $T = 0.35$ mm; (b) Fluid-structure geometry; (c) Number of finite elements for the mesh definition: $n_\theta = 10$, $n_\text{t} = 5$, $n_\text{h} = 10$, $n_\text{r} = 10$.

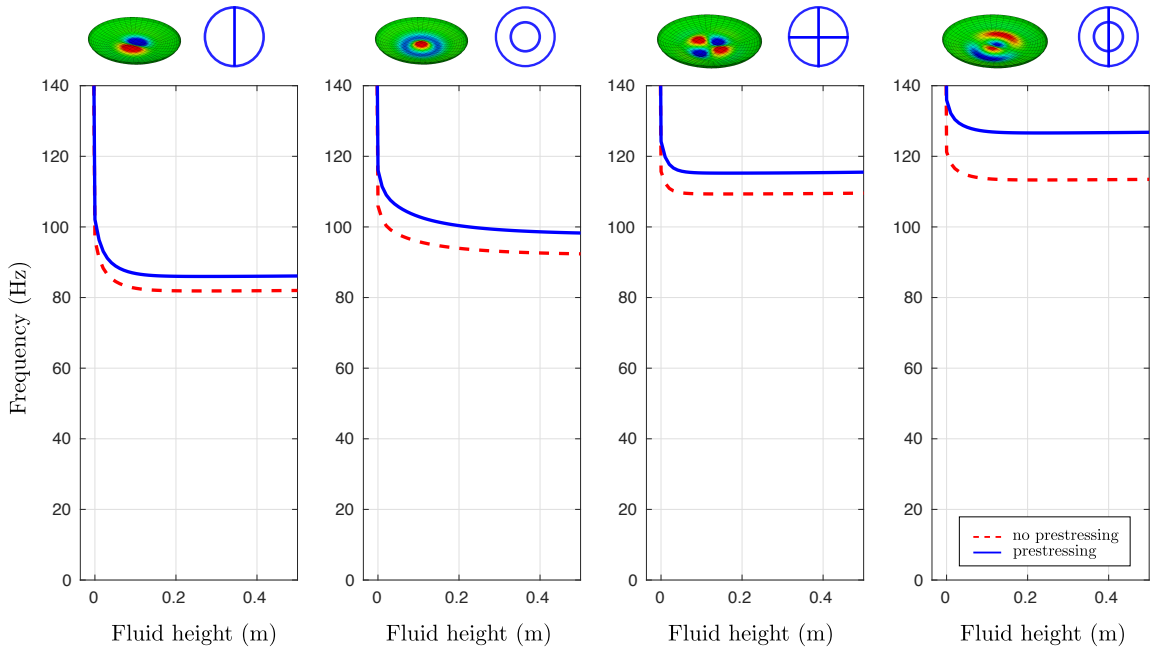

Figure 3: Evolution of natural frequencies as function of the fluid height for $h \in [0, 0.5]$ m. The 4 plots are respectively associated to mode 2, 3, 4 and 5 (30 dry modes are used for each fluid height).

In Fig. 3, the hydroelastic coupled natural frequencies of modes 2, 3, 4 and 5 have been plotted as function of the fluid height. For each fluid height, the eigenfrequencies are obtained either with or without prestressing. We can thus observe on those results the influence of the nonlinear prestressed effect, which is not at all negligible in this specific example.

5 CONCLUSION

This work concerns the computation of vibrations of a structure in contact with an internal free surface liquid. We consider that the hydrostatic pressure exerted by the incompressible internal fluid on the flexible walls of the tank causes large displacements, thus leading to a geometric nonlinear equilibrium state. The change of stiffness related to this prestressed state induces a shift in the resonance frequencies of the coupled linear vibration problem. A reduced order model, based on the projection of the coupled system on the dry structural modes, is also proposed and allows us to compute parametric solutions with low numerical costs and thus quantify the shift of resonance frequencies for various tank filling levels. Future investigations are undertaken to validate the proposed approach on more complex systems and to reduce the hydoelastic vibrations using active/passive damping treatments.

REFERENCES

[1] M. Chiba. Nonlinear hydroelastic vibration of a cylindrical tank with an elastic, bottom containing liquid. Part I: Experiment. *Journal of fluids and structures*, 6(2):181–206, 1992.

[2] H. J.-P. Morand and R. Ohayon. *Fluid Structure Interaction*. Wiley, 1995.

[3] C. Hoareau and J.-F. Deü. Nonlinear equilibrium of partially liquid-filled tanks: A finite element/level-set method to handle hydrostatic follower forces. *International Journal of Non-Linear Mechanics*, 113:112–127, 2019.

[4] C. Hoareau, J.-F. Deü, and R. Ohayon. Prestressed vibrations of partially filled tanks containing a free-surface fluid: Finite element and reduced order models. *In Proceedings of the 8th International Conference on Coupled Problems in Science and Engineering, ECCOMAS Thematic Conference, Sitges, Spain*, 2019.

FRICTION POWER LOSSES PREDICTION OF SPUR GEAR PAIRS WITH CONSIDERING DYNAMIC EFFECTS

Nabih Feki[1,2], Maroua Hammami[1], Olfa Ksentini[1], Mohamed Slim Abbes[1] and Mohamed Haddar[1]

[1] Laboratory of Mechanics, Modelling and Manufacturing (LA2MP)
University of Sfax, National Engineering School of Sfax, BP 1173, 3038 Sfax, Tunisia
Email: fekinabih@gmail.com, hammamimaroi@gmail.com, olfa.ing@gmail.com, slim.abbes@enis.tn, Mohamed.haddar@enis.rnu.tn

[2] University of Sousse, Higher Institute of Applied Science and Technology of Sousse, ISSATSo, 4003, Sousse, Tunisia
Email: nabih.feki@issatso.u-sousse.tn

ABSTRACT

This paper deals with the investigation of the dynamic effects on the friction power losses prediction. The proposed nonlinear dynamic model account for the actual time varying gear mesh stiffness with considering the frictional effects between meshing gear teeth. Constant and local coefficient of friction are introduced in the model formulation under several operating conditions. The equations of motions are developed by deriving the equations of Lagrange and solved the implicit scheme of newmark coupled with the Newton Raphson algorithm. Several numerical simulation results have been presented in order to highlight the dynamic effects on lubricated spur gear pairs and predict its corresponding friction power losses. Simulation results are confronted with experimental results obtained for FZG C40 spur gear pairs which running under several operating conditions (different loads and speeds).

1 INTRODUCTION

The friction in meshing gear power loss is a critical factor affecting the gears efficiency in drive trains, gearboxes and transmissions [1]. It impacts not only the efficiency of the mechanical system but also influences vibration and noise behavior.

The gear friction problem was already dealt in a significant number of studies by several authors in previous works as reviewed by references [2,3]. These studies were based on experimental measured power loss using roller test machine [1] and even FZG machine [4], on empirical formulae that are extensively used in gear transmission applications and can be found in the literature [1] and on EHL model [1].

In order to have accurate power losses predictions, a correct friction formulation is very important especially since it depends on several parameters like sliding and rolling velocities, load or contact pressure, radii of curvature of the surfaces in contact, surface roughness, and lubricant viscosity [1].

A spur gears studied in previous work [4], were analyzed under different operating conditions considering constant coefficients of friction. In the present work a twelve degree of freedom dynamic of one stage gear system model including EHL based frictional formulation has been developed. The main objective of this work is a comparison between two coefficient of friction approaches in gear power losses prediction including dynamic effects. The average power loss in dynamic stabilized conditions using a local coefficient of friction is compared with experimental results and with the one predicted using the classical methods (constant COF).

2 MODEL PRESENTATION

A twelve-degree-of-freedom gear dynamics model is presented in Figure 1 [4]. The gear system is accounted for by 4 nodes and to each node is associated 3 degrees of freedom (2 translational and 1 torsional displacements).

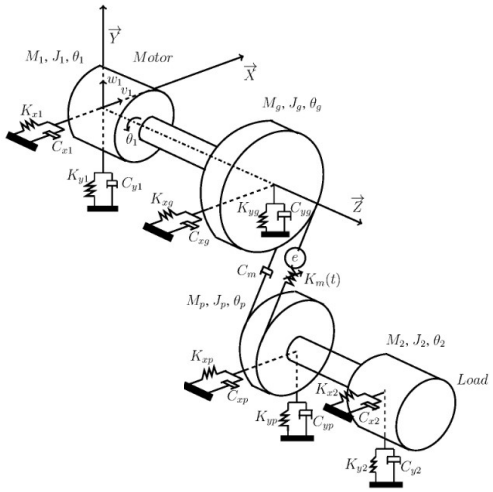

Figure 1. Gear Model presentation [4].

The equation of motion describing the dynamic behavior of the system has been developed by deriving the Lagrange equations with including frictional effects (constant or local COF μ) and neglecting centrifugal and gyroscopic effects. The equation of motion is detailed as [4]:

$$[M]\{\ddot{X}\}+[C]\{\dot{X}\}+\left[\left[K\left(t,\{X\}\right)\right]+\left[K_{\mu}\left(t,\{X\}\right)\right]\right]\{X\}=\left\{F\left(\mu,t,\{X\}\right)\right\} \quad (1)$$

where $[M]$, $[C]$, $\left[K\left(t,\{X\}\right)\right]$, $\left[K_{\mu}\left(t,\{X\}\right)\right]$ are respectively the are the global mass, damping, nonlinear stiffness and frictional stiffness matrices; $\{X\}$ is the DOF's vector and

$\{F(\mu,t,\{X\})\}$ is a vector including motor and load torques and internal frictional excitation.

In order to consider the local coefficient of friction in the gear dynamic simulations, an EHL-based μ formula has been inserted in the mathematical formulation of the model. The equations (2) and (3) present the EHL theoretical model of Xu and Kahraman [1].

$$\mu = e^{f(SR,P_h,\nu_0,S)} P_h^{b2} |SR|^{b3} V_r^{b6} \mu_0^{b7} R^{b8} \tag{2}$$

$$f(SR,P_h,\nu_0,S) = b_1 + b_4 |SR| P_h \log_{10}(\nu_0) + b_5 e^{-|SR|P_h \log_{10}(\nu_0)} + b_9 e^{S} \tag{3}$$

where SR, P_h, ν_0, S, V_r , μ_0, R are respectively the slide to roll ratio, maximum Hertzian pressure, dynamic viscosity, surface roughness, rolling velocity, kinematic viscosity and equivalent radius of curvature; the coefficients b_1 to b_9 of equations (2) and (3) are given in Table 1 for axle gear oil.

b_1	-8.916465	b_2	1.03303	b_3	1.036077	b_4	-0.354068	b_5	2.812084
b_6	-0.100601	b_7	0.752755	b_8	-0.390958	b_9	0.620305		

Table 1. Coefficients for equations (2) and (3).

3 RESULTS AND DISCUSSIONS

All the following simulated and experimental results are obtained for FZG C40 spur gear pairs. The geometric parameters of this type of gear are detailed in Table 2.

	Z	m (mm)	a (mm)	α (°)	β (°)	b (mm)
Pinion	16	4.5	91.5	20	0	40
Wheel	24					

Table 2. FZG C40 gear geometric parameters [4].

Figure 2 presents the constant and the local coefficient of friction for C40 spur gear geometry at load stage K8 (Tm=171.585 N.m) and for two rotational speed (250 and 1000 rpm). The time varying local COF is calculated based on Xu and Kahraman EHL theoretical formulation (equations (2) and (3)).

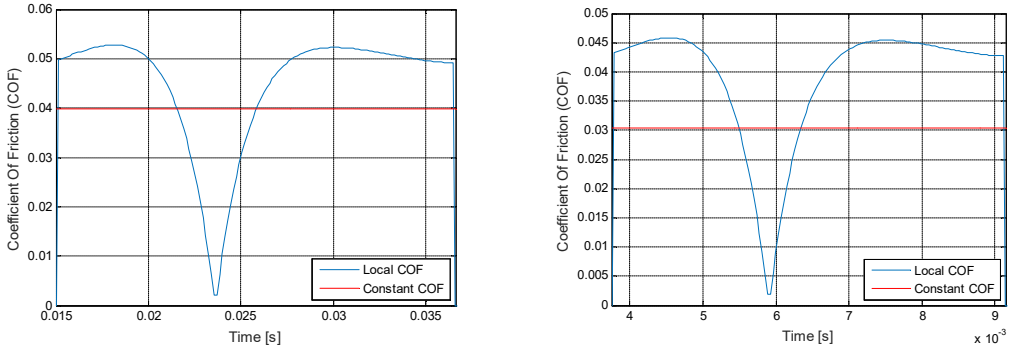

(a) COF at 250 rpm (b) COF at 1000 rpm

Figure 2. Coefficient of friction variation for C40 spur gears at K8.

Figure 3 shows the total friction power losses estimations for C40 gear geometry under quasi static and dynamic conditions. This figure presents the effect of two COF approaches (Constant and local COF). In fact, an increase of the friction power loss level is observed when using the time varying local COF and when increasing the rotational speed. These observations are experimentally validated as shown in Table 3. The simulations using local COF are closer to the experimental results than the ones with a constant COF.

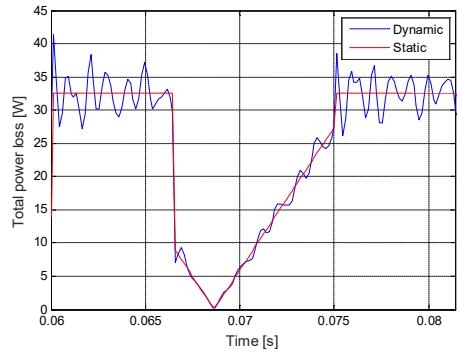

(a) with constant COF at 250 rpm

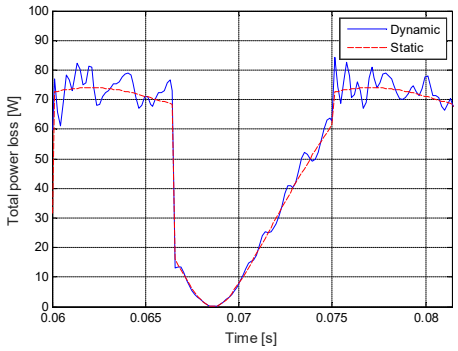

(b) with local COF at 250 rpm

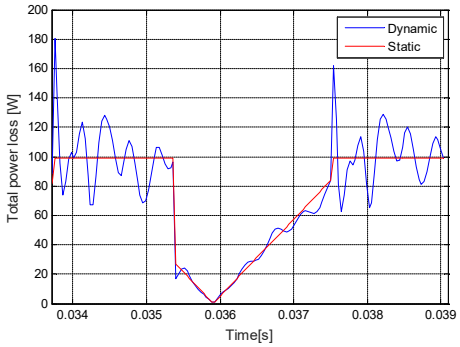

(c) with constant COF at 1000 rpm

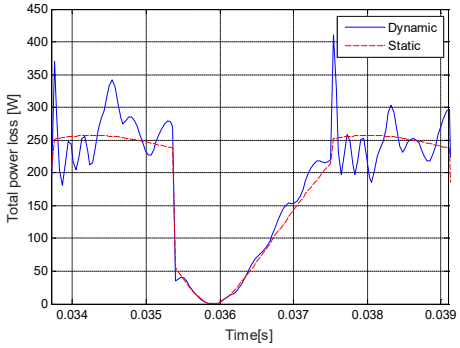

(d) with local COF at 1000 rpm

Figure 3. Friction power loss simulations for C40 spur gears at K8.

K8	$P_{VZP\ Exp}$ [W]	$P_{VZP\ constant\ COF}$ [W]	$P_{VZP\ Local\ COF}$ [W]	Error [%] ($P_{VZP\ constant\ COF}$ / $P_{VZP\ Exp}$)	Error [%] ($P_{VZP\ Local\ COF}$ / $P_{VZP\ Exp}$)
250 rpm	51.87	37.18	47.84	28.32	7.77
1000 rpm	157.24	112.80	146.07	28.26	7.1

Table 3. Experimental and simulated total friction power losses.

4 CONCLUSIONS

A dynamic model of a one stage spur gear system was developed in order to evaluate the total power loss considering frictional effects. The coefficient of friction is a key factor in predicting an accurate meshing spur gear power loss. The presented results prove the difference between simulations with constant and local COF. This difference can be explained with its dependency to load distribution variation affecting the Hertzian pressure. The selected EHL approach in simulations was validated by experimental results.

REFERENCES

[1] H. Xu, and A. Kahraman. Prediction of friction-related power losses of hypoid gear pairs. *Proc. of the Inst. of Mech. Eng. Part K: J. of Multi-body Dyn.*, 221(3):387–400, 2007.

[2] R.C. Martins, J.H.O. Seabra, A. Brito, Ch. Seyfert, R. Luther, and A. Igartua. Friction coefficient in FZG gears lubricated with industrial gear oils: biodegradable ester vs. mineral oil. *Tribology International*, vol. 39, no 6, p. 512-521, 2006.

[3] H. Dong, Z.-Y. Liu, L. Duan, and Y-H. Hu. Research on the sliding friction associated spur-face gear meshing efficiency based on the loaded tooth contact analysis. *PLoS ONE 13(6)*, 2018.

[4] M. Hammami, N. Feki, O. Ksentini, T. Hentati, M.S. Abbes, and M. Haddar. Dynamic effects on spur gear pairs power loss lubricated with axle gear oils. Accepted for publication in *Proc. of the Inst. of Mech. Eng., Part C: J. of Mech. Eng. Science* (22-October-2019).

CRASHWORTHY DESIGN OF AN AIRCRAFT WING LEADING EDGE TO WITHSTAND BIRD IMPACT EVENTS

F. Di Caprio[1*], A. Sellitto[2], S. Saputo[2], M. Guida[3] and A. Riccio[2]

[1]CIRA – Italian Aerospace Research Centre
via Maiorise snc, Capua (CE), Italy
Email: f.dicaprio@cira.it

[2]University of Campania "Luigi Vanvitelli"
via Roma 29, Aversa (CE), Italy
Email: andrea.sellitto@unicampania.it, salvatore.saputo@unicampania.it, aniello.riccio@unicampania.it

[3]University of Naples "Federico II"
p.le Tecchio 80, Naples, Italy
Email: michele.guida@unina.it

ABSTRACT

This paper aims to investigate the crashworthiness capability of a metallic sandwich leading edge of a commercial aircraft subjected to bird strike events.
A sensitivity analysis is presented, in order to determine the influence of the skin parameters (inner and outer faces and core thicknesses) on the leading edge crashworthiness and to determine, among the configuration able to withstand a birdstrike event, the best compromise in terms of weight and structural performances. In order to easily manage the design parameters and the output data, the ModeFrontier code was used in conjunction with the FE code Abaqus/Explicit. A dedicated python routine has been developed to define a fully parametric simplified vertical tail leading edge model. In order to fulfil the aerodynamic requirements, the external surfaces have been considered fixed during the sensitivity analysis and thus only the internal leading edge's components have been modified to study their influence on the structural response.
The global mass of the model, the maximum deformation, and the energy dissipated due to material failure and to the plastic deformations have been monitored and used to compare and assess the behavior of each configuration.

1 INTRODUCTION

Damages resulting from birdstrike on aircraft can be extremely dangerous for the structural health. Therefore, extensive research studies have been focused on reducing the human and aircraft losses, by developing new materials and design configurations of the parts more exposed to the risks of birdstrikes, and by developing birds control programs at airports to reduce the birdstrike frequency. Thus, strict requirements were selected and continually updated by the aviation safety agencies (FAA and EASA) [1] in the certification procedures of each component of the aircraft. By the development of numerical features for design and simulation, these agencies allowed numerical bird proof qualification of the aircraft components, which presents a faster and low-cost approach to the aircraft design and test stages. In the use of these numerical features, three main aspects have to be considered when analysing the bird impact phenomena on the aircraft structures, which are: the bird model, the mutual interaction between the bird and the structure, and the structural response of the aircraft component to the impact. Especially when dealing with high velocity impacts, an appropriate numerical description of these aspects is mandatory to obtain a reliable analysis. In the literature, the bird modelling was deeply investigated [2,3]. Among the others, the Smooth Particle Hydrodynamic (SPH) technique was found the most representative approach for this problem [4]. The response of structure under bird impact was investigated in different works [5,6], and innovative material configurations were analysed in order to satisfy the agencies requirements. In order to limit the weight increase related to the adoption and to the development of structures able to withstand birdstrikes, composite and sandwich materials are usually employed. In this work, a metallic sandwich leading edge subjected to birdstrike is presented. SPH has been used to numerically simulate the bird and its interaction with the structure. A sensitivity analysis has been performed in order to find, among the configurations able to withstand a birdstrike phenomenon, the best compromise between weight and structural performances.

2 SENSITIVITY ANALYSIS ON THE LEADING EDGE

The investigated subcomponent is representative of the vertical tail leading edge of a general aviation aircraft. The presented model, shown in Figure 1, has been previously validated in [6]. The impact trajectory is normal to the leading edge at the central point. The impact velocity is equal to 129 m/s and the bird mass is 3.68 kg.

The structure has been discretized by means of linear shell elements, while the bird has been discretized by SPH elements. In particular, the skin was modelled by means of layered elements in order to simulate the sandwich structure. An elasto-plastic material with failure option and a strain rete dependency has been considered for the structure.

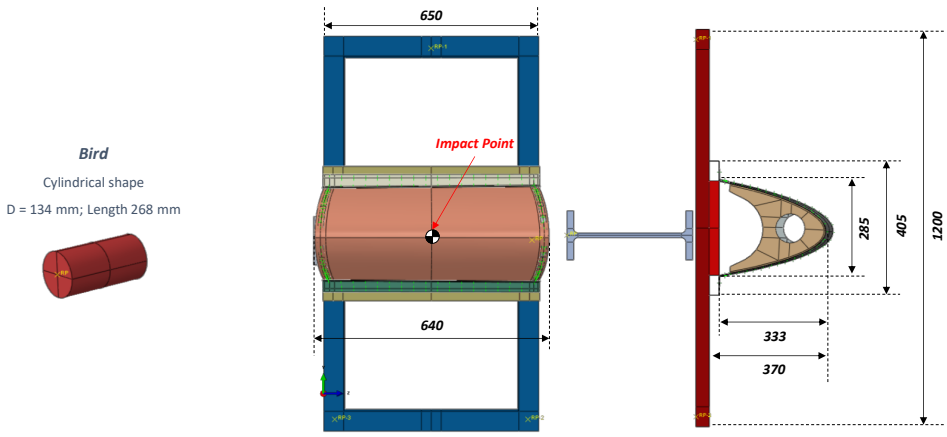

Figure 1. Bird and tested structure.

A parametric procedure has been established in order to assess the influence of the design parameters on the deformation and on the total mass of the structure. The procedure has been implemented in the ModeFrontier code. The design parameters of the sensitivity analysis are the thicknesses of the inner face, of the outer face, and of the core of the leading edge, as reported in Table 1, where the starting values of these parameters are reported in red bold style. As output, the masses of the inner, of the outer, and of the core (and thus the total skin mass), the plastic and the damage energies of the skin, and the displacement of the central point of the skin have been considered. A configuration is considered feasible if the safety requirements are satisfied, in particular: the maximum displacement (along the impact direction) of central point of the skin must not exceed 370 mm (that is the distance between the inner skin and the main spar) and no penetration must occur. The plastic and the damage energies provide global information regarding the capability of the structure to dissipate the impact energy, which can result in a catastrophic or in a non-catastrophic failure mode.

	Inner face: *Al2024-T3*	**Outer face:** *Al2024-T3*	**Core:** *Hexcel – hexweb aluminum flexcore*
Analyzed values [mm]	**0.4** – 1 – 1.4 – 2	0.4 – 1 – **1.4** – 2	3.125 – **6.35** – 9.375 – 12.7

Table 1. Design parameters

According to the sensitivity analysis, an increase of the outer and inner sandwich faces thicknesses leads to a decrease of the maximum displacement, while increasing the total mass. Moreover, it has been observed that similar effects are obtained by increasing the honeycomb core thickness; however, the effects in terms of the total mass increase are less relevant respect to the outer and inner face variations, as shown in Figure 2, where the central point displacement as a function of the components thicknesses and the total mass is reported. For sake of clarity, Figure 2 does not report all the possible parameters combinations. In particular, each curve represents the variation of the thickness value of the single sandwich component (Inner face, Outer face, Core), while the other two thicknesses are set equal to their starting values.

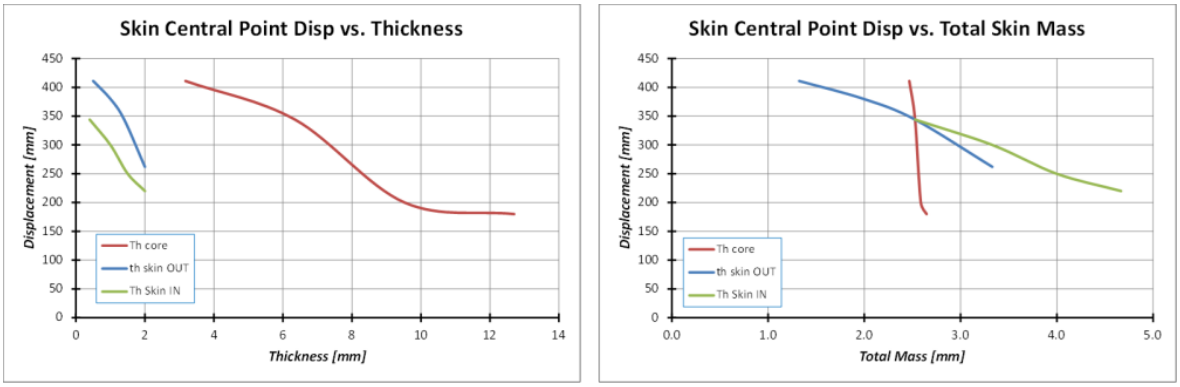

Figure 2. Sensitivity analysis results.

64 configurations have been analysed and, in this context, only the best and the worst configurations, in terms of global deformation, are reported.

	Starting configuration	**Worst configuration**	**Best configuration**
Inner thickness [mm]	0.4	0.4	0.4
Outer thickness [mm]	1.4	0.4	1.4
Core thickness [mm]	6.35	6.35	12.7

Table 2. Design parameters of the starting, the best and the worst configuration

Figure 3 shows a comparison among the starting, the best, and the worst configurations in terms of global deformation at the end of the event. The worst configuration, which is the one with the minimum thickness for all sandwich components, is characterized by a catastrophic damage status; indeed, the bird penetrates the structure. The reduced frame tips distance, thus, is not a reasonable parameter to take into account to evaluate the performances as the displacement of the central point. The best configuration, on the contrary, shows a consistent performance improvement. Indeed, the frame tips distance was increased of about 93% and the central point displacement was reduced of about 40%. On the other hand, an increase of the total mass of about 5% is observed, which can be considered a good compromise respect to the performance improvement.

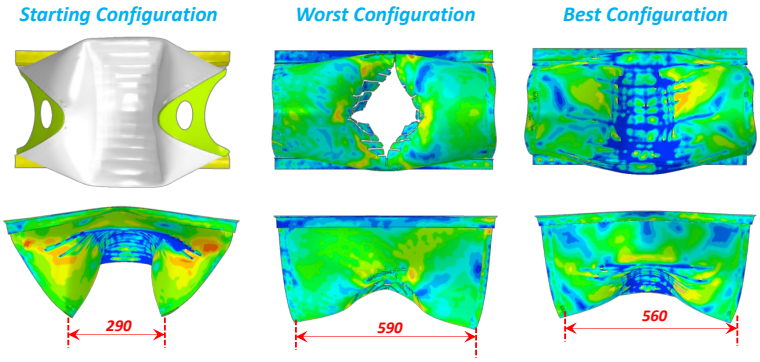

Figure 3. Deformation comparison

3 CONCLUSION

In this work, a sensitivity analysis on a metallic sandwich leading edge subjected to a birdstrike phenomenon has been presented. Different configurations have been investigated, with different thickness of the sandwich inner and outer skins and of the sandwich core. According to the analyses, the impact behaviour is strongly influenced by the investigated parameters. As a matter of facts, the configuration characterized by the minimum thicknesses is the one most damaged during the impact. On the other side, the best configuration is the one which offers the best compromise between the structural performances (the central point displacement is reduced of about 40% respect to the starting configuration) and weight (which is increased of 5% respect to the starting configuration).

REFERENCES

[1] Federal Aviation Administration, Policy for Bird Strike, U.S. Department of Transportation, 2002

[2] M. Guida, F. Marulo, M. Meo, M. Riccio. Analysis of bird impact on a composite tailplane leading edge. *Applied composite materials*. 15(4-6):241-257, 2008.

[3] V.K. Goyal, C.A. Huertas, T.J. Vasko. Bird-strike modeling based on the Lagrangian formulation using LS-DYNA. *American Transactions on Engineering & Applied Sciences.* 2(2):57-81, 2013.

[4] J.L. Lacome. Smoothed particle hydrodynamics (sph): a new feature in ls-dyna. *Proceedings of the 7th International LS-DYNA Users Conference*, 2002.

[5] A. Riccio, R. Cristiano, S. Saputo, A. Sellitto. Numerical methodologies for simulating bird-strike on composite wings. *Composite Structures.* 202: 590-602, 2018.

[6] F. Di Caprio, D. Cristillo, S. Saputo, M. Guida, A. Riccio. Crashworthiness of wing leading edges under bird impact event. *Composite Structures*. 216: 39-52, 2019.

OPTIMAL DESIGN OF RAINBOW METAMATERIALS

Han Meng[1*], Dimitrios Chronopoulos[1] , Adriano. T Fabro[2], Waiel Elmadih[3] and Richard Leach[3]

[1]Institute for Aerospace Technology & The Composites Group
University of Nottingham, Nottingham, UK
Email: han.meng@nottingham.ac.uk, dimitrios.chronopoulos@nottingham.ac.uk

[2] Department of Mechanical Engineering
University of Brasilia, Brasilia, Brazil

[3] Manufacturing Metrology Team, Faculty of Engineering, University of Nottingham, Nottingham, UK

ABSTRACT

Nonperiodic metamaterials with appropriately designed resonator distributions can have superior vibration attenuation capabilities compared to periodic metamaterials. In this study, we present an optimization scheme for the resonator distribution in rainbow metamaterials that are constitutive of a Π-shaped beam with parallel plate insertions and spatially varying cantilever-mass resonators. To improve the vibration attenuation of rainbow metamaterials at specific design frequencies, two optimization strategies are proposed, aiming at minimizing the maximum and average receptance values. Objective functions are set up with the frequency response functions predicted by the displacement transfer matrix model. The masses of the two sets of resonators, clamped at different side walls of the Π-shaped beams, constitute the set of design variables. Optimization functions are solved using a genetic algorithm method. Results of case studies showed that the receptance values of the nonperiodic metamaterial is greatly reduced within the optimization frequency range, in comparison to the periodic metamaterial.

1 INTRODUCTION

Metamaterials are a new class of artificial composites engineered to have novel properties that cannot be found with natural materials. Metamaterials have attracted much attention in many research fields [1-5]. Metamaterials were originally introduced to tailor electromagnetic optical waves [1-2]. Nowadays, the concept of the metamaterial has expanded to include acoustic and elastic waves which are the focus of this work. New properties, such as negative effective mass, negative effective dynamic stiffness and negative bulk modulus, can be obtained using elastic/acoustic metamaterials. An important feature of elastic/acoustic metamaterials is the existence of bandgaps within which no waves can propagate [3-4]. Locally resonant bandgaps, relying on the resonance of internal oscillators, occur at frequencies much lower than those due to Bragg scattering.

A large number of elastic/acoustic metamaterials have been proposed with various local resonators. Most of the proposed metamaterials are periodic structures. Although these periodic metamaterials are applicable for manipulating wave propagation and providing low-frequency vibration attention, broad bandgaps are difficult to achieve. Few researchers have presented nonperiodic metamaterials with spatially varying resonators. Sun et al. [3] and Pai [4] made the first attempt at investigating metamaterials with spatially varying mass-spring-damper subsystems. They found that their metamaterials could have better vibration attenuation with properly designed nonperiodic resonators. Their design procedures were, however, mainly based on trial and error, which is unlikely to give optimal designs and possibly leaves a large design space unexplored.

In this paper, we propose a design approach for the distribution of resonators in nonperiodic metamaterials. Optimization objective functions are set up on the basis of the displacement transfer matrix model. A genetic algorithm optimization method is employed to search the optimal nonperiodic distributions of resonator masses that can generate optimal receptance values at the frequencies of interest.

2 ANALYTICAL MODELLING METHOD FOR THE RAINBOW METAMATERIAL

Figure 1 shows the schema of the proposed rainbow metamaterial. The Π-shaped beam is partitioned into substructures by periodic plate insertions. Non-symmetric cantilever-mass subsystems are clamped to the two side walls of the Π-shaped beam in each substructure. Instead of being periodic, the resonating subsystems are spatially varying along the length of the beam, hence the term "rainbow".

An analytical model built on the basis of the displacement transfer matrix model (see [5] for a more in depth description of the model) is employed to determine the receptance function R_{ec} of the rainbow metamaterial, as

$$R_{ec} = 20\log_{10}\left|w_{m,r}\right|_{x=L} / F\left| \right. \tag{1}$$

where F is the excitation force on the metamaterial beam and $w_{m,r}\big|_{x=L}$ is the displacement of the beam.

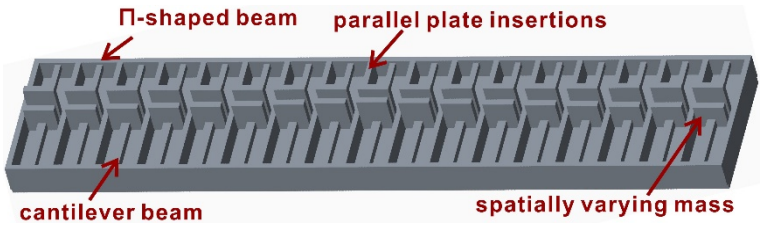

Figure 1. Illustration of the global view of the rainbow metamaterial.

3 OPTIMIZATION STRATEGY

In order to maximize the vibration attenuation of rainbow metamaterials in a prescribed frequency range, two optimization strategies are proposed that use two objective functions individually. One objective function is set based on the maximum receptance value within the prescribed frequency range, given by

$$\min \quad \max\left(R_{ec}\left(\mathbf{M}_1,\mathbf{M}_2,\mathbf{\Phi}\right)\right) \tag{2}$$

where $\mathbf{M}_1=\left(m_{11},m_{12},...,m_{1t}\right)$ and $\mathbf{M}_2=\left(m_{21},m_{22},...,m_{2t}\right)$ represent the mass of the resonators at different sides of the complex beam respectively, t is the total number of segments in the metamaterial beam and $\mathbf{\Phi}=\left(f_1\sim f_2\right)$ is the prescribed frequency regime. The receptance within the prescribed frequency range is low when the maximum value remains minimal; the vibration attenuation is thus optimized. The mass of each resonator cannot be less than zero, constraints of the design variables are hence given by

$$s.t. \quad m_{ij}\geq 0.\ i=1,2.\ \ j=1,2,...,t \tag{3}$$

The mean value is another indicator of the receptance value quality within a prescribed frequency range, therefore, the other objective function is set based on the mean receptance value within the prescribed frequency range, given by

$$\min \quad \frac{\int_{\mathbf{\Phi}} R_{ec}\left(\mathbf{M}_1,\mathbf{M}_2,\mathbf{\Phi}\right)df}{f_2-f_1}. \tag{4}$$

The constraints on the design variables defined by Eq. (4) are similarly applicable to the maximum value-based optimization objective function. A genetic algorithm method is employed to solve the objective functions in Eqs. (2) to (4).

4 OPTIMIZATION EXAMPLES

For the purpose of reducing vibration at low frequencies, a prescribed frequency range 130 Hz to 150 Hz, which is around the first resonance frequency of the backbone beam, is used for the optimization examples. Receptance values of the rainbow metamaterials with optimal resonator mass distributions obtained by the two optimization strategies are compared with those of complex beams of the same mass but without resonators, as shown in Figs. 2(a) and (b) . As can be seen, both of the two optimal rainbow metamaterials show bandgaps within the prescribed frequency range, hence, the receptance values are significantly reduced. The optimal metamaterial in Fig 2(a) has a maximal receptance approximately 38 dB less than that of the structure without resonators. The mean receptance difference between the optimal structure and the no-resonator beam, shown in Fig 2(b), is approximately 33 dB. Both maximum and mean displacements within 130 Hz to 150 Hz can be reduced by a factor of more than 70 with the optimization process.

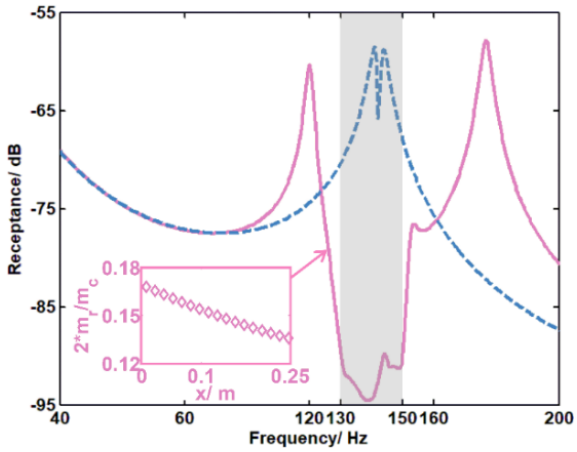

(a)

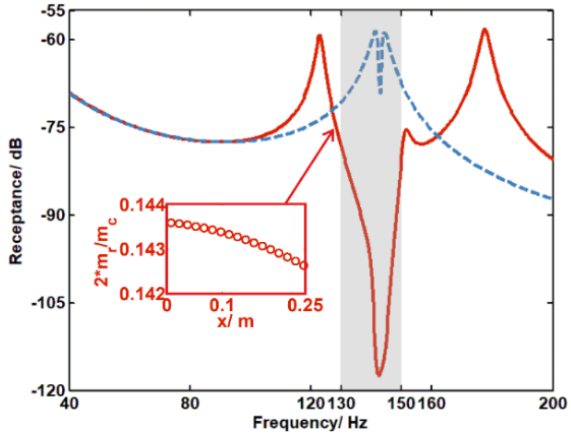

(b)

Figure 2. Receptance value comparison between optimal rainbow metamaterial beams (solid line) by maximal receptance value based objective function (a) and by average value based objective function (b) and no-resonator Π-shaped beam (dashed line) of the same mass. The ratios of resonator masses to that of the backbone structure of the optimal beams are plotted in the subfigure.

In addition, as shown in Figs. 2(a) and (b), the optimal structure, derived using a maximum value based objective function, has a broader bandgap of higher receptance value within the prescribed frequency range, which is opposite to the optimal structure derived by the mean value based objective function. The optimization strategy can be chosen according to the requirements of different applications.

ACKNOWLEDGEMENTS

We would like to acknowledge the support acquired by the H2020 DiaMoND project (Grant Agreement ID: 785859), Royal Society Grant: PURSUIT, the Brazilian Na-tional Council of Research CNPq (Grant Agreement ID: 420304/2018-5) and the Brazilian Federal District Research Foundation (Grant Agreement ID: 0193.001507/2017).

REFERENCES

[1] J.B. Pendry, Negative Refraction Makes a Perfect Lens. *Physical Review Letters*, 85: 3966-3969, 2000.

[2] J.B. Pendry, Negative refraction. *Contemporary Physics*. 45:191-202, 2004.

[3] H. Sun, X. Du, P.F. Pai, Theory of metamaterial beams for broadband vibration absorption. *Journal of Intelligent Material Systems and Structures*. 21: 1085-1101, 2010.

[4] P.F. Pai, Metamaterial-based broadband elastic wave absorber, *Journal of Intelligent Material Systems and Structures*, 21: 517-528, 2010.

[5] H. Meng, D. Chronopoulos, A. T. Fabro, W. Elmadih, I. Maskery, Rainbow metamaterials for broadband multi-frequency vibration attenuation: Numerical analysis and experimental validation. *Journal of Sound and Vibration*, 465: 115005, 2019.

MACHINE HEALTH DIAGNOSTICS USING ACOUSTIC IMAGING AND ALGORITHMS FOR MACHINE LEARNING

Alessia Aulitto[1], Ines Lopez Arteaga[2], Dragan Kostić[3], Faysal Boughorbel[3], Sergio De Rosa[1] and Giuseppe Petrone[1]

[1] Università degli Studi di Napoli "Federico II", Italy
E-mail: al.aulitto@studenti.unina.it, sergio.derosa @unina.it, giuseppe.petrone@unina.it

[2]Eindhoven University of Technology, The Netherlands
Email: I.Lopez@tue.nl

[3]ASM Pacific Technology
6641 TL Beuningen, The Netherlands
Email: dkostic@alsi.asmpt.com, fboughorbel@alsi.asmpt.com

ABSTRACT

Nowadays monitoring health conditions of machines is necessary to reduce costs and repairing time and to secure the quality of the products. Therefore, the potential of acoustic measurements in combination with machine learning techniques for non-invasive diagnostics of machine performance has been investigated. The idea is to establish relations between the acoustic images produced by a sound camera and the machine conditions and then create a strategy for processing the images using Convolutional Neural Networks. Several working conditions of the machine have been considered and experiments have been performed both under nominal and abnormal conditions of the machine, obtained by mimicking the presence of a disturbance. The use of the algorithms for image classification allows isolation of the faults in the machine behaviour by the definition of the primary sound sources. The procedure shows promising results with a short computational time, easy application and high accuracy.

1 INTRODUCTION

The semiconductor manufacturing is one of the most technology-evolving market sectors. In order to reach a competitive position in semiconductor industry the most important challenges that a fabrication plant must face are the reduction of costs and the increase of production. Predictive

maintenance is one possible way to address these challenges. Many manufacturing stations are already equipped with sensors, such as accelerometers, and data coming from these sensors are often processed with Machine learning algorithms. However, a body-mounted sensor represents an extraneous mass and it affects the dynamics of the system. This problem leads to the necessity to find a measurement equipment for non-intrusive condition monitoring and a sound camera shows promising results in this sense. The idea is to establish relations between the acoustic images produced by the camera and the machine conditions using Machine Learning algorithm in order to predict the behaviour of the system by artificially simulating the presence of a disturbance.

2 PREPARATION

The experiments are performed on a wire-bonder machine produced by ASM Pacific Technologies [1]. The sound emitted by this machine during operations is recorded with the sound camera Sorama CAM64 [2] that comes with a Portal to analyse the produced acoustic images. The images will be used to feed a Convolutional Neural Network (CNN), built using Python and TensorFlow [3].

2.1 Wire-bonder and abnormal conditions

The wire-bonder machine has three orthogonal stages moving along three orthogonal axes and the motion of each stage is controlled by a closed loop. Detailed instruction on the wire-bonder are in [4]. Focusing on the feedback controller in the loop, increasing its gain means increasing the bandwidth so the dynamics of the system can be affected by abnormal vibrations at resonance frequencies. Working on the feed-forward controller instead it is possible to insert an artificial force which mimics the braked response with friction or to introduce a random force that simulates the vibrations coming from the environment. All these disturbances will introduce new frequencies of the oscillation that can be found by analysing the sound emitted from the machine.

2.2 Sound camera and acoustic images

Sorama CAM64 can record the sound coming from a sound source and it can produce different kinds of acoustic images. Further information about the camera can be found in [5]. In the intent of the project the spectrograms will be considered: they are frequency-vs- time chosen to identify which axis or combination of axes of the machine are performing operations by the analysis of the emitted sound.

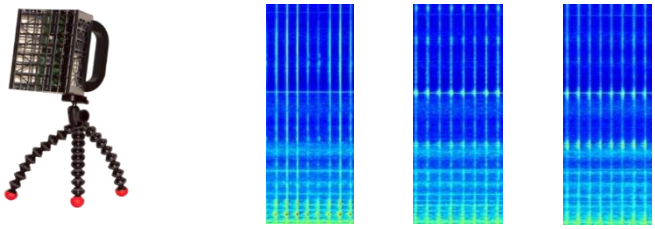

Figure 1: Sound camera and portions of spectrogram

In Figure 1 three portions of the spectrograms collected during the experiments are presented and by observation a user can recognize which stage is moving. The scope of the project is to teach to a computer to learn directly from the images collected.

2.3 Convolutional Neural Network

Machine learning techniques and Convolutional Neural Networks (CNN), exploit the capability of computers to receive data and to learn from them, by modifying the algorithms step-by-step. More information about the use of CNN can be found in [6]. Images coming from the Sorama Portal should

be frameless, then cut in slices and then resized to be squared ones. Each image comes with a label that underlines which stage of the machine was acting when the image was collected. Furthermore, the images are split in two groups: a training set, used to insert in the network the recognition and classification phase and a test set, to test the capability of prediction. The workflow of the process is presented in Figure 2.

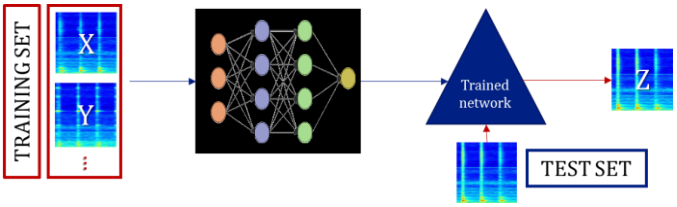

Figure 2: Map of the process using CNN

3 STATEMENT OF THE PROBLEM

Several working conditions of the machine are tested. First set of measurement is collected during the motion of the stages with a given trajectory and a fixed acceleration. To test the robustness of the procedure other three trajectories in normal conditions are tested and a smaller dataset is created. Then, new images are collected by artificially simulating the three types of abnormal behaviour mentioned in the paragraph 2.1.

3.1 Prediction in healthy conditions

The images in the first dataset are 2896, squared, with pixel value between 0 and 255 and then rescaled in the range 0,1. They are then converted in greyscale in order to reduce the computational cost and then organized in 8 classes, with 8 different labels. The accuracy is around 95%. Testing the images coming from different trajectories there is an expected reduction of the accuracy that oscillates around 85%, according to the reduction of the number of images in the dataset.
In Figure 3, an example of the classes in the network is presented.

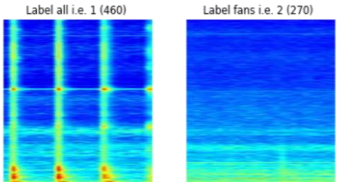

Figure 3: Example of the classes of the network in healthy conditions

3.2 Prediction in artificial unhealthy conditions

The first type of abnormal behaviour is simulated by increasing the gain of the feedback controller. Some frequencies will show a higher SPL and, in the spectrum, it will result in a higher peak at some resonant frequencies, as presented in Figure 4.

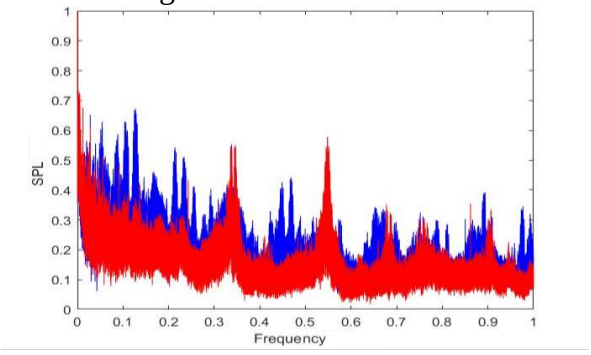

Figure 4: Spectra in presence of resonance frequencies (blue) and in normal conditions (red)

The values presented in the plot have been normalized due to confidential issues. Furthermore, to mimic the effect of the friction a force will be introduced: this force is given by a constant Coulomb friction component and a viscous one depending on the velocity. In this case new frequencies will show a tail behaviour. In the case of random vibration, it should be underlined that a horizontal line in the spectrogram is representative of a harmonic function. In the spectrogram three groups of horizontal lines will appear, due to the definition of the chosen disturbance. In addition to the first network, three networks will be built by using the images coming from these three experiments. The fourth network is representative of all the disturbance sources and it is composed by 28 classes, instead of the eight classes of the network for the healthy conditions. In Figure 5 the result of the complete network is presented.

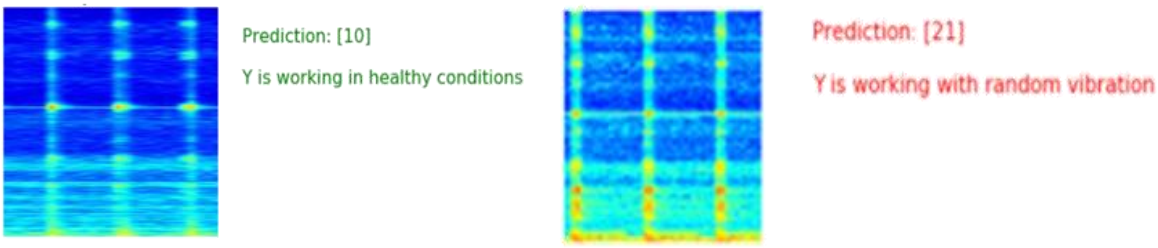

Figure 5: Results of the prediction phase

4 CONCLUSIONS AND FUTURE APPLICATIONS

The final network can recognize which stage or combination of sage is performing operations, if the wire bonder is working in healthy conditions or if one of the disturbance sources is changing the dynamics of the machine. In conclusion, the behaviour of the machine influences the frequencies of the emitted sound and using a sound camera is possible to detect the deviances from the normal conditions. The initial hypothesis about the use of spectrograms to get suitable information for neural network application is confirmed and, despite the reduced number of layers, the accuracy of the image classification procedure is high. In the end, the application of the sound camera shows promising results in condition monitoring without changing the dynamics of the machine. In the coming future, further application of the mentioned procedure will lead to a deeper knowledge of the problem: new kinds of disturbances will be tested also on several machines in the workstations. New images, such as the hologram can give information about the spatial distribution of the emitted sound in order to identify the locations of the primary sound sources during the motion of two stages. Furthermore, new types of Machine Learning techniques can perform the classification tasks directly on the recorded sound without using the acoustic images. So, the project opens the way to new possibility to investigate in the field of application of sound camera for non-intrusive condition monitoring and predictive maintenance.

5 REFERENCES

[1] ASM Center of Competency, https://alsi.asmpt.com/

[2] Sorama Cam64, https://www.sorama.eu/cam64

[3] Tensorflow, https://www.tensorflow.org/

[4] ASM Technology Singapore, *Wire bonding apparatus comprising rotary positioning stage*, 2012.

[5] Sorama, *Guided Preparation - Preparation Help*, 2017.

[6] Stanford University, CS231n: Convolutional Neural Networks for Visual Recognition, 2019.

UNCERTAINTIES IN WAVE CHARACTERISTIC OF TWO-DIMENSIONAL PERIODIC MEDIA USING THE FUZZY WAVE FINITE ELEMENT METHOD

R. P. Singh[1,2*], S. De Rosa[1], F. Franco[1], O. Bareille[2], M. Ichchou[2] and G. Petrone[1]

[1]Laboratory for promoting experiences in aeronautical structures and acoustics
Department of Industrial Engineering
University of Naples "Federico II", Via Claudio 21, 80125 Napoli, Italy
Email: ravipratap.singh@unina.it, sergio.derosa@unina.it, francesco.franco@unina.it, giuseppe.petrone@unina.it

[2]Vibroacoustic and Complex Media Research Group, LTDS,
Ecole Centrale de Lyon,
36 Avenue Guy de Collongue, 69134 Ecully, France
Email: ravi-pratap.singh@ec-lyon.fr, olivier.bareille@ec-lyon.fr, mohamed.ichchou@ec-lyon.fr

ABSTRACT

The periodic structures exhibit a considerable amount of scattering in material properties during the manufacturing process and mechanical properties evaluations. Due to imprecision and non-availability of the information about the parameter, the uncertainty is modelled as fuzzy variable. In this paper wave finite element method in conjunction with fuzzy logic and algebra defined as fuzzy wave finite element method has been applied for free wave propagation in the two-dimensional periodic structure. The formulation is derived for the direct form where frequency is imposed, and wavenumber dispersion is obtained. The dispersion curves for the out of plane flexural waves with fuzzy parameters have been used to illustrate the proposed approach. In the numerical simulation, target is to look for the possibility to find the variation of the frequency band gap (frequency region, where waves cannot propagate). The validation of the presented method is carried out for the free wave propagation for the periodic plate by comparison with WFEM MCS results.

1 INTRODUCTION

The design of periodic media is generally based on deterministic models without considering the effect of intrinsic uncertainties existing in these media. In general, the design is aimed at controlling as much as possible the mechanical waves; however, inherent uncertainty may affect their characteristics [1]. Periodic media are diffused in all the transportation engineering and demand a high level of robustness, which can be ensured with the careful consideration of the presence of uncertainty in the numerical models. The uncertainties, in terms of material properties and geometrical parameters, are mostly exhibited in both the manufacturing and assembly processes [2]. The exact sources of uncertainty are rarely found since their identification represents a difficult task. When faced with incomplete information about the uncertainties, the adoption of the probabilistic

approach can result in very challenging evaluations. In this scenario, the fuzzy set theory offers a way to approximating the uncertainty distribution in the form of the confidence interval through fuzzy membership functions [3]. These are equivalent representations for the characterization of the linguistic, vague and missing data uncertainties [4].

To predict the wave characteristics of the periodic media in the presence of imprecise uncertainties, the wave finite element method (WFEM) in conjunction with fuzzy logic and algebra is developed and named as fuzzy wave finite element method (FWFEM) [4]. For two-dimensional wave propagation, firstly, the most significant input parameters such as Young's modulus and mass density are identified and then fuzzified using the membership functions. The triangular membership functions have been used in this paper. Then, the fuzzy uncertainty propagated using the α-cut approach. The dispersion curves for the out of plane flexural waves with fuzzy parameters have been used to illustrate the proposed approach. In the numerical simulation, targete is to look for the possibility to find the variation of the frequency band gap (frequency region, where waves cannot propagate). The validation of the presented method is carried out for the free wave propagation for the periodic plate by comparing the result with the WFEM Monte Carlo Simulation (WFEM MCS) results.

2 FWFEM FORMULATION FOR TWO-DIMENSIONAL PERIODIC MEDIA

The fuzzy variables are modelled using the fuzzy membership functions. Every term in the formulation, denoted with subscript α is the fuzzy membership level. The symbol $()$ denotes the fuzzy arithmetic operations. The definition of the fuzzy membership function and α-cut (fuzzy membership level) can be referred in the one-dimensional formulation in the previous paper by the same authors [4]. If imprecision is present in the material properties, which contribute to the stiffness and mass matrix and introduce fuzzy uncertainty in the dynamic matrix, then the global fuzzy dynamic equilibrium [5] of a substructure represented as the time-harmonic equation of motion as

$$\left(K_\alpha - \omega_\alpha^2 M_\alpha\right)(.) q_\alpha = f_\alpha \tag{1}$$

where K_α is the fuzzy stiffness matrices, M_α is the fuzzy mass matrices, ω_α is the fuzzy circular frequency, f_α is the fuzzy nodal forces vector, and q_α is the fuzzy nodal displacements vector. The Eq. (1) is used to form the fuzzy spectral problem involving wavenumber in x direction (k_x), wavenumber in y direction (k_y) and fuzzy circular frequency ω_α. The fuzzy dynamic stiffness matrix can be expressed as $D_\alpha = K_\alpha - \omega_\alpha^2 M_\alpha$.

Introducing the periodic structure theory for the unit cell and considering a time-harmonic response [6] the fuzzy harmonic equation of motion Eq. (1) leads to fuzzy eigenvalue problem. Considering that the frequency ω and one wavenumber is known, it this case the fuzzyeigenvalue problem can be formulated as fuzzy quadratic eigenproblem in λ_{x_α} form, when λ_{x_α} is unknown and $(\omega_\alpha, \lambda_{y_\alpha})$ are given

$$\begin{aligned}\big[(D_{21_\alpha}(+)D_{43_\alpha}(+)D_{41_\alpha}(.)\lambda_{y_\alpha}^{-1}(+)D_{23_\alpha}(.)\lambda_{y_\alpha})(+)\mu_{i_\alpha}(.)(D_{11_\alpha}(+)D_{22_\alpha}(+)D_{33_\alpha}(+)D_{44_\alpha}\\ (+)(D_{31_\alpha}(+)D_{42_\alpha})(.)\lambda_{y_\alpha}^{-1}(+)(D_{13_\alpha}(+)D_{24_\alpha})(.)\lambda_{y_\alpha})\\ (+)\,\mu_{i_\alpha}^2(.)(D_{12_\alpha}(+)D_{34_\alpha}(+)D_{32_\alpha}(.)\lambda_{y_\alpha}^{-1}(+)D_{14_\alpha}(.)\lambda_{y_\alpha})\big](.)\left(\Phi_{q_\alpha}\right)_i = 0\end{aligned} \tag{2}$$

where (D_{ij_α}) $i, j = 1, 2, 3, 4$ are the element from the fuzzy reduced dynamic stiffness matrix. $\lambda_{x_\alpha}, \lambda_{y_\alpha}$ are the fuzzy propogation constatins in x and y direction respectively. Φ_{q_α} are the fuzzy eigenvector matrix. The fuzzy quadratic eigenproblem solved using the α-cut method and propagating wavenumber in x direction (k_{x_α}) and y direction (k_{y_α}) are identified.

3 NUMERICAL RESULTS

In this section, the validation of the FWFEM formulation is presented for two-dimensional perioidic plate case. The schematic of periodic plate is reported in Fig. 1a. The periodic plate unit cell is modeled with four noded elements with three degree of freedoms at each node. The sides of the unit cell are $L_x = L_y = 0.1\ m$ with thickness $h = 0.005\ m$. The unit cell is made of two isotropic materials and material properties are reported in Table 1.

The validation of the developed FWFEM formulation is presented for the out of plane flexural wavenumber in the considered periodic plate. The considered frequency range is [0-3000] Hz.

Table 1: Material properties for the periodic plate

Property	Value
Young's modulus of Material 1	$70 \times 10^9\ Pa$
Young's modulus of Material 2	$210 \times 10^9\ Pa$
Poission's ratio of Material 1 and Material 2	0.3
Mass density of Material 1	$2700\ kg/m^3$
Mass density of Material 2	$7800\ kg/m^3$

The Young's modulus of sub-plate type A and sub-plate type B are considered imprecise. The variation of (10%) about the nominal values of Young's modulus is studied. The elasticity of sub-plate type A (material 1) and sub-plate type B (material 2) are fuzzified using triangular membership function and shown in Fig. 1b and Fig. 1c. The WFEM MCS with 10000 samples is considered

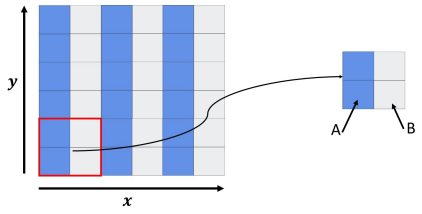

(a) Schematic of the periodic plate and unit cell

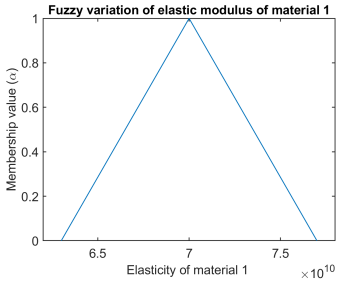

(b) Fuzzified material 1

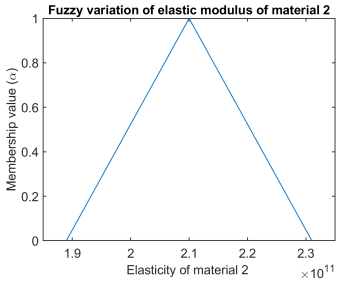

(c) Fuzzified material 2

Figure 1: Schematic of periodic plate and fuzzified material properties with 10% uncertainty. The unit is (Pa)

as the reference solution for the validation. The out of plane flexural wavenumber dispersion is computed from FWFEM formulation at α-cut=0 (maximum variation) and obtained fuzzy upper and lower bound is compared with the ones carried out by WFEM MCS approach. The comparison of the upper and lower bound is shown in Fig. 2. The comparison shows the excellent agreement of the FWFEM results with the reference results. It verifies the applicability of FWFEM formulation for periodic plate case. From the comparison presented in Fig. 2, it can be observed the band gap starting approximately around 2352 Hz. Near around the same frequency, the variation of the upper and lower bound is maximum see as in Fig. 2(b). Also inferring to Fig. 2 inside the band gap zone there is a very minimum variation of out of plane flexural wavenumber. It confirms the validity of the FWFEM formulation for the periodic plate case.

3.1 Elapsed time comparison for FWFEM two-dimensional periodic media

Another important result is related to the computation cost and a comparision between FWFEM and WFEM MCS is computed. The numerical costs involved in computation is compared with that of MCS with 10000 samples. The numerical test ran on the mobile workstation with the following characteristics, Intel® Core™ i7 7820 HQ CPU@2.90GHz with 32 GB RAM. The comparison of elapsed time is reported in Table 2. It can be seen from Table 2 that computational effort by

Table 2: Elapsed time comparison for FWFEM

	WFEM MCS (10000 samples)	FWFEM (11 α-cut level)
Two-dimensional direct form	14400 seconds	122.52 seconds

application of FWFEM direct form is 99.1% less compared to WFEM MCS.

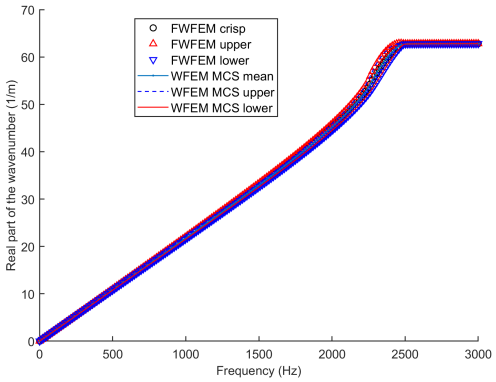

(a) Comparision of the out of plane flexural wavenumber (fuzzy Young's modulus)

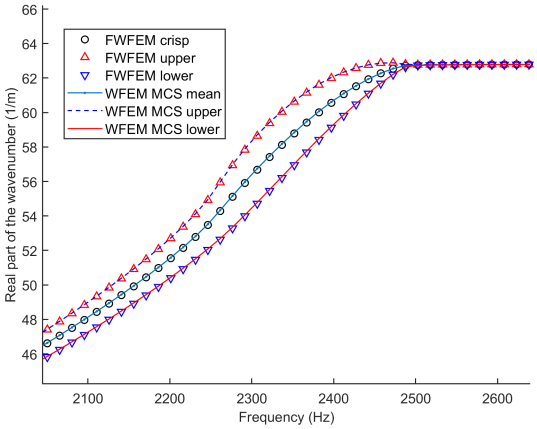

(b) Zoomed part

Figure 2: Periodic plate validation

4 CONCLUSIONS

A computationally inexpensive fuzzy spectral approach to study the uncertainties effects in two-dimensional periodic media is presented in this paper. The formulation applied to periodic plate up for the frequency range [0-3000] Hz. The validation of present results is performed by comparing with the WFEM MCS results and it provides excellent agreement. For periodic plate case, uncertainties affect the out of plane flexural wavenumber and maximum bound of the flexural wavenumber occurs near the band gap edge frequency. The analysis presented in this paper suggest that the uncertainties have a significant impact on the band gap frequencies. It is highly desirable to include the uncertainties when designing and analysing the periodic structures. In terms of computation cost, developed formulation offers substantial cost savings and can be a good point for the optimisation and reliability study under uncertainties of complex periodic structures.

REFERENCES

[1] R. P. Singh, S. De Rosa, F. Franco, M. Ichchou, and O. Bareille. A literature review for the analysis of structured and unstructured uncertainty effects on vibroacoustic. In *MEDYNA 2017: 2nd Euro-Mediterranean Conference on Structural Dynamics and Vibroacoustics*, pages 170–174, 2017.

[2] R. P. Singh, C. Droz, S. De Rosa, F. Franco, O. Bareille, and M. N. Ichchou. A study of structured uncertainties in wave characteristic of one-dimensional periodic structures. In *International Conference on Noise and Vibration Engineering (ISMA 2018)*, pages 4731–4740, 2018.

[3] B. K. Patle, Chetan K. Hirwani, Ravi P. Singh, and Subrata K. Panda. Eigenfrequency and deflection analysis of layered structure using uncertain elastic properties – a fuzzy finite element approach. *International Journal of Approximate Reasoning*, 98:163–176, 2018.

[4] R. P. Singh, M. Ichchou, O. Bareille, F. Franco, and S. De Rosa. Uncertainties in wave characteristic of one-dimensional periodic media using the fuzzy wave finite element method. In *9th ECCOMAS Thematic Conference on Smart Structures and Materials (SMART 2019)*, pages 1169–1182, 2019.

[5] Qing Liu and Singiresu S. Rao. Fuzzy finite element approach for analysis of fiber-reinforced laminated composite beams. *AIAA Journal*, 43(3):651–661, 2005.

[6] Brian R. Mace and Elisabetta Manconi. Modelling wave propagation in two-dimensional structures using finite element analysis. *Journal of Sound and Vibration*, 318(4-5):884–902, 2008.

VIBROACOUSTIC SIMULATION FE METHODOLOGIES: EXTERNAL GEAR PUMP CASE STUDY

Giuseppe Miccoli[1*] and Karim Hamiche[2]

[1]C.N.R. - IMAMOTER Institute
Via Canal Bianco, 28, Ferrara, ITALY
Email: g.miccoli@imamoter.cnr.it

[2]Siemens Digital Industries Software
Interleuvenlaan, 68, Leuven, BELGIUM
Email: karim.hamiche@siemens.com

ABSTRACT

Accurate predictions of the noise field emitted by an 8.5 cc/rev external gear pump are presented in this paper, making use of hybrid numerical-experimental integrated approaches together with some acceleration measurements on the gear pump external casing. The noise field radiated by the gear pump was computed by means of finite element vibroacoustic simulations involving the structural dynamic response as excitation boundary condition. A first two-step approach was carried out consisting in a structural FEM (Finite Element Method) model linked to an acoustic BEM (Boundary Element Method) model. Moreover, some acoustic numerical methods were investigated as integrated fluid-structure coupling approaches developed in the commercial software Simcenter 3D.

1 THE NUMERICAL-EXPERIMENTAL INTEGRATED APPROACH

The main aim of the original methodologies here proposed consists in predicting and reducing the vibroacoustic field emitted by external gear pumps. Two reasons at least make this topic remarkable and challenging. Firstly, gear pumps are components widely used for energy transmission in hydraulic and fluid power systems installed in a lot of machines and vehicles. Secondly, the current regulations and directives impose lower noise emission limits in the transport field. Moreover, a great advantage of these methodologies consists in considering the pump as a "black box", this way disregarding the complex dynamics of the gear tooth meshing process and consequent fluid pressure/load distribution.

The methodology (Figure 1) essentially consists in the development of external gear pump FEM models and computation of the vibroacoustic response as radiated acoustic field. An essential step is the acquisition of some experimental vibration spectra only in some different positions on the pump surface, as excitation boundary condition and system dynamic response estimation [1].

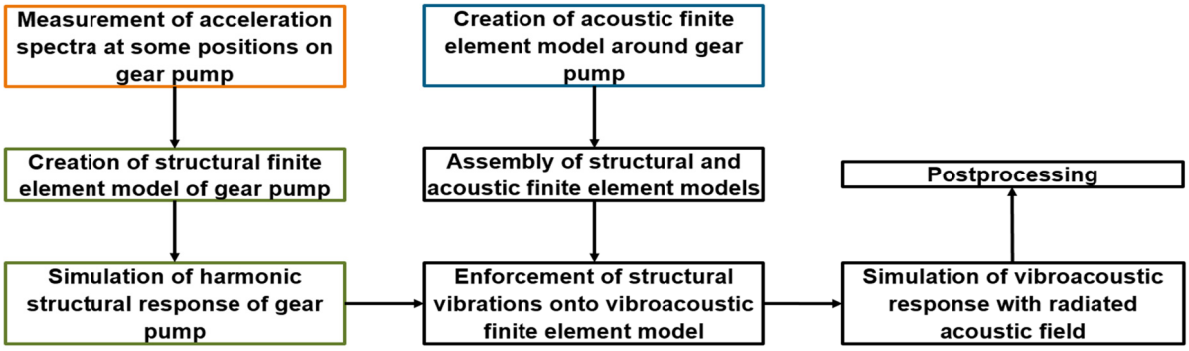

Figure 1. Flowchart of the numerical-experimental integrated approach.

The numerical-experimental approach was applied to an 8.5 cc/rev external gear pump with 12 teeth (Figure 2, left). The system dynamic response is estimated by the identification of the lowest number of acceleration spectra which leads to acceptable results of the radiated acoustic field. Eight positions were located on the pump casing surface and its support and 4 different subsets of acceleration spectra acquired for results quality comparison (Figure 2, right). The FEM structural model (Figure 3, left) consisted of 60779 nodes and 34880 hexahedral/tetrahedral elements. The output of the FEM structural response analysis (ANSYS, computation time 10 h, 95 GB results file size, Dell pc, W7, 4 cores, 16 GB RAM) represented the input as excitation boundary conditions to the BEM model (3115 nodes and 6093 triangular shell elements (Figure 3, right), analysis up to 8000 Hz, indirect variational BEM approach for the acoustic field computation).

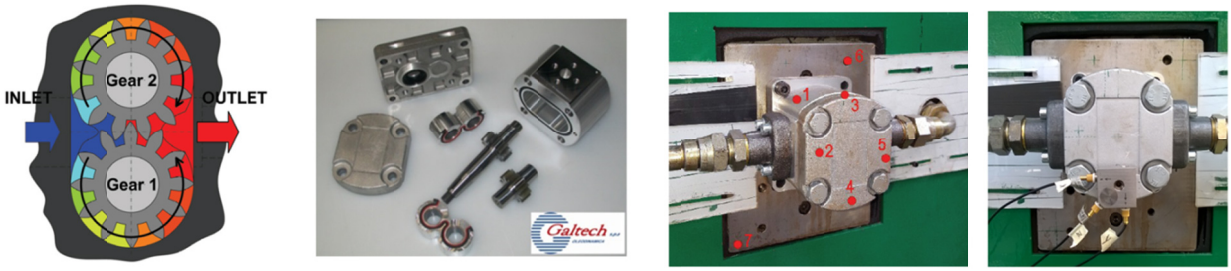

Figure 2. External gear pump (left) and accelerometer positions for test measurements (right).

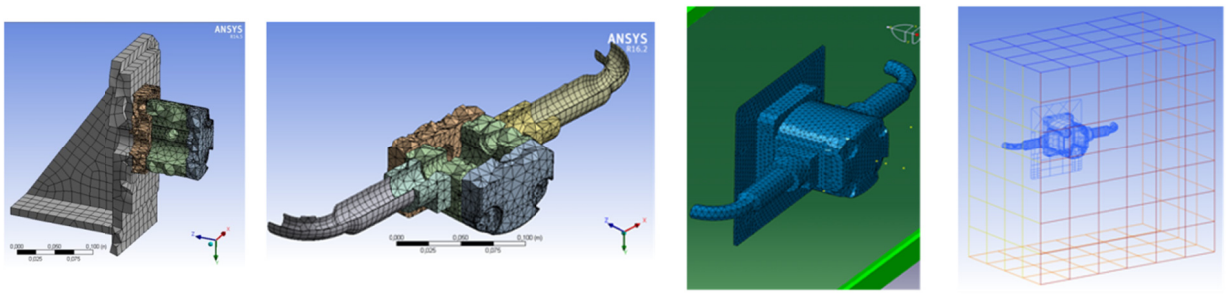

Figure 3. FEM model mesh (ANSYS, left) and BEM model mesh (Siemens PLM Virtual.Lab) with field points grid enclosing the pump (right).

For a matter of computational results validation, the sound power spectra of the tested pump were also experimentally acquired on a test rig complying with the requirements of ISO 16902-1 [2] by sound power measurements.

Three different pump operating conditions A, B and C were tested, referring to pump shaft speed and outlet pressure, so to check the reliability of this approach: A: 1500 rpm-50 bar, B: 1500 rpm-150 bar, C: 2500 rpm-50 bar.

For each operating condition, the numerical and experimental overall sound power levels match very well. Figure 4 reports a comparison in terms of overall and partial sound power levels. The sound power spectra were numerically computed on the field points grid (Figure 3, right) overlapping that defined for the experimental sound power tests: the partial sound power was calculated for each single face, and the total sound power for the whole surface.

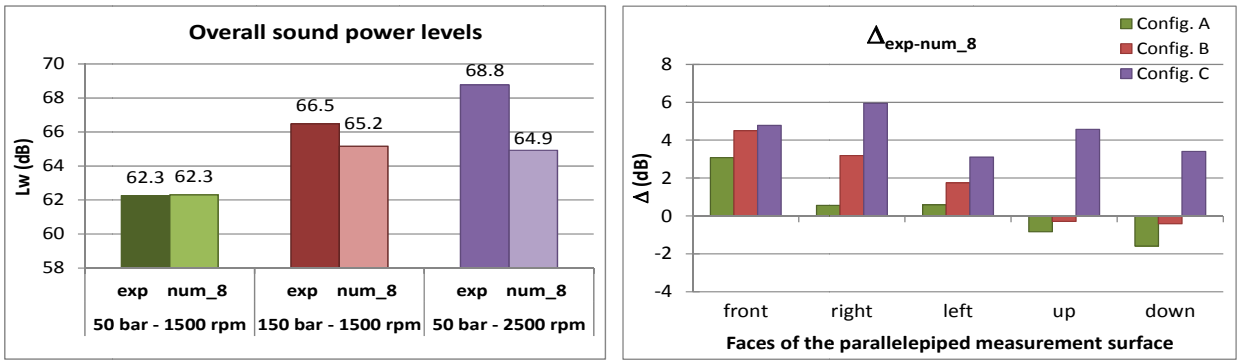

Figure 4. Numerical and experimental results obtained with 8 experimental acceleration spectra. Overall sound power levels (left), and partial sound power levels (right).

2 FULLY-INTEGRATED SIMCENTER 3D IMPLEMENTATION

An alternative numeric solution to that previously described consists in the Simcenter 3D implementation of a global workflow with a fully-integrated set-up from the geometry preparation up to the vibroacoustic solution within a single environment.

As a starting point, the available CAD geometry of the pump is imported into Simcenter 3D and optimised and discretised to generate the structural FEM mesh (Figure 5).

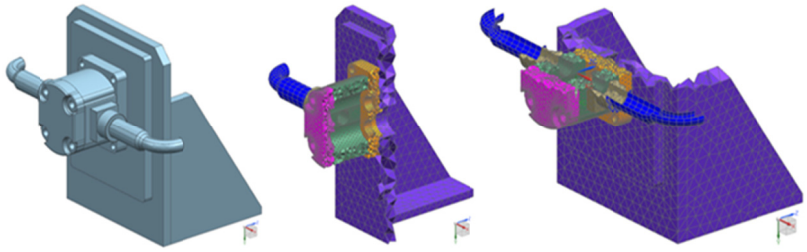

Figure 5. Pump modelling, Simcenter 3D: geometry (left), and structural mesh (middle and right).

The air around the pump is modelled with a 3D acoustic FEM mesh composed of 26749 nodes and 130096 linear tetrahedral elements. Some computation tools are used in order to account for the wave reflections against the wall on which the pump is fixed and against the ground. As well as an efficient absorption is simulated of the acoustic waves leaving the computation domain by means of a convex shape of the mesh suitable to support the AML (Automatically Matched Layer) boundary condition (Figure 6).

The FE AML acoustic (coarse) mesh (5226 nodes and 21059 elements, Figure 6, bottom left) allows better computation performance if integrated with the FEMAO (FEM Adaptive Order) solution method: the vibroacoustic response over the all frequency range (3000 Hz) is obtained in 1 h 5 min only, instead of 3 h 13 min needed with the classical FEM approach (Intel® Xeon® Silver 4116 CPU 2.10 GHz, 24 cores, 128 GB installed memory). Experimental vs computation overall and partial sound power levels show a deviation lower than 2 dB for both acoustic meshes.

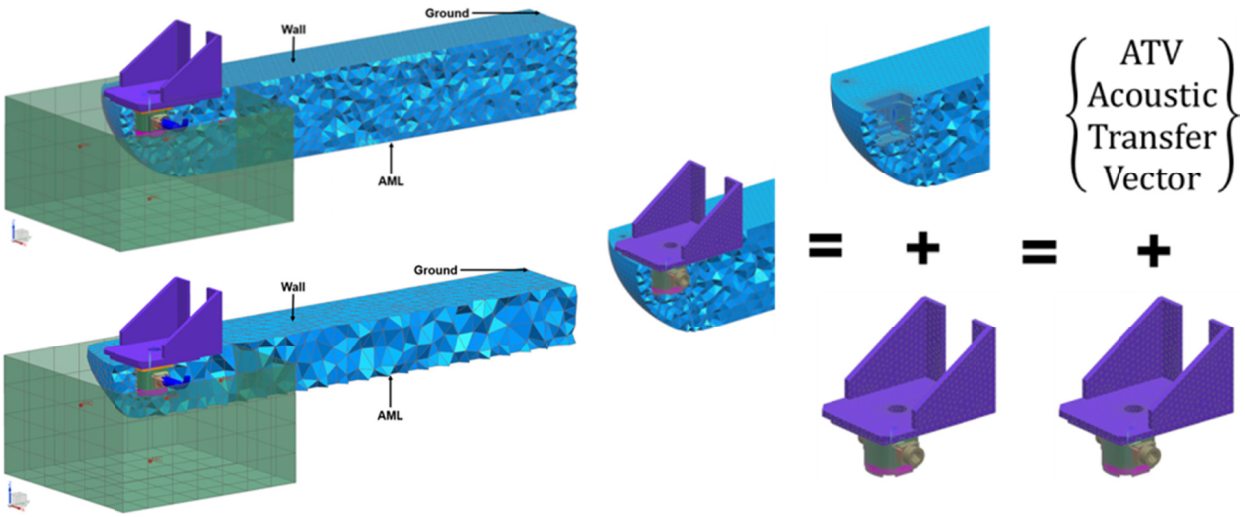

Figure 6. Gear pump modelling in Simcenter 3D - FEM AML acoustic mesh (blue) and field point grid (green). Fine mesh for classical FEM (top left) and coarse mesh for FEMAO (bottom left). Gear pump modelling equivalence, full FEM and ATV (right).

The ATV (Acoustic Transfer Vector) approach was also checked for comparison. It consists in computing the transfer matrix linking the acoustic pressure at some microphones with unit normal velocities on the vibrating structural surface. Two steps are required: Step 1 - computation of ATV without structure (purely acoustic and only once), Step 2 - computation of vibroacoutic response by multiplication by the actual structural vibrations, i.e. {Pressure} = [ATV] x {Structural Vibrations}. Figure 6 right shows the equivalence between the two pump modelling approaches. The vibroacoustic response computation times result in 193 min for the full FEM representation, in comparison with 19 min only with ATV (plus 68 min for Step1). As Step 1 is computed only once, a benefit of the ATV method consists in faster simulations for multiple load cases (multi-RPMs, different operating conditions, etc.).

3 CONCLUSIONS

The combination of experimental measurements with numerical set-ups to predict the acoustic field emitted by gear pumps is shown to be a suitable approach to estimate the system dynamic response from a limited number of accelerations acquired on the pump surface. Among the Simcenter 3D fully-integrated numerical models validated, the innovative FEMAO and ATV approaches exhibit interesting computational performance and impressive solution time reduction. The implementation of a multi-physics approach is considered now by the authors as a methodology future development, linking the pump inner pressure distributions as output of a CFD (Computational Fluid Dynamics) analysis and structural excitation to the Simcenter 3D fully-integrated numerical models.

REFERENCES

[1] E. Carletti, G. Miccoli, F. Pedrielli, and G. Parise. Vibroacoustic Measurements and Simulation Applied to External Gear Pumps. An Integrated Simplified Approach. Archives of Acoustics. 41(2):285-296, 2016.

[2] ISO 16902-1:2002, Hydraulic Fluid Power – Test Code for the Determination of Sound Power Levels of Pumps using Sound Intensity Techniques: Engineering Method – Part1: Pumps, 2002.

"BANDGAP INVESTIGATION OF HIERARCHICAL ISOVOLUMETRIC PERIODIC CORES WITH NEGATIVE POISSON RATIO"

S. Del Broccolo[1*], M. Ouisse[1], E. Foltete[1] and F. Scarpa[2]

[1] Univ. Bourgogne Franche-Comté - FEMTO-ST – Institute CNRS/UFC/ENSMM/UTBM
Department of Applied Mechanics, 25000 BESANÇON-FR

[2] Bristol Composites Institute (ACCIS), University of Bristol
Queen's Building, University Walk, Bristol BS8 1TR, United Kingdom

ABSTRACT

The use of periodic media as passive mechanical and acoustic vibration filters has become a research topic of great interest. The classic cores dynamic characteristics have been widely studied and only for very few configurations revealed partial Bragg bandgaps using simple beam models. In this paper, an innovative negative Poisson's ratio cellular core, derived from the classic re-entrant core geometry is proposed and optimized maintaining constant its overall volume and mass, with the aim of improving its vibration filtering capabilities while leaving its static properties unvaried. The numerical method used to perform this is the Wave Finite Element Method (WFEM) and the optimization focused on obtaining the widest full in-plane bandgap. Harmonic numerical analyses using commercial FEA software are also carried out to validate the bandgaps.

1 INTRODUCTION

Periodic structures can be found in almost every engineering domain. Periodicity is a feature that can be found in the structure's geometry as well as in its constituent materials. The industrial world has moved in favour of such strategy mainly because it represented a cost-effective solution but lately, this characteristic has also been exploited for acoustic and mechanical wave annihilation or transmission. Impedance mismatches caused by the periodic features will passively filter unwanted and potentially dangerous structure Bourne vibrations because the injected wave will experience internal reflection and consequent destructive interaction within the structure [1]. Sandwich panels are a well-fitting example of periodic engineered building bricks for complex structures which had to be light and withstand high loads and solicitations. Sandwich panels are made with two laminate skins and a light-weight core to separate them which can be made of porous media like a foam or a cellular structure. Amongst the latter, the hexagonal cell periodic core is the one with the higher stiffness to mass ratio [2] and this translates in high static properties. The configuration which has been found to possess the most interesting filtering properties amongst the classic ones is indeed the re-entrant also known as the inverted hexagonal. Whilst static performance might be the only requirement for some structures, increasing effort in improving the dynamic properties of sandwich panels has been made lately. Most adopted solutions though cause an increase in mass (addition of viscoelastic patches, foam inserts, resonating elements) and may become non-trivial manufacturing or assembly tasks. The solution presented in this paper instead is an improved re-entrant cellular structure that maintains constant volume and mass and static out of plane properties.

2 NOVEL RE-ENTRANT CELL

This cellular core is derived from the classic re-entrant configuration, which exhibited directional wave propagation characteristics [3] when exposed to out of plane solicitation. Although this is an interesting feature, the availability of a cellular core producing full Bragg bandgaps is also of great interest. The Directionality and hierarchy concepts [4] in this case were used as a tool to create a full in-plane bandgap by placing "child" re-entrant cells of smaller size and different orientation onto the main frame constituted from "parent" re-entrant cells. The starting configuration is therefore the classical re-entrant cell and as we increase the size of the "child" cell (e), the cell's wall thickness is reduced to maintain the core's encumbrance and mass constant [5], as shown in *Figure 1*. The overall cell encumbrance is 20mm*12.125mm*15mm.

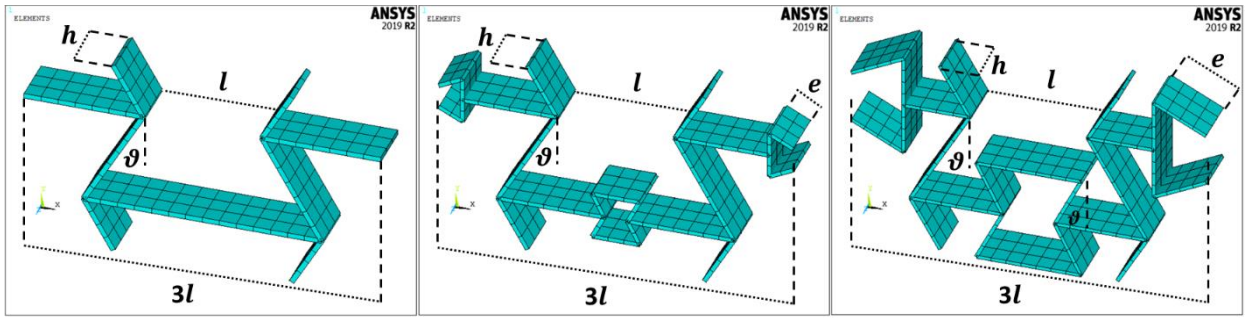

Figure 1 - Re-entrant unit cell (left), Optimised cell evolution (middle), Optimised unit cell (right)

3 NUMERICAL METHODS

Numerical tools were developed to perform WFEM and investigate wave propagation. the 2D in-plane periodicity dynamic analysis was carried out adopting the inverse WFEM formulation [6-9], based on the Floquet-Bloch periodic boundary conditions, in which the reduced wavenumber is

imposed, and the output frequency calculated. The tool is a synergy between MATLAB 2019 and ANSYS APDL 19.0 R2. The model parameters used for the simulation are listed in *Table 1*. Initially, the dispersion curve for the classic re-entrant configuration will be produced and then the geometrical optimization is carried out.

MODEL DETAILS		MATERIAL PROPERTIES (MDF)	
Element Type	SHELL 181	Young's Modulus	4.20 GPa
Element Size	1.00 mm	Density	818 kg/m^3
Element thickness	0.30 - 0.19 mm	Poisson's Ratio	0.33

Table 1 - Model and material details

3.1 Re-entrant cell

The unit cell for the re-entrant core is shown in *Figure 2* as well as the dispersion curves for the frequency range 0-10 kHz. This geometry clearly shows some partial bandgaps across the XY plane direction for all types of waves traveling the media (AB & BC in the k-space). The steep branch starting from zero is a compression mode which translates that there is no compression bandgap within this frequency range along the X and Y direction. Directional (X-axis) in-plane and out of plane bending bandgaps are present.

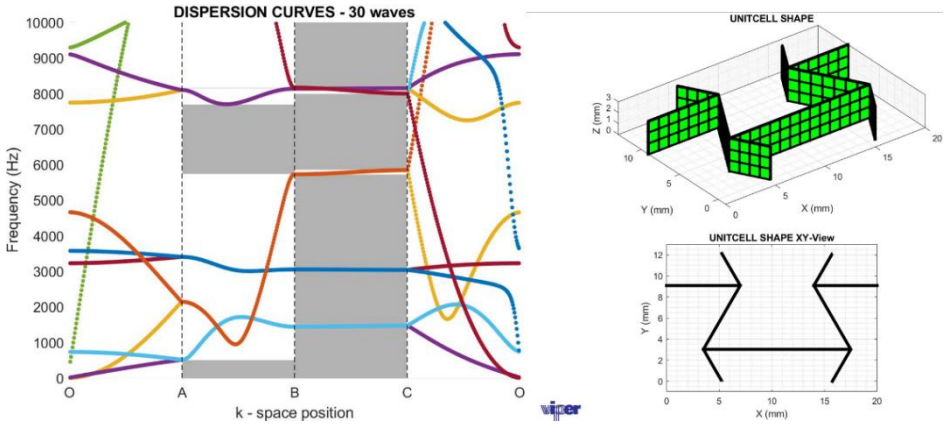

Figure 2 - Re-entrant unit cell and dispersion curves

3.2 Optimized cell

The optimized re-entrant unit cell is shown in *Figure 3* as well as the dispersion curves for the frequency range 0-10 kHz. *Figure 3* clearly shows show a full bandgap of noticeable width (1.1 kHz) which is found between 4.9 kHz and 6.0 kHz.

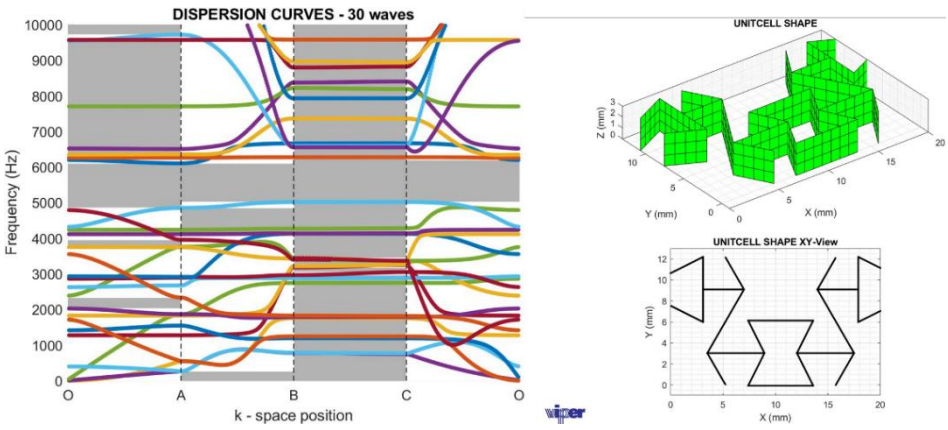

Figure 3 - Optimised re-entrant unit cell and dispersion curves

4 CONCLUSIONS

The auxetic core has interesting partial and directional Bragg bandgaps but further improvement seemed necessary. The optimisation conducted in this work produced a wide full Bragg bandgap which represents a valid improvement of the dynamic behaviour of the "parent" cellular core. The overall full bandgap evolution can be observed in *Figure 4* as parameter *e* is increased to its maximum admissible value. An experimental campaign will be conducted to complete the validation.

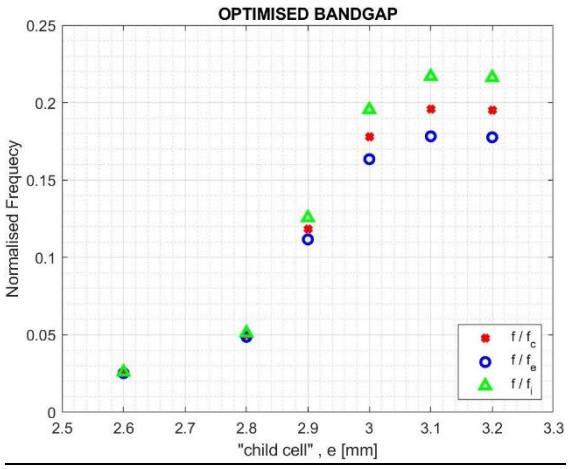

Figure 4 - Bandgap width evolution during geometrical optimisation (f_c = central frequency ; f_i = initial frequency ; f_e = end frequency)

REFERENCES

[1] L. Brillouin. Wave propagation in periodic structures, electric filters and crystal lattices. Dover, 1953.

[2] Lorna J, Gibson MFA. Cellular Solids. 2nd Ed. Cambridge University Press, 1997

[3] F. Scarpa, M. Ruzzene - Wave beaming effects in two-dimensional cellular structures, *Smart Materials and Structures*, 12, 363 – 372, 2003

[4] Mechanics and band gaps in hierarchical auxetic rectangular perforated composite metamaterials, K. Billon, I. Zampetakis, F. Scarpa, M. Ouisse, E. Sadoulet-Reboul, M. Collet, A. Perriman, A. Hetherington, *Composite Structures*, 160, 1042-1050, 2017

[5] L.Boldrin, F.Scarpa, R.Rajasekaran, Thermal conductivities of iso-volume centre-symmetric honeycombs, Composite Structures, 113, 498-506, 2014

[6] D.J. Mead. Wave propagation in continuous periodic structures: research contributions from Southampton 1964-1995. *J. Sound Vib*., 190(3):495-524, 1996.

[7] Brian R. Mace, Denis Duhamel, Michael J. Brennan - Finite element prediction of wave motion in structural waveguides, *The J. of the Acoustical Society of America* – 117, 2835-2843, 2005.

[8] Brian R. Mace, E. Manconi - Modelling wave propagation in two-dimensional structure using finite element analysis, *Journal of Sound and Vibration* 318, 844 – 902, 2008.

[9] M. I. Hussein, M. J. Leamy, and M. Ruzzene. Dynamics of phononic materials and structures: Historical origins, recent progress and future outlook. *Applied Mechanics Reviews*, 66(4):040802, 2014.

This project has received funding from the European Union's Horizon 2020 research and innovation programme under Marie Curie grant agreement No 675441

TOWARDS FULL-FIELD MODAL ANALYSIS: COMBINING OPTICAL TECHNIQUES WITH STRUCTURAL DYNAMICS TESTING

E. Di Lorenzo[1] , D. Mastrodicasa[1] , L. Wittevrongel[2], P. Lava[2] and B. Peeters[1]

[1]Siemens Industry Software
Interleuvenlaan 68, 3001, Leuven, BELGIUM
Email: emilio.dilorenzo@siemens.com

[2]MatchID
Deinsesteenweg 94A, 9031, Gent, BELGIUM

ABSTRACT

The main objective of this work is to make a step further to bridge the gap between two different worlds and bring together the use of optical measurement techniques with structural dynamics testing and analysis. The recent advances in both fields allow to combine the use of cameras with modal analysis tools in order to reconstruct the dynamic behavior of a structure in a large frequency band and with a very high spatial resolution. The use of Digital Image Correlation (DIC) is gaining popularity in many application fields and here it is applied to obtain the full-field mode shapes of different type of structures, from lab experiments to a full aircraft. This is a clear advantage especially in proximity of connection points and for lightweight structures where it becomes complex or impossible to instrument the specimen by means of contact transducers such as accelerometers or strain gauges. Of course, the data acquisition and processing has some challenges to overcome. Laser Doppler Vibrometry and accelerometers are used to compare the results obtained by means of DIC.

1 INTRODUCTION

Nowadays, there has been an increase in applications of lightweight and composites materials in the automotive, aerospace and other advanced manufacturing industries. At the state of the art testing and validation for mechanical numerical models are mostly performed using a certain number of transducers (e.g accelerometers, strain gauges, fiber optics, etc...). However, accelerometers may mass-load the structure and can only provide measurements at discrete locations. Furthermore, placing transducers is a labour intensive and time consuming task and it could introduce electrical noise to the measured signals due to the extensive and unavoidable wiring. These are the main reasons behind the development of image processing techniques to perform modal analysis of mechanical structures without contact and without having to instrument the specimen. An optical method such as Digital Image Correlation (DIC) has recently received special attention in the structural dynamics field because it can be used to obtain full field measurements, [1, 2]. At the state of the art DIC is mostly used for static applications like structural testing and material identification. In the last years the use of DIC for measuring vibrations is gaining popularity. Particularly DIC for vibration analysis was mostly performed on aerospace and automotive components and rotating structures like turbine blades, helicopter rotors[3]. In this paper, DIC technique is used to get the full-field displacement time histories of the unity under test. These information are then used in combination with Siemens Simcenter Testlab to identify the dynamic characteristics of the structures. Two real life examples were considered: an helicopter tail blade in lab conditions and an aircraft in the hangar.

2 DIGITAL IMAGE CORRELATION

DIC only requires a set of cameras and a specimen which has been speckled (i.e. a gradient must be present in the tested specimen, which can be created with spray paint, a marker, stickers, etc.) for point tracking. The first image of camera 1 is used as a reference image to which the image of the second camera (taken at the same time) is compared. The corresponding points can be triangulated into a three-dimensional point in space if the orientation of the cameras is known (by performing a pre-test calibration). The same points matching can be done over time so that each measurement point can be tracked over time, leading to a total deformation tracking of the surface area of a specimen.
This process holds some intrinsic requirements towards the images: a gradient, as well as contrast, must be present so that features can be tracked. The size of these features lead to the minimal size of the so-called subset which is tracked throughout the set of images. This is needed since a single pixel is not a unique item due to the limited amount of gray scales which are stored in an image (usually 8 bit cameras are used, so a maximum of 256 grey scales are available). A cluster of pixels is however a unique set of data which can be tracked. This subset is restricted in the way it can deform by assigning a so-called “shape function” to it, leading to an even higher amount of robustness against noise. This, together with image interpolation for sub-pixel accuracy, leads to high-quality and precise measurements of shapes and displacements.

3 EXPERIMENTAL ANALYSIS

Different test beds were investigated in order to analyze the challenges related to the use of Digital Image Correlation for the dynamic characterization of aeronautical structures. More specifically, an helicopter tail blade was analyzed by using high speed cameras. Afterwards the F16 airplane was speckled and measured by using DIC together with accelerometers and a Scanning Laser Doppler Vibrometer (SLDV).

3.1 Helicopter Tail Blade

The objective of this study is to perform a full-field modal analysis of an helicopter tail blade in lab conditions. The specimen on which a white base coat has been applied is shown in Fig. 1(a). The same specimen after the application of the white coat which was needed to create enough contrast after applying the speckles (i.e. features), is shown in Fig. 1(b). Finally, the specimen used for the DIC test is shown in Fig. 1(c). The structure was clamped on the right hand side using an heavy mass to apply a fixed constraint. The experimental setup for the high speed cameras configuration includes two iX 720 high speed cameras in a stereo DIC setup to grab the pictures of the specimen

during the controlled excitation. MatchID software was used both for the image acquisition and data processing. 8253 images were acquired and 10200 points were analyzed. Only the Z Degree-of-Freedom (DoF) (out of plane motion) was considered due to the high computational cost to process all the 3 DoFs.

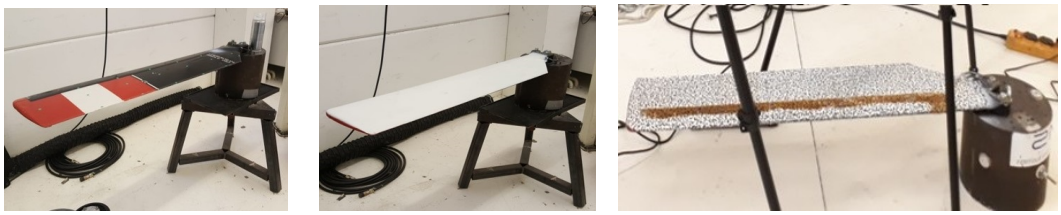

Figure 1: Experimental set up: speckled blade.

The blade was pulled at its free-end and the free vibrations were recorded by using the stereo setup. Operational Polymax was then used to perform Operational Modal Analysis (OMA) in order to get the modal parameters estimation with the help of Siemens Simcenter Testlab. An Optomet Scanning Laser Doppler Vibrometer (SLDV) device was also used to measure the vibrations of the helicopter blade to obtain reference results to compare with the DIC estimated modal parameters. Tab. 1 and Fig.2 show the comparison in terms of natural frequencies, damping ratios and mode shapes.

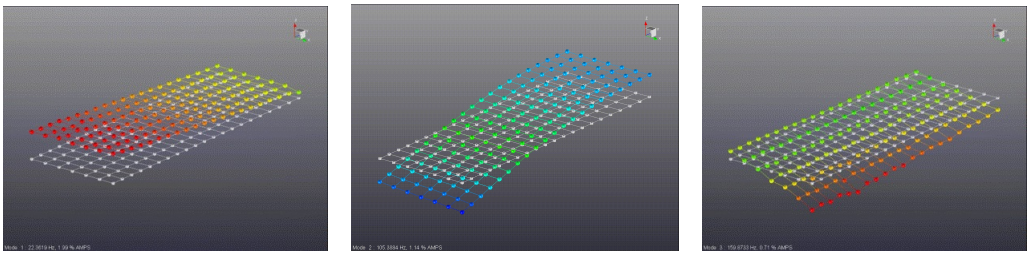

(a) 1^{st} Mode shape SLDV. (b) 2^{nd} Mode shape SLDV. (c) 3^{rd} Mode shape SLDV.

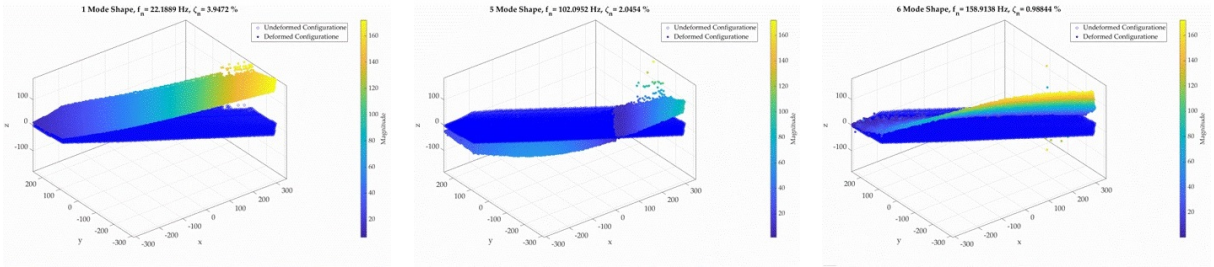

(d) 1^{st} Mode shape DIC. (e) 2^{nd} Mode shape DIC. (f) 3^{rd} Mode shape DIC.

Figure 2: Mode shapes comparison.

Mode	SLDV		DIC	
	f_n **(Hz)**	ζ_n **(%)**	f_n **(Hz)**	ζ_n **(%)**
1	22.36	1.99	22.19	3.95
2	105.40	1.14	102.10	2.05
3	159.90	0.71	158.91	0.99

Table 1: Modal parameters comparison.

A good match between DIC and SLDV results in terms of natural frequencies is achieved, but DIC is overestimating the damping for all the three analyzed modes. Further studies will be conducted to improve the damping estimation.

3.2 F16 aircraft

A F16 aircraft was used as test bed to prove the reliability and robustness of the technique. The structure was speckled using A4 paper sheets glued on the two wings and part of the fuselage as shown in Fig. 3. The system was also instrumented using accelerometers and using the Optomet SLDV to have a reliable modal model for the comparison with the DIC results. Only the out of plane motion was considered. 932 images were acquired and 13959 points were analyzed. Fig. 4 shows the comparison between SLDV + accelerometers and DIC. A very good match both in terms of natural frequencies and mode shapes can be highlighted. The damping is again overestimated.

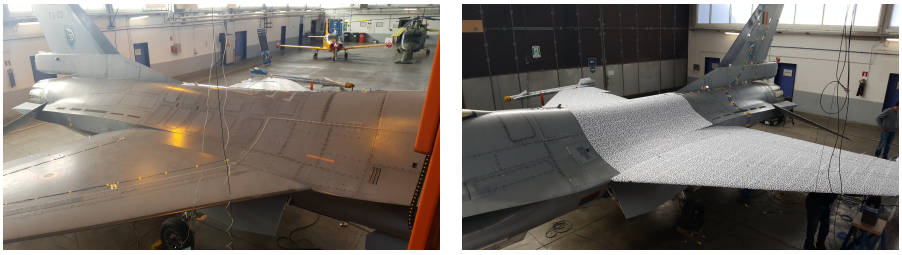

Figure 3: Experimental set up: speckled aircraft.

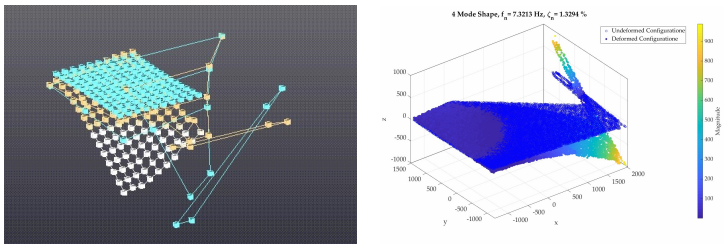

(a) SLDV + accelerometers mode shape (7.40 Hz, 0.43 %).

(b) DIC mode shape (7.32 Hz, 1.33 %).

Figure 4: Mode shapes comparison.

4 CONCLUSIONS

In this paper, the use of DIC for modal analysis is investigated. Different experimental measurements results which combine conventional modal analysis (SLDV/accelerometers) with the novel DIC experimental modal analysis are presented. The quality of the measured DIC data is very good and its application in the modal analysis field in order to enrich the conventional modal analysis results with high density data is very promising. Further studies will be conducted to establish a streamline solution covering the full measurement and processing chain.

REFERENCES

[1] E. Di Lorenzo, P. Lava, R. Balcaen, S. Manzato, and B. Peeters. Full-field modal analysis using high-speed 3d digital image correlation. *Journal of Physics: Conference Series*, 1149:012007, 12 2018.

[2] V. Srivastava, K. Patil, J. Baqersad, and J. Zhang. A multi-view dic approach to extract operating mode shapes of structures. In C. Niezrecki and J. Baqersad, editors, *Structural Health Monitoring, Photogrammetry & DIC, Volume 6*, pages 43–48, Cham, 2019. Springer.

[3] A. Molina-Viedma, E. Lopez-Alba, L. Felipe-Sese, F. Diaz, J. Rodriguez-Ahlquist, and M. Iglesias-Vallejo. Modal parameters evaluation in a full-scale aircraft demonstrator under different environmental conditions using hs 3d-dic. *Materials*, 11:230, 02 2018.

Investigation of the sound transmission loss with the use of the inner-resonance and the veering effect of a multi-layer core topology system

N. Guenfoud[1,2], C. Droz[1], M. Ichchou[1*], O. Bareille[1], E. Deckers[2, 3] and W. Desmet[2, 3]

[1]Vibroacoustics & Complex Media Research Group, LTDS - CNRS UMR 5513, Ecole Centrale de Lyon, Ecully, 69134, France
Email: mohamed.ichchou@ec-lyon.fr, olivier.bareille@ec-lyon.fr

[2]Noise and Vibration Research Group, Dept. Mechanical Engineering, section LMSD, KU Leuven, Celestijnenlaan 300 B, B-3001, Heverlee, Belgium
Email: elke.deckers@kuleuven.be, wim.desmet@kuleuven.be

[3]DMMS lab, Flanders Make, Belgium

ABSTRACT

The purpose of this paper is to analyze the veering effect occurring in the wave propagation of multi-layer core topology systems (MLCTS) and to study its influence on the acoustic efficiency. The structure is modeled with two methods considering either the entire unit cell or the skins and the core separately applying the Transfer Matrix Method (TMM). Both are combined with the Wave Finite Element Method (WFEM). MLCTS turns out a veering effect coupling shear waves propagating in the core and flexural waves of the structure compared to standard structures with the same mass. The interaction between an incident acoustic wave impinging the structure with a specific angle and the veering effect allow to remove the coincidence frequency due to the internal resonance of the core which dissipates the energy of flexural waves. This mechanism can be compared to internal resonators. Finally, it is shown that the veering effect and thus, the internal resonance can be controlled by modifying either the geometry of the core or by shifting core layers.

***Keywords*:** *TMM-WFE / multi-layer periodic structure / Sound Transmission Loss / Veering effect / Internal resonance*

1 INTRODUCTION

The acoustic efficiency of lightweight structures became a widespread research topic these last years. Studies are mainly focused on the analysis of the wave propagation through structures obtained with the Wave Finite Element Method (WFEM) [1]. Recently, many methods were developed to model the acoustic properties calculating the sound transmission loss of sandwich panels made of periodic cores [2-4]. Dispersion curves and more specifically flexural waves can be used to predict coincidence frequencies and critical frequencies of sandwich panels. However, in some cases two different waves can be coupled in the structure and creates a veering effect at a specific frequency as it is explained by Mace and Manconi [5-6]. This veering effect can be increased depending on the damping of the structure. In addition, it is shown that such an effect occurs when coupled systems with string coupling are considered. In this paper, veering effects are observed in MLCTS depending on the shift between layers. The main purpose is to interact them with acoustic waves and to investigate the effect on the Sound Transmission Loss (STL). Firstly, a MLCTS is compared to a standard structure to show the veering effect occurring. Then, the calculation of the sound transmission loss is performed for a specific angle of an acoustic wave and coupled with the veering effect. Finally, the effect of several geometrical parameters is investigated.

2 VEERING EFFECT IN MLCTS

In this section, a standard sandwich panel made of a rectangular core (Fig. 1a) is compared with a MLCTS made of 4 layers of rectangular cores (Fig. 1b). In this configuration, the 2 middle layers are shifted to obtain the MLCTS.

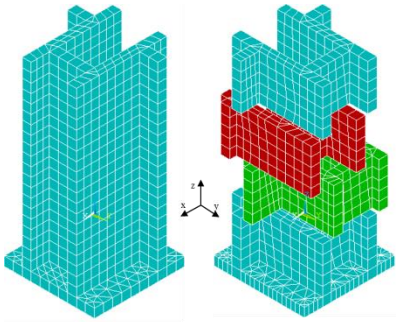

(a) (b)

Figure 1. (a) standard structure (b) MLCTS.

The size of the unit cell is fixed to Lx = 10 mm and Ly = 10 mm. The depth of each layer is 5 mm. The thickness of the skins and the core is 1 mm. The sandwich panel is made of ABS since the 3D printing technic is commonly used to manufacture these structures, with E = 1,8 x 10^9 Pa, $\rho = 985$ kg/m^3 and $\upsilon = 0{,}35$. The damping η is evaluated at 2 %. These values were acquired using a DMA test.

After applying the WFEM, the dispersion curves are obtained in the x-direction as illustrated in Fig. 2. The flexural and shear wave are represented. The shear wave corresponds to waves travelling in the core. As it can be seen, according to the angle θ and φ of the acoustic wave, the coincidence frequency is changed. In the case of an angle $\theta = 75°$ and $\varphi = 0°$, the acoustic wave intersects the flexural wave of both structures which creates a coincidence frequency in the STL. The azimuth angle $\varphi = 0°$ involves an acoustic wave travelling in the x-direction of the structure while θ is the grazing angle. In addition, in the case of MLCTS a veering effect is observed between 7000 and 8000 Hz. At this frequency, the flexural and shear wave are coupled. As explained by Manconi et Mace [5], the veering effect is due to a coupled system. In the case of MLCTS, the two-middle layer are connected

to the first and last layers by point contact which involve impedance discontinuities and a drop of mechanical properties. Therefore, the flexural wave number is higher than standard structures (more rigid). Finally, the analogy with string-mass systems can be done considering that the skins attached to the first and last layer are connected with two middle layers with a less rigid string coupling and lead to the veering effect. It is then interesting to investigate how the coincidence frequency evolves when the coincidence frequency region occurs at the same frequency of the veering effect occurring when $\theta = 59°$ and $\varphi = 0°$.

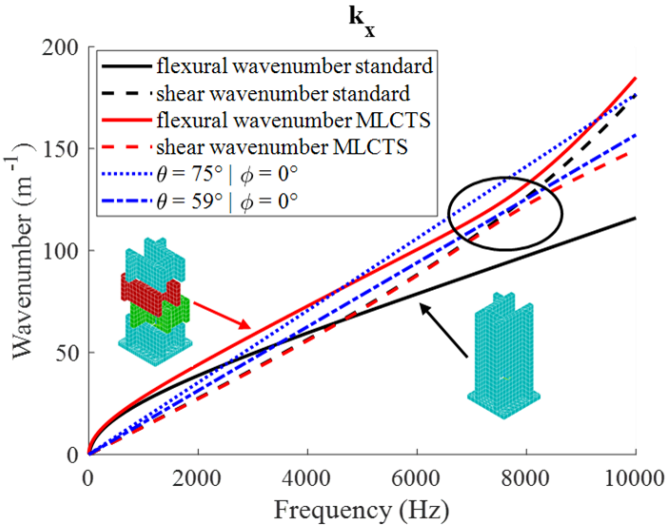

Figure 2. Flexural, shear and acoustic wavenumber of the standard structure compared to the MLCTS in the x-direction.

3 VEERING EFFECT AND ACOUSTIC WAVE INTERACTION

Two methods are applied and described in [2, 3] to calculate the STL. Christen et al. [2] considers the entire unit cell whereas Parrinello et al. [3] uses the TMM to be able to separate the calculation of the transfer matrix of the skins and the core which reduces drastically the computational cost. Results are depicted in Fig. 3. It is shown that the coincidence frequency is completely removed in case of MLCTS. The behavior of the MLCTS in this coincidence region is similar to resonating behavior. At this frequency, the wave mode shape is mainly due to the shear core effect which

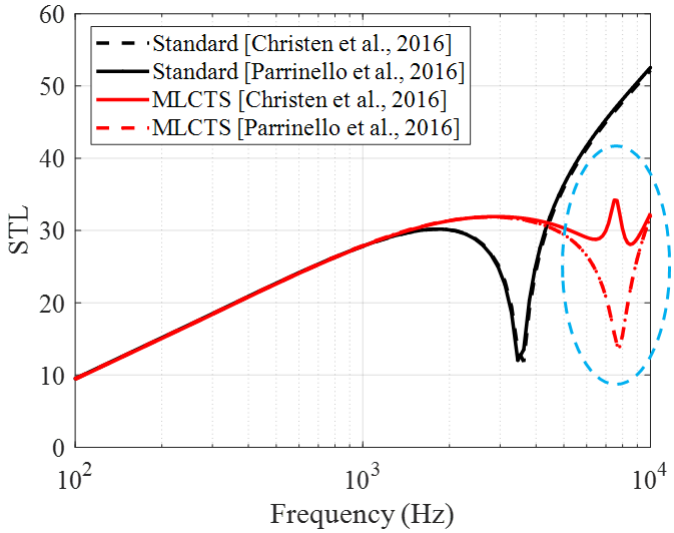

Figure 3. STL of the standard structure compared to the MLCTS for an acoustic wave with $\theta = 59°$ and $\varphi = 0°$.

dissipates the strain energy related to flexural waves as shown in Fig. 4. Therefore, the 2 middle layer cores act as internal resonators and lead to an improvement of the STL. This effect is observable if the dynamic behavior of the entire unit cell is considered and thus, the influence of the dynamic behavior of the core on the skins.

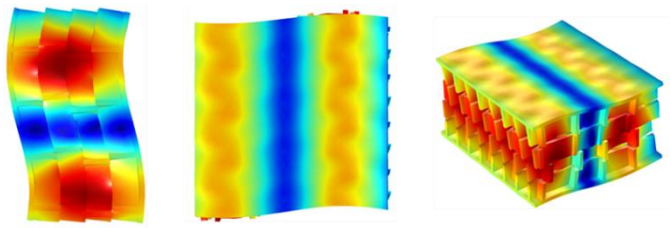

Figure 4. Wave mode shape of the MLCTS in the veering frequency region.

4 CONCLUSIONS

It has been shown that MLCTS can produce a veering effect at a specific frequency. This veering effect is due to the interface between layers which creates a low rigid coupling between both skins. Therefore, the flexural wave and the core shear wave are coupled. In the case of the MLCTS, the energy of the flexural wave is dissipated in the core. This later then, acts as an internal resonator and leads to an improvement of the STL. Such an improvement is obtained when the acoustic wavenumber and the frequency in which the veering effect occurs are similar. The coincidence frequency is then eliminated. Finally, these results can be obtained keeping the mass constant compared to standard honeycomb sandwich panels using shifting cores.

ACKNOWLEDGEMENTS

This project has received funding from the European Union's Horizon 2020 research and innovation program under the Marie Sklodowska-Curie grant agreement No. 675441. The author would like to gratefully acknowledge everyone involved in the VIPER project. The research work of Elke Deckers is financed by a post-doctoral grant of the Research Foundation-Flanders (FWO).

REFERENCES

[1] B., Mace and E., Manconi. Modelling wave propagation in two-dimensional structures using finite element analysis. *Journal of Sound and Vibrations*, vol. 318, no 4-5, 2008.

[2] J-L., Christen and M., Ichchou and A-M., Zine and B., Troclet. Wave finite element formulation of the acoustic transmission through complex infinite plates, *Acta Acustica united with Acustica*, vol. 102, no 6, 2016.

[3] A., Parinello and G.L., Ghiringhelli. Transfer Matrix representation for periodic planar media. *Journal of Sound and Vibration*, vol. 371, 2016.

[4] E., Deckers and S., Jonckheere and L.V., Belle and C., Claeys and W., Desmet. Prediction of transmission, reflection and absorption coefficients of periodic structures using a hybrid wave based finite element unit cell method, *Journal of Computational Physics*, vol. 356, 2018.

[5] E., Manconi and B., Mace. Veering and Strong Coupling Effects in Structural Dynamics. *Journal of Vibration and Acoustics*, vol. 139, no 2, 2017.

[6] B., Mace and E., Manconi. Wave motion and dispersion phenomena: Veering, locking and strong coupling effects, *The Journal of the Acoustical Society of America*, vol. 131, no 2, 2012.

VIBRO-ACOUSTIC CHARACTERIZATION OF A MILITARY SHELTER SYSTEM

M. Lomasto[1*], M. Viscardi[1*], R. Molitierno[2]

[1] *Vibration, Acoustic & Smart Structure Lab*. Università degli studi di Napoli Federico II
massimo.viscardi@unina.it , mar.lomasto@gmail.com

[2]MBDA Italia Spa
raffaele.molitierno@mbda.it

ABSTRACT

The main goal of the present study is the development of a numerical model well representing the system in terms of vibro-acoustic response to the effecting noise and vibration sources.
The Shelter System has been designed and modeled with finite elements (FEM) considering both a structural and acoustic mesh of the internal air volume. A vibroacoustic numerical test with NASTRAN was then conducted to predict the level of acoustic pressure inside the cavity and more precisely close to the human ear; the main results obtained concern the acoustic pressure levels, inside the shelter, generated by the action of the power unit (PGU).
Numerical data have been compared with results of a dedicated experimental campaign to check and update the numerical assumptions.

1. INTRODUCTION

The Shelters are able to withstand extreme conditions of use both structural and meteorological, providing the operator with optimal comfort conditions.
The main requirements that must be kept under control in a shelter enclosure are mainly the temperature and internal noise level. With reference to this latter aspect, personnel shall be provided an acoustical environment that will not cause personnel injury, interfere with voice or any other communications, cause fatigue, or in any other way degrade system effectiveness. Noise affects human health and performance in several ways. Apart from environmental considerations, the most critical effects include noise-induced hearing injury and the impact of signal comprehension on communications, survivability, and mission effectiveness.
The aim of this paper is to develop a vibro-acoustic model of a shelter system, in order to be able to predict the internal acoustics noise of a manned shelter system during the drafting phase. After

numerical model validation due to experimental testing, some strategies will be proposed to reduce the internal noise of the shelter.
The shelter that has been taken into is composed by: an operating cabin where devices are set up to carry out the mission, a central compartment occupied by an antenna that can be raised in the operational phase and at the end we have a power unit and a cooling system outside. The shelter has four large paws that separate it from the ground, thanks to which it can be positioned horizontally compared to ground.

2. ACOUSTIC PROBLEM

Main interest of the work will be the structural transmission of low-frequency noise; the noise vibration load, that is considered, is generated only by the PGU that work at 50Hz. Tonal noise, or tonality, as a component of environmental noise can be an important factor in the annoyance of people listening to that noise. Environmental noise with audible tonal components generally results in higher levels of annoyance than broadband noise at a similar level.

3. NUMERICAL MODELING

Shelter structure can be considered as a complex structure. Due to this fact, modelling the structure accordingly to the actual structure might be difficult. Therefore, major simplification in modelling the structure was carried out when constructing the finite element model of the shelter system. Most of joints, iso-corners and door were all neglected during the model. The Shelter structure is composed by aluminium truss and aluminium sandwich panels with thermal acoustic insulation foam inside.

4. MODAL ANALYSIS

The numerical modal analysis was performed on the both structural and acoustic parts separately and at least it was performed also on the full model considering the fluid-structure interaction.
As shown below the main normal modes all fall within a range of 50Hz, therefore a strong fluid structure will be achieved.

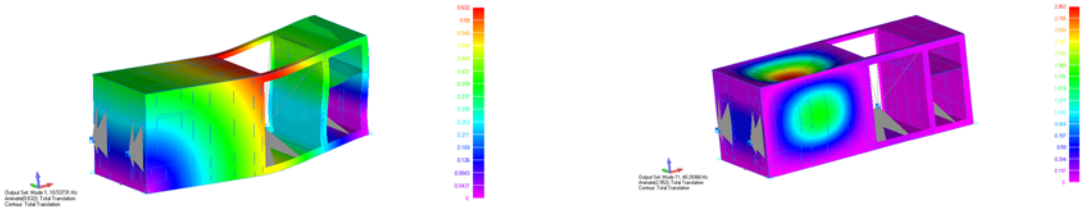

(a) (b)

Figure 1 Main structural normal modes: (a):10,5Hz; (b):48,3Hz

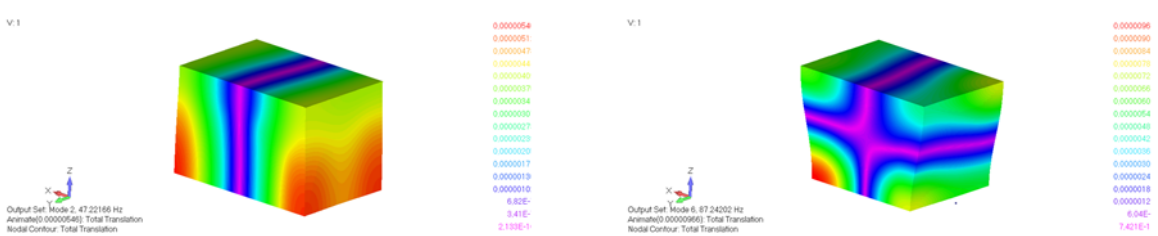

(a) (b)

Figure 2 Main acoustic normal modes: (a):47,2Hz; (b) 87,2Hz

5. EXPERIMENTAL TESTING

5.1 Vibrational and Operating deflection shape

An operating deflection shape (ODS) is defined as any forced motion of two or more points on a structure. Specifying the motion of two or more points defines a shape. Stated differently, a shape is the motion of one point relative to all others. Motion is a vector quantity, which means that it has both a location and a direction associated with it. Motion at a point in a direction is also called a Degree of Freedom, or DOF.
This technique has been performed so as to simplify the setting setup of the boundary condition, in fact it was used the operative configuration; an accelerometer has been positioned on the power units (Master accelerometer) and other satellites accelerometer (Slave) has been positioned in a lattice position on structure as shown in the following figure.

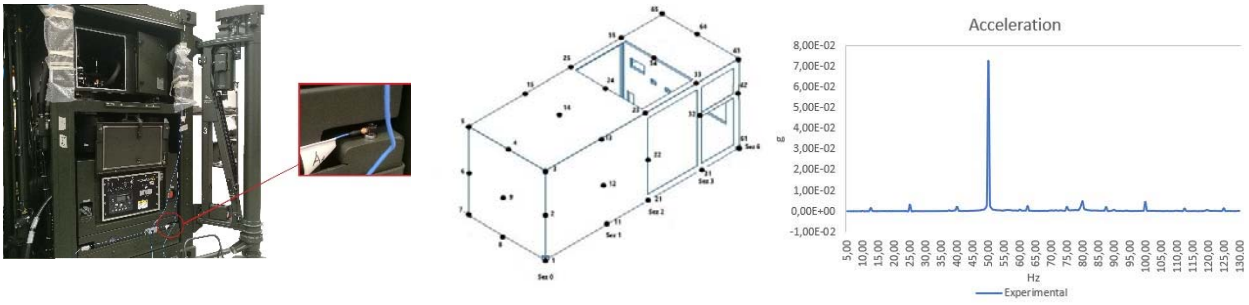

Figure 3 Accelerometers disposition (a); Acquisition maesh (b) ; vibration spectra (c)

Experimental tests show that the noise source is mainly tonal at 50hz which is the regime where the power unit works.

5.2 SPL - Sound pressure level

At the same time the sound pressure level inside the shelter was measured while the current generator was switched on. The measurement was carried out thanks to the use of two microphones placed inside the passenger compartment; as shown in figure 8 (b) also in this case the vibro-acoustic noise is mainly tonal at 50Hz.

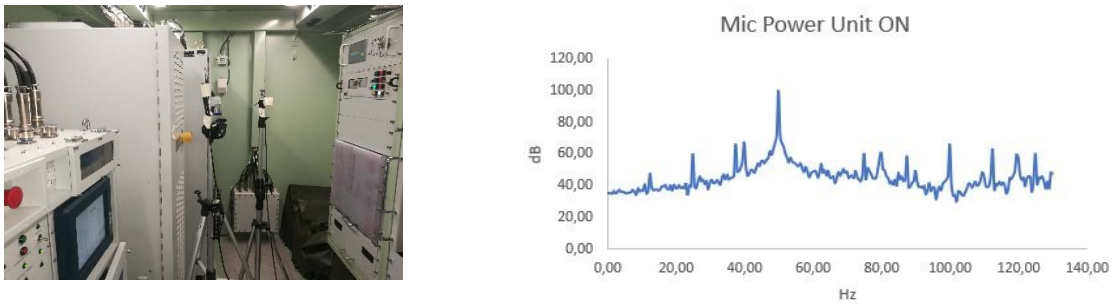

Figure 4 Sound pressure level: (a): Test setup; (b): SPL (dB)

6. NUMERICAL FREQUENCY RESPONSE

To validate both the structure and the acoustic volume it is necessary to carry out a numerical frequency response analysis on the whole model, with which it could be possible to make the comparison with the ODS.

6.1 Load calibration

The force calibration was performed through an iterative process, where at first a unitary force was placed in the PGU's centre of mass and then thanks to the accelerometric acquisition it was possible to calibrate that force.
After the forcing calibration it was possible to make a cross correlation between all the experimental and numerical acquisitions. Where necessary the following validation process was used to achieve a good correlation with the actual structure.
Only some of the calibrated accelerometers are shown below, they show the experimental-numerical accelerometric trend.

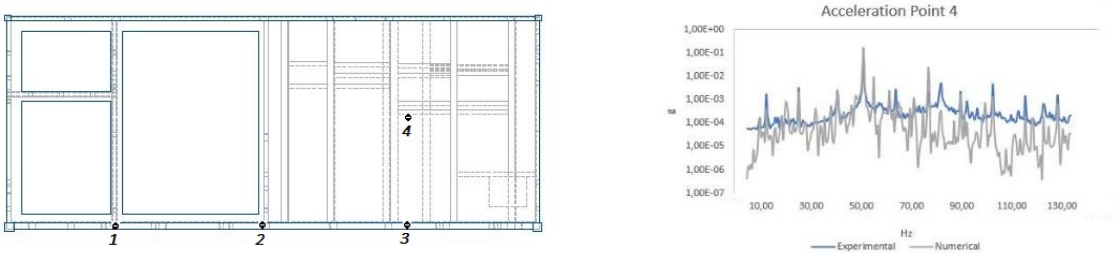

(a) (b)

Figure 1 Numerical and experimental frequency response correlation: (b): correlation in point 4.

At the same time, the numerical frequency response analysis provided information about the SPL inside the shelter; to validate the acoustic cavity, the numerical analysis was compared with the microphones acquisition placed inside the operating area.

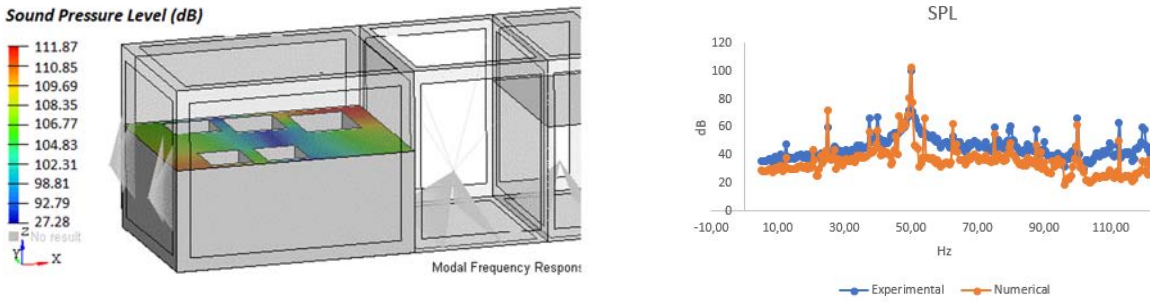

(a) (b)

Figure 2 Acoustic analysis - SPL: (a): acoustic noise on human ear level; (b): Numerical and experimental correlation of SPL

7. CONCLUSION

The present study concerned with the vibro-acoustic assessment of a shelter system based on numerical modelling and experimental data correlation. The result of this investigation showed that some discrepancies are unavoidable when constructing model for a complex structure such a shelter because of inaccuracies in parameters assumption and simplification in process of modelling; nevertheless these deviations can be fully accepted for the scope of the work. On these basis, optimization processes can be started in terms of acoustic comfort parameters inside the shelter.

REFERENCES

[1] Yong, J.S., Wang, D. Impact of noise on hearing in the military. Military Med Res 2, 6 (2015) doi:10.1186/s40779-015-0034-5

FLUTTER ANALYSIS OF A LARGE CIVIL AIRPLANE EQUIPPED WITH MORPHING WING FLAPS

Rosario Pecora*, Maria Chiara Noviello

Smart Structures Unit, Industrial Engineering Department
University of Naples "Federico II", Naples, Italy
*Email: rosario.pecora@unina.it

ABSTRACT

Mechanical systems based on structural components in relative motion represent a mature technology to efficiently enable wing-camber morphing for large civil airplanes.
On the other hand, the use of multiple hinged connections imposes a careful analysis of the effects induced at aircraft level by any degradation of their mechanical performance, overall system malfunction or local failures. This is even more relevant in case the addressed mechanical system is conceived to enable load control and alleviation functionalities. In the framework of the CleanSky2, a research program in aeronautics among the largest ever founded by the European Union, a camber-morphing flap specifically tailored for EASA CS-25 category aircraft has been investigated. The shape transition is obtained through a smart architecture based on segmented (finger-like) ribs with embedded electromechanical actuators. Three tabs were located at the flap trailing edge to actively control the shape of the wing in cruise and to enhance the aerodynamic efficiency by effectively redistributing the loads along the span. Aeroelastic phenomena related to these flap components were duly addressed since the very preliminary design stage to prevent the maturation of a potentially unstable architecture; rational approaches compliant with applicable airworthiness requirements were implemented -and herein presented- to model and analyze the influence of the flap tabs on the aeroelastic behavior of the aircraft both in nominal working conditions of the embedded tab mechanisms and in case of malfunction or failure.

Keywords: morphing structures, morphing flap, finger-like ribs, mechanical systems, aeroelasticity, large aeroplanes, industrial standards, airworthiness requirements, free-plays, failures

1 INTRODUCTION

In the framework of the CleanSky2, the largest funded project on aeronautics currently running in Europe, several researches are carried out to improve the efficiency of the next generation regional aircraft through a rational implementation of conventional and emerging technologies. Among the emerging technologies, an innovative morphing flap has been deeply investigated ([1]) and is expected to reach a maturity level (TRL) of 6 out of 9 thanks to experimental validation campaigns to be carried out on true scale ground demonstrators and large scale (1:3) wind tunnel models.

The flap is characterized by three different morphing modes which are activated according to the specific flight condition of the aircraft ([2]):

Morphing mode 1, flap deployed: the camber of the entire flap airfoil is morphed to improve high lift aircraft performances during take-off and landing phases.

Morphing mode 2, flap stowed: the last portion of the flap (nearly the 10% of its local chord) is exposed to the airflow when the flap is stowed in the wing. This portion can be moved upwards and downwards during high speed operations (max upwards/downwards deflection: 10°) to rationally distribute the aerodynamic loads along the wing thus increasing its aerodynamic efficiency.

Morphing mode 3, flap stowed: to enable also load alleviation functionalities, the last portion of the flap, exposed to the airflow in stowed configuration, can be twisted to smartly affect the equivalent twist angle distribution along the wing. The twist is obtained through the differential deflection of three tabs located on the trailing edge of the flap while, during morphing mode 2, the three tabs are deflected synchronously.

In force of the multi-zone and multi-modal morphing functionalities to be enabled, an adaptive architecture based on mechanical systems was considered as an effective solution to implement selective motion of subcomponents: the flap was conceived as a multi-box arrangement characterized by articulated finger-like ribs (Figure 1, [2]) properly connected to a smart system by means of actuation lines driving the ribs' shape change according to the desired morphing modes.

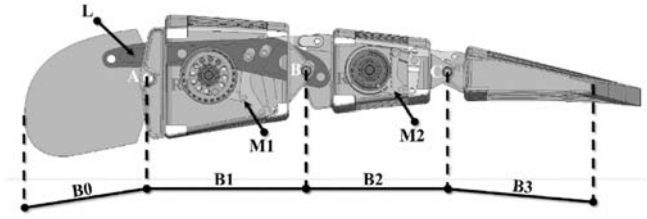

Figure 1. Finger like rib and inner mechanism, [2]

The articulated rib is composed by four consecutive blocks (B0, B1, B2, B3) connected to each other by means of cylindrical hinges (A, B, C) located on the airfoil camber line.

A linking beam element (L) – hinged on not Adjacent blocks B0 and B2 – forces the camber line segments to rotate according to specific gear ratios. The inner leverage (M1), hosted by rib block (B1), connects blocks B1 and B2 and amplifies the torque provided by an external rotary actuator the shaft (R1). A secondary leverage (M2), hosted by rib block (B2), links B3 (flap tab rib) to B2 and is driven by the rotation of the actuator acting around the shaft R2. Therefore, this inner mechanism (M2) makes rib block B3 to rotate around the hinge C thus enabling the tab-like motion required by morphing modes 2 and 3. Six actuators arranged along six separate transmission lines drive the motion of the entire flap according to the mechanics described for the single rib (Figure 3).

All the actuators are activated to implement morphing mode 1; during morphing mode 2 and 3, just the rear line of actuators is activated and is responsible for the deflection of the three tabs.

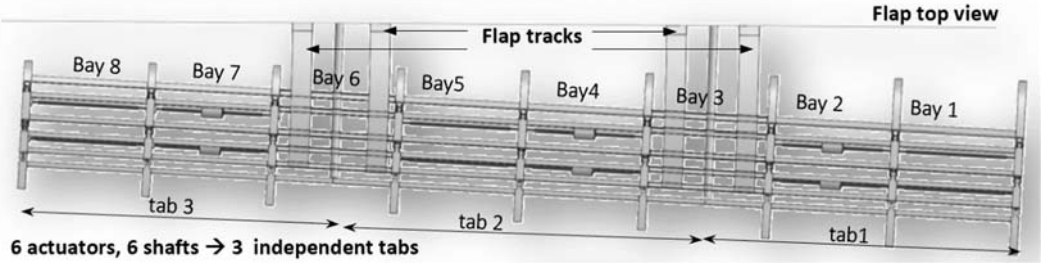

Figure 2. Flap top view, [2]

2 AEROELASTIC MODEL

A suitable aeroelastic model of a reference regional aircraft equipped with the six unconventional tabs (three per each wing side) was realized and aeroelastic stability analyses by means of theoretical modes association were performed both in nominal conditions and in case of failures or malfunction (free-plays) of tabs' control lines. The dynamic model of the entire aircraft was generated by referring to an equivalent beam representation of the lifting surfaces, fuselage and control surfaces ([3]). The elasticity of the joints between macro-structural elements (wing and fuselage, empennages and fuselage) was simulated by means of stiffness matrices reduced at significant grids of the interface regions. All control surfaces (elevator, rudder and aileron) were modelled as locked, or in other terms, constrained with respect to the rotation around their hinge axis.

Flap tabs rotations around their hinge axis was instead allowed and considered counteracted by a torsion spring accounting for the stiffness provided by the tab control mechanism (K_{cm}, Figure 4).

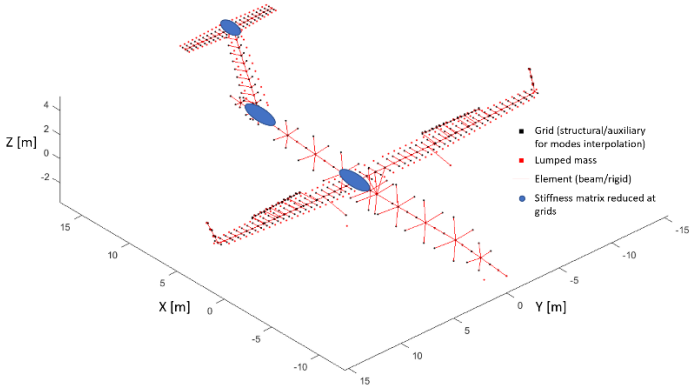

Figure 3. Aircraft dynamic model, [2]

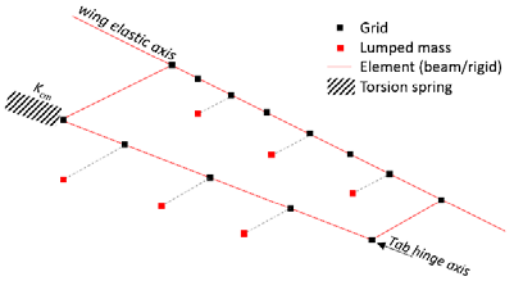

Figure 4. Flap tab dynamic model, [2]

The stiffness of the tab control mechanism was evaluated by means of a FE-based static analysis. In order to effectively implement the double lattice method for the evaluation of the unsteady aerodynamic influence coefficients ([3]), a 3D flat panels model of the entire aircraft was generated. The model consisted of 20 macro-panels further meshed into elementary boxes; interference panels were added to account for the aerodynamic influence of the fuselage. The interpolation of modal displacements along the centers of the aerodynamic boxes, was obtained by means of surface spline functions attached to structural (or auxiliary) grids of the dynamic model.

The in-house developed code, SANDY3.0 by M. and R. Pecora ([2]), was used to estimate the critical flutter speed of the reference aircraft. Dynamic instabilities were evaluated by referring to PK-English method [3] under the following general assumptions:

- Association of the theoretical elastic modes up to 50 Hz; natural frequencies and shapes evaluated by means of Lanczos method ([3]) applied to the dynamic model described in the previous paragraph; modal damping conservatively set to 1% for all the elastic modes;
- all control surfaces locked; sea-level flight altitude,
- flight speed range: [0:1.15VD] ([0:280m/s], certification envelope according to [4]).

3 FLUTTER ANALYSIS AND CONCLUDING REMARKS

In correspondence of the nominal value of the stiffness, K_{cm}, provided by the control mechanisms against the rotation of the tabs around their hinge axes (965.8 Nm/rad, [2]), and considering all tabs unbalanced, no flutter was detected in the flight speed investigation range (Figure 5). On the other hand, a bell-shaped damping trend of curve 33 (mode 27) was evident, with a very small residual damping (< 0.5%) at nearly 200 m/s.

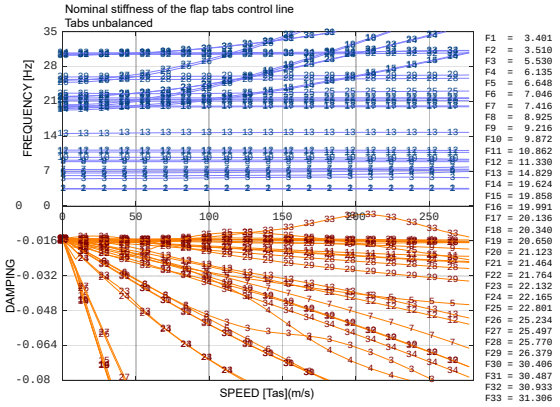

Figure 5. VG plot, nominal stiffness of tabs control lines

The bell-shaped damping trend was found to be essentially due to the unbalanced motion of the tabs that induces a weak coalescence of tabs harmonics and wing bending modes at high frequencies (>20 Hz). Although no flutter was found in the flight certification envelope, it was considered anyway necessary to add enough mass-balance to the tabs so to increase the damping of mode 27 at V_D and in nominal conditions, as well as to avoid critical instabilities in case of control mechanism failure.

Being the failures of movables control mechanisms the most critical events from the flutter standpoint, the minimum safe mass-balancing of the tabs was determined in correspondence of K_{cm} = 0 Nm/rad for all tabs. If Kcm=0 then all the tabs are free to rigidly rotate and, as shown in Figure 6, the coalescences of tabs harmonics with wing bending mode is anticipated with respect to the nominal case, thus leading to several flutters at low speeds (flutter of curves 21 and 27).

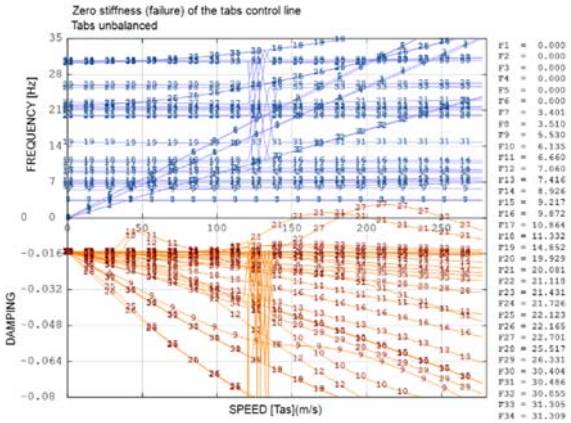

Figure 6. VG plot, zero stiffness of tabs control lines

Starting from the unbalanced configuration, flutter analyses were repeated at increasing levels of tabs' mass balancing in order to find the minimum value of massbalancing assuring the clearance from flutter in case of control mechanisms failures. In correspondence of a degree of massbalancing equal to 50%, no flutter occurred up to 1.5 V_D. The nominal mass-balancing of each tab was then set to this value and a new analysis proving the persistence of the flutter clearance was carried out in correspondence of the nominal stiffness of tabs' control line; a wider damping margin with respect to those of Figure 5 was obtained. The efficacy of the massbalancing was finally proved also in case of free-plays due to malfunctioning of the control mechanisms. Free-plays were treated as a degradation of the nominal stiffness (K_{cm}) provided by the control mechanisms against the rotation of the tabs around their hinge axis. Four different values of free-plays amplitude (δ) were considered; in correspondence of each free-play, the maximum amplitude for the tab oscillation (A) was set equal to $\delta+\delta_e$, being δ_e the elastic rotation of the tab under the maximum operative loads and in correspondence of the nominal value of control mechanisms stiffness (evaluated by FEM). For each δ, and A, an equivalent (reduced) stiffness was evaluated by means of the harmonic balance method and used in place of K_{cm} to run flutter analyses. For each case of Table 1, no flutter was detected; the bell-shape trend of mode 27 is characterized by a residual damping at V_D that decreases (in module) while the f.play increases; the obtained residual damping is anyway adequate to assure adequate margins of safety with respect to the onset of flutter at V_D, thus proving the robustness of the tabs' massbalancing.

Free-play (±δ°)	Residual modal damping at V_D (mode 27)
± 1°	-2.26E-02
± 3°	-2.14E-02
± 5°	-2.06E-02
± 7°	-2.01E-02 (worst case)

Table 1. Free-plays and residual damping of the flutter mode

4 REFERENCES

[1] Pecora, R. et al., "Multi-parametric flutter analysis of a morphing wing trailing edge", Aero. Journal, Vol. 118, Issue 1207, 2014
[2] Pecora, R. et al., "Flutter analysis of a large civil aircraft in case of free-plays and internal failures of morphing wing flaps mechanical systems", Proc. of SPIE Smart Structures and NDE Conf., Denver (CO), USA, 2019
[3] Broadbent, E. G., Flutter and Response Calculations in Practice, AGARD Manual on Aeroelasticity, Vol. 3, NASA, February 1963
[4] EASA, "CS-25, Certification specifications and acceptable means of compliance for large aeroplanes", Amendment 11, July 2011

Multimodal control of interior random sound pressure using optimized tuned mass dampers

E. Mrabet[1,2], M. Ichchou[3] and N. Bouhaddi[4]

[1]Laboratoire de Mécanique, Modélisation et Productique (ENIS)
University of Sfax, Sfax, TUNISIA
[2]ISSAT Kasserine, University of Kairouan, TUNISIA
Email: elyes.mrabet@isetkr.rnu.tn

[3]LTDS UMR5513 Ecole Centrale de Lyon
Université de Lyon, Ecully, France
Email: mohamed.ichchou@ec-lyon.fr

[4] FEMTO-ST Institute, CNRS/UFC/ENSMM/UTBM, Department of Applied Mechanics
University of Bourgogne Franche-Comté, BESANÇON, France
Email: noureddine.bouhaddi@univ-fcomte.fr

ABSTRACT

The present work deals with a vibro-acoustic system presenting several resonant modes and a multimodal control of the interior random sound is achieved, in the low frequency range, using Tuned Mass Dampers (TMDs). The system is composed by a randomly driven vibrating plate weakly coupled to a rectangular cavity filled with air. By making use of a stochastic acoustic optimization strategy, a multi-objective optimization of the TMDs parameters is performed and a set of optimal solutions are obtained. To help the designer decision-making, the self organizing maps (SOM) have been used and "the best" solution showed good performance of the multimodal control.

1 INTRODUCTION

The control of the interior sound, achieved in the low frequency range, has been for long considered by several research works. Indeed, reducing the interior sound is of major importance for several industrial sectors like the automotive one, where the comfort of passengers is primordial, and the aerospace where the safety of the payload bays of launchers should be improved [1].

Depending on the specificities of the considered problem several techniques can be used to achieve the interior sound control [2]. In the present work, a randomly driven vibrating plate weakly coupled to a rectangular cavity filled with air is considered and the passive control, using optimized TMDs, is adopted. Assuming linear behavior, a stochastic acoustic multi-objective optimization is performed and a set of optimal solutions is obtained. To help the designer making-decision, the SOM are used and the "best" solution showed good global performance.

2 GOVERNING EQUATIONS AND MULTIMODAL CONTROL

Consider the vibro-acoustic system equipped with TMDs as shown in Figure 1. Let *Na* and *Ns* be the number of modes considered for the plate and the acoustic cavity, respectively. In addition, let *N* be the number of the deployed TMDs, the modal coupling approach can be applied and the governing equations of the system are

$$\mathbf{M}\ddot{\mathbf{q}} + \mathbf{D}\dot{\mathbf{q}} + \mathbf{K}\mathbf{q} = \mathbf{\Phi}^{\mathrm{T}} F_z \tag{1}$$

where $\ddot{\mathbf{q}}$ and $\dot{\mathbf{q}}$ are the time derivatives of $\mathbf{q} = (\mathbf{w}^{\mathrm{T}}, \mathbf{p}^{\mathrm{T}}, \mathbf{z}_T)^{\mathrm{T}}$; $\mathbf{w}$ is the $(Ns \times 1)$ vector of the plate modal participation factor, $\mathbf{p}$ is the $(Na \times 1)$ vector of the acoustic modal participation factor and $\mathbf{z}_T$ is the $(1 \times N)$ displacement vector of the TMD devices; $\mathbf{\Phi} = (\boldsymbol{\varphi}_F \quad \boldsymbol{\psi}_0 \quad 0)$ where $\boldsymbol{\varphi}_F$ is the $(1 \times Ns)$ vector of the plate mode shapes computed at force location $\mathbf{r}_F = (x_F, y_F)^{\mathrm{T}}$ and $\boldsymbol{\psi}_0$ is a $(1 \times Na)$ vector of zeros; F_z is a stationary zero mean Gaussian white noise point force. Furthermore, let Λ_m and ω_m be the modal mass and the corresponding *in-vacuo* natural frequency of the plate, respectively, and let Λ_n, ω_n be those of the cavity (rigid-walled), respectively; m_{T_j}, c_{T_j} and k_{T_j} (j=1,..,N) are the mass, the damping coefficient and the stiffness of a TMD, respectively. The matrices defined in Equation (1) are

$$\mathbf{M} = \begin{bmatrix} \mathbf{\Lambda}_m & \mathbf{0} & \mathbf{0} \\ S\mathbf{C}_{nm} & \dfrac{1}{\rho_0 c_0^2}\mathbf{\Lambda}_n & \mathbf{0} \\ \mathbf{0} & \mathbf{0} & \mathbf{m}_T \end{bmatrix}, \mathbf{\Lambda}_m = \begin{bmatrix} \mathrm{O} & & \\ & \Lambda_m & \\ & & \mathrm{O} \end{bmatrix}, \mathbf{\Lambda}_n = \begin{bmatrix} \mathrm{O} & & \\ & \Lambda_n & \\ & & \mathrm{O} \end{bmatrix}; \mathbf{m}_T = \begin{bmatrix} m_{T_1} & & \\ & \mathrm{O} & \\ & & m_{T_N} \end{bmatrix};$$

$$\mathbf{D} = \begin{bmatrix} \mathbf{D}_m + \mathbf{\Phi}_c^{\mathrm{T}}\mathbf{C}_T\mathbf{\Phi}_c & \mathbf{0} & -\mathbf{\Phi}_c^{\mathrm{T}}\mathbf{C}_T \\ \mathbf{0} & \mathbf{D}_n & \mathbf{0} \\ -\mathbf{C}_T\mathbf{\Phi}_c & \mathbf{0} & \mathbf{C}_T \end{bmatrix}, \quad \mathbf{D}_m = \begin{bmatrix} \mathrm{O} & & \\ & 2\xi_m\omega_m\Lambda_m & \\ & & \mathrm{O} \end{bmatrix}, \quad \mathbf{D}_n = \frac{1}{\rho_0 c_0^2}\begin{bmatrix} \mathrm{O} & & \\ & 2\xi_n\omega_n\Lambda_n & \\ & & \mathrm{O} \end{bmatrix};$$

$$\mathbf{K} = \begin{bmatrix} \mathbf{K}_m + \mathbf{\Phi}_c^{\mathrm{T}}\mathbf{K}_T\mathbf{\Phi}_c & -S\mathbf{C}_{nm}^{\mathrm{T}} & -\mathbf{\Phi}_c^{\mathrm{T}}\mathbf{K}_T \\ \mathbf{0} & \mathbf{K}_n & \mathbf{0} \\ -\mathbf{K}_T\mathbf{\Phi}_c & \mathbf{0} & \mathbf{K}_T \end{bmatrix}, \quad \mathbf{K}_m = \begin{bmatrix} \mathrm{O} & & \\ & \omega_m^2\Lambda_m & \\ & & \mathrm{O} \end{bmatrix}, \quad \mathbf{K}_n = \frac{1}{\rho_0 c_0^2}\begin{bmatrix} \mathrm{O} & & \\ & \omega_n^2\Lambda_n & \\ & & \mathrm{O} \end{bmatrix},$$

$$\mathbf{\Phi}_c^{\mathrm{T}} = \left[\boldsymbol{\varphi}_{c_1}^{\mathrm{T}} \ldots \boldsymbol{\varphi}_{c_N}^{\mathrm{T}}\right], \ \mathbf{C}_T = \begin{bmatrix} c_{T_1} & & \\ & \mathrm{O} & \\ & & c_{T_N} \end{bmatrix}, \ \mathbf{K}_T = \begin{bmatrix} k_{T_1} & & \\ & \mathrm{O} & \\ & & k_{T_N} \end{bmatrix}, \text{ where } S = l_x \times l_y, \ \mathbf{C}_{nm} \text{ is the coupling}$$

matrix [3] and $\boldsymbol{\varphi}_{c_j}$ is the $(1 \times Ns)$ vector of the plate mode shapes calculated at a TMD location $\mathbf{r}_{c_j} = (x_{c_j}, y_{c_j})$; ξ_m and ξ_n are the damping ratios of the plate and the cavity, respectively. It should be noted that a proportional damping is assumed (in both plate and cavity) so that $\xi_i = \alpha/2\omega_i + \beta\omega_i/2$; α and β are two coefficients to be calculated by imposing a targeted damping value ξ_0 for the two frequencies bounds of the range of interest.

For the plate, the targeted damping ratio is set to 2% whereas it's set to 0.5% for the cavity.

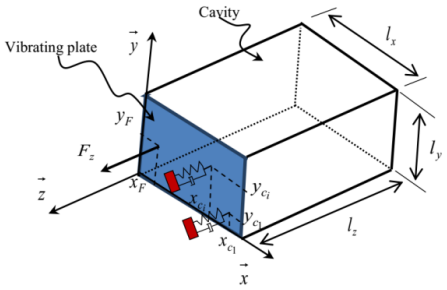

Figure 1. The vibro-acoustic system equipped with TMDs.

Once the governing equations are obtained, a spectral analysis can be made and the root mean square acoustic pressure, measured at a given microphone location $\mathbf{r}_a = (x, y, z)^{\mathrm{T}}$ into the cavity, can be obtained $\sigma_p(\mathbf{r}_a, \mathbf{r}_F) = \sqrt{\int_{\omega^l}^{\omega^u} S_{\tilde{p}\tilde{p}}(\mathbf{r}_a, \mathbf{r}_F, \omega) d\omega}$; ω^l and ω^u are the lower and upper bounds of a certain bandwidth of interest $\Delta f = [\omega^l, \omega^u]$ centred at a given resonant frequency ϖ. The power spectral density (PSD) of the acoustic pressure is $S_{\tilde{p}\tilde{p}}(\mathbf{r}_a, \mathbf{r}_F, \omega) = \left|H(\omega, \mathbf{r}_a, \mathbf{r}_F)\right|^2 S_{FF}$; $H(\omega, \mathbf{r}_a, \mathbf{r}_F)$ represents the acoustic pressure frequency response function and S_{FF} is the PSD of the excitation force.

The multimodal control of the vibro-acoustic system can be then performed by carrying out a multi-objective optimization defined as finding $\mathbf{d}_j = (\omega_{T_j}, \xi_{T_j}, \mu_j, \mathbf{r}_{c_j})^{\mathrm{T}}$ to minimize the vector

$$\boldsymbol{\sigma}_p(\mathbf{r}_a, \mathbf{r}_F, \mathbf{d}) = (\sigma_{p1}, \sigma_{p2}, ..., \sigma_{pN})^{\mathrm{T}} \quad \text{subject to} \quad \sum_{i=1}^{N} \mu_i \le \mu_{adm} \tag{2}$$

where $\mathbf{d} = (\mathbf{d}_1, ..., \mathbf{d}_N)^{\mathrm{T}}$; ω_{T_j}, ξ_{T_j} and $\mu_j = m_{T_j} / m_{\text{plate}}$ are the natural frequency, the damping ratio and the mass ratio of a given TMD, whereas μ_{adm} is an admissible mass ratio defined in a pre-design phase. It should be noted that the length of the vector $\boldsymbol{\sigma}_p$ depends on the number the resonant modes, to be controlled, and consequently on the number of TMDs (one TMD for each one of the resonant modes).

3 NUMERICAL EXAMPLE

In the present work $\mathbf{r}_a = (0.35,\ 0.1,\ -0.875)^{\mathrm{T}}$, $\mathbf{r}_F = (0.05,\ 0.05)^{\mathrm{T}}$ and $\mu_{adm} = 7\%$ .The parameter values of the vibro-acoustic system shown in Figure 1 are l_x=0.5m, l_y=0.5m, l_z=1.1m, h=3mm, E=7.1010Pa, ρ_s=2700kg.m^{-3}, ρ_0=1.21kg.m^{-3}, υ=0.3 and c_0= 344 m.s^{-1}. The number of modes are set Na=100, Ns=21 and $S_{FF} = 0.1$ N^2.Hz^{-1}. The frequency range of interest was [0- 400] Hz.

The modal analysis of the uncontrolled plate-cavity system arises five resonant modes therefore five TMDs should be used and one had to find 25 TMD parameters that should simultaneously minimize the five objective functions corresponding to the resonant modes. The multi-objective optimization has been performed using the genetic algorithm routine available in Matlab and 38 optimal solutions. To help the designer making-decision, the SOMs have been used (Figure 2 (a)) and four optimal solutions have been of particular interest (S26, S19, S16 and S14). Indeed, in view of the PSD responses, shown in Figure 2 (b), one can see that significant attenuations are achieved especially when the solution S26 is considered.

The optimal TMDs parameters corresponding to the solution S26 are ω_{T_1} =98.25 Hz, ξ_{T_1} =0.088; μ_1 =1.34%, $\mathbf{r}_{c_1}$ = (0.2; 0.15); ω_{T_2} =128.51Hz, ξ_{T_2} =0.11; μ_2 =1.32%, $\mathbf{r}_{c_2}$ = (0.19; 0.15); ω_{T_3} =282.97Hz, ξ_{T_3} =0. 22; μ_3 =2.92%, $\mathbf{r}_{c_3}$ = (0.31; 0.13); ω_{T_4} =311.47Hz, ξ_{T_4} =0.22; μ_4 =0.45%, $\mathbf{r}_{c_4}$ = (0.38; 0.11); ω_{T_5} =342.64Hz, ξ_{T_5} =0.005; μ_5 =0.87%, $\mathbf{r}_{c_5}$ = (0.05; 0.09). For the solution S26, a minimum reduction of 26.47 dB has been observed in the vicinity of the fourth resonant mode and it can be considered as the "best" one among the set of the optimal solutions.

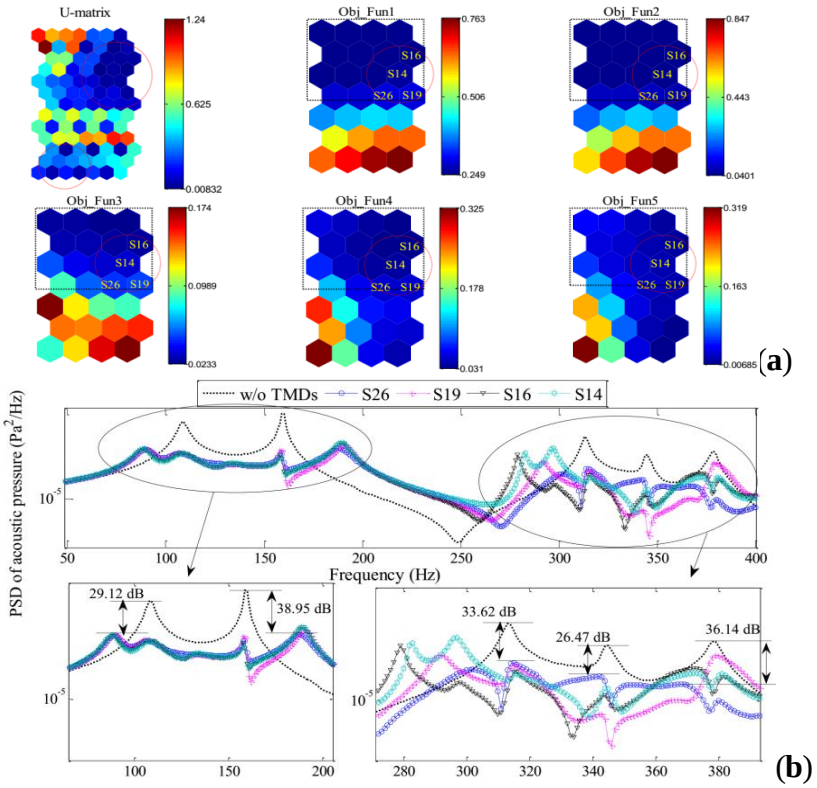

Figure 2. (**a**) The SOM; (**b**) The PSD responses

4 CONCLUDING REMARKS

In the present work a multimodal control of a vibro-acoustic system is achieved using optimized TMDs. By making use of a stochastic acoustic strategy, a multi-objective optimization of the TMDs parameters is performed and the control has been achieved using only five TMDs, corresponding to the five resonant modes of the uncontrolled system. The obtained solutions showed good performances of the TMDs and significant attenuations in PSD responses have been recorded.

REFERENCES

[1] C. Q. Howard, C. H. Hansen, and A. Zander. Vibro-acoustic noise control treatments for payload bays of launch vehicles: Discrete to fuzzy solutions. *Applied Acoustics*. 66: 1235-1261, 2005.

[2] E. Mrabet, M. N. Ichchou, and N. Bouhaddi. Random vibro-acoustic control of internal noise through optimized Tuned Mass Dampers. *Mechanical Systems and Signal Processing*. 130: 17-40, 2019.

[3] N. K. Jain and V. R. Sonti. Structural Acoustics of a Rectangular Panel Backed by a Cavity: An Analytical Matrix Approach. *Journal of Vibration and Acoustics*. 139: 031004-031004-8, 2017.

VIBRO-ACOUSTIC PERFORMANCE ANALYSIS OF A TURBOPROP INSULATION PACKAGE

Giuseppe Bizzarro[1], Massimo Viscardi[1], Valerio Maria Porpora[2], Giuliano Di Paola [2]

[1]Vibration, Acoustic & Smart Structure Lab. Università degli studi di Napoli Federico II
massimo.viscardi@unina.it , giuse.bizzarro@hotmail.it

[2]Protom SPA, Via Vicinale S.M. del Pianto – CPN, Ed. 6 80143 – Napoli
valerio.portpora@protom.com , giuliano.dipaola@protom.com

ABSTRACT

Control of interior noise levels in turboprop aircraft has been a significant research area over the last two decades. The reason is that, the turboprops, are more fuel efficient than jets on shorter, slower routes but present a strong potential for unacceptably high structure-borne noise levels in the aircraft fuselage. These high noise levels would require very efficient fuselage sidewall transmission loss at a propeller blade passage frequency in the range of 150 to 300 Hz. To meet these technical requirements in terms of internal noise reduction, the use of insulating materials between interior trim panels and the fuselage is required. The methodological process is based on a vibro-acoustical numerical Finite Element approach, to evaluate the Sound Pressure Level (SPL) at passenger ear level.
Based on the target of the study, different materials and possible stratifications have been experimentally studied in terms of acoustic properties and performances.

INTRODUCTION

These work was part of the European project CLEAN SKY2 S.P.A.I.N. (Smart Panel for SAT Aircraft Cabin Insulation). Project had the purpose to improve the acoustic for General Aviation Aircrafts by providing a performant, cost effective and lightweight cabin insulation system. The Topic manager of the project was the Czech aircraft manufacturer Evektor, while the companies involved in the project where Protom, with rules of project Coordinator and system design and TI&A, partner for the construction and installation of the insulation system on a demonstrator (EV-55 aircraft). Unina has supervised the numerical modelling and the experimental test on laboratory coupon and samples.

The main project innovation was a new mounting configuration which provide the insulation blanket linked to the Cabin lining panels instead of the primary fuselage structure (skin) and allows faster access to wiring and an easier replacement of the blankets.

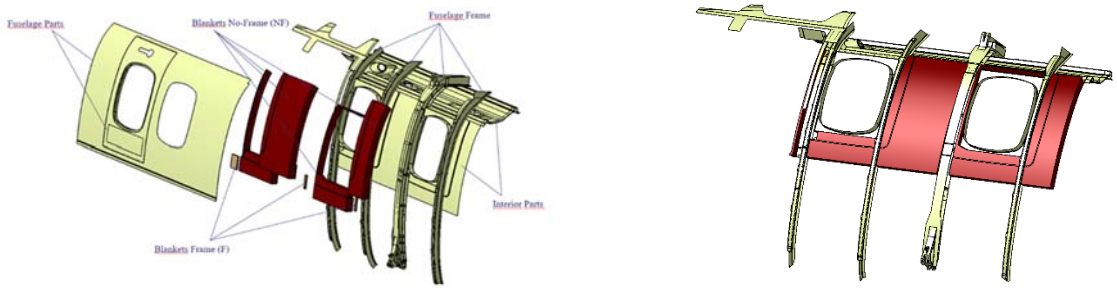

(a) (b)

Figure 1: (a) New Mounting Configuration; (b) Analysed Panel and Available Acoustic Cavity

Different blanket's configuration have been considered in terms of different insulation materials stratification in relation to critical frequencies, external pressure and maximum acoustic cavity located in different aircraft areas and define the insulation system optimization without losing sight, the acoustic and total weight requirements.
To achieve this aim, a methodological process has been used, based on a numerical Vibro-acoustic Finite Element approach, to evaluate the Sound Pressure Level (SPL) at passenger ear level.

TURBOPROP INTERIOR NOISE INVESTIGATION

Generally speaking, an aircraft is affected by several noise sources; the noise level and spectrum depending on the aircraft configuration, the engine power unit, the broadband excitations related to the turbulent boundary layer, propulsion system and flight phase.
Results of preliminary noise and vibration measurements are presented here. These measurements were realized by EVEKTOR on the EV-55 airplane without interior panel during flight test FL100 RPM 2200 (Cruise condition); microphones were step by step located in 3 points (mark of points = UZL). A B&K 2238 analyser was used for the measurement.

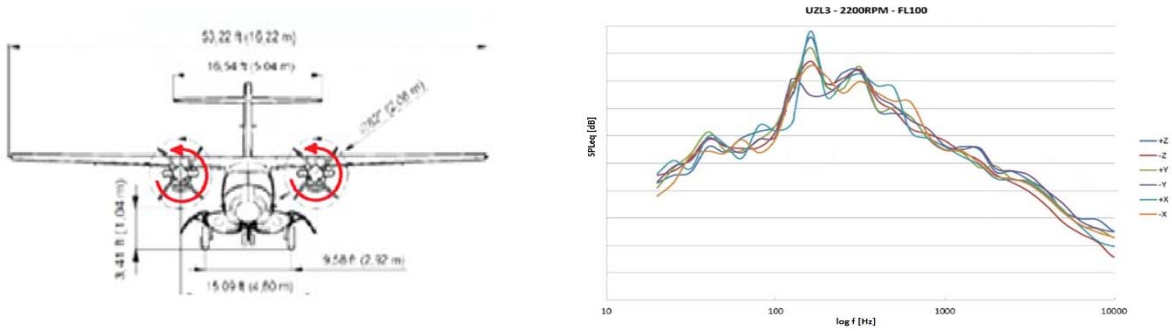

Figure 2 (a) In flight SPL at UZL2 ;(b) In flight SPL at UZL3

FUSELAGE FEM ANALYSIS AND EXPERIMENTAL COMPARISON

Modeling approach

FEM based structural and acoustical analyses have been assessed and the SPL response has been compared with the in-flight measurement to validate the model.
Once verified under the initial conditions, a subsequent forecast of the internal fuselage noise with different deck configurations has been performed.

Figure 3 (a) Fuselage CAD model; (b) Fuselage FEM model

Mesh has been realized on the basis of the fuselage CAD supplied by Evektor. The model, has been initially simplified ; all stringers have been made with 1D elements (BEAM), whit same section of the CAD model and the spars modelled with 2D element (spar web) and 1D element (spar caps).

Modal analysis

To identify the structural and acoustical resonant frequencies a modal analysis has been made to evaluate contribution at the interior noise of both.
In the acoustic characterization, the acoustic cavity has been modelling with PFluid hexa-element and the air property in FL100 condition, has been considered.
Particular attention has been given to the identification of the "coincident" resonance frequencies whose excitation would cause intensive energy exchanges between fluid and structure. An example of structural and acoustic modes have been reported:

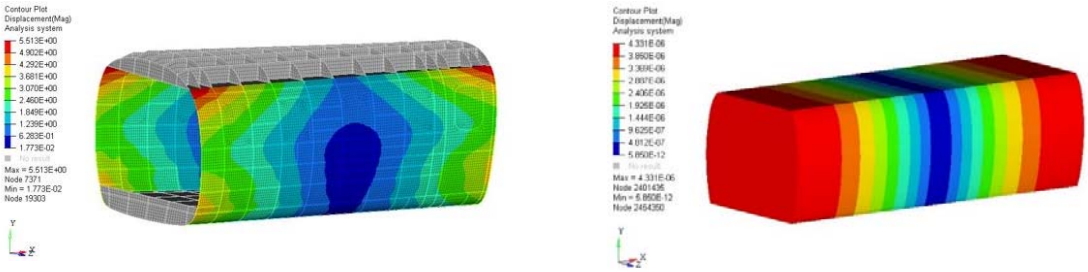

Figure 4 (a)Structural Modal Shapes at 36.85Hz and (b) Acoustic Modal Shapes at 36.41Hz

Pressure fields modeling

To estimate the aerodynamic load caused by the passage of the blade, the sound pressure level in operational flight has been analysed in a reverse engineering approach; consequently, the equivalent pressure distribution on the outside of the fuselage was calculated.
This was achieved by setting the SPL on the UZL2 microphone and verifying the numerical correspondence with the reading of the UZL3 microphone.

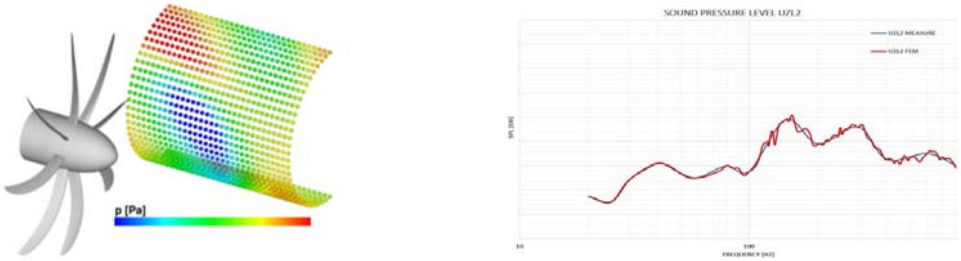

Figure 5 (a) Evektor Co-rotating Propeller; (b) Generic Pressure Distribution Acting on Fuselage

PRELIMINARY INSULATION SYSTEM EXPERIMENTAL ANALYSIS

Different insulation materials have been analysed and compared to define the best blanket stratification opting for materials already certified in the aeronautical field (CS23 / FAR23) and using as a benchmark, the weight to cost and performance ratio.
Blankets have been designed in relation to the available acoustic cavity (considering structural frames and cabin wiring) and external pressure acting on the fuselage.
The parameters of absorption, transmission loss and impedance has been measured, for all the package, with a kundt tube.
The preliminary insulation blankets configuration has then been realized, setting on the interior panel and the full system has been analysed in the operative mounting.

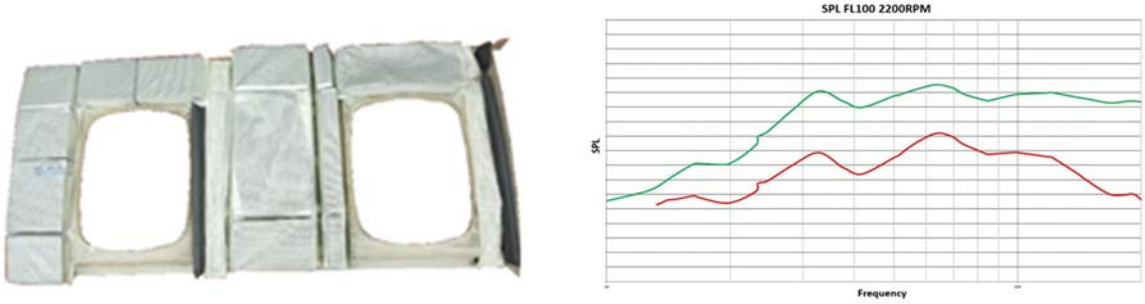

Figure 6 (a) Preliminary configuration *(b)* Experimental Noise Reduction

PREDICTED FUSELAGE NOISE REDUCTION

After the preliminary insulation package experimental measurements, the value of the impedance for the interior system (whit all designed stratification and considering the interior trim panel) has been determined with the Kundt tube.
This value has been employed in FEM model whit the use of Frequency-Dependent Acoustic Absorber Element (CAABSF) and the SPL on the passenger ear level in the worst frequencies of interest has been determined:

CONCLUSION

In the contest of the SPAIN project, an innovative thermo-acoustic blanket configuration has been studied and assessed. The availability of a FE predictive model made possible to study different blanket configurations, forecasting the overall performance at aircraft level, also based on the knowledge of experimental acoustic impedance of the multi-layered configurations at coupon level. The designed configuration seemed to fulfil the design technical requirements; in flight test have been planned as a further step.

ACHIEVEMENT

This work has been funded under H2020 Clean Sky 2 program Grant Agreement n. 714486

REFERENCES

[1] M. Klaerner, S. Marburg, L. Kroll, “FE based measures for structure borne sound radiation,” 43rd International Congress on Noise Control Engineering, November 16-19, 2014.

[2] Viscardi M, Arena M, Siano D. Vibro-acoustic response of a turboprop cabin with innovative sidewall viscoelastic treatment in “Proceedings of 24th International Congress on Sound and Vibration, ICVS24”. London, UK, 2017.

[3] Official Evektor company webpage: https://www.evektor.cz/en/ev-55-outback

DYNAMIC PROPERTIES OF METAMATERIALS WITH DIFFERENT RESONATOR CONNECTION METHODS

Han Meng[1*] and Dimitrios Chronopoulos[1]

[1] Institute for Aerospace Technology & The Composites Group
University of Nottingham, Nottingham, UK
Email: han.meng@nottingham.ac.uk,

ABSTRACT

This paper investigates the influences of resonator connection methods on the dynamic properties of the elastic metamaterials. A large number of metamaterials with multiple resonators were developed for the purpose of generating multiple bandgaps or broadening the bandwidth. The multiple resonators in a unit cell could be connected end to end in a line, i.e. in series connection, or connected individually to the substrate, i.e. in parallel connection. Resonators connection methods caused considerable differences to the dynamic properties of the metamaterials, it would hence be meaningful to investigate in depth the influences of connection methods, which could offer theoretical basis and foundation for the design of metamaterials with multiple resonators. An analytical model is first built to calculate the dynamic properties of metamaterial beams with periodical single/in-series/in-parallel resonators respectively. After that, comparisons are made among the calculated frequency response functions of metamaterial beams with resonators of the same mass but different connections methods. It is found that in-series resonators could lead to lower frequency bandgaps, nonetheless, their bandwidth cannot exceed that by single resonators. On the contrary, in-parallel resonators can results in bandgaps at higher frequencies with enlarged bandwidth compared with single resonators. Moreover, the beam with single resonators has the deepest bandgaps than those with multiple resonators.

1 ANALYTICAL MODEL OF METAMATERIAL BEAMS

As shown in the Figs. 1(a)-(c), the metamaterial beams are composed of beams with periodically attached single, in-series and in-parallel resonators.

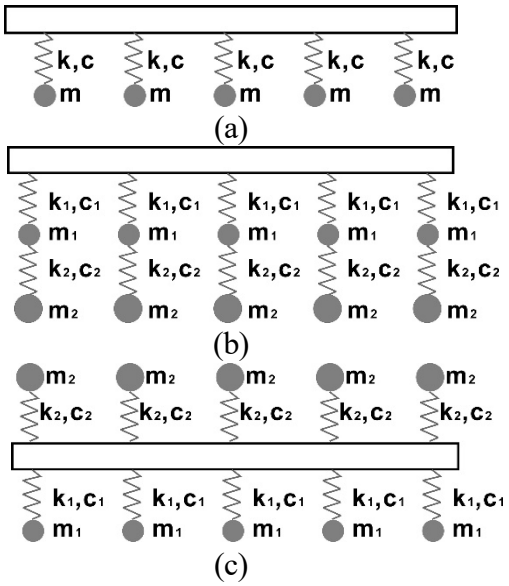

Figure 1. Illustration of metamaterial beams with different resonator connection methods, (a) single resonator, (b) resonators connected in series, (c) resonators connected in parallel

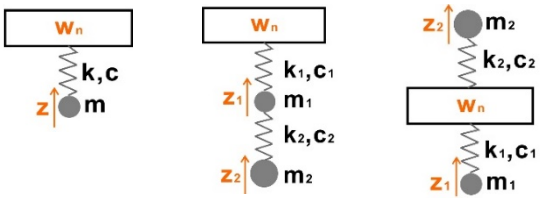

Figure 2. Unit cell of metamaterial beams with (a) single resonator, (b) resonators connected in series, (c) resonators connected in parallel

Unit cells of the three beams are shown in Fig. 2(a)-(c). The displacements of the beam before and after the attached resonator are related by,

$$\begin{aligned} w_{n,l}\big|_{x=x_r} &= w_{n,r}\big|_{x=x_r} \\ w'_{n,l}\big|_{x=x_r} &= w'_{n,r}\big|_{x=x_r} \\ w''_{n,l}\big|_{x=x_r} &= w''_{n,r}\big|_{x=x_r} \\ EI_z\, w'''_{n,l}\big|_{x=x_r} + F_r &= EI_z\, w'''_{n,r}\big|_{x=x_r} \end{aligned} \quad , \tag{1}$$

where E and I_z are the Young's modulus and the second moment of area of the beam. x_r is the location of the resonator on the beam, $w_{n,l}$ and $w_{n,r}$ are the displacements of beam before and after the attached resonators. F_r is the interaction force between the resonator and the beam. For beam with single resonators, in-series and in parallel resonators, the interaction force should be

$$F_r = \begin{cases} \dfrac{\omega^2 ms}{-\omega^2 m + s} w_n & \text{single resonator} \\ \left(\dfrac{s_1^2}{s_1 + s_2 - m_1\omega^2 - s_2^2 / \left(-m_2\omega^2 + s_2\right)} - s_1 \right) w_n & \text{in-series resonator} \\ \left(\dfrac{\omega^2 m_1 s_1}{-\omega^2 m_1 + s_1} + \dfrac{\omega^2 m_2 s_2}{-\omega^2 m_2 + s_2} \right) w_n & \text{in-parallel resonator} \end{cases} , \tag{2}$$

where $s = k + \mathrm{i}\omega c$, $s_1 = k_1 + \mathrm{i}\omega c_1$ and $s_2 = k_2 + \mathrm{i}\omega c_2$. m , k , c are the mass, stiffness and damping ratio of the single resonator. m_1 and m_2 , k_1 and k_2 , c_1 and c_2 are the masses, stiffnesses and damping ratios of the dual resonators. ω denotes the angular frequency. w_n is the displacement of the beam at the connecting point.

The receptance functions of the beam is given as,

$$R_{ec} = 20\log_{10}\left|\frac{w_L}{F}\right| , \tag{3}$$

where is the F is the excitation force on the beam, and w_L is displacement at one end of the beam.

2 NUMERICAL STUDY

Receptance functions of beams with different resonator connection methods are compared in Fig. 3. The three beams are of the same mass and length. The total masses of resonators are 30% of that of the three substrate beams. It can be seen from Fig. 3 that the beams with various resonator connection methods could result in different resonance frequencies, bandwidths and receptance reductions within the bandgap regions.

The beams with dual resonators have two bandgaps in the considered frequency range. The two bandgaps of the metamaterial beam with in-series resonators are separated, and the second bandgap is less obvious regarding the bandwidth and receptance reduction than that of the first bandgap. As a contrary, the beam with in parallel resonators has two bandgaps generated by each oscillator. The two bandgaps could be integrated to a single wide bandgap with close resonance frequencies [1-3].

In addition, the first bandgap of the beam with in series resonators occurs at lowest frequencies, but its bandwidth and receptance reduction in the bandgap region are smaller than that of the beam with single resonators. On the contrary, the beam with resonators connected in parallel has bigger resonance frequencies, which leads to enlarged bandwidth and less receptance reduction as a result.

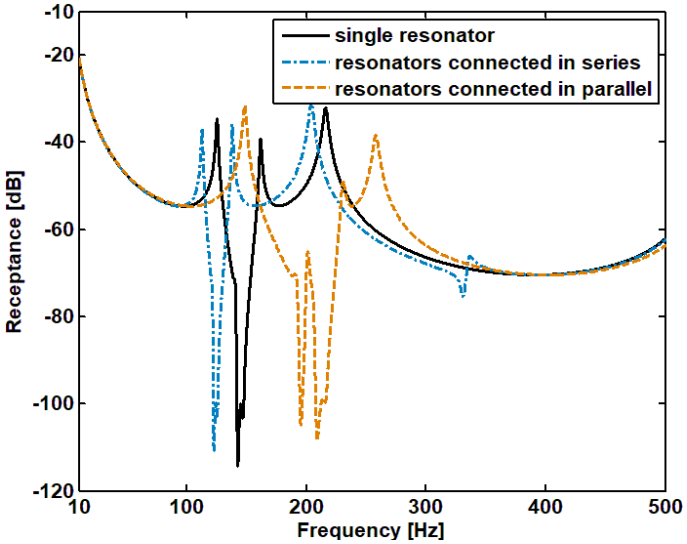

Figure 3. Unit cell of metamaterial beams with (a) single resonator, (b) resonators connected in series, (c) resonators connected in parallel

ACKNOWLEDGEMENTS

We would like to acknowledge the support acquired by the H2020 DiaMoND project (Grant Agreement ID: 785859), Royal Society Grant: PURSUIT.

REFERENCES

[1] X. Xiao, Z. C. He, Eric. Li, A. G. Cheng. Design multi-stopband laminate acoustic metamaterials for structural-acoustic coupled system. *Mechanical Systems and Signal Processing*. 115: 418–433, 2019.

[2] Miranda Jr, E. J. P., E. D. Nobrega, A. H. R. Ferreira, and J. M. C. Dos Santos. Flexural wave band gaps in a multi-resonator elastic metamaterial plate using Kirchhoff-Love theory. *Mechanical Systems and Signal Processing*. 116: 480-504, 2019.

[3] H. Peng, E. P. F. Pai, and H. Deng. Acoustic multi-stopband metamaterial plates design for broadband elastic wave absorption and vibration suppression. *International Journal of Mechanical Sciences*. 103: 104-114, 2015.

BEST PRACTICES FOR SPACECRAFT ACOUSTIC ANALYSIS AND ASSESMENTS

M. Cordaro

MSC Software & Politecnico di Torino
Turin, Italy
Email: mattia.cordaro@studenti.polito.it

ABSTRACT

Acoustic loads are one of the major concern in the structural design of SpaceCrafts (SCs); they are mostly caused by the launcher fairing sound pressure level during lift-off and ascending phase.
In this work a number of acoustic assessments have been performed by using MSC Actran SW and by referring to a real S/C structure and a real launch acoustic environment.
Three types of acoustic analysis are available in MSC Actran for the purpose: Modal and Direct frequency analysis and Virtual SEA, each one implies different assumptions and different computational effort, which may be noteworthy.
The aim of this work is to make a well though engineering evaluation about which is the type of acoustic analysis most suitable for the analysis, as a good compromise between accuracy and computational costs.
The second part of this work is devoted to the simulation of the Direct Acoustic Field Noise testing, which is a new promising and convenient trend for acoustic testing. More specifically the uniformity of the field generated by loudspeakers is evaluated.

1 INTRODUCTION

Concerning the spacecrafts, design the launch phase is particularly critical due to gross noise levels that impacts on the structure within the launcher shroud, for this reason is important to study the noise effect on the payload. When we have to analyse heavy and complex models like spacecraft, there are many problems connected to computational time and RAM consumption, furthermore, the designer could need an initial estimate of displacements, forces and accelerations; the main goal of this work is to set correctly in Actran the acoustic analysis of the S/C subject to acoustic loads of a real launcher and find a good compromise between fast computation and reliable results.
In this work will be considered a specific node of the structure to compare all the analysis.

2 MODAL VS DIRECT FREQUENCY ANALYSIS

2.1 Different Step Modal Comparison

The following analysis have been compared:

- Two logarithmic with 150 frequencies analysed, with different number of parallels and samples;
- Two logarithmic with 200 frequencies analysed, with different number of parallels and samples.

In the following table are listed the analysis with their respective parameters, computational times and peak memory consumption.

	STEP	# samples	# parallels	Computational time	Peak memory consumption [Mb]
1	Linear 0.5	20	8	7d, 7h, 16min	64384
2	LOG 150	20	8	10h, 15min	34098
3	LOG 150	25	10	20h, 40min	34404
4	LOG 200	20	8	13h, 3min	34458
5	LOG 200	25	10	1d, 3h, 36min	34850

Table 1

Focusing on the g-acceleration along z-axis of a specific node, as can be seen from Figure 1, the trend for logarithmic coarser analysis is quite the same of the detailed one with linear step; this can also be verified by means of RMS value of the PSD (Power Spectral Density), the percentage differences from the detailed one is almost never beyond 10% and in the most of cases around 5%. For the specific node of this case study we have the following percentage differences:

	LINEAR	LOG150	LOG150	LOG200	LOG200+
Z	5.9343	+10.66%	-11.79%	+2.59%	-4.17%

Table 2

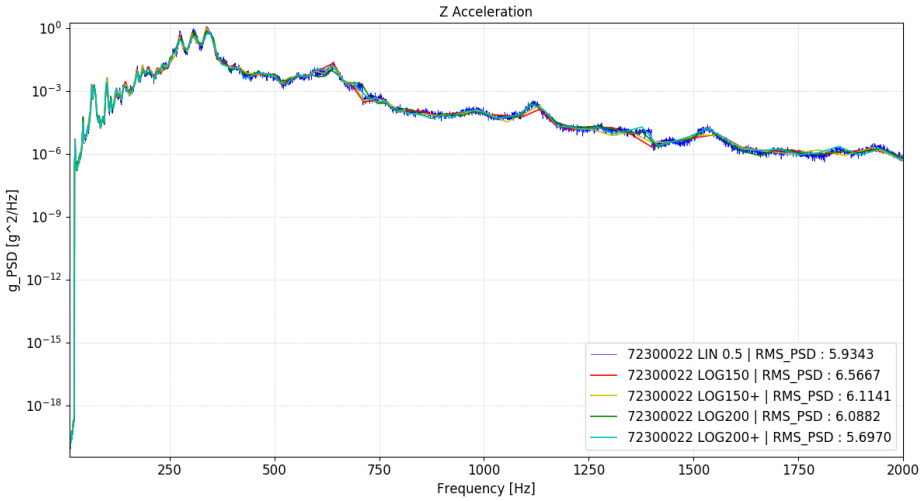

Figure 1

According to Figure 2 we can see that, for all the analysis, the problem is the loss of peak values, this is important, in particular for mid-lower frequencies up to 400Hz; this phenomenon is more evident for analysis 4 and 5 (LOG200), but depends on frequencies analysed – if are immediately after or before of a spike – and in particular to this node: increasing the number of frequencies the result will be more accurate.

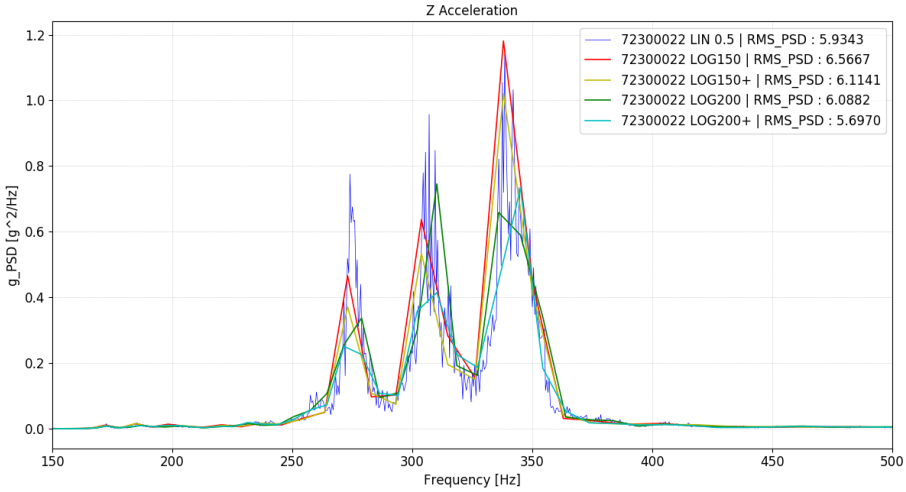

Figure 2

In view of the results a good compromise between all analysis shown is the one with a logarithmic step for 150 frequencies, this allows to save 7 days compared to the most precise with step 0.5Hz, where frequencies analysed are 3981, but adding just 3.5 hours compared to a coarser one (LOG100); this allows the designer to have, since the beginning of the analysis, an idea of loads that the structure will be subjected of.

For this reason, taking into account of computational times and results accuracy, if the analyst wants to have an initial estimate of values that will occur in the structure, the suggestion is to use a lower value of samples and parallels with a sufficient number of frequencies analysed.

2.2 Modal and Direct Comparison

Since the beginning of this section emphasis must be placed on the high complexity of the direct analysis, this is due to the fact that the creation of the exterior acoustic mesh comes with an high RAM consumption and very long computational times; for this reason this kind of analysis cannot be done on a normal pc if we want to evaluate a wide band of frequencies (10 ÷ 2000Hz), even with 128Gb the analysis can stop if parameters are not set up well.

These problems are connect mainly to the creation of the finite and infinite fluid at lower frequencies: starting the analysis at 10Hz – according to the standard mesh criterion – means that the software has to create a bubble of 34m radius to be fitted with elements dependent on the upper frequency of its sub-band domain.

In Figure 3 are plotted results obtained for both the modal analysis of paragraph 2.1 with linear step of 0.5Hz and logarithmic for 150 frequencies and the direct analysis with logarithmic step for 80 frequencies.

It is noted that values are lower for the direct analysis, this may be due to the masking effect of the air surrounding the structure; the value of RMS of PSD in this case is less different from the modal detailed analysis then the coarser one is.

This analysis, although with few frequencies analysed took 6 days, quite the same computational time needed for the high detailed modal, and a peak memory consumption of 117Gb.

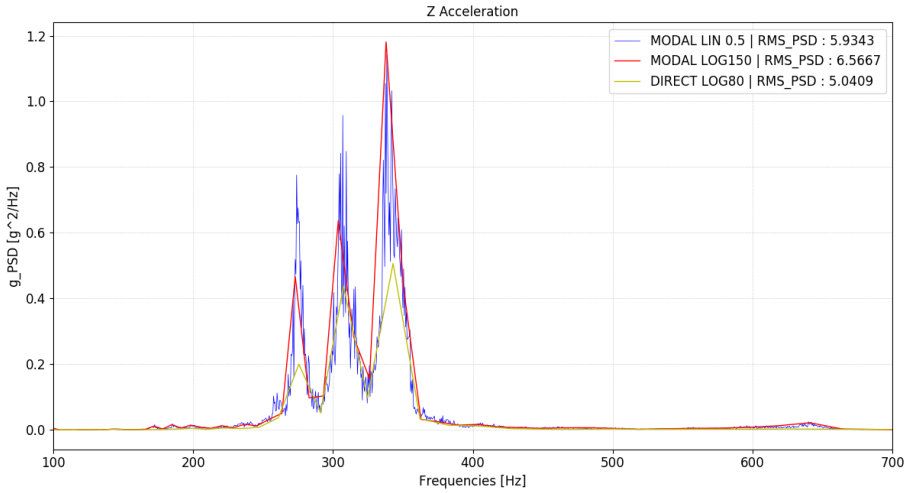

Figure 3

In conclusion my advice is to use the modal analysis in order to save time and memory consumption, at the very beginning of the study with a logarithmic step with 150 or more frequencies analysed in order to have really fast results and increasing this value for having more accurate results.

3 DIRECT FIELD ACOUSTIC NOISE TESTING SIMULATION

For the Acoustic Testing scenario, the excitation sources are noise generators like loudspeakers and horn-speaker, today's standard practice is to use dedicated buildings like reverberant rooms, here the acoustic field is uniform and diffuse, the aim is to replicate the spectrum that the spacecraft will be subjected to during launch inside of the shroud. However there are many problems connected to this kind of test, in fact, the need to move the structure from various facilities, leads to increased costs and risks; for these reasons has been developed the DFAN (Direct Field Acoustic Noise), here the speakers and audio equipment can be trucked to different sites so it can be very portable, allowing convenience in spacecraft scheduling [3].

In order to achieve the acoustic levels and the diffuse field effects of a reverberation chamber, is important to have an acoustic field as uniform as possible, meaning the same SPL anywhere in the acoustic volume, the target of this simulation was to understand if the acoustic field around the structure was comparable to a properly diffuse field.

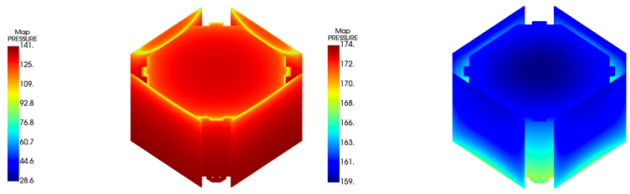

Figure 4

In exclusion of some areas that change with the frequency the field can be considered quite uniform and similar to a diffuse field.

REFERENCES

[1] Best Practices for Spacecraft Acoustic Analysis in Actran and Assesments, MSc thesis, M.Cordaro
[2] Actran 19.0 Users Guide VOL1
[3] Direct-Field-Acoustic-Noise-Testing, SIEMENS community, consulted on November 2019

IDENTIFICATION OF FORCES IN EULER-BERNOULLI BEAMS : BAYESIAN UPDATING

Abdelmalek Zine [1], Alexandre Kawano[2]

[1] Institut Camille Jordan (ICJ), Ecole Centrale de Lyon, Écully, France (*abdel-malek.zine@ec-lyon.fr*)
[2] Escola Polytechnica da Universidad de Sao Paulo, SP, Brazil (*akawano@usp.br*)

ABSTRACT

The beam is among the most important structural elements, and it can fail by different causes.In many cases it is important to access the loading acting on them. The determination of loading on beams is important, to model calibration purposes and/or to estimate remaining fatigue life, for example. In this work, we first prove that identification of the loading is theoretically possible from the observation of the displacement of small portion of the beam and for an arbitrary small interval of time. Ande then, we propose a method to infer the spatial distribution of forces acting upon a beam from the measurement of the displacement of one of its points.
The Bayesian method is used to combine measurements taken from different points at different times. This method enables an effective way of reducing the practical amount of time for obtaining meaningful loading estimates.

1 INTRODUCTION

The load determination over beams is viewed as an inverse problem related to vibration. The aim of this work is to idenfiy forces acting in a beam, using a new method based on almost periodic distributions, see Kawano, Zine [1]. We first prove that the data at our disposal is sufficient for the unique recovery of the loading, and then give a recovery method based on Bayesian updating scheme. Let $L > 0$ and $T_0 > 0$ given parameters. Let u be the displacement of the beam, the main equation in this inverse problem is

$$\begin{cases} \rho\dfrac{\partial^2 u}{\partial t^2} + \nu\dfrac{\partial u}{\partial t} + EI\dfrac{\partial^4 u}{\partial x^4} - T\dfrac{\partial^2 u}{\partial x^2} = F(t,x), & \text{in }]0,T_0[\times]0,L[, \\ u(0,x) = \frac{\partial u}{\partial t}(0,x) = 0, & \forall x \in]0,L[, \\ u(t,x) = \frac{\partial^2 u}{\partial x^2}(t,x) = 0, & \forall t \in]0,T_0[,\ \forall x \in \{0,L\}. \end{cases} \tag{1}$$

Here we assume a source term of the form $F(t,x) = g(t)f(x)$, $(t,x) \in [0,T_0]\times\Omega$, where, $g \in \mathcal{C}^1([0,T_0])$, $g(0) \neq 0$, assumed to be known, is a time–dependent attenuation factor and $f \in H^1(]0,L[)$, an unknown distribution to be identified, is a space–dependent source magnitude. Let $]0,T_0[$ be an arbitrary open set and $x_0 \in \left\{x \in]0,L[;\ \sin(\frac{n\pi x}{L}) \neq 0,\ \forall n \in \mathbb{N}\right\}$. The available data in this inverse problem is the set

$$\Gamma_{T_0,x_0} = \{u(t,x_0);\ t \in]0,T_0[\}, \tag{2}$$

2 THE DIRECT PROBLEM

A formal solution to Problem (1) may be obtained using Galerkin method. More precisely, consider the eigenproblem, $S \in H_0^1(]0,L[)$;

$$\begin{cases} \dfrac{EI}{\rho}\dfrac{\partial^4 S}{\partial x^4} - \dfrac{T}{\rho}\dfrac{\partial^2 S}{\partial x^2} = \beta S, & \text{in }]0,L[, \\ S(0) = S(L) = 0,\ \ S''(0) = S''(L) = 0. \end{cases} \tag{3}$$

The eigenvectors S_n and corresponding eigenvalues β_n are given by :

$$S_n(x) = C_n \sin(\frac{n\pi x}{L}), \quad \beta_n = \frac{EI}{\rho}\left(\frac{n\pi}{L}\right)^4 + \frac{T}{\rho}\left(\frac{n\pi}{L}\right)^2. \tag{4}$$

The constant $C_n = \sqrt{2/L}$ is chosen so that $\|S_n\|_{L^2(]0,L[)} = 1$. The set $\{S_n;\ n \in \mathbb{N}\}$ is orthogonal and dense in $H_0^1(]0,L[)$, as well as orthonormal in $L^2(]0,L[)$. Moreover, the set $\left(\frac{S_n}{n}\right)_{n\in\mathbb{N}}$ forms an orthonormal Hilbert basis of $H_0^1]0,L[$. Then, any function in $H_0^1]0,L[$ can be expressed as $\sum_{n=1}^{+\infty} A_n\dfrac{S_n}{n}$, with $(A_n)_{n\in\mathbb{N}} \in \ell^2$. Similarly, any distribution $h \in H^{-1}(]0,L[)$ can be uniquely expressed as $h = \sum_{n=1}^{+\infty} \tilde{A}_n n S_n$, $(\tilde{A}_n)_{n\in\mathbb{N}} \in \ell^2$. Finally, as $f \in H^{-1}(]0,L[)$, we get

$$f = \sum_{n=1}^{\infty} A_n S_n, \quad (A_n/n)_{n\in\mathbb{N}} \in \ell^2. \tag{5}$$

Assuming separation of variables, the dynamic response of $u(t,x)$ can be represented by:

$$u(t,x) = \sum_{n=1}^{\infty} G_n(t)S_n(x). \tag{6}$$

Using (5), (6) and the fact that u is a solution to (1), we get, for $t \in [0,T_0]$ and $x \in [0,L]$:

$$u(t,x) = \int_0^t g(t-\tau)\left[e^{-\frac{\nu}{2\rho}\tau}\sum_{n=1}^{\infty}\frac{A_n}{\omega_n}\sin(\omega_n\tau)S_n(x)\right]d\tau, \quad \omega_n = \sqrt{\beta_n - (\frac{\nu}{2\rho}\tau)^2}. \tag{7}$$

3 THE INVERSE PROBLEM

From (7), one may define the operator $\mathcal{K} : L^2(0,T_0) \to L^2(0,T_0)$;
$\mathcal{K}\psi(t) = \int_0^t g(t-s)\psi(s)\,ds, \quad \forall t \in]0,T_0[$. Define the space $\mathcal{G} = \left\{\eta \in L^2(0,T_0);\ (g,\eta)_{L^2(0,T_0)}\right\}$
and the projection operator $\mathcal{P} : L^2(0,T_0) \to \mathcal{G}$. On may show the following result :
$\exists\, c_1, c_2 > 0; \quad c_1 \left\|\mathcal{P}\mathcal{K}\ \psi\right\|_{L^2(0,T_0)} \leq \left\|\psi\right\|_{H^{-1}(0,T_0)} \leq c_2 \left\|\mathcal{P}\mathcal{K}\psi\right\|_{L^2(0,T_0)}$.
Applying this continuity result to (7), and the data $\Gamma_{T_0,x_0} = \{0\}$, to conclude that

$$\sum_{n=1}^{\infty} \frac{A_n}{\omega_n} \sin(\omega_n \tau) S_n(x_0) = 0, \quad \forall \tau \in [0,T_0[. \tag{8}$$

From [1], we get $A_n = 0$. And then, we conclude that the data $\Gamma_{T_0,x_0} = \{0\}$ is enough to determine uniquely $(A_n)_{n\in\mathbb{N}}$, and consequently the distribution $f \in H^{-1}(]0,L[)$.

3.1 Recovery procedure

To recover the source term $f \in H^{-1}(]0,L[)$, we consider a truncation of the Fourier series of g to the interval $[-T_0,T_0]$ given by, $g_M(t) = \sum_{k=0}^{M} k_m \cos(\tilde{\omega}_m t), \ \ \tilde{\omega}_m = \pi m t/T_0, \ \ M \in \mathbb{N}$.
Solving (1) for g replaced by g_M, and after some technical computations, we obtain :
$u_M(t,x) = \sum_{n=1}^{+\infty} \alpha_n e^{\imath\lambda_n t}$,
The idea is to approximate each α_n which depends on t, to a constant mean value in time. Following [1], we use a family of functions $\phi_{1,m,\tau}(\xi) = \frac{[\sin((\xi-\lambda_m)\tau)]^2}{(\xi-\lambda_m)^2\tau^2}, \quad \forall m \in \mathbb{N}, \forall \tau > 0$.
And, define

$$V_m = \langle w(\cdot,x), \widehat{\phi_{1,m,\tau}}\rangle, \ \ P_\tau(m,n) = \phi_{1,m,\tau}(\lambda_n), \ \ m,n \in \mathbb{N}.$$

Consider the operator $T : \ell^2 \to \mathcal{S}'$, $(\alpha_n)_{n\in\mathbb{N}} \to (V_m)_{m\in\mathbb{N}}$. Formally, applying T can be interpreted as performing a product with an infinite order matrix. Truncating of the previous infinite system we obtain :

$$\mathbf{T}_N\ \boldsymbol{\alpha} = \mathbf{V}; \ \ \mathbf{T}_N \in \mathbb{R}^{N\times N}, \ \ T_{m,n} = P_\tau(m,n), \quad \boldsymbol{\alpha}, \mathbf{V} \in \mathbb{R}^N. \tag{9}$$

By solving the linear system (9), we get the first elements of the desired sequence $(\alpha_n)_{n\in\mathbb{N}}$.

3.2 Bayesian updating

The Bayesian updating method makes it possible to incorporate previous experimental results and even subjective expert opinion into the analysis. We suppose in this section that vector $\mathbf{V}$ in (9) is corrupted by noise. That is, $\mathbf{V}$ is replaced by

$$\tilde{\mathbf{V}} = \mathbf{V} + \boldsymbol{\mathcal{E}}, \ \ \boldsymbol{\mathcal{E}} \text{ is a random variable, normally distributed with zero mean.}$$

Let $\sigma_\epsilon^2\,\mathbf{I}$ be a covariance matrix of $\boldsymbol{\mathcal{E}}$. The likelihood function for $\boldsymbol{\alpha}$, given the observation $\tilde{\mathbf{V}}$ is

$$\mathcal{L}(\boldsymbol{\alpha}\,|\,\tilde{\mathbf{V}}) = \frac{1}{(\sigma_\epsilon\sqrt{2\pi})^N} \exp\left[\sigma_\epsilon^{-2N}\left(\tilde{\mathbf{V}} - \mathbf{T}_N\ \boldsymbol{\alpha}\right)^t \left(\tilde{\mathbf{V}} - \mathbf{T}_N\ \boldsymbol{\alpha}\right)\right]. \tag{10}$$

If we attach to $[\alpha]$ a probability density functions in the Bayesian sense, we can assign to $[\alpha]$ a prior and a posterior probability density functions, f_{prior} and f_{post} respectively, [2].

By the Bayes rule, we have $f_{post}(\boldsymbol{\alpha}) = \dfrac{\mathcal{L}(\alpha\,|\,\tilde{\mathbf{V}})\, f_{prior}(\boldsymbol{\alpha})}{K(\tilde{\mathbf{V}})}$, where $K(\tilde{\mathbf{V}})$ is a normalizing constant defined so that $\int f_{post}(\boldsymbol{\alpha}) = 1$.
After the posterior distribution is obtained, it can be reused as a new prior for a new application of the Bayes rule, when new data is acquired. This is one of the advantages of the Bayesian method. The first prior employed in the beginning of the process incorporates subjective opinion regarding the parameters, about their joint distribution, mean and dispersion.

4 NUMERICAL EXPERIMENTS

To illustrate the theory above, we show some numerical experiments. Consider a beam that models a span of $L = 100m$ under traction with the following parameters :
$EI = 2.7 \times 10^7$, $\rho = 1.3 \times 10^1$, $T = 5.0 \times 10^5$, $\nu = 0.1$.
The excitation force used to simulate the dynamics of the system is
$F(t,x) = \cos(\tilde{\omega}_1 t) f(x)$, with $\tilde{\omega}_1 = 6$, $g(x) = \sum_{j=1}^{15} A_n \sqrt{2/L} \sin(\pi j x/L)$.
Function g is an approximation for an unit uniformly distributed load spanning from $x = 0.5L$ and $0.8L$. A random noise uniformly distributed over $[-\epsilon, \epsilon]$, $\epsilon = 0.01$ was added to $w(t, x_0)$, the function generated with the above data. This disturbed data is used for the recovery of the first five elements of (A_n).
Solving (9), we get $\tilde{\alpha}_n$, $n = 1, \ldots, 16$. Then, from $\tilde{\alpha}_n$ we obtain A_n.
The measurements are done in intervals of time of $T_0 = 20$ and $T_0 = 40$ seconds at point $x_0 = \frac{5}{11}L$. The Bayesian updating scheme can combine measurements taken at different points, the quality of the result is far superior if just one measurement is taken with no regularization besides truncation.

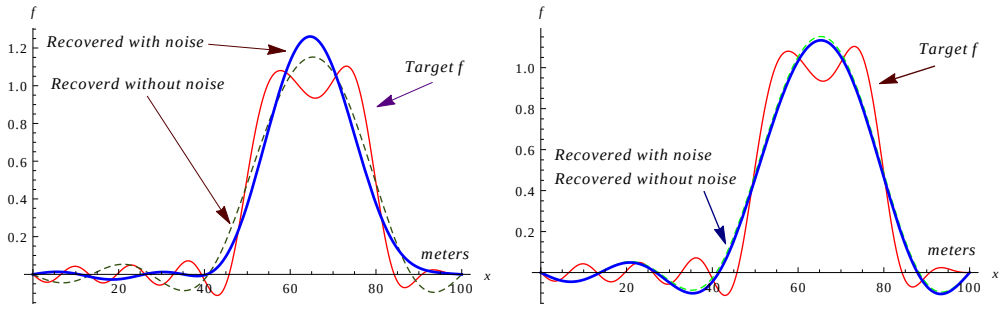

Figure 1. Recovered f, $T_0 = 4$ seconds; one and and three observation points, with Bayesian updating

5 CONCLUSION

In this paper we proved that the spatial distribution of the loading acting on an elastic beam can be uniquely determined by knowing the displacement of a point over an arbitrarily small interval of time. The Bayesian updating scheme gives very accurate results.

REFERENCES

[1] A Kawano and A Zine. Uniqueness and nonuniqueness results for a certain class of almost periodic distributions. *SIAM Journal of Mathematical Analysis*, 43(1):135–152, 2011.

[2] Jari Kaipio and E. Somersalo. *Statistical and Computational Inverse Problems*. Springer, 2005.

INVESTIGATION ON THE ARTIFICIAL NEURAL NETWORKS PREDICTION CAPABILITIES APPLIED TO VIBRATING PLATES IN SIMILITUDE

A. Casaburo[1*], G. Petrone[1], V. Meruane[2], F. Franco[1], S. De Rosa[1]

[1]pasta-Lab
Department of Industrial Engineering, Aerospace section, Università degli Studi di Napoli Federico II, Via Claudio 21, 80125 Napoli, ITALY
Email: alessandro.casaburo@unina.it, giuseppe.petrone@unina.it, francof@unina.it, sergio.derosa@unina.it

[2]Department of Mechanical Engineering, Universidad de Chile, Beauchef 850, Santiago, CHILE
Email: vmeruane@uchile.it

ABSTRACT

The prediction capabilities of artificial neural networks in similitude field are investigated. They have been applied to plates in similitude with two objectives: prediction of natural frequencies and model identification. The results show that the method is able to give accurate predictions and that an experimental training set can be created if the models are well characterized.

1 INTRODUCTION

Similitude methods are valuable tools for experimental tests, allowing money and time saving, and simplifying the test setup by testing reduced scale models instead of full-scale prototypes. However, manufacturing limits or errors are the causes of distorted models production. For these models, there is no univocal law that allows the reconstruction of the prototype dynamic response [1]. ANNs (Artificial Neural Networks) [2] pattern recognition capabilities, already explored in [3], are thus investigated for two purposes: 1) prediction of the natural frequencies of clamped-free-clamped-free aluminium plates in similitude using a training set made, mainly, by distorted models; 2) model identification in terms of geometrical scale factors, using response parameters to characterize the models. For both the tasks, a sensitivity analysis has been executed in order to identify the best architecture and number of training examples returning an acceptable performance.

2 PREDICTION OF NATURAL FREQUENCIES

In the first task, the models are characterized in terms of geometrical scale factors (length, width, and thickness); the output to predict are the first nine natural frequencies. Two training sets are used: both analytical, one of them polluted with numerical random normally distributed noise, in an attempt to reproduce the experimental uncertainties.

Fig. 1 shows the predictions of the natural frequencies. Five panels, on which experimental tests were performed, are used to test the generalization capabilities of the ANN: the prototype, two complete similitudes and two distorted similitudes.

The blue dots are the predictions of the ANN trained on the analytical data, with architecture 20 – 15 – 10 and 4000 training examples. The red dots are the predictions of the ANN trained on polluted data, with architecture 10 – 10 and 6000 training examples. The predictions of the ANN are very close to the reference, the blue line. This is a proof of the efficiency and robustness to noise of ANNs. The results are validated by the experimental (black) dots, close to the values returned by the ANN. However, the number of training examples is prohibitive, and an experimental training set cannot be generated, at least with the model characterization herein used.

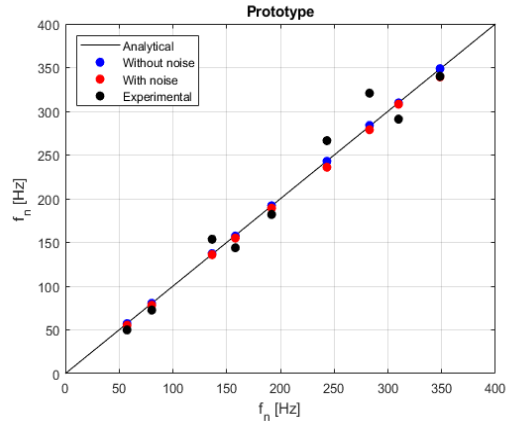

(a)

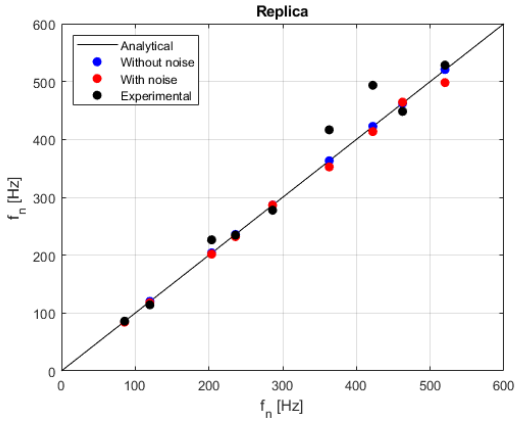

(b)

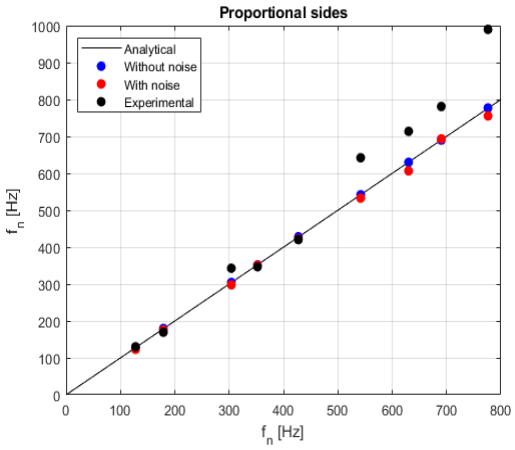

(c)

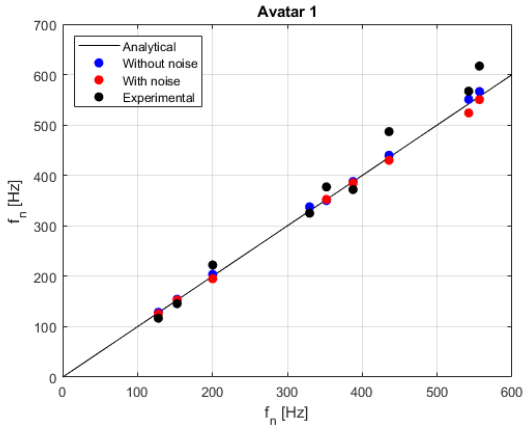

(d)

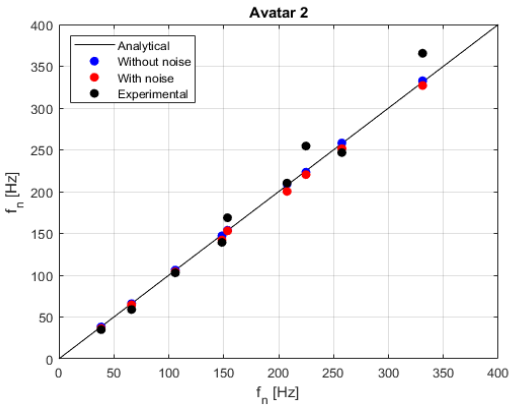

(e)

Figure 1 - Comparison among the experimental natural frequencies and those predicted by the ANN in both the cases of polluted and not polluted training sets, for the prototype (a), replica (b), proportional sides (c), avatar 1 (d), avatar 2 (e).

3 MODEL IDENTIFICATION

In this task, model identification is performed. The aim is to distinguish replicas (all the geometrical dimensions scale in the same way), proportional sides (length and width scale in the same way) and avatars (all the geometrical dimensions scale differently).

The network architecture is 5 – 7 and uses 200 training samples. The dynamic response is used as input, characterized in terms of first and second natural frequencies, modal density and the first eigenvalue extracted by applying PCA (Principal Component Analysis) to the frequency response function of each model.

Table 1 lists the prediction of the scale factors of the five experimental panels. The prototype is perfectly identified. Length and width scale factors of the proportional sides are not quite the true ones, however the model can be still identified as proportional sides. Both the avatars are perfectly identified. The thickness scale factor of the replica, instead, deviates of 3% from the real scale factor. The error is not very high, but it prevents a complete model identification.

To have an idea of the error made on all the predictions, Fig. 2 shows the relative error map evaluated on 27,000 examples. In general, the errors are very low, around 1% – 2%. For each scale factor there is a region of higher error, in which peaks of 11% are reached. However, being maps of relative error, this is always in the range [-0.05, 0.05] for all the scale factors. Therefore, it is not very high, although it prevents an accurate model identification.

Table 1 – Predictions of the scale factors of the experimental plates.

	True (r_a, r_b, r_h)	**Predicted (r_a, r_b, r_h)**
Prototype	1.00, 1.00, 1.00	1.00, 1.00, 1.00
Replica	0.67, 0.67, 0.67	0.67, 0.67, 0.65
Proportional sides	0.67, 0.67, 1.00	0.66, 0.66, 1.00
Avatar 1	0.67, 1.00, 1.00	0.67, 1.00, 1.00
Avatar 2	0.99, 0.70, 0.67	0.99, 0.70, 0.67

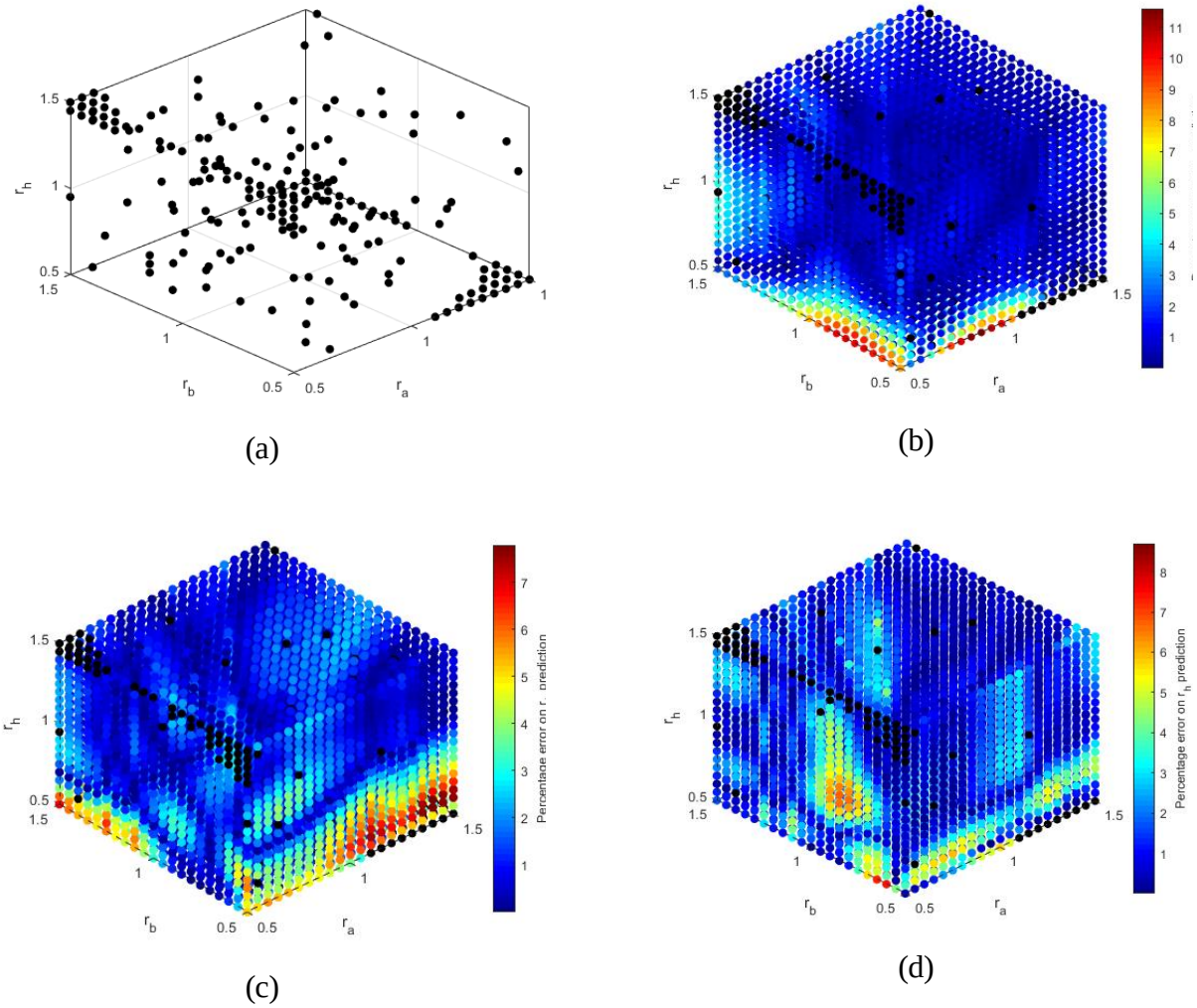

Figure 2 - Maps of the relative errors made by the ANN when predicting the scale factors. Subplot (a) shows the training examples, the other subplots the errors when predicting r_a (b), r_b (c), and r_h (d).

4 CONCLUDING REMARKS

The results demonstrated that ANNs have good potentialities in similitude fields, although too many samples are still required and the architecture cannot be defined *a priori*. However, the model identification task proved that, with a good characterization of input and output, it is possible to reduce significantly the number of training examples. ANNs proved to be also robust to noise. Using the method and analysing the results with critical thinking can make the application of ANNs an useful tool to support numerical simulations and experimental tests.

REFERENCES

[1] A. Casaburo, G. Petrone, F. Franco, and S. De Rosa. A review of similitude methods for structural engineering. *Applied Mechanics Reviews* 71(3), 2019.

[2] M. T. Hagan, H. B. Demuth, M. H. Beale and O. De Jesùs. Neural Network Design, 2nd Edition, Martin Hagan, USA, 2014.

[3] A. Casaburo, G. Petrone, V. Meruane, F. Franco and S. De Rosa, Prediction of the Dynamic Behavior of Beams in Similitude Using Machine Learning Methods. *Aerotecnica Missili e Spazio*, doi: https://doi.org/10.1007/s42496-019-00029-y, 2019.

TUNING OF SHUNTED ELECTRO-MAGNETIC ABSORBES BASED ON ELECTRICAL POWER DISSIPATED

E. Turco[1*], L. Dal Bo and P. Gardonio[1]

[1]Laboratorio di Controllo e Regolazione Automatica
University of Udine, Udine, ITALY
Email: turco.emanuele.1@spes.uniud.it, dalbo.loris@spes.uniud.it, paolo.gardonio@uniud.it

ABSTRACT

This paper discusses an innovative tuning approach of shunted electro-magnetic absorbers for broadband vibration control of a single-degree-of-freedom system. The control performances of the shunted absorber are numerically assessed considering the minimization of the time-averaged kinetic energy of the system. Classical tuning approaches for mechanical absorbers are based on the minimization of a cost function related to the kinetic energy of the system. In this paper, besides the time-averaged kinetic energy of the hosting system, the time-averaged electrical power dissipated by the transducer is analysed. It is found that the shunt parameters that minimise the kinetic energy of the system correspond to the values that would maximise the electrical power dissipated by the transducer. Therefore, the electrical power dissipated by the transducer, which can be measured locally, can be used as the cost function to tune the shunted electro-magnetic absorber in place of the kinetic energy of the hosting system, which, considering for example distributed flexible structures such as plates or cylinders, is a global function that cannot be measured straightforwardly.

1 INTRODUCTION

This paper discusses the tuning of shunted electro-magnetic vibration absorbers [1] based on time-averaged cost functions of the kinetic energy of the hosting system and of the dissipated electrical power by the absorber. In the work presented in Ref. [2], it was mathematically proved that, for a classical mechanical vibration absorber, the absorber parameters, *i.e.* natural frequency and damping ratio, which minimise the time-averaged kinetic energy of the primary structure, correspond to the values that maximise the mechanical power dissipation in the absorber. This concept has been recently extended also to electro-mechanical systems. In particular, in Ref [3] a simulation study regarding the

tuning of shunted piezoelectric absorber is presented and in Ref. [4] a similar numerical and experimental study concerning active electro-magnetic inertial actuators is discussed.

A series resistive inductive shunt circuit connected to an electro-magnetic absorber is considered. The equivalent mechanical effects of the shunt parameters can be expressed in terms of an equivalent spring and equivalent damper [1]. Therefore, the shunt parameters affect the dynamic behaviour of the absorber, *i.e.* natural frequency and damping ratio. A simulation study based on the time-averaged kinetic energy of the hosting system and electrical power dissipated by the absorber is assessed. The control and electrical dissipation effects are evaluated in terms of the kinetic energy and dissipated electrical power Power Spectral Densities (PSDs) functions. The simulation study shows that the shunt parameters that minimise the kinetic energy cost function correspond to the values which would maximise the electrical dissipated power cost function.

2 MODEL

As shown in Figure 1, a single-degree-of-freedom (*sdof*) hosting system is considered, which is equipped with an electro-magnetic absorber connected to a shunt. The shunt is used to vary the stiffness and damping properties of the absorber so that it can be conveniently tuned to control the vibration of the hosting system. The mass, stiffness and damping elements of the hosting system are m_1, k_1 and c_1 respectively. The lumped parameter model of the absorber is composed of a mass m_a suspended on a base mass m_b. The suspension system is modelled with a spring k_a and a damper c_a connected in parallel. The inherent electrical effects of the coil are modelled with a resistance R_e and an inductance L_e. The shunt circuit is composed by a resistance R_s and an inductance L_s connected in series. The physical properties of the primary system and of the electro-magnetic transducer are reported in Table 1. The hosting system is excited by a stochastic white noise force f. The vibration control performances and the electrical power dissipation by the electromagnetic absorber are assessed in terms of the kinetic energy and dissipated power PSDs functions. Furthermore, to better contrast the results obtained with different combinations of the shunt parameters, the time-averaged kinetic energy and time-averaged dissipated power are evaluated.

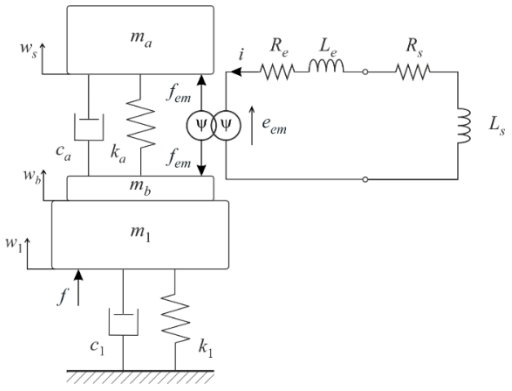

Figure 1. Scheme of the *sdof* system equipped with the shunted electro-magnetic absorber.

	Parameter	Value
Primary structure	m_1	3.35 kg
	k_1	1688 kN/m
	c_1	2.14 Ns/m
	f_n	112 Hz
Electro-magnetic transducer	m_b	0.105 kg
	m_a	0.185 kg
	k_a	2314 N/m
	c_a	9.10 Ns/m
	R_e	22.5 Ω
	L_e	4.35 mH
	ψ	22.5 N/A

Table 1. Parameters of the primary structure and electro-magnetic transducer.

The constitutive equations of the transducer are:

$$f_{em}(t) = \psi\, i(t) \tag{1}$$

and

$$e_{em}(t) = \psi\, (\dot{w}_s - \dot{w}_b)\,, \tag{2}$$

where f_{em} is the reactive force between the magnet and the external cylinder produced by the current i flowing in the coil and e_{em} is the back electro-motive force generated by the relative velocity

between the magnet $\dot{w}_b$ and ferromagnetic ring and coil components $\dot{w}_s$. Finally, ψ is the transduction coefficient. Preliminary studies [1] have shown that the RL shunt considered in this study generates an equivalent mechanical effect which could be interpreted as an equivalent spring

$$k_{es} = \psi^2/(L_e + L_s) \tag{3}$$

and an equivalent dashpot

$$c_{es} = \psi^2/(R_e + R_s)\,. \tag{4}$$

Equations (3) and (4) clearly indicate that the considered shunt circuit can be used to change the tuning frequency and damping ratio of the shunted absorber.

2.1 Mathematical model

The coupled equation of motion for system are derived considering Newton's law of motion for the primary system and for the suspended mass of the absorber and Kirchhoff's voltage law applied to the electrical circuit. The resulting differential equations can be casted in matrix form as:

$$\begin{bmatrix} m_1+m_b & 0 & 0 \\ 0 & m_a & 0 \\ 0 & 0 & 0 \end{bmatrix} \begin{Bmatrix} \ddot{w}_1 \\ \ddot{w}_s \\ \ddot{\imath} \end{Bmatrix} + \begin{bmatrix} c_1+c_a & c_a & 0 \\ -c_a & c_a & 0 \\ -\psi & \psi & L_e+L_s \end{bmatrix} \begin{Bmatrix} \dot{w}_1 \\ \dot{w}_s \\ i \end{Bmatrix} + \begin{bmatrix} k_1+k_a & -k_a & \psi \\ -k_a & k_a & -\psi \\ 0 & 0 & R_e+R_s \end{bmatrix} \begin{Bmatrix} w_1 \\ w_s \\ i \end{Bmatrix} = \begin{bmatrix} 1 \\ 0 \\ 0 \end{bmatrix} f\,. \tag{5}$$

The kinetic energy PSD and the absorbed power PSD are defined as [3,5]:

$$S_K(\omega) = \tfrac{1}{2} m_1 \lim_{T\to\infty} E\left[\tfrac{1}{T}\, \dot{w}_1{}^*(\omega)\dot{w}_1(\omega)\right], \tag{6}$$

$$S_P(\omega) = \lim_{T\to\infty} E\left[\tfrac{1}{T}\, i(\omega)i^*(\omega)\right](R_e + R_s)\,. \tag{7}$$

where $\dot{w}_1(\omega)$ and $i(\omega)$ are the complex amplitudes of the time-harmonic velocity of the primary system and of the electrical current in the coil. Also, the time-averaged kinetic energy $\bar{K}$ and the time-averaged electrical power dissipated $\bar{P}$ functions result [3,5]:

$$\bar{K} = \int_0^{+\infty} S_K(\omega)\ \mathrm{d}\omega\,, \tag{8}$$

$$\bar{P} = \int_0^{+\infty} S_P(\omega)\ d\omega\ . \tag{9}$$

3 SIMULATIONS

Figure 2 shows the maps of the time-averaged kinetic energy (a) and of the electrical dissipated power (b) for different combinations of the shunt resistance R_s and shunt inductance L_s. Plots (a) and (b) present a second horizontal axis, which corresponds to the natural frequency f_A of the shunted absorber. The kinetic energy in plot (a) presents a bell-like surface, with a minimum marked by the cyan dot. Similarly, the electrical dissipated power in plot (b) presents a mirror surface, characterised by a maximum marked with the purple dot. The combination of the shunt parameters which guarantee the minimum of the kinetic energy closely corresponds to the couple of parameters which maximise the electrical power dissipated. The kinetic energy PSDs of the primary system without (solid black line) and with the shunted absorber are contrasted in plot (c). Here, the results obtained with the shunt parameters that minimise the kinetic energy are shown with the solid cyan line while the dotted purple line represents the results obtained with the shunt parameters that maximise the electrical power dissipated. The two coloured curves overlap quite closely, confirming that the tuning approach based on the maximisation of the electrical power dissipated by the shunted absorber produces the same effect as the tuning based on the minimisation of the kinetic energy of the primary system. Finally, plot (d) shows the spectra of the dissipated power PSD when the shunt parameters that minimise the kinetic energy (solid cyan line) and maximise the power dissipation (dotted purple line) are adopted.

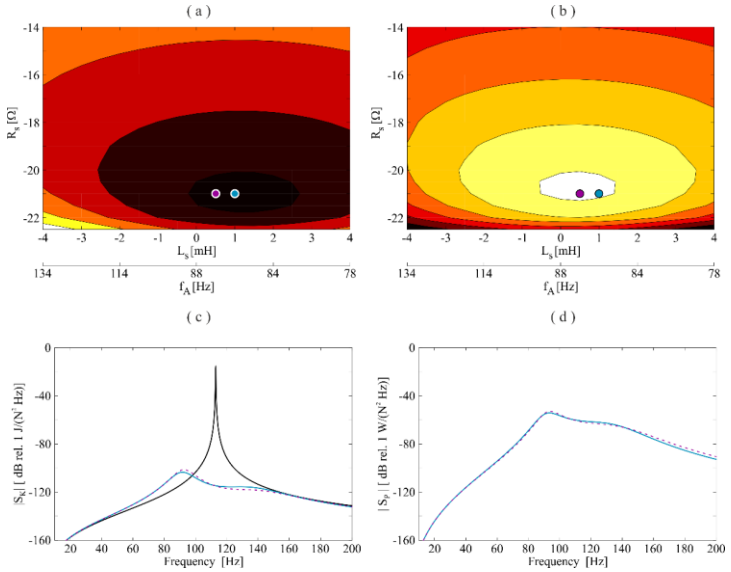

Figure 2. Time-averaged kinetic energy (a) and dissipated power (b), PSDs of the kinetic energy (c) and of the dissipated power (d). Minimum of the kinetic energy is depicted by the blue dot while maximum of the power dissipated by the purple dot.

4 CONCLUDING REMARKS

This paper has presented a simulation study concerning the tuning of shunted electromagnetic vibration absorber on a single-degree-of-freedom primary system to control broadband vibrations. The tuning criteria are related to the minimisation of the time-averaged kinetic energy of the primary system and the maximisation of the time-averaged electrical power dissipated by the transducer.

The preliminary numerical results presented in this paper show that the shunt parameters that minimise the time-averaged kinetic energy closely corresponds to the values that would maximise the time-averaged electrical power dissipated. This result offers an interesting practical application, since the tuning of shunted electromagnetic absorbers could be achieved considering a local function, *i.e.* the dissipated electrical power, which can be measured locally using few electrical components, instead of a global function, *i.e.* the kinetic energy, which requires a more complex measurement setup, particularly when distributed hosting structures are considered.

ACKOWLEDGEMENTS

The authors would like to acknowledge the DEVISU project which was supported by the Ministero dell'Istruzione, dell'Università e della Ricerca research funding programme PRIN 2017 and the Programma operativo del Fondo sociale europeo 2014/2020 della Regione Friuli Venezia Giulia - Progetto "HEaD HIGHER EDUCATION AND DEVELOPMENT" OPERAZIONE 1 UNIUD (FP1619942002, canale di finanziamento 1420AFPL01)

REFERENCES

[1] E. Turco, and P. Gardonio. Sweeping shunted electro-magnetic tuneable vibration absorber: design and implementation. *J. Sound Vib*. 407: 82-105, 2017.

[2] M. Zilletti, S. J. Elliott, and E. Rustighi. Optimisation of dynamic vibration absorbers to minimize kinetic energy and maximize internal power dissipation. *J. Sound Vib*. 331:4093-4100, 2012.

[3] P. Gardonio, M. Zientek, and L. Dal Bo. Panel with self-tuning shunted piezoelectric patches for broadband flexural vibration control. *Mech. Syst. Signal Process.* 134:106299-106321, 2019.

[4] S. Camperi, M. G. Tehrani, and S. J. Elliott. Local tuning and power requirements of a multiple-input multiple-output decentralized velocity feedback with inertial actuators. *Mech. Syst. Signal Process.* 117:689-708, 2019.

[5] P. Gardonio, S. Miani, F. Blanchini, D. Casagrande and S. J. Elliott. Plate with decentralized velocity feedback loops: power absorption and kinetic energy considerations. *J. Sound Vib*. 331(8):1-14, 2012.

BAND GAP OPTIMIZATION OF PERIODIC BEAMS USING FOURIER SHAPE COEFFICIENTS

V. D. Lima and J. R. F. Arruda

School of Mechanical Engineering
University of Campinas, Campinas, Brazil
Email: vinidiaslima@gmail.com, arruda@fem.unicamp.br

ABSTRACT

Periodic elastic waveguides such as rods and beams exhibit frequency bands where wave reflections at impedance discontinuities cause strong wave attenuation by Bragg scattering, thus avoiding the building up of standing waves, i.e., normal modes. Such frequency bands are known as stop bands, or band gaps. This work proposes the shape optimization of periodic beams using, as optimization parameters, the spatial Fourier coefficients that describe the periodic shape and/or material properties along the beam length. The objective may be the widening of a given wave band gap of the periodic beam caused by Bragg scattering, as done here, lowering the initial band gap frequency, or opening a bang gap around a target frequency. Using the Fourier coefficients is convenient, as they are the input of the Plane Wave Expansion (PWE) method commonly used to obtain the dispersion relations that indicate the band gaps. In this work, the proposed technique is applied to a simple straight beam with circular cross section and the first band gap is widened by optimizing the beam radius. In a second example case, both the internal and external radii of a hollow beam are optimized. The optimization is performed using sequential a quadratic programming in the MATLAB® environment. We explain how to impose geometrical constraints to the Fourier coefficient parameters to avoid non physical aberrant solutions in the optimization. The proposed technique can be easily extended to two and three-dimensional structures and easily adapted for different cost functions. The forced response of the arbitrarily shaped periodic beam is computed using a spatial state-space formulation of the elastodynamic equations of the beam. Euler-Bernoulli and Timoshenko theories are used.

1 INTRODUCTION

Periodic structures exhibit frequency bands where elastic waves of certain types cannot propagate, as they are canceled by multiple reflections caused by the periodic impedance variations (Bragg scattering). This phenomenon has been known since the seminal works of Lon Brillouin in quantum physics, Gaston Floquet in mathematics and Felix Bloch in nuclear physics in the early XXth century. Concerning mechanical waves, Lord Rayleigh had already commented on the possibility of Bragg canceling in periodic lattices in the XIXth century[1]. More recently, results and methods developed in solid state physics (photonic crystals) have been translated for elastic wave phenomena (phononic crystals).

Band gaps can be computed using the Plane Wave Expansion (PWE) method, which consists in expanding the material and geometrical properties of the elastic structure in its elastodynamic equations. Using the Floquet-Bloch theorem, the displacements and forces are written as a periodic kernel multiplied by an exponential, of which the exponent is the wavenumber (Bloch wave vector) multiplied by the period length. The expanded elastodynamic equation can be transformed into an eigenvalue problem using the orthogonality of the Fourier series expansion. Given that the shape of the periodic structure is described by the spatial Fourier series coefficients, we propose to use these coefficients to optimize the shape of the structure with a band-gap-based objective, such as widening the band gap or opening a bang gap in a target frequency range.

In this work we apply the proposed method to a simple straight beam with circular cross section (solid and hollow). The first band gap is widened by optimizing the beam radius (external and also internal in the hollow case). After optimizing the shape, the forced response of the arbitrarily shaped periodic beam is computed using a spatial state-space formulation of the elastodynamic equations of the beam[2] .

2 PLANE WAVE EXPANSION METHOD

The governing equation of a uniform one-dimensional mechanical waveguide can be written as [3]

$$\frac{\partial^q}{\partial x^q}\left[\alpha(x)\frac{\partial^q u(x,t)}{\partial x^q}\right] = \beta(x)\frac{\partial^2 u(x,t)}{\partial t^2}, \tag{1}$$

where x and t denote, respectively, spatial and time (independent) variables, q is the order of the differential equation, α is related with elastic properties, β related with mass properties and $u(x,t)$ is the displacement at position x and time t. Applying the Fourier transform with respect to the independent variable t, one obtains

$$\frac{\partial^q}{\partial x^q}\left[\alpha(x)\frac{\partial^q}{\partial x^q}\hat{u}(x,\omega)\right] + \omega^2\beta(x)\hat{u}(x,\omega) = 0. \tag{2}$$

where ω is the angular frequency and $\hat{u}(x,\omega)$ is the displacement in the frequency domain. Due to the periodicity, the Floquet-Bloch condition can be applied, and $\hat{u}(x+a,\omega) = \hat{u}(x,\omega)e^{jka}$. Expanding α and β in Fourier series results in the following eigenvalue problem

$$\sum_{m=-\infty}^{+\infty} \hat{\alpha}_{r-m}(k+g_m)^q(k+g_r)^q c_m = \omega^2 \sum_{m=-\infty}^{+\infty} \hat{\beta}_{r-m}c_m, \qquad r \in \mathbb{Z}, \tag{3}$$

with $r = m + n$. More details on the PWE method can be found in [4].

Assis et al. [2] recently proposed a methodology which allows to obtain the forced response of a phononic crystal with arbitrary shape writing the wave equation in a state-space first order system of equations and transforming them in a Riccati-type matrix equation, which can be integrated it in the spatial domain, as the boundary conditions give the impedance at the structure ends.

3 SHAPE OPTIMIZATION OF BAND GAPS IN BEAMS

The governing equation representing a beam is obtained using $q = 2$. In this case, the properties are $\alpha(x) = E(x)I(x)$ and $\beta(x) = \rho(x)S(x)$. Without loss of generality we use constant material

properties E and ρ and the Fourier coefficients of interest in the optimization are the resultant from the expansion of the cross-sectional area $S(x)$ and area moment of inertia $I(x)$. Imposing the cell symmetry, $S(x)$ and $I(x)$ are even functions, and therefore can be expanded in cosine form

$$S(x) = S_0 + 2\sum_{\ell=1}^{\gamma} S_\ell \cos(2\pi\ell x/a), \qquad I(x) = I_0 + 2\sum_{\ell=1}^{\gamma} I_\ell \cos(2\pi\ell x/a), \tag{4}$$

and the optimized parameters (decision variables) are

$$p = [S_0 \quad \cdots \quad S_{\gamma-1} \quad S_\gamma \quad I_0 \quad \cdots \quad I_{\gamma-1} \quad I_\gamma]^T. \tag{5}$$

Imposing the cross section area limits S_{min} and S_{max} and the moment of inertia limits I_{min} and I_{max}, the maximization of the first band gap by the shape optimization of a straight beam is described by the minimization problem

$$\min_p f(p) = \frac{1}{\omega_2 - \omega_1}$$

subject to

$$Ap - b \leq 0,$$

with matrices $\mathbf{A}$ and $\mathbf{b}$

$$\mathbf{A} = \begin{bmatrix} -\mathbf{\Theta}_S & \mathbf{0} \\ \mathbf{\Theta}_S & \mathbf{0} \\ \mathbf{0} & -\mathbf{\Theta}_I \\ \mathbf{0} & \mathbf{\Theta}_I \end{bmatrix}, \qquad \mathbf{b} = \begin{bmatrix} -S_{\min} \\ S_{\max} \\ -I_{\min} \\ I_{\max} \end{bmatrix}. \tag{6}$$

The cross section area and moment of inertia can be independently optimized. However, if the geometric shape of the cross section is imposed, those geometric characteristics become linked and the number of decision variables decreases.

4 NUMERICAL SIMULATION RESULTS

The proposed method was applied for two numerical examples. In the first example, the beam is assumed as solid with circular cross-section, made of aluminum with $E = 77.6\ GPa$ and $\rho = 2730\ kg/m^3$. The unit cell length is $0.2\ m$ and the maximum and minimum radii imposed are $0.1\ m$ and $0.05\ m$, respectively. The optimization problem was solved with a sequential quadratic programming algorithm available in the *fmincon* package of MATLAB®.

The initial and optimized geometries are shown in Figure 1a. The first band gap has a significant widening, from $7.6 - 8.9\ kHz$ to $5.5 - 10.1\ kHz$, i.e. 3.5 times wider than the initial band gap. Moreover, it is still covering the bandwidth of the initial band gap. Figure 1c compares the forced responses of the initial and final shapes.

The second example is a hollow circular cross-section beam. The initial values for the external radius are the same of the solid beam, now adding an inside radius restricted to be within the interval $[0.015\ , 0.04\ ]$m. In this case, the first band gap changes from $7.0 - 8.7\ kHz$ to $5.8 - 10.9\ kHz$. Note that it is slightly larger than the band gap obtained for the solid beam case with same external limits, but less material.

5 CONCLUSIONS

The proposed method allowed a straightforward shape optimization of a beam element aiming at widening the first wave band gap, caused by Bragg scattering. The optimized geometry in the simple examples treated here is predictable, converging to the highest possible impedance discontinuity. However, the proposed method has the potential to generate less predictable results if different optimization objectives are sought, such as a simultaneous band gap for flexural, longitudinal and torsional waves of a frame element with more complex geometrical and material properties. Functionally graded structural elements can be optimized. Furthermore, the method can be easily extended do two- and three-dimensional structures, such as spatial frames and plates. The authors are currently investigating these applications.

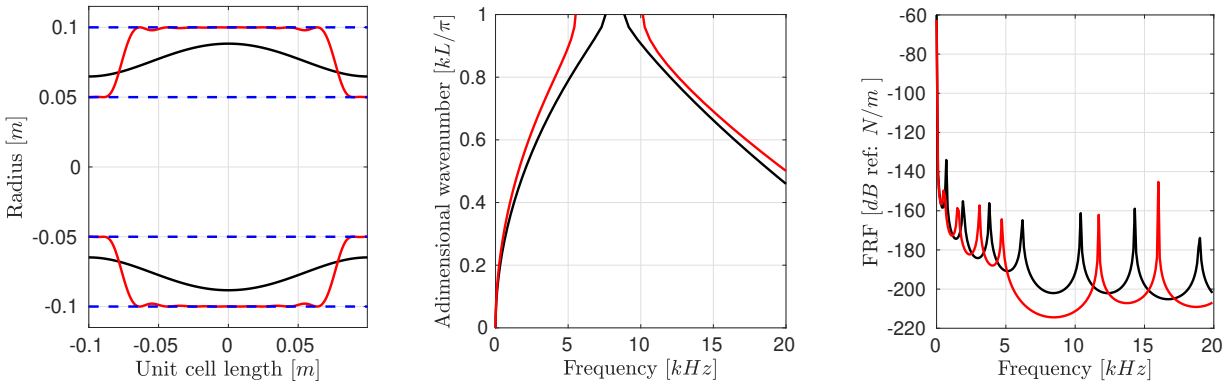

(a) (b) (c)

Figure 1: Comparison between initial (black) and final (red), solid beam case: (a) geometry, (b) dispersion diagrams and (c) forced responses for a beam with 5 unit cells.

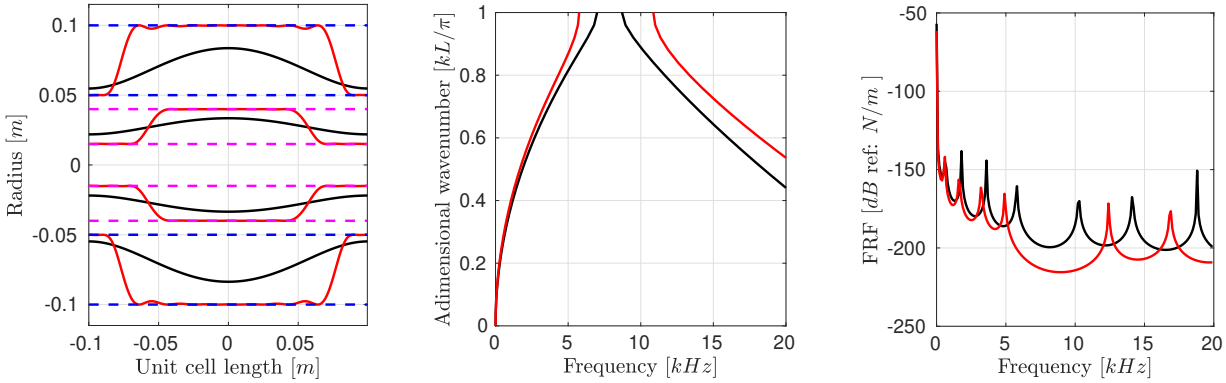

(a) (b) (c)

Figure 2: Comparison between initial (black) and final (red) hollow beam case: (a) geometry, (b) dispersion diagrams and (c) forced responses for a beam with 5 unit cells.

ACKNOWLEDGMENTS

The authors gratefully acknowledge the support of the So Paulo State Foundation (FAPESP Grant Reference Number 2018/15894-0).

REFERENCES

[1] Lord Rayleigh. On the maintenance of vibrations by forces af double frequency, and on the propagation of waves through a medium endowed with a periodic structure. *Phylosophical Magazine*, 24(147):145–159, 1887.

[2] G. F. C. A. Assis, D. Beli, E. J. P. de Miranda Jr., J. F. Camino, J. M. C. Dos Santos, and J. R. F. Arruda. Computing the complex wave and dynamic behavior of one-dimensional phononic systems using a state-space formulation. *International Journal of Mechanical Sciences*, 163:105088, 2019.

[3] J.F. Doyle. *Wave Propagation in Structures: Spectral Analysis Using Fast Discrete Fourier Transforms*. Mechanical Engineering Series. Springer New York, 1997.

[4] M. Sigalas and E. N. Economou. Band structure of elastic waves in two dimensional systems. *Solid State Communications*, 86(3):141–143, 1993.

INTELLIGENT SLIDING MODE REFERENCE CONDITIONING CONTROLLER

M. Haddar[1*], R. Chaari[1], S.C. Baslimisli[2], F.Chaari[2], and M.Haddar

[1] Laboratory of Mechanics, Modelling and Production (LA2MP), National School of Engineering of Sfax, University of Sfax, Tunisia
Email: maroua.haddar@enis.tn, rchaari@yahoo.fr, fakher.chaari@gmail.com, Mohamed.haddar@enis.rnu.tn

[2] Department of Mechanical Engineering Hacettepe University Beytepe, Ankara, 06800 Turkey
Email: caglar.baslamisli@gmail.com

ABSTRACT

This paper proposes a new intelligent control algorithm for half car system. A combination between a model free controller based on a non-asymptotic observer with a sliding mode reference conditioning scheme. Merging different advantages such as limiting the level of vertical acceleration and using online observer can be helpful for conserving the ride comfort requirement.A comparative analysis with passive system, classical PID and SMRC+PID is presented. Results obtained from the introduced control scheme show a robust fault tolerant controlling to sprung mass variation and sensor noise

1 INTRODUCTION

In order to achieve high level performance objectives in terms of the comfort of vehicle and passenger safety, several technical skills are required. Indeed, to improve the dynamics of the vehicle, both effective observation strategies and control are essential in addition to knowledge of automotive mechanics. It is very important that the research community prove that the proposed theoretical strategies can lead to real workable solutions that meet the needs of the industry.

The main objectives of this paper are to develop new methodologies and innovative solutions, for the studying vehicle behaviour, for the observation online of critical situations, detection and

control with robustness the half car dynamic. In addition, one of the main objectives of the solutions developed in this work is to improve passenger comfort under different kind of unpredictable perturbations .Several approaches are developed to ensure the supervision and observation of driving situations, in order to avoid the use of many sensors [1-2]. For example Haddar et al [1] used the development of algebraic estimators, both for estimation and compensation of unknown dynamics in control algorithms for quarter car model.

For these raisons, a new scheme of control is developed in this paper. A combination between the effectiveness of two kind of controller that allows driver to getting a good ride comfort and robustness to exogenous and endogenous perturbations.

2 MULTIBODY SUSPENSION SYSTEM

The model of a half-car suspension represented as a combination of two-quarter car model for giving born to a linear four degree of freedom system. All used mechanical components are linear. Additive servo-hydraulic actuators are integrated into the architecture to generate active power. The parameters and required performances are detailed in the work of León-Vargas et al [1].

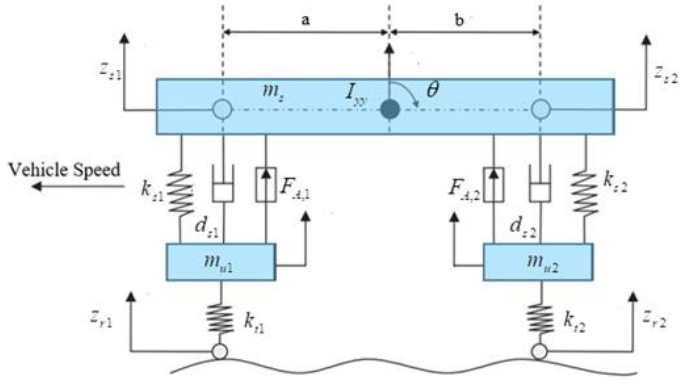

Figure 1. Half car model

The equations of motion of Half Car Model are illustrated as following:

$$m_s \ddot{z}_s = -k_{s1}(z_{s1} - z_{u1}) - k_{s2}(z_{s2} - z_{u2}) - d_{s1}(\dot{z}_{s1} - \dot{z}_{u1}) - d_{s2}(\dot{z}_{s2} - \dot{z}_{u2}) + F_{A,1} + F_{A,2} \quad (1)$$

$$I_{yy}\ddot{\theta} = k_{s1}(z_{s1} - z_{u1})a - k_{s2}(z_{s2} - z_{u2})b + d_{s1}(\dot{z}_{s1} - \dot{z}_{u1})a - d_{s2}(\dot{z}_{s2} - \dot{z}_{u2})b - F_{A,1}a + F_{A,2}b \quad (2)$$

$$m_{u1}\ddot{z}_{u1} = k_{s1}(z_{s1} - z_{u1}) + d_{s1}(\dot{z}_{s1} - \dot{z}_{u1}) - k_{s1}(z_{u1} - z_{r1}) - F_{A,1} \quad (3)$$

$$m_{u2}\ddot{z}_{u2} = k_{s2}(z_{s2} - z_{u2}) + d_{s2}(\dot{z}_{s2} - \dot{z}_{u2}) - k_{t2}(z_{u2} - z_{r2}) - F_{A,2} \quad (4)$$

Two relations between the body displacement and the pitch rate can give the expressions of displacements of sprung mass at front and rear tyres respectively: $z_{s1} = z_s - a\theta$ and $z_{s2} = z_s + b\theta$.

3 IMPLIMENTED CONTROLLERS

The novelty in this paper is the use of an i-PD controller as a new controller for half car model. Furthermore, the combination between the introduced SMRC controller and the intelligent controller is introduced for getting more effective controller in amelioration ride comfort.The i-PD is classified as a model free controller that is able to reject all kind of perturbations online and without need to a

new calibration. In fact, the knowledge of the mathematical model and the features of noise are avoidable. The equation of control process and non-asymptotic observer can be written as following:

$$F_{A,i} = \underbrace{-\frac{\hat{\phi}_i}{\alpha_i}}_{\text{Cancellation term}} + \underbrace{\frac{y_{ref,i} - \left(K_{P,i}e + K_{D,i}\dot{e}\right)}{\alpha_i}}_{\text{Closed loop tracking}} \tag{5}$$

$$\hat{\phi}_i = [\hat{\dot{z}}_s]_e - \hat{F}_{A,i}(t-\tau) \tag{6}$$

$F_{A,i}$ are the actuators forces. $y_{ref,i}$ are the suspension deflections. $K_{P,i}$, $K_{D,i}$ are the PD gains. α_i is a scaling parameter. $[\hat{\dot{z}}_s]_e$ and $\hat{F}_{A,i}(t-\tau)$ are the estimated signals from algebraic non-asymptotic observer.

4 SIMULATION RESULTS

4.1 Control under noisy condition

In real time application, the problem of noisy signals is an important issue and especially in the field of automotive applications. As indicated by Haddar et al [1], digital filters implemented in Model Free controller are useful for extracting a noiseless signal. In this simulation, we try to show the variation of sprung mass acceleration for evaluating the ride comfort criteria. Then, a measurement noise was added in the simulated measurements of sprung mass acceleration to investigate the robustness of i-PD+SMRC to sensors default. From the results depicted in Figure 2 -(a) , it is show that i- PD+SMRC and PD+SMRC show better vibration isolation characteristics compared to passive suspension ,PID and i-PD. In fact, this attenuation is related to SMRC that allows to set up a limit values for the acceleration between 1.2 m/s^{-2} and -1.2 m/s^{-2}.However, Figure 2 -(b) demonstrate that SMRC is sensitive to the noise in the absence of intelligent term $\hat{\phi}$. From Figures 2(c-d), the algebraic filters are effective tools for low-pass filtering noisy data.

4.2 Variation of loads

Theoretically, the mass of the vehicle can be determined based on provided information about the geometry and the masses of the bodies. However, these measures cannot take into account a certain number of factors that influence the ride comfort such as the addition of the driver numbers, passengers and baggage, and whose effect is not negligible on the total mass. From the results depicted in Figure 3, it is show that the classical PID and PID+SMRC are unable to dealing with the sprung mass variation and are sensitive to this kind of uncertainty. However, the scheme that include a non-asymptotic observer are unsusceptible to the load variation. As indicated by [1], the intelligent term is able to conserve the stability of the vehicle dynamic and avoid the process of recalibration of controller gains.

5 CONCLUDING REMARKS

As part of this paper, an evaluation of a fault-tolerant control approach for half car model. It is therefore necessary in the suspension architecture chosen; these systems are placed under the supervision of a supervisor in charge of detecting the failures of the systems, and to adapt the laws of control in case of fault. Fault Tolerant Active Control, which consists of automatically correcting the effects of failures by performing two tasks: detect and identify faults, adapt the control laws to the present fault as sprung mass variation and sensor default.

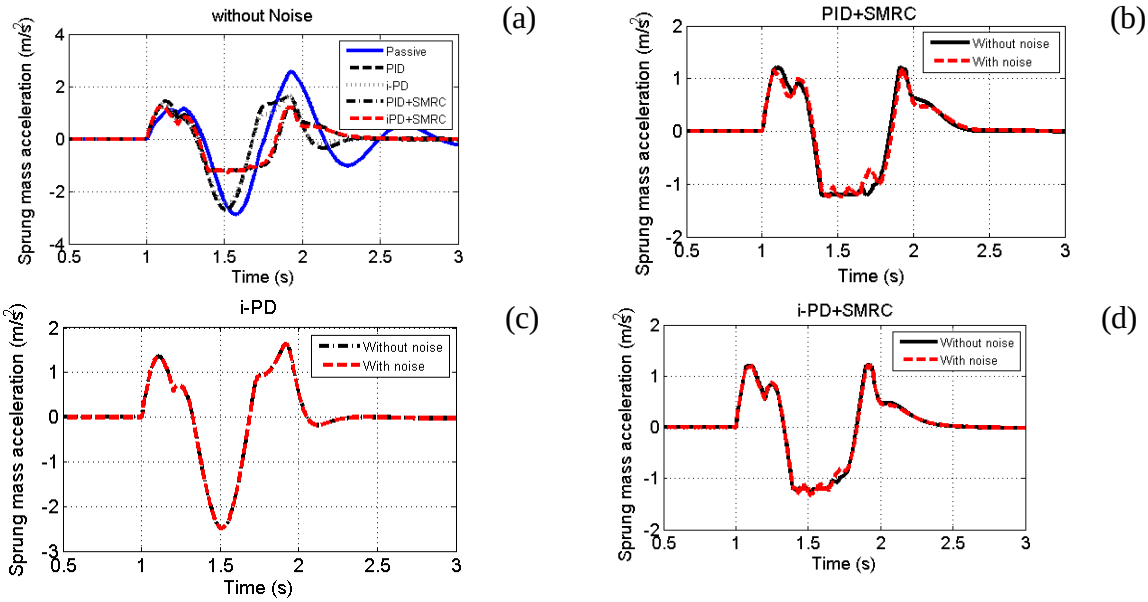

Figure 2. The car body acceleration with sensor default

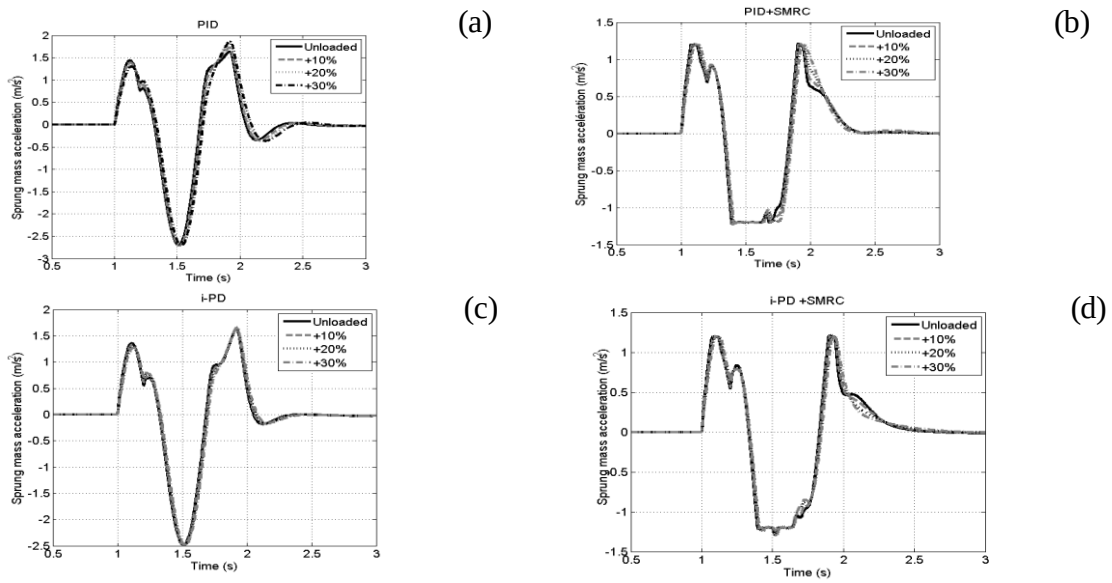

Figure 3. Variation of Body sprung mass

REFERENCES

[1] M.Haddar ,R.Chaari, S.C. Baslamisli, F. Chaari, and M. Haddar. Intelligent PD controller design for active suspension system based on robust model-free control strategy. *Proceedings of the Institution of Mechanical Engineers, Part C: Journal of Mechanical Engineering Science*, 2019.

[2] F.León-Vargas, F. Garelli, and M. Zapateiro.Limiting vertical acceleration for ride comfort in active suspension systems. *Proceedings of the Institution of Mechanical Engineers, Part I: Journal of Systems and Control Engineering*, 232(3), 223-232, 2018.

INVESTIGATING THE APPROXIMATION OF HIGHER-ORDER NONLINEAR BEHAVIOUR INTO NON-INTRUSIVE REDUCED-ORDER MODELS

A. J. Elliott[1*] and A. Cammarano[1]

[1]University of Glasgow
University Avenue, Glasgow, G12 8QQ, United Kingdom
[*]Email: a.elliott.1@research.gla.ac.uk

ABSTRACT

This study compares the implicit condensation and enforced displacement methods in terms of the way in which they approximate the effect of nonlinear behaviour for high displacement levels. These non-intrusive reduced-order methods are typically applied to commercial finite element software to approximate the calculations made by their nonlinear solvers. To overcome the fact that it is not possible to access the source code for these programmes, this paper uses quintic-order discrete and continuous Galerkin models as the "full" system. This allows the comparison of the polynomial coefficients in the reduced-order models with those in the full system, as well as the assessment of the manner in which these adapt to capture higher-order behaviour.

1 INTRODUCTION

The ability to quickly and accurately capture nonlinear vibrations continues to be an active area research, motivated by the development of increasingly lightweight and flexible mechanical structures. While it is possible to accurately model this behaviour using finite element (FE) software, the number of degrees-of-freedom (DOFs) required to do so can often be prohibitive. In particular, simulations can often take a number of days to run or require access to high-performance computing facilities. To overcome this, it is possible to produce a non-intrusive reduced-order model (NIROM), which applies a number of simpler cases in the FE software and approximates the nonlinear effects based on these results.

This work considers two leading NIROM techniques – namely, the implicit condensation (IC) [1] and enforced displacement (ED) [2] methods – and applies them first to a quintic-order discrete model, and then a quintic-order Galerkin model. The NIROM polynomial coefficients can then be compared directly with the full model in terms of how these adapt to account for variations in the magnitude of the nonlinearities. As such, this work can be considered as an extension of the analysis performed in [3].

2 NON-INTRUSIVE REDUCED-ORDER MODELLING TECHNIQUES

A full overview of the IC and ED methods can be found in [1] and [2], respectively. Of primary importance to the present study is the observation that the methodology of the two techniques is largely identical, with both applying a series of static cases so that the force-displacement relationship can be approximated using as a cubic polynomial. The mathematical expression for the n^{th} equation of these static cases is given by

$$\omega_n^2 q_n + \sum_{i=1}^{N}\sum_{j=1}^{N}\sum_{k=1}^{N} A_{ijk}^{(n)} q_i q_j q_k + \sum_{i=1}^{N}\sum_{j=1}^{N} B_{ij}^{(n)} q_i q_j = F_{q,n}, \tag{1}$$

where q_n denotes the displacement of the n^{th} mode, ω_n is the n^{th} natural frequency, $F_{q,n}$ is the n^{th} modal force, and N is the number of modes retained in the modal basis. The A and B coefficients are found via regression analysis of a number of static cases made up of modal displacements and forces. In the IC method, is the modal forces that are applied, with the resulting displacements outputted from the FE software, and vice versa for the ED technique. This difference in strategy results in similar static cases, but with the modal compositions differing between the two. The work of the following sections investigates the effect that this has on the results.

3 DISCRETE MODEL

The simplest implementation of higher-order terms can be achieved by introducing quintic terms to the cubic nonlinear springs that have been used in previous studies [3]. As such, the nonlinear force term is given by

$$\mathbf{F}_{\text{NL}}(\mathbf{x}) = k_3 \begin{pmatrix} (x_2 - x_1)^3 \\ -x_2^3 \\ 0 \end{pmatrix} + k_5 \begin{pmatrix} (x_2 - x_1)^5 \\ -x_2^5 \\ 0 \end{pmatrix}, \tag{2}$$

where k_3 and k_5 are constant coefficients. These can be projected onto the modal basis to give expressions of the form

$$F = \sum_{\rho_i+\rho_j+\rho_k=3} R^{(1)}_{\rho_i\rho_j\rho_k} q_i^{\rho_i} q_j^{\rho_j} q_k^{\rho_k} + \sum_{\rho_i+\rho_j+\rho_k+\rho_l+\rho_m=5} S^{(1)}_{\rho_i\rho_j\rho_k\rho_l\rho_m} q_i^{\rho_i} q_j^{\rho_j} q_k^{\rho_k} q_l^{\rho_l} q_m^{\rho_m} \tag{3}$$

where the R and S coefficients arise in the expression of the physical coordinates in terms of the modal coordinates.

In both methods, the magnitude of the static cases is left to the user. Figure 1 explores the accuracy of the model as this is varied. It can be observed that, when this coefficient is higher, the region over which the approximated backbone curve remains close to that of the full model is

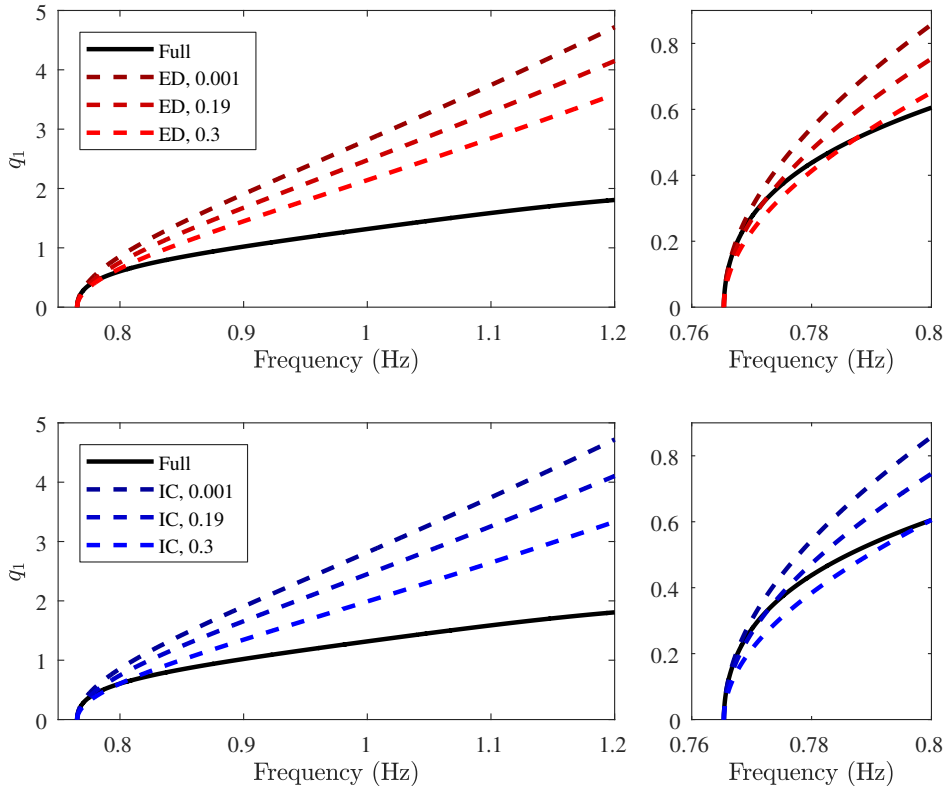

Figure 1: Backbone curves for the 3DOF spring-mass model, generated using the full model, as well as with the IC and ED methods.

extended. As such, it can be observed that both methods attempt to condense the effects of the quintic terms into the cubic coefficients. This is achieved to a greater extent in the IC method as a result of the displacement of membrane modes that is not present in the ED technique.
It must be further noted that the accurate replication of the cubic coefficients is actually seen to be detrimental for the accuracy of the backbone curve at higher amplitudes.

4 DISCRETE MODEL

This investigation is extended by the continuous Galerkin model for a pinned-pinned beam with a rotational spring at one tip, which has previously been observed to exhibit modal interactions [4]. The model is extended to include higher-order tension terms, as outlined in [5]. Figure 2 displays the backbone curves for a number of maximum static displacements and the condensation of the higher-order terms into the cubic coefficients can again be observed. While the observations regarding the fundamental component of the backbone curves remain true in this case, the inaccurate approximations generated using displacements of 10^{-1} and 1 highlight the importance of using realistic static cases.
The inset panel of Figure 2 demonstrates how the coefficients adapt to model the internal resonance tongue. It can be seen that, as the static displacement (and hence triggering of the modal interaction) is increased, the tongue moves towards the dashed grey line denoting the full model.

5 CONCLUSIONS

This paper presents a preliminary investigation of the implicit condensation and enforced displacement method through their application to analytical nonlinear systems, as opposed to those developed using commercial finite element software. A number of key observations have been made and are summarised as follows:

- The accurate recreation of full nonlinear coefficients by the NIROM does not guarantee an accurate reproduction of the response. In fact, this has proven to be detrimental to the prediction. This reassures the user that access to the nonlinear solvers of commercial FE packages

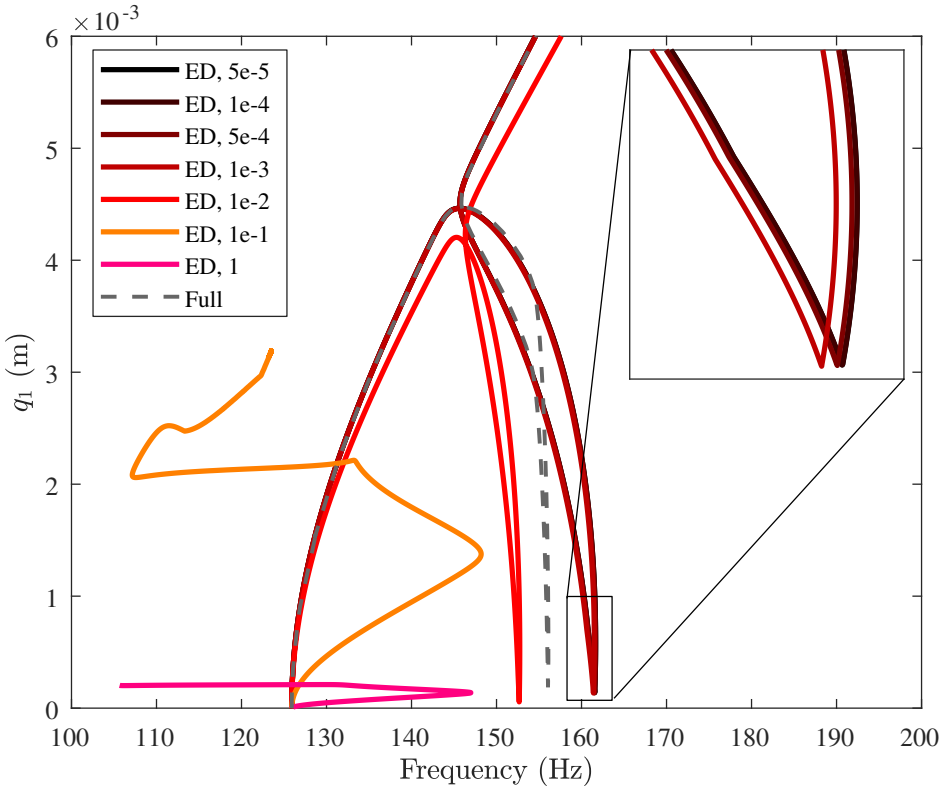

Figure 2: Backbone curves calculated by applying the ED method to the higher-order Galerkin model.

does not prohibit the development of accurate ROMs.

- Both techniques are observed to condense the effect of the higher-order terms into the cubic order polynomial approximation. This is more pronounced in the IC method, due to its triggering of membrane effects when modal forces are applied. This is consistent with observations made in a previous study [3], in which a cubic system was used as the full model. In this case, the ED coefficients were invariant to changes in the static displacements, whereas the IC method varied in a similar way to that observed in the current work.
- Variations in the coefficients are capable of improving the prediction of both the fundamental section of the backbone curve and of internal resonance tongues. Again, this can reassure the user of the potential of these techniques, though this is an area in which further investigation may prove useful.

REFERENCES

[1] M. I. McEwan, J. R. Wright, J. E. Cooper, and A. Y. Y. Leung. A combined modal/finite element analysis technique for the dynamic response of a non-linear beam to harmonic excitation. *Journal of Sound and Vibration*, 243:601–624, 2001.

[2] A. A. Muravyov and S. A. Rizzi. Determination of nonlinear stiffness with application to random vibration of geometrically nonlinear structures. *Computers and Structures*, 81:1513–1523, 2003.

[3] I. Tartaruga, A. J. Elliott, T. L. Hill, A. Cammarano, and S. A. Neild. The effect of nonlinear cross-coupling on reduced-order modelling. *International Journal of Non-Linear Mechanics*, 116:7–17, 2019.

[4] T.L. Hill, A. Cammarano, S.A. Neild, and D.A.W. Barton. Identifying the significance of nonlinear normal modes. *Proceedings of the Royal Society A*, 473, 2017.

[5] A. J. Elliott. Accurate approximations for nonlinear vibrations. PhD Thesis, 2019.

TOWARDS A COUPLED FLUID-STRUCTURE MODEL FOR SLUG FLOW IN A FLEXIBLE RISER

A.J. Elliott[1*], G. Hunt[1], A. Cammarano[1], and G. Falcone[1]

[1]University of Glasgow
University Avenue, Glasgow, G12 8QQ, United Kingdom
[*]Email: a.elliott.1@research.gla.ac.uk

ABSTRACT

This paper outlines the initial stages in the development of a coupled fluid-structure model for the prediction of hydrodynamic behaviour in a flexible riser. Initially, the two models will be considered separately, with the computational fluid dynamics analysed first and results applied to the solid structure separately. A discussion of the most appropriate outputs to stimulate the structural response is provided, considering the conversion of pressure fluctuations into forces and the assessment of frequencies in the variation of liquid hold up. The overall aim of this project is to develop fully-coupled model that can be used for the prediction of experimental results. The methodology presented in this paper offers a significantly lower computational cost than fully-coupled fluid-structure solvers and provides a faster platform to predict the system behaviour. These characteristics make this tool the perfect candidate to assess the influence of different parameters in the early stages of the design process and instruct the model selection by reducing the risk of undesired behaviour.

1 INTRODUCTION

While there exists an extensive list of potential multiphase flow regimes, it is the occurrence of slugging that is widely considered to have the highest destructive potential [1]. Despite the development of a number of modelling techniques for the treatment of this complex behaviour [2], the majority of the existing works mostly focus either on the fluid or on the structure behaviour, largely simplifying the remaining field. Such simplifications call for meticulous validation of the model accuracy through comparison with experimental data, but such experiments can be particularly costly due to the need for a closed-loop multiphase system capable of providing the specific set of flow parameters to accommodate slug flow. In particular, the structural response in flexible risers remains largely uninvestigated, leaving a great deal of uncertainty in the design process. This observation provides the motivation for the development of a coupled fluid-structure model capable of reproducing accurately the structural behaviour, and provide quantitative estimations of the force and displacement levels.

2 REPRESENTATIVE STRUCTURE

In this study, a slender, flexible riser is modelled numerically. Long pipes are required for the development of slug flow in computational fluid dynamics (CFD) models, and, to this end, the pipe comprised three sections: an initial 1 m horizontal section, a curved riser, and a vertical 1 m section. The curved riser was based on a quarter ellipse with major axis of 14 m and minor axis of 8.6 m. As such, the total length of the pipe was 10 m. The pipe has an interior diameter of 50 mm and wall thickness of 7 mm. Additionally, due to the asymmetric nature of slug flows – as well as their irregularity – it was required that the simulations were carried out using three-dimensional geometries.

Due to the interest in interaction at the surface between the multiphase flow and the solid enclosing pipe, an inflation zone of five layers was used in the generation of the mesh. The resulting mesh contained 487,888 elements and 198,254 nodes. A time-step of 10^{-3} s was chosen after a number of test simulations, as this was able to encapsulate the desired multiphase flow features while maintaining a reasonable computational load.

2.1 Mathematical modelling

The computational simulations have been performed using ANSYS Fluent, applying the volume of fluid (VOF) model and k-ϵ turbulence model.

2.1.1 Volume of fluid model

The volume of fluid model uses the assumption that there exist two or more fluids, which are not interpenetrating. Within the cells of the mesh all properties and variables are functions of the phase fractions (see ANSYS user guide). For the purpose of this study, two phases were used, one liquid and the other gas. The liquid and gas chosen for this are water and air respectively.

2.1.2 k-ϵ turbulence model

The k-ϵ turbulence model represents a compromise between numerical demands and stability, resulting in its extensive application in industry. Belonging to the two-equation eddy-viscosity turbulence type of model, there are many variants which are applied depending upon specific requirements. In the k-ϵ model, the k represents the turbulent kinetic energy and the ϵ is the turbulent dissipation term. Reynolds decomposition is applied to the various fields, splitting the instantaneous value into an average value and a value representing a fluctuation. Thus an additional set of two conservation equations are required to be solved to realise the Reynolds stresses.

3 RESULTS

3.1 Slug flow development

The key aim of this study is to assess the impact of slug flow on the vibrations of a flexible pipeline riser. Therefore, the initial step was the selection of flow parameters that lead to the development of hydrodynamic slugging in the riser. Advised by studies in the literature [2], the flow parameters were varied until slug flow was achieved.

Through the application of these conditions, it was possible to establish slugging in the test section, as can be observed in Figure 1. The first panel of Figure 1 show the gas volume fraction (GVF) of the developed slug flow, whereas the second panel displays the corresponding pressure values. It can be observed that the pressure is greatest at the tip of each gas slug, which will potentially lead to a pseudo-periodic forcing of the structure.

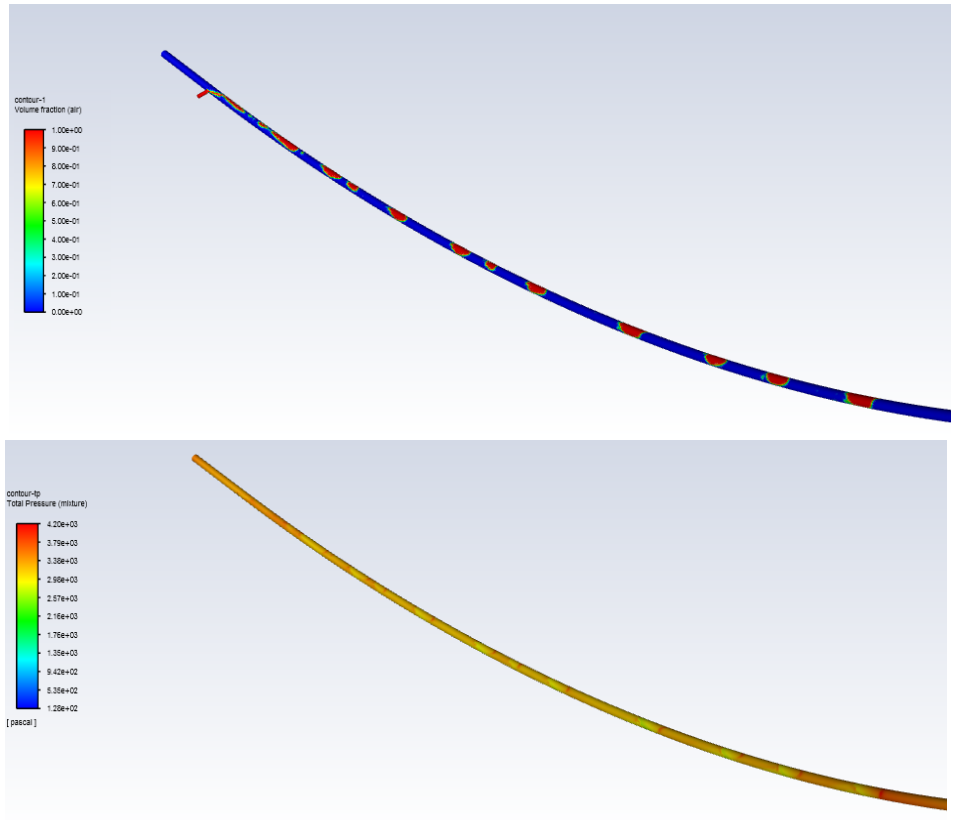

Figure 1. Visualisation of the developed slug flow in terms of GVF and pressure values.

3.2 Applying CFD outputs as structural excitation

There are a number of ways in which the outputs of the CFD model could be applied to a structural model without coupling, though the authors have identified to primary strategies. Of course, in the fully-coupled model, this would not be an issue, but the consideration of both of these cases will allow an examination of methods that may provide accurate results without the need for complex simulations. The two strategies identified are as follows:

- Pressure values can be recorded at the fluid-structure boundary and used to calculate the forces experienced in the solid structure. These can then be applied to a structural model with identical geometry.
- Variations in the GVF can be recorded and the frequencies of these can be extracted from the time history via Fourier transform. The structural model can then be periodically excited at these frequencies.

Naturally, there are positive and negative aspects to both of these methods. While the first gives a more direct representation of the fluid-induced forcing of the pipe, it can be computationally expensive. Alternatively, the second method provides useful insight without the explicit application of extensive time history data.

4 NEXT STEPS

As discussed above, the work presented here represents the initial steps towards the development and assessment of a coupled fluid-structure model that can be used to predict the structural response of an experimental flexible riser. The overall strategy, including both components that have been completed and additional steps, is summarised as follows:

- *Development of slug flow using CFD:* This provides an initial numerical case that can be adapted in the following steps.
- *Application of structural excitation methods:* The results of these can be compared in terms of their consistency and used to make initial suggestions for experiment design.
- *Development of coupled fluid-structure model:* The initial stages of this process allow the forces from the fluid flow to be directly inputted into the structural model at each time step. Subsequently, the influence of the structural response on the flow regime can also be added.
- *Application in experiment design:* The anticipated forces and displacements can be used to advise the design and measurement strategy of a real riser subjected to internal slug flow, taking into account the uncertainty related to the numerical predictions.
- *Comparison with experimental data:* The recorded data from the experimental setup can be used as a validation of the initial numerical predictions.
- *Updates to coupled model:* Where necessary, differences between the numerical and experimental results can be used to highlight areas in which the model is inaccurate. Appropriate updates to the model can then be applied.

5 CONCLUSIONS

This paper provides insight into the initial steps and overall strategy for the development of a methodology for predicting the vibration response of an experimental flexible riser subjected to internal slug flow. A CFD model for the development of slug flow in a representative structure has been presented. This has allowed the identification and measurement of a number of potential outputs that can be applied as an excitation for a solid finite element model. In particular, observed variations in the GVF and pressure provide a useful indication as to the nature of a potential pseudo-periodic forcing. The results presented here play an important role in the design of experimental rigs featuring interactions between slug flow and structural dynamics. In this work, in particular, they have been successfully used to outline a strategy for the development of the project.

REFERENCES

[1] M. A. Farghaly. Study of severe slugging in real offshore pipeline riser-pipe system. *Society of Petroleum Engineers*, 1987.

[2] V. Talimi, Y. S. Muzychka, and S. Kocabiyik. A review on numerical studies of slug flow hydrodynamics and heat transfer in microtubes and microchannels. *International Journal of Multiphase Flow*, 39:88–104, 2012.

UNSUPERVISED LEARNING ALGORITHM AND A SENSOR SWARM FOR STRUCTURAL HEALTH MONITORING OF A BRIDGE

N. Roveri[1], S. Milana[1], A. Culla[1], P. Conte[1] and A. Carcaterra[1]

[1]Department of Mechanical and Aerospace Engineering,
Sapienza, University of Rome, ITALY
Email: nicola.roveri@uniroma1.it, silvia.milana@uniroma1.it, antonio.culla@uniroma1.it,
conte.1660849@studenti.uniroma1.it, antonio.carcaterra@uniroma1.it

ABSTRACT

A Model-free approach to Structural Health Monitoring allows the damage detection without the needs of any a priori information about the response of the undamaged structure. The present paper proposes an unsupervised early-stage damage detection method, which relies on the combined application of the Principal Component Analysis, for features extraction and dimensionality reduction, and Symbolic Data Analysis, for automatically cluster different patterns. The structure considered is a Warren truss bridge, which is numerically simulated by a Finite Element Model, it is excited by a thermal cycle and a static load; the damage is modelled as a sudden reduction of the area of the section; vibration data are acquired on a number of sensors distributed over the whole structure. The validity of the proposed algorithm is numerically tested over one month of vibration data: the damage is properly identified by some PCAs, which show a sudden amplitude variation or a change of shape, in respect to the damage application; furthermore Symbolic Data Analysis allows an effective clustering of damaged and undamaged PCA samples. Robustness of the algorithm is tested at different noise level, timing of damage, damage position and depth, the influence of the sensors' number is also tested.

1 INTRODUCTION

Structural health monitoring (SHM) allows the real-time characterization of a structure in order to improve its safety and to optimise the maintenance procedures. The first issue in SHM is the early stage damage detection, which is generally carried out analysing vibration data coming from the monitored structure [1-5]. Several techniques employed in SHM are based on the determination of modal properties through an identification process [1-3], which imply the filtering of the signal that generally mask the damage signature in respect to the raw data. In addition, modal components are essentially describing an equivalent linear behaviour, which may be not exact for the analysis of damaged systems. To overcome the problem, several damage detection methods presented in recent years are based on signature principles, which generally require a time-frequency analysis of the acquired signal [4-5], they generally provide better performances regarding the early stage detection, however their results are still hard to be generalised in an automatic detection procedure when real life structures are considered. In addition, working with raw data imply to deal with large data sets, which makes the analysis process very demanding.

This paper draws inspiration by a research project between the department of Mechanical and Aerospace Engineering of Sapienza University of Rome and BASF Italy Spa, concerning an unconventional structural restoration of a train bridge, located over Bormida river, in northern Italy. Instead of using traditional steel bars reinforcements, Glass Fibers Reinforced Polymers are employed, with an embedded set of Fiber Bragg Grating (FBG) strain sensors for monitoring the structural health (SHM) of the reinforced existing structure. FBG sensors allow continuous acquisition and distributed sensing over significant areas, as a result, a huge amount of data is generated: this paper provides indeed a SHM algorithm, for the damage detection level 1 problem according to Rytter's classification, which involves data compression via Principal Component Analysis (PCA), to limit the dimensionality of the problem, and data clustering, by Symbolic Data Analysis (SDA), for an easy implementation of an automatic detection procedure. Furthermore, it is also investigated how the sensor number and locations affect the identification of the damage.

2 DAMAGE DETECTION ALGORITHM

Truss bridges are particular kind of bridge with its load-bearing structures composed of a series of wooden or metal triangles, known as trusses. The model here analysed is made up by one large span divided into 5 equilateral triangles. The system is numerically studied by FEM considering a number of sensors distributed over the structure.

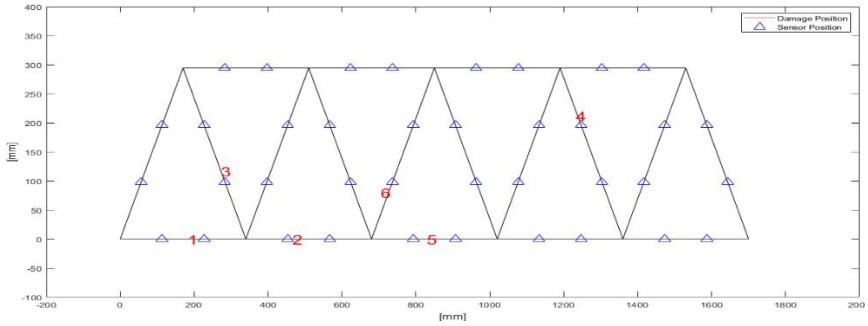

Figure 1. Sensor and Damage positions

The structure undergoes a punctual static load, applied in the second base chord and a thermal cycle, which varies from 15 degress to 40 degrees according to a sinusoidal distribution that simulate 24 hours in a typical summer day reaching the maximum temperature at 12pm. The presence of damage is simulated by a sudden cross section reduction, which goes from 1 to 30%, different damage positions are also studied. Numerical vibration data is also corrupted with white noise with zero mean and 1% rms. The numerical displacements of the sensors are processed by PCA, data are organized in

an *n* x *m* input matrix where rows are for the time samples and columns for the sensors. PCA is applied to the input matrix, producing another *n* x *m* matrix, where the Principal Components are organised in columns. The first PCAs are those with the largest variance and are related to the global *modal* properties of the structures, which are not sensitive to the damage presence, while the presence of damage is identified in some PCAs starting from the 5th. As an example, Figure 2 shows the 5th PC where the damage is located at the sudden amplitude jump. Please note that the 10th PC doesn't show any discontinuities in that time correspondence, however the damage presence is still detectable since the curve has different shapes before and after the damage occurs.

In order to enhance the performance provided by PCA and for an easy implementation of an automatic detection procedure SDA is also employed. One month data is considered: in the first 15 days the structure is intact, then the damage occur in the 16th day and remain damaged until the 31st day of the month. PCA is performed for each day and, for each PCA, a new input *d* x *m* matrix is generated, where rows are for different days and columns for time samples: each input matrix is then processed by k-means and hierarchical tree, which divide observations in a set of clusters.

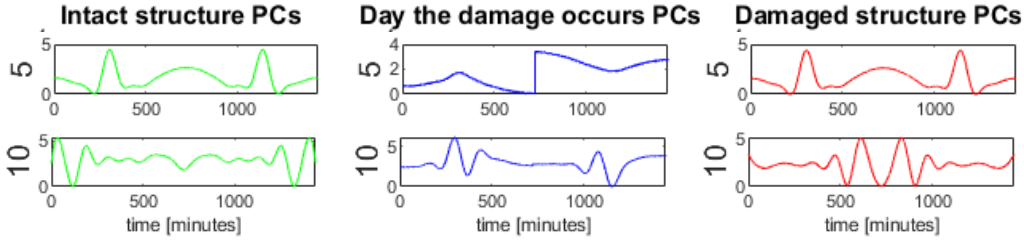

Figure 2. 5th and 10th PCs of a day structure is intact (green), the day damage occurs (blue) and a day structure is damaged (red).

3 RESULTS AND DISCUSSION

Many tests have been conducted in order to prove the robustness of the algorithm: different damage depth, location and time occurrence have been tested in order to prove that the method is not time depending: in each case it is possible to identify at least a Principal Component, for example the 5th, that shows a sudden jump that reveals the presence of the damage. This result is obtained independently of the noise level considered, whose rms ranges from 1% to 10%.

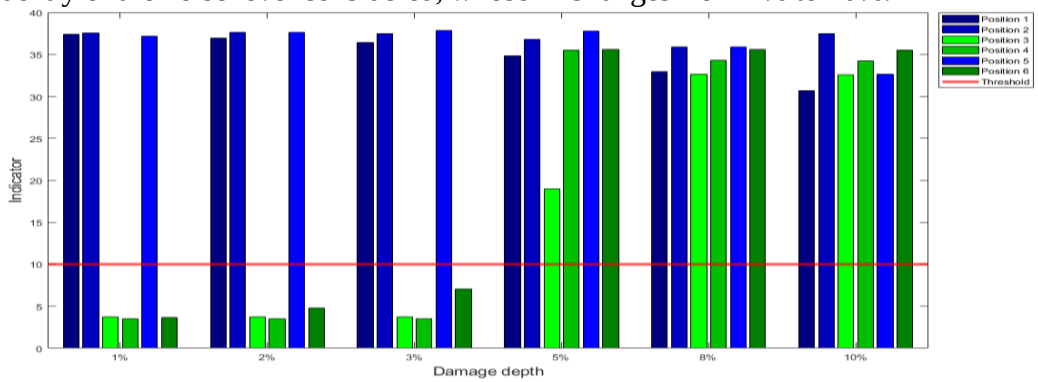

Figure 3. Damage indicator plotted versus the damage depth, for different damage positions.

With reference to the Figure 3, the algorithm achieves to detect damage until 1% of area reduction, when the section damaged is placed on the base of the truss and 5% of area reduction when it is placed on a lateral member. Below these values damage can be detected in higher PCs, i.e. 7th and 8th, but the procedure become less robust. Note that from 30% of damage intensity, also the firsts PC becomes sensitive to the damage presence. The influence of the sensor number is also considered: very good performances are obtained when at least one sensor per truss member is considered. On the other hand, if the number of sensors is low, i.e. much smaller than the total number of members, a positioning problem arise: damage is well detected only when there are sensors nearby.

Finally, the effect of SDA is described. With reference to Figure 4, clustering functions achieve to separate two different cluster when 5th PC is selected: cluster 2 separates the sample in the single day on which the damage occur, i.e. the 16th day, from the samples in cluster 1, which refers to other 1-15 and 17-31 days. When the 10th PC is selected three different groups arises: cluster 1 contains all the undamaged days labelled from 1 to 15, cluster 2 contains all the damaged days labelled from 17 to 31 and cluster 3 contains the day 16th on which the damage occurs.

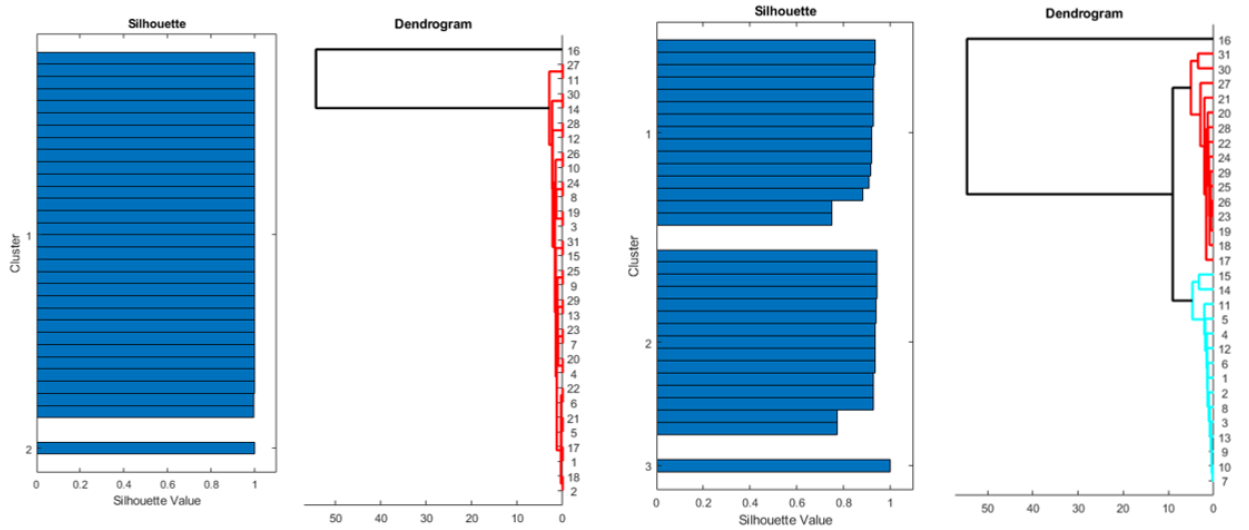

Figure 4. Silhouette and dendrogram of 5th PC selection (left) and 10th PC selection (right).

4 CONCLUSIONS

A novel technique for the early stage damage detection is here presented, which is based on the combinate use of PCA and SDA. The damage is properly identified by some PCAs which show a sudden amplitude variation, i.e. the 5th and the 6th, or a change of shape, i.e. the 10th, in respect to the damage application. The effect of the number of sensors has been also analysed, studying how PC are sensitive to the damage presence varying the number of the measurement points along the structure: very good performance are obtained when at least one sensor per truss member is considered, while if the number of sensors is much smaller than the total number of members, the damage is well detected only when there are sensors nearby. The application of SDA furtherly improves the performance provided by PCA and allows an automatic detection procedure: when the 10th PC is selected three different groups arises, separating the damaged and undamaged days and the day on which the damage occurs.

REFERENCES

[1] O. S. Salawu, Detection of structural damage through changes in frequency: a review, Eng. Struct. 1997; 19, 9, 718–723.

[2] S. W. Doebling, C. R. Farrar, M. B. Prime, A summary review of vibration-based damage identification methods, Shock Vib. Dig.; 30, 2, 91–105, 1998.

[3] C.R. Farrar, D.A. Jauregui, Comparative study of damage identification algorithms applied to a bridge: I. Experiment. Smart Materials and Structures; 7, 704–719, 1998.

[4] N. Roveri, A. Carcaterra. Unsupervised identification of damage and load characteristics in time-varying systems. Continuum Mechanics and Thermodynamics, 27.4-5: 531-550, 2015.

[5] N. Roveri, A. Carcaterra. Damage detection in structures under traveling loads by Hilbert–Huang transform. Mechanical Systems and Signal Processing, 28: 128-144, 2012.

WAVE PROPAGATION IN AN AIRCRAFT WING SLAT FOR DE-ICING PURPOSES

D. Raffaele[1*], T. P. Waters[1] and E. Rustighi[1]

[1]Institute of Sound and Vibration Research
University of Southampton, Highfield, Southampton SO17 1BJ, United Kingdom
Email: D.Raffaele@soton.ac.uk

ABSTRACT

Ice accretions on aircraft lifting surfaces must be removed in flight to avoid catastrophic accidents. Conventionally, this is done effectively but inefficiently by bleeding hot air from the engines prompting a number of low energy approaches to be explored that use high amplitude shock or vibration. One recently proposed method, which has so far been successfully implemented for a beam, generates a shock response at a target position by focusing elastic waves in time and space from a single actuator. However, prior knowledge of the dispersion characteristics of such waves is required.
In order to extend the applicability of the technique, this paper aims to predict the dispersion curves of waves propagating along the leading edge of a Boeing 737 wing slat. A semi-analytical finite element (SAFE) model is implemented in Comsol Multiphysics software. By assuming a spatially harmonic displacement field in the direction of propagation only the 2-D cross section of the waveguide needs to be meshed.
Dispersion curves are presented for the leading edge portion of the erosion shield under several assumed sets of boundary conditions. The dispersion curves are compared with measured results from laboratory tests conducted on the real wing slat and found to be in good qualitative agreement. The model will be further developed to predict interfacial shear stresses between the wing skin and accreted ice under transient loading.

1 INTRODUCTION

Wings and other aircraft lifting surfaces must be kept free from ice to maintain aerodynamic performance and controllability. Traditional methods of ice protection depend on aircraft size and include pneumatic de-icing boots, electro-thermal systems, glycol based fluid and bleed air. Each has its own drawbacks such as weight, cost, complexity, unreliability, high maintenance or power consumption. To overcome these difficulties a number of electromechanical de-icing concepts have been proposed over the years. They are low-energy solutions that use mechanical pulses or vibrations to break the bond between the ice accretion and the structure. An overview of the state-of-the-art can be found in [1].
Ultrasonic vibration methods, specifically for rotorcraft, have been pioneered by researchers from Pennsylvania State University, and these activities are summarised in [2]. The main limitations relate to the capacity of piezoelectric actuators to deliver sufficient force and, relatedly, the need to drive them at resonance causing them to heat up and crack. To circumvent this problem Waters proposed the use of transient, chirp excitations which achieve amplification through wave focussing instead of resonance [3]. This approach has been shown capable of delaminating an ice substitute from a beam [4]. Extension of this method to realistic wing structures requires prior knowledge of free wave propagation along the wing leading edge where ice accumulates in order to negate and even exploit the effects of wave dispersion.
For structures with complicated cross-sections dispersion curves must be found numerically. A method which is readily applicable to uniform waveguides is the semi analytical finite element (SAFE) method. In this paper, the SAFE method is used to model the leading edge of a Boeing 737 wing slat, the results of which are partially validated through laboratory experiments.

2 FREE WAVE PROPAGATION MODEL OF WING SLAT

The SAFE method assumes uniformity along the length of the waveguide. Whilst the Boeing 737 wing slat shown in Figure 1a-1b has periodic ribs these extend only as far as the forward spar, and so the aluminium erosion shield is modelled approximately as a uniform curved plate, as shown in Figure 1c. Its cross-section is approximately 80 by 100 mm with a skin thickness of 1.5 mm. Three different models were considered, with hinged, simply supported and clamped boundary conditions, as shown in Figure 2. In addition, three different meshes have been considered for each model: 45 linear elements, 180 linear elements and 180 quadratic elements.

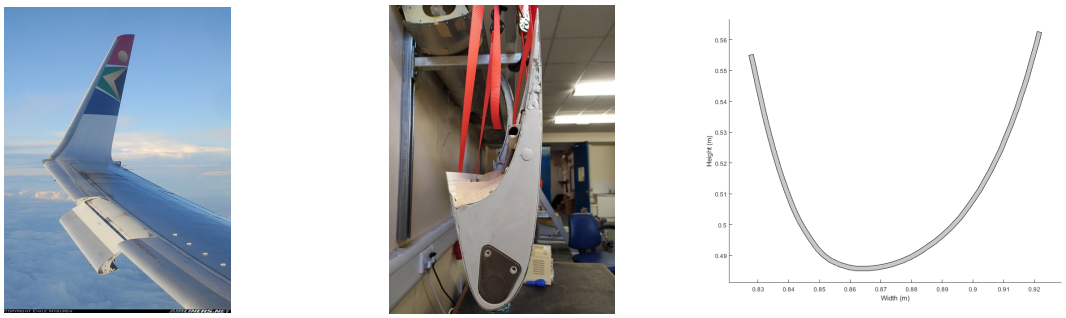

(a) (b) (c)

Figure 1: Boeing 737 wing slat: (a) leading edge slats on a Boeing 737. Image with kind permission of Emile Myburgh, (b) cross-section of the wing slat and (c) cross-section of the model.

The numerical results were obtained using COMSOL Multiphysics finite element software [5] and implementing the SAFE problem through its *Coefficient Form PDE Interface* as proposed in [6]. Dispersion curves in the form of wavenumber against frequency were obtained from the solutions of the eigenvalue problem yielded by the SAFE method for a set of frequencies from 0 to 10 kHz. The first four cut-off frequencies for the corresponding three models and three mesh configurations are reported in Table 1. Mesh convergence has not yet been achieved due to computational limitations, and a finer mesh will be required for future studies.

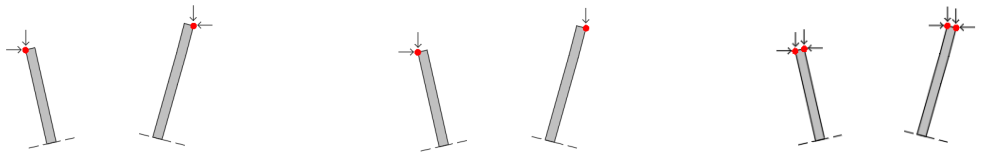

(a) Hinged (b) Simply supported (c) Clamped

Figure 2: Boundary conditions of the wing slat models: (a) hinged, (b) simply supported, and (c) clamped.

Boundary condition	Mesh	Cut-off frequencies (Hz)			
		1^{st}	2^{nd}	3^{rd}	4^{th}
Hinged	45 linear elements	513.13	1662.68	2935.83	4788.86
	180 linear elements	337.82	1100.31	1962.59	3226.41
	180 quadratic elements	239.18	788.21	1445.34	2429.59
Simply supported	45 linear elements	125.20	830.87	1922.02	3282.33
	180 linear elements	87.99	551.16	1256.68	2165.85
	180 quadratic elements	69.38	394.46	882.07	1551.95
Clamped	45 linear elements	832.48	2329.72	3961.79	5951.52
	180 linear elements	558.37	1541.84	2621.96	3998.57
	180 quadratic elements	418.46	1115.88	1901.71	2994.22

Table 1: First four cut-off frequencies of the wing slat models discretised by three different meshes.

3 EXPERIMENTAL VALIDATION

Vibration measurements were conducted on the 3.5 m long wing slat which was suspended by ratchet straps. One end was buried in a box of dry sand of tapered depth to provide some reduction of reflections. The wing slat was excited using a micro impulse hammer (PCB 086E80) and the acceleration was measured with a miniature accelerometer (PCB 352C22). Transfer function measurements were then acquired using a Data Physics Quattro spectrum analyser. In total, 26 accelerance transfer functions were measured, in the centre section of the wing to minimise contamination by near fields, with a spatial array of length 0.6 m and a sensor spacing of 0.025 m. The measurements were then repeated at a different chordwise position, slightly behind the stagnation point, to improve the possibility of sensing all wave types. Dispersion curves were then estimated from the transfer functions using the correlation method proposed in [7].
Figure 3 shows the estimated dispersion curves from the combined sets of transfer functions. Multiple branches are apparent corresponding to different wave types. Also shown are the predicted results from the SAFE model with 180 linear elements and simply supported boundary conditions. Whilst the mesh is not fully converged, these boundary conditions best replicate the measured cut-off frequencies at around 500 Hz, 1300 Hz, 3000 Hz and 6600 Hz.

4 CONCLUSIONS

A SAFE model of the leading edge of an aircraft wing slat has been implemented using commercial software to obtain dispersion curves of elastic propagating waves. There is qualitative agreement with measurements on a real slat from a Boeing 737 aircraft, notwithstanding the limited extent of the model.
In future work, the model will be extended to compute the forced response due to a chirp-like input waveform chosen to focus waves at a target position. An accretion will be added enabling interfacial stresses between the wing skin and accretion to be predicted.

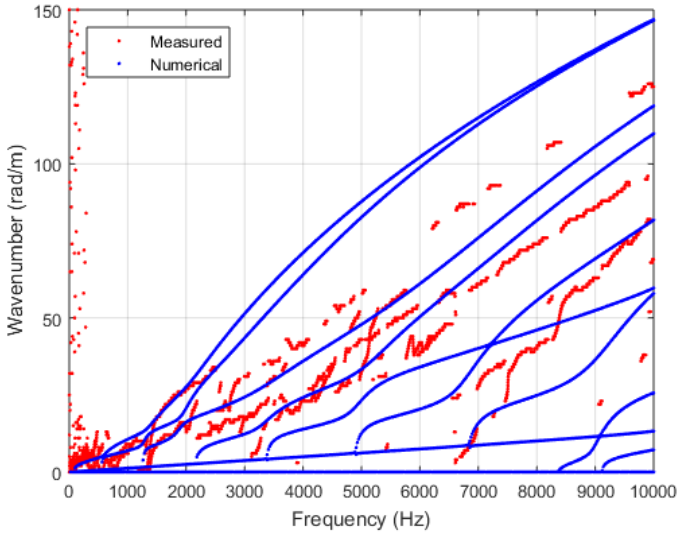

Figure 3: Measured and numerical dispersion curves for the simply supported wing slat model discretised by 180 linear elements.

ACKNOWLEDGEMENTS

The authors are grateful to Ultra Electronics PLC for their financial support and provision of the wing slat.

REFERENCES

[1] Z. Goraj. An overview of the deicing and antiicing technologies with prospects for the future. 24th International congress of the aeronautical sciences, 29, 2004.

[2] J. Palacios. A review of ultrasonic vibration for de-icing of aircraft. Internacional conference on Vibration and Vibro-acoustics, China, 2014.

[3] T. P. Waters. A chirp excitation for focussing flexural waves. Journal of Sound and Vibration, 439, pp. 113-128, 2019.

[4] T. P. Waters, P. Harris, H. Mulchandani, and I. Stothers. Focussing flexural waves for accretion removal from a beam. International Conference on Noise & Vibration Engineering (ISMA), 2018.

[5] COMSOL Multiphysics Reference Manual. Comsol ab. Stockholm, Sweden, 2018.

[6] M.V. Predoi, M. Castaings, B. Hosten, and C. Bacon. Wave propagation along transversely periodic structures. *The Journal of the Acoustical Society of America*, 121(4):1935–1944, 2007.

[7] N. S. Ferguson, C.R. Halkyard, B. Mace, and K.H. Heron. The estimation of wavenumbers in two-dimensional structures. *International Conference on Noise & Vibration Engineering (ISMA)*, pages 799–806, 01 2002.

TORSIONAL ENERGY FLOW THROUGH A TOUGH HYDROGEL VIBRATION ISOLATOR

L. Kari

The Marcus Wallenberg Laboratory for Sound and Vibration Research (MWL)
KTH Royal Institute of Technology, 100 44 Stockholm, SWEDEN
Email: leifkari@kth.se

ABSTRACT

The potential to use a tough hydrogel vibration isolator in a torsional energy flow noise abatement application is investigated. The tough, single, three-dimensional macro-molecule hydrogel network contains both chemical and physical cross-links; the former being permanent, covalent cross-links while the latter being temporary cross-links. It is possible to match the frequency for maximum loss factor for hydrogel shear modulus to the rigid body-resonance frequency of the vibration isolation system, resulting in a very low energy flow transmissibility peak as compared to that of an ordinary vibration isolation system. This feature is an important advantage since the rigid body-resonance frequency range is unwanted but often unavoidable for torsional axial excitation moment of the source. A possible extension is to control the energy flow transmission in a more realistic vibration isolation system by individually and adaptively tuning the frequencies of maximum loss factor of all including tough hydrogel vibration isolators in the system.

1 INTRODUCTION

Tough, doubly cross-linked, single network hydrogels concurrently containing both chemical and physical cross-links *e.g.* [1–10] are an interesting material not only for tissue engineering but also for noise abatement engineering. Those hydrogels contain permanent, covalently cross-linked (chemical cross-links) macro-molecules shaping a three-dimensional polymer network that are swollen with water and including additional temporary physical cross-links. It is possible to tune the frequency $f_{\max}$ for maximum loss shear modulus by choosing a distinct metal ion to adjust the kinetics and thermodynamics of the adhesion–deadhesion activity of the physical cross-links [6]. This conference paper investigates the potential to use vibration isolators made of tough, doubly cross-linked, single network hydrogels in torsional energy flow noise abatement applications.

2 MODEL

2.1 Torsional vibration isolator

Consider the torsional vibration isolator in Figure 1 of length l, radius a and density ρ, made of tough hydrogel and excited at one end ($z = 0$) by angular displacement

$$\hat{u}_\theta = \phi \mathrm{e}^{\mathrm{i}2\pi f}, \tag{1}$$

while being blocked at the other end ($z = l$). The torsional driving point and torsional transfer

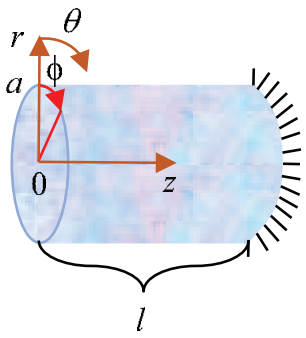

Figure 1: Torsional tough hydrogel vibration isolator of length l and radius a, excited at one end and blocked at the other end.

stiffness *e.g.* [11]

$$k_{\mathrm{D}} \overset{\mathrm{def}}{=} \frac{\hat{M}_\theta|_{z=0}}{\hat{u}_\theta|_{z=0}} = ka^4\hat{\mu}\,\frac{\pi}{2\tan(kl)} \tag{2}$$

and

$$k_{\mathrm{T}} \overset{\mathrm{def}}{=} \frac{\hat{M}_\theta|_{z=l}}{\hat{u}_\theta|_{z=0}} = ka^4\hat{\mu}\,\frac{\pi}{2\sin(kl)}, \tag{3}$$

respectively, where torsional wave number and wave velocity

$$k = \frac{2\pi f}{c} \text{ and } c = \sqrt{\frac{\hat{\mu}}{\rho}}, \tag{4}$$

i and $\hat{\mu}$ are imaginary unit and shear modulus, respectively.

2.2 Shear modulus

The shear modulus [10]

$$\hat{\mu} = \mu_\infty \frac{1 + (1 + \triangle)\sqrt{\mathrm{i}f/f_{\max}}}{1 + \sqrt{\mathrm{i}f/f_{\max}}}, \tag{5}$$

where μ_∞ is equilibrium shear modulus and $\triangle$ is stress relaxation intensity.

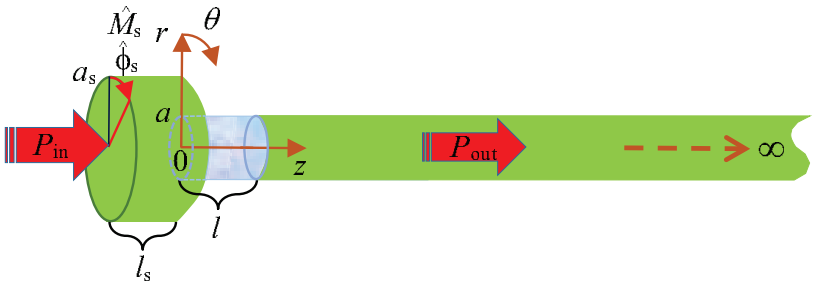

Figure 2: Torsional energy flow from a source via a hydrogel vibration isolator into a semi-infinite cylinder.

2.3 Energy flow

Consider the torsional source in Figure 2 modelled as a rigid cylindrical mass of length l_s, radius a_s, density ρ_s and axial torsional moment of inertia $J_s = \pi l_s \rho_s a_s^4/2$, excited by a torsional axial moment of $\hat{M}_s$ resulting in a angular displacement of $\hat{\phi}_s$. The time averaged energy flow in the system $P_{in} = \Re[\hat{M}_s \,\mathrm{conj}(2\pi \mathrm{i} f \hat{\phi}_s)]/2$ and out of the system $P_{out} = \Re[(k_T\hat{\phi}_s - k_D\hat{\phi}|_{z=l})\,\mathrm{conj}(2\pi \mathrm{i} f \hat{\phi}|_{z=l})]/2$, where $\mathrm{conj}(\cdot)$ denotes complex conjugate of $(\cdot)$ and $\Re$ denotes real part.

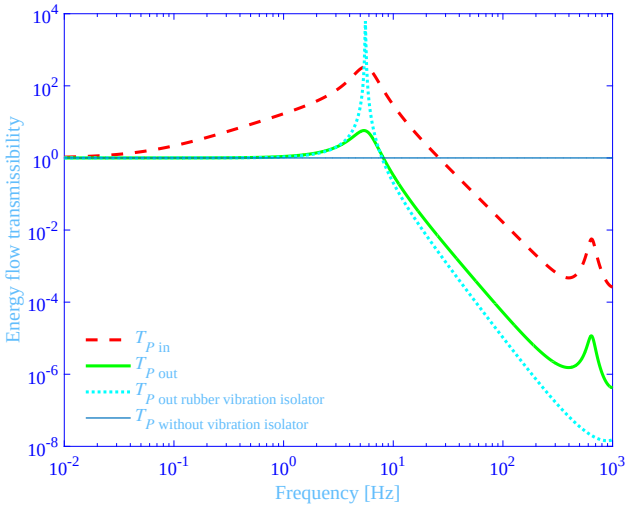

Figure 3: The energy flow transmissibility into the semi-infinite cylinder $T_{P\,out}$ and into the isolator $T_{P\,in}$ versus frequency together with corresponding result $T_{P\,without\,vibration\,isolator}$ as a reference and that of an ordinary vibration isolation system $T_{P\,out\,rubber\,vibration\,isolator}$.

3 RESULTS

The energy flow transmissibility into the semi-infinite cylinder $T_{P\,out} = P_{out|\mathfrak{with}}/P_{out|\mathfrak{without}}$ and into the isolator $T_{P\,in} = P_{in|\mathfrak{with}}/P_{in|\mathfrak{without}}$ are shown in Figure 3 versus frequency, where subscript are $\mathfrak{with}$ and $\mathfrak{without}$ vibration isolator. Data used are $l = 0.01\,\mathrm{m}$, $a = 0.006\,\mathrm{m}$, $\rho = 1000\,\mathrm{kg/m^3}$, $\mu_\infty = 20\,\mathrm{kN/m^2}$, $\triangle = 9$, $f_{max} = 60\,\mathrm{Hz}$, $l_s = 0.005\,\mathrm{m}$, $a_s = 0.02\,\mathrm{m}$, $\rho_s = 7800\,\mathrm{kg/m^3}$ and $\mu_{cyl} = 80\,\mathrm{GN/m^2}$. Furthermore, the energy flow transmissibility $T_{P\,without\,vibration\,isolator}$ without vibration isolator is shown as a reference. Clearly, energy flow transmissibility is close to one in the low-frequency region, peaking at the rigid body-resonance frequency and is diminishing rapidly with frequency above that resonance frequency. It is in this frequency range, well above the rigid body-resonance frequency, where vibration isolation is effective ($T_{P\,out} \ll 1$). The transmissibility peak in the high-frequency range is due to an internal anti-resonance in the vibration isolator. The energy flow transmissibility into the vibration isolator is in general substantially higher than the corresponding flow into the semi-infinite cylinder, in average 127 times higher; thus, showing that vibration damping is present in addition to vibration isolation. Finally, the hydrogel isolator

is substituted with a standard isolator of identical length $l = 0.01\,\mathrm{m}$, made of natural rubber with material properties from Ref. [12] and where the radius is adjusted ($a = 0.0031\,\mathrm{m}$) to result in approximately the same rigid body–resonance frequency as above. Clearly, the energy flow transmissibility peak into the semi-infinite cylinder for $T_{P\,\mathrm{out\,rubber\,vibration\,isolator}}$ is more than 1000 times higher for ordinary isolator than that of the hydrogel isolator. Not surprising as the loss factor peak for hydrogel ($45\,\%$) is adjusted to be approximately at the rigid body-resonance frequency $6\,\mathrm{Hz}$ $= f_{\max}/(\triangle + 1)$ being ($6.4\,\%$) for the ordinary isolator at the same frequency. The adaptively high damping at the rigid body-resonance frequency for hydrogel vibration isolator is an important advantage as this frequency range for torsional axial excitation moment of the source is unwanted but often unavoidable.

4 EXTENSION

An interesting extension of this conference paper is to the control energy flow transmission in a more realistic vibration isolation system by individually and adaptively tuning the frequencies $f_{\max}$ for maximum loss shear modulus of all including tough hydrogel vibration isolators in the system.

REFERENCES

[1] W. C. Lin, W. Fan, A. Marcellan, D. Hourdet, and C. Creton. Large strain and fracture properties of poly(dimethylacrylamide)/silica hybrid hydrogels. *Macromolecules*, 43:2554–2563, 2010.

[2] K. Mayumi, A. Marcellan, G. Ducouret, C. Creton, and T. Narita. Stress–strain relationship of highly stretchable dual cross-link gels: Separability of strain and time effect. *ACS Macro Lett.*, **2**:1065–1068, 2013.

[3] S. Rose, A. Dizeux, T. Narita, D. Hourdet, and A. Marcellan. Time dependence of dissipative and recovery processes in nanohybrid hydrogels. *Macromolecules*, 46:4095–4104, 2013.

[4] R. Long, K. Mayumi, C. Creton, T. Narita, and C. Y. Hui. Time dependent behavior of a dual cross-link self-healing gel: Theory and experiments. *Macromolecules*, 47:7243–7250, 2014.

[5] R. Long, K. Mayumi, C. Creton, T. Narita, and C. Y. Hui. Rheology of a dual crosslink self-healing gel: Theory and measurement using parallel-plate torsional rheometry. *J. Rheol.*, 59:643–665, 2015.

[6] S. Czarnecki, T. Rossow, and S. Seiffert. Hybrid polymer-network hydrogels with tunable mechanical response. *Polymers*, 8:82, 2016.

[7] J. Guo, R. Long, K. Mayumi, and C. Y. Hui. Mechanics of a dual cross-link gel with dynamic bonds: Steady state kinetics and large deformation effects. *Macromolecules*, 49:3497–3507, 2016.

[8] J. Zhao, K. Mayumi, C. Creton, and T. Narita. Rheological properties of tough hydrogels based on an associating polymer with permanent and transient crosslinks: Effects of crosslinking density. *J. Rheol.*, 61:1371–1383, 2017.

[9] M. Liu, J. Guo, C. Y. Hui, C. Creton, T. Narita, and A. Zehnder. Time–temperature equivalence in a pva dual cross-link self-healing hydrogely. *J. Rheol.*, 62:991–1000, 2018.

[10] L. Kari. Effective visco-elastic models of tough, doubly cross-linked, single network polyvinyl alcohol (pva) hydrogels— additively separable fractional derivative based models for chemical and physical cross-links. *Continuum Mech. Thermodyn.*, Submitted, 2019.

[11] L. Kari. Torsional wave propagation in tough, rubber like, doubly crosslinked hydrogel. In *Constitutive Models for Rubber X*, pages 423–426, Leiden, The Netherlands, 2017. CRC Press/Balkema.

[12] L. Kari, P. Eriksson, and B. Stenberg. Dynamic stiffness of natural rubber cylinders in the audible frequency range using wave guides. *Kaut. Gummi Kunstst.*, 54:106–111, 2001.

ACTIVE OPTIMAL CONTROL FOR FLUTTER IN SUSPENSION BRIDGES

E. Paifelman[1*], G. Pepe[2] and A. Carcaterra[2]

[1]Institute of Marine Engineering, National Research Council of Italy INM-CNR
Rome, Italy
Email: elena.paifelman@inm.cnr.it

[2]Sapienza University of Rome
Rome, Italy
Email: gianluca.pepe@uniroma1.it, antonio.caraterra@uniroma1.it

ABSTRACT

Long-span suspension bridges are characterized by a high bending-torsional slenderness. Such high compliance together with the high width-to-depth ratio of the typical boxed, sharp-edge, deck cross sections emphasize the dynamic effects of the aerodynamic loads ensuing from wind-structure interaction. Thus, when subject to severe wind excitations, suspension bridges may be affected by dynamic instability phenomena, such as flutter or galloping, that can be damaging to the in-service limit states and, in extreme cases, can also lead to the failure of the structure.
The mitigation strategies of such instabilities principally make use of passive control systems (i.e: nonlinear vibration absorbers) that improve the aerodynamic stability of bridges. In this work, authors propose a novel active optimal control algorithm for the minimization of flutter instabilities. The aerodynamic nonlinearities are described by the quasisteady aerodynamic theory, originally formulated for thin airfoils by Theodorsen, which is a typical section for a suspended bridge. This fluid-structure interaction problem is represented by integro-differential equation of motion in the time domain. Optimal control problems governed by integral-differential equations (IDEs) have been a major research topic in applied mechanics and control theory. Authors propose a novel indirect variational optimal control method applied to IDEs which is an extension of the Pontryagin theory normally applied to differential equations and also its feedback extension via model predictive control (integral MPC). Numerical results show how the integral MPC is able to totally control the flutter instabilities. Moreover, the novel algorithm shows better results than standard LQR control method in term of minimization of the cost function.

1 INTRODUCTION

This paper proposes a novel optimal control method for the control of flutter instabilities in suspension bridges. The typical bridge cross-section can be modelled as an elastic airfoil moving in the flow field with integro-differential mathematical counterpart.
Normally, the control strategies of such instabilities principally make use of passive control systems (i.e: nonlinear vibration absorbers) that improve the aerodynamic stability of bridges. In this work, proposes a novel active optimal algorithm consists in the formulation of the Pontryagin's theory for IDEs model and its feedback extension via model predictive control (MPC). The proposed integral MPC has been already formulated by the authors for the vibrations control of autonomous underwater vehicles [1, 2].

2 MATHEMATICAL MODEL OF TYPICAL BRIDGE SECTION

Theodorsen's airfoil model [3] for this problem is employed to achieve the mathematical model of the typical bridge transversal section. This theory provide the generalized unsteady aerodynamic forces due to an arbitrary motion of the airfoil. The airfoil is a simple two degree-of-freedom

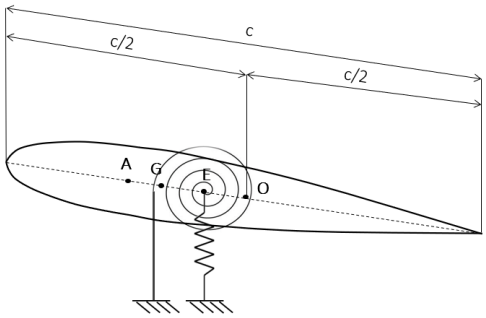

Figure 1. Elastic airfoil model: bridge typical transversal section

system, elastically constrained by a pair of translational and torsional equivalent linear springs, oscillating in plunge (υ) and pitch (α) as Figure 1 shows. The elastic axis, *E*, is located at a distance $OE = a_h c/2$ from the mid-chord, while the mass center, *G*, is located at a distance $EG = x_\alpha c/2$ from the elastic axis. The aeroelastic equations of the typical section are:

$$\begin{cases} \ddot{\upsilon} + x_\alpha \ddot{\alpha} + \Omega^2 \upsilon + (\ddot{\upsilon} - a_h \ddot{\alpha} + U\dot{\alpha})\dfrac{1}{\mu} + \dfrac{2U}{\mu} K_W(t) * \dot{w}(t)_{3/4} = 0 \\ \dfrac{x_\alpha}{r_\alpha^2}\ddot{\upsilon} + \ddot{\alpha} + \alpha - [a_h(\ddot{\upsilon} - a_h\ddot{\alpha}) + \dfrac{1}{2}U(1-a_h)\dot{\alpha} - \dfrac{1}{8}\ddot{\alpha}]\dfrac{1}{\mu r_\alpha^2} + \dfrac{U(1+2a_h)}{\mu r_\alpha^2} K_W(t) * \dot{w}(t)_{3/4} = 0 \end{cases} \tag{1}$$

where $\Omega = \omega_\upsilon/\omega_\alpha$, being ω_υ and ω_α the uncoupled natural frequencies of heave and pitch modes, respectively; $r_\alpha = \sqrt{4J/mc^2}$ is the dimensionless radius of gyration about the elastic axis; $\mu = \pi\rho c^2/4m$ is the mass ratio, $w_{3/4}(t)$ is the downwash, $K_W(t)$ is the Wagner function [4], $U = 2V/c\omega_\alpha$ the dimensionless inflow velocity and *V* is the inflow velocity, oriented along the x-axis. The integral terms represent the circulatory part of the lift, due to the wake generation.
Using the property of the convolution, the system in state-space matrix form becomes:

$$\dot{\mathbf{x}} = \mathbf{A}\mathbf{x} + \mathbf{\Sigma}(\mathbf{t}) * \mathbf{x} + \mathbf{b}\mathbf{u} \tag{2}$$

where the new state vector is $\mathbf{x} = \{\mathbf{x_1}, \mathbf{x_2}\}^\mathbf{T} = \{\mathbf{q}, \dot{\mathbf{q}}\}^\mathbf{T}$ and $\mathbf{q} = \{\upsilon, \alpha\}^\mathbf{T}$; $\mathbf{A}$ is the dynamical matrix, $\mathbf{\Sigma(t)}$ the convolution matrix and u is the control variable. Equation (2) is completed with the initial conditions $\mathbf{x}(\tau)$=$\mathbf{x_0}(\tau)$, $\tau \in (-\infty, t]$.

3 INDIRECT VARIATIONAL METHOD FOR IDES & MODEL PREDICTIVE FEEDBACK FORMULATION

The presence of integral-differential equations of motion requires a nonstandard optimal control startegy.
The cost function of the variational optimal control problem is described by the quadratic functional $\widetilde{J}$, and the optimal control problem is stated as:

$$\begin{aligned} &min\ \widetilde{J} = \int_{-\infty}^{T_f} \frac{1}{2}\mathbf{x^T Q x} + \mathbf{\frac{1}{2}u^T r u}\ \mathbf{dt} \\ &\text{subjected to} \\ &\mathbf{\dot{x} = Ax + \Sigma(t) * x + bu} \end{aligned} \tag{3}$$

where $\mathbf{Q}$ and r are the gain parameters. Introducing the Lagrange multiplier vector λ and minimizing the functional J in terms of the variations $\delta\mathbf{x}$, $\delta\dot{\mathbf{x}}$, $\delta\lambda$, $\delta\mathbf{u}$, the Euler-Lagrange associated system is founded as follow:

$$\begin{cases} \dot{\lambda} = \mathbf{Qx - A^T}\lambda - \displaystyle\int_{\mathbf{t}}^{\mathbf{T_f}} \mathbf{\Sigma^T}(\tau - \mathbf{t})\lambda(\tau)\ \mathbf{d}\tau \\ \mathbf{\dot{x} = Ax + br^{-1}b^T}\lambda + \displaystyle\int_{-\infty}^{\mathbf{t}} \mathbf{\Sigma(t-\tau)x}(\tau)\ \mathbf{d}\tau = \mathbf{0} \\ \mathbf{x}(\tau) = \mathbf{x_0}(\tau),\ \tau \in (-\infty, \mathbf{t}] \\ \lambda(\mathbf{T}) \end{cases} \tag{4}$$

where the control law is $\mathbf{u = r^{-1}b^T}\lambda$. Equations (4) are solved by applying implicit forward finite differences technique and solving the discrete matrix solution which follows:

$$\left\{ \begin{array}{c} \chi_{\mathbf{x}}^{(\mathbf{1,N})} \\ \chi_{\lambda}^{(\mathbf{0,N-1})} \end{array} \right\} = \mathbf{\Omega}^{(\mathbf{0,N-2})^{-1}} \mathbf{\Lambda}^{(\mathbf{0,N-1})} \left\{ \begin{array}{c} \zeta_{\mathbf{x}}^{(\mathbf{0})} \\ \mathbf{0} \end{array} \right\} \tag{5}$$

where the vector of unknowns is $\{\chi_{\mathbf{x}}^{(\mathbf{1,N})}, \chi_{\lambda}^{(\mathbf{0,N-1})}\}^{\mathbf{T}}$, $\chi_{\mathbf{x}}^{(\mathbf{1,N})}$=$\{\mathbf{x_1}, ..., \mathbf{x_i}, ..., \mathbf{x_N}\}^{\mathbf{T}}$, $\chi_{\lambda}^{(\mathbf{0,N-1})}$=$\{\lambda_\mathbf{0}, \lambda_\mathbf{1}, ..., \lambda_\mathbf{i}, ..., \lambda_{\mathbf{N-1}}\}^{\mathbf{T}}$, where *(N,M)* indicates dependence on the time values of t_i for $i \in [N, M]$. Analogusly, $\{\zeta_{\mathbf{x}}^{(\mathbf{0})}, \mathbf{0}\}^{\mathbf{T}}$ where $\zeta_{\mathbf{x}}^{(\mathbf{0})}$=$\{\mathbf{x_0}\}$. Equation (5) reveals that the system response depends only on the initial condition of the system giving an open loop solution. In order to found a feedback solution of the optimal control problem, a model predictive control strategy has been formulated. The MPC strategy does not implies the use of the complete solution shown before, but we use only the first output for $\mathbf{u}$, associated at the time $t = t_0$, to which is also associated the first output for the state at the time $t = t_1$. We can iterate this process and at the generic *k-th* step one obtains:

$$\left\{ \begin{array}{c} \chi_{\mathbf{x}}^{(\mathbf{k,N})} \\ \chi_{\lambda}^{(\mathbf{k-1,N-1})} \end{array} \right\} = \mathbf{\Omega}^{(\mathbf{k-1,N-2})^{-1}} \mathbf{\Lambda}^{(\mathbf{k-1,N-1})} \left\{ \begin{array}{c} \zeta_{\mathbf{x}}^{(\mathbf{0,k-1})} \\ \zeta_{\lambda}^{(\mathbf{0,k-2})} \\ \mathbf{0} \end{array} \right\} \tag{6}$$

4 NUMERICAL SIMULATIONS & CONCLUDING REMARKS

Different numerical simulation have been performed to test the proposed integral MPC method in order to minimize the instable behaviour of a suspended bridge, when it is in flutter condition, by controlling the 2-dof of its typical transversal section. Specif dynamic and geometrical parameters have been chosen and the algorithm has been applied to the IDE model at the flutter velocity $V_f = 0.1m/s$ and it has been compared with the standard LQR method. In particular, Figure 2 shows the evolution in time of the displacement and velocity of both degree-of-freedom (heave and pitch) when the airfoil is in the flutter condition ($u = 0$, green line), when the integral MPC is controlling the system (blue line) and the respective results when the LQR is applied (red line). It is evident

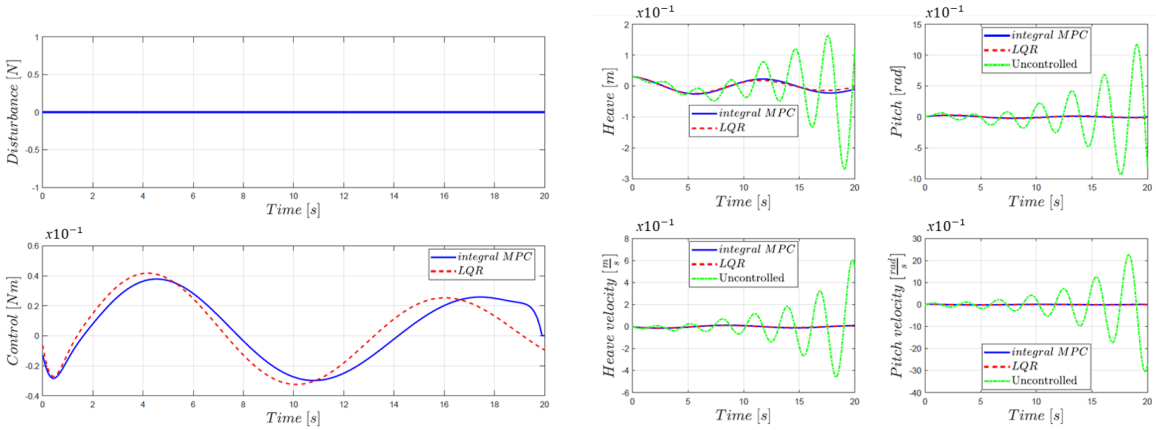

Figure 2: Right: System disturbances, control law: integral MPC vs LQR; Left: Pitch & Heave displacement and velocity: flutter condition vs controlled system (integral MPC vs LQR)

that the integral MPC succeded in the total control of the airfoil flutter instabilities. Moreover, Figure 3 reports the values of the objective function J computed in different simulations in which external random disturbances are acting on the system. At increasing level of standard deviation σ, the integral MPC presents better results than LQR method in terms of minimization of J, as required by the statement of the optimal problem in equation (3).

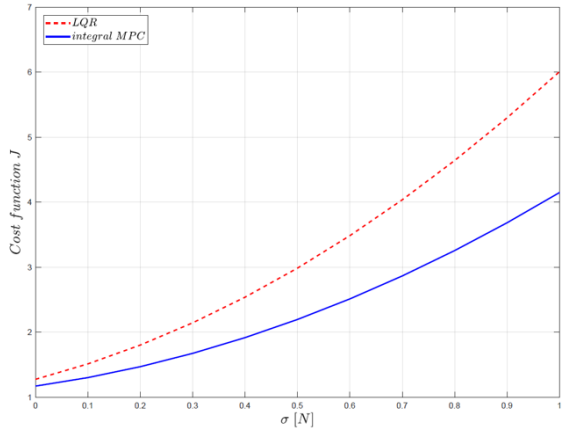

Figure 3: Cost function J value in presence of external random disturbances: integral MPC vs LQR

REFERENCES

[1] Elena Paifelman, Gianluca Pepe, Francesco La Gala, and Antonio Carcaterra. Control of fluctuations of a tethered unmannedunderwater- vehicle. In *ISMA 2018 Proceedings*, 2018.

[2] E. Paifelman, G. Pepe, and A. Carcaterra. An optimal indirect control of underwater vehicle. *International Journal of Control*, pages 1–27, mar 2019.

[3] T. Theodorsen. *General theory of aerodynamic instabilities and the meccanism of flutter*, volume 496. Naca report, 1935.

[4] R.T. Jones. *The unsteady lift of a wing of finite aspect ratio*, volume 681. Naca report, 1940.

RESONANT STOP BAND ANALYSIS USING AN INHOMOGENEOUS RE-ENTRANT HONEYCOMB CORE STRUCTURE

M.A. Campana[1*,2,3] , M. Ouisse[3], E. Sadoulet-Reboul[3], F. Scarpa[1,2]

[1]Bristol Composites Institute
University of Bristol, Bristol BS8 1TR, UK
Email: mc16271@bristol.ac.uk, f.scarpa@bristol.ac.uk

[2]Dynamics and Control Research Group (DCRG), Civil, Aerospace and Mechanical Engineering (CAME)
University of Bristol, BS8 1TR Bristol, UK

[3]Univ. Bourgogne Franche-Comte, FEMTO-ST Department of Applied Mechanics, CNRS/UFC/ENSMM/UTBM
Besancon 25000, FR
Email: morvan.ouisse@femto-st.fr, emeline.sadoulet-reboul@univ-fcomte.fr

ABSTRACT

Different ways to analyse the role of resonators for a vibroacoustic control taking a re-entrant unit cell as an hosting structure is done using classical WFEM tools. The core of the structure is analysed using the Floquet-Bloch theorem and resonators are added to the structure to understand the physical impact they bring in the case of a complex and inhomogeneous 3D structure. A parametric analysis on the resonator using a modified version of the Transfer Matrix Method is used to get the frequency responses of the finite structure to quickly identify the resonant stop bands. The 2D inverse WFEM is performed to analyse the type of waves travelling through the structure in order to understand how to improve the vibroacoustics performances by tuning the resonators keeping a constant mass to the overall system.

$\rho\ [kg.m^{-3}]$	1040	L [mm]	6	$\rho_R\ [kg.m^{-3}]$	variable	L_r [mm]	$\sqrt{3}L$
E [GPa]	8.1	t [mm]	0.3	E_R [GPa]	E	b_r [mm]	1.33
ν	0.2	h [mm]	10	ν_R	ν	h_r [mm]	0.3

Table 1. Standard material and geometrical properties of the unit cell considered

1 INTRODUCTION

Classical studies involving resonator analyses for wave propagation control are mainly done using the support of discrete systems or homogeneous structures like simple beams [1] or plates [2]. Under those considerations, wave propagation analyses involving resonant system can lead to straightforward studies for the stop bands location and width thanks to their relation with the resonators eigenfrequencies. An approximate equation can also be used to determine the values of the boundaries of the band gap with a simple 1D discrete resonant system using the properties of the negative mass effect [3]. However, for inhomogeneous structures like honeycombs, the resonator and the core of the hosting structure are coupled, meaning that the relation between the eigenfrequency of the resonator and the location/width of the resonant band gaps no longer exists. In addition, waves related to the hosting structure are also present and can disturb the system leading to a loss of efficiency of the resonators. The research shows an example where such a case is occurring, and a solution to move the resonant stop band from an obstructive wave in order to get the full efficiency of the resonator in a inhomogeneous 3D hosting structure is suggested.

2 UNIT CELL MODEL AND SIMULATION TOOLS

2.1 Unit Cell model

A re-entrant honeycomb including resonators represented by simple thin plates attached from one side to the other side of the core is considered as a unit cell in this study. The shape of the unit cell is shown Fig. 1 and the geometrical and material properties associated are presented table 1. E, ρ and ν represent respectively the density, the Young Modulus and the Poisson's ratio of the hosting structure while E_r, ρ_R and ν_R relate to the resonators. The finite element model software used to create the unit cell is ANSYS APDL and the type of elements considered are shell181.

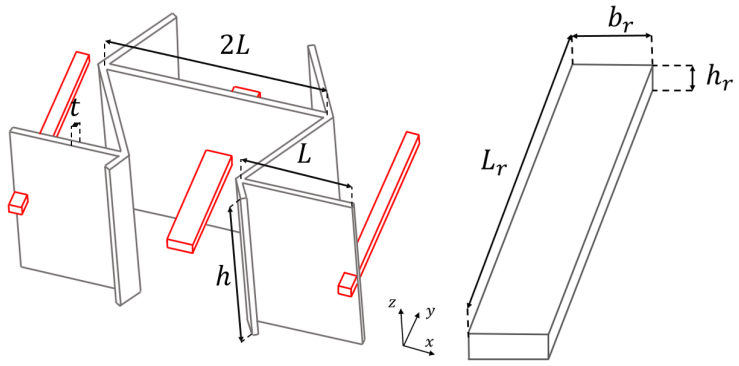

Figure 1. Unit cell and resonator geometrical parameters

2.2 Simulation tools

Floquet-Bloch theorem is applied to the unit cell performing the inverse WFEM for two-dimensional periodic structures. Floquet boundary conditions linking the sides of the unit cell are written under the following form :

$$q_R = e^{j\mu_x} q_L,\ q_T = e^{j\mu_y} q_B \tag{1}$$

Segment	$[O-A]$	$[A-B]$	$[B-C]$	$[C-O]$
μ_x	[0, π]	π	[π, 0]	0
μ_y	0	[0, π]	π	[π, 0]

Table 2. Values of μ_x and μ_y for the dispersion contour

where q_L, q_R, q_B and q_T are the degrees of freedom for left, right, bottom and top side of the unit cell. μ_x and μ_y represent the non dimensional wave numbers in x and y direction respectively. The computation is done for values corresponding to the Irreducible First Brillouin Zone [O-A-B-C-O] where the values are referred table 2.

Finite structure analyses are done using a band of several unit cells in the y direction (8 here) in which a modified version of the Transfer Matrix Method inspired by Dazel et al. [4] is applied to get the frequency response of the periodic structure.

3 RESULTS

Only out-of-plane waves are considered as an interest for stop band investigation in this study. For that reason, the design of the resonators has been thought in a way that their thickness is higher in the (x, y) plane than in the (y, z) plane. Doing so, the out-of-plane stiffness is lower than the in-plane stiffness to encourage the stop band opening for out-of-plane waves in low frequency area.

Fig. 2a shows results using the inverse WFEM while Fig. 2b represents the frequency response of the finite structure using a density of $\rho_R = 10\rho$. A new unit cell made with a combination of 8 of the single unit cell in the y direction is built, and the TMM is applied to the new unit cell created that way by repeating it 25 times in the x direction, equivalent to simulate a finite panel made of 8×25 unit cells. The frequency response is then performed using the TMM applying an out-of-plane force F_z at one extremity of the structure. A mean of displacement of several nodes of the structure for the out-of-plane degree of freedom u_z is calculated to get the response.

The dispersion curve exhibits that a resonant band gap is created between 2.6 kHz and 3kHz. However, this band gap is obstructed by a wave belonging to the hosting structure, making it almost not visible on the frequency response. The coupling between the resonators and the hosting structure on that case makes not trivial to separate the waves since the resonator has an impact on the hosting structure and vice versa. One of the solution chosen in this paper to move the band gap in lower frequency is to decrease the out-of-plane thickness of the resonators to reduce their stiffness while increasing their density. In order to keep the mass constant, the new density ρ_{R_n} of the resonators has to be taken in consideration using the following rule :

$$\rho_{R_n} = \rho_R \frac{h_R}{h_{R_n}} \tag{2}$$

where h_{R_n} is the new value of height of the resonator. By tuning the parameters such as $\rho_{R_n} = 14\rho$ and $h_{R_n} = 0.2143$, the new dispersion curve and the frequency response are computed and results are presented Fig. 3 and effectively shows a stop band shift to lower frequencies.

4 CONCLUSION

An example of how can be tuned a resonator in order to get a relevant result for wave propagation control is shown in this paper. The study also shows the limitation of the finite structure analysis, very useful to get fast frequency response results using the Transfer Matrix Method but not sufficient enough to detect obstructing structural waves for which the dispersion curve analysis is necessary.

5 ACKNOWLEDGEMENTS

This project has received funding from the European Union's Horizon 2020 research and innovation programme under Marie Curie grant agreement No 675441. This work was performed in cooperation with the EUR EIPHI program (ANR 17-EURE-0002).

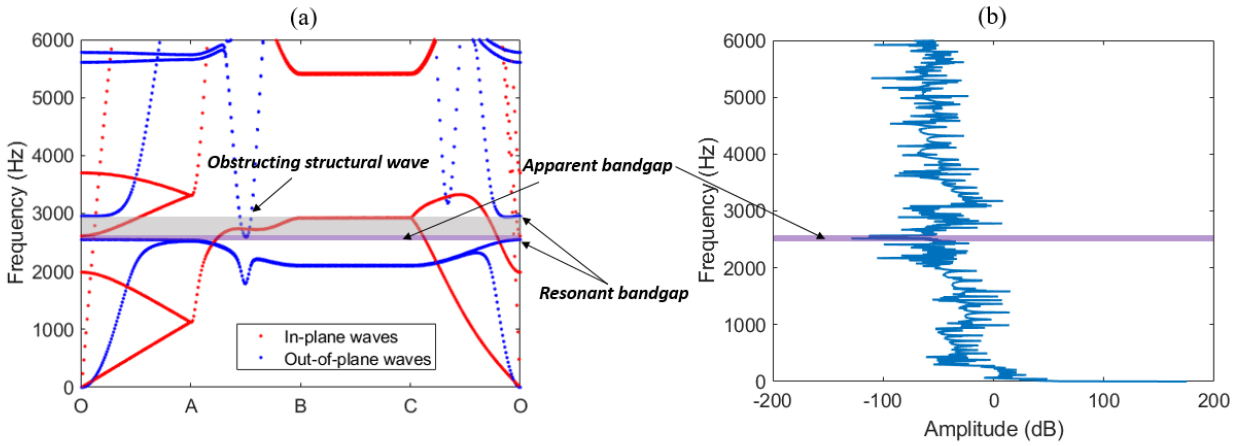

Figure 2. Results with $\rho_R = 10\rho$ using Inverse WFEM (a) and TMM (b)

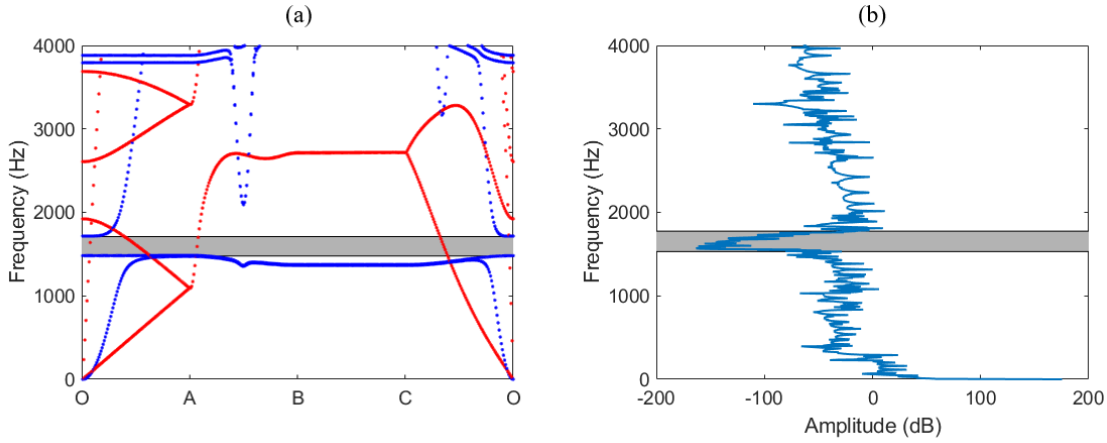

Figure 3: Results after changing the density and the height of the resonators using Inverse WFEM (a) and TMM (b)

REFERENCES

[1] J.S. Chen, B. Sharma, and C.T. Sun. Dynamic behaviour of sandwich structure containing spring-mass resonators. *Composite Structures*, 93(8):2120 – 2125, 2011.

[2] Claus C. Claeys, Karel Vergote, Paul Sas, and Wim Desmet. On the potential of tuned resonators to obtain low-frequency vibrational stop bands in periodic panels. *Journal of Sound and Vibration*, 332(6):1418 – 1436, 2013.

[3] Shanshan Yao, Xiaoming Zhou, and Gengkai Hu. Experimental study on negative effective mass in a 1d mass–spring system. *New Journal of Physics*, 10(4):043020, apr 2008.

[4] O. Dazel, J.-P. Groby, B. Brouard, and C. Potel. A stable method to model the acoustic response of multilayered structures. *Journal of Applied Physics*, 113(8):083506, 2013.

UTILIZING A LUMPED PARAMETER MODEL FOR ANALYZING THE SOUND RADIATION OF A SPINNING PLATE

M. Maeder[1], R. D'Auria[1,2], E. Grasso[1,2], G. Petrone[2], S. De Rosa[2], M. Klaerner[3], L. Kroll[3] and S. Marburg[1]

[1]Chair of Vibroacoustics of Vehicles and Machines
Technical University of Munich, Munich, GERMANY
Email: Marcus.Maeder@tum.de

[2]Laboratory for Promoting experiences in Aeronautical STructures and Acoustics
Università degli Studi di Napoli "Federico II", Naples, ITALY

[3]Department of Lightweight Structures and Polymer Technology
Chemnitz University of Technology, Chemnitz, GERMANY

ABSTRACT

Circular spinning discs are commonly used in the industry for cutting structures. Next to the mechanical instabilities that can occur when critical rotational speeds are applied, investigating the acoustic sound radiation of these discs is an interesting objective especially when health-related issues come into play. Since multiple physical effects interact with each other, take the stiffening effect of Coriolis and centrifugal forces, fluid structure interaction and acoustic short circuits, the system is complex and analytical solutions are challenging to derive. To investigate these complex systems, numerical methods are usually used, e.g. the finite element method. Despite the ongoing development of high-performance computer systems, analyzing industry relevant problems usually requires significant computational resources. Therefore, simplified theories and methods that yield reasonable solutions have been developed.
In this paper, the authors investigate the sound radiation of spinning circular discs utilizing a lumped parameter model. The resulting sound power estimates show that acoustic short circuits can be analyzed depending on the frequency of interest and the rotational speed. Last but not least, the question will be answered, whether mode splitting of the forward and backward traveling wave is audible.

1 INTRODUCTION

Investigating the sound radiation of vibrating and spinning discs is still a challenging topic due to various mechanical effects such as Coriolis and centrifugal effects, but also due to acoustic effects, e.g. acoustic short circuits or source acceleration. Difficulties arise because of the complex mechanical behavior when taking elastic deformation and rotation into account, as well as fluid structure interaction (FSI) [1] and sound radiation into an exterior domain [2]. Numerous contributions towards the analysis of rotating structures in general [3], circular plates [4–6] and their stability[7], as well as the associated sound radiation [8–10] have been published. In order to analyze industry relevant examples, numerical methods have proven to be suitable tools, especially the finite element method (FEM). Despite the continuously evolving computer technologies, simplified models have been developed in order to efficiently compute the sound radiation of flat surfaces [11–13].

In this paper, the authors investigate the sound radiation of a vibrating and spinning disc utilizing a lumped parameter model (LPM). The results show that acoustic short circuits are captured and that they are only present for low rotational speeds. Finally, the question, whether the so called mode splitting is audible, is addressed.

2 NUMERICAL MODEL

For the numerical investigations, a disc with an outer radius of $r_o = 400\,\mathrm{mm}$, an inner radius of $r_i = 30\,\mathrm{mm}$ and a thickness of $t = 3.5\,\mathrm{mm}$ is considered. An adequate FEM model with a sufficiently fine mesh consisting of quadratic hexahedral 3D elements was created in Abaqus 6.14. [14]. Following the outlines of Klaerner et al. [12], the LPM was implemented in Python as a post processing routine utilizing NumPy and SciPy libraries. It must be noted that the surface normal velocity was homogenized for each surface element. This simplification is valid as long as the single elements can be seen as compact with respect to the acoustic wave length. In addition, the plate is considered as baffled with respect to the acoustic domain.

In the simulations, a harmonic unit force excitation normal to the disc surface acting at the outer radius r_o was applied, while the frequency range of interest was limited between $f = 1\,\mathrm{Hz}$ and $f = 200\,\mathrm{Hz}$. The position of the force was kept constant with respect to a stationary observer. Further, a clamped boundary condition was applied to the surface area defined by the inner radius r_i and $r_{bc} = 60\,\mathrm{mm}$.

3 RESULTS

In Figure 1, the sound power calculated using the LPM is plotted over the frequency range of interest for various rotational speeds. It can be seen that for the case where the disc does not

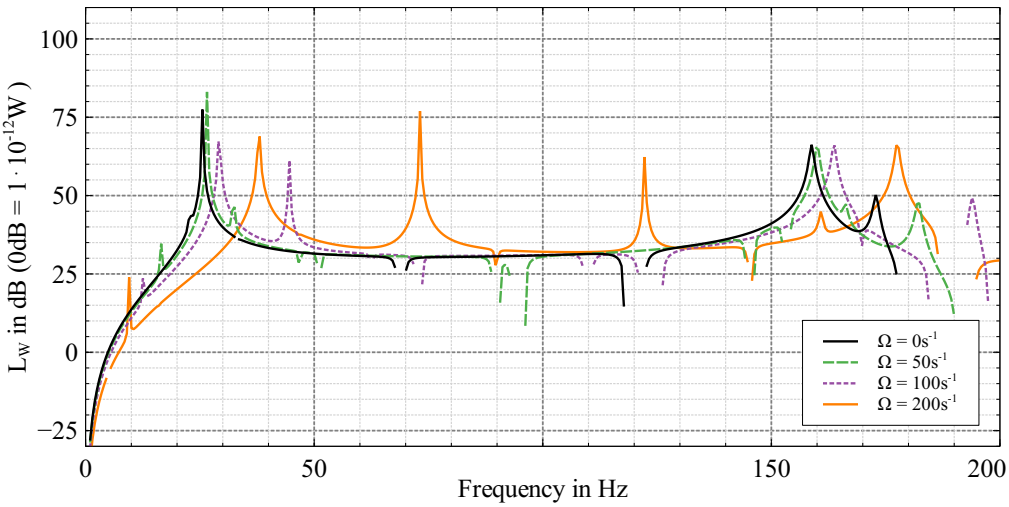

Figure 1. Sound power levels for varying rotational speeds.

rotate, some resonances occur. These resonances are associated with elastic deformations, where circular nodal lines are present with respect to the main disc surface. Deformations, where radial

nodal lines are present, develop acoustic short circuits in the low frequency regime and no sound radiation is recognizable. The associated frequencies are indicated by the gaps in the plotted lines, where numerical difficulties arise due to the handling of small values. The first plate deformation with radial nodal lines is found at $f = 172\,\mathrm{Hz}$. At this frequency, no acoustic short circuits develop anymore.

As the rotational speed increases, the stiffening effect of the centrifugal forces can be noticed as the resonance peaks shift to higher frequencies. Further, mode splitting is present for the resonance around $f = 172\,\mathrm{Hz}$. Looking at the results for $\Omega = 50\,\mathrm{s}^{-1}$, one notices that the two split peaks appear at $f = 157\,\mathrm{Hz}$ and $f = 181\,\mathrm{Hz}$. Interestingly, as the rotational speed increases up to $\Omega = 200\,\mathrm{s}^{-1}$, additional resonances occur. The authors believe that this is due to the high rotational speed preventing acoustic short circuits from developing, even in the low frequency range.

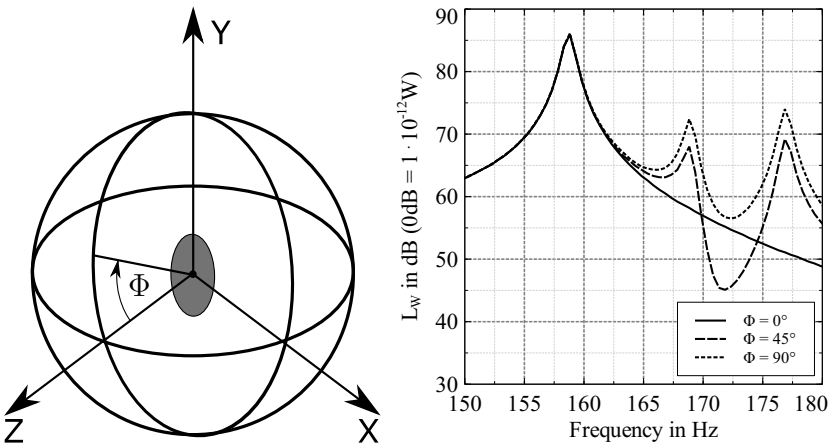

(a) Definition of angle Φ (b) Magnitude of sound pressure

Figure 2: Sound radiation at different angular coordinates for $\Omega = 25\,\mathrm{s}^{-1}$ in a distance of $z = 1.5\,\mathrm{m}$.

As a final step, the authors want to address the question, whether the mode splitting is audible or not. To answer the question, the sound pressure was calculated at a distance of $z = 1.5\,\mathrm{m}$. See Figure 2(a) for a definition of the angle Φ. Three different angles from the z-axis for a rotational speed of $\Omega = 25\,\mathrm{s}^{-1}$ are calculated. As depicted in Figure 2(b), it can be seen that mode splitting is audible. Only at the vicinity of the rotational axis, the two resonances vanish.

4 CONCLUDING REMARKS

As a conclusion, the authors emphasize the following outcomes. It is a valid approach to utilize the LPM as a simplified tool for investigating the sound radiation of spinning discs. Further, it is seen that acoustic short circuits are present on the disc surface for small rotational speeds but vanish as the speed increases. Last but not least, mode splitting is audible but not in the vicinity of the rotational axis.

REFERENCES

[1] G. Hou, J. Wang, and A. Layton. Numerical methods for fluid-structure interaction - a review. *Communications in Computational Physics*, 12(2):337–377, 2012.

[2] S. Marburg and B. Nolte, editors. *Computational Acoustics of Noise Propagation in Fluids - Finite and Boundary Element Methods*. Springer-Verlag, Berlin, Heidelberg, 2008.

[3] T. Kiesel and S. Marburg. Simulation of mode-locking phenomena in a complex nonlinear rotor system using 3d solid finite elements. *Proceedings of the Institution of Mechanical Engineers, Part C: Journal of Mechanical Engineering Science*, 230(6):959–973, 2016.

[4] C. D. Mote and L. T. Nieh. On the foundation of circular-saw stability theory. *Wood and Fiber Science*, 5(2):160–169, 2007.

[5] H. Lamb and R. V. Southwell. The vibration of a spinning disk. *The Royal Society Publishing*, 1921.

[6] S.C. Huang and W. Soedel. Effects of coriolis acceleration on the free and forced in-plane vibrations of rotating rings on elastic foundation. *Journal of sound and vibration*, 115(2):253–274, 1987.

[7] U. Heisel, T. Stehle, and H. Ghassemi. Experimental investigation into parameters influencing roll tensioning of circular saw blades. *Journal of Machine Engineering*, 15, 2015.

[8] R.C. Chanaud. Experimental study of aerodynamic sound from a rotating disk. *The Journal of the Acoustical Society of America*, 45(2):392–397, 1969.

[9] M.-r. Lee and R. Singh. Analytical formulations for annular disk sound radiation using structural modes. *The Journal of the Acoustical Society of America*, 95(6):3311–3323, 1994.

[10] H. Lee and R. Singh. Acoustic radiation from out-of-plane modes of an annular disk using thin and thick plate theories. *Journal of Sound and Vibration*, 282(1):313 – 339, 2005.

[11] J. B. Fahnline and G. H. Koopmann. Numerical implementation of the lumped parameter model for the acoustic power output of a vibrating structure. *The Journal of the Acoustical Society of America*, 102(1):179–192, 1997.

[12] M. Klaerner, M. Wuehrl, L. Kroll, and S. Marburg. Fea-based methods for optimising structure-borne sound radiation. *Mechanical Systems and Signal Processing*, 89:37 – 47, 2017.

[13] D. Fritze, S. Marburg, and H.-J. Hardtke. Estimation of radiated sound power: A case study on common approximation methods. *Acta Acustica united with Acustica*, 95(5):833–842, 2009.

[14] P. Langer, K. Sepahvand, C. Guist, J. Bär, A. Peplow, and S. Marburg. Matching experimental and three dimensional numerical models for structural vibration problems with uncertainties. *Journal of Sound and Vibration*, 417:294 – 305, 2018.

ENHANCEMENTS IN STRUCTURAL OPTIMIZATION OF AUTOMOTIVE UNDERBODY PANELS SUBJECTED TO WATER WADING LOAD

Andreas Daving, Flavio G. Pezzani, Yanyan Huang, Michael Hauenstein

Autoneum Management AG
Schlosstalstrasse 43, Winterhur, SWITZERLAND
Email: andreas.daving@autoneum.com, flavio.pezzani@autoneum.com, yanyan.huang@autoneum.com, michael.hauenstein@autoneum.com

1 INTRODUCTION

Vehicle water wading test is a standard test procedure in automotive development process. Within this procedure the vehicle traverses through water in specific test facilities, at different speeds and with various water depths. This set of tests are designed to put the vehicle under high load conditions and check for part failures, mainly on the underbody.

The most typical failure on underbody parts under such conditions is a combination of "pull-out" and "shear-through" failure modes, the latter meaning respectively out-of-plane and in plane breaking of the material.

Due to limited test data acquisition (normally failure or no failure) and lack of simulation capabilities in this field, the failure of parts is detected in a late state of the development process, which leads to expensive redesigns and time delay.

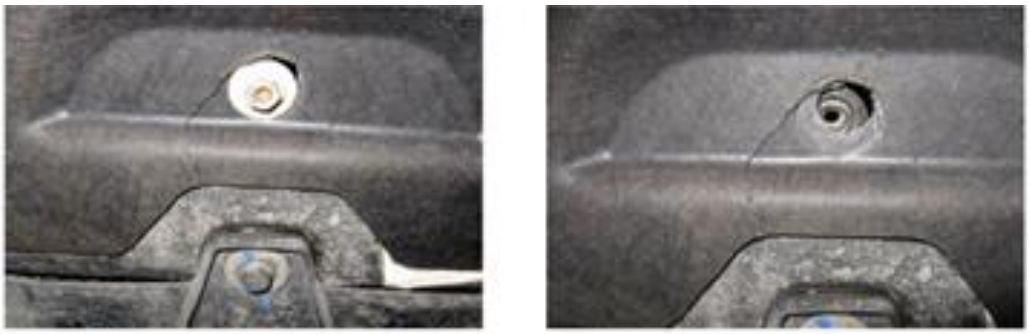

Figure 1: Typical under engine shields failure modes during water wading tests

Typically a total/average load on the part was used to calculate maximum stresses and deformation which often led to over-engineered solutions that compromise the use of light-weight materials.

2 METHODOLOGY

With the increasing need to understand and identify part failure in a wading test, Autoneum has developed a multiphase Computational Fluid Dynamics (CFD) simulation tool in StarCCM+ in order to predict the loads on the under body panels. The loads are represented as surface pressures, where stresses and displacements are calculated using the structural simulation tools provided from Altair, such as OptiStruct. This methodology is validated using force and displacement sensor data acquired by physical testing in a real world water wading test campaign realized in collaboration with a European OEM.

2.1 CFD Simulation

The water wading process is simulated using a transient CFD simulation. Simulating the full car in a transient manner allows for an accurate representation of the impact load in order to define the critical load case. The CFD simulation was carried out using Siemens StarCCM+ [1].

The motion of the car was modelled using the overset methodology which allows a body to move on a background mesh domain without the need to re-mesh between time steps. This powerful tool reduces the simulation time significantly. The multiphase interaction is modelled using the volume of fluid (VOF) methodology. This Eulerian methodology models the two phases by locating the free surface. Unsteady RANS equations are solved in each fluid domain.

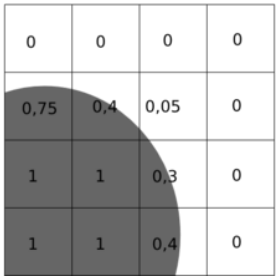

Figure 3: Volume of Fluid Methodology Scheme (volume fraction of fluid) [2]

Figure 2: Volume of Fluid Visualisation

CFD simulation provides insight on the water wading test allowing a definition of the critical load cases and produces the pressure maps for the structural simulation and optimization. The simulations were based on the generic DrivAer car model [3] which is a fusion of two typical medium class vehicles (Audi A4 and BMW 3 Series).

The water wading test channel dimensions were chosen to have the following dimensions:

- Width: 3.5 m, Ramp length: 15 m
- Ramp inclination: 3 °
- Water height: 400 mm
- Vehicle speed: 10 kph

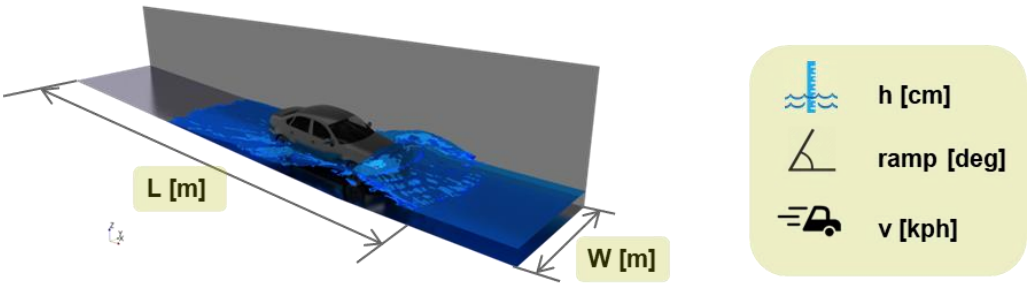

Figure 4: Wading basin with dimensions

2.2 Structural Simulation

From the CFD simulation one or several pressure maps, depending on the loading history, can be extracted and fed into a Finite Elements based structural solver to compute stress and deflection.
Topographical optimizations are traditionally used for optimizing geometrical stiffness, such as adding beads. With the use of topological optimization, it is also possible to identify the optimal fixation point position. Having a design volume of solid elements between the part and boundary conditions (BIW), the solver is reducing the element density where material is not needed. This can be represented as a geometrical result to visualize where a connection between the part and BIW is most needed in order to achieve the highest stiffness. These results are then used to quantify increased part performance by comparing with the original part design.

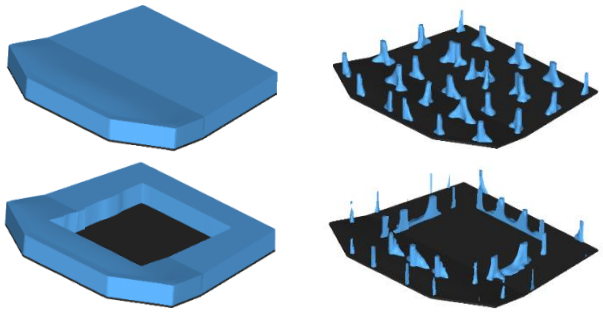

Figure 5: Initial optimization results with alternative design space (blue)

3 RESULTS

Initial simulations show that, with this method, it is possible to achieve a significant increased part performance by repositioning the fixation points.

Depending on the allowed design volume, it is possible to tune the output results from the optimization to better suit the application. For instance, on a typical underbody part, many restrictions on where fixation points are allowed must be taken into account. This is highly dependent on the vehicle body in white (BIW) structure design. A design change on the BIW is in most cases not feasible due to cost and complexity of such change on a vehicle program.

4 OUTLOOK

Correlation of the loads in test and simulation is not trivial. Variables such as vehicle speed during wading, exact vehicle position (pitch) and alignment to the wading channel are not fully controllable during the test. A sensitivity analysis with respect to this factors where performed, but in general CFD loads could be validated on a simpler geometry impacting water in more controlled conditions.

During the study it was noticed that in some measurement positions the predicted load presented a big deviation from the tested ones. To understand the cause of the deviation the occurrence of buckling in the part shape was investigated with a dynamic simulation and eventually confirmed. This highlights the need for a fully coupled fluid-structure simulation of the test that adapts the fluid domain to the current deflected shape of the part.

The use of meshless method could allow us to exploit a fully coupled Fluid-Structure simulation environment. Even though it has to be compared against typical Finite Volume methods results, in terms of accuracy and solution time.

REFERENCES

1. ISO 527-1 “Plastics – Determination of tensile properties”
2. ISO 527-3 “Plastics – Tensile properties of films and sheets”
3. ISO 178 “Plastics – Determination of flexural properties”
4. Altair Optistruct User Guide
5. Altair Radioss™ Reference Manual
6. Von Ikosaeder - Eigenes Werk, CC BY-SA 3.0, https://commons.wikimedia.org/w/index.php?curid=31554492
7. StarCCM+ https://www.plm.automation.siemens.com/global/en/products/simcenter/STAR-CCM.html
   DrivAer Model
   Angelina I. Heft, Thomas Indinger and Nikolaus A. Adams, Introduction of a New Realistic Generic Car Model for Aerodynamic Investigations, SAE International, 2012-01-0168

MANUFACTURING TOLERANCE IMPACT ON STATIC CHARACTERISITICS FOR A TILTING PAD JOURNAL BEARING

Mingyang Lou [1,2] , Olivier Bareille[2] , Wenqi Chai[2] , Mohamed Ichchou[2] , Wei Chen[1]

[1]Key Laboratory of Ministry of Education for Modern Design & Rotor Bearing System, Xi'an Jiaotong University , Xi an Shannxi 710049, CHINA
Email: loumingyang123@gmail.com,

[2]Laboratoire de Tribologie et Dynamique des Systèmes, Ecole Centrale de Lyon , 36 Avenue Guy de Collongue, 69310 Ecully Cedex FRANCE
Email: olivier.bareille@ec-lyon.fr

ABSTRACT

A tiny difference between the normal dimensions and the processing dimensions in the range of manufacture tolerance can cause a great change in characteristics of tilting pad journal bearing (TPJB). The first order sensitivity index of the static characteristics of a five pad TPJB including capacity, power loss and inlet flow using the Fourier Amplitudes Sensitivity Test (FAST) method have been analyzed and evaluated for five processing parameters: pad internal radius, shaft radius, pivot radius, pivot position and pad angular extent which all these parameters obey the normal distribution respectively. The results show that under the given machining precision, the pivot position and pad angular extent have no influence on the static characteristics while the pivot radius is relatively important than shaft radius for capacity and power loss in which pad internal radius shows non important. For inlet flow the shaft radius is most important, pivot radius is important and pad internal radius is less important. The solution can be used for the purpose of choosing the reasonable machining precision for a TPJB designed for reducing the change between the experienced characteristics and that expected.

1 INTRODUCTION

In a practical machining process of journal bearing, the inevitable error between the real dimension and nominal dimension leads to a variation of performance. These errors come from the tolerance and the distribution of studied parameters [1, 2]. As a key part of a mechanical system, bearing

performance affect a lot the whole system, thus the importance is self-evident to understand and determine which parameters have effect on the bearing characteristics most and which that have no effect so that conclusion drawn in bearing studies is robust and stable. So it is necessary to conducting a sensitivity analysis (SA). In reference [3,4,5], cylindrical journal bearing, four-lobe journal bearing, five-pad journal bearing are studied, authors confirmed that bearing characteristics are affected by manufacturing error which must be considered for an accurate prediction. While these three references above used a Local SA.

Over the last decade, Global SA has gained considerable attention among practitioners due to its advantages over Local SA [6,7]. Many reviews of Global SA have been published in different fields. Methods for conducting a Global SA are developed [8, 9]in which variance-based methods including Fourier amplitude Sensitivity Test method [10]and Sobol' [11] method are widely used.

For the best of our knowledge, few comprehensive and up-to-date paper studied titling-pad journal bearing using Global SA. In this paper, we introduce Global SA to titling-pad journal bearing, in a way of quantitative and robustness to identify important processing size affecting static characteristics of tilting-pad journal bearing and to determine which one explain most of the model sensitivity. We take a model of five-pad journal bearing; conduct a FAST method to study the sensitivity of bearing characteristics including capacity, power loss and inlet flow to five studied parameters: pad internal radius, shaft radius, pivot radius, pivot position and pad angular extent.

2 TILTING PAD BEARING GEOMETRICAL DESCRIPTION

Figure 1 show the specific geometrical characteristic of the tilting pad journal bearing.

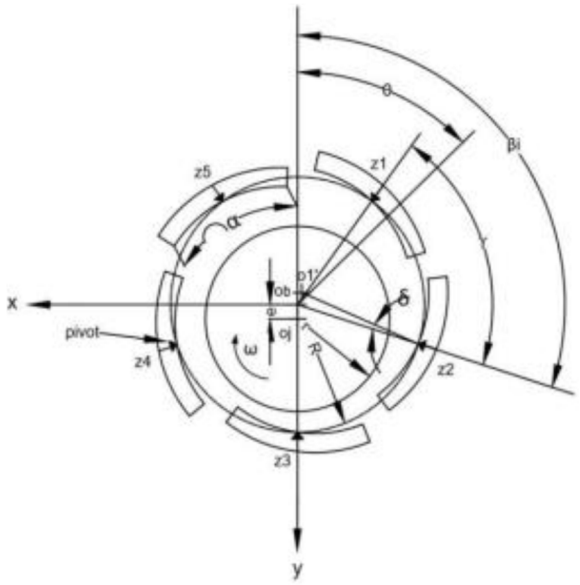

Figure 1 – Geometry of tilting-pad journal bearing

The main parameters that will analyzed with respect to their influence on the bearing performances are:

- e, the excentricity (m), at the center of the figure;
- d, the bearing diameter;
- δ, pad's inclination angle (rad);
- θ, attitude angle (rad);
- α, pad extent angle (rad);
- R, pad internal radius (m);
- β_I, pivot location of pad I (rad)

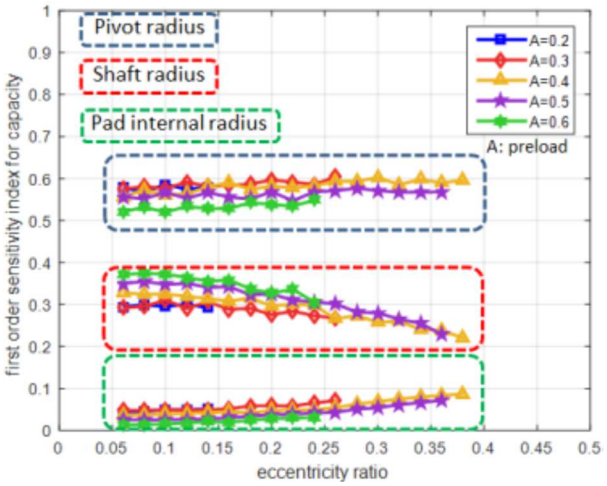

a- capacity

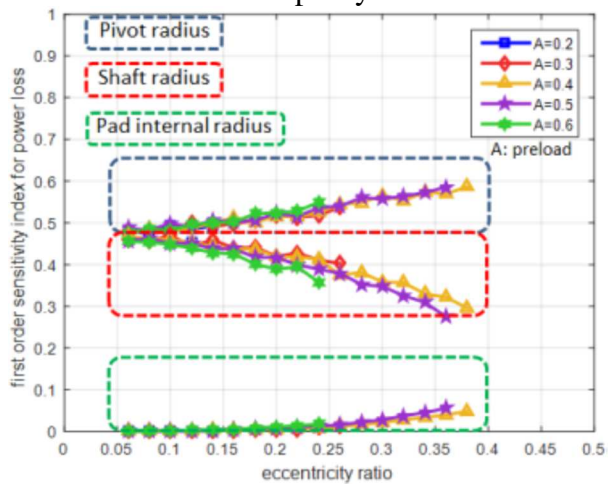

b- power loss

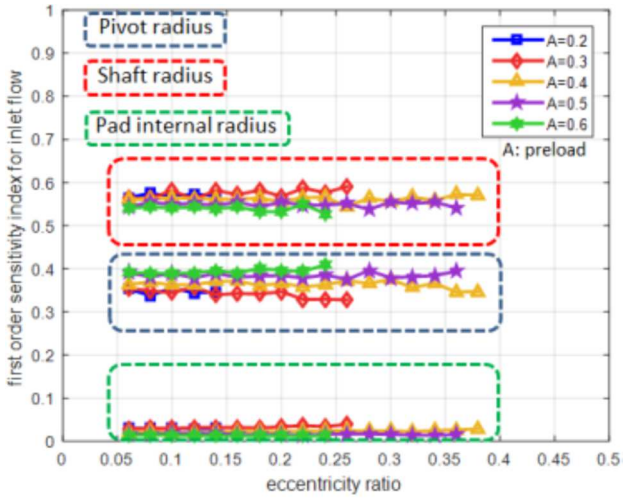

c- inlet flow

Figure 2 - Main results of first order sensitivity index of studied parameters to manufacturing tolerance: a- capacity, b- power loss, c- inlet flow

3 RESULTS

Figure 2-a shows that for capacity, as the eccentricity ratio increasing, the trend of the sensitivity of pivot radius remain the same while that of shaft radius shows a decreasing tendency, internal radius of pad 3 increases with the eccentricity ratio for each preload. Meantime when different preloads are given, the tendency and the order of the sensitivity have no change. Figure 2-b shows that for power loss, pivot radius and internal radius of pad 3increasewith eccentricity ratio, while shaft radius shows an opposite tendency for each preload. Similar tendency can be obtained when different preload are given. Figure 2-d shows that for inlet flow, pivot radius, shaft radius and internal radius of pad 3 remain constant with the increase of eccentricity ratio. For different preload, the tendency has no change also.

4 CONCLUSION

For an effective calculation, geometrical preload and eccentricity ratio should be determined to avoid pad unloaded and negative oil film thickness. Under the condition of a given normal distribution of five studied parameters, the variation of pivot position and pad angular extent have no influence on static characteristics, pivot radius, shaft radius and internal radius of pad3 affect a lot the static characteristics, while pivot radius is important relatively. Little change is seen in sensitivity when eccentricity ratio increases. Load applied do not change the order of the sensitivity. For obtain a good economy, reasonable processing precision should be chosen according to a practical application.

REFERENCES

[1] C. Tong, F. Graziani, A practical global sensitivity analysis methodology for multi-physics applications, *Comput. Methods in Transport: Verification and Validation,* Springer, 277-299, 2008

[2] M. Shin, J.H. Guillaume, B.F. Croke, A.J. Jakeman, Addressing ten questions about conceptual rainfall-runoff models with global sensitivity analysis in R, *Journal of Hydrology*, 503:135-152, 2013.

[3] K. Iwamoto, S. Oishi, Influence of manufacturing error characteristics bearing, *Tribology Series,* 40:495-501, 2002.

[4] K. Iwamoto, K. Tanaka, Influence of manufacturing error of roundness for characteristics of cylindrical journal bearing, *Tribology and Interface Engineering Series,* 48:751-754, 2005.T

[5] M. Fillon, W. Dmochowski, A. Dadouche, Numerical study of the sensitivity of tilting pad journal bearing performance characteristics to manufacturing tolerances: steady-state analysis, *Tribology Transactions,* 50(3):387-400, 2007.

[6] A. Saltelli, P. Annoni, How to avoid a perfunctory sensitivity analysis, *Environmental Modelling Software,* 25(12):1508-1517, 2010.

[7] F. Ferretti, A. Saltelli, S. Tarantolla, Trends in sensitivity analysis practice in the last decade, *Science of the total environment,* 568:666-670, 2016.

[8] A. Saltelli, M. Ratto, T. Andres, F. Campolongo, J. Cariboni, D. Gatelli, M. Saisana, S. Tarantola, Global sensitivity analysis, *John Wiley & Sons,* 2008.

[9] F. Pianosi, T. Wagener, A simple and efficient method for global sensitivity analysis based on cumulative distribution functions, *Environmental Modelling Software,* 67:1-11, 2015.

[10] A. Saltelli, S. Tarantola, K.-S. Chan, A quantitative model-independent method for global sensitivity analysis of model input, *Technometrics,* 41(1):39-56, 1999

[11] I.M. Sobol, Sensitivity estimates for nonlinear mathematical models, *Mathematical modelling and computational experiment,* 1(4):407-414, 1993

OPTIMIZATION OF PASSIVE AND ACTIVE SOUNDPROOFING FOR AN ADVANCED TURBO-PROP AIRCRAFT CABIN

R. Lombardi[1], P. Vitiello[2], I. Dimino[2], G. Petrone[3], M. Barbarino[2]

[1]Noesis Solutions, Gaston Geenslaan, 11 B4 - 3001 Leuven, Belgium
riccardo.lombardi@noesissolutions.com

[2]Italian Aerospace Research Centre (C.I.R.A.), via Maiorise snc, 81043 Capua, Italy
p.Vitiello@cira.it, i.Dimino@cira.it, m.Barbarino@cira.it

[3]Università degli Studi di Napoli Federico II, via Claudio 21, 80125 Napoli, Italy
giuseppe.petrone@unina.it

ABSTRACT

Turbo-prop aircraft are subjected to significant acoustic loads, mainly generated by the propeller blades and the turbulent boundary layer.
In this paper, the cabin noise is reduced using an optimized combination of active and passive technologies. Due to the extension of the analyzed frequency range, and the characteristics of the investigated soundproofing methodologies, both Finite Element method (FEM) and Statistical Energy Analysis (SEA) have been used to study the global fluid-structure interaction phenomena of the whole cabin. The significant difference in computational effort between the different methodologies has been exploited to create a stepped optimization; the best lining panel configuration, in terms of different performance metrics described in the paper, identified using the SEA, has been used as starting point for the tailoring of the FEM-modelled, active technologies.
The results, in terms of percentual reduction of the noise metrics compared with the variation of the total cabin weight, support the claim that, through optimization, improvement of the passengers' comfort can be achieved without reduction of the overall aircraft performances.

1 INTRODUCTION

The soundproofing of a T/P aircraft requires to carefully balance passengers and crew comfort with construction requirements as well as installation and operation costs; the current trend toward composite airframes, although allowing for lighter, and therefore more fuel-efficient, aircraft, represent a significant challenge in terms of internal noise. The higher stiffness and lower dampening of the carbon fiber structures improve the transmission of the pressure loads, both in terms of high frequency (500 to 10k Hz), Turbulent Boundary Layer (TBL) and lower frequency, propeller blades. To reduce the cabin noise multiple, often concurrent, approaches are available, each with specific advantages, ranges of efficacy, and requisites. Furthermore, the airframe is subjected to tight installation, geometrical, weight and power constraints, that limit the number of solutions that can be effectively used. Optimization would allow searching for the solution that respects the afore-mentioned constraints while improving internal comfort. However, several key enablers are required to pursue this objective: parameterized numerical models able to efficiently characterize the response of the airframe to different technologies; accurate descriptions of the involved technologies; explicit representations of the constraints; non-ambiguous definition targets; algorithms and methodologies to extract and analyse the technologies impact with a limited numerical effort. The first element has been achieved developing both a FEM model, suited to investigate the active technologies and the tonal frequency range and a SEA model, used for the higher part of the spectrum as well as broad-band analyses of lining panels and thermo-acoustic blankets. Both models have been parametrized to allow for explicit control of soundproofing-related elements, such as lining panels composition and configuration. Secondly, each technology has been characterized outside the main model, its feature studied and prepared for the integration. The analysis of the airframe clarified the constraints that had to be respected, specifically in terms of allowable space and weight. The performed cabin noise optimization is part of the Clean Sky 2 project CASTLE, which has among its objectives the development of innovative, lighter and more environmentally friendly seats, stowage bins and interiors. Improvements achieved in the other fields allowed for wider upper weight constraints with respect to the nominal configuration. Due to the size of the cabin, the range of the investigated frequencies and the overall target of passenger and crew acoustic comfort improvement, the two main metrics used to lead the optimization process have been the cabin average noise and the service area maximum noise, both evaluated in A-weighted format to better represent the human response. Finally, a Process Integration and Design Optimization (PIDO) software has been used to wrap the analyses and prepare the with pre- and post-processing elements that automatically take care of the models' customization according to the desired soundproofing configuration. The overall objective is to effectively investigate how new materials and approaches affect the passengers, identifying critical aspects and highlighting solutions of potential interest for more in-deep investigations.

2 CABIN MODELS DESCRIPTION

For the SEA analyses, the cylindrical section of the fuselage has been modeled using the software VA One. In view to distinguish the SPL along the fuselage at the different stations, necessary to evaluate the noise level at various distances from the noise source, the fuselage trunk has been divided into several subsections. An isometric view of the SEA fuselage model is shown in the left side of Fig. 1, where it can be noted the internal subdivision through the cavities, the different colors of the skins (according to material and properties), the application of the external loads and the Semi-Infinite Fluids (SIF). For comparison, the corresponding FEM model is illustrated on the right. Instead of volumes, the pressure levels have been investigated using two planes of microphones, whose height from the cabin floor is equivalent to the passenger's standing and seated ears position.

The nominal passive soundproofing configuration of the cabin exploits fiberglass reinforced, laminated, lining panels with Nomex core, and aeronautical glass wool thermoacoustic blankets.

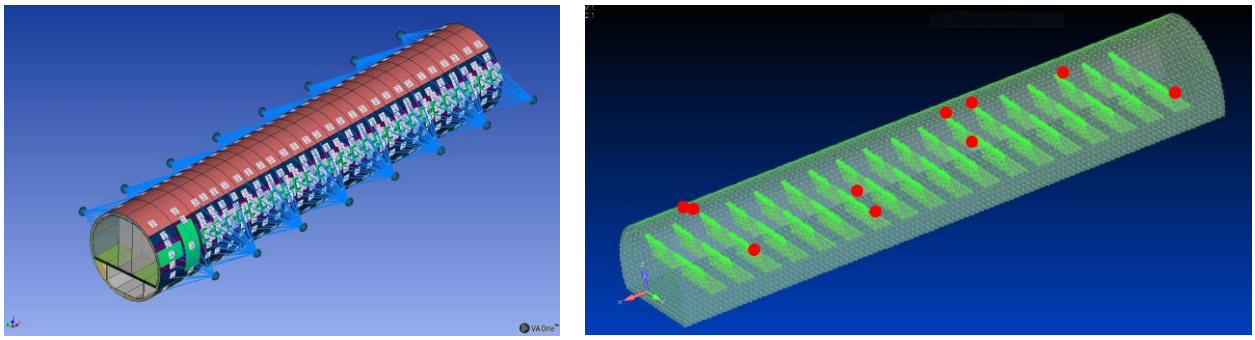

Figure 1. Developed SEA (left) and FEM (right) models.

This configuration has been previously optimized for a similar size, aluminum alloy built, T/P airframe and has been analyzed and used as a reference to evaluate the changes in terms of weight and noise environment properties. Lining and blanket weight have been determined using their known (blanket) or estimated (lining) densities, thicknesses, and model-measured total surface. Besides, soundproofing is achieved utilizing thermo-acoustic blankets (SEA model only), Dynamic Vibration Absorbers (DVA) tuned to counter the first blade frequency and an Active Noise Control system (ANC) (both evaluated on the FEM model only).

3 OPTIMIZATION PROCEDURE

The optimization has been carried out splitting the analyses into two separated phases with different design variables. During the initial one, the SEA model has been used to investigate the higher frequencies and determine the lining panel and thermoacoustic blanket configurations able to provide a quantifiable noise reduction at the cost of an acceptable total weight increment. Then, the most promising configurations have been used as starting points for the FEM model investigation of the ANC sources phase and amplitude. Several reasons led to the adoption of this stepped approach, both from engineering and mathematical perspectives. A single FEM analysis is significantly more expensive in terms of time and computational resources than the SEA one for the same frequency and cannot be reasonably used beyond 300 Hz. Furthermore, the blankets and the lining panels have a significant impact on the TBL reduction, but are less relevant for the tonal loads, that in turn are addressed by the DVAs (whose contribution outside their design frequency is mostly negligible). This led to an initial SEA optimization of the passive technologies with geometric and weight constraints and a subsequent FEM one of the ANC. Both optimizations have been performed using surrogate models of the cabin response developed from the data gathered by running and combining several Design of Experiments (DOE). The exploitation of the response models allowed for a significant improvement in operational flexibility and time reduction, at the cost of a few additional analyses required to validate the results of the identified configurations.

4 RESULTS

The optimization of the passive technologies addressed as multi-objective optimization, Fig. 2, highlighted that the achievable improvement with respect to the reference configuration had to be paid in terms of added weight, as clearly illustrated by the Pareto front. The observed trend to reduce the cabin noise as a result of the optimization is to increase the lining panel core thickness, which leads to thinner glass fiber layers to preserve the overall panel stiffness (active constraint) and

overall lighter lining panels. The saved weight is then dedicated to increasing the thermo-acoustic blanket thickness.

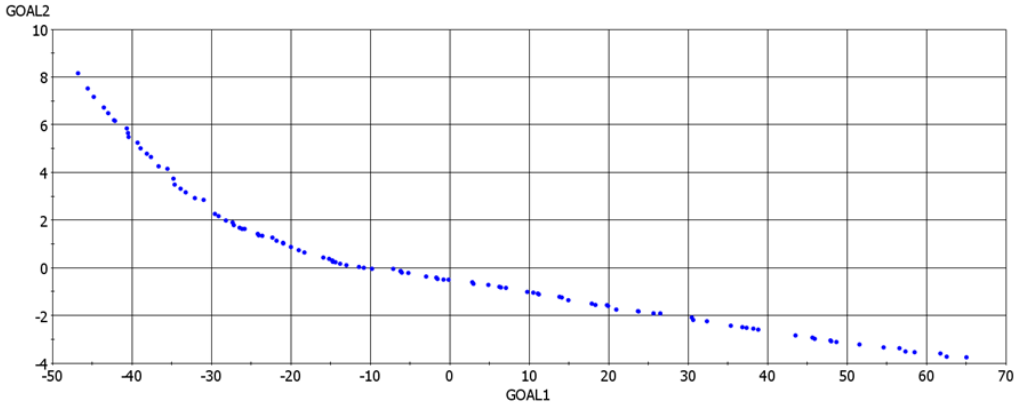

Figure 2. Pareto front evaluated from multi-objective minimization of both total soundproofing weight variation % (GOAL1) and Passengers OSPL variation % (GOAL2).

The results for the optimizations of the ANC parameters, using fixed actuators positions and free to vary phase and amplitude, are summarised in Table 1. Variations have been evaluated with respect to the reference configuration. The most significant impact of the ANC is the sharp decrease in cabin maximum values, whereas average and crew area effects are limited.

	Pax Max OSPL variation	Pax Average OSPL variation	Crew Max OSPL variation	Crew Average OSPL variation
Nomex	-15.26%	-1.26%	-0.34%	-0.75%
Metamaterial	-14.90%	-1.33%	-0.13%	-0.68%
Tegracore	-15.20%	-1.39%	-0.72%	-0.76%

Table 1. OSPL variations induced by ANC optimization from different lining panels configurations.

5 CONCLUSIONS

The performed optimization demonstrates that it is possible to successfully combine staggered, SEA and FEM analyses targeted to different spectral ranges and soundproofing technologies to reduce the noise in a T/P aircraft, therefore improving the comfort of both crew and passengers. The full paper will detail the used models and procedures and debate the full extent of the results.

6 ACKNOWLEDGEMENTS

The results have been achieved in the framework of CASTLE – (CAbin Systems design Toward passenger welLbEing) Core Partnership of Clean Sky 2 Programme. CASTLE has received funding from the Clean Sky 2 Joint Undertaking under the European Union's Horizon 2020 research and innovation programme under grant agreement n° CS2-AIR-GAM-2014-2015-01. The SEA and FEM models developed for the numerical analysis has been derived from the CAD model of the Clean Sky 2 demonstrator, provided by Leonardo Aircraft Division as one of the project input data. The Leonardo Aircraft Division also provided the applied acoustic loads (TBL and propeller). The contents of this paper reflect only the author's views and the Clean Sky 2 Joint Undertaking and the European Commission are not liable for any use that may be made of the information contained therein.

PERIODIC AND RANDOM LONG-RANGE INTERACTIONS IN METAMATERIALS

F. Mezzani[1*], A.S. Rezaei[1*] and A. Carcaterra

[1]Department of Mechanical and Aerospace Engineering
Sapienza University of Rome, Rome, ITALY
Email: federica.mezzani@uniroma1.it, amirsajjad.rezaei@uniroma1.it,
antonio.carcaterra@uniroma1.it

ABSTRACT

This work investigates the dynamic behavior of a periodic one-dimensional longitudinal metamaterial characterized by the presence of non-local interactions. Two topological configurations are considered for the long-range connections: i) periodic rectangular windows, symmetrically distributed along the main axis, and ii) randomly spread connections. These configurations, both analytically approached through successive approximations method, produce unconventional dispersion relationship and disclose wave stopping phenomenon in the former case and a jagging and thickening of the dispersion curve for the latter.

1 INTRODUCTION

The effects of long-range interactions embedded within a one-dimensional wave-guide have already been investigated [1]. The idea behind this work is to provide a further description of the different topological configuration non-local connections can perform, so to complete the propagating characterization of the obtainable dynamic scenarios. Periodic rectangular windows distributed along the length of the wave-guide and connections with random intensity are the two considered schemes.

Metamaterials enjoy widespread attention due to the unexpected results they produce in many applications. In electromagnetics, metamaterials are frequently related to anomalous dissipation and diffraction properties of electromagnetic media that lead to negative group velocity, light stopping and fast light [2]. In mechanics, metamaterials change the connectivity scheme of a structure and induce micropolar, higher-gradient and nonlocal elasticity. In this context, metamaterials are thought as conventional elastic materials equipped with long-range interactions, the source of integral

contributions in the equation of motion. The effect of these long-range interactions has been investigated in [3-5], but only considering specific kernels which provide analytical solutions. In this work, analytical solutions are achieved in both cases: i) the dynamics of the configuration of periodic rectangular windows, natural extension of [6], is treated through the Fourier Transform, ii) the successive iteration method is applied in case of random interactions. Long-range interactions, changing the topology of the connections, represent a breakthrough in the conventional concept of particle-particle interaction between closest neighbors. When the connection is extended either to one-to-all particles or to all-to-all particles, the introduced modification becomes source of sophisticated propagation behavior, here discussed.

2 PERIODIC RECTANGULAR WINDOWS

The system composed by long-range connections, confined in a succession of rectangular windows, is shown in **Errore. L'origine riferimento non è stata trovata.**

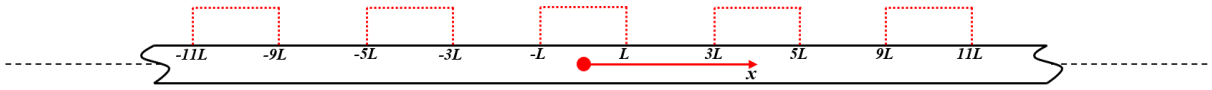

Figure 1. Long-range wave-guide with periodic non-localities.

The dynamics of such structure is described by:

$$\rho \frac{\partial^2 u(x,t)}{\partial t^2} - E \frac{\partial^2 u(x,t)}{\partial x^2} - \tilde{k} \int_{-\infty}^{+\infty} [u(x) - u(\xi)] H(x-\xi) d\xi = 0 \tag{1}$$

Where $\tilde{k}$ resembles the stiffness modulation of the elastic connections, $H(x)$ indicates the window confining the interactions. Setting L as the length of the window and n the number of windows in case of an unbounded wave-guide, the kernel in Equation (1) assumes the form:

$$H(x) = \begin{cases} 1, (4n-1)L \le x \le (4n+1)L \\ 0, (4n+1)L \le x \le (4n+3)L \end{cases} \tag{2}$$

The dynamic response is first analyzed in terms of dispersion relationship, obtained applying the Fourier Transform both in space and time to Equation (1):

$$\rho\omega^2 - Ek^2 + 2\tilde{k}NL - \frac{j\tilde{k}(1-e^{2jkL})}{k} \sum_{q=0}^{N-1} e^{j(1-2N+4q)kL} = 0 \tag{3}$$

being N the number of considered windows, symmetrically distributed around the midpoint of the structure. Eventually, the non-dimensional counterpart of the dispersion relationship is considered:

$$\Omega^2 - K^2 + 2N\chi - \frac{j\chi(1-e^{2jK})}{K} \sum_{q=0}^{N-1} e^{j(1-2N+4q)K} = 0 \tag{4}$$

with $\Omega = \omega L\sqrt{\rho/}$ $K = kL$ and $\chi = L^3\tilde{k}/E$.
Figure 2 compares the trend of the non-dimensional dispersion relationship for three different values of N, i.e. $N = 1$, $N = 3$, $N = 5$, and, for the same values, Figure 3 shows the corresponding group velocities.

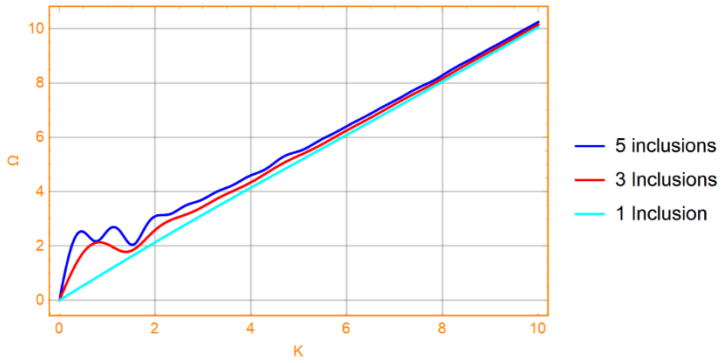

Figure 2. Dispersion curves of long-range wave-guide for different numbers of windows.

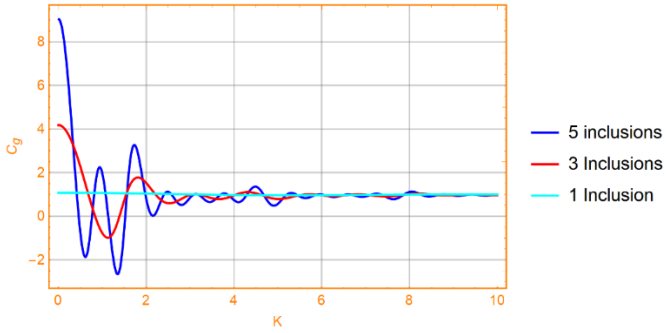

Figure 3. group velocity of long-range wave-guide for different numbers of windows.

It is apparent how the increasing of the number of windows induces a new phenomenon, the wave-stopping, absent in case of single interaction area.

3 RANDOM LONG-RANGE INTERACTIONS

This configuration considers a periodic elastic wave-guide, shown in Figure 4, in which all particles are interacting with each other through long-range connections of random intensity. The associated kernel is in the form:

$$K(x) = \sum_i C_i \cos(\tilde{k}_i x) \tag{5}$$

where C_i are the random coefficients.

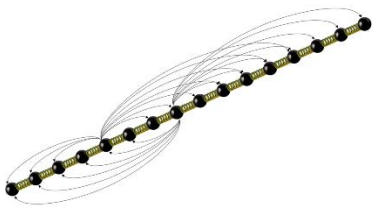

Figure 4. Long-range wave-guide with random non-localities.

The related equation of motion is given by:

$$\rho \frac{\partial^2 u(x,t)}{\partial t^2} - E \frac{\partial^2 u(x,t)}{\partial x^2} - \lambda \sum_i C_i \int_{-\infty}^{+\infty} (\tilde{k}_i (x-\xi) u(\xi) d\xi = 0 \tag{6}$$

The solution is obtained by applying the successive iteration method, which considers:

$$\begin{gathered} u_0 \; such \; that \; \rho \frac{\partial^2 u_0(x,t)}{\partial t^2} - E \frac{\partial^2 u_0(x,t)}{\partial x^2} = 0 \\ u_n \; such \; that \; \rho \frac{\partial^2 u_{n-1}(x,t)}{\partial t^2} - E \frac{\partial^2 u_{n-1}(x,t)}{\partial x^2} - \lambda \sum_i C_i \int_{-\infty}^{+\infty} (\tilde{k}_i(x-\xi) u_{n-1}(\xi) d\xi = 0 \end{gathered} \tag{7}$$

Even considering a 3-step iteration strategy only, the solution already unveils some peculiar phenomena. Indeed, the related dispersion relationship, shown in Figure 5, with respect to the conventional propagation (straight black line), presents a thickening and a jagging behavior, typical of in-homogeneous systems.

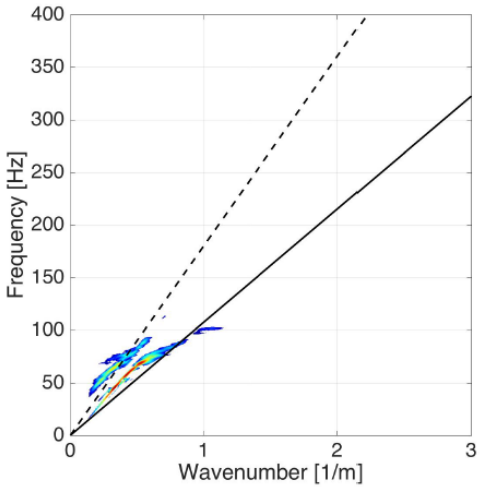

Figure 5. dispersion relationship in case of random long-range interactions.

REFERENCES

[1] A. Carcaterra, F. Coppo, F. Mezzani, S. Pensalfini. Long-Range Retarded Elastic Metamaterials: Wave-Stopping, Negative, and Hypersonic or Superluminal Group Velocity. *Physical Review Applied*. 11.1: 014041, 2019.

[2] V. Laude, M.E. Korotyaeva. Stochastic band structure for waves propagating in periodic media or along waveguides. *arXiv preprint arXiv:1801.09914*, 2018.

[3] F. Mezzani, F. Coppo, A. Carcaterra. Long-range coupling of waveguides. *Proceedings of ISMA 2018 - International Conference on Noise and Vibration Engineering and USD 2018 - International Conference on Uncertainty in Structural Dynamics.* 2018.

[4] F. Mezzani, F. Coppo, S. Pensalfini, N. Roveri, A. Carcaterra. Twin-waves propagation phenomena in magnetically-coupled structures. *Procedia engineering*, 199, 711-716. 2017.

[5] F. Coppo, A.S. Rezaei, F. Mezzani, S. Pensalfini, A. Carcaterra. Wave path in an elastic membrane with selective nonlocality. *Proceedings of ISMA 2018 - International Conference on Noise and Vibration Engineering and USD 2018 - International Conference on Uncertainty in Structural Dynamics*. 2018.

[6] F. Mezzani, A.S. Rezaei, A. Carcaterra. Wave propagation phenomena in nonlinear elastic metamaterials. *Nodycon Conference proceedings.* 2019.

SYNTHESIS AND CHARACTERIZATION OF NATURAL FIBERS REINFORCED EPOXY COMPOSITE

M. F. Zhang[1], M. Salvia[1*] and O. Bareille[1]

[1] Ecole Centrale de Lyon - LTDS, University of Lyon, 36 avenue Guy de Collongue
69134 Ecully, France

Email: mingfa.zhang@ec-lyon.fr, michelle.salvia@ec-lyon.fr, olivier.bareille@ec-lyon.fr

ABSTRACT

The purpose of this job is to study the mechanical properties of flax fiber reinforced bio-epoxy composites and to explore its feasibility as an external reinforcement for building components. Patches of natural flax fabric layer reinforced composites were made by hand lay-up method. DSC tests were conducted for the thermal study. The mechanical characterization was performed using DMA test. In addition, the durability of the composite underwater immersion was also mentioned. The results showed that the durability tests reduce the mechanical properties of the flax/epoxy composite. It had also been observed that degradations of the composite can be partly healed after initiating the second curing stage due to the two-stage curing of the epoxy system. Both the mechanical and durable properties give the possibility of this composite as an external strengthening application.

1 INTRODUCTION

The failure of materials involved in large infrastructures, such as bridges or roads, may cause a huge loss of life, economy or a loss of services [1]. In order to prevent these phenomena, scientists and engineers have been working from both theoretical and application fields. An attractive solution to upgrade existing infrastructures and increase their life-span is to bond fiber reinforced thermosetting composite patches to strengthen the damaged structure and to prevent failure growth. And in doing so, understanding the mechanical properties as well as failure mechanism of the bonded thermosetting composites is important. Unlike isotropic materials, whose crack growth occurs by simple enlargement of the initial defect without branching or directional changes, damage mechanism in composite materials are more complex. Initiations and growths of defects occur during almost all life of the composite up to final failure which occurs by coalescence of previous

damages (cumulative damage). Hence, how to detect the latent cracks in materials and how to fix the damaged materials with more cost-effectively ways are research emphasizes.

As a non-destructive inspection method, in-situ Structural Health Monitoring (SHM) has obtained increasing attention [2]. It implies the use of sensors, such as piezoelectric ceramics (PZT), which are embedded within a structural material and provide real-time performance feedback based on the measurement, such as electrical impedance. These sensors can be used to monitor the health state of thermosetting composites, from their curing process to the propagation of microcracks then to the end of their life cycle, which is useful for analysing the fabrication or failure procedure of materials. By monitoring the change in the impedance spectrum which is linked to the changes of matrix viscoelastic properties as cure progressed, we can understand the different steps of the epoxy cure regarding molecular motion, viscosity change, crosslinking density and their consequences on the mechanical properties of the material.

Compared to the high cost of refabrication, being repaired by the material itself would be a better deal. From this point of view, the concept of "self-healing" has become the research hotspot. Self-healing is a terminology that mimicked from a "bleeding" biological method, which can be described as the ability of a material to repair damages [3]. Many literature has expounded the rationale of self-healing: after the appearance of damages or cracks, reactive substances in the system are released to the site of injury and fix it to some certain extent. Essentially, the core idea about self-healing is the existence of reactive substances, which can polymerize after some microcracks appear. Hence, instead of adding new reactive materials into the material, preserving the reactants during manufacturing procedures, and trigger another reaction after damage appears using external stimulus is another way to fabricate self-healing materials.

2 MATERIALS AND EXPERIMENTS

In this work, the resin for fabricating the patch composite is designed for ambient temperature cure. Its prepolymer is a low molecular weight "green" epoxy resin that made from bio-based epichlorhydrine. The hardener used is Cardolite NX5619, a solvent-free, low viscosity phenalkamine curing agent made through the Mannich reaction of cardanol from cashewnuts, formaldehyde, and amines. The natural fiber used is flax, a *quasi-unidirectional fabric* made of untwisted rovings. The weft and warp ratio is 9/91 and the areal density is 200 g/m^2. The manufacturing of the natural fiber reinforced epoxy composite was accomplished by the use of wet hand lay-up process (2 plies) at room temperature.

The DSC analyses of the epoxy resin were carried out with a METTLER DSC822e thermal analyzer to measure the glass transition temperature (Tg) and to monitor the curing degree. As for the experiment, the prepared resin samples of 5-10 mg were placed in aluminum pans and were scanned from -80°C to 300°C with different heating rates 5, 10, 15 and 20°C/min.

The dynamic mechanical behaviors of epoxy resin samples and flax fibers reinforced bio-epoxy composites were analyzed by using a DMA equipment (DHR2, TA Instrument). The experiments were performed under tensile-compression mode. Rectangular specimens of $20 \times 10 \times 3$ mm^3 were prepared for the tests. The testing temperature ranged from -80 °C to 150 °C at a rate of 1 °C/min with different frequencies of from 0.1 to 30 Hz.

The technique used for monitoring in this job was based on the measurement of the electrical impedance of a piezoelectric PZT ceramic disc which embedded inside the composite materials as its impedance is linked to the characteristics of the surrounding medium, which varies as cure progresses. In general, the curing process is the transition that thermosettings change from viscous liquid state to infusible cross-linked solid (3D-network). This transformation may involve two main transitions: gelation when the viscous liquid prepolymer is transformed into an infusible, insoluble

gel or rubber-like material and vitrification, which corresponds to rubber-glass transition. At vitrification, the rate of the cure reaction may be reduced due to molecular mobility.

3 RESULTS AND DISCUSSION

The typical DSC thermograms of the non-isothermal scan of the whole curing process is shown in Fig. 1. It can be observed that there are two broad and relatively independent exothermic peaks, which is a characteristic of the dual-curing epoxy crosslinking reaction. By analysing the DSC heat flow curves, we can find that the heating rates have little influence on the total reaction heat: $\Delta H_{total} = 280 \pm 3$ J/g. Besides, the gap temperature between two peaks is about 100 degrees, which is a quite considerable data for the property of separated curing. The percentage of the second peak increases with the increasing heating rates, that is due to the thermal hysteresis of the tested sample and it stands out as the quality of the test sample increase.

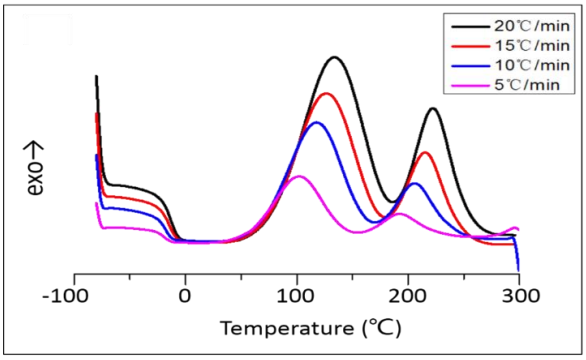

Figure 1. the DSC curve of the epoxy resin

Fig.2A shows the DMA results of composite with different curing levels. The specific curves with black, red and blue represent the curing conditions of in the fridge, at room temperature and at 90℃. With increasing curing temperature, the conversion of degree increases too, given by the evidence of higher Tg temperature and lower value of tan delta. The result of aging experiment is given in Fig.2B. The specific curve with black color corresponds to the samples that soaked in water for two weeks, while the red curves represent the samples that soaked in water for 2 weeks then post-cured at 140℃ for 24 hours. We can find that the healing process increases the Tg and decreases the tan delta. This phenomenon is due to the special dual-curing epoxy resin.

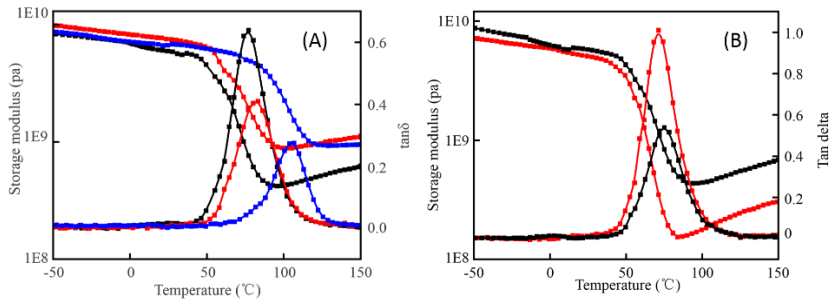

Figure 2 (A) DMA results of composites with different curing levels and (B) DMA results of composites before and after aged

The variation of impedance versus time has a sigmoidal shape, as shown in Fig 3. At the very beginning, the thermoset mixture is composed of low-molecular pre-polymers. As the reaction proceeded, chain extension occurs to produce relatively high molecular weight reaction products resulting in an increase in impedance. Gelation which corresponded to the first appearance of an infinite cross-linked network may be related to the time at which the first significant increase in stiffness. While vitrification is associated with the transition from a rubbery modulus to a glassy modulus. Beyond, the impedance continued to increase slowly long after the vitrification: the reaction dramatically slows, since the cure mechanism was controlled by the molecular diffusivity, but does not come to end. Besides, similarly, the same monitoring process is ongoing for the composites tests and the composite failure tests.

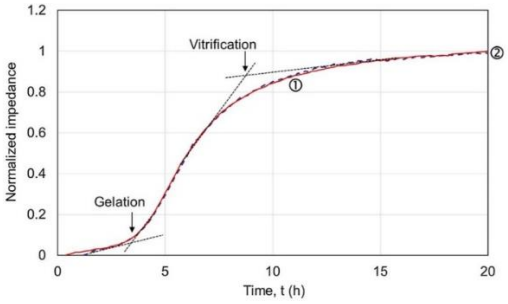

Figure 3 Normalized impedance vs time during cure at RT of two different plates (arrows indicate gelation and vitrification)

4 CONCLUSION

In our work, natural fiber reinforced composites were fabricated using a novel two-stage curing process. After the first curing of epoxy resin, the excellent mechanical properties of composite are endowed. Meanwhile, the potential reactivity of epoxy at elevated temperature is also reserved. When the mechanical properties of the material in use decrease to a critical point, the “self-healing process” is triggered under temperature increase allowing to recover the materials to some extent, avoiding the risk of collapse in the short term before extended repairing. As a result, the conversion rate, crosslinking density, glass transition temperature as well as tensile strength of the composite can be improved further. Differential scanning calorimetry (DSC), dynamic mechanical analysis (DMA) and PZT tests were applied to characterize the feasibility of two-stage curing process, the conversion rate, the mechanical strength and the real-time electrical impedance feedback of composite respectively.

REFERENCES

[1] F. Regina, R. M. William, B. Derrick, A. Purvis, A. Tiwari, and G. D. M. Serugendo "Self-healing and self-repairing technologies". *The International Journal of Advanced Manufacturing Technology*, 69(5-8),1033-1061, 2013.

[2] G. Park, H. Sohn, C. R. Farrar and D. J. Inman "Overview of piezoelectric impedance-based health monitoring and path forward". *Shock and Vibration Digest*, 35(6), 451-463, 2006.

[3] D. G. Bekas, K. Tsirka, D. Baltzis and A.S. Paipetis "Self-healing materials: a review of advances in materials, evaluation, characterization and monitoring techniques". *Composites Part B: Engineering*, 87, 92-119, 2016.

RELIABILITY ASSESSMENT OF DAMAGE DETECTION TECHNIQUES BASED ON GUIDED ULTRASONIC WAVES

Fabrizio Ricci[1*], Vittorio Memmolo[1], Leandro Maio[1], Natalino Boffa[1] and Ernesto Monaco[1]

[1]Dept. of Industrial Engineering, University of Naples "Federico II"
Via Claudio 21, 80125 Naples, ITALY
Email: fabricci@unina.it

ABSTRACT

Guided wave (GW) Structural Health Monitoring (SHM) allows to assess the health of aerostructures thanks to the great sensitivity to delamination and/or debonding appearance. Due to the several complexities affecting wave propagation in composites, an efficient GW SHM system requires its effective quantification associated to a rigorous statistical evaluation procedure. Probability of Detection (POD) approach is a commonly accepted measurement method to quantify NDI results and it can be effectively extended to an SHM context. However, it requires a very complex setup arrangement and many coupons. When a rigorous correlation with measurements is adopted, Model Assisted POD (MAPOD) is an efficient alternative to classic methods. This paper is concerned with the identification of small emerging delamination in composite structural components. An ultrasonic GW tomography focused to impact damage detection in composite plate-like structures recently developed by authors is investigated, getting the bases for a more complex MAPOD analysis. Experimental tests carried out on a typical wing composite structure demonstrated the effectiveness of modeling approach in order to detect damages with the tomographic algorithm. Environmental disturbances, which affect signal waveforms and consequently damage detection, are considered simulating a mathematical noise in the modeling stage. A statistical method is used for an effective making decision procedure. A Damage Index approach is implemented as metric to interpret the signals collected from a distributed sensor network and a subsequent graphic interpolation is carried out to reconstruct the damage appearance. A model validation and first reliability assessment results are provided, in view of performance system quantification and its optimization as well.

1 INTRODUCTION

Failure of aerospace structures can lead to drastic reduction of safety for passengers with a catastrophic impact on the flight operator and the manufacturer as well. Although the aircraft design

adopting composite materials allows to obtain lighter and more efficient structural components, they show really complex damage mechanisms. Hence, it is difficult to fully exploit the potentiality of that designed materials, constraining the design phase with the reduction of the allowable stresses. Although a great effort has been made in the damage prediction after low velocity impacts [1], an active Structural Health Monitoring (SHM) is actually the only way to increase the safety, reducing the design constraints and inspection frequency as well.

In this context ultrasonic guided waves (GWs) appear to be suitable for many SHM applications due to the good compromise between sensitivity to damage, extent of the area monitored, and time required for inspection. Many approaches and reconstruction algorithms have been validated and correctly applied to composite specimens and full-scale components [1]. However, it is quite challenging to get to practice the implementation of the SHM approaches because it is difficult to quantify the system performances. For that reason, it is important to define the probability of detection of the adopted methodology. To achieve the reliability assessment of a prescribed approach, many coupons would be necessary in order to vary the damage condition and the inspection parameters. To reduce the number of experimentally tested coupons, numerical aiding is strongly demanded in a model assisted probability of detection approach [2].

This paper concerns with the model validation of a finite element approach oriented to the reliability assessment of a damage detection methodology already developed by the authors. Much effort is provided with multiple analysis in order to achieve a reasonable modelling of both propagation and damage interaction behavior. The main issue is the feasibility to adopt experimental data in order to only assess the modelling stage. Then, the large amount of data required for statistical assessment could be extracted from simulated environment with few efforts. The remainder of this paper is organized as follows: the methodology for damage detection is explained with its peculiarities, highlighting the way to perform the making decision procedure. Several approaches available in the context of FE modelling are briefly presented with their peculiarities, justifying the given choice. Then, a multiple validation is provided, accounting vibrational as well as damage interaction properties revealed during experimentations. Finally, the results obtained until now by processing of experimental data and modelling procedure are discussed, in view of the next possibilities oriented to reliability assessment of SHM systems within simulated environments.

2 DAMAGE DETECTION APPROACH

Lamb wave propagation is used to detect early emerging flaws in composite structures. The pitch catch configuration is used for the detection of Lamb waves: the wave is excited and detected in the direct line of sight. The converse and direct piezoelectric effects are exploited for excitation and detection purposes respectively, by means of a variable voltage input. Circular transducers are employed generating omnidirectional waves. The enclosed area is monitored using all possible pairs of sensors. Individually activating each transducer, a network of paths gathering information of wave field is thus obtained (see [3][2] for further details). Then, through signal processing techniques, several wave features can be extracted and used for assessing structural health along such paths. A baseline interrogation is performed on the pristine structure storing the undamaged condition of the structure. The health monitoring is finally operated via scheduled interrogations tracking any change in the dynamic response. A DI formulation is provided for the network paths comparing the current response with the baseline reference, as reported in Equation (1)

$$DI = \frac{|CS - BS|}{BS} \tag{1}$$

where CS and BS are the representative feature of the signal recorded on the operating structure and the pristine structure, respectively.

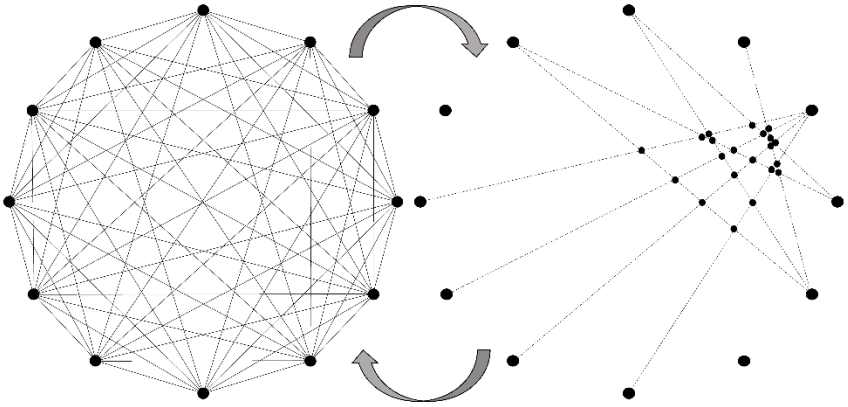

Figure 1. Damage reconstruction network.

To assess the effective network gathering successful information on the damage occurrence a statistical decision-making strategy is employed. To this end, the noise is characterized via concurred measurements every time the interrogation is scheduled estimating the decision DI via statistical analysis. From the intersection points of the selected network (see Figure 1), the damage can be identified, located and reconstructed using the detecting procedure proposed in [4].

3 MODELLING STRATEGY

The ABAQUS® Explicit package is used here to solve the dynamic equation of motion, evaluating the group velocity of the first antisymmetric Lamb wave mode propagating in laminated composite structures. The equivalent single layer approach based on the First Shear Deformation Plate theory (FSDT) is used to idealize the structure. To this purpose, the S4R element available in the Abaqus explicit library (a 4-node, reduced integration and hourglass control finite element) is adopted, allowing to control the shear effects as well. Figure 2 (a) depicts the scheme employed in the simulated environment. From the recorded signals, the group velocity of the propagating A_0 mode is evaluated by means of Short Time Fourier. Figure 2 (b) shows the comparison between numerical results and measurements highlighting the reasonable result obtained (maximum percentage error of 5 %).

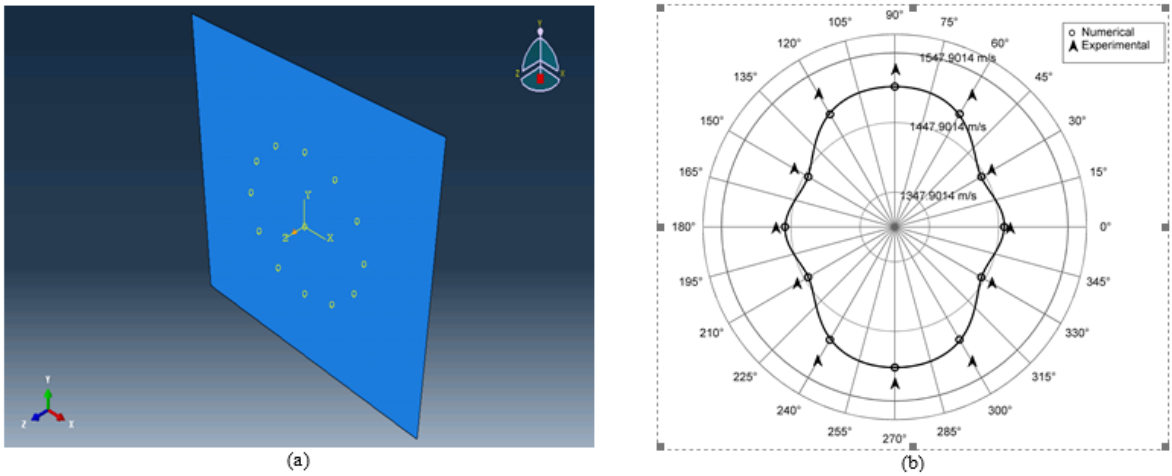

(a) (b)

Figure 2. Overall scheme adopted in the simulation environment for the arrival time correlation (a) and group velocity comparison (b). Max percentage error of 5%.

After validating the model for wave propagation in pristine condition, the case of damage interaction is addressed by idealizing the damage as a stiffens reduction of the whole section affected by the flaw.

The damage indicators are in line with experimental findings and the damage detection is operated by the described reconstruction algorithm. Mathematical noise is introduced in the signals to simulate the making-decision strategy as well and different damage size are simulated to define the POD. The results are reported in figure 3 and demonstrate the reasonable results obtained by model assisted reliability assessment.

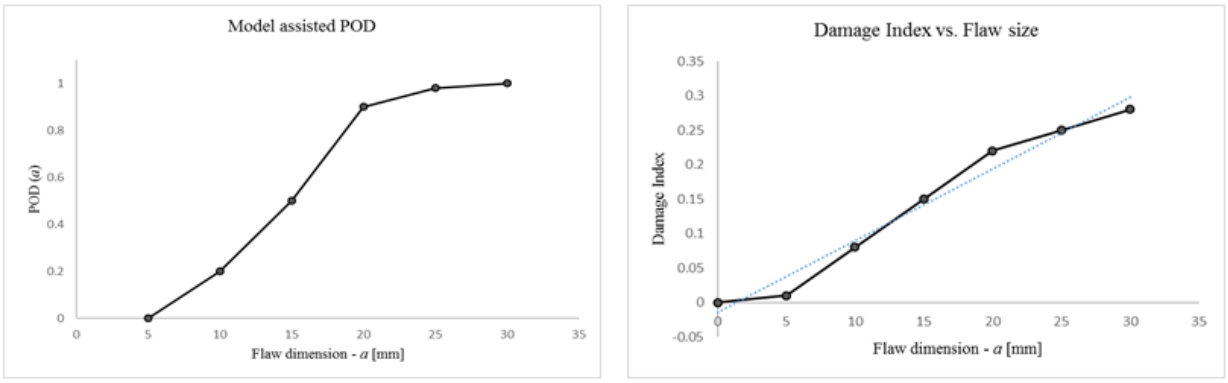

(a) (b)

Figure 3. Estimated POD data for the active diagnostic system through simulated hit miss analysis (a) and indicative Damage Index Profile evaluated along single path.

4 CONCLUDING REMARKS

In the present work a comprehensive analysis of the modelling validation for the reliability assessment of a SHM system is presented. In view to investigate a more complex MAPOD analysis to establish the system performance, the damage detection system is briefly introduced, mostly addressing the reasonable results obtained. The interaction of guided waves A0 mode with through thickness delamination carries important information on the damage location. The Finite Element simulations carried out adopting FSDT based equivalent single layer approach provide a good understanding of the interaction process. Moreover, a good agreement between simulations and experimental results has been achieved in terms of wave propagation, wave-defect interaction and damage detection. The noise simulation is demonstrated to be a reasonable replication of experimental uncertainties and allows to simulate the decision-making procedure as well. The early results show the sensitivity of proposed DI respect to the in-plane dimension and depth of damage. Finally, the reliability approach opens interesting scenarios in view of the application of a more sophisticated *a vs. a* MAPOD analysis.

REFERENCES

[1] Maio, L., Monaco, E., Ricci, F., Lecce, L., "Simulation of low velocity impact on composite laminates with progressive failure analysis," Composite Structures, 103, 75-85 (2013)

[2] Cobb, A. C., and Fisher, J., "Model-assisted probability of detection for ultrasonic structural health monitoring," in 4th European-American Workshop on Reliability of NDE, Berlin, Germany, 24–26 June 2009

[3] Memmolo, V., Monaco, E., Boffa, N.D., Maio, L., Ricci, F., "Guided wave propagation and scattering for structural health monitoring of stiffened composites," Composite Structures, 184, pp. 568-580, 2018.

[4] Memmolo, V., Boffa, N.D., Maio, L., Monaco, E., Ricci, F., "Damage localization in composite structures using a guided waves based multi-parameter approach," Aerospace, 5 (4), 2018.

COMPARISON OF DAMPING PERFORMANCES OF CONSTRAINED VISCOELASTIC LAYERS AND PASSIVE PIEZOELECTRIC NETWORKS

L. Rouleau[1*] , B. Lossouarn[1] , R. Darleux[1] and J.-F. Deü[1]

[1]LMSSC - Conservatoire national des arts et métiers
292 Rue Saint-Martin, 75003, Paris, FRANCE
Email: lucie.rouleau@lecnam.net, boris.lossouarn@lecnam.net, robin.darleux@lecnam.net, jean-francois.deu@cnam.fr

ABSTRACT

This work aims at comparing the damping performances of two passive treatments based on piezoelectric or viscoelastic patches. The motivation for such a comparison stems from the fact that the two damping treatments have been developed fairly independently, and are rarely compared. Firstly, the dynamic response of a simply supported metallic plate, equipped with constrained viscoelastic patches or piezoelectric patches connected to an electrical network, is measured experimentally. Secondly, a numerical model of the structure is set up and validated to evaluate the damping performances of both passive treatments under different configurations (for instance equal-mass and equal-thickness configurations). Finally, with regard to this work, the advantages and the limitations in using viscoelastic or piezoelectric treatments are discussed.

1 INTRODUCTION

In the context of noise and vibration mitigation, several damping technologies are proposed in the literature. Among them, purely passive treatments generally lead to low-cost and robust structural vibration control. These can be achieved by bonding constrained viscoelastic patches to the structure or by using piezoelectric patches connected to an electrical network. With piezoelectric patches, the vibrational energy is transfered to an electric circuit and dissipated in resistive components ; while with viscoelastic patches, it is transfered to the viscoelastic layer (undergoing shear deformations) and is dissipated in the damping material. Resonant piezoelectric shunts are commonly tuned to a single mechanical natural frequency to be controlled [1]. However, broadband vibration reduction can be obtained with multimodal damping, where the structure is coupled to a multi-resonant electrical network [2]. On the other hand, due to the frequency dependent damping properties of viscoelastic materials, viscoelastic patches naturally provide broadband damping [3]. The goal of this work is to provide an experimental and a numerical comparison of the damping performances of constrained viscoelastic layers and passive piezoelectric networks. Comparisons are carried out on a simply supported metallic plate, equipped with constrained viscoelastic patches or piezoelectric patches connected to an electrical network. The efficiency of both passive treatments usually depends on the volume of material used, so that the performance is generally limited by weight and size constraints. Therefore, numerical models of the damped panels are implemented and validated in order to test the two damping technologies under different configurations, such as equal-mass and equal thickness configurations.

2 EXPERIMENTAL COMPARISON

The structure under study is an aluminium panel, of dimensions $420 \times 360 \times 3$ mm^3. 42 viscoelastic or piezoelectric patches are periodically distributed on the panel, as indicated in Figure 1. Each patch is of dimensions 50×50 mm^2.
Viscoelastic patches are composed of a 120 m viscoelastic layer (Smacwrap®) and a 1.04 mm composite laminate which acts as a constraining layer. Piezoelectric patches are made of PIC 153 (PI Ceramic) and are 0.5 mm thick. A vacuum bonding technique is used to assemble all the layers. These damping solutions lead to a 15% added mass for the viscoelastic patches and a 33% added mass for the piezoelectric patches, not taking into account the mass of the electrical components.
The electrical network that interconnects the piezoelectric patches consists of 42 identical unit cells made of passive components such as inductors and transformers. Their values and interconnections are chosen so as to create, in the electrical domain, the analogue of the plate to be controlled [4]. This generates a multi-resonant network whose natural frequencies are tuned to that of the mechanical plate in order to obtain the equivalent of a multimodal tuned mass damper.
Panels are mounted in a specific frame to approximate simply supported boundary conditions [5, 6]. The whole structure is suspended and excited by a shaker, while the structural dynamic response is measured by a laser vibrometer. The location of the shaker is given by the coordinates $x = 0.12$ m, $y = 0.15$ m and $z = 0.003$ m, and a pseudo-random excitation is generated. The frequency response of the structure is measured at the excitation point, in the frequency range $0 - 900$ Hz, with a frequency step of 0.156 Hz. Three panels are tested: a bare aluminium panel, an aluminium panel with viscoelastic patches and an aluminium panel with piezoelectric patches connected to a multi-resonant network. The measured frequency response functions are plotted in Figure 2. Both damping treatments induce a drastic reduction of the dynamic response over the whole frequency range. Multi-resonant piezoelectric damping is more efficient than viscoelastic damping for the first vibration modes. However, they offer similar damping performances above 400 Hz.

3 NUMERICAL COMPARISON

For practical reasons, the configurations considered for piezoelectric and viscoelastic damping do not correspond to equal-mass or equal-thickness configurations. In order to compare the two passive treatments in a more objective manner, numerical models of the damped panels are implemented [2, 7] and experimentally validated.
Weight and dimensions being classical constraints in the design of a damping treatment, two configurations are studied : equal-mass and equal-thickness. To that purpose, the dimensions of the

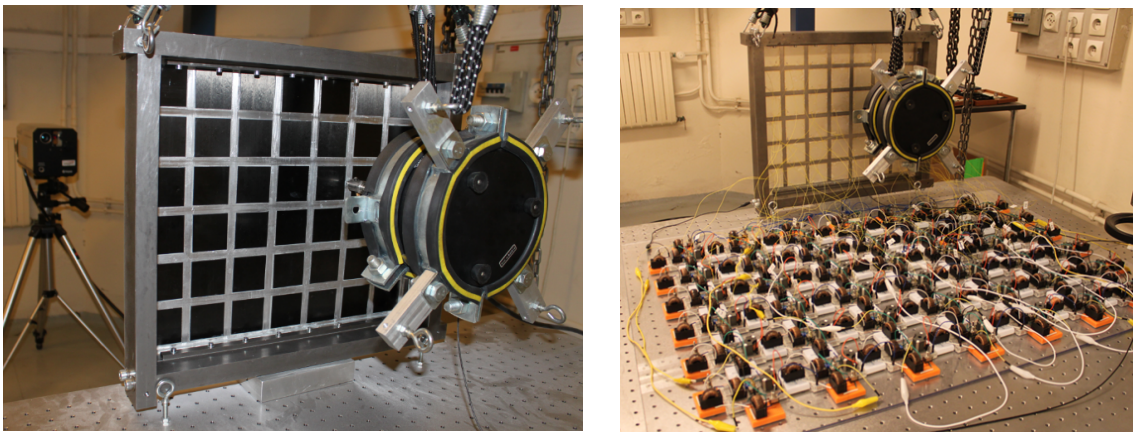

(a) (b)

Figure 1: Experimental set-up for the panel with viscoelastic patches (a) and the panel with piezoelectric patches connected to an electrical network (b).

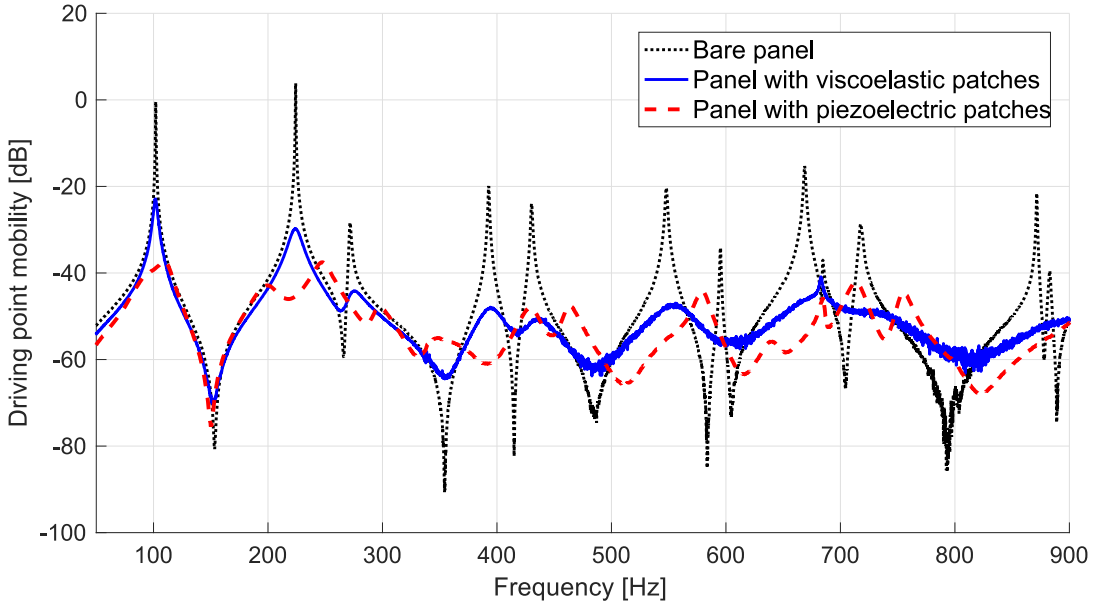

Figure 2: Frequency response functions measured on the bare aluminium panel, the panel with viscoelastic patches and the panel with piezoelectric patches.

piezoelectric or the viscoelastic patches have been modified in the numerical models. Results show that for the equal-mass configuration, the damping performances of the piezoelectric patches are better than those of the viscoelastic patches below 400 Hz. Above 400 Hz, the inverse tendency is observed. For the equal-thickness configuration, the piezoelectric solution is identified as the most efficient damping technique in terms of vibration damping, over the whole frequency range.

4 CONCLUSION

The goal of this work was to compare the damping performances of two passive treatments based on constrained viscoelastic layers or on piezoelectric patches connected to a multi-resonant electrical network. To this end, experimental and numerical tests have been carried out on a metallic panel, equipped with viscoelastic or piezoelectric patches. Numerical models of both panels have been experimentally validated, which enables the numerical study of two configurations: equal-mass and equal-thickness configurations.
The main conclusions of this work are :

- The damping performances of piezoelectric networks are generally more advantageous than those of viscoelastic materials to damped the first vibration modes.
- To damp higher modes of vibrations, the most efficient damping technique depends on the considered mass and dimension constraints.

The impact of other design constraints, such as cost, integrability or temperature, should be further investigated for an objective comparison of the damping performances of both passive treatments.

5 ACKNOWLEDGEMENTS

We acknowledge gratefully Safran Aircraft Engines for their contribution to the realization of the panel with viscoelastic patches.

REFERENCES

[1] O. Thomas, J. Ducarne, and J.-F. Deü. Performance of piezoelectric shunts for vibration reduction. *Smart Materials and Structures*, 21(1):015008, 2012.

[2] B. Lossouarn, J.-F. Deü, M. Aucejo, and K.A. Cunefare. Multimodal vibration damping of a plate by piezoelectric coupling to its analogous electrical network. *Smart Materials and Structures*, 25(11):115042, 2016.

[3] L. Rouleau, R. Pirk, B. Pluymers, and W. Desmet. Characterization and modeling of the viscoelastic behavior of a self-adhesive rubber using dynamic mechanical analysis tests. *Journal of Aerospace Technology and Management*, 7(2):200–208, 2015.

[4] B. Lossouarn, M. Aucejo, J.-F. Deü, and K.A. Kunefare. Design of a passive electrical analogue for piezoelectric damping of a plate. *Journal of Intelligent Material Systems and Structures*, 29(7):1301–1314, 2018.

[5] O. Robin, J.-D. Chazot, R. Boulandet, A. Berry, and N. Atalla. A plane and thin panel with representative simply supported boundary conditions for laboratory vibroacoustic tests. *Acta Acustica united with Acustica*, 102:170–182, 2016.

[6] O Robin, A. Berry, N. Atalla, M. Aucejo, B. Lossouarn, L. Rouleau, J.-F. Deü, C. Marchetto, and L. Maxit. Setting up plane and thin panels with representative simply supported boundary conditions: comparative results and applications in three laboratories. In *Proceedings of Internoise 2018*, Chicago, Illinois, August 2018.

[7] L. Rouleau, A. Legay, and J.-F. Deü. Interface finite elements for the modelling of constrained viscoelastic layers. *Composite Structures*, 204:847–854, 2018.

ATTENUATION PERFORMANCE DUE TO CORRELATED DISORDER IN RAINBOW METAMATERIALS

A.T. Fabro[1], H. Meng[1] and D. Chornopolous[2]

[1]Department of Mechanical Engineering
University of Brasilia, Brasília-DF, BRAZIL
Email: fabro@unb.br

[2]Institute for Aerospace Technology & The Composites Group
University of Nottingham, Nottingham, UK
Email: han.meng@nottingham.ac.uk, dimitrios.chronopoulos@nottingham.ac.uk

ABSTRACT

Metastructures are typically composed of periodic unit cells designed to present enhanced dynamic properties in which either single or multiple resonators are periodically distributed. Even though the periodic metamaterials can obtain outstanding vibration attenuation when compared to the single resonator design, the bandgap width can still be narrow for some practical applications. Rainbow metamaterial have been proposed based on gradient or random profiles providing further improved attenuation. Nonetheless, the effects of correlated random disorder, i.e., spatial correlation on the resonator properties, on the attenuation performance remains an open challenge. This work presents a numerical investigation on the effects of correlated disorder on the vibration attenuation performance in metamaterials. A transfer matrix approach is used to calculate transfer receptance in a finite length metastructure composed of evenly spaced non-symmetric resonators attached to a beam with Π-shaped cross-section, thus a multi-frequency metastructure. Individual samples of correlated random fields are used to show the effects of the correlated disorder in the attenuation performance of the metastructure. It is shown that the band gap can be further widened when compared to the uncorrelated disorder. These results open new and innovative ways for the design of metastructures.

1 INTRODUCTION

Most of the proposed metamaterials are periodic structures in which either single or multiple resonators are periodically distributed. Even though the periodic metamaterials can obtain good

vibration attenuation within bandgap regions when compared to the traditional single resonator design, the width of the bandgap can still be narrow for some practical applications.

The use of the so-called rainbow metastructure is an interesting concept for achieving broad-band wave attenuation. Originally proposed in the context of optical waves [1], this concept has been further developed for acoustic [2], ultrasonic [3] and elastic waves [4]. Moreover, Meng et al. [5] have shown that optimal spatial distribution of the tuning frequency of each resonator can be further explored for different performance criteria in multi-frequency metamaterials, opening new and innovative possibilities for metamaterial design. In order to enlarge the bandgap of locally resonant metamaterials, a deviation from the typical periodic design, using near-periodic, quasi-periodic or a-periodic approaches is capable to significantly improving the dynamic performance of metastructures. Recently, Celli et al. [6] have shown that random disorder in rainbow metamaterial can provide improved wave attenuation when compared to graded configurations. Nonetheless, the effects of correlated random disorder, i.e., spatial correlation on the resonator properties, on the bandgap widening performance remains unexplored to the best of the authors knowledge, and an open challenge to be addressed.

The aim of this work is to present an investigation of the effects of correlated disorder on the vibration attenuation performance in rainbow metamaterials. Section 2 briefly introduces metastructure with non-symmetric resonators for rainbow design, based on a previously proposed design [5,7]. Section 3 presents the correlated disorder model and some numerical results, Finally, section 4 gives some concluding remarks.

2 METAMATERIAL BEAM WITH NON-SYMMETRIC RESONATORS

In this section, the proposed rainbow metastructure and an analytical model for beam with two non-symmetric resonators is, shown in Figure 1, based on the design proposed by Meng et al. [7] is briefly presented. The metastructure is composed of a total of 17 unit cells, with two non-symmetric cantilever-mass attached acting like local resonators, as presented in Figure 1. In the proposed design, each resonator can act independently such that it is possible to create two separate band gap regions, thus broadening the total attenuation band.

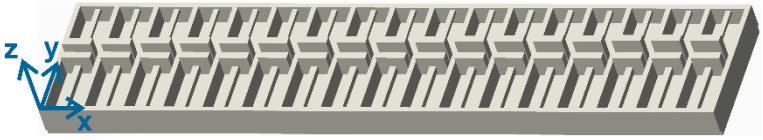

Figure 1: Schematic representations of the metamaterial beam with non-symmetric resonators at each unit cell [7].

An analytical model based on transfer matrix approach has been previously proposed and experimentally validated [7]. It is assumed a Euler-Bernoulli beam theory for both the baseline host structure and the cantilever-mass resonator. Each resonator is modelled as a beam point attached to the baseline structure at one end and a lumped mass with negligible inertia at the other. Additionally, the periodic plate insertions are modelled as added masses to the Π-shaped beam at the ends of each segment.

For a periodic structure, the transfer matrix $\mathbf{T}_n$ is identical for every segment. Consequently, according to the Bloch theorem [8], a wavenumber k_n can be defined from the propagation constant $\mu_n = \exp(-ik_n L_d)$, for a unit cell of length L_d, which is given from the transfer matrix of the periodic metamaterial such that $|\mathbf{T}_n - \mu_n \mathbf{I}| = 0$. However, this assumption does not hold when the metastructure is no longer periodic. In this sense, an equivalent wavenumber k_T can also be defined from the propagation constant $\mu_T = \exp(-ik_T L)$ of the finite length L metastrucure with spatially

varying properties, i.e. near-periodic, as [7] $|\boldsymbol{\Xi} - \mu_T \mathbf{I}| = 0, \text{where } \boldsymbol{\Xi} = \mathbf{T}_m \mathbf{T}_{m-1} \dots \mathbf{T}_1$. The equivalent wavenumber k_T can be also interpreted as the wavenumber when the finite rainbow metamaterial is a periodic unit of an infinite complex beam and it represents the total phase change and attenuation of a travelling wave over m unit cells. It is used as a tool to understand the wave-like behaviour of non-periodic structures. Note that the total phase and attenuation change $k_T L$, which is a complex number for the case of metastructure, is not generally equal to the contribution of the phase and attenuation change at each segment in the near periodic metastructure, i.e., $k_T L \neq \sum_{n=1}^{m} k_n L_d$. This is because of the additional scattering created due to the differences in neighbouring segments.

3 NUMERICAL RESULTS

In this section, a numerical analysis is carried out considering a metastructure produced from 3D printing by a powder bed fusion method with Nylon-12 employed to fill the powder bed material and geometrical properties as described in [7] with a total of 17 unit cells and total beam length $L_T = 257$ mm. The tip mass in both resonators at each unit cell is assumed to have a mean value of 1 g. Note that, in this case, the difference in length of the beams produces the differences in the resonance frequencies and therefore in the band gaps. The numerical results are presented only the band gap of higher frequency. The correlated disorder is introduced in by varying the tip masses of the resonators according to

$$\mathbf{m}_{1,2} = m_{0_{1,2}}(\mathbf{1} + \sigma_m \boldsymbol{\xi}_{\mathrm{m}}), \tag{1}$$

where $m_{0_{1,2}}$ is the nominal values of the resonators tip masses in the periodic design, $\mathbf{1}$ is a vector $m \times 1$ vector filled with 1 and σ_m controls the level of statistical dispersion of the random vector $\boldsymbol{\xi}_{\mathrm{m}}$, which represents a discrete Gaussian homogeneous random field, with autocorrelation function given by $C(\tau) = \exp(-\tau/c_l)$, where c_l is the correlation length, i.e., the level of statistical fluctuation of the spatial variability. In other words, this parameter controls the smoothness of the spatial variation, given the spatial profile of the tip masses of the resonators along the beam. The uncorrelated disorder corresponds to the case in which the correlation length equal zero, i.e., the values of the tip masses are statistically independent, giving a white-noise type of spatial profile. For increasing correlation length, the spatial variation of masses becomes increasingly smooth, such that for infinitely large correlation correspond to a homogeneous profile, thus the periodic design.

Figure 2(a) presents the amplitude of the transfer receptance around the second band gap frequency considering uncorrelated disorder, $c_l = 0.1L$ and $c_l = 1L$. The three cases are produced a single sample of a random field with the same random seeds, such that only the smoothness of the spatial profile is affected. Note that the correlated disorder has a clear effect of further widening the band gap when compared to the uncorrelated disorder case. Figure 2(b) presents the imaginary part of $k_T L$, i.e. the attenuation change defined over the length of the metastructure. It has a similar interpretation of imaginary part of the wavenumber in periodic structures. Negative values indicate wave attenuation, and it clearly shows a similar behaviour in terms of vibration attenuation.

4 CONCLUDING REMARKS

In this work, an investigation of the effects of correlated disorder on the vibration attenuation performance in rainbow metamaterials is presented. An analytical model based on the transfer matrix method of a finite length metastructure is used to calculate the transfer receptance to a point harmonic force. The metastructure is composed of evenly spaced non-symmetric resonators attached to a beam with Π-shaped cross-section, thus a multi-frequency metastructure. Correlated disorder is introduced by varying the tip masses of the resonators according to a single sample of a homogeneous Gaussian random field with a given correlation function. Its correlation length is used to vary the correlation

level of the disorder. For increasing correlation length, the spatial variation of masses becomes increasingly smooth. It is shown in terms of the transfer receptance and total wave attenuation that the band gap can be further widened when compared to the uncorrelated disorder. These results open new and innovative ways for the design of metastructures

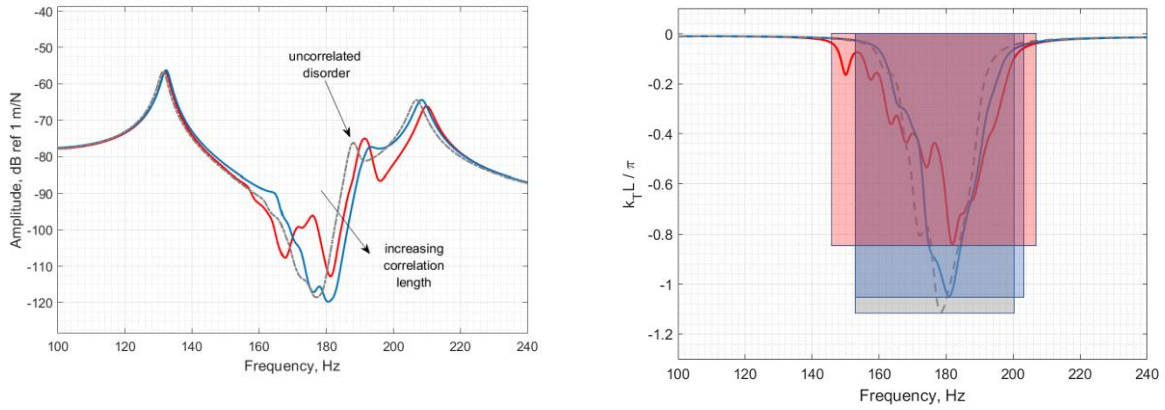

(a) (b)

Figure 2: (a) Amplitude of the transfer receptance around the second band gap frequency and (b) attenuation change defined over the length of the metastructure, considering uncorrelated disorder (grey dashed line), $c_l = 0.1L$ (red line) and $c_l = 1L$ (blue line).

ACKNOWLDEGMENTS

The authors would like to acknowledge the support acquired by the H2020 DiaMoND project (Grant Agreement ID:785859), Royal Society Grant: PURSUIT, the Brazilian National Council of Research CNPq (Grant Agreement ID: 420304/2018-5) and the Federal District Research Foundation FAPDF (Grant Agreement ID: 0193.001507/2017).

REFERENCES

[1] K.L. Tsakmakidis, A.D. Boardman, O. Hess, 'Trapped rainbow' storage of light in metamaterials, Nature. 450 (2007) 397–401. https://doi.org/10.1038/nature06285.
[2] J. Zhu, Y. Chen, X. Zhu, F.J. Garcia-Vidal, X. Yin, W. Zhang, X. Zhang, Acoustic rainbow trapping, Sci. Rep. 3 (2013) 1728. https://doi.org/10.1038/srep01728.
[3] Z. Tian, L. Yu, Rainbow trapping of ultrasonic guided waves in chirped phononic crystal plates, Sci. Rep. 7 (2017) 40004. https://doi.org/10.1038/srep40004.
[4] J. Sanchez-Dehesa, A. Arreola-Lucas, G. Baez, F. Cervera, A. Climente, R. Mendez-Sanchez, Mechanical rainbow trapping and Bloch oscillations in chirped metallic beams, J. Acoust. Soc. Am. 141 (2017) 3810–3810. https://doi.org/10.1121/1.4988421.
[5] H. Meng, D. Chronopoulos, A.T. Fabro, I. Maskery, Y. Chen, Optimal design of rainbow elastic metamaterials, Int. J. Mech. Sci. (2019) 105185. https://doi.org/10.1016/j.ijmecsci.2019.105185.
[6] P. Celli, B. Yousefzadeh, C. Daraio, S. Gonella, Bandgap widening by disorder in rainbow metamaterials, Appl. Phys. Lett. 114 (2019) 091903. https://doi.org/10.1063/1.5081916.
[7] H. Meng, D. Chronopoulos, A.T. Fabro, W. Elmadih, I. Maskery, Rainbow metamaterials for broadband multi-frequency vibration attenuation: Numerical analysis and experimental validation, J. Sound Vib. (2019) 115005. https://doi.org/10.1016/j.jsv.2019.115005.
[8] F. Bloch, Über die Quantenmechanik der Elektronen in Kristallgittern, Z. Für Phys. 52 (1929) 555–600. https://doi.org/10.1007/BF01339455.

NON-LINEAR FREE VIBRATIONS OF FUNCTIONALLY GRADED NON-UNIFORM BEAMS WITH DISCONTINUITIES

M.Chajdi[1*] , A. Adri[2] , K. El bikri[1] and R. Benamar[3]

[1]Mohammed V University in Rabat, ENSET - Rabat, MSSM, B.P.6207, Rabat Instituts, Rabat, Morocco
Email: mohcine.chajdi@um5s.net.ma, k.elbikri@um5s.net.ma

[2]Hassan II University of Casablanca, EST - Casablanca, LMPGI, B.P.8012, Oasis Casablanca, Morocco
Email: ahmedadri@gmail.com

[3]Mohammed V University in Rabat, EMI - Rabat, LERSIM, B.P.765 Agdal, Rabat, Morocco
Email: rhali.benamar@gmail.com

ABSTRACT

This paper presents a semi-analytical approach to investigate the geometrically non-linear free vibrations of functionally graded beams with discontinuities. The theoretical model is based on the Euler-Bernoulli beam theory and the Von Kármán geometrical non-linearity assumptions. The neutral surface approach is developed to reduce the problem examined to that of an equivalent isotropic homogeneous non-uniform beam. The harmonic motion is assumed in the non-linear analysis. Hamilton's Principle is applied to the discretised expressions for the beam total strain and kinetic energies, so as to obtain a non-linear algebraic system solved using an approximate explicit method. The numerical results, validated via comparisons with few available results, shows the effects of crack depth and position on the dynamic behaviour.

1 INTRODUCTION

The dynamic behaviour of structures made from functionally graded materials has been a topic of active research over the last few decades, owing to the outstanding properties of this type of material characterised by the smooth and continuous transition in both compositional profile and material properties. In this respect, numerous methods, based on analytical, semi-analytical and numerical techniques, address the problem of functionally graded beam (FGB) vibrations presenting discontinuities with different end conditions. The discontinuities in the beam can be caused by an intermediate support, an attached mass, a transverse edged crack or a step jumps in cross section. The purpose of the present work is to investigate the geometrically non-linear free vibrations of functionally graded non-uniform cracked beams, based on the Euler-Bernoulli beam theory, the Von Kármán geometrical non-linearity assumptions and the rotational spring crack model. The material properties of the FG non-uniform beam examined are assumed to vary according to a power law distribution along the beam thickness. A homogenisation method based on the neutral surface approach, used previously in [1], was employed to reduce the problem under consideration to that of an equivalent isotropic homogeneous non-uniform cracked beam. The closed-form solutions are employed and solved iteratively using the Newton Raphson algorithm. Afterwards, by expanding the non-linear multi-cracked beam transverse displacement function as a series of the linear modes calculated before, the non-linear case was examined. Using the model developed in [2], the modal functions obtained in the linear analysis have been used as trial functions in the development of the so-called second formulation, leading to a multimode approach of the non-linear free response problem. Satisfactory comparison is made with previous analytical results to demonstrate the effectiveness of the proposed procedure considered in the linear case. A quite comprehensive parametric study was performed by varying the crack position to investigate its effect on the dynamic behaviour of a FG non-uniform beam.

2 PROBLEM FORMULATION

2.1 Mechanical properties of the FGB

Consider a straight non-uniform rectangular FG Euler-Bernoulli beam containing discontinuities in the form of cracks and step changes in cross section located at a distance $\xi_n = \frac{x_n}{L}$ from the left end and having a geometrical characteristic shown in Figure 1.

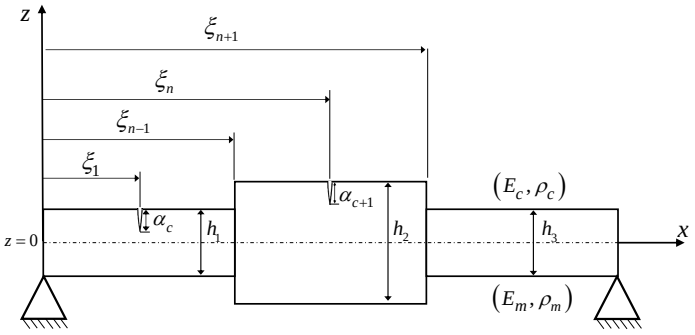

Figure 1: Physical model of the FG non-uniform cracked beam.

The present work formulation based on the neutral surface approach, by considering the change of variable $\overline{z} = z + \delta$ since the neutral plane does not coincide with the middle plane in case of the FGB. The material properties vary smoothly along the thickness direction as follows:

$$P_n(\overline{z}) = (P_{c_n} - P_{m_n}) \left(\frac{z+\delta}{h_n} + \frac{1}{2} \right)^k + P_{m_n} \tag{1}$$

Where P_m and P_c are the corresponding properties of the metal and ceramic, respectively. k is the volume fraction of the FG non-uniform beam and δ is the distance separating the two planes defined by:

$$\delta_n = \int_{-\frac{h_n}{2}}^{\frac{h_n}{2}} zE(z)\,dz \Big/ \int_{-\frac{h_n}{2}}^{\frac{h_n}{2}} E(z)\,dz \tag{2}$$

As in [1], the crack is assumed to be perpendicular to the beam surface and remains always open. Based on the rotational spring model, the bending stiffness K_τ of the cracked section is related to the flexibility C by [3]:

$$C_n = \int_0^{\alpha_n} \frac{72\pi(1-\nu^2)\alpha_n f^2\left(k, \frac{\alpha}{h}\right)}{E_n(\alpha)h_n^2}\, d\alpha_n = \frac{1}{K_{\tau_n}} \text{ with } E_n(\alpha) = (E_{c_n} - E_{m_n})\left(1 - \frac{\alpha_n - \delta_n}{h_n}\right)^k + E_{m_n} \tag{3}$$

Where α_n/h_n is the crack depth, $f^2\left(k, \frac{\alpha}{h}\right)$ is called the crack correction function given in [1] and $E_n(\alpha)$ is the effective elastic modulus at the crack tip.

2.2 Non-linear vibrations analysis

Taking into account Equation (2) in mind, neglected the axial inertia, the expression of the total strain energy V of the symmetrical FG non-uniform cracked beam can be written as follows :

$$V = \sum_{n=1}^{N+1} \frac{(ES)_{\text{eff}_n}}{8L}\left[\int_{\xi_{n-1}}^{\xi_n}\left(\frac{\partial w_n}{\partial x_n}\right)^2\right]^2 + \sum_{n=1}^{N+1}\frac{(EI)_{\text{eff}_n}}{2}\int_{\xi_{n-1}}^{\xi_n}\left(\frac{\partial^2 w_n}{\partial x_n^2}\right)^2 dx_n \tag{4}$$

Equation (4) is effective for replacing the non-uniform FGB problem with an equivalent isotropic non-uniform beam, where $(ES)_{\text{eff}_n} = \overline{A}_{11_n}$ and $(EI)_{\text{eff}_n} = \overline{D}_{11_n}$ are the effective axial and bending stiffness, respectively. The kinetic energy T and the strain energy of the crack V_c are given by:

$$T = \sum_{n=1}^{N+1}\frac{1}{2}\int_{\xi_{n-1}}^{\xi_n}\int_{-\frac{h_n}{2}-\delta_n}^{\frac{h_n}{2}-\delta_n}\rho_n(\overline{z})\left(\frac{\partial w_n}{\partial t}\right)^2 dx_n d\overline{z}_n;\; V_c = \sum_{n=1}^{N+1}\frac{(EI)^2_{\text{eff}_n}}{2K_{\tau_n}}\left(\frac{\partial^2 w_n}{\partial x_n^2}\right)^2_{x_n=x_c} \tag{5a,b}$$

Using the dimensionless formulation, for a general parametric study $w_n(x_n) = h_n w_n^*\left(\frac{x_n}{L}\right)$, assuming harmonic motion and expanding the transverse displacement in the form of a finite series $w^*(x^*,t) = a_i w_i^*(x^*)sin(\omega^* t)$ in which w_i^* are the FG non-uniform cracked beam linear mode shapes and by applying Hamilton's principle, the following set of nonlinear algebraic equations is obtained:

$$2a_i\left(K_{ir}^* - \omega^{*2}M_{ir}^*\right) + 3a_i a_j a_k B_{ijkr}^* = 0,\ \text{r=1,2,..,m} \tag{6}$$

Where K_{ir}^*, M_{ir}^* and B_{ijkr}^* stand for the dimensionless classical rigidity tensor, the mass tensor and the nonlinear rigidity tensor, respectively defined by:

$$K_{ij}^* = \int_0^1 \frac{\partial^2 w_i^*}{\partial x^{*2}}\frac{\partial^2 w_j^*}{\partial x^{*2}}dx^* + \sum_{c=1}^{N_c}\frac{(EI)_{\text{eff}_n}}{K_{\tau_n}^c}\frac{\partial^2 w_i^*}{\partial x^{*2}}\bigg|_\xi \frac{\partial^2 w_j^*}{\partial x^{*2}}\bigg|_\xi;\; M_{ij}^* = \int_0^1 w_i^* w_j^* dx^* \tag{7a,b}$$

$$B_{ijkl}^* = \sum_{n=1}^{N+1}\frac{(ES)_{\text{eff}_n}h_n^2}{4\,(EI)_{\text{eff}_n}}\int_{\xi_{n-1}}^{\xi_n}\frac{\partial w_{i_n}^*}{\partial x_n}\frac{\partial w_{j_n}^*}{\partial x_n}dx_n^*\int_{\xi_{n-1}}^{\xi_n}\frac{\partial w_{k_n}^*}{\partial x_n}\frac{\partial w_{l_n}^*}{\partial x}dx_n^* \tag{8}$$

3 NUMERICAL RESULTS AND DISCUSSION

In order to perform and verify the proposed above procedure, the first three modal frequencies of FGB with three step changes in cross section with Simply Supported end conditions are calculated in Table 1 after normalisation by $\beta = \frac{\omega L^2}{h}\sqrt{\frac{\rho_m}{E_m}}$ using the classical Euler-Bernoulli beam theory and compared to those obtained by Timoshenko beam theory developed in [4], where the neutral surface is assumed to be the middle one corresponding to $k = 2$, $\alpha/h = 0.4$ located at the middle of steps in each case, $h_1 = h_3 = 0.1\text{m}$ and $h_2 = 0.2\text{m}$. It can be shown that the two theories have the same trend when the crack depth increases. The FG non-uniform cracked beam under investigation in Figure 1, has the following material and physical parameters: the top surface of the FGM $E_c = 380\text{Gpa}$, $\rho_c = 3960\text{Kg/m}^3$, the bottom surface of the FGM $E_c = 70\text{Gpa}$, $\rho_m = 2702\text{Kg/m}^3$, $\nu_c = \nu_m = 0.3$ and slenderness ratio $L/h = 30$ with $h_1 = h_3 = 0.01\text{m}$ and $h_2 = 0.02m$. The effect

Mode	intact beam		Single crack			
			First step		Second step	
	Present	[1]	Present	[1]	Present	[1]
1	4.354	4.161	3.993	4.053	3.961	4.040
2	15.125	14.338	13.432	13.756	15.074	14.338
3	45.352	42.188	40.715	40.512	36.597	39.079

Table 1: Comparison of natural frequencies of FG non-uniform beam with differently cracked steps.

of crack with depth $a/h = 0.3$ on the non-linear frequency of S-S FGB with two symmetrical step changes for $k = 2$, located in the first scenario at $\xi = 1/6$ and in the second at $\xi = 1/2$ corresponding to equally step length is examined and presented in Figure. 2. It can be concluded from the curves that the beam slightly affected when the crack located at the first step, compared with crack located at the second step.

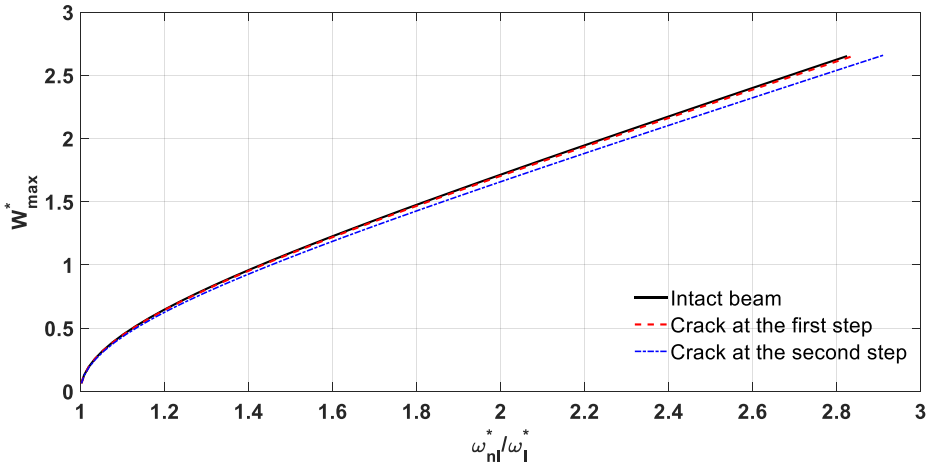

Figure 2: Amplitude frequency dependence of FG non-uniform beam in the vicinity of the first mode for three scenarios.

CONCLUSION

The problem of geometrically non-linear free vibrations of functionally graded non-uniform cracked beam is investigated in this paper. The main feature of the present contribution is that the non-linear analysis of the symmetrical FG non-uniform cracked beam can be treated by the proposed homogenisation procedure based on the neutral surface approach, the numerical techniques and software developed for non-uniform isotropic cracked beams. Numerical results have been given to illustrate the effects of the crack parameters on the dynamic behaviour of symmetrical FG non-uniform beams.

REFERENCES

[1] M. Chajdi, H. Fakhreddine, A. Adri, K.E. bikri, R. Benamar, Geometrically non-linear forced vibrations of fully clamped functionally graded beams with multi-cracks resting on intermediate simple supports. *J. Phys. Conf. Ser.*, (1264) 012023, 2019.

[2] M. El kadiri, R. Benamar, R.G. White, Improvement of the semi-analytical method, for determining the geometrically non-linear response of thin straight structures. Part I: application to clamped–clamped and simply supported–clamped beams. *J. Sound Vib.*, (249) 263–305, (2002).

[3] K. El Bikri, R. Benamar, M.M. Bennouna, Geometrically non-linear free vibrations of clamped–clamped beams with an edge crack, *Comput. Struct.*, (84) 485–502, 2006.

[4] N.T. Khiem, T.V. Lien, V.T.A. Ninh, Natural Frequencies of Multistep Functionally Graded Beam with Cracks. *Iran. J. Sci. Technol. Trans. Mech. Eng.*, 2018.

SIMPLIFIED 3D TIRE MODEL INFRASTRUCTURE FOR DYNAMIC AND FREQUENCY ANALYSIS

A. Sakhnevych[1], V. M. Arricale[1], F. Farroni[1], A. Genovese[1] and F. Timpone[1]

[1]Dipartimento di Ingegneria Industriale
Università degli Studi di Napoli, Napoli, ITALY
Email: ale.sak@unina.it, vincenzomaria.arricale@unina.it, flavio.farroni@unina.it,
andrea.genovese2@unina.it, francesco.timpone@unina.it

ABSTRACT

The tires play an important role for an aircraft during taxing on the ground, take-off and landing phases. Therefore, knowledge of the tire dynamic behavior and its properties becomes particularly crucial in order to be able to satisfy the requirements in terms of stability, comfort, wear and NVH performances. In this paper, a physical multibody 3D tire model, called RCH-tire (Research Comfort and Handling), allowing to evaluate the shape of the tire dynamic contact patch with local pressure and velocity distributions, is presented. The physical RCH-tire model structure is represented by a three-dimensional array of interconnected lumped-mass nodes by means of tension and rotational spring and damper elements, attached to the rim modelled as a rigid body. The illustrated model structure becomes notably suitable to be effectively characterized by means of non-destructive static and specifically developed dynamic test procedures presented.

1 INTRODUCTION

The tires play a fundamental role for an aircraft during taxing on the ground, take-off and landing phases and with the landing gear system have to meet the JAR/FAR (airworthiness authority organisation) regulations in order to obtain an airworthiness certificate.
In this regard, several authors have developed tire models using the FEA approach to simulate the aircraft tire-ground interaction [1][2][3], the understanding of tire dynamics, as well as the ability to reproduce the tire behaviour in the simulation environment is one of the key factors to pursue in order to guarantee the required level of reliability of the overall aircraft system in all the design and development phases [4].

Tire behaviour deeply depends on the compound and carcass structural characteristics linked to the operating tire conditions, as a function of contact pressure and sliding speed distributions within the contact patch, temperature distribution within the tire structure, inflation pressure and road texture. The knowledge and the ability to govern the above properties is fundamental since the vehicle stability and comfort, and tire wear and NVH performances are deeply affected by the optimum employment of tires.

There is a variety of tire models available in literature whose aim is to reproduce both static and dynamic tire characteristics, based on Pacejka formulation, FEA studies and multibody approaches [5][6][7][8]. However, the main difficulties linked with the employment of the above tire models concern the correct parametrization, this is the reason why the physical multibody 3D tire model, called RCH-tire (Research Comfort and Handling) has become a necessity within the UniNa Vehicle Dynamics research group. RCH-tire models [9][10]the tire as a three-dimensional array of interconnected masses, linked with each other by means of tension and rotational spring and damper elements to reproduce the equivalent tread viscoelastic characteristics and to take into account the dissipative effect due to the composite matrix, and coupled to the rim, hypothesized rigid by means of radial spring and damper non-linear elements. At the current stage, RCH-tire is able to completely reproduce the tire normal interaction in both static and dynamic working conditions with the minimum number of the equivalent parameters, representing a physical base infrastructure for further coupling a brush model within the contact patch to evaluate the tangential interaction phenomena.

2 MODELLING ASSUMPTIONS

The assumptions underlying the RCH tire model structure can be summarized as follows:

- rim is considered rigid and cylindrically shaped interacting with the vehicle motion by means of suspension system fastenings and wheel spindle, and has *6* degrees of freedom: three linear motions along x,y, z directions and three rotations around the same axis;
- tire is considered slick and geometrically symmetrical towards the *zx* longitudinal plane;
- tire belt properties are differentiated towards the tire meridian *yz* and parallel *zx* planes, with physical inertial and structural properties assumed to be identical within the same planes.

Starting from the real tire geometry, the model is meshed in a certain number *n* of lumped masses nodes, interconnected by means of structural elements, whose characteristics deeply depend on their position within the real tire structure, as illustrated in the figure 1. Indeed, the colours blue and green highlight different inertial and physical properties, characterizing each tire structural zone, assigned respectively to sidewall and belt nodes.

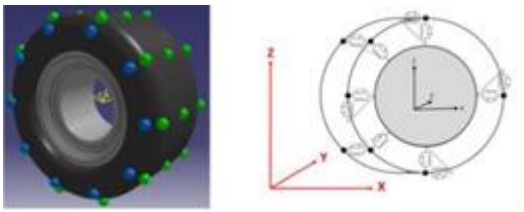

Figure 1. Tire node scheme

Since each tire structure node has *3* DoF, the total number of the RCH-tire model degrees of freedom and therefore the length of the state vector is *3n+6*.

3 RCH MODEL

In order to study the motion that results from the application of a force (or, in general, the application of multiple forces) to a particle, it is necessary the kinematics has been properly studied to describe quantitatively the forces that act on a particle; to determine the motion that results from the application of these forces using postulated laws of physics and to analyse the motion.

On each node $P_{k,j}$, five kinds of forces are considered [7]:

$$R_{k,j} = F_{structural,k} + F_{structure,b} + F_{pressure} + F_{road} + F_{gravity} \quad (1)$$

Where:

- *Fstructural,k* are the internal force due to deformation of the tire (belt and sidewall)
- *Fstructural,b* are the internal force due to dissipation effects within the tire structure
- *Fpressure* are the internal forces due to effect of inflation pressure p_{in}
- *Froad* are the external forces due to the interaction with road pavement (at current development step the only external forces due to the interaction with road is the sum of the normal reaction to the road profile – the tangential tire-road interaction has not been implemented)
- *Fgravity* is the gravitational force.

The rigid body, differently from the particles can undergo both translational and rotational motion. Consequently, two balance laws, one for translation and another for rotation, are required to specify completely the motion of a rigid body. The resultant and the resultant moment of the above forces are the terms $\overline{R_{rim}}$ and $\overline{M_{rim}}$, which can be therefore obtained by the following expressions

$$\begin{aligned} \bar{R}_{rim} &= \bar{F}_{vehicle} + m_{rim}g\bar{k} + \sum_{k=1}^{n} \bar{R}_{k,j=1} + \sum_{k=1}^{n} \bar{R}_{k,j=m} \\ \bar{M}_{rim} &= \bar{T}_{vehicle} + \sum_{k=1}^{n} \bar{R}_{k,j=1} \times \overline{GP}_{k,j=1} + \sum_{k=1}^{n} \bar{R}_{k,j=m} \times \overline{GP}_{k,j=m} \end{aligned} \quad (2)$$

4 TESTING PROCEDURES

To properly characterize the RCH-tire in order to employ the model in the entire range of the possible tire operating conditions, both static and dynamic characterization testing methodologies have been performed on the real tire to find an optimum set of equivalent parameters, able to completely represent all the tested conditions.

The tire static characterization test considers the non-rolling tire, loaded at the wheel spindle. The induced lowering is then measured at different values of the inflation pressure, vertical load and camber angle to evaluate the radial displacement of the rim centre and the contact patch extension, in terms of shape and pressed area.

The dynamic tire characterization considers the non-rolling tire, subjected to the cycling deformation routine at different load values and frequencies. In particular, the energy dissipated by the tire as a result of cyclic deformations is called Strain Energy Loss (SEL) and the equivalent cyclic deformations occur with a frequency corresponding to the tire rotational speed. The result of each routine is a hysteresis cycle, represented in a force vs displacement diagram, for which the area is calculated in steady state conditions, considered as an index of the dissipated power, converted in heat.

5 RESULTS

5.1 Static characterization

The results obtained from the RCH-tire model simulation of a static radial test carried out under three different load configurations.

In the steady-state conditions the RCH-tire model behaviour can be compared with the acquired data obtained from the static characterization procedure. It is important to highlight that the parameters adopted in the analysis (stiffness and damping) are constant. The aim of the first version of the RCH-

tire model was understand if the RCH-tire multibody approach could be appropriate to describe the large deformation of the tire structure even with completely linear elements.

5.2 Dynamic characterization

The RCH-tire model results are compared to the acquired one obtained by means of a radial SEL test. Despite the completely linear behaviour of all the structural parameters involved, the RCH-tire model achieves a good result, reproducing good global trends, as a function both of imposed vertical load and of excitation frequency.

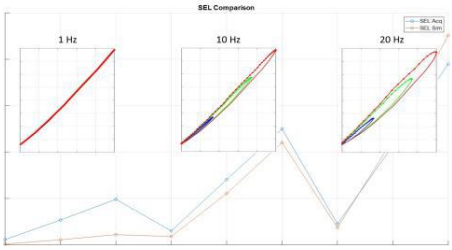

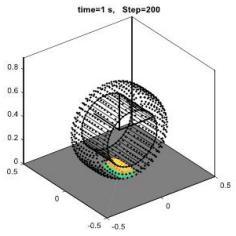

Figure 2. Results

6 CONCLUSION

In this work a brief description of the physical multibody 3D tire model is reported. To validate the model a tire test characterization procedure, both in static and dynamic, has been performed.
The tyre model is able to obtain the shape of the tire dynamic contact patch with local pressure and velocity distributions. A simulation of a normal interaction test on a flat road is reported. The trends of the numerical results obtained are presented. Moreover, the model achieves a good result in a radial SEL test simulation.
Further developments could introduce the non-linear structural elements behaviour, function of induced strain, internal pressure and finally working temperature, to completely reproduce the tyre carcass behaviour and to model the tangential interaction.

REFERENCES

[1] Johnson, A. R., Tanner, J. A., & Mason, A. J. (1999). Quasi-static viscoelastic finite element model of an aircraft tire.

[2] H. Guo, C. Bastien, M.V. Blundell, G. Wood. A detailed aircraft tyre finite element model for hard landing safety assessment, *9th European LS-DYNA Conference*. 2013, pp. 240–250.

[3] Kondé, A. K., Rosu, I., Lebon, F., Brardo, O., & Devésa, B. (2013). On the modeling of aircraft tire. Aerospace Science and Technology, 27(1), 67-75.

[4] Rimyalegdo KIEBRE. Contribution to Modeling of Aircraft Tyre-road Interaction. *PhD thesis*, Université de Haute-Alsace, 2010.

[5] S. T. Jansen, L.Verhoeff, R. Cremers, A. J. Schmeitz, and I. J. Besselink. Mf-swift simulation study using benchmark data. *Vehicle System Dynamics*. 2005, 43(sup1):92–101.

[6] Gipser, M. Ftire: a physically based application-oriented tyre model for use with detailed mbs and finite-element suspension models. *Vehicle system dynamics*. 2005, 43(sup1):76–91.

[7] Gallrein, A. and Bäcker, M. Cdtire: a tire model for comfort and durability applications. *Vehicle System Dynamics*. 2007, 45(S1):69–77.

[8] Kim, S., Nikravesh, P. E., and Gim, G. A two-dimensional tire model on unevenroads for vehicle dynamic simulation. *Vehicle system dynamics*. 2008, 46(10):913–930.

[9] Farroni, F., Sakhnevych, A., and Timpone, F. A three-dimensional multibody tire model for research comfort and handling analysis as a structural framework for a multi-physical integrated system. Proceedings of the Institution of Mechanical Engineers, Part D: *Journal of Automobile Engineering*, 233(1), 136–146.

[10] Farroni, F., Russo, M., Sakhnevych, A., and Timpone, F. (2019). TRT EVO: Advances in real-time thermodynamic tire modeling for vehicle dynamics simulations. Proceedings of the Institution of Mechanical Engineers, Part D*: Journal of Automobile Engineering*, 233(1), 121–135.

FIRST MODELS FOR STRUCTURAL ENERGY TRANSMISSION DECOUPLING

G. Mazzeo[1*] , M. Ichchou[1], G. Petrone[2], O. Bareille[1], F. Franco[2] and S. De Rosa[2]

[1]Vibroacoustic and Complex Media Research Group, LTDS
École Centrale de Lyon, Lyon, FRANCE
Email: giulia.mazzeo@ec-lyon.fr, mohamed.ichchou@ec-lyon.fr, olivier.bareille@ec-lyon.fr

[2]Pasta-Lab, Department of Industrial Engineering – Aerospace Section
University of Naples Federico II, Naples, ITALY
Email: giuseppe.petrone@unina.it, francesco.franco@unina.it, sergio.derosa@unina.it

ABSTRACT

For the analysis of the vibrational response of structures subjected to aerodynamic excitations, wind tunnel facilities are equipped with "test bench" structures. Clearly, for the sake of the measurements' purity, it is important that the test bench does not transmit part of its vibrational energy to the test structure. For this reason, it is important to define design rules with which it is possible to project "smartly" a test bench which ensures an energy transmission decoupling. This work has been carried out focusing in the high frequency domain (HF), exploiting the possibility to assume an aerodynamic excitation as the Turbulent Boundary Layer (TBL) approximated to an Equivalent Rain-on-the-roof excitation. The method invoked here was based on Statistical Energy Analysis (SEA). For the analysis of vibrational response, a simplified model was conceived: it is wanted to determine the effective design rules for the structure and material properties; this means that it is wanted to guarantee the possibility of different material choices for a test bench project and, at the same time, to ensure a test bench versatility.

1 INTRODUCTION

The Turbulent Boundary Layer (TBL) is one of the most relevant sources of vibration and noise for high speed transport vehicle as automotive, railway, aircraft and spacecraft. The study of the dynamic behaviour of structures subjected at this aerodynamic load is measured in terms of vibrational velocity response in a wide frequency band. Wind tunnels facilities thus need particular test benches which should ensure the correctness of sample panels' vibroacoustic measurements. In fact, mechanical impedances mismatch can cause an energy transmission between test bench and sample panel which can return false data. Therefore, a "smart" design of test bench can be a solution for different aspects: guaranty of measurements, smart choice of material for design test bench considering also the versatility of sample panels. The development of these design rules starts considering the vibrational response at high frequencies, characteristic of airplanes at cruise speed. The Statistical Energy Analysis (SEA) [1–3] has been used as methodology for the representation and analysis of energy transmission among subsystems of same structure. For what concerning the expression of a TBL excitation, an Equivalent rain-on-the-roof [4] excitation has been taken into account.

The application of SEA for design rules simplifies considerably the description of the energy transmission, giving one the opportunity to establish a fast pre-design of material choice and foresee the energy path among the subsystems. Therefore, an application with SEA on a simple structural assembly is carried out to outline the first design rules taking into account isotropic and orthotropic materials to ensure the test bench performances and the versatility of sample panels which would be mounted on it.

2 DESIGN RULES WITH STATISTICAL ENERGY ANALYSIS

For what concerning the study of energy decoupling among subsystem of a structure, a SEA model has been created for the study of energy transmission between two subsystems: one representing a test bench and the other the sample panel, bot described as two plates.

The approximation of a test bench to a simple structure plate has been applied taking into account the work of Finnveden in [5].

The design rules are developed considering the principle of the conservation of energy applied to an SEA model, represented in Fig.1.

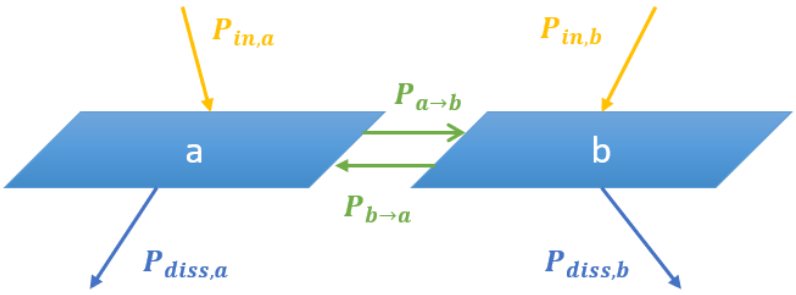

Figure 1. Representation of a 2-plates system for SEA application.

In fact, considering the power equilibrium (Eq.(1a)) on subsystem a, which can represent the test panel, it is possible to obtain the relation between the two subsystems vibrational

responses directly dependent on the ratio of their modal densities and masses.

$$P_{in,a} + P_{ba} = P_{diss,a} + P_{ab} \tag{1a}$$

$$P_{ba} \ll P_{diss,a} + P_{ab} \tag{1b}$$

$$\langle v_b^2 \rangle \ll \left(\frac{\eta_a + \eta_{ab}}{\eta_{ab}} \right) \frac{n_b(\omega)}{n_a(\omega)} \frac{M_a}{M_b} \langle v_a^2 \rangle \tag{1c}$$

In fig.2, it is showed as example the direct vibrational response gain (in dB) that can be got working on the subsystems' effective parameters: just a scale 1:7 for the thickness can determine almost 17 dB of difference between the two subsystems with characteristics in Table 1. It is possible to work directly with their effective parameters as Young modulus, density, etc. when the subsystems are made with simple materials as the isotropic one.

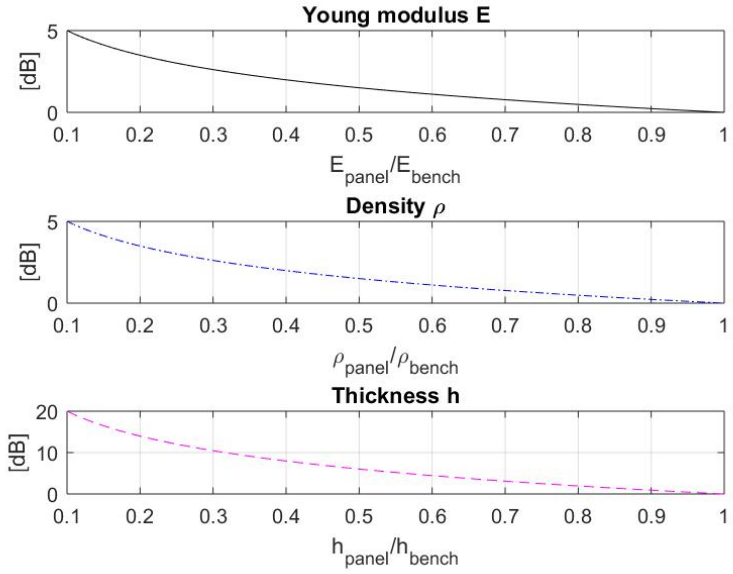

Figure 2: Vibrational response gain (in dB) in function of subsystems' effective parameters ratios (Young Modulus, density, thickness).

	$\rho\ (kg/m^3)$	E (Pa)	ν	h (m)
Panel (a)	2700	$6.9\text{x}10^9$	0.33	$1\text{x}10^3$
Bench (b)	7820	$20\text{x}10^9$	0.33	$7\text{x}10^3$

Table 1: Details for two-plates SEA assembly (subsystem a in aluminium and subsystem b in steel).

For what concerning materials more complex to describe, as an orthotropic one, a wave propagation analysis can be necessary to obtain the wavenumbers behaviour at high frequencies, which are essential for the modal density description. In Table 2, are reported the gain in dB that ratios of wavenumbers, group velocities and masses with the total velocities gap between the vibration velocities of two panels: the first one in simple aluminium and the second in composite (unidirectional fibre) having the same geometry. A wavenumber average over the directivity angle [6] has been applied to get an equivalent behaviour of the orthotropic panel.

$L_{\langle v^2 \rangle}$	L_k	L_{c_g}	L_M
12.9 dB	6.4 dB	11.3 dB	-2.4 dB

Table 2: Vibrational velocity gap in dB between two plates with same geometry, but different material: plate (a) is in aluminium and plate (b) is in composite unidirectional fibre; the gain in dB of wavenumber ration, group velocity ratio and mass ratio is reported.

3 CONSIDERATIONS

The structural design rules want to take into account different kind of materials, from the simplest one as the isotropics, to other types more complex as the orthotropic one. An investigation and categorization has been carried out for different wavenumbers, taking into account the prevalent wavenumber effect at high frequency for a right performance of the SEA application. Considering the Equivalent rain on the roof excitation lets one get a valuable approximation of the TBL effect on a structure; using it in a Statistical Energy analysis allows to define the right materials for the design of a test bench taking care of the required versatility for different sample panels study.

4 ACKNOWLEDGEMENTS

This work did receive a FERED/FSE Rhône-Alpes funding under the frame of the collaborative project IJES. Authors warmly acknowledge the institutional support for this research. G.M. also wants to warmly thank Christophe Droz for the useful discussions.

REFERENCES

[1] R.H. Lyon and R.G. Dejong. *Theory and Application of Statistical Energy Analysis*. Butterworth-Heinemann, U.S.A., 1995.

[2] T. Lafont, N. Totaro, and A. Le Bot. Review of statistical energy analysis hypotheses in vibroacoustics. *Proceedings of the Royal Society A*, 470:20130515, 2014.

[3] T. Lafont, N. Totaro, and A. Le Bot. Coupling strength assumption in statistical energy analysis. *Proceedings of the Royal Society A*, 473:20160927, 2017.

[4] M.N. Ichchou, B. Hiverniau, and B. Troclet. Equivalent "rain on the roof" loads for random spatially correlated excitations in the mid-high frequency range. *Journal of Sound and Vibration*, 322:926–940, 2009.

[5] S. Finnveden. Evaluation of modal density and group velocity by a finite element method. *Journal of Sound and Vibration*, 273:51–75, 2004.

[6] C. Droz, Z. Zergoune, R. Boukadia, O. Bareille, and M.N. Ichchou. Vibro-acoustic optimisation of sandwich panels using the wave/finite element method. *Composite Structures*, 156:108–114, 2016.

IMPROVED STRUCTURAL HEALTH MONITORING FEATURES ON 3D PRINTED STRUCTURES BY PIEZOELECTRIC IMPLANTS

A. Xiaopeng CUI[1], B. Olivier Bareille[1*] and C. Michelle SALVIA[1]

[1] Laboratoire de Tribologie et Dynamique des Systèmes
Ecole Centrale de Lyon, Ecully, FRANCE
Email: xiaopeng.cui@ec-lyon.fr, olivier.bareille@ec-lyon.fr

ABSTRACT

In this research, mechanical properties of 3D-printed specimens were studied by tensile test. The samples were designed with different filament orientations and raster width, thus verifying the parametric influence of mechanical properties and to identify the possible application to the design of a 3D-printed damping structure. Dynamic thermomechanical analysis (DMA) test and Differential scanning calorimetry (DSC)were carried on as well, in order to obtain a clearer view of dynamic response of this printing material and the polymer characters associated to the overall mechanical properties. Through the method to implant piezoelectric sensors inside a structure, it is possible to monitor real-time response of damage of a structure. Researches have been done to identify the preference of parameters and a possible acoustic mode indicating occurrence of delamination inside of a 3D-printed structure.

1 INTRODUCTION

Additive manufacturing (AM), usually known as 3D printing, has been defined as the process of joining materials to make parts from a 3-dimensional model data one layer at a time. The first-of-all drawback of fused filament fabricating (FFF)technology is the lower mechanical properties compared to conventional manufacturing process. The mechanical properties of 3D-printed structure depend on the way of layer stacking sequence and orientation. [1] Mechanical performance (strength and stiffness) of 3D-printed parts could be improved by adding chopped fiber reinforcement into printing process even if void occurrence and fiber/matrix adhesions are all

amongst the existing issues in 3D printing of fiber composites. The introduction of fillers within filaments can lead to blockage and wear at nozzle level and then 3D printers are designed for specific reinforced resins. Carbon fibers are currently the most commonly used because of their abrasiveness and small diameter compared to glass fibers. Natural fiber is also a possibility because their low abrasiveness, but there are no filaments made of natural fiber/TP for commercial printer at current time. The 3D printed polymer parts are built up in layers, which results in porosities widely observed inside of 3D-printed parts, between the deposit filaments which is actually an unavoidable defect.

Through the use of sensors embedded within a structural material it is possible to monitor real-time knowledge of damage (Structural Health) of a structure during its life cycle in its application environment, and adjust life prediction strategy. There are a variety of sensors that can be used to monitor the health of composite structures such as optical fiber, carbon fiber, piezoelectric ceramics or polymers. The technique used in this work is based on the measurement of the electrical impedance of piezoelectric ceramic. Piezoelectric materials are widely used sensor because they are lightweight, inexpensive, and come in a variety of forms ranging from thin rectangular patches to complex shapes.

2 RESULTS

2.1 Tensile test

2.1.1 ABS

The mechanical behavior of tensile test is quite different among varied raster orientations. For ABS0, the orientation of which is collinear with that of tensile force, the strength is much higher than ABS45 and ABS90. A reasonable cause of this phenomena is that the connection of interface between filaments is much weaker than the strength inside a filament. Observed from the tensile curves, the ABS45 and ABS 90 show an evident brittle behavior. The photo from SEM shows that, at the surface of crack, the interface is rather smooth without much bonging material from another filament. Comparing with injected ABS sample, the 3D-printed samples showed a lack of plasticity, even for the ABS0 samples which have similar strength to injected ABS, the strain at failure is much lower. Under SEM, not much plastic deformation can be observed at crack of ABS0 and ABS ±45. The higher strain for ABS±45 may come from the re-orientation of filaments when tensile load is applied.

	ABS0	ABS45	ABS90	ABS±45	ABS injection
E (GPa)	2.35±0.07	2.01±0.04	1.80±0.08	1.92±0.10	1.95±0.17
Strength (MPa)	33.83±0.46	20.28±0.71	17.76±0.38	25.83±0.25	31.55±1.19
Strain	2.83±0.07	1.84±0.24	1.74±0.10	6.42±0.76	27.25±11.40

Table.1. Statistic data of ABS tensile tests

The mechanical behaviour of tensile test is quite different among varied raster orientations. For ABS0, the orientation of which is collinear with that of tensile force, the strength is much higher than ABS45 and ABS90. A reasonable cause of this phenomena is that the connection of interface between filaments is much weaker than the strength inside a filament. Observed from the tensile curves, the ABS45 and ABS 90 show an evident brittle behavior. The photo from SEM shows that, at the surface of crack, the interface is rather smooth without much bonding material from another filament. Comparing with injected ABS sample, the 3D-printed samples showed a lack of plasticity,

even for the ABS0 samples which have similar strength to injected ABS, the strain at failure is much lower. Under SEM, not much plastic deformation can be observed at crack of ABS0 and ABS ±45. The higher strain for ABS±45 may come from the re-orientation of filaments when tensile load is applied.

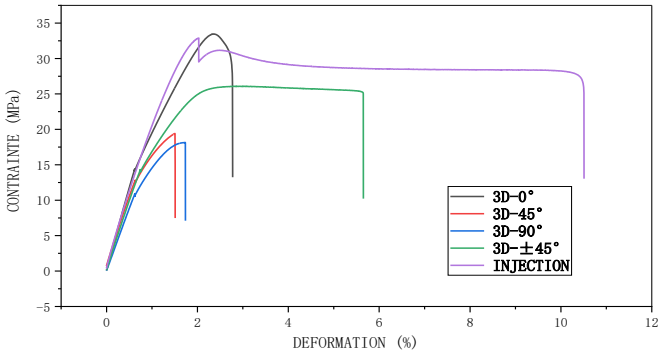

Figure.1. Tensile test of 3D-printed ABS specimens

Secondly, a series of porosity is observed between filaments. These porosities are formed with the fabrication of 3D-printed material, and theoretically will cause degradation of mechanical properties.

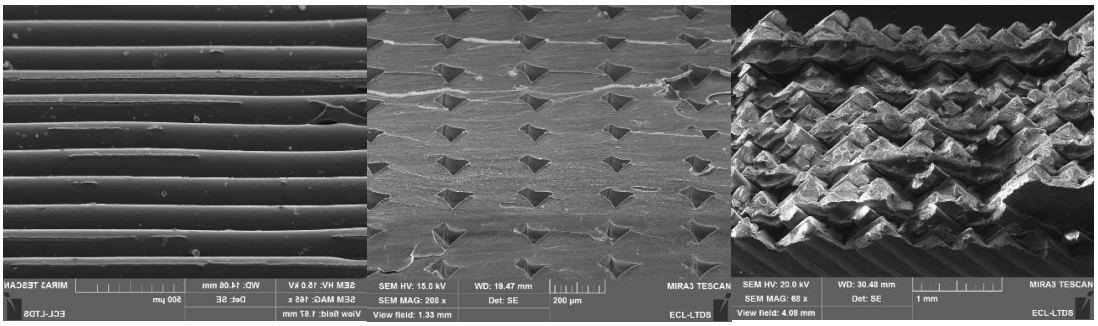

Figure.2. a) ABS90, b) ABS0, c) ABS±45

2.1.2 PLA

The 3D-printing method has a similar influence to the mechanical properties of PLA. The plasticity will be reduced, and the ±45 orientation samples show better strength and deformation capacity. Photo taken by SEM gives an evidence of plastic deformation of each filament printed and the original orientation of filaments was modified by the tensile load. And the nearly non-adhesive interface can be also observed in the figure of PLA 090.

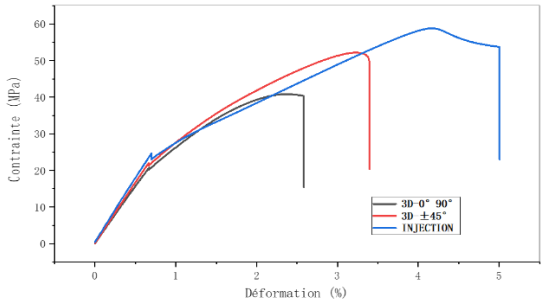

Figure.3. Tensile test of 3D-printed PLA specimens

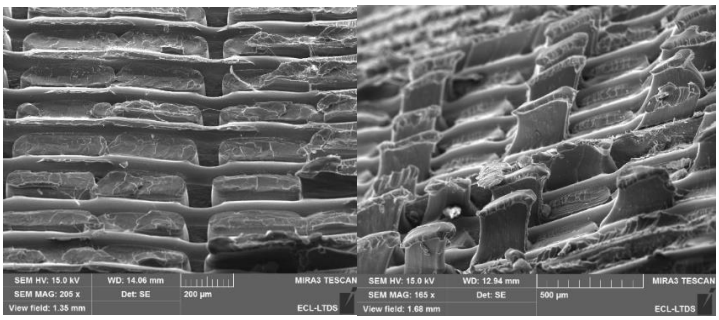

Figure.4. a) PLA090, b) PLA±45

	PLA090	PLA±45	Injected PLA
E(GPa)	3.20±0.04	3.37±0.05	3.46±0.12
Strength (MPa)	41.92±0.80	52.80±0.65	54.70±4.04
Strain	2.68±0.08	3.30±0.12	4.08±0.95

Table.2. Statistic data of PLA tensile tests

3 CONCLUSIONS

The tensile tests showed an orientation preference of different applications. In a 3D-printed structure, the heavier loaded parts should be studied and then filaments are better ranged following the orientation of maximum of deformation and stress. For complicated loading situations, a cross 45 degrees method will be capable for various challenges. The 90 degrees' arrangement can be utilised as a pre-created defects in order to induce the occurrences of cracks and absorb impact energy.

REFERENCES

[1] R.J. Zaldivar, D.B. Witkin, T. McLouth, D.N. Patel, K. Schmitt, J.P. Nokes.Inuence of processing and orientation print effects on the mechanical and thermal behavior of 3D-Printed ULTEM R 9085 Material. *Additive Manufacturing.* 13:71-80, 2017

[2] Z.N. Yin, L.F. Fan, T.J. Wang, Experimental investigation of the viscoelastic deformation of PC, ABS and PC/ABS alloys. *Materials Letters.* 62:2750-2753, 2008.

[3] D. Young, N. Wetmore, M. Czabaj, Interlayer fracture toughness of additively manufactured unreinforced and carbon-fiber-reinforced acrylonitrile butadiene styrene. *Additive Manufacturing*. 22:883 -890, 2018·

[4] K. Sugiyama, R. Matsuzaki, M. Ueda, A. Todoroki, Y. Hirano, 3D printing of composite sandwich structures using continuous carbon fiber and fiber tension. *Composites Part A.* 113:114-121, 2018.

ELIGIBILITY OF ELECTROSPUN NANOFIBERS FOR AERONAUTICAL THERMOACOUSTIC INSULATION BLANKETS

M. Guida[1], T. Polito[1], F. Marulo[1], F. Branda[2], B. Vitolo[3]

[1] University of Naples Federico II – Dipartimento di Ingegneria Industriale, Napoli, Italy
E-mail: michele.guida@unina.it; tiziano.polito@unina.it; francesco.marulo@unina.it

[2] University of Naples Federico II - Dipartimento di Ingegneria Chimica, dei Materiali e della Produzione Industriale, Napoli, Italy
E-mail: francesco.branda@unina.it

[3] Geven SPA, via Boscofangone, Nola, Italy
E-mail: bonaventura.vitolo@geven.com

ABSTRACT

This paper deals with the activities funded in the framework of the European research project Clean Sky 2 for airframe platform named 'CASTLE', in cooperation between GEVEN and the University of Naples Federico II.

The final focus is the design and the production of a new solution for thermoacoustic insulation blankets intended for applications in commercial aviation based on electrospinning, which has been recognized as an efficient technique for the fabrication of polymer nanofibers. In this paper, an eco-friendly water resistant self-extinguishing polyvinylpyrrolidone, acoustically effective at low frequencies, was considered to design an insulation blanket. Once the prototypical blanket was installed in a fullscale fuselage barrel, the acoustical performance of the manufactured nanofibers at various frequencies was measured.

INTRODUCTION

Thermal insulation is used to reduce heat losses from the cabin to the surroundings. These insulation layers often play the role in thermal as well as in noise insulation, Figure 1. Requirements for insulation in the aircraft are following:

- Thermal, noise and fire resistance;
- Low weight;
- Not electrically conductive;
- Not causing corrosion of neighboring structures;
- Must allow inspection of the fuselage structure;
- Must not absorb large amount of water;
- Must not have adverse environmental and/or healthy/safety effects during fabrication and installation, or in-service use and disposal;
- Must fulfil requirements of CS23 / FAR23 regulations.

Figure 1. Example of PVP sample.

The constant increase in passenger traffic and the strong competition present between the various airlines to guarantee ever-increasing spaces on the market mean that passenger comfort is one of the main parameters to have a significant impact on the commercial success of one or the other operator; the attention is therefore maximum, from the early stages of design. Exposure to high levels of noise pollution has a decidedly negative influence on the quality of service offered to passengers. The design phase therefore has, among the main objectives, the control and reduction of noise and vibrations present in the cabin.
However, the research and development of sound-absorbing solutions cannot ignore the knowledge of the main sound sources in the aeronautical field. It is therefore essential, for the definition of an adequate solution for the thermo-acoustic insulation of the cabin of a civil transport aircraft, the identification of the emission characteristics of the main noise sources, which vary, even considerably, depending on the type of aircraft and engines, and their contribution to the total sound level perceived on board. In general, as reported in the figure 2 it is possible to distinguish in:

- external sources (engine noise transmitted by air or through structural vibration, fluid-structure interaction, structure vibrations).
- internal sources (air conditioning systems, pressurization systems and associated ducts, noise generated by the occupants of the cabin, sound devices).

The overall noise, which affects passenger comfort, is given by the combined action of the internal and external sources; in particular engines and aerodynamic disturbances provide the most significant contributions. There are different noise measurement indices, and among them, some of the most used to "quantify" the level of acoustic comfort of an aircraft are:

- Overall Sound Pressure Level (OASPL), expressed in dB and defined by the total sound energy logarithm, measured over a wide frequency spectrum, generally between 0 and

16 kHz. It is typically used in applications where high frequencies dominate (jet aircraft) or characterized by energy values spread over a wide frequency spectrum.

- dB (A), is the Overall calculated on the spectrum (0-12.5 KHz) to which the "A" weighting curve is applied, which takes into account the variation in sensitivity of the human ear with frequency; that is, in order for the ear to perceive the same sensation, different sound levels are required at different frequencies. In particular, the ear is less sensitive to lower frequencies and more others. It is generally used for applications where low frequencies are predominant (helical aircraft).
- SIL (Speech Interference Level) is a measure of acoustic disturbance in speech frequencies; in particular the SIL3 is the arithmetic average of the SPL in the Octave bands 500, 1K, 2K Hz; SIL4 is the arithmetic average of the SPL in the Octave bands 500, 1K, 2K, 4K Hz. This parameter is generally used for the characterization of aircraft with high internal comfort (Business Jet).

Typical SPL values measured on transport aircraft equipped with turbofan engines are between 75 and 80 dB (A), with peaks up to 85 dB (A). The maximum levels of OASPL in the cab tend to reach 95 dB with external values of 135 dB, while the SIL indicator typically assumes values between 65 and 70 dB. In the case of propeller aircraft, with piston engines, the stress spectrum is dominated by the propeller's tonal characteristics, depending on the number of blades, the propeller actuator disk diameter and its minimum distance from the fuselage, with values peak rates of higher SPLs.

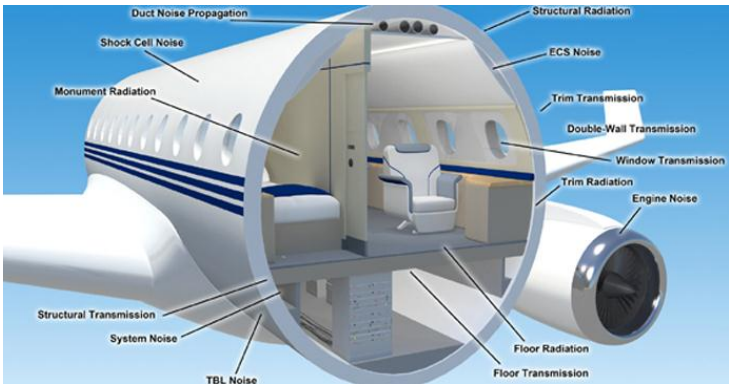

Figure 2. Example of a figure.

1 ELECTOSPUN MATS

The silica particles were prepared through Stöber method using tetraethyl orthosilicate (TEOS) as as a precursor. TEOS (7 mL) was added to a distilled ethanol (160 mL) water (13.4 mL) and a precursor. TEOS (7 mL) was added to a distilled ethanol (160 mL) water (13.4 mL) and ammonium hydroxide solution (30–33% NH3 in H2O) (5.38 mL) under stirring. After 2 h the particles were recovered by centrifugation (11500 rpm per 10 min) and washed three times with ethanol.
The scheme of the electrospinning apparatus, shown in Figure 1, consists of a high voltage electric source, a syringe pump (Harvard Apparatus (Cambridge, MA, USA), Pump 11 Plus) holding a 12 mL plastic syringe (Nipro, Osaka, Japan) with a needle (inner diameter of 0.6 mm and average length of 4 cm) acting as the cathode and a rigid copper foil collector acting as the anode.

2 EXPERIMENTAL MATERIALS

A Noise Reduction test was performed aimed to compare transmission loss characteristics of two different layups were investigated, the first one consists of a microlite blanket and an

honeycomb panel and the other one of a PVP blanket, coupled with the same honeycomb panel. The adopted solutions allow us to investigate the different behaviour of the core.
Outside of the 4 meters long A321 aircraft fuselage barrel an active loudspeaker was placed, able to reproduce pink noise. A ½" microphone was placed close to the external skin fo the barrel, whereas two ½" microphones ware installed in the aircraft cabin.

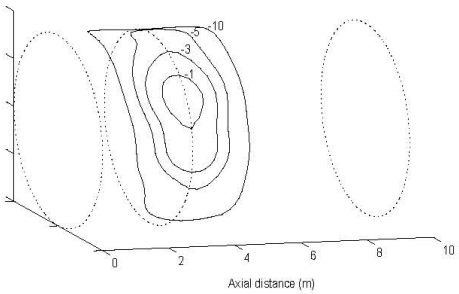

Figure 4. Example of pressure distribution map

Figure 5. Schematic setup

REFERENCES

[1] Manville, J. OEM Insulations Division. www.jm.com. Available online: https://www.tricityinsulation.com/ cms/wp-content/uploads/2010/11/Microlite-Blankets1.pdf (accessed on 2 June 2019).

[2] Passaro, J., Russo, P. Bifulco, A., Martino, M., Granata, V., Vitolo, B., Iannace, G., Vecchione, A. Marulo, F., Branda, F. Water Resistant Self-Extinguishing Low Frequency Soundproofing Polyvinylpyrrolidone Based Electrospun Blankets. Polymers, vol. 11, 1205, 2019. DOI: 0.3390/polym11071205

[3] Duan, G.; Liu, S.; Jiang, S.; Hou, H. High-performance polyamide-imide films and electrospun aligned nanofibers from an amidecontaining Diamine. J. Mater. Sci. 2019, 54, 6719–6727.

[4] Khan, W.S.; Asmatulu, R.; Yildirim, M.B. Acoustical Properties of Electrospun Fibers for Aircraft Interior Noise Reduction. J. Aerosp. Eng. 2012, 25, 376–382. [CrossRef]

[5] Xiang, H.; Tan, S.; Yu, X.; Long, Y.; Zhang, X.; Zhao, N.; Xu, J. Sound absorption behavior of electrospun polyacrylonitrile nanofibrous membranes. Chin. J. Polym. Sci. 2011, 29, 650.

[6] Iannace, G. Acoustic Properties of Nanofibers. Noise Vib. Worldw. 2014, 45, 29–33.

ON THE PERFORMANCE OF A FLOW ENERGY HARVESTER USING TIME DELAY

Zakaria Ghouli[1], Mohamed Belhaq[1] and Mustapha Hamdi[2]

[1]Faculty of Sciences Ain Chock
University Hassan II-Casablanca, Morocco
Email: ghoulizakaria@gmail.com, mbelhaq@yahoo.fr

[2]FST-Al Hoceima
University Abdelmalek Essaadi, Tetouan, Morocco
Email: hamustapha2000@yahoo.fr

ABSTRACT

This paper explores periodic vibration-based energy harvesting (EH) in a delayed harvester device consisting of a delayed nonlinear oscillator subject to galloping excitation and coupled to an electric circuit through a piezoelectric coupling mechanism. It is assumed that the delay amplitude is modulated such that the frequency of the modulation is near twice the natural frequency of the oscillator. Application of the method of multiple scales gives approximation of the amplitude of periodic vibrations and the corresponding power extracted from the harvester device. Results show that the presence of modulated delay amplitude in the mechanical component increases significantly the amplitude of vibrations and the output power in a certain range of the wind speed. Numerical simulation is conducted to support the analytical predictions.

1 INTRODUCTION

Vibration-based EH in a delayed oscillator with time-periodic delay amplitude has been amply investigated. In [1] it was reported that in a delayed van der Pol oscillator with modulated delay amplitude coupled to an electromagnetic energy harvester, quasi-periodic (QP) vibrations can be exploited to scavenge energy in broadband of parameters with good performance. The time delay was introduced in the mechanical subsystem. The case where the time delay is introduced in both mechanical component and electrical circuit was studied in [2]. Recently, it was reported that in a delayed Duffing oscillator, the modulation of the delay amplitude near the delay parametric resonance gives rise to large-amplitude QP vibration which is exploited to extract energy with better performance comparing to the periodic output power [3].

Yet, in certain harvester systems under aerodynamic and base excitations, it was shown that QP vibrations cause a substantial reduction in the harvested power [4, 5] beyond the flutter speed and then extracting energy from such systems should be avoided in the QP regime. Nevertheless, it was demonstrated that in the presence of time delay, QP vibrations can have a beneficial effect and can be exploited in EH [1–3]. Taking advantages of the time delay effect in EH, the present work studies vibration-based periodic EH in a nonlinear delayed electromechanical harvester device in cross flow. The system consists of a bluff body of mass m subjected to a periodic excitation and coupled to an electrical circuit through a piezoelectric mechanism as shown in the shematic presenred in Fig. 1.

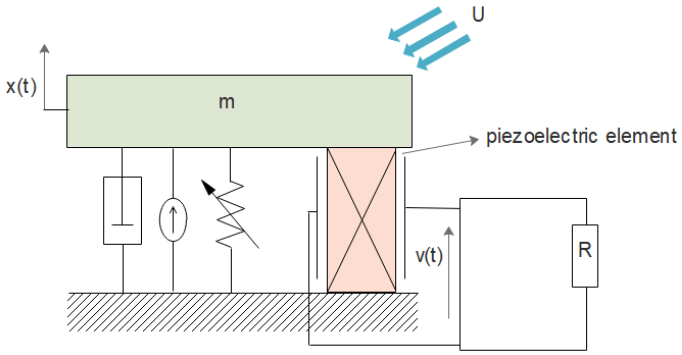

Figure 1. Schematic description of the EH system

It is assumed that the delay is present in the mechanical component of the harvester such that the dimensionless governing equations for the system can be written as

$$\ddot{x}(t) + \mu x(t) + \xi_1 \dot{x}(t) + \xi_3 \dot{x}(t)^3 + \gamma x(t)^3 - \kappa v(t) = \lambda(t) x(t-\tau) \tag{1}$$

$$\dot{v}(t) + \alpha v(t) + \dot{x}(t) = 0 \tag{2}$$

where $x(t)$ is the transverse displacement of the mass m and $v(t)$ is the voltage across the load resistance. The coefficients ξ_1, ξ_3 are, the mechanical damping components, μ the naturel frequency of the harvester, γ the stiffness, κ the piezoelectric coupling term in the mechanical attachment, and α the reciprocal of the time constant of the electrical circuit. The parameter $\lambda(t)$ is the feedback gain and τ is the time delay. It is supposed that the delay amplitude $\lambda(t)$ is modulated with a certain frequency such that

$$\lambda(t) = \lambda_1 \cos(\omega t) \tag{3}$$

where λ_1, ω are, respectively, the amplitude and the frequency of the modulation. The coefficients ξ_1, ξ_3 in (1) are defined by

$$\xi_1 = 2[\xi_m - m a_1 U], \quad \xi_3 = \frac{2 m a_3}{U} \tag{4}$$

where ξ_m is the mechanical damping ratio, m is the flow to harvester mass ratio, U is the reduced wind speed and the coefficients a_1 and a_3 account for the different geometries and aspect ratios of the bluff body. The present work can be considered as an extension of the results given in [6] in which only the undelayed case was considered.

2 MAIN RESULTS

Here the response of the system is investigated near the delay parametric resonance for which the frequency of the delay modulation is near twice the natural frequency of the oscillator. Using the multiple scales method [7], approximation of the periodic response is obtained and used to extract energy from the harvester device.

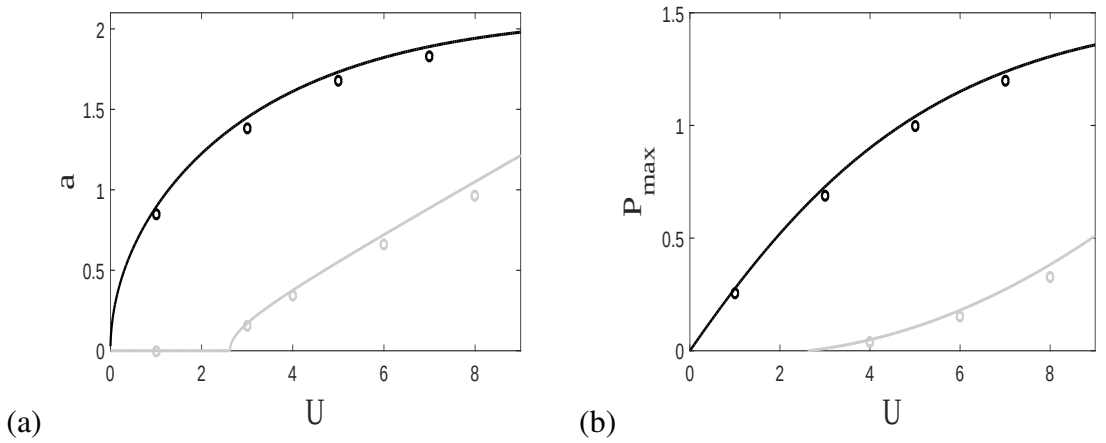

(a) (b)

Figure 2: Vibration and power amplitudes vs U. *Black* lines for the delayed case ($\lambda_1 = 0.3$, $\omega = 2.1$, $\tau = 2\pi$.) and *grey* lines for the undelayed case [6].

Figure 2 shown the variation of the amplitudes of periodic response (Fig. 2a) as well as the maximum output power amplitudes (Fig. 2b) versus the reduced wind speed U for $\lambda_1 = 0$ (undelayed case, *grey* lines) [6] and for $\lambda_1 = 0.3$, $\omega = 2.1$, $\tau = 2\pi$ (delayed case, *black* lines). The analytical prediction are compared to numerical simulation (circles) obtained by using `dde23` algorithm [8] for the delayed system and by using the method of Runge-Kutta of order 4 for the undelayed one. It can be observed from Fig. 2 that in the presence of a modulated delay amplitude in the mechanical component causes a significant increase of vibrations and the output power in a certain range of the reduced wind speed U (Fig. 2, *black* lines).

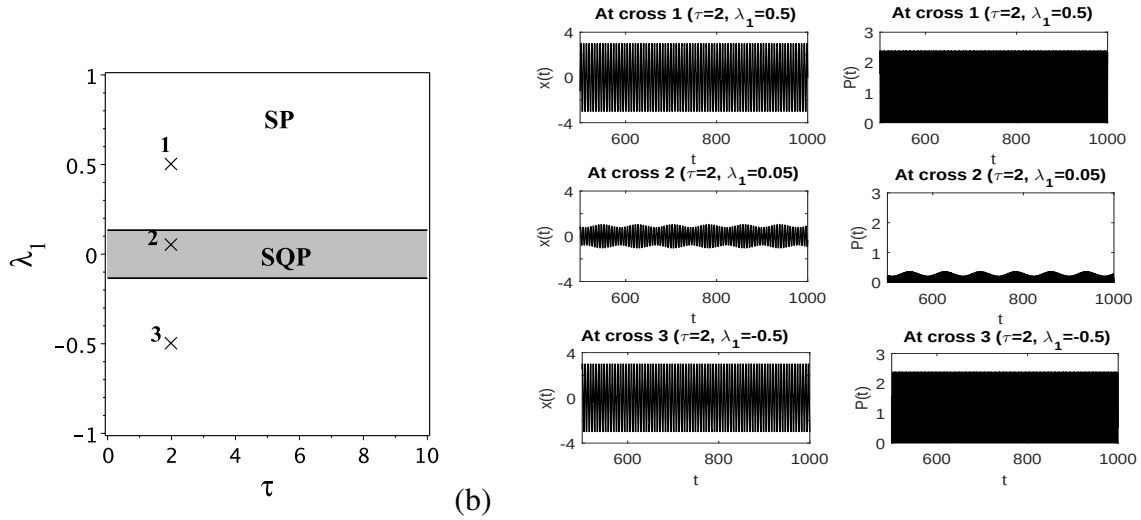

(a) (b)

Figure 3: (a) Stability chart in the plane (λ_1, τ), (b) time and power histories corresponding to different regions picked from (a). SP: stable periodic, SQP: stable QP; $\omega = 2.1$, $U = 8$, $\mu = 1.175$, $\gamma = 0.024$, $\kappa = 10^{-2}$, $m = 6.83.10^{-4}$, $\xi_m = 3.10^{-3}$, $a_1 = 2.5$ and $a_3 = 130$.

To guarantee the robustness of the vibrations during energy extraction operation, the stability chart is presented in Fig. 3a in the parameter plane (λ_1, τ) for $\omega = 2$ indicating the *white* regions corresponding to stable periodic (SP) solutions and the *grey* one where stable QP (SQP) solutions

take place. In Fig. 3b are shown time histories and the corresponding output power responses related to crosses labelled 1, 2, 3 in Fig. 3a. From cross 1 or 3 to cross 2 the response bifurcates from SP to SQP oscillations via secondary Hopf bifurcation producing a decrease of the amplitude response and the corresponding output power at cross 2.

3 CONCLUDING REMARKS

Periodic vibration-based EH has been investigated in a delayed nonlinear oscillator subject to galloping excitation and coupled to an electric circuit through a piezoelectric mechanism in the case where the delay amplitude is modulated with a frequency in the vicinity of the delay parametric resonance. Application of the method of multiple scales enables the approximation of the amplitudes of vibration and the output power. It is shown that the modulation of the delay amplitude near the delay parametric resonance produces a significant increase in the amplitude of vibrations producing power with better performance.

REFERENCES

[1] M. Belhaq, M. Hamdi, Energy harversting from quasi-periodic vibrations. Nonlinear Dynamics, **86**, 2193-2205, (2016).

[2] Z. Ghouli, M. Hamdi, M. Belhaq, Energy harvesting from quasi-periodic vibrations using electromagnetic coupling with delay. Nonlinear Dyn, **89**, 1625-1636, (2017).

[3] Z. Ghouli, M. Hamdi, M. Belhaq, Energy Harvesting in a Duffing Oscillator with Modulated Delay Amplitude. I. Kovacic, S. Lenci (eds) IUTAM Symposium on Exploiting Nonlinear Dynamics for Engineering Systems. ENOLIDES 2018. IUTAM Bookseries, **37**, Springer, Cham, (2020).

[4] A. Abdelkefi, A.H. Nayfeh, M.R. Hajj, Design of piezoaeroelastic energy harvesters. Nonlinear Dynamics, **68**, 519-530, (2012).

[5] A. Bibo, M.F. Daqaq, Energy harvesting under combined aerodynamic and base excitations. Journal of Sound and Vibration, **332**, 5086-5102, (2013).

[6] A. Bibo, A.H. Alhadidi, M.F. Daqaq, Exploiting a nonlinear restoring force to improve the performance of flow energy harvesters. Journal of Applied Physics, **117**, 045103 (2015).

[7] A.H. Nayfeh, D.T. Mook, Nonlinear Oscillations. Wiley, New York (1979).

[8] L.F. Shampine, S. Thompson, Solving delay differential equations with dde23. PDF available on-line at http: //www.radford.edu/∼ thompson/webddes/tutorial.pdf (2000).

SIMULATION OF THE TBL INDUCED VIBRATIONS OF A PLATE USING VIRTUAL SOURCES

A. Pouye[1,2] , L. Maxit[1], C. Maury[2] and M. Pachebat[2]

[1]Laboratoire Vibrations-Acoustique
INSA de Lyon, Lyon, FRANCE
Email: augustin.pouye@insa-lyon.fr, laurent.maxit@insa-lyon.fr

[2]Laboratoire de Mécanique et d'Acoustique
Centrale Marseille, Marseille, FRANCE
Email: maury@lma.cnrs-mrs.fr, pachebat@lma.cnrs-mrs.fr

ABSTRACT

Finding an alternative to common test means (reverberant chamber, wind tunnel facilities, in-situ measurements, etc.) is of particular interest to the transportation industry (automobile, aeronautics, etc.) for the reproduction of the vibroacoustic response of structures under random excitations such as the diffuse acoustic field or the turbulent boundary layer. In this paper a method of achieving this goal using a single acoustic source and the synthetic array principle is proposed. To assess the validity of this method, an academic case study consisting of a simply supported thin aluminum plate under turbulent boundary layer excitation is presented. The vibroacoustic response of the plate is determined with the proposed process and compared to results from random vibration theory and direct measurements in an anechoic wind tunnel facility. This comparison shows good agreement between the proposed approach and both the theoretical and wind tunnel results.

1 INTRODUCTION

The experimental characterization of structures under random excitations such as the diffuse acoustic field (DAF) and the turbulent boundary layer (TBL) is of great interest to the transportation industry. However, the test facilities used (reverberant chamber for the DAF and anechoic wind tunnel/*in-situ* tests for the TBL) can sometimes be complex and costly. Moreover, the results obtained for a given structure can be very different from one facility to another even though the same setup is implemented. In this paper an alternative method is proposed and aims at simulating the vibroacoustic response of structures under these random excitations independently of the environment. This paper is organized as follows: first the proposed approach is briefly described. Secondly, the theoretical background on the vibroacoustic response of a simple structure under random excitation is given. Finally, some results are presented.

2 PROPOSED APPROACH

The experimental reproduction of the TBL induced vibrations using an array of acoustic sources has been theoretically shown some decades ago. But due to technical limitations, this method could not be experimentally validated back then. Since 2000, many researchers have addressed this problem using various approaches. Maury, Bravo, Elliott and Gardonio [1–4] have widely discussed the reproduction of a TBL excitation using an array of loudspeakers. This method works well when it comes to the reproduction of a DAF excitation but due to the limited number of sources in the array, it fails to simulate the wall-pressure fluctuations of a subsonic TBL excitation because of the high wavenumbers involved. In order to circumvent this limitation, a denser array of sources must be used. This is achieved by relying on the synthetic array principle which describes the effects of a full array of sources as the sum of the effects of each source. A single acoustic source is spatially displaced to different positions thereby virtually creating an array of sources.

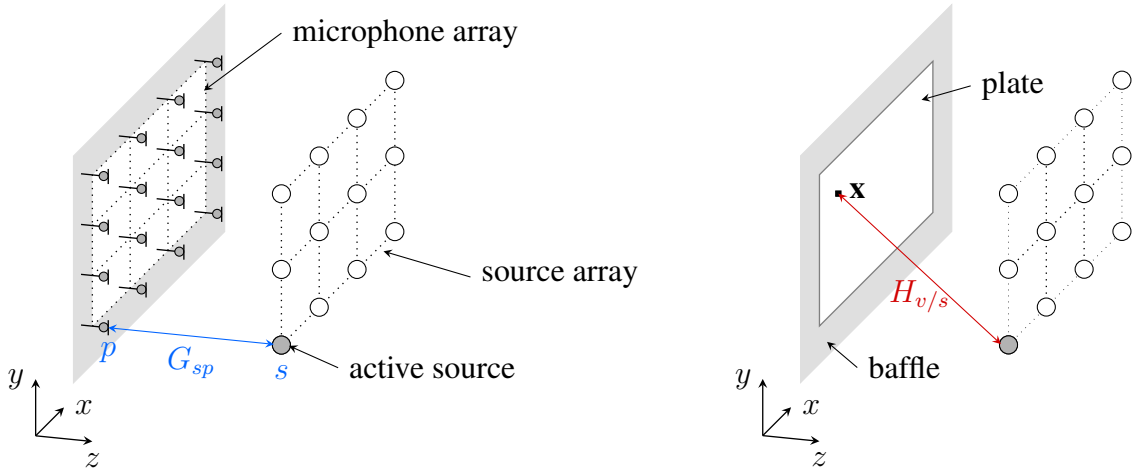

(a) Measurement of G_{sp}

(b) Measurement of $H_{v/s}$

Figure 1. Problem geometry and parameters.

The proposed approach is based on the mathematical formulation of the problem in the wavenumber domain. This formulation is used because it allows an explicit separation of the contributions of the excitation *via* the wall-pressure cross-spectrum density (CSD) function from those of the vibroacoustic behavior of the structure *via* the sensitivity functions. Given a target pressure field $p(\mathbf{k}, \omega)$ consisting of wall-pressure plane waves of wave-vector $\mathbf{k} = (k_x, k_y)$, there are three main steps for the reproduction of this target pressure field using the synthetic array principle:

1. Characterization of the acoustic source: measurement of the transfer functions (G_{sp}) between source positions s and observation points p on the plate (microphones), see Figure 1a.

2. Computation of the source amplitudes Q_s at each position by inversing the equation below:

$$\sum_s Q_s(\mathbf{k}, \omega) G_{sp}(\omega) = p(\mathbf{k}, \omega) \tag{1}$$

3. Synthesis of the target pressure field on the plate surface by adding up the effects of the source at each position and simulation of the vibroacoustic response in a post-processing step.

3 SIMULATION OF THE TBL INDUCED VIBRATIONS OF A PLATE

3.1 Principle

Let us consider a simple test case consisting of a baffled and simply supported aluminum plate with the following dimensions: $480 \times 420 \times 3\,\mathrm{mm}^3$. The auto-spectrum density function of the flexural velocity response noted $S_{vv}(\mathbf{x}, \omega)$ at some point $\mathbf{x}$ of the plate under random excitation is approximately given in the wavenumber domain by the following equation [5]:

$$S_{vv}(\mathbf{x}, \omega) = \frac{1}{4\pi^2} \sum_{\mathbf{k} \in \Omega_\mathbf{k}} |H_v(\mathbf{x}, \mathbf{k}, \omega)|^2 S_{pp}(\mathbf{k}, \omega)\, \delta\mathbf{k} \tag{2}$$

$H_v(\mathbf{x}, \mathbf{k}, \omega)$ is the sensitivity function which corresponds to the vibration response of the structure to a wall-pressure plane wave of wave-vector $\mathbf{k}$ and $S_{pp}(\mathbf{k}, \omega)$ is the pressure CSD function that describes the excitation.

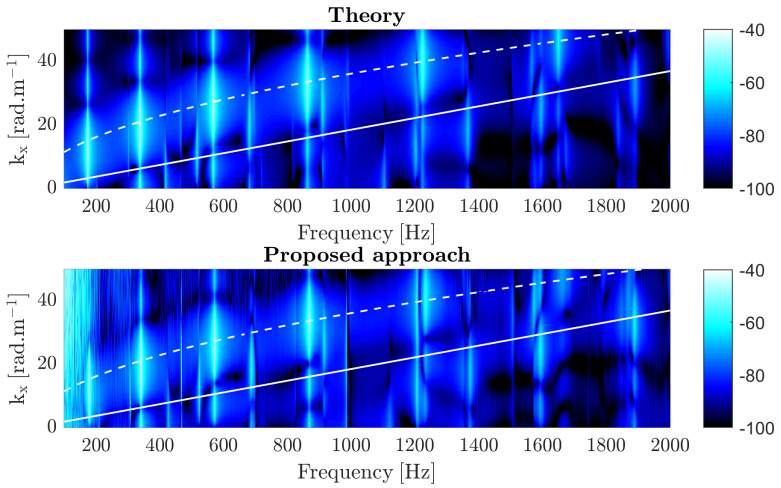

Figure 2: Squared value of the sensitivity function $|H_v(\mathbf{x}, \mathbf{k}, \omega)|^2$ (dB, ref. : $1\,\mathrm{m}^2\,\mathrm{s}^{-2}$) along k_x (for $k_y = 0$). Flexural wavenumber k_f (dashed line), acoustic wavenumber k_0 (continuous line).

Assuming that $S_{pp}(\mathbf{k}, \omega)$ is known, only the experimental measurement of the sensitivity functions of the structure is required in order to determine the response of the structure to the considered excitation by post-processing. The sensitivity functions of the structure are determined as follows: first the transfer functions between the different source positions and a point $\mathbf{x}$ of the plate are measured. This transfer function between one source position s and the point $\mathbf{x}$ is denoted $H_{v/s}(\mathbf{x}, \omega)$, see Figure 1b. Second, after the source amplitudes Q_s have been determined at each source position using Equation (1) which is solved in the least squares sense with $p(\mathbf{k}, \omega) = e^{-j\mathbf{kx}}$, the sensitivity functions are computed with the following equation:

$$H_v(\mathbf{x}, \mathbf{k}, \omega) = \sum_s Q_s(\mathbf{k}, \omega)\, H_{v/s}(\mathbf{x}, \omega) \tag{3}$$

3.2 Results

Figure 2 shows a comparison between the theoretical and experimental sensitivity functions. The source used for the experiment was only efficient from approximately $300\,\mathrm{Hz}$ to $7000\,\mathrm{Hz}$: this is the reason the experimental sensitivity function do not exactly match the theoretical one below $300\,\mathrm{Hz}$. Outside that frequency range and for the considered wavenumber domain, the results are in good agreement: the modal frequencies of the plate can be located around the flexural wavenumber where the response of the plate is maximum.
In Figure 3, the vibration response of the plate to a TBL excitation determined from vibration theory, anechoic wind tunnel measurements and the proposed approach are compared. The TBL

excitation parameters are taken from a previous paper [5]. In this study, the CSD function of the wall-pressure fluctuations was measured in the spatial-frequency domain and the parameters were adjusted to the TBL model of Mellen, the free stream velocity of the TBL was set at $20\,\mathrm{m\,s^{-1}}$.

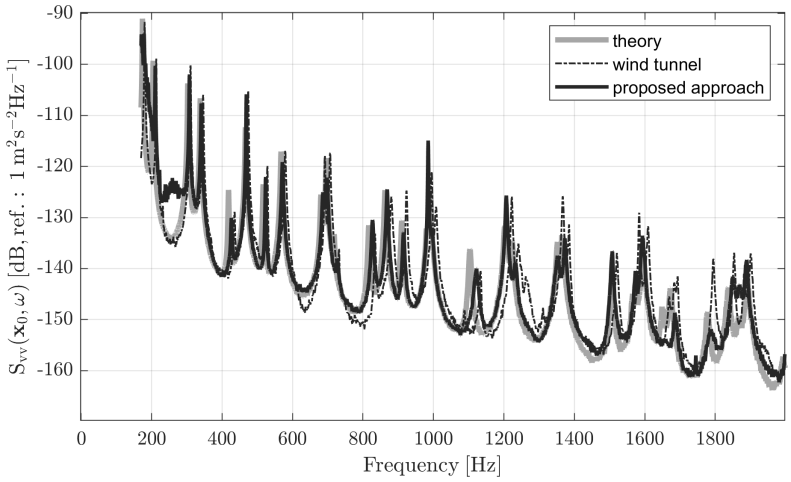

Figure 3. Vibration response of the plate at point $\mathbf{x} = (0.06\,\mathrm{m}, 0.3\,\mathrm{m})$.

As one can observe in Figure 3, the vibration response determined with the proposed approach does not match those obtained from the theory and the wind tunnel measurements under $300\,\mathrm{Hz}$: this is due the fact that the source is not efficient in that frequency range as stated before. The vertical offsets that can be observed at some frequencies are due to the fact that for the theoretical and proposed approach cases, the modal damping of the plate is taken constant in the entire frequency range. As for the horizontal offset, it is certainly due to the difference of boundary conditions between the theory, where the boundary conditions are perfect, and the experimentations, where they are not and differ from one setup to another. Overall, the three results are in good agreement.

4 CONCLUSION

The results obtained with the proposed approach for the simulation of the TBL induced vibrations of a simple were compared to analytical results and those determined from anechoic wind tunnel measurements. This comparison shows good agreement and that the proposed method is promising.

ACKNOWLEDGMENTS

This work was funded by the French National Research Agency (VIRTECH project, ANR-17-CE10-0012).

REFERENCES

[1] C. Maury, S. J. Elliott, and P. Gardonio. Turbulent Boundary-Layer Simulation with an Array of Loudspeakers. *AIAA Journal*, pages 706–713, 2004.

[2] S. J. Elliott, C. Maury, and P. Gardonio. The synthesis of spatially correlated random pressure fields. *The Journal of the Acoustical Society of America*, pages 1186–1201, March 2005.

[3] T. Bravo and C. Maury. The experimental synthesis of random pressure fields: Methodology. *The Journal of the Acoustical Society of America*, pages 2702–2711, October 2006.

[4] C. Maury and T. Bravo. The experimental synthesis of random pressure fields: Practical feasibility. *The Journal of the Acoustical Society of America*, pages 2712–2723, October 2006.

[5] C. Marchetto, L. Maxit, O. Robin, and A. Berry. Experimental prediction of the vibration response of panels under a turbulent boundary layer excitation from sensitivity functions. *The Journal of the Acoustical Society of America*, pages 2954–2964, 2018.

DYNAMIC BUCKLING INVESTIGATION OF AIRCRAFT COMPOSITE STANCHIONS SUBJECTED TO CYCLIC LOADING CONDITIONS

F. Di Caprio[1*], A. Sellitto[2], S. Saputo[2], M. Guida[3] and A. Riccio[2]

[1]CIRA – Italian Aerospace Research Centre
via Maiorise snc, Capua (CE), Italy
Email: f.dicaprio@cira.it

[2]University of Campania "Luigi Vanvitelli"
via Roma 29, Aversa (CE), Italy
Email: andrea.sellitto@unicampania.it, salvatore.saputo@unicampania.it,
aniello.riccio@unicampania.it

[3]University of Naples "Federico II"
p.le Tecchio 80, Naples, Italy
Email: michele.guida@unina.it

ABSTRACT

This work is focused on the investigation of the structural behavior of a composite floor beam, located in the cargo area of a civil aircraft, subjected to cyclical low frequencies compressive loads. In a first stage, the numerical models, able to correctly simulate the investigated phenomenon, have been defined. Different analyses have been performed, aimed to an exhaustive evaluation of the structural behavior of the test article. In particular, implicit and explicit analyses have been considered to preliminary assess the capabilities of the FE code. Then, explicit non-linear analysis under dynamic loads have been considered, to predict the behavior of the composite structure under cyclic loading conditions.

1 INTRODUCTION

Buckling is an instability phenomenon typical of "thin" structures (characterized by at least one very small dimension compared to the others). Usually, the buckling has been considered a

purely static phenomenon. The classic example is that of the Euler beam in which a beam stuck at one end is loaded from the tip to the other, with a compressive load lower than the limit of elasticity of the material. Theoretically, if the force is perfectly centred and the beam is free of imperfections, the latter would remain in equilibrium under the action of any load. In order for the instability to occur, it is mandatory to destabilize the beam by means of an external action, immediately removed. After the perturbation, three cases can occur, depending on the applied load: the beam returns to the initial equilibrium configuration (stable equilibrium); the beam moves to a new equilibrium condition different from the initial one (indifferent equilibrium); the beam moves away indefinitely from the initial equilibrium configuration (unstable equilibrium). The so-called buckling load is the lowest of the loads for which equilibrium is indifferent.

However, buckling can also be caused by loads that vary over time. The application of a time-dependent axial load to a beam, which then induces lateral vibrations and can eventually lead to instability, is something that has been investigated by many authors [1-3].

Dynamic buckling has a relatively recent history. One of the first researchers to study dynamic buckling can be found in [4], where a theoretical solution for the case of a simply supported rectangular plate subjected to varying floor loads over time has been developed. In [5], a criterion that related dynamic buckling to the duration of the load has been introduced. The effects of a high intensity and short duration load have been studied in [6]. According to the investigation, long lasting critical dynamic buckling loads may be of lesser intensity than the corresponding static buckling loads.

In this work, the structural behaviour of a composite floor beam subjected to low-frequency cyclic load conditions has been investigated, assessing the structural response by considering three different loads (below, close, and above the static critical buckling load).

2 TEST CASE DESCRIPTION

The investigated test case, which has been previously validated in [7], is representative of the composite floor beam of the cargo area of a civil aircraft. The geometrical model and the numerical model, discretized in the ABAQUS Finite Element (FE) environment, are reported in Figure 1, while the mechanical properties of the composite lamina are reported in Table 1. The stacking sequence of the beam is [-45; 45; 90; 45; -45; 0; 0; 0; 0; 0; -45; 45; 90; 45; -45].

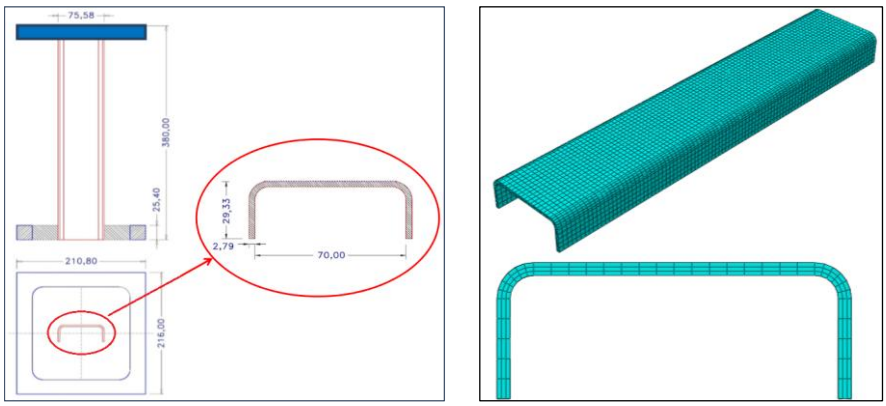

Figure 1. Left: geometrical model; right: numerical model.

ρ [g/cm^3]	th [mm]	E_{11} [MPa]	E_{22} [MPa]	G_{12} [MPa]	G_{13} [MPa]	G_{23} [MPa]	ν_{12}	Xt [MPa]	Xc [MPa]	Yt [MPa]	Yc [MPa]	Sc [MPa]
1.6	0.186	135000	8430	4160	4160	3328	0.26	2257	800	75	171	85

Table 1. Mechanical properties of the lamina.

3 RESULTS AND DISCUSSION

A preliminary compressive analysis has been performed on the investigated test case. In particular, two different formulations, implicit and explicit, have been considered, and the results of both approaches have been compared. Very similar results have been obtained for both approaches, as shown in Figure 2, which compares the load vs applied strain curves of the implicit and explicit formulations, and Figure 3, which reports the damages in the composite laminate evaluated by using the Hashin's failure criteria.

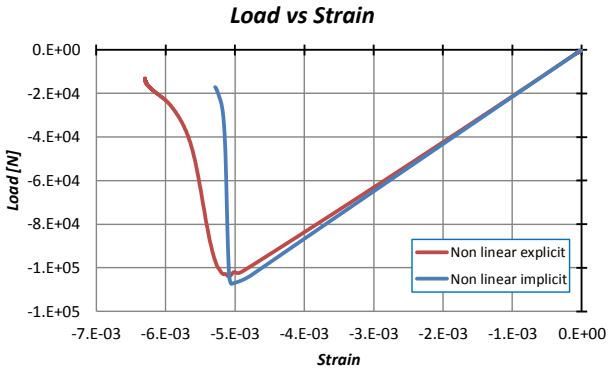

Figure 2. Load vs applied strain.

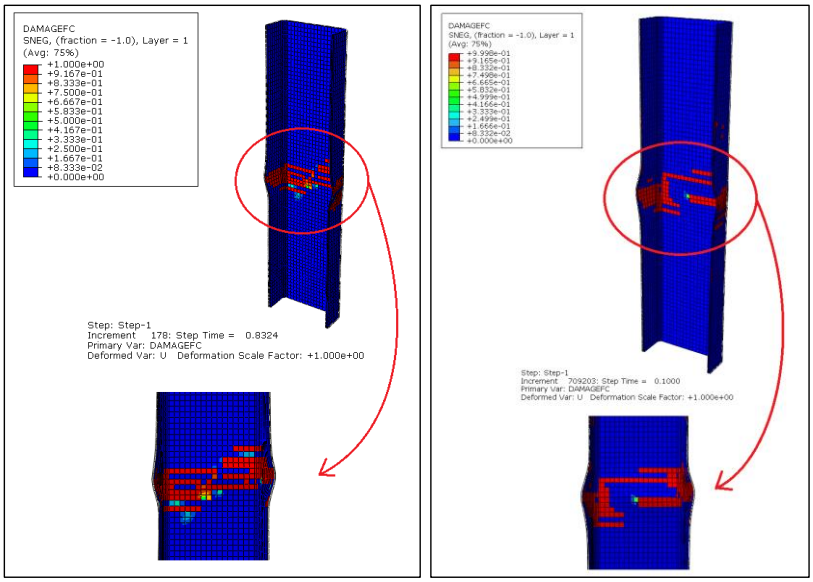

Figure 3. Fibre compressive damages. Left: implicit analysis; right: explicit analysis.

Then, explicit low-cycle analyses have been considered. Three different loads have been applied on the investigated test case. In particular, 10 Hz sinusoidal displacements have been considered, characterized by different applied displacements: 1 mm (below the critical displacement), 1.53 mm (equal to the critical displacement), and 2 mm (above the critical displacement).

Figure 4 reports the results, in terms of stiffness variation, considering the different applied loads.

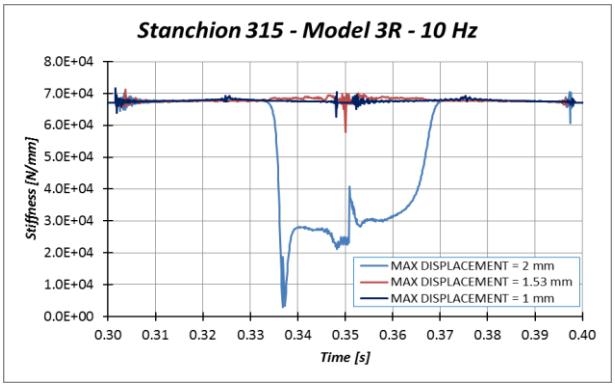

Figure 4. Stiffness variation over a load cycle for different load levels at a 10 Hz frequency.

According to the numerical results, the investigated test case does not experience instabilization under cyclic compressive load below or close to the critical static buckling value. On the other side, the instability occurs if the compressive displacement is above the critical static buckling value.

4 CONCLUSION

In this work, the structural behaviour of a composite floor beam subjected to cyclical low-frequency compressive loads has been presented. Explicit non-linear analyses were then carried out considering dynamic 10 Hz frequency compressive loads. Load cycles with different amplitudes have been considered: 1 mm (about 70% of the static buckling value), 1.53 mm (close to the static buckling value), and finally 2 mm (above the static buckling value).

The results showed that low frequency cyclic loads (compared to the test article's own frequencies) with peak values lower than the static buckling load value are not capable of trigger significant instability. This behaviour is confirmed by comparing the stiffness of the models as a function of time for the different load levels applied at the same 10 Hz frequency.

REFERENCES

[1] M. Amabili, M.P. Païdoussis. Review of studies on geometrically nonlinear vibrations and dynamics of circular cylindrical shells and panels, with and without fluid-structure interaction. *Applied Mechanics Reviews*. 56(4):349-356, 2003.

[2] F. Alijani, M. Amabili. Non-linear vibrations of shells: A literature review from 2003 to 2013. *International Journal of Non-Linear Mechanics*. 58:233-257, 2014.

[3] T. Kubiak. Static and dynamic buckling of thin-walled plate structures. *In. Static and Dynamic Buckling of Thin-Walled Plate Structures*, 2013.

[4] G.A. Zizicas. Dynamic buckling of thin elastic plates. *Transactions of the ASME*. 74(7):1257, 1952.

[5] B. Budiansky, R.S. Roth. Axisymmetric dynamic buckling of clamped shallow spherical shells. *NASA TN D-1510*: 597-606, 1962.

[6] H.E. Lindberg, A.L. Florence. Dynamic Pulse Buckling, 1987.

[7] A. Riccio, A. Raimondo, F. Di Caprio, M. Fusco, P. Sanità. Experimental and numerical investigation on the crashworthiness of a composite fuselage sub-floor support system. *Composites Part B: Engineering*. 150:93-103, 2018.

A NEW FRICTION MODEL TO DESCRIBE THE FREE DYNAMIC RESPONSE OF A SLIDING OSCILLATING SYSTEM UNDER LUBRICATION

J. Perret-Liaudet[1*], A. Hriouech[1,2], M. Belin[1], and M.I. De Barros[1]

[1]Univ. Lyon, Ecole Centrale de Lyon, ENISE, ENTPE, CNRS,
Lab. de Tribologie et Dynamique des Systèmes LTDS, UMR5513, F69134, Ecully, FRANCE
[*]Email: joel.perret-liaudet@ec-lyon.fr

[2]PSA, Centre technique de Vélizy
Vélizy, F78140, FRANCE

ABSTRACT

In this study we introduce a new friction model which can describe lubricated sliding contact under unsteady or transient dynamic conditions. It is developed on the basis of a state variable friction model resting on a friction force equation and a state ones. An effective film thickness is introduced as the internal variable. Its lag or relaxation behaviour to reach the steady state film thickness is governed by a first order differential equation. The role of this film thickness on friction force is interpreted as a sharing effect between solid interaction or confined lubricant and the lubricant film itself. Experimental results consisting on free dynamic responses of a sliding oscillating system under lubrication are compared with ones obtained by the proposed theoretical approach.

1 INTRODUCTION

Friction is a phenomenon that occurs in a lot of mechanical systems including contacts. In order to simulate and analyse the dynamic behaviour of such systems, it is necessary to choose friction law that can be able to describe and model it. A classical way to describe friction is to use the Coulomb friction or viscous friction models, or the combination of both [1]. Such friction models are very useful thanks to their simplicity. However, in many circumstances, they cannot accurately describe tribological behaviours, especially for lubricated contacts. Other models have been used to reproduce the well-known Stribeck behaviour, but they usually ignore the dynamic effects [2].

In other ways, we have designed and built a dynamic tribotest device in order to quantify in a simple way general trends of friction as a function of the sliding velocity [1,3]. This experimental setup, described in Figure 1, is based on the measurement of transient responses $x(t)$ of an underdamped frictional single-degree-of-freedom mass-spring oscillator. For this dynamic tribometer, the moving mass m slides in contact with the tribological system under study. The governing equation of motion can be written as follows

$$m\ddot{x} + kx = -T = -\mu(\dot{x})N \tag{1}$$

where k is the spring stiffness, N the normal contact force, T the friction force and μ the coefficient of friction.

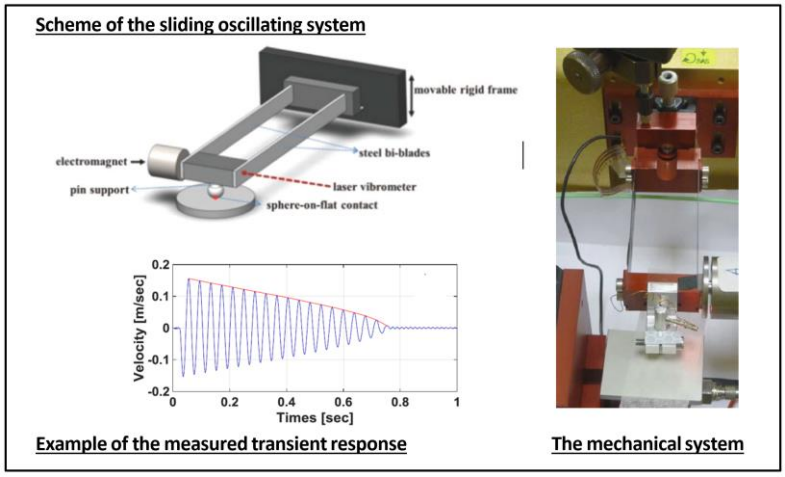

Figure 1. Description of the dynamic tribometer.

General trends of friction is then determined by identifying and analysing the decaying envelope (or the energy decay curve) of the oscillating transient response. To this end, we have described the dependency of the friction coefficient μ on sliding velocity $v = \dot{x}$ by a pseudo-polynomial function given by

$$\mu(v) = \sum_{p=0}^{p=n} \mu_p v^p \mathrm{sgn}(v)^{p+1} \tag{2}$$

where the sign function is introduced in order to preserve the odd property of the coefficient of friction. To determine coefficients μ_p, we have developed a suitable and accurate procedure based on the Krylov-Bogolyubov average method, and then demonstrated the capability of this original technic to obtain in a very simple way the general trends of friction [4]. Nevertheless, complementary experimental measurements of the contact electrical resistance showed that the dynamic phenomena are poorly described by the introduced friction law, equation (2). Indeed, for lubricated contacts, the

lubricant film thickness, not included in the law, plays an important role as it shares friction forces between solid, confined lubricant and/or fluid forces.

In this context, the main goal of this study is to introduce a new friction model by considering the film thickness as the internal state variable.

2 THE SUGGESTED FRICTION MODEL

In order to improve friction models, it is often proposed to introduce internal state variables in constitutive laws. In this approach, modelling consists on a friction force equation coupled to a state equation. Formally, these two equations are written as

$$\begin{cases} T = & \mathcal{F}(v, y) \\ \dot{y} = & \mathcal{G}(v, y) \end{cases} \tag{3}$$

where y is the internal state variable and $\mathcal{F}(\cdot)$ and $\mathcal{G}(\cdot)$ are two nonlinear functions to be precise. To give a first example, we can cite the rate-and-state-variable friction law, which is formulated in term of an average contact lifetime as the internal state variable[5]. As a second example, the LuGre model [6] includes transition from static friction to kinetic one by introducing the mean deflection of bristles as the internal state variable. In this model, it includes also the Stribeck effect obtained for the case of constant sliding velocities. So, in a similar approach, we propose to build a state variable model by introducing the instantaneous film thickness as the internal state variable y. Indeed, this is the key to interpret transition between boundary and full film hydrodynamic regimes. For the state equation, we can heuristically introduced the following differential equation

$$\dot{y} = (Y_{ss}(v) - y)/\tau \tag{4}$$

where $Y_{ss}(v)$ represents the film thickness to be reached, and which corresponds to the steady state film thickness associated to the instantaneous sliding velocity $V = v(t)$. Conceptually, $Y_{ss}(v)$ is a monotonic even function which can be expressed as a power of velocity as follows

$$Y_{ss}(v) = Y_0 + (Y_\infty - Y_0)\left(\frac{|v|}{V^*}\right)^n \tag{5}$$

Concerning the total friction force, it is introduced by the concept of a mixed law for which it is shared between forces induced by the lubricant film itself, T_{EHL}, and by the solid interactions (or the confined lubricant), T_{BL}. So, the total force is written as the following weighted sum

$$T = \alpha T_{BL} + (1 - \alpha) T_{EHL} \tag{6}$$

where $(1 - \alpha)$ is a shifted monotonic sigmoid function of the film thickness, y, which increases from 0 to 1. Without loss of generality, T_{BL} is assumed to be almost constant and $T_{EHL}(v)$ to be a viscous force. Finally and considering the oscillating free responses obtained by our dynamic tribometer, the governing equation can be written in the following first order equation

$$\begin{cases} \dot{x} = & v \\ m\dot{v} = & -m\omega^2 x - T(v, y)\ \mathrm{sign}(v) \\ \dot{y} = & (Y_{ss}(v) - y)/\tau \end{cases} \tag{7}$$

3 RESULTS

In order to simulate the free dynamic response, we have integrated equations (7) by using a Runge-Kutta scheme of order 4. Figure (2-a) shows an example of velocity responses which begins with a convex envelop and finish by a concave one. This behaviour is well captured by our model (see Figure (2-b)). As we can see in Figure (2-d), this can be interpreted by a transition from a full lubricant film force contribution to a dominant solid force contribution. This interpretation is confirmed by

measurement of the electrical contact resistance (ECR) presented in Figure (2-c). At the beginning, the separation between solids is total (the ECR is very high) and at the end full electrical contact is observed (the ECR has a low value).

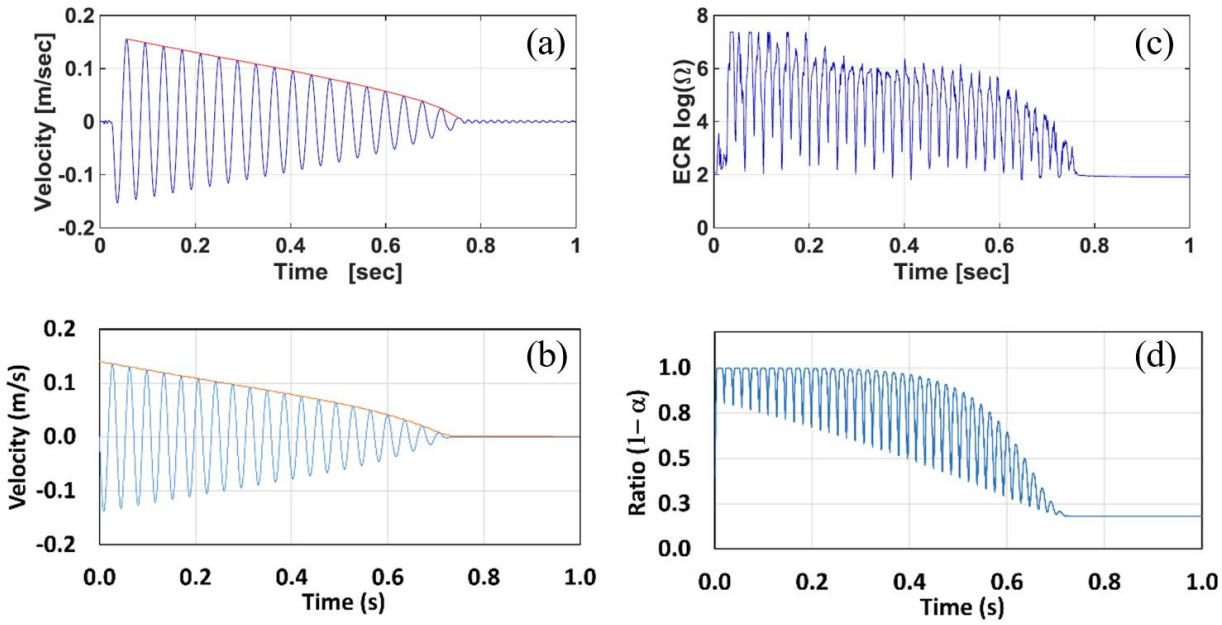

Figure 2. (a) Experimental and (b) theoretical velocity responses; (c) experimental contact resistance; ratio $(1-\alpha)$ of the lubricant film force contribution.

4 CONCLUSION

The relevance of the proposed model is demonstrated in the light of comparisons between numerical results and experimental ones. In particular, our new model can capture the transition related to the instantaneous film thickness which separates the two sliding surfaces, including the lag effect of the thickness dynamics. Now, ongoing work is conducted in order to relate the model parameters to the physical properties of the tribological contact.

REFERENCES

[1] E. Rigaud, J. Perret-Liaudet, M. Belin, L. Joly-Pottuz, J.-M. Martin, A dynamical tribotest discriminating friction and viscous damping, *Tribol. Int.* 43 (2010) 320–329.
[2] J. Juel Thomsen, A. Fidlin, Analytical approximations for stick–slip vibration amplitudes, *Int. J. Non-Linear Mech.* 38 (2003) 389–403.
[3] F. Majdoub, M. Belin, J.M. Martin, J. Perret-Liaudet, M. Kano, K. Yoshida, Exploring low friction of lubricated DLC coatings in no-wear conditions with a new relaxation tribometer, *Tribol. Int.* 65 (2013) 278–285.
[4] F. Majdoub, J. Perret-Liaudet, M. Belin, J.M. Martin, Decaying law for the free oscillating response with a pseudo-polynomial friction law: Analysis of a superlow lubricated friction test, *J. Sound Vib.* 348 (2015) 263–281.
[5] J.-C. Gu, J.R. Rice, A.L. Ruina, S.T. Tse, Slip motion and stability of a single degree of freedom elastic system with rate and state dependent friction, *J. Mech. Phys. Solids.* 32 (1984) 167–196.
[6] D. Pikunov, A. Stefanski, Numerical analysis of the friction-induced oscillator of Duffing's type with modified LuGre friction model, *J. Sound Vib.* 440 (2019) 23–33.

ACOUSTIC CHARACTERISTICS OF INNOVATIVE MATERIALS THROUGH ELECTROSPINNING

G.Iannace[3], F.Branda[1], F.Marulo[2], G.Ciaburro[3], J.Passaro[1], A.Bifulco[1], P.Russo[2]

[1] Department of Chemical Materials and Industrial Production Engineering (DICMaPI), University of Naples Federico II, P.leTecchio 80, 80125 Naples, Italy
E-mail: francesco.branda@unina.it; jessica.passaro@unina.it; aurelio.bifulco@unina.it

[2] Department of Industrial Engineering, Aerospace Division, University of Naples Federico II, Via Claudio 21,80125 Naples, Italy
E-mail: francesco.marulo@unina.it; pa.russo15@gmail.com

[3] Department of Architecture and Industrial Design, University of Campania Luigi Vanvitelli Borgo San Lorenzo, 81031 Aversa (Caserta), Italy
E-mail: giuseppe.ciaburro@unicampania.it; gino.iannace@unicampania.it

ABSTRACT

The produced PVP/silica samples have better sound absorption properties, in the lower frequency range, than materials, of the same thickness. The purpose of this paper is to provide a theoretical model for predicting the sound absorption coefficient of PVP/silica samples. Starting from the knowledge of the physical properties (such as resistivity, porosity and the structure factor) measured for each range of particle size, by the application of a theoretical model, it is possible to obtain the coefficient of absorption of the tested material. Measurements of the absorption coefficient were made using an impedance tube (tube of Kundt). Then the theoretical developments were compared with the experimental ones in function of the frequency.

INTRODUCTION

New materials composed of nanofibers are diffusing also in the field of noise control and correction of acoustic environments. It is possible to get the advantage of improving the acoustic characteristics of traditional materials without increasing their weight and size. The possible applications of these new materials are the automotive and the aerospace industry where there are weight reduction needs. Polymers electrospinning raised very great interest for

the preparation of polymer nanofibers with respect to conventional spinning processes is the possibility of producing micro/nanofibers ranging from two nanometers to several micrometers [1-4]. Light polymeric soundproofing materials that are of interest for the transportation industry fabricated through electrospinning were recently proposed [5, 6] consisting of blankets of electrospun polyvinylpyrrolidone (PVP), with an average fiber diameter in the range 1–3 μm. The electrospun PVP/silica samples may have better sound absorption properties, in the lower frequency range, than materials, of the same thickness, that are usually used in both the civil and aerospace engineering fields

RESULTS AND DISCUSSION

The measurements of the absorption coefficient at normal incidence have been performed with the impedance tube, with an internal diameter of 100 mm. The dimensions of the tube are such that the measure of the absorption coefficient is satisfying in a frequency range between 200 Hz - 2.0 kHz. The acoustic absorption coefficient is obtained from the combination of the transfer functions measured in the two measuring microphones, placed inside the tube in accordance with ISO 10534-2 (2001) [7]. While with the same specimens used for the measurement of the absorption coefficient were used for the measurement of the resistivity R1, this measurement is performed with the method of the alternate air flow, using a rotary cam system, which realizes an alternate air flow at a frequency of 2.0 Hz , in accordance with EN 29053(1994) [8]. Furthermore the porosity Y is defined as the ratio between the volume occupied by the air (Va) and the one occupied by all the material (Vm). The porosity is determined knowing the density of the material prior to the shredding and the density of the granular material; ρm (kg/m^3) is the apparent density of the material, ρsolid (kg/m^3) is the density of the material which the skeleton is made of:

$$Y = \frac{Va}{Vm} = 1 - \frac{\rho_m}{\rho_{solid}}$$

The apparent density (ρm) was evaluated by weighing different volumes of material into a graduated glass tube, while the density of the solid (ρsolid). The structure factor s, is obtained in an indirect way, because it is not easy to measure directly [9], by the knowledge of the first value of the maximum of the absorption coefficient, according to the following relation:

$$s = \left[\frac{c_o (2n+1)}{4\ d\ f_{2n+1}} \right]^2 \qquad n = 0,1,2,.....$$

c_o [m/s] is the speed of the sound in the air, n = integer (n = 0 corresponds to the first value of the maximum); d [m] is the thickness of the specimen; f_{2n+1} [Hz] the corresponding frequency of the first value of the maximum of the absorption coefficient.

Theoretical model for the determination of the absorption coefficient

In literature are available mono-parametric models in function of the only resistivity R_1 (Delany and Bazley, Mechel [10]), and semi empirical models based on other acoustic parameters [11] for the theoretical evaluation of the absorption coefficient, but usually the trends obtained are not in good agreement with the measured data for the granular materials. Therefore, for the evaluation of the absorption coefficient is taken a phenomenological model based on the knowledge of three non- acoustical parameters that can be measured; this phenomenological model was elaborated to estimate the acoustic parameters, so it can be used for nano materials. The numerical model requires of the resistivity, the porosity and the structure factor of the

material [12, 13]. The complex wave number k_m and the characteristic impedance Z_m are evaluated, in agreement with the following relations:

$$k_m = k_0 (s\gamma)^{1/2} \left(1 - j\frac{f_\mu}{f}\right)^{1/2} \left[1 - \frac{1-\frac{1}{\gamma}}{1 - j\frac{f_\theta}{f}}\right]^{1/2}$$

$$Z_m = \frac{\rho_0 c}{Y} (s\gamma)^{1/2} \left(1 - j\frac{f_\mu}{f}\right)^{1/2} \left[1 - \frac{1-\frac{1}{\gamma}}{1 - j\frac{f_\theta}{f}}\right]^{1/2}$$

$k_o = \omega/c_o = 2\pi f/c_o$ is the wave number [m^{-1}]; f is the frequency [Hz]; c_o is the speed of sound in the air [m/s]; s is the structure factor; $\gamma = c_p/c_v$ is the ratio of the specific heat at a constant pressure and volume of the air ($\gamma = 1.41$); ρ_o is the air density (kg/m^3). Y is the porosity, R_1 is the resistivity (Ns / m^4), f_μ and f_θ are defined as follows:

$$f_\mu = \frac{1}{2\pi}\frac{R_1 Y}{\rho_0 s}$$

$$f_\theta = \frac{R_1}{2\pi\rho_0 N_{Pr}}$$

N_{Pr} is the Prandtl number ($N_{Pr} = 0.71$). The Prandtl number is defined as the ratio of momentum diffusivity (kinematic viscosity) to thermal diffusivity $Pr=\nu/\alpha$, where ν is the kinematic viscosity (m^2/s), α is the thermal diffusivity (m^2/s). In heat transfer problems, the Prandtl number controls the relative thickness of the momentum and thermal boundary layers. For a porous material, with a thickness of d, on a rigid wall is defined the acoustic impedance Z, per unit area, as a function of the complex wave number k_m and of the characteristic impedance Z_m, such as:

$$Z = -jZ_m \cot(k_m d)$$

Defining the acoustic impedance per unit area $\zeta = Z/\rho_o c_o$ ($\rho_o c_o = 407$ kg m^{-2} s^{-1}) characteristic impedance to the air), it is possible to define the value of the absorption coefficient for a normal incidence:

$$\alpha_0 = \frac{4\,\mathrm{Re}(\zeta)}{|\zeta|^2 + 2\,\mathrm{Re}(\zeta) + 1}$$

The trends of the absorption coefficient are reported as a function of the frequency in the range 200 Hz - 2.0 kHz. Figure 1 shows the trends of the absorption coefficient of the PVP/SiO_2 sample (weight 7.11 gr; thickness 0.015 m), which have good sound absorption characteristics. It is possible to note a good agreement between the measured and calculated trends.

REFERENCES

[1] Agarwal, S.; Greiner, A.; Wendor, J.H., Functional materials by electrospinning of polymers. Prog. Polym. Sci. **2013**, 38, 963–991.

[2] Bhardwaj, N.; Kundu, S.C., Electrospinning: A fascinating fiber fabrication technique. Biotechnol. Adv. **2010**,28, 325–347.
[3] Teo, W.E.; Ramakrishna, S., A review on electrospinning design and nanofibre assemblies. Nanotechnology **2006**, 17, R89–R106.
[4] Iannace, G.; Acoustic properties of nanofibers. Noise and Vibration Worldwide 2014, 45(10), 29-33.
[5] Avossa, J.; Branda, F.; Marulo, F.; Petrone, G.; Guido, S.; Tomaiuolo, G.; Costantini, A., Light ElectrospunPolyvinylpyrrolidone Blanket for Low Frequencies Sound Absorption. Chin. J. Polym. Sci. **2018**, 36, 1368–1374.
[6] Del Sorbo, G.R.; Truda, G.; Bifulco, A.; Passaro, J.; Petrone, G.; Vitolo, B.; Ausanio, G.; Vergara, A.; Marulo, F.; Branda, F., Non Monotonous E_ects of Noncovalently Functionalized Graphene Addition on the Structure and Sound Absorption Properties of Polyvinylpyrrolidone (1300 kDa) Electrospun Mats. Materials **2019**, 12, 108.
[7] ISO 10534-2 (2001), Acoustics - Determination of sound absorption coefficient and impedance in impedance tubes - Part 2: Transfer-function method.
[8] EN 29053 (1994) "Acoustics. Materials for acoustical applications. Determination of airflow resistance"
[9] Champoux, Y.; Stinson, M.R., Measurement of the tortuosity of porous materials and applications for acoustic modelling, J. Acoust. Soc. Am. **1990**, 106 (3), 1416-1419.
[10] Delany, M.E.; Bazley E.N., Acoustical properties of fibrous materials, Applied Acoustics, **1970**, 3, 105-116.
[11] Champoux Y., Stinson M. R., On acoustical models for sound propagation in rigid frame porous materials and the influence of shape factors, J. Acoust. Soc. Am. **1992**, 92(2), 1120–1131.
[12] Berengier M.C., Stinson M.R., Daigle G. A., Hamet J. F., Porous road pavements: Acoustical characterization and propagation effects, J. Acoust. Soc. Am. **1997**, 101(1), 155-162. Doi; http://dx.doi.org/10.1121/1.417998
[13] Hamet, J.F., Bérengier, M., Acoustical characteristics of porous pavements: A new phenomenological model, Proceedings. Internoise 93, Leuven, Belgium, **1993**, 641-646.

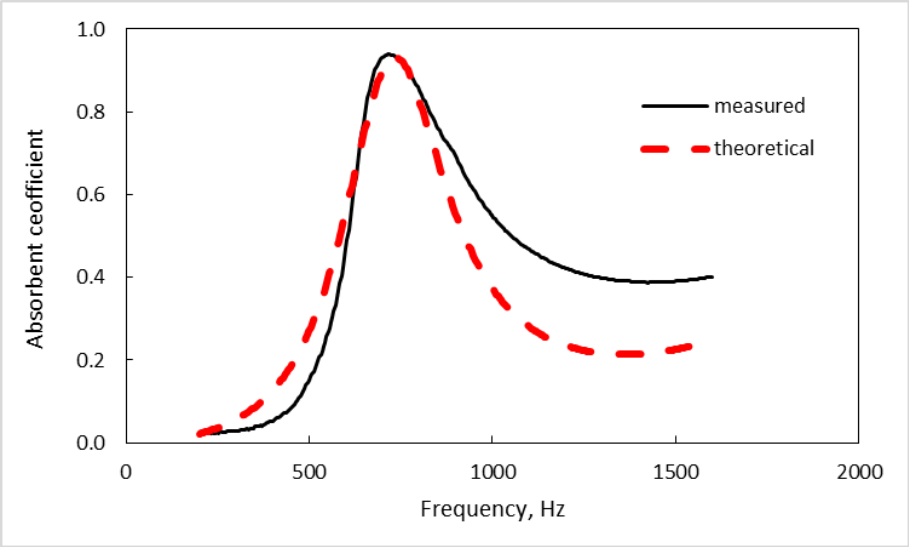

Fig.1 Plots of the sound absorption coefficient as a function of frequency measured compared with theoretical one

THE DYNAMICS OF DELAYED BIRHYTHMICITY OSCILLATOR WITH MODULATED DELAY AMPLITUDE

Mustapha Hamdi[1], Mohamed Belhaq[2] and Zakaria Ghouli[2]

[1]FST-Al Hoceima
University Abdelmalek Essaadi, Tetouan, Morocco
Email: hamustapha2000@yahoo.fr

[2]Faculty of Sciences Ain Chock
University Hassan II-Casablanca, Morocco
Email:mbelhaq@yahoo.fr, ghoulizakaria@gmail.com

ABSTRACT

This paper studies the dynamics of a delayed birhythmicity oscillator in a modified form of the classical delayed van der Pol oscillator in which the time delay amplitude is modulated around a mean value with a certain amplitude and frequency. The time-periodic delay amplitude is introduced to investigate the control of birhythmicity in the oscillator. Averaging method is applied to approximation the different amplitudes of stable and unstable limit cycles of the birhythmic oscillator near a parametric resonance for which the frequency of the delay amplitude modulation is near twice the natural frequency of the oscillator. Analytical approximations supported by numerical simulations show the influence of the modulated time delay on the regions where birhythmic behavior exists. Depending on the system parameters, the system may exhibit birhythmicity, monorhythmic or quasiperiodiity.

1 INTRODUCTION

In a recent work [1], the dynamics and control of a delayed van der Pol oscillator with time-periodic delay amplitude was investigated in the case where the delay amplitude in the position is modulated with a certain amplitude and a resonant frequency. Perturbation method was performed o approximate the amplitude of periodic and quasi-periodic vibrations of the oscillator near a parametric resonance for which the frequency of the delay amplitude modulation is near twice the natural frequency of the oscillator. The obtained result demonstrated that the modulation of the delay amplitude in the position gives birth to quasi-periodic vibrations with large amplitude in a broad range of parameters. This finding has been successfully exploited in energy harvesting from quasi-periodic vibrations [2–4].
In [1] the undelayed classical van der Pol oscillator have one limit cycle. In the present study, we consider the case where the undelayed van der Pol oscillator presents a birhythmitic phenomenon in which two stable limit cycles separated by an unstable limit cycle having different amplitudes and frequencies may coexist.
The interest to investigate mulistability in van der Pol oscillator is that the birhythmitic phenomenon occurs in many natural and artificial systems [5–7]. In [8] The influence of time delay on the dynamics of a multicycle van der Pol oscillator has benn considered. It was shown that depending on the strength of delay the bifurcation space can be divided into two subspaces for which the dynamical response of the system is generically distinct. Also, depending on the parameter space the system also exhibits a transition between birhythmicity and monorhythmic behavior. Control of birhythmicity was also investigated in [9] for three birhythmic oscillators from diverse fields of natural science.
The intent of the present work is to study analytically and using numerical simulation the influence of time-periodic delay amplitude on birhythmiticity in a delayed van der Pol oscillator in the case where the delay amplitude in the position is periodically modulated around a nominal value with a certain amplitude and a resonant frequency.
Consider a modified form of a classical equation of van der Pol oscillator in which the damping part contains an additional higher nonlinear term comparing with the standard van der Pol oscillator. The dimensionless form of the model is given by the following equation

$$\ddot{x} + x - \epsilon(\alpha - \beta x^2 + \alpha_2 x^4 - \beta_2 x^6)\dot{x} = (\lambda_1 + \lambda_2 \cos \omega t)x(t-\tau) + \lambda_3 \dot{x}(t-\tau) \qquad (1)$$

where α, β, α_2 and β_2 are the damping coefficients of the multicycle van der Pol oscillator, and λ_1, λ_2 and λ_3 denote, respectively, the gains in position and velocity and τ is the time delay. Note that the present paper can be considered as an extension of a previous work [1] where the multicycle behavior was absent (the case of Eq. (1) with $\alpha_2 = \beta_2 = 0$).

2 MAIN RESULTS

We investigate the response of the system near the delay parametric resonance for which the frequency of the delay modulation is near twice the natural frequency of the oscillator. Application of the averaging method [11] enables the approximation of the response of the periodic vibrations.

Figure 1 shown the variation of the amplitudes of periodic response versus ω. The analytical prediction are obtained by using the averaging method. Solid line corresponds to stable solutions and dashed lines indicate unstable ones. It can be observed from Fig. 1 that near the resonance two stable limit cycle exist, one with small amplitude and other with large amplitude. Away from the resonance only the one with large amplitude which is not affected by time delay persists. Time histories of the two responses are shown inset in Fig. 1 for $\omega = 2$ providing numerical validation of the analytical predictions.

Figure 2 illustrates in the parameter plane (α_2, β_2) the bifurcation curves delimiting regions of existence of limit cycles. In region II two stable limit cycles (birhythmiticity) occurs and in region I only one stable limit cycle exists (monorhythmicity). The tick line correspond to the delayed case while the thin line is related to the undelayed case.

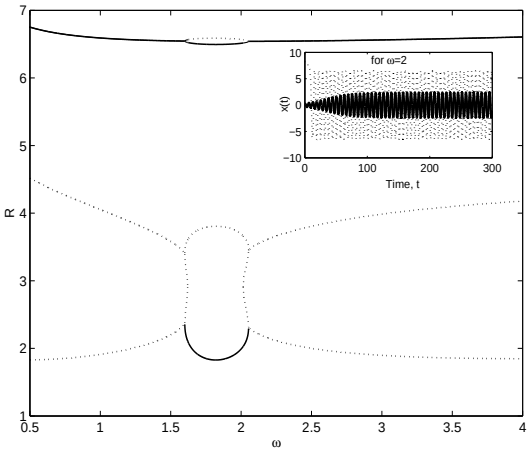

Figure 1. Vibration amplitudes versus ω for $\alpha_2 = 0.15$, $\beta_2 = 0.004$, $\alpha = 1$, $\beta = 1$ and $\tau = 1.58$.

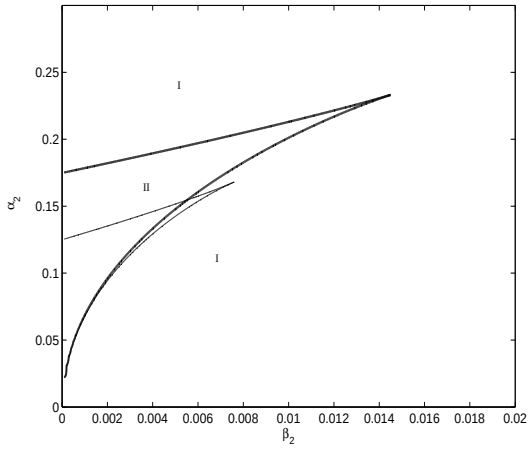

Figure 2: Bifurcation curves in the parameters plane (α_2, β_2), $\alpha = 1$, $\beta = 1$, $\omega = 2.1$ and $\tau = 1.58$.

3 CONCLUDING REMARKS

A birhythmic behavior was studied in a modified form of a classical delayed van der Pol oscillator in which the damping component contains an additional higher nonlinear terms. We consider the case where the delay amplitude in the position is modulated around a nominal value with a certain amplitude and frequency. The averaging method has been used to approximate the solutions near the primary delay parametric resonance for which the frequency of the modulation is near twice that of the natural frequency of the oscillator. The influence of the modulated delay amplitude on the dynamics of the oscillator was examined. It was shown that the modulation of the delay amplitude can widen the region of birhythmicity over which a large-amplitude stable limit cycle persists. This result can be of great interest in energy harvesting for which a large-amplitude limit cycle is desired. This problem is under consideration and results will be presented elsewhere.

REFERENCES

[1] M. Hamdi and M. Belhaq, Quasi-periodic vibrations in a delayed van der Pol oscillator with time-periodic delay amplitude. J. Vib. Control, **24**, 57265734, (2018).

[2] M. Belhaq, M. Hamdi, Energy harversting from quasi-periodic vibrations. Nonlinear Dynamics, **86**, 2193-2205, (2016).

[3] Z. Ghouli, M. Hamdi, M. Belhaq, Energy harvesting from quasi-periodic vibrations using electromagnetic coupling with delay. Nonlinear Dyn, **89**, 1625-1636, (2017).

[4] Z. Ghouli, M. Hamdi, M. Belhaq, Energy Harvesting in a Duffing Oscillator with Modulated Delay Amplitude. I. Kovacic, S. Lenci (eds) IUTAM Symposium on Exploiting Nonlinear Dynamics for Engineering Systems. ENOLIDES 2018. IUTAM Bookseries, **37**, Springer, Cham, (2020).

[5] A. Goldbeter, Biochemical Oscillations and Cellular Rythms. The molecular basis of periodic and chaotic behavior (Cambridge University Press, 1996).

[6] A. Goldbeter, Computational approaches to cellular rhythms, Nature **420**, 238245, (2002).

[7] A. N. Pisarchik and U. Feudel, Control of multistability, Phys. Rep. **540**, 167 (2014).

[8] P. Ghosh, S. Sen, S.S. Riaz, D.S Ray, Controlling birhythmicity in a self-sustained oscillator by time-delayed feedback, Phys. Rev. E **83**, 036205, (2011).

[9] D. Biswas, T. Banerjee, J. Kurths, Control of birhythmicity: A self-feedback approach, CHAOS, **27**, 063110, (2017).

[10] Mustapha Hamdi and Mohamed Belhaq, Quasi-periodic vibrations in a delayed van der Pol oscillator with time-periodic delay amplitude. Journal of Vibration and Control 24(2015), 5726-5734.

[11] A.H. Nayfeh, D.T. Mook, Nonlinear Oscillations. Wiley, New York (1979).

[12] L.F. Shampine, S. Thompson, Solving delay differential equations with dde23. PDF available on-line at http: //www.radford.edu/∼ thompson/webddes/tutorial.pdf (2000).

VIBROACOUSTIC PERFORMANCES OF AN ACOUSTIC BOX THROUGH HYBRID FE-SEA METHOD

G. Piccirillo Sibiano[1], G. Petrone[1] and G. Bizzarro[2]

[1]Pasta-Lab
Università degli Studi di Napoli Federico II, Naples, Italy
Email: ge.piccirillosibiano@studenti.unina.it, giuseppe.petrone@unina.it

[2]Leonardo Helicopter Division, Interior Acoustics - Aerodynamics
via G. Agusta 520, Cascina Costa di Samarate, 21017, Italy
Email: giuseppe.bizzarro@leonardocompany.com

ABSTRACT

A numerical FE-SEA model of a box-shaped test article has been made in order to compare numerical with experimental results and to mark the improvement due to the addiction of local details with respect to pure SEA. The hybrid FE-SEA method is computationally efficient to investigate the behavior of the structure and the acoustic performances of the fluid volume inside the box, especially in the mid frequency range. The subsystems with long wavelength behavior are modeled deterministically with FE, while the subsystems with short wavelength behavior are modeled statistically with SEA. Although this method provides results as ensemble average response for each subsystem subject to small variations in terms of mass and geometrical properties, the numerical results shows a good level of agreement with the experimental ones.

1 INTRODUCTION

The dynamic behavior of a structure is strictly linked to the frequency range of interest. Typically, at low frequencies it is characterized by global modes and relatively long wavelength behavior, conversely at high frequencies it shows local mode shapes and short wavelength behavior. For this reason, at low frequencies finite element method (FEM) is widely used. When the frequency arises, FEM computational cost increases until it becomes unaffordable. Hence, at high frequencies statistical energy analysis (SEA) is mostly used, also because this approach is well suited when local modes are predominant. Nevertheless, there are some cases in which, in a certain frequency range, some components of the structure show a long wavelength behavior while other ones have a short wavelength behavior.

The hybrid FE-SEA method is especially useful in this kind of situations. In fact, the former components are modelled with FEM and the latter with SEA.
In this paper the hybrid FE-SEA method is used in order to obtain numerical results comparable with experimental ones. The use of hybrid method enables the introduction of FE details into a standard SEA analysis [1].

In particular, in this paper a box-shaped test article (Figure 1) has been analyzed in order to become familiar with this method. It is made up of a set of six panels which are pinned on a stiffer trapezoidal frame. Mechanical properties of the structure are listed in Table 1. The frequency range of interest is 200-4000 Hz.

2 EXPERIMENTAL SETUP

The boundary condition of the structure is free, so in laboratory it was simulated by suspending the system with four ropes. For each panel a series of accelerometers (both triaxial and monoaxial) provided the acquisition of the vibrational level. A pair of microphones was set inside the box to measure the SPL of the cavity. The load was given by a shaker and the generated signal was a white noise in the range of interest.

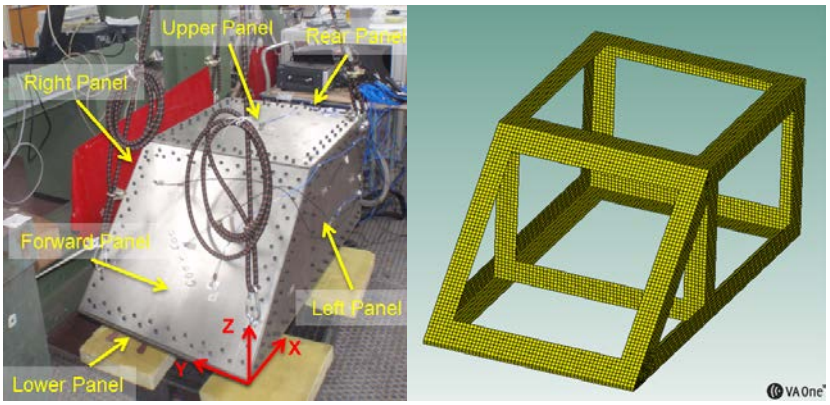

Figure 1- On the left: experimental setup of the box with specification of the panels name.
On the right: internal frame modeled with VA ONE software.

	FRAME	PANELS
MATERIAL	Steel	Aluminum
t [mm]	8.3	1.0
E [GPa]	190	73
ν	0.30	0.30
ρ [kg/m^3]	7852	2780
DLF	1%	1%

Table 1- Material and mechanical properties of the system components.

3 MODELING

Two numerical models have been made: a pure SEA and a hybrid FE-SEA. The first thing to do in an FE-SEA model is establish which components are best modeled with FEM or SEA. In order to do so, it is important to analyze the modal density of each subsystem [2]. The frame is sufficiently stiff such that it has only 271 modes in the frequency range of interest and, so, it has been modeled with FEM, in particular, CQUAD4 elements with plate properties. For the six panels the flexural wavefield has been modeled through SEA plates, while the extensional and shear wavefields has been described with FEM, in particular CTRIA3 elements with membrane properties [3].

In order to decrease the level of uncertainty introduced by the SEA subsystems, FE punctual junctions between FE membranes and the FE frame have been taken into account and added in proper positions inside the virtual model. Hybrid line junctions have been provided on the edges of the box. They establish the coupling among adjacent SEA plates and FE membranes on each of their boundary. In fact, on each edge, the energy flows in the following manners:

- between an SEA plate and the correspondent FE membrane;
- between two SEA plates;
- between two FE membranes.

The acoustic part has been concerned introducing an SEA acoustic cavity with 1% absorption and some SIFs linked to the SEA panels. SEA area junctions have been used to allow energy flowing between the flexural wavefield and the cavity, while hybrid area junctions have simulated the energy exchange between the extensional wavefield and the cavity [4].

In the pure SEA model, every subsystem has a statistical formulation and information about punctual connections between frame and panels can’t be taken into account.

The software used for the analyses is VA One [5], which provides the possibility to combine in one work environment the SEA and FEM, in order to take advantage of both using the hybrid method.

4 RESULTS

In order to compare experimental and numerical results, the measured accelerations for each panel have been averaged such that a subsystem could be described by a single level of acceleration, that is the same result coming from SEA or hybrid FE-SEA method.

The numerical simulation shows that the numerical results are in good agreement with the experimental ones (Figure 2-3). SEA modeling brings to an overestimation of rear and upper panels acceleration level, but for the remaining panels it is near to the mean response starting from 800 Hz. This observation can be also successful extended to the acoustic noise transfer function (NTF), evaluated starting from the SPL of the SEA cavity.

Referencing to the hybrid FE-SEA results, it can be observed that panels acceleration levels and acoustic cavity SPL are very similar to the experimental ones starting in the whole analyzed range, both in terms of amplitude and peaks/valley behavior.

5 CONCLUSIONS

In this example the hybrid FE-SEA method reveals how much the SEA formulation can be improved by adding deterministic details and, on the other side, how much it can be beneficial to decrease the computational cost introducing an SEA formulation for appropriate subsystems.

The numerical discrepancies in terms of natural frequencies and amplitude could be due to the lack of information about the effective DLF spectra (the assumption of constant 1% is suggested by literature) and to an unvalidated model of the frame.

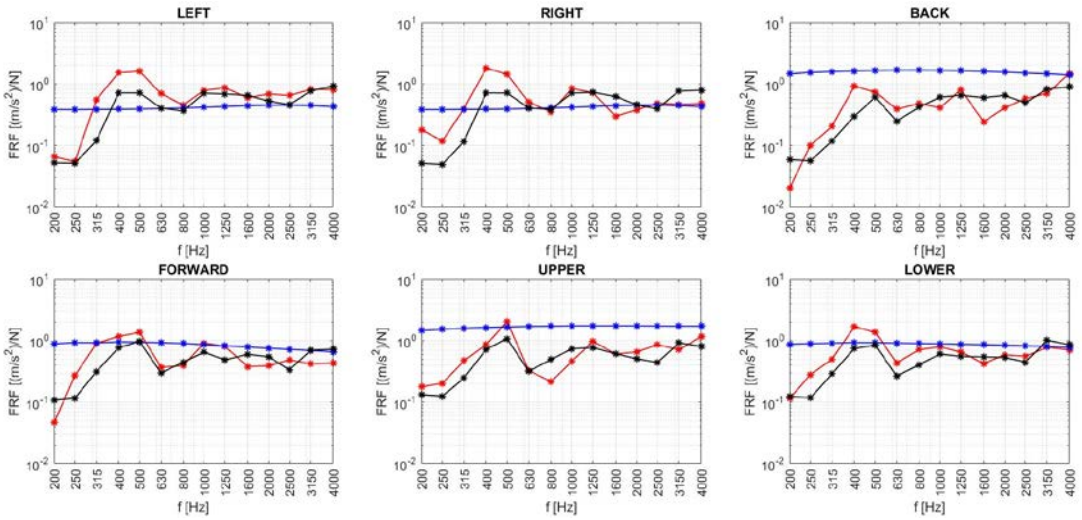

Figure 2- Comparison between experimental (red line), pure SEA (blue line) and hybrid FE-SEA (black line) results in terms of mean flexural acceleration FRF of the structure panels.

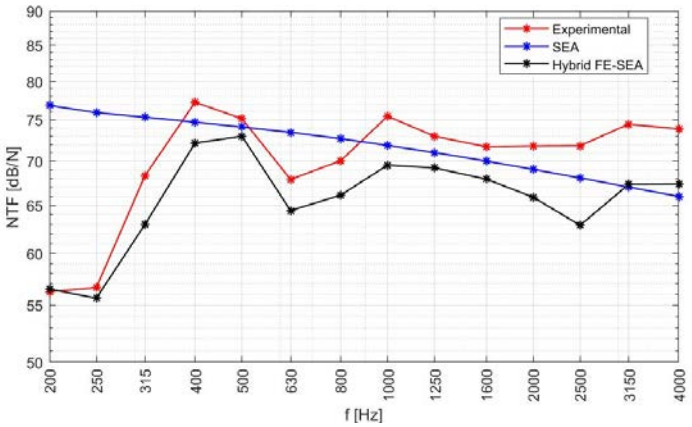

Figure 3- Comparison between experimental, pure SEA and hybrid FE-SEA results in terms of acoustic NTF for the cavity inside the analyzed box.

6 ACKNOWLEDGEMENT

All the authors would like sincerely to acknowledge prof. G. Ghiringhelli from Politecnico di Milano who gently provided the experimental test article.

7 REFERENCES

[1] P.J. Shorter, R.S. Langley, Vibro-acoustic analysis of complex systems. *Journal of Sound and Vibration*. 288(3): 669-699, 2005.

[2] I. Vaz, K. Washburn, L. De Vries, Improvement of an SEA model of cab interior sound levels through use of a hybrid FE/SEA method. *SAE Technical Paper*. 2011-01-1706, 2011.

[3] V. Cotoni, P. Shorter, R. Langley, Numerical and experimental validation of a hybrid finite element-statistical energy analysis method. *The Journal of Acoustic Society of America*.122(1): 259, 2007.

[4] B. Gardner, P. Shorter, V. Cotoni, Vibro-acoustic analysis of large space structures using the hybrid FE-SEA method. *46th AIAA/ASME/ASCE/AHS/ASC Structures, Structural Dynamics & Materials Conference*. AIAA 2005-1987.

[5] The ESI Group, VA One 2016.5 User's Guide, 2016.

Reliability and optimization of embedded mechatronic systems

A. EL HAMI
Laboratory of Mechanics of Normandy LMN
INSA Rouen, France,
Email: abdelkhalak.elhami@insa-rouen.fr

ABSTRACT

Reliability-Based Design Optimization (RBDO) in embedded electronics and mechatronic system is a very important part in several industrial fields. The RBDO analysis of industrial systems is a very important engineering issue, in order to guarantee their functional behavior. Most of the critical failures are generated by the interactions between the sub-systems, implemented in different technologies, e.g. mechanics, electronics, and software. Therefore, the analysis of the system as a whole is not enough and it is necessary to study all the interactions in order to estimate the system reliability. In this paper, we will present the last developments of Reliability-based Design Optimization in embedded electronics and mechatronic system.

1 INTRODUCTION

In the embedded electronics and mechatronical system design, it is very important tominimize the structural cost and to maximize safety. Few designers (or researchers) can work with these two opposite philosophies. The basic idea is to know the role ofeach parameter in our design using advanced technologies in CAD (Computer-Aided Design) domain such as sensitivity analysis, optimization concept and reliability analysis. Our main challenge is to integrate the reliability analysis in the optimization procedure that allows us to define the best compromise between cost and safety. This model is called Reliability-Based Optimization. We applied reliability-based optimization on the three structural optimization families.
Model 1: The Reliability-Based Design Optimization (RBDO) consists of the integration of reliability analysis into the optimization procedure. The classical RBDO approach is carried out in two spaces: normalized space and physical one. Therefore, the nested problems necessitate a high computational time. In order to overcome this problem, we propose a new hybrid formulation consisting in solving the problem in a Hybrid Design Space (HDS), containing all numerical information about the optimization process. Application of Dynamical and fatigue of structures.
Model 2: The Reliability-Based Shape Optimization (RBSO) consists of the coupling between several models: geometrical modeling, numerical simulation, and reliability analysis and

optimization methods. The hybrid method can be used efficiently to reduce the computational time. Since the structural geometry may be updated during the optimization process, a flexible model has to be used. After having studied different ways of geometrical modeling, we select a parametric boundary description such as B-spline curves. Furthermore, the design model may be different than the mechanical one and may then give inaccurate results of the structure behavior. We study the relationship between CAD and FEA (Finite Element Analysis) models in order to define the suitable method that updates the geometry with a small cost. Furthermore, the optimization process generally needs gradient evaluations at each iteration. Two problems can be found: the computing time and the result accuracy. Therefore, we propose a new numerical derivative to balance the computing time and the precision. Application of
Model 3: The Reliability-Based Topology Optimization (RBTO) is based on the introduction of the reliability criteria into the topology optimization procedure. The resulting reliability-based topologies are different than the resulting deterministic one.Moreover, the advantage of RBTO is to provide the designer with several solutions in function of the target reliability. This paper presents a numerical investigation of the probabilistic approach in estimating the reliability of wire bonding, and develops a reliability-based design optimization Methodology (RBDO) for microelectronic devices structures.

2 PROBLEM DEFINITION

The device studied is the electronic package (wire bonding type) developed for engine environments but also have Venus planetary exploration applications in harsh environments (The temperature at the surface of venis is 450 °C). This device is of stack configuration. The silicon chips are soldered into insulating substrates typically made of a ceramic layer (Al2O3 or AIN) sandwiched between two thin copper layers, and the entire assembly of the die and the direct copper bonded (DCB) is soldered to a copper base plate. Gold wire bonds and the bus bars interconnect the die, substrate and module terminals. Schematic drawings of the module construction are given in Fig.1.

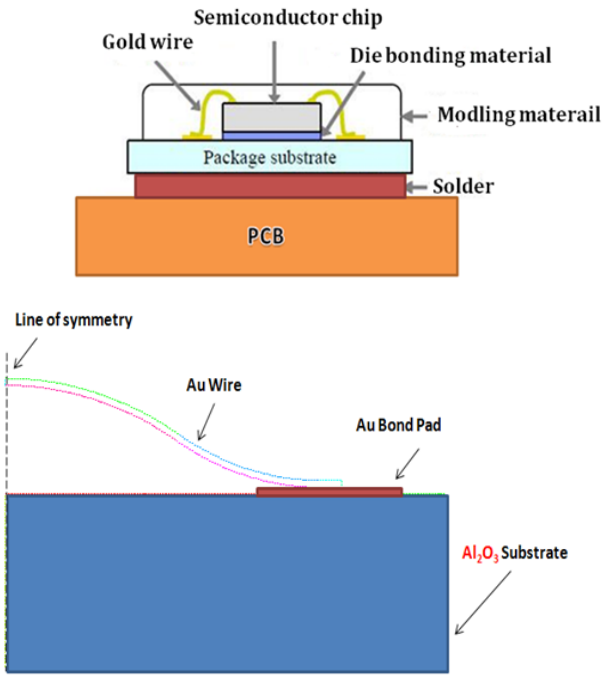

Fig.1. Structure of the electronic package (wire bonding type)

For high temperature electronics and sensors, the temperature range to which the devices are exposed to be much wider compared with that for conventional electronics. Thus the thermo-mechanical properties of the devices in particular those of wirebonds are critically important to the reliability of chip-level electrical interconnection systems because the devices are subject to a very

wide temperature variation. The thermo-mechanical stress in wirebonds due to the differences in material properties of wirebonds, especially, coefficient of thermal expansion (CTE) mismatch between the metal wire, bond pads, chip and substrate materials may cause degradation and failure of wirebonds. The most common failure mode of wirebonds is delamination/cracking at wire/bond-pad and bond-pad/chip (or substrate) interfaces. The failure of wirebonds may cause open and shorted circuits. The performance of these structures also depends on the design; they may be more sensitive to random variations in material and load uncertainties. Hence, the objective of this work is to develop a reliability-based design and optimization methodology to improve the performance and reliability of power device. To demonstrate the methodology, results are shown for a wire wedge bond, but the methodology is generally applicable to other structures. The failure of the system is modeled by a functional relation G(X), called limit state function, this function can either be implicit (e.g., the outcome of a numerical FEM code), or explicit (e.g., an approximate equation obtained using the response surface method). The limit between the state of failure G(X) <0 and the state of safety G(X)>0 is known as the limit state surface G(X) = 0. Given this formulation, the reliability design optimization problem of the wire bonding interconnection can be written as:

Find $X_d = [x_{d1}, x_{d2}, \ldots, x_{dn}]$ and $X_r = [x_{r1}, x_{r2}, \ldots, x_{rn}]$

Such that to minimize $P_f = P_f[G(X_d, X_r) \leq 0]$

Subjected to $\cos t(X_d) \leq C_0$; $X^{lb} \leq X \leq X^{ub}$

Were C_0 is the allowable cost, which is a function of a vector of design variable X_d, Pr [.] is the probability operator and is the failure probability corresponding to the performance function G.

In this problem, the designer is to find the design, X_d that minimizes the probability of system failure of wire bonding under the cost constraint corresponding to the structural volume. Such a problem requires a very high computation cost, which is mainly due to the calculation of gradients, especially when a finite element model is used. To solve this problem the concept of response surface methodology combined to the sensitivity analysis give a useful tool to establish an approximate explicit functional relationship between input variables and output response through regression analysis for the range of expected variation in the input parameters. The calculation of the reliability index is carried out in the normalized space (U) (see Fig.2):

1 Input the initial values of the variable vector u of the studied model,

2 Evaluate the objective function d(U),

3 Calculate the limit state constraint $H(U) \leq 0$,

4 Test the convergence constraint $H(U) \leq 0$, if not converged, update u and go to step 2, else, converged, stop.

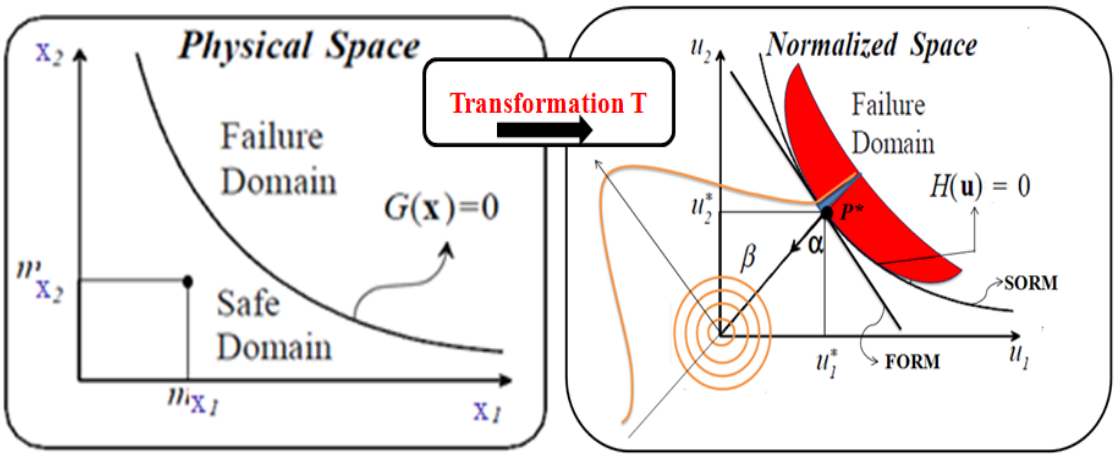

Fig.2. Physical and normalized spaces

CONCLUSION

In this study, a probabilistic approach combined to a nonlinear thermo-mechanical finite element analysis is used to predict the reliability of the bonding wire of an electronic power module. The F.E. model developed in this paper is used to investigate the reliability of the wire bonding by considering the thermo-mechanical coupling effects within a power chip and its environment. The 2D FE model takes into account the bonding wires and the material nonlinearity properties of plastic behavior of the wire bonds.

This study reveals the interest to use the reliability analysis to predict the effects of the delamination and the wire-bonding lift-off of the microelectronic devices. The uncertainties related to geometrical dimensions and to the material properties such as Young's modulus, can lead to mechanical failure. The probabilistic approach can be used to ensure more design robustness. Furthermore, the use of reliability based design optimization model reduces the structural weight in uncritical regions. It does not only provide an improved design but also a higher level of confidence in the design.

REFERENCES

[1] EL HAMI, PH. POUGNET, Embedded Mechatronic Systems - Volume 1: Analyse of failures, prédictive reliability, (237 pages) ISTE, ELSEVIER, ISBEN: 9781785480133, London, june 2015

[2] EL HAMI, PH. POUGNET, Embedded Mechatronic Systems - Volume 2: Analyse of failures, Modeling, Simulation, optimization (247pages) ISTE, ELSEVIER,ISBEN:9781785480140, London, june 2015

[3] S.KADRY, A. EL HAMI, Numerical Methods for Reliability and Safety Assessment Multiscale and Multiphysics Systems, Springer, (805 pages), ISBN 978-3-319- 07166-4. New York and London 2015.

[4] EL HAMI, PH. POUGNET,Les systèmes mécatroniques embarqués,Volume1:Analyse des causes de défaillances, Fiabilité et contraintes, ISBN 978-1-78405-057-3, 230 pages, ISTE, London, mars 2015.

[5] EL HAMI, PH. POUGNET, Les systèmes mécatroniques embarqués Volume2: Analyse des causes de défaillances, Modélisation, simulation et optimisation, ISBN 978-1-78405-057-3, (270 pages) ISTE, London mars 2015

[6] EL HAMI, B. RADI, Incertitude, Optimisation et Fiabilité des Structures, Hermes- Lavoisier, ISBN : 9782746245167, 400 pages. Paris, 2013

[7] EL HAMI, B. RADI, Uncertainty and Optimization in Structural Mechanics, WILEY/ISTE, ISBN : 978-1-84821-517-7, 144 pages. New York & Londre, 2013

Thermal modeling of high power transistor HEMT

A. AMAR[1], A. EL HAMI[2] and B. RADI[3]
[1]LLaboratory of Mechanics of Normandy LMN
INSA Rouen, France,
Engineering, Industrial Management and Innovation Laboratory (IM2I)
FST SETTAT, Morocco
Email: abdelhamid.amar@insa-rouen.fr
[2] Laboratory of Mechanics of Normandy LMN
INSA Rouen, France
Email: abdelkhalak.elhami@insa-rouen.fr
[3] Engineering, Industrial Management and Innovation Laboratory (IM2I)
FST SETTAT, Morocco
Email: bouchaib.radi@yahoo.fr

ABSTRACT

Among the very important components in these systems is the transistor. There is an electronic element that has created a revolution in the design and development of such systems by controlling, amplifying and lowering signals. When we talk about the most developed systems such as airborne systems, we find that most of its failures come from its high-power amplifiers (HPAs). According to various studies, a large percentage of these failures are due to high-power transistors, including gate burial, degradation of ohmic contacts, deformation of the AlGaN layer... these failures have a relationship with the operating temperature that exceeds critical values by heating the transistors. So the operating temperature has a great influence on the performance of the latter. In this work, we will propose a very realistic thermal model of the transistor under conditions similar to those of the operating environment, then we will use the finite element method with COMSOL software to perform numerical simulation to observe the temperature distribution over the entire structure. In the following we will start a study of thermomechanical behavior thanks to the combination of thermal and mechanical study.

1 INTRODUCTION

The robust design of mechatronic systems is a very important technical issue, whose failures that occurred during the first manufacturing versions before the manufacture of the new versions must be

taken into account, in this context digital simulation does not allow to observe and have much information on these failures, using the finite element method, with software such as ANSYS and COMSOL. With all these tools we can interpret the behavior and operation of the systems and detect failures as early as the design phase before reaching the manufacturing stage, we undergo our system under all conditions of use and environment.

2 HIGH POWER TRANSISTORS HEMT

The HEMT transistor appears to be a major evolution of the MESFET. The difference is that the HEMT uses a heterojunction, i. e. a junction between materials having different energy bands, so that the electrons constituting the drain-source current in a non-doped semiconductor, in order to reduce the time of transit and thus increase frequency performance. The electron velocity is in effect is even greater when the doping of the semiconductor is low, because the dispersion of ionized impurities is reduced [1] [3].

3 THERMAL MODELING OF HEMT TRANSISTOR

3.1 Thermal transfer to one's own of a HEMT

The energy dissipated in the active transistor zone, in the form of heat flux, can be transferred and evacuated to the external environment through different mechanisms of conduction, convection and radiation[2].

- Conduction: Thermal conduction refers to the heating and propagation of heat in a body, without the displacement of matter. It is caused by the oscillations of the atoms, proportional to the temperature gradient and the coefficient characterizing the thermal conductivity of the material. The elementary vectors of heat transfer are phonons and free electrons. The heat flow is linked to the temperature gradient by Fourier's law.

$$\vec{\varphi} = -K_{TH}\, A\, \overrightarrow{grad}(T) \tag{1}$$

With K_{TH} thermal conductivity [W/m/K]
and A the exchange surface in m^2

R. Meanddru et al presented a thermal transfer study in the HEMT transistor, for temperatures above ambient temperature, we observe that the contribution of radiation and convection is about 1.5% compared to the contribution of conduction. This is why we neglected heat transfer by radiation and even by convection in the rest of our study[3].

3.2- construction of a thermal model

To ensure the reliability of mechatronic systems through the reliability of transistors, it is necessary to build a thermal model specific to this component, which resembles reality. This will allow to control its thermal behavior and observe any temperature variation according to the chosen parameters, the power dissipated, the reference temperature…

3.2.1- Thermal properties of materials

The construction of a thermal model of the transistor requires the definition of the thermal properties (thermal conductivity and mass thermal capacity) of the different materials represented in this model. There are many articles giving values, which depend in particular in the case of GaN on the crystalline

quality of the material [4]. In our models, we have taken values from the literature [5] and previous work [6] [1].

3.2.2- Boundary conditions

To carry out a thermal simulation requires the definition of the conditions to the limits to be imposed on our system, in this case we have two which are very important:

- The reference temperature
- The dissipated power

4-DIGITAL SIMULATION OF THERMAL EXCHANGES

The purpose of this simulation is to know the influence of the different parameters including the dissipated power, the reference temperature, on the operating temperature of the transistor.

4.1- Influence of the reference temperature:

To quantify the influence of this effect on the component operating temperature, we performed several thermal simulations on our model, at different TRéf reference temperatures, at the grids in the center and periphery of the transistor.

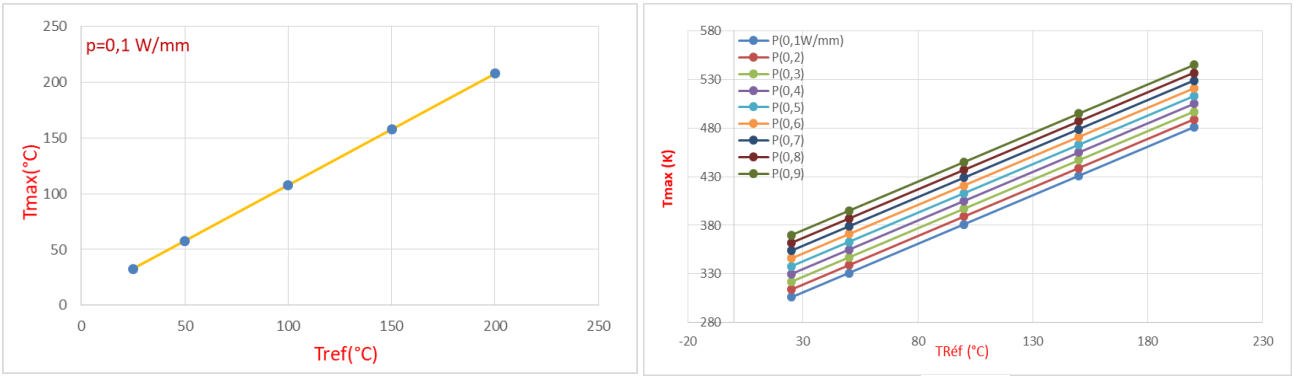

(a) (b)

Figure 3: Tref influnec on Tmax for a dissipated power of 0.1W/mm (a), Tref influence on Tmax for different dissipated powers(b)

The figure shows the variation of the maximum temperature as a function of the operating temperature, with a fixed dissipation power of 0.1W/mm, it can be clearly seen that the component temperature increases with the Tref variation.
To observe this influence, the figure shows the component temperature variation as a function of the reference temperature for the different values of the dissipated power.
From this figure, it is clear that the reference temperature influences the operating temperature of the transistor, even in the different values of the dissipated power.

4.2-Influence of the dissipated power:

In order to observe the influence of this effect on the component operating temperature, we carried out several thermal simulations on our model, at different values of the dissipated power, at the level of the grids in the middle and periphery of the transistor

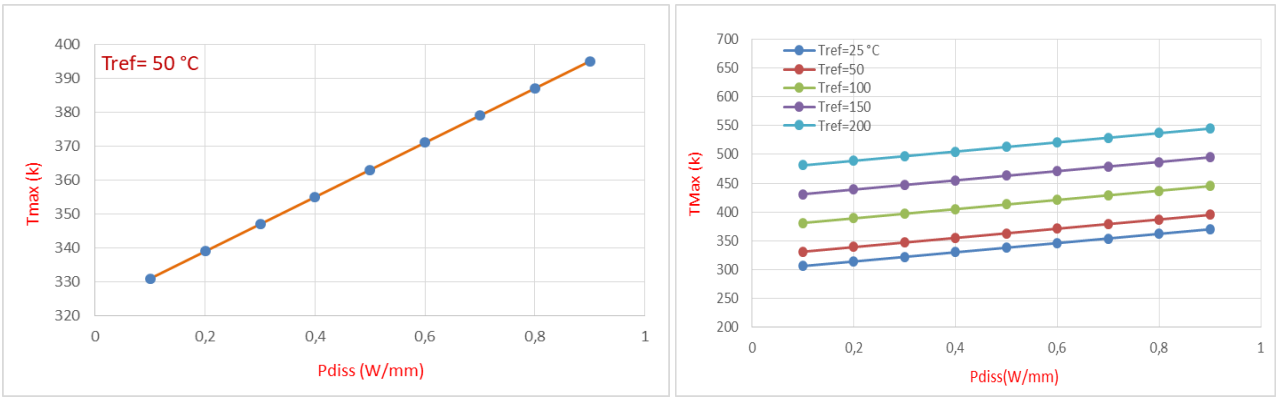

(a) (b)

Figure 5: influence of dissipated power on Tmax for a Tref of 50°C(a), influence of dissipated power on Tmax for the different Tref values(b)

In order to observe the influence of this effect on the component operating temperature, we carried out several thermal simulations on our model, at different values of the reference temperature, at the level of the grids at the middle and periphery of the transistor.
From this figure it is clear that the maximum transistor temperature increases with the variation of the dissipated power and the different values of the reference temperature.

CONCLUSION

In this paper we have done a thermal modeling of the high power transistor which is one of the essential components in a mechatronic system. It allowed to observe the influence of the dissipated power and the reference temperature on the maximum transistor operating temperature using the finite element model solved by the COMSOL software.
In order to ensure a robust manufacture of high-power transistors, i. e. mechatronic systems, it is necessary to carry out a study to optimize the dissipated power, it is necessary to study other types of failures from other origins.

REFERENCES

[1] J.-C. Jacquet *et al.*, "Analytical transport model of AlGaN/GaN HEMT based on electrical and thermal measurement."
[2] O. Jardel *et al.*, "InAlN/GaN HEMTs based L-band high-power packaged amplifiers," *Int. J. Microw. Wirel. Technol.*, vol. 6, no. 6, pp. 565–572, Dec. 2014.
[3] R. Mehandru *et al.*, "Thermal simulations of high power , bulk GaN rectifiers," vol. 47, pp. 1037–1043, 2003.
[4] J. Zou, D. Kotchetkov, A. A. Balandin, D. I. Florescu, and F. H. Pollak, "Thermal conductivity of GaN films: Effects of impurities and dislocations," *J. Appl. Phys.*, vol. 92, no. 5, pp. 2534–2539, Sep. 2002.
[5] R. S. Pengelly, S. M. Wood, J. W. Milligan, S. T. Sheppard, and W. L. Pribble, "A review of GaN on SiC high electron-mobility power transistors and MMICs," *IEEE Transactions on Microwave Theory and Techniques*, vol. 60, no. 6 PART 2. pp. 1764–1783, 2012.
[6] A. Sarua *et al.*, "Thermal boundary resistance between GaN and substrate in AlGaN/GaN electronic devices," *IEEE Trans. Electron Devices*, vol. 54, no. 12, pp. 3152–3158, Dec. 2007.

PASSIVE NOISE CONTROL ORIENTED DESIGN OF AIRCRAFT HEADRESTS

V. Giannella[1], R. Citarella[1], M. Barbarino[2], P. Vitiello[2], D. Bianco[2], G. Petrone[3]

[1] Department of Industrial Engineering
University of Salerno, Fisciano (SA), 84084, ITALY
Email: vgiannella@unisa.it, rcitarella@unisa.it

[2] Italian Aerospace Research Centre (C.I.R.A.)
via Maiorise snc, 81043 Capua, ITALY
Email: , m.barbarino@cira.it, p.vitiello@cira.it, d.bianco@cira.it

[3] Università degli Studi di Napoli Federico II
via Claudio 21, 80125 Napoli, ITALY
Email: giuseppe.petrone@unina.it

ABSTRACT

Two Passive Noise Control (PNC) concepts were numerically evaluated in terms of their impact on the Sound Pressure Level (SPL) perceived by passengers of an aircraft flight.
A concept was based on the shape optimization of the headrests, whereas the second one was based on the adoption of a high absorbing material, i.e. a nanofiber textile, to improve the acoustic performances of the headrests.
To this aim, an aircraft seat was modelled with the Boundary Element Method (BEM) and loaded with a spherical distribution of monopole sources surrounding the seat. Different configurations of headrest shape and covering textiles were then compared in terms of the SPL calculated at passengers' ears.
The work shows how an acoustic-oriented design of the aircraft headrests could achieve an average SPL reduction for passengers up to 3 dBA.

1 INTRODUCTION

This work presents the development of two Passive Noise Control (PNC) concepts aiming at improving the acoustic comfort inside an aircraft cabin via numerical simulation. A concept is based on the shape optimization of the seats' headrests to reduce the Sound Pressure Level (SPL) perceived by passengers. The second concept is based on the adoption of a high absorbing materials, i.e. nanofibrous textiles, to improve the absorbing performances of the headrests, thus in turn reducing the perceived SPL.

To simplify the Design of Experiment (DoE), the current numerical simulations were performed considering the turbulent boundary layer aero-acoustic load as the unique noise contributor. The related data was available from [1] and has been here adopted as acoustic load applied around a single aircraft seat modelled with the Boundary Element Method (BEM). Such BEM model was then used to evaluate different configurations of headrest shapes and headrest covering textiles, i.e. a nanofiber textile [2-3], in terms of their acoustic performances.

Application of the BEM to problems in solids and structures can be found in [4-5] whereas some applications in aeronautic and railway fields can be found in [6-7]. In particular, in [6] a FEM-BEM modelling technique was used to predict the vibro-acoustic response of an aircraft fuselage, whereas BEM was used in [7] for the acoustic scattering of large and complex aircraft.

2 NUMERICAL ANALYSES

The starting CAD model of two aircraft seats adopted for the acoustic assessments o is shown in Fig. 1a. Such CAD model was imported in VA One [8] and a simplified BEM model was created, see Fig. 1b. Preliminary BEM analyses were aimed at reducing the size of the BEM model to handle and the resulting BEM modelling is here presented. Such "baseline" model comprised only one seat with cushion, backrest and headrest; the whole supporting structure did not give any appreciable contribute to the SPL calculated at passengers' ears height, therefore its modelling was neglected.

The final BEM model comprised nearly 7000 linear boundary elements with an average size equal to 14 mm, thus 6 elements per wavelength were used at maximum frequency of 4 kHz. The BEM fluid was air with bulk modulus equal to 142,4 kPa and mass density equal to 1,21 kg/m^3.

Two different shapes for the headrest were considered on such baseline model (Fig. 2); such shapes were representative of the smallest and largest headrest that were envisaged for such a headrest shape optimization process. Moreover, various combinations of headrest shapes as well as headrest covering textiles were considered as part of the design of experiment. For all the simulations, the same data recovery surfaces (Figs. 1-2) were considered as the areas on which the SPLs were output. Such SPLs were then compared among the various configurations allowing to realize how much the impact of both, geometry and fabric, would be on the passengers' perceived noise.

The headrest was considered as covered by different textiles: a traditional one, termed "reference", and two new-generation nanofibrous textiles [2-3], whereas the backrest and cushion were covered with the reference textile for all the analyses. The related absorbing coefficients are shown in Fig. 2c. All the material data were obtained experimentally using a Kundt's tube.

The BEM simulations were performed across a frequency domain of 200 ÷ 4000 Hz, with a 200 Hz constant bandwidth. All the analyses were based onto several uncorrelated monopole sources located at equal distance of 2 m from the centre of the backrest's surface. Such sources were positioned spherically, so as to reproduce a diffuse acoustic field surrounding the seats. All the monopoles were set up in such a way to generate a pressure distribution providing a SPL at the data recovery surfaces equal to that calculated by the full SEA modelling of the fuselage [1].

(a) (b)

Figure 1: (a) CAD model of two aircraft seats; (b) simplified BEM model of one seat surrounded by the monopole sources.

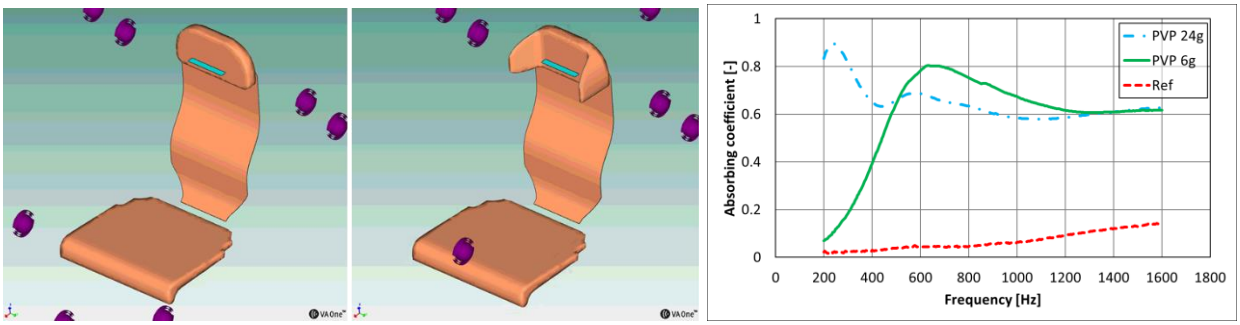

(a) (b) (c)

Figure 2: BEM model with headrest (a) without caps or (b) with caps; data recovery surfaces to output the SPLs shown in azure; (c) acoustic absorbing coefficient for textiles.

3 RESULTS

Results in terms of SPL were calculated on the data recovery surfaces (Figs. 1-2), so as to represent the average SPL that the passenger perceives as cabin interior noise. Fig. 3 shows the aforementioned SPL values for various configurations of headrest shape and headrest covering textile.

Such results demonstrated that using both, a headrest and an appropriate absorbing material, it was possible to reduce the SPL values perceived by the passengers. In particular, the usage of a headrest with lateral caps seemed to provide significant advantages only when used in combination with high absorbing covering textiles such as the here considered nanofibrous textiles.

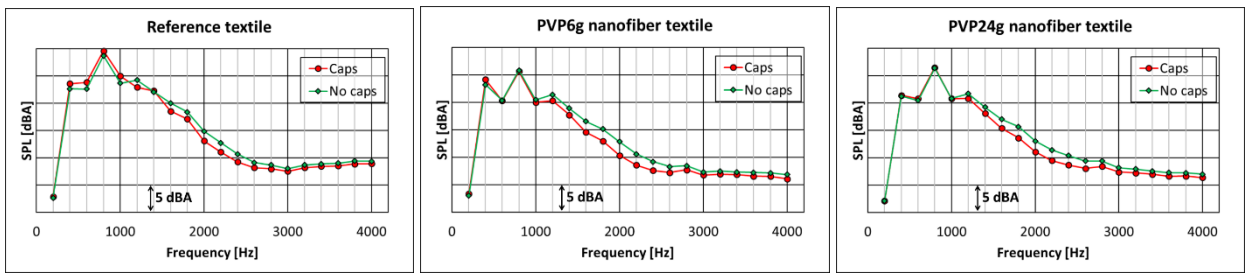

(a) (b) (c)

Figure 3. SPL [dBA] on the data recovery surfaces considering headrest with/without caps and surface impedance of: (a) reference textile, (b) PVP6g nanofiber textile, (c) PVP24g nanofiber textile

4 CONCLUSIONS

The two PNC concepts of headrest shape optimization and covering textiles demonstrated to be effective in lowering the noise perceived by the passengers inside the cabin of an aircraft turboprop.

The adoption of a headrest with lateral caps seemed to play a positive effect for all the frequencies higher than 1 kHz. The adoption of high absorbing materials, such as the nanofibrous textiles, turned out to be effective in lowering the SPL perceived by passengers.

It is worth noting that the adoption of the PVP24g nanofibrous textile allowed an interesting noise reduction (-1 dBA) even at frequency as low as 200 Hz, thus foreseeing the possibility to adopt PNC even at such low frequencies. At higher frequencies, the adoption of a nanofibrous textile allowed a reduction in SPL up to nearly 3 dBA. For high frequency, the adoption of PVP6g seemed to be the most effective since the it demonstrated to be the most performant and also lightweight textile.

5 ACKNOWLEDGEMENTS

The results have been mainly achieved in the framework of CASTLE – (CAbin Systems design Toward passenger welLbEing) Core Partnership of Clean Sky 2 Programme. CASTLE has received funding from the Clean Sky 2 Joint Undertaking under the European Union's Horizon 2020 research and innovation programme under grant agreement n° CS2-AIR-GAM-2014-2015-01. The contents of this paper reflect only the author's views and the Clean Sky 2 Joint Undertaking and the European Commission are not liable for any use that may be made of the information contained therein.

Authors thank Prof. Branda (University of Naples, Italy) for providing the nanofiber textiles.

REFERENCES

[1] Petrone G., Melillo G., Laudiero A., De Rosa S., "A Statistical Energy Analysis (SEA) model of a fuselage section for the prediction of the internal Sound Pressure Level (SPL) at cruise flight conditions", Aerospace Science and Technology, in press (2019)

[2] Avossa J., Branda F., Marulo F., Petrone G., Guido S., Tomaiuolo G., Costantini A., "Light Electrospun Polyvinylpyrrolidone Blanket for Low Frequencies Sound Absorption", Chinese Journal of Polymer Science, 36 (12), 1368-1374 (2018)

[3] Del Sorbo G.R., Truda G., Bifulco A., Passaro J., Petrone G., Vitolo B., Ausanio G., Vergara A., Marulo F., Branda F., "Non monotonous effects of noncovalently functionalized graphene addition on the structure and sound absorption properties of Polyvinylpyrrolidone (1300 kDa) electrospun mats", Materials, 12(1), 108 (2019)

[4] Becker A., "The Boundary Element Method in Engineering", McGraw-Hill, London (1992)

[5] Brebbia C.A., Telles J.C.F., Wrobel L.C., "Boundary Element Techniques", Springer-Verlag, Berlin (1984)

[6] Koukounian V.N., Mechefske C.K., "Computational modelling and experimental verification of the vibro-acoustic behavior of aircraft fuselage sections", Applied Acoustics, 132, pp. 8-18 (2018).

[7] Barbarino, M., Bianco, D., "A BEM-FMM approach applied to the combined convected Helmholtz integral formulation for the solution of aeroacoustic problems", Computer Methods in Applied Mechanics and Engineering", 342, 585-603 (2018)

[8] VA One, User's Guide (2017)

GEOMETRICALLY NON-LINEAR FREE VIBRATION OF RECTANGULAR PLATES SIMPLY SUPPORTED AT TWO OPPOSITE EDGES AND CONNECTED BY DISTRIBUTED TRANSLATIONAL AND ROTATIONAL SPRINGS AT THE TWO OTHER EDGES

Ahmed BABAHAMMOU[1], RHALI BENAMAR[1]

University Mohammed V in Rabat, E.M.I, BP 765, Rabat, Morocco
Email: ahmedbabahammou@gmail.com, rhali.benamar@gmail.com

ABSTRACT

A complementary study of the works available on geometrically non-linear rectangular plate vibrations is presented, corresponding to a new combination of edge conditions, involving edges elastically supported. In addition to its theoretical interest, this study may be of a crucial importance in experimental identification. A plate is simply supported (SS) at two opposite edges and connected by distributed translational and rotational springs (DTRS) at the two other edges is examined using trial functions defined as products of appropriate beam functions in the x and y directions. The general formulation of the non-linear problem, based on Hamiltons principle and spectral analysis, is presented, followed by a case study, leading to the backbone curves for plates having different combinations of stiffness.

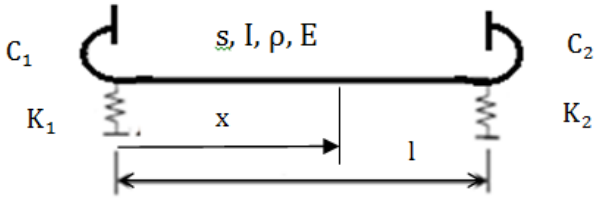

Figure 1: Beam connected by translational and rotational spring at ends x=0,l

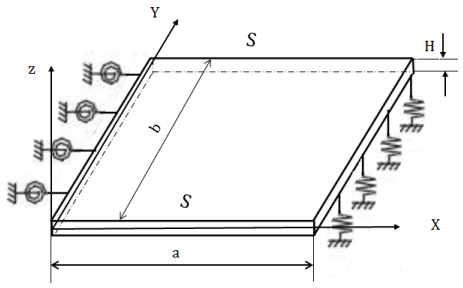

Figure 2: Plate connected by translational and rotational spring at edges x=0,a and SS at edges y=0,b

1 INTRODUCTION

The analysis of rectangular plate vibrations is a topic of a crucial importance in the structural design in many fields. In the linear case, analytical solutions exist only in the case of two opposite edges simply supported [1]. The other edge conditions, corresponding to free (F), simply supported (SS) and clamped (C) edges, are usually examined by the Rayleigh-Ritz method but yet many of the edge combinations have not been treated. In the non-linear regime, Benamars method has been applied to few combinations of boundary conditions ([2],[3]). A complementary work is presented here, corresponding to non-linear vibrations and a new combination of edge conditions, namely a plate SS at two opposite edges and connected by distributed translational and rotational springs (DTRS) at the two other edges. The mode shapes of beams attached to elastic supports are first determined in order to be used in building the corresponding plate trial functions, defined as products of beam functions in the x and y directions. The general formulation of the non-linear problem and a case study are then presented. The backbone curves are given for plates having different combinations of stiffness and aspect ratios.

2 LINEAR ANALYSIS OF BEAMS ATTACHED TO ELASTIC SUPPORTS AT THE TWO ENDS.

Consider the beam shown in Figure 1 attached at the two ends x=0 and x=a to two translational springs of stiffness K_1 and K_2, and two rotational springs of stiffness C_1 and C_2. If $\mathbf{w}(x,t)$ denotes the transverse deflection the beam shown in Figure 1, the beam vibration is governed by [4]:

$$\frac{d^4\mathbf{w}}{dx^4} + .\beta.\mathbf{w} = 0 \qquad \text{In witch} \qquad \beta^4 = \omega^2 \frac{\rho.S}{E.I} \tag{1}$$

The general solution of Equation 1 can be written as [5]:

$$W_i(x) = C_1 \sin(\beta_i.x) + C_2.\cos(\beta_i.x) + C_3.\sinh(\beta_i.x) + C_4 \cosh(\beta_i.x) \tag{2}$$

The $\beta_i's$ are frequency parameters depending on the beam end conditions, to be determined with C_1 to C_4 by setting the system determinant equal to zero. The symbolic calculation and fzero command in Maltlab was used to solve the transcendental equation giving the elastically supported beam parameters $\beta_i.l^2$

3 LINEAR VIBRATION OF PLATES WITH ELASTIC RESTRAINTS ALONG TWO OPPOSITE EDGES

Consider linear free vibrations of the plate shown in Figure 2 (for clarity, only the rotational and linear springs are shown here at x=0 and x=a respectively). If the time and space functions are supposed to be separable and harmonic motion is assumed, the transverse displacement can be written as:

$$\mathbf{W}(x,y,t) = w(x,y).\sin(\omega.t) \qquad \text{where} \qquad w(x,y) = \sum_{k=1}^{N} a_k.w_k(x,y) \tag{3}$$

The kinetic energy of the plate can be expressed as [2]:

$$T = \frac{1}{2}.\rho.H.\int_S \left(\frac{\partial w}{\partial t}\right)^2 dxdy \tag{4}$$

If one put $D = \dfrac{E.H^3}{12.(1-\nu^2)}$ the bending stiffness, H plate thickness and ν Poisson's ratio so the plate strain energy is the sum of the energy due to the bending V_b [5] and the energy stored in the elastic edge restraints V_{edg} [6]:

$$V_b = \frac{D}{2}\int_S \left(\frac{\partial^2 w}{\partial x^2} + \frac{\partial^2 w}{\partial y^2}\right)^2 + 2.(1-\nu).\left(\left(\frac{\partial^2 w}{\partial x \partial y}\right)^2 - \frac{\partial^2 w}{\partial x^2}.\frac{\partial^2 w}{\partial y^2}\right) dS \tag{5}$$

$$V_{edg} = \frac{1}{2}\int_0^b \left(K_1.w^2 + C_1\left(\frac{\partial w}{\partial x}\right)^2\right)_{x=0} dy + \frac{1}{2}.\int_0^b \left(K_2.w^2 + C_2.\left(\frac{\partial w}{\partial x}\right)^2\right)_{x=a} dy \tag{6}$$

The basic plate functions (Equation (3)) are constructed as [6] $w_k(x,y) = P_I(x).Q_J(y)$, with $P_I(x)$ and $Q_J(y)$ being the beam functions presented in section 2. $k = n.(I-1) + J$, where n is the number of beam functions used. After discretization, and by applying Hamilton's principle, the plate vibration is governed by the following linear equation [2]:

$$2.[K].\{A\} - 2.\omega^2.[M].\{A\} = \{0\} \tag{7}$$

$\{A\}$ is the column vector of the basic function contribution coefficients, K,M are the rigidity and mass matrices, well known in linear theory. The fundamental frequencies $\Omega = \omega.a^2\sqrt{\dfrac{\rho H}{D}}$ of rectangular plate, simply supported in y-direction, clamped at $x = 0$ and elastically restrained at $x = a$ (CSES), are shown in Table (1) for various combinations of the spring stiffnesses $K^* = \dfrac{a^3 K_2}{D}$ and $C^* = \dfrac{aC_2}{D}$.

C^*	$K^*=0$		$K^*=100$		$K^*=\infty$	
	a	b	a	b	a	b
0	12.74	12.69	19.24	19.22	23.65	23.65
10	13.44	13.41	19.41	19.40	26.56	26.56
100	13.66	13.65	19.48	19.48	28.56	28.55
∞	13.69	13.69	19.49	19.49	28.96	28.95

Table 1: Frequency parameter of CSES a square plate (a) present results, (b) results given by Ref [6].

4 NON-LINEAR VIBRATION OF A RECTANGULAR PLATE ATTACHED TO ELASTIC SUPPORTS

The membrane strain energy V_m of the plate supposed now to exhibit non-linear vibrations is given by [6]:

$$V_m = \frac{3D}{2H^2}\int_S \left[\left(\frac{\partial W}{\partial x}\right)^2 + \left(\frac{\partial W}{\partial y}\right)^2\right]^2 dS \tag{8}$$

Equation (7) becomes:

$$2.[K].\{A\} + 3.[B\{A\}].\{A\} - 2.\omega^2.[M].\{A\} = \{0\} \tag{9}$$

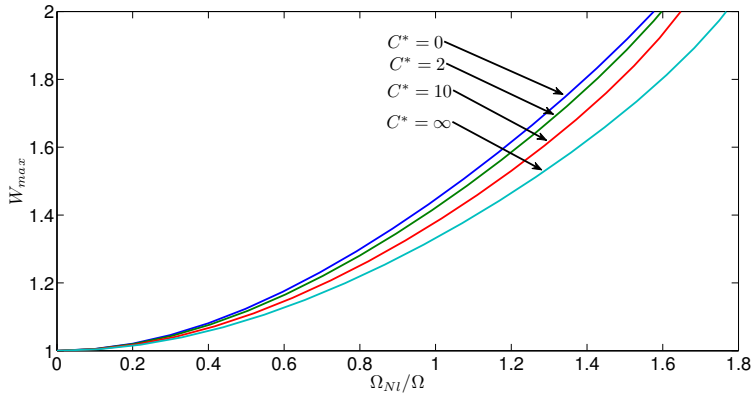

Figure 3: Backbone curve of a simply supported plate at all edges in addition to rotational spring at edges $x = 0, a$ with various stifnesses C^*.

$B\{A\}$ is the non-linear geometrical rigidity. Equation (9) is Benamars adaptation of the Rayleigh-Ritz method to the nonlinear problem, to be solved numerically or explicitly. Pre-multiplying the two hand sides of Equation (9) by $\{A\}^T$ and using the single mode approach (SMA) one obtain [3]:

$$\Omega_{Nl} = \frac{K_{11}}{M_{11}} + a^2 \frac{3}{2} \frac{B_{1111}}{M_{11}} \tag{10}$$

In which K_{11}, M_{11}, B_{1111} correspond to the single mode parameters used in the SMA formulation. Figure 3 gives the various backbone curves corresponding to various values of rotational spring stiffness at the edges $x = 0$ and $x = a$ for SSSS rectangular plate.

5 CONCLUSION

Benamar's method has been successfully applied to examine in the geometrically non-linear free vibration of rectangular plates simply supported at two opposite edges and attached to distributed translational and rotational springs at the two other edges. Analytical details have been given and the numerical results were compared to those available in literature. The backbone curves are presented for plates having different combinations of stiffness and aspect ratios giving quantitatively the expected hardening type of non-linearity.

REFERENCES

[1] Arthur W Leissa. The free vibration of rectangular plates. *Journal of sound and vibration*, 31(3):257–293, 1973.

[2] R Benamar, M Bennouna, and RG White. The effects of large vibration amplitudes on the mode shapes and natural frequencies of thin elastic structures, part ii: fully clamped rectangular isotropic plates. *Journal of sound and vibration*, 164(2):295–316, 1993.

[3] M El Kadiri and R Benamar. Improvement of the semi-analytical method, for determining the geometrically non-linear response of thin straight structures: Part ii first and second non-linear mode shapes of fully clamped rectangular plates. *Journal of sound and vibration*, 257(1):19–62, 2002.

[4] AK Igor. Olga, l. l. 2001, formulas structural dynamics.

[5] Z Beidouri, R Benamar, and M El Kadiri. Geometrically non-linear transverse vibrations of c–s–s–s and c–s–c–s rectangular plates. *International Journal of Non-Linear Mechanics*, 41(1):57–77, 2006.

[6] WL Li and M Daniels. A fourier series method for the vibrations of elastically restrained plates arbitrarily loaded with springs and masses. *Journal of Sound Vibration*, 252:768–781, 2002.

IMPROVED WAVE DISPERSION PROPERTIES IN A PERIDYNAMIC BAR

R. Alebrahim[1], U. Galvanetto[1], P. Packo[2] and M. Zaccariotto[1*]

[1]Industrial Engineering Department, University of Padova, v. Venezia 1, Padova 35131, ITALY
Email: Reza.Alebrahim@unipd.it, mirco.zaccariotto@unipd.it, ugo.galvanetto@unipd.it

[2]Department of Robotics and Mechatronics, AGH – University of Science and Technology, Krakow, POLAND
Email: pawel.packo@agh.edu.pl

ABSTRACT

In this study wave propagation in a Peridynamics (PD) bar is investigated. Initially, dispersion properties of the one-dimensional bond-based PD model are computed. Its dispersion characteristic is optimized through minimizing the error between the exact and the numerical solution. A weighted residual technique is employed and the weighting coefficient corresponding to every bond is then defined. The proposed method is able to significantly improve the description of wave dispersion phenomena in the 1-D PD model.

1 INTRODUCTION

Peridynamics has been intensively developed over the last two decades. This theory was initially proposed by Silling [1] to study crack propagation problems in solid bodies. Peridynamics has been found successful in modelling static and quasi-static problems [2] and it has recently been applied to simulate wave propagation phenomena [3]. The comparison of wave dispersion in discrete and continuum systems modelled using PD was addressed in [4], where a method to modify wave dispersion in bond-based (BB) discrete systems at low frequencies is introduced. Detailed analysis of wave dispersion in nonlocal models in 1-D and 2-D framework was presented in [5]. It was clearly shown that the BB Peridynamics shows dynamically softening behaviour.

This study is focused on the improvement of wave dispersion in a one-dimensional bond-based PD model. Galerkin method is employed and the correction factor of each bond is computed. Results are compared and verified against the exact solution.

2 NUMERICAL DISPERSION IN BOND BASED PERIDYNAMIC BAR

For analysing dispersion in Peridynamics we start with the equation of motion [1] of a 1-D discretized bar with nonlocal interactions as shown in Figure (1).

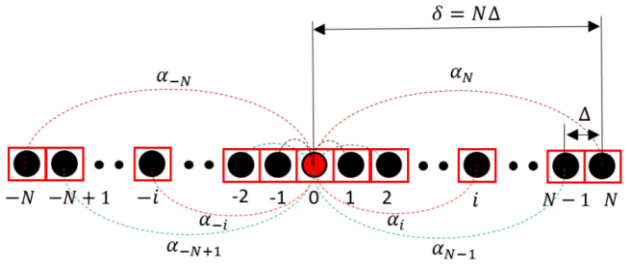

Figure 1. Numbering of the family nodes of a source node inside its horizon, dashed line represents the bond between nodes.

$$\rho u_{0,tt} = \frac{2E}{\delta^2}\sum_{i=-N}^{+N}\frac{1}{|i|}\alpha_i(u_i - u_0) \tag{1}$$

2N is the number of the family nodes within the horizon radius δ, $\delta = N\Delta$ is the horizon radius, Δ is the grid spacing, ρ is the density of the material and E is the Young's modulus. u_i in Equation (1) represents the displacement of i^{th} node and α_i is the correction factor of i^{th} bond (see Figure 1). After discretization in time, Equation (1) can be used to compute displacements in subsequent time steps for a 1-D infinite domain. Wave propagation characteristics are found from Equation (1) assuming a single, unit amplitude, wave solution for a linear, homogeneous, isotropic medium of the form $u_n(n\Delta, t) = e^{ikn\Delta}e^{-i\omega t}$. For a regular grid of nodes, the following phase relation holds between any family node and the considered central node n

$$u_{n\pm i} = u_n e^{\pm \mathrm{i}ki\Delta}, \tag{2}$$

considering Equation (2) and after doing some manipulations, Equation (1) becomes

$$\left\{\frac{2E}{\Delta^2 N^2}\sum_{i=-N}^{+N}\frac{1}{|i|}\alpha_i(1 - e^{\mathrm{i}ki\Delta}) - \omega^2\rho\right\}u_0 = 0, \tag{3}$$

with the non-trivial solution for the quantity in brackets $\{\cdot\} = 0$, yielding the dispersion relation for a 1-D peridynamic bar

$$\omega^2 = \frac{4E}{\rho\Delta^2 N^2}\sum_{i=1}^{N}\alpha_i\frac{1-\cos(ki\Delta)}{i}. \tag{4}$$

2.1 Modified optimal 1-D BB-PD model

The Galerkin method is applied to find the unknown weight coefficients $\boldsymbol{\alpha}$ in Equation (4)

$$\int_0^{\frac{\pi}{\Delta}}\bar{\bar{\boldsymbol{K}}}R\,dk = \int_0^{\frac{\pi}{\Delta}}\bar{\bar{\boldsymbol{K}}}(\bar{\boldsymbol{K}}^T\boldsymbol{\alpha} - k^2)dk = 0, \tag{5}$$

where $\bar{\boldsymbol{K}}$, $\bar{\bar{\boldsymbol{K}}}$ and $\boldsymbol{\alpha}$ are defined as follows

$$\bar{\boldsymbol{K}} = \frac{4}{\Delta^2 N^2}\left[\frac{1-\cos(k\Delta)}{1}, \frac{1-\cos(2k\Delta)}{2}, \dots, \frac{1-\cos(Nk\Delta)}{N}\right]^T, \tag{6}$$

$$\bar{\bar{\boldsymbol{K}}} = \frac{4}{\Delta^2 N^2}\left[\frac{1-\cos(k\Delta)}{1}, \frac{1-\cos(2k\Delta)}{2}, \dots, \frac{1-\cos((N-1)k\Delta)}{N-1}\right]^T, \tag{7}$$

$$\boldsymbol{\alpha} = [\alpha_1, \alpha_2, \dots, \alpha_N]^T, \tag{8}$$

the problem formulated in Equation (4) consists of N unknowns $\boldsymbol{\alpha}$. Therefore, N equations must be constructed to uniquely solve the problem. According to Equations (5-8), it can be found that

the statement $\bar{\bar{\boldsymbol{K}}}(\bar{\boldsymbol{K}}^{\boldsymbol{T}}\boldsymbol{\alpha} - k^2)$ in Equation (5) provides $N-1$ independent equations. Thus, an additional equation is required to find all unknown weight coefficients. It should be noted that Equation (5) should satisfy two physically-motivated conditions, i.e. zero static error (i.e. for $\omega = k = 0$) and correct group velocity at $\omega \to 0$ and $k \to 0$. Hence, one more constraint may be imposed on the parameters $\boldsymbol{\alpha}$ to enforce correct solution at long wavelength limit. Recalling Equation (4) for dispersion at long wavelength limit, yields

$$\omega^2 = \frac{4E}{\rho N^2}\sum_{i=1}^{N}\alpha_i\frac{1-\cos(ki\Delta)}{i\Delta^2} = V^2k^2\frac{2}{N^2}\sum_{i=1}^{N}i\alpha_i\,, \tag{9}$$

the group velocity condition at $k \to 0$ then requires that

$$\sum_{i=1}^{N}i\alpha_i = \frac{N^2}{2} \text{ or } \mathbf{i}^T\boldsymbol{\alpha} = \frac{N^2}{2}, \quad \mathbf{i} = [1, 2, \dots, N]^T \tag{10}$$

Equation (10) provides an additional equation to the set defined in Equation (5).

3 RESULTS AND DISCUSSION

3.1 Optimal BB-PD model for *N=1&2*

Assuming *N = 1*, i.e. only the closest neighbors are included in the horizon, there is a single weighting parameter α_1. Following Equation (10) we have α_1 = 1/2. Using the dispersion relation of Equation (9), $\omega^2 = 2\alpha_1V^2k^2 = V^2k^2$ which perfectly agrees with the group velocity at the long wavelength limit. Including second neighbors, i.e. *N = 2*, yields two weighting parameters α_1 and α_2. From (10) we have the group velocity constraint $\alpha_1 = 2(1-\alpha_2)$. Using Equation (5), one will obtain $\alpha_1 = 3.72$ and $\alpha_2 = -0.86$. Numerical study for optimal BB-PD $N \in \{1, 2\}$ are introduced and validated in Figures (2(a) and 2(b)). It can be observed that there is a good fit between dynamic transient simulation and exact solution.

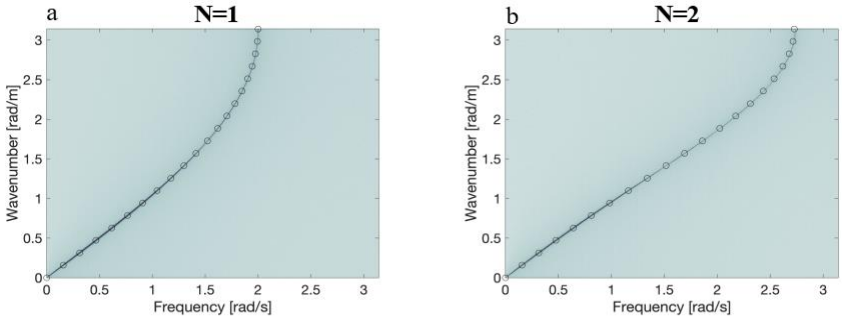

Figure 2: Comparison of the solution obtained using Equation (4) (black markers) to numerical dispersion (grey colormaps) in the modified BB-PD. Model parameters: Δ *=1, E =1,* ρ *=1,* Δt *=0.1*

3.2 Optimal BB-PD model for *N≥3*

Optimal dispersion properties of 1-D PD for $N \geq 3$ is computed. Exact, modified and original wave dispersion curves for *N=5* are drawn in Figure (3). It can be seen that through employing Galerkin method wave dispersion improves significantly. Increasing the N value to 10, more accurate results can be achieved. The weighting coefficients of the PD bonds for $N \in \{3, 5, 10\}$ are tabulated in Table 1. As pointed out in [6] negative weighting coefficients can lead to some difficulties using standard bond-breakage methods to simulate damage propagation.

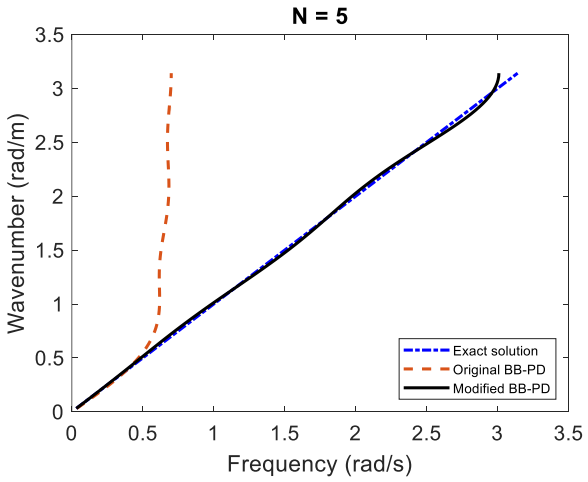

Figure 3. Comparison of wave dispersion, *N=5*.

N	3	5	10
α_1	9.08	25.03	99.99
α_2	-4.34	12.44	-50.01
α_3	1.37	8.42	33.31
α_4	-	-6.13	-25.03
α_5	-	2.32	19.96
α_6	-	-	-16.71
α_7	-	-	14.23
α_8	-	-	-12.56
α_9	-	-	11.04
α_{10}	-	-	-4.79

Table 1. Weight coefficients values.

4 CONCLUDING REMARKS

In this study dispersion properties of a nonlocal bond-based PD model were investigated. A weighted residual technique was employed and wave dispersion in a 1-D uniform grids model was then optimized. A set of weight coefficients was computed for all PD bonds inside the horizon region using Galerkin method. It was observed that wave dispersion in the modified PD model is significantly improved. It was also found that by increasing the number of nodes inside the horizon region more accurate results can be obtained.

ACKNOWLEDGEMENTS

U. Galvanetto and M. Zaccariotto would like to acknowledge the support they received from MIUR under the research project PRIN2017-DEVISU and from University of Padua under the research projects BIRD2018 NR.183703/18 and BIRD2017 NR.175705/17.

REFERENCES

[1] S.A. Silling. Reformulation of elasticity theory for discontinuities and long-range forces. *Journal of the Mechanics and Physics of Solids*, 48(1):175–209, 2000.

[2] T. Ni, M. Zaccariotto, Q.-Z. Zhu, and U. Galvanetto. Static solution of crack propagation problems in peridynamics. *Comput. Methods Appl. Mech. Eng.*, 346: 126–151, 2019.

[3] R. Alebrahim. Peridynamic modeling of lamb wave propagation in bimaterial plates. *Composite Structures*, 214:12–22, 2019.

[4] V.S. Mutnuri and S. Gopalakrishnan. A comparative study of wave dispersion between discrete and continuum linear bond-based peridynamics systems: 1d framework. Mechanics Research Communications, 94:40 – 44, 2018.

[5] Z.P. Bazant, W. Luo, V.T. Chau, and M.A. Bessa. Wave dispersion and basic concepts of peridynamics compared to classical nonlocal damage models. *Journal of Applied Mechanics, Transactions ASME*, 83(11), 11 2016.

[6] R.A. Wildman. Discrete Micromodulus Functions for Reducing Wave Dispersion in Linearized Peridynamics. *J. of Peridynamics and Nonlocal Modeling*, 1(1): 56-73, 2019.

INNOVATIVE SOUNDPROOFING MATERIALS THROUGH ELECTROSPINNING

F.Branda[1], F.Marulo[2], B.Vitolo[3],G.Iannace[4], J.Passaro[1], A.Bifulco[1], P.Russo[2]

[1]Department of Chemical Materials and Industrial Production Engineering (DICMaPI), University of Naples Federico II, P.leTecchio 80, 80125 Naples, Italy
E-mail: francesco.branda@unina.it; jessica.passaro@unina.it; aurelio.bifulco@unina.it

[2]Department of Industrial Engineering, Aerospace Division, University of Naples Federico II, Via Claudio 21,80125 Naples, Italy
E-mail:francesco.marulo@unina.it; pa.russo15@gmail.com

[3]Geven SPA, via Boscofangone, Nola, Italy
E-mail: bonaventura.vitolo@geven.com

[4]Department of Architecture and Industrial Design, University of Campania Luigi Vanvitelli Borgo San Lorenzo, 81031 Aversa (Caserta), Italy
E-mail: Gino.IANNACE@unicampania.it

ABSTRACT

Water resistant sound absorbers with reduced thickness and excellent sound-absorption properties in the low and medium frequency range, that pass the fire tests (Federal Aviation Regulation FAR 25.853 and FAR 25.855) which are mandatory in many engineering areas, were produced through an eco-friendly electrospinning process.
It is shown that the produced PVP/silica samples may have better sound absorption properties, in the lower frequency range, than materials, of the same thickness, that are usually used in both the civil and aerospace engineering fields.
Preliminary results suggest that the mats have potential application for thermal insulation.

INTRODUCTION

In recent years, polymers electrospinning raised very great interest for the preparation of polymer nanofibers with a broad range of complex architectures [1-3]. A very great advantage

with respect to conventional spinning processes is the possibility of producing micro/nanofibers ranging from two nanometers to several micrometers [1-3]. This is the reason why it has been recently proposed for the production of soundproofing materials [4]. The high specific surface area, 100 to 10000 times greater than that of the traditional acoustical fibrous materials, is expected, in fact, to give high sound absorption coefficients, as a consequence of the higher friction between the air molecules of sound waves and the electrospun fibers and/or rubbing of the fibers. As it is known noise pollution is one of the most widespread problems in modern society and constitutes a real danger to human health [5]. In the transportation industries, the need to produce soundproofing materials remains a big problem to cope with. The available soundproofing materials, in fact, do possess good sound absorption properties in the high frequency range but little in the low and medium frequency range (250–1600 Hz), for which human sensitivity is high [6].
Light polymeric soundproofing materials (density = 63 kg/m3) that are of interest for the transportation industry fabricated through electrospinning were recently proposed by the authors [7-9] consisting of blankets of electrospun polyvinylpyrrolidone (PVP), with an average fiber diameter in the range 1–3 μm. The blankets were obtained by stacking disks of electrospun mats on each other.
PVP does possess a unique combination of properties, such as good solubility in both water and a range of organic solvents, a remarkable capacity to interact with a wide variety of organic and inorganic compounds, good biocompatibility, and non-toxicity to living tissues. The PVP good solubility in polar solvents allowed us to obtain blankets through electrospinning of its ethanol solutions, with obvious advantages in term of process eco-friendliness with respect to the use of polymers insoluble in polar solvents. The drawback is that the good solubility in water does strongly limit the applications of the blankets. A solution was found [9] by heat treating blankets of PVP added with silica particles in order to make PVP molecular chains to crosslink. The silica was necessary to prevent samples shrinkage.

RESULTS AND DISCUSSION

Fig. 1 shows the silica particles used in the present work. They were produced by means of the Stöber method that allows to obtain particles dimensionally quasi monodisperse through the well known reactions of Sol-Gel methodology of hydrolysis and polycondensation of low molecular alcoxide molecules at room temperature.

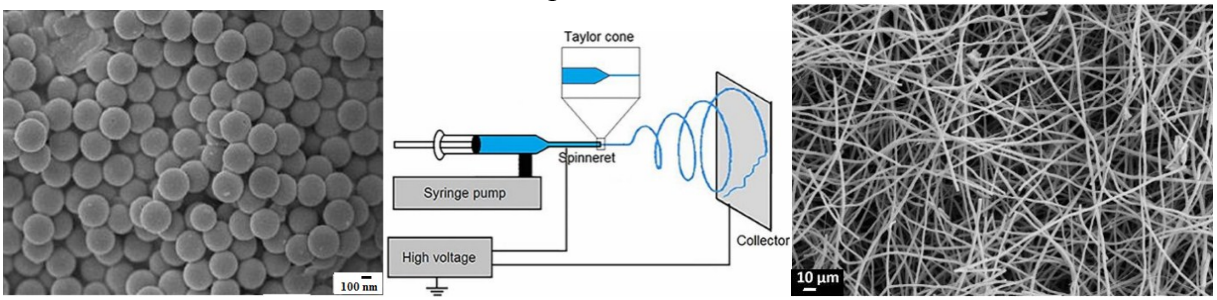

Fig.1 SEM micrograph of silica particles; Fig.2 Electrospinning apparatus schematic setup; Fig.3 SEM micrograph of heat treated PVP/SiO_2 mat

The silica particles were dispersed in an ethanol solution of polyvinylpyrrolidone, PVP (MW: 1,300,000 g ml^{-1}). The PVP and silica particles concentrations were 10 and 20 wt. %, respectively. The suspension in ethanol was electrospun so as reported elsewhere [9]in an electrospinning apparatus whose schematic setup is shown in Fig 2. A proper thermal cycle was defined [9] for the successful PVP networking. The SEM micrograph reported in Fig.3 (similar to the, not reported, not heat treated sample) shows that the heat treated PVP/SiO_2 mat has the typical aspect of the woven non woven fabrics. The fibers have a bimodal distribution of diameters: 1.6±0.4 μm, and 330±30 nm. It was shown [9] that the particles are tightly arranged

inside the fibers separated by thin polymer layers. This may be the consequence of strong absorption interactions between the silanols (Si-OH) groups present on the surface of silica particles and polar groups of PVP.

Three randomly selected samples of heat treated PVP/SiO_2 mat were submitted to a water resistance test reported in the literature. They were placed in 30 mL distilled water. After 24 h, the samples were removed and gently rinsed with distilled water. The water resistance, WS, was determined as:

$$WS = (S° - S)/S$$

where S° and S are the weights of the samples before and after immersion in water, both evaluated after drying at 105° C for 24 h. The weight percentage change measured on three samples was 1.42±0.50%. The not heat treated sample, instead, rapidly disintegrated when exposed to water. The good water resistance may be attributed to cross-linking occurring during thermal treatment.

The heat treated PVP/SiO_2were submitted to two tests required by the Federal Aviation Administration (FAA) (Federal Aviation Regulation FAR 25.853 and FAR 25.855) in order to assure, in civil aircraft, prescribed levels of fire safety:

1) Vertical Bunsen Burner Test for Cabin and Cargo Compartment Materials.
2) Smoke Test for Cabin Materials.

The Vertical Bunsen Burner Test determines the resistance of materials to flame. The samples exhibited [9] good self-extinguishing properties that may be attributed to the structure consisting of tightly assembled silica particles and to the partial thermal degradation that occurred during heating until the temperature reached 200°C.

According to the Smoke Test for Cabin Materials the Specific Optical Density is a dimensionless measure of the amount of smoke produced per unit area by a material when it is burned. This is an important test because smoke excessively dense prevents us from seeing escape routes and may provoke panic. The medium measured Specific Optical Density was 32.3 much lower than the maximum allowed value of 200 [9].

Thermal conductivity was measured [9] with a Differential Scanning Calorimeter (DSC) at the Indium melting point (156°C). The value measured (0.044 Wm^{-1} K^{-1}) for the heat treated PVP/SiO_2sample is close to the one (0.061 Wm^{-1} K^{-1} at 149 °C) reported for Microlite®AA, a well known Aircraft Acoustical and Thermal Insulation [10].

Fig. 4 shows the acoustical results collected with an impedance tube according to ASTM E 1050-12 and ISO 10534-2. As can be seen the acoustical response of the samples is represented by bell shaped curves with maximum sound absorption coefficient greater than 0.9. The curves shift towards lower frequency and become sharper by increasing the number (and total mass) of the disks. A second relative maximum is observed for some curves. The second maximum of curves occurred at a frequency of about 3 times the one of the first maximum.

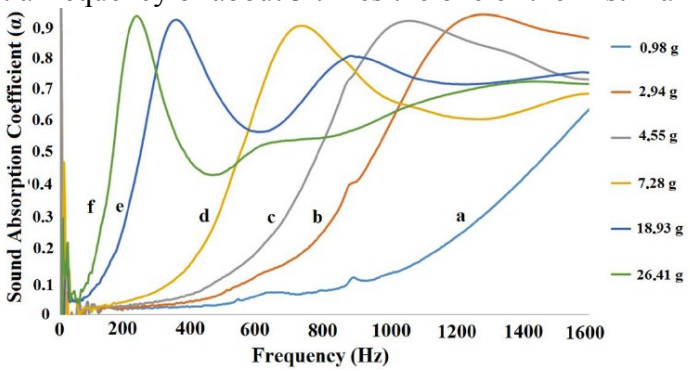

Fig.4 Plots of the sound absorption coefficient as a function of frequency for various heat treated PVP/SiO_2disks piles.

Fig.5 shows that electrospun PVP/silica samples may have better sound absorption properties, in the lower frequency range, than materials, of the same thickness, that are usually used in both the civil and aerospace engineering fields.

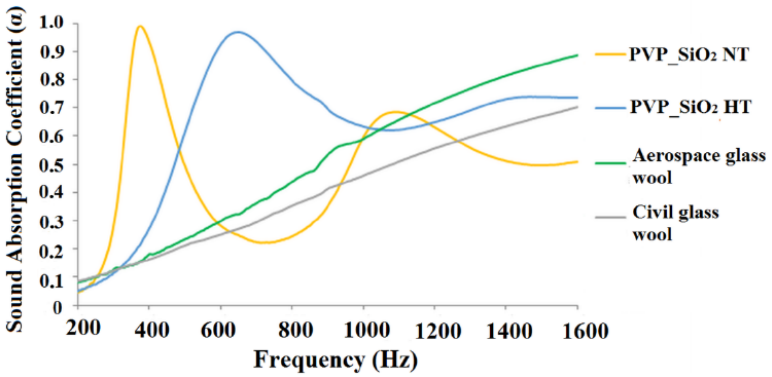

Fig.5 Comparison of the acoustical behaviors of electrospun PVP/silica mats and glass wool samples marketed in civil and aerospace engineering fields of same thickness (2.5 cm).

REFERENCES

[1] Agarwal, S.; Greiner, A.;Wendor_, J.H. Functional materials by electrospinning of polymers. Prog. Polym. Sci. **2013**, 38, 963–991.

[2] Bhardwaj, N.; Kundu, S.C. Electrospinning: A fascinating fiber fabrication technique. Biotechnol. Adv. **2010**,28, 325–347.

[3] Teo,W.E.; Ramakrishna, S. A review on electrospinning design and nanofibre assemblies. Nanotechnology **2006**, 17, R89–R106.

[4] Khan, W.S.; Asmatulu, R.; Yildirim, M.B. Acoustical Properties of Electrospun Fibers for Aircraft Interior Noise Reduction. J. Aerosp. Eng. **2012**, 25, 376–382.

[5] Crocker, M.J. Handbook of Noise and Vibration Control; John Wiley & Sons: Hoboken, NJ, USA, 2007;ISBN 978-0-471-39599-7.

[6] Arenas, J.P.; Crocker, M.J. Recent Trends in Porous Sound-Absorbing Materials. Sound Vib. **2010**, 44, 12–18.

[7] Avossa, J.; Branda, F.; Marulo, F.; Petrone, G.; Guido, S.; Tomaiuolo, G.; Costantini, A. Light ElectrospunPolyvinylpyrrolidone Blanket for Low Frequencies Sound Absorption. Chin. J. Polym. Sci. **2018**, 36, 1368–1374.

[8] Del Sorbo, G.R.; Truda, G.; Bifulco, A.; Passaro, J.; Petrone, G.; Vitolo, B.; Ausanio, G.; Vergara, A.; Marulo, F.Branda, F. Non Monotonous E_ects of Noncovalently Functionalized Graphene Addition on the Structure and Sound Absorption Properties of Polyvinylpyrrolidone (1300 kDa) Electrospun Mats. Materials **2019**, 12, 108.

[9] Jessica Passaro, Paolo Russo, Aurelio Bifulco, Maria Teresa De Martino , Veronica Granata, Bonaventura Vitolo, Gino Iannace, Antonio Vecchione, Francesco Marulo and Francesco Branda, Water Resistant Self-ExtinguishingLowFrequencySoundproofingPolyvinylpyrrolidoneBasedElectrospunBlankets, Polymers 2019, 11, 1205; doi:10.3390/polym11071205.

[10] Manville, J. OEM Insulations Division. www.jm.com. Available online: https://www.tricityinsulation.com/cms/wp-content/uploads/2010/11/Microlite-Blankets1.pdf (accessed on 2 June 2019).

NONLINEAR VIBRATIONS OF VARIABLE-STIFFNESS PLATES USING DIFFERENT SEMI-ANALYTICAL MODELS

A.Y. Cheng[1] , R. Vescovini[1] and E.L. Jansen[2]

[1]Dipartimento di Scienze e Tecnologie Aerospaziali
Politecnico di Milano, Milano, ITALY
Email: chengangelo.yan@mail.polimi.it, riccardo.vescovini@polimi.it

[2]Institute of Structural Analysis
Leibniz University Hannover, Hannover, GERMANY
Email: e.jansen@isd.uni-hannover.de

ABSTRACT

Semi-analytical strategies are presented for the nonlinear vibration analysis of variable-stiffness plates. The formulations are developed within a mixed variational framework, where the out-of-plane displacements and the Airy stress functions are the unknowns of the problem, approximated using the Ritz method. Three different strategies are presented for solving the discrete set of equations originating from the Ritz expansion: direct time integration, an iterative procedure based on the Harmonic Balance Method (HBM) and the Method of Averaging. In addition, a single-mode perturbation approach is developed, and is proposed as a suitable way for efficiently assessing the nonlinear vibration problem of variable-stiffness plates. Comparison against results from literature confirms the validity of the proposed models.

1 INTRODUCTION

Considerable attention has been devoted in the past decades to vibration problems for plates and shells involving moderately large displacements [1]. The motivations can be found in the theoretical relevance of the phenomenon along with several practical applications, in many cases related with structural stability problems. Several studies can be found in the literature for classical isotropic or composite configurations [1, 2]. However, relatively few works cover this topic in relation with variable-stiffness configurations [3, 4]. This work aims at presenting semi-analytical formulations as a viable alternative to finite element techniques for analyzing with improved efficiency the nonlinear vibrations of variable-stiffness plates. Different solution strategies are implemented and comparison against reference results is shown.

2 THEORETICAL FRAMEWORK

The approach is developed for the analysis of thin composite plates, obtained by the stacking of plies with non-uniform properties, i.e. variable-stiffness plates (VSP). The orientation of the fibers of a generic ply is specified according to the notation $\langle \alpha | \beta \rangle$, where α and β are the fiber's orientations at the center and the edges of the plate. The formulation is based on thin-plate theory, where a mixed variational functional [5, 6] is introduced for expressing the equilibrium and the compatibility requirements. The functional, expressed in terms of the out-plane deflections and the Airy stress function and including for the contribution due to inertial forces, reads:

$$\begin{aligned}\Pi^* = &-\frac{1}{2}\int_{\mathrm{A}} \left(\mathbf{F}^{\mathrm{T}}\mathbf{a}(x,y)\mathbf{F} - \mathbf{k}^{\mathrm{T}}\mathbf{D}(x,y)\mathbf{k} + F_{,yy}w_{,x}^2 - 2F_{,xy}w_{,x}w_{,y} + F_{,xx}w_{,y}^2\right)\,\mathrm{dA} + \\ &-\int_{\mathrm{A}} \left(F_{,yy}w_0w_{,xx} - 2F_{,xy}w_0w_{,xy} + F_{,xx}w_0w_{,yy}\right)\,\mathrm{dA} + \int_{\mathrm{A}} I_0 w_{,tt} w\,\mathrm{dA} + \Pi^*_{load}\end{aligned} \tag{1}$$

where $\mathbf{F}$ and $\mathbf{k}$ are the vectors collecting the second derivatives of the Airy stress function and out-of-plane displacements; the matrices $\mathbf{a}$ and $\mathbf{D}$ are the in-plane compliance and the bending stiffness, both function of the position x, y due to the variability of elastic properties over the plane x-y; the out-of-plane deflections and the initial imperfections are denoted with w and w_0, respectively. In-plane inertia effects are neglected, and just the out-of-plane moment of inertia I_0 is considered. Following Wu et al. [7] the expansion of the unknowns is performed referring to Legendre polynomials and boundary functions, where the membrane stresses are split into a part related to the distribution at the boundaries and another contribution specifying the behaviour inside the plate domain.

Direct time integration

A first strategy for solving the nonlinear dynamic problem consists in integrating the equations of motion. The Ritz approximation is substituted into Eq. (1) and, after imposing the functional to be stationary, the set of nonlinear equations expressing membrane compatibility and dynamic equilibrium along the out-of-plane direction are retrieved. Whenever the loads are directed in the out-of-plane direction, as it is considered here, the compatibility equations are time-independent. Therefore, the problem can be statically condensed into one single set of equations expressing the equilibrium requirements. Referring to a base of n modes, these equations are obtained as:

$$\ddot{q}_i + c_i\dot{q}_i + k_iq_i + \sum_{jk=1}^{nn} a_{ijk}q_jq_k + \sum_{jks=1}^{nnn} b_{ijks}q_jq_kq_s = p_i \qquad \text{for} \quad i = 1, 2, ...n \tag{2}$$

where the coefficients k_i, a_{ijk} and b_{ijks} are obtained by numerical integration of the stiffness-related contributions of the functional Π^* and successive projection onto the modal basis. Viscous damping can be added through the term c_i. The equations are integrated using the Matlab ode23s scheme, based on a modified Rosenbrock formula of order 2.

Iterative procedure

A second strategy relies upon an iterative procedure based on the Harmonic Balance Method (HBM), which can be employed for evaluating the forced steady-state response and the nonlinear free vibrations. In the former case, the response of the nonlinear system is approximated as:

$$\mathbf{q} \cong \mathbf{Q_0} + \sum_{k=1}^{5} \left[\mathbf{Q_{c,k}} \cos(k\omega t) + \mathbf{Q_{s,k}} \sin(k\omega t) \right] \tag{3}$$

where ω is the frequency of the forcing term, so super-harmonic contributions are taken as multiples of the fundamental frequency up to the fifth order. Substitution of Eq. (3) into the equation of motion, and successive balancing of the harmonics allows to derive the system of $11n$ nonlinear equations, which are solved using a Newton-Raphson technique.

Method of averaging

The method of averaging is based on an initial description of the problem as per Eq. (2), where a two-mode approximation is performed, q_1 and q_2 being the modal coordinates. By applying the averaging procedure to eliminate time-dependence, i.e. by replacing the vibration amplitudes and phases with their average values over the time period, the governing equations are found as a set of four algebraic equations. Clearly, the single-mode approximation can be retrieved as a special case, reducing the number of unknowns from four to two.

Perturbation approach

An effective strategy for analysing the nonlinear vibration response relies on a perturbation approach [8], which is essentially an extension of Koiterś approach to the case of vibrations. Main advantage is that the nonlinear problem is transformed into a sequence of linear problems. The unknowns, after introducing the Ritz approximation, are approximated using a perturbation expansion: the out-of-plane deflections are approximated as $w = \xi w^{(1)} + \xi^2 w^{(2)} + ...$, where ξ is the perturbation parameter, and similarly is done for the Airy function.

3 RESULTS

Exemplary results are presented to illustrate the comparison between the different methods presented above and reference numerical simulations from the literature [4, 9]. The full plate properties are not reported here for the sake of conciseness, but can be found in the referenced works. In all the examples, the boundary conditions are those of a fully clamped panel with immovable edges. The first example deals with a variable-stiffness plate with stacking sequence given by $[\langle 135|90\rangle, \langle -90|-45\rangle, \langle 90|45\rangle, \langle 45|0\rangle]_{\mathrm{s}}$. The nonlinear free vibration response is assessed in Figure 1(a), where the comparison is presented against the backbone curve obtained in Ref. [4]. Note, due to the close matching between the results, they are presented using markers and not continous curves. In the case of the direct integration approach, the procedure is quite cumbersome, as integration needs to be carried-out for a sufficiently large number of periods. Furthermore, several frequency response curves need to the traced to derive the final backbone plot. In this example, a 11-dof model is considered, with a concentrated force applied at the center of the plate (magnitude $f = 0.7N$) and accounting for a slight damping factor ($\xi_{1,1} = 0.0325$).
A second example regards the forced nonlinear response of the variable-stiffness plate analyzed by Akhavan [9], whose lay-up is $[\langle 90|45\rangle, 90, \langle 90|45\rangle]_{\mathrm{s}}$. The load is introduced in the form of a uniform pressure with magnitude equal to $2 \times 10^4\ N/m^2$. No damping is accounted for. The results are reported in Figure 1(b) in terms of maximum nondimensional deflection versus nondimensional frequency $\overline{\omega} = \omega a \sqrt{\rho / E_{22}}$. Even in this case, close matching can be observed between the present results and those of Ref. [9], where the p-version finite element and third-order plate theory are used. In both cases, computations are carried out very effectively, with times ranging from 0.5 s to few minutes (on a laptop with Intel i7 4.00 GHz, 32 GB of RAM). The perturbation technique is particularly effective, as fractions of a seconds are needed to trace the plots with a two-term expansion. Iterative procedure and method of averaging require, in general, few seconds, while

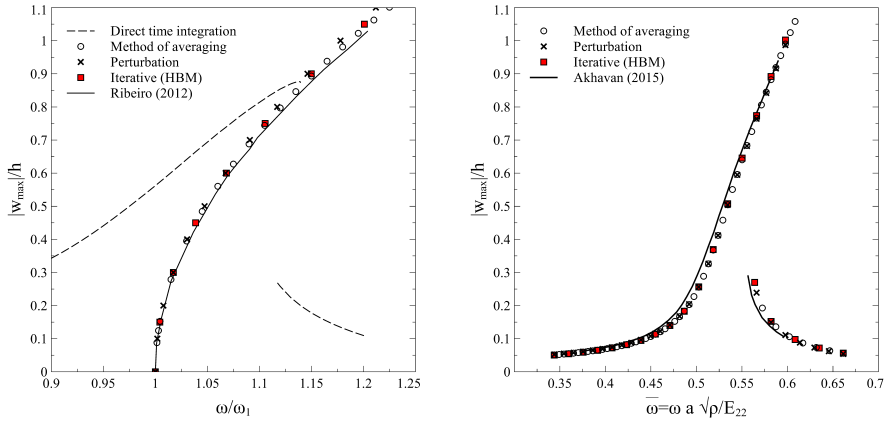

(a) (b)

Figure 1: Comparison between different methods and reference results: (a) backbone curves, (b) frequency response curves.

numerical integration is the most computationally intensive approach, requiring a total time of the order of a few minutes.

4 CONCLUDING REMARKS

A semi-analytical strategy has been presented for analyzing the nonlinear vibration response of variable-stiffness plates. The formulation is general enough to allow any set of flexural boundary conditions to be studied, while free, movable and immovable edges can be considered with respect to the in-plane motion. Four different strategies were proposed for solving the nonlinear equations available from the Ritz discretization: direct time integration can be relatively time-consuming, but the three other strategies are extremely attractive in terms of computational time. This is particularly true for the single-mode perturbation approach: the solution is obtained as a sequence of linear problems, and fractions of a second are required for the problem to be solved. These features render the proposed approaches particularly suited for gathering insight into the nonlinear vibration response of variable-stiffness configurations, a relatively new field demanding further investigation.

REFERENCES

[1] M. Amabili. *Nonlinear Vibrations and Stability of Shells and Plates*. Cambridge University Press, 2008.

[2] F. Farbod and M. Amabili. Non-linear vibrations of shells: A literature review from 2003 to 2013. *International Journal of Non-Linear Mechanics*, 58:233–257, 2014.

[3] P. Ribeiro and H. Akhavan. Non-linear vibrations of variable stiffness composite laminated plates. *Composite Structures*, 94(8):2424–2432, 2012.

[4] P. Ribeiro. Non-linear free periodic vibrations of variable stiffness composite laminated plates. *Nonlinear Dynamics*, 70(2):1535–1548, 2012.

[5] V. Giavotto. Sulla meccanica dei pannelli anisotropi ed eterogenei. *Memorie dell' Istituto Lombardo - Accademia di Scienze e Lettere*, XXV(5), 1969. [Italian].

[6] C. Bisagni and R. Vescovini. Analytical formulation for local buckling and post-buckling analysis of stiffened laminated panels. *Thin-Walled Structures*, 47(3):318–334, 2009.

[7] Z. Wu, P.M. Weaver, G. Raju, and B.C. Kim. Buckling analysis and optimisation of variable angle tow composite plates. *Thin-Walled Structures*, 60:163–172, 2012.

[8] L.W. Rehfield. Nonlinear free vibrations of elastic structures. *International Journal of Solids and Structures*, 9(5):581–590, 1973.

[9] H. Akhavan. Non-linear vibrations of tow placed variable stiffness composite laminates. Ph.D. Thesis, Universidade do Porto, 2015.

A SIMPLIFIED FINITE ELEMENT MODELLING OF A FULL-SCALE FUSELAGE SECTION FOR CRASHWORTHINESS DESIGN

M. Manzo[1], A. De Luca[1], D. Perfetto[1], L. Di Palma[2], M. Waimer[3], P. Schatrow[3]

[1]Department of Engineering
University of Campania "Luigi Vanvitelli", Aversa, ITALY
Email: mario.manzo1@unicampania.it, alessandro.deluca@unicampania.it, donato.perfetto@unicampania.it

[2]Italian Aerospace Research Centre (CIRA)
Via Maiorise s.n.c. 81043, Capua, ITALY
Email: L.DiPalma@cira.it

[3]Institute of Structures and Design
German Aerospace Center (DLR), Stuttgart, GERMANY
Email: matthias.waimer@dlr.de, paul.schatrow@dlr.de

ABSTRACT

In the aerospace field, passive safety of aircraft is among the most critical aspects to take into account during the current design practice. For this reason, several tools are nowadays available to improve the aircraft crashworthiness performances. Among these, numerical modelling plays an important role and numerical optimization procedures, which require the use of light, in terms of computational costs, and flexible models, are increasingly used. This article deals with the development of a simplified finite elements (FE) numerical model, for optimization purpose. The modelling starts from an established FE model of a full-scale composite fuselage section, already validated with respect to an experimental test, under a vertical drop test loading condition. The main goal is to reduce computational costs with respect to this FE model and, thus, to have a starting point for an optimization process for crashworthiness design purposes. In this paper, the FE model and its simplification procedure are described. Subsequently, a numerical-numerical comparison has been herein presented in terms of structural behavior under vertical drop test condition.

1 INTRODUCTION

Numerical modelling is assuming an increasingly important role in the current design practice, especially for the development of aeronautical structures with focus on crashworthiness. It allows using less human and economic resources as well as saving time; for instance, the complexity of setting up experimental tests for drop tests of fuselage sections [1,2]. Numerical simulations have been becoming necessary especially in the pre-test phase to predict phenomena that may occur during the real experimental tests [3-4]. Virtual structural optimizations take on a fundamental position in this framework, allowing improving crashworthiness performance characteristics of a preliminary model, which however should be light, since the large number of scenarios that may be analyzed. It follows that, to achieve solutions in reasonable simulation times, many answers have been came up [5, 6]. In addition, such simplifications can be also useful for further structural improvement methods being not properly optimizations [5-8].

In this paper, a simplified model of a fuselage section for crashworthiness improvement simulations will be discussed.

2 FE MODEL AND LOAD CASE DISCUSSION

The starting point for this work is a FE model of a fuselage section, entirely made of composite materials, already used to simulate in detail a vertical drop test event to which a full-scale test article was presented by authors in [1]. In previous works, a good correlation was achieved and shown, both in terms of accelerations and failures, in accordance with the experimental data [1, 4, 9, 10]. The current idea is to exploit this model to carry out structural optimization analysis in order to obtain better crashworthiness performances. Of course, the first step should be to make a simplified version of the numerical model to cut down computational costs. Herein, this phase is going to be discussed.

As first thing, a subsection consisting in only two frames has been extracted from (Figure 1).

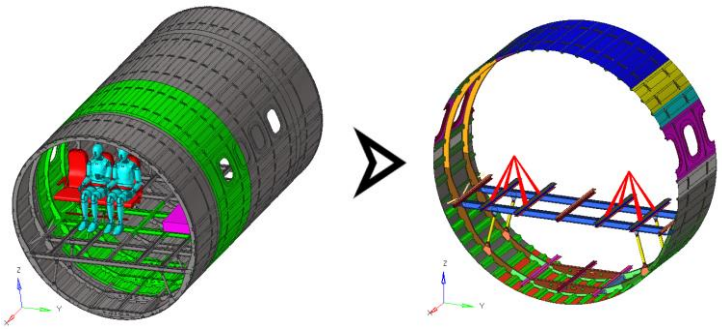

Figure 1. Extrapolation of the simplified model from the complete one.

Then, many simplifications have been made, among which the most noticeable are: replacement of seats, dummies and the balancing mass with concentrated masses (Figure 1); replacement of floor beams solid bolts and struts pins with 1D rigid elements (Figure 2), letting the rotation around their main axis free; modelling the material behavior of the parts above the floor as purely elastic, since failures are not detected in this zone; deletion of various components which do not influence significantly the results.

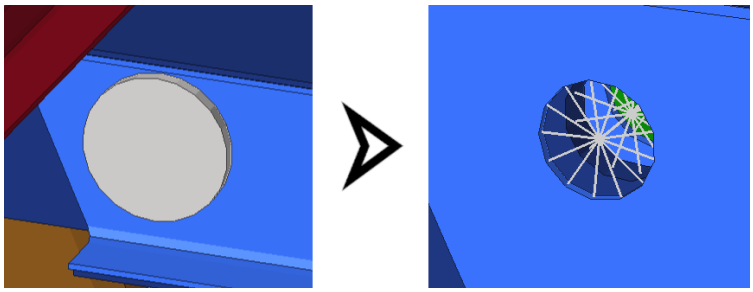

Figure 2. Example of simplification.

In addition, in order to take into account the effects of the removed fuselage sections, symmetry constraints have been applied to the nodes positioned on the two cutting planes of the simplified model. The loading condition consists of a vertical drop test onto a rigid wall. In order to develop a reliable simplified model, the energy aspect has been considered: its starting kinetic energy must be equals to the maximum internal energy of the subsection belonging the complete model under the same impact condition. As a result, it is possible to set up both mass and initial velocity necessary for the execution of the load case of interest.

3 RESULTS AND CONSIDERATIONS

The explicit solution has been run by using the commercial code LS-DYNA® for 100 ms of simulation. The calculation time is about 6 hours; a considerable reduction compared to about 47 hours of the complete model (≈ -87%) [1, 9]. A comparison of structural response between the simplified and the complete models is shown in the Figure 3.

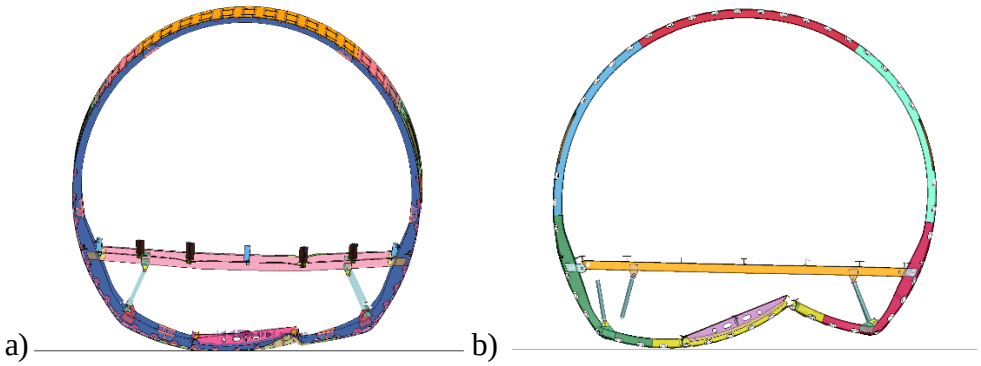

Figure 3. Failures involving both complete (a) and simplified (b) models.

Larger failures for the simplified model are evident, especially with respect to rigids substituting bolts and pins. Besides, the plot of the internal energy comparison is illustrated in the Figure 4.

The disagreement between the two curves remains within about 10%, demonstrating the reliability of the simplified model. However, improvements are certainly possible.

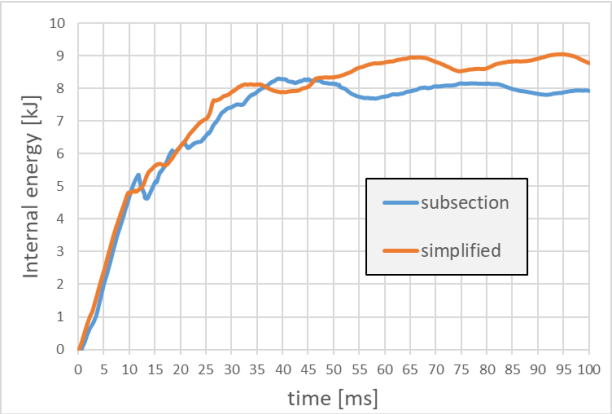

Figure 4. Comparison of internal energies.

REFERENCES

[1] L. Di Palma, F. Di Caprio, A. Chiariello, M. Ignarra, S. Russo, A. Riccio, A. De Luca and F. Caputo. *Vertical Drop Test of Composite Fuselage Section of a Regional Aircraft*, AIAA Journal, 2019

[2] J. D. Littel. *A Summary of Results from Two Full-Scale Fokker F28 Fuselage Section Drop Tests*. NASA/TM–2018-219829, 2018.

[3] M. Guida, A. Manzoni, A. Zuppardi, F. Caputo, F. Marulo, A. De Luca, Development of a multibody system for crashworthiness certification of aircraft seat, Multibody System Dynamics, 44 (2): 191-221, 2018.

[4] D. Perfetto, A. De Luca, G. Lamanna, A. Chiariello, F. Di Caprio, L. Di Palma, F. Caputo, Drop test simulation and validation of a full composite fuselage section of a regional aircraft, Procedia Structural Integrity, 12: 380-391, 2018.

[5] F. di Napoli, A. De Luca, F. Caputo, F. Marulo, M. Guida and B. Vitolo. *Mixed FE–MB methodology for the evaluation of passive safety performances of aeronautical seats*. International Journal of Crashworthiness, 24 (3): 314-325, 2018.

[6] F. Caputo, A. De Luca, F. Marulo, M. Guida, and B. Vitolo. *Numerical-Experimental Assessment of a Hybrid FE-MB Model of an Aircraft Seat Sled Test*. Hindawi, International Journal of Aerospace Engineering, Article ID 8943826, 2018.

[7] F. Caputo, G. Lamanna and A. Soprano. *Residual Strength Improvement of an Aluminium Alloy Cracked Panel*. The Open Mechanical Engineering Journal, 7: 90-97, 2013.

[8] F. Caputo, A. Soprano and G. Monacelli. *Stochastic design improvement of an impact absorber*. Latin American Journal of Solids and Structures, 3: 41-58, 2006.

[9] D. Perfetto, G. Lamanna, M. Manzo, A. Chiariello, F. Di Caprio, L. Di Palma. *Numerical and experimental investigation on the energy absorption capability of a full-scale composite fuselage section*. International Conference on Fracture and Damage Mechanics (FDM), Rhodes, 2019.

[10] F. Caputo, M. Manzo, D. Perfetto, A. De Luca, L. Di Palma, A. Chiariello, F. Di Caprio. *Crashworthiness Investigation on a Composite Fuselage Section under a Drop Test through the FE Method*. International Conference on Stress Analysis (AIAS), Assisi, 2019.

EXPERIMENTAL STUDY OF GRAPHENE AND CARBON NANOTUBES THERMAL SENSING PROPERTIES

D. Passato [1] , M. Akermo[2], P. Hallander[3], S. De Rosa[1] and G. Petrone[1]

[1]PASTA Lab
Universita' degli Studi di Napoli Federico II, Napoli, Italia
Email: d.passato@studenti.unina.it, sergio.derosa@unina.it, giuseppe.petrone@unina.it

[2]Aeronautical and Vehicle Engineering
KTH, Stockholm, Sweden
Email: akermo@kth.se

[3]SAAB AB SE-581 88
Linkoping,Sweden

ABSTRACT

Today there are several new and interesting Nano-particle materials on the market providing good electrical conductivity. Examples are carbon Nano-tubes and different versions of graphene derivatives, often provided as powder. In particular, the materials available were Multi-Walled Carbon Nanotubes in Epoxy matrix and Reduced Graphene Oxide (rGOH). An initial literature survey underlined the lack of measurements and information about the conductivity of these materials during heating up or curing. This work is part of a larger project aiming at producing "sensing structural composite material", i.e. a composite material with integrated Nanoparticles, as eg. Carbon-nano-tubes or graphene, working as sensors reporting the status of the material during heating up, curing and/or tensioning. The principal results concerns the evaluation of the specific conductivity during heating for both materials (rGOH and MWCNT in Epoxy Matrix) with the realization of an experimental model for the gradient of the specific conductivity with temperature. The linearity underlines the possibility of using the properties of these materials to create sensors, not only for strain (with the advantage of high Gauge Factors), but also for temperature.

1 INTRODUCTION: CARBON NANOTUBES AND GRAPHENE

The principal aim of this experimental work is to study thermal sensible properties of Graphene and Multi Walled Carbon Nanotubes (MWCNT). In particular, the materials available for experimental investigations are Carbon Nanotubes in Epoxy matrix and Reduced Graphene Oxide (rGOH).

Carbon nanotubes (CNTs) are tubes made of carbon with diameters typically measured in nanometers. Carbon nanotubes often refers to single-wall carbon nanotubes (SWCNTs) with diameters in the range of a nanometer. They were discovered independently by Iijima and Ichihashi [1] and Bethune et al. [2] in carbon arc chambers similar to those used to produce fullerenes. Carbon nanotubes also often refer to multi-wall carbon nanotubes (MWCNTs, also sometimes used to refer to double- and triple-wall carbon nanotubes) consisting of nested single-wall carbon nanotubes. Carbon nanotubes can exhibit remarkable electrical conductivity. They also have exceptional tensile strength and thermal conductivity, because of their nanostructure. These properties are expected to be valuable in many areas of technology, such as electronics, optics, composite materials (replacing or complementing carbon fibers), nanotechnology, and other applications of materials science.

A more detailed view has been considered on the effect of CNT inside Epoxy matrix. The mechanical and electrical properties of the composite with different weight percentages of nanotubes have been investigated in [3]. Conductivity measurements on the composite samples showed that the insulator-to-conductor transition took place for nanotube concentration between 0.5% and 1 wt.%. The electrical and thermal conductivities of epoxy composites containing $0.005 \setminus 0.5$ wt% of single-walled (SWNTs) or multi-walled (MWNTs) carbon nanotubes have been also studied in [4]. The MWNT composites had an electrical percolation threshold of 0.005 wt%, whereas the thermal conductivity of the same samples increased very modestly as a function of the filler content.

Graphene is an allotrope of carbon in the form of a single layer of atoms in a two-dimensional hexagonal lattice in which one atom forms each vertex. Graphene has a special set of properties which set it apart from other allotropes of carbon. In proportion to its thickness, it is about 100 times stronger than the strongest steel. It conducts heat and electricity very efficiently and is nearly transparent. In its traditional form, graphene is one atomic layer thick and usually exists as a film of sorts; however, the proliferation of graphene research and testing has led to the creation of various graphene forms, each used for unique purposes. These forms include graphene films produced through chemical vapor deposition (CVD), graphene oxide (GO), reduced graphene oxide (rGO) and graphene nanoplates (GNPS). The material studied in this thesis project was Reduced Graphene Oxide. There are numerous ways to produce rGO such as annealing, hydrazine vapor treatment, and microwave reduction.

Studies conducted on thin graphene layers underline the possibility of temperature sensing applications. In [5], a temperaturedependent study of thermal (10300 K) and electrical (103000 K) transport in annealed RGO films indicates the potential application of RGO films for sensing temperatures across an extremely wide range. Also applications with a highperformances flexible temperature sensor composed of polyethyleneimine and rGO have been realised [6]. The prepared sensor exhibits high sensitivity (1.30% $^{\circ}\mathrm{C}^{-1}$), linearity (R2 = 0.999), accuracy (0.1 $^{\circ}\mathrm{C}$), and durability (60 d) for temperature sensing between 25 and 45 $^{\circ}\mathrm{C}$.

2 EXPERIMENTAL

2.1 Set-Up

Principally the evaluation of the specific conductivity of the different materials has been realized by a Bio-Logic Potentiostat and two different ovens. Temperature measurements in the ovens have been made by a thermocouple and the different geometric data have been measured using a caliber. To collect data from different sources a LabView Script has been realized. Finally Matlab has been used to post process results.

2.2 MWCNTs in Epoxy Matrix

As concerns the CNTs forest impregnated by a epoxy film (from Hexcel) on Steel Sheets, the mean value of conductivity for cured samples is about 0.24 (S/m). Moreover the variance of the values obtained from different samples (with different number of layers and different geometry) is

6.7×10^{-4}. It was also interesting to collect data on the level of current during heating up in order to study the sensing properties of the Carbon Nanotubes.

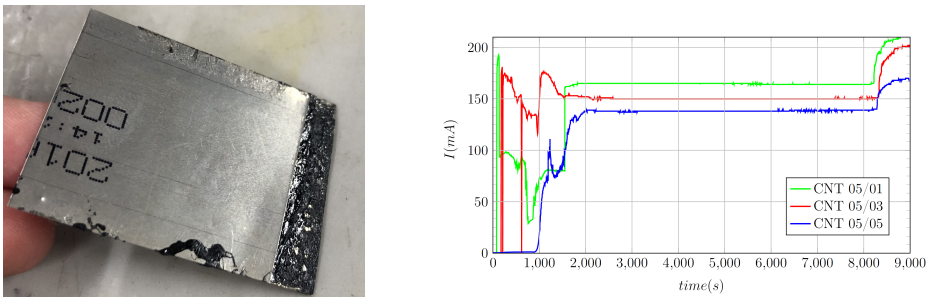

Figure 1. Sample and Measurements during curing

Considering the geometry of the sample a value of $d\sigma/dT$ $(S/m)/°\mathrm{C}$ has been get. The mean value of $d\sigma/dT$ is 3.45E-4 $(S/m)/°\mathrm{C}$. The value of conductivity during the cure has been also measured. On average the value of conductivity has been increased by the treatment (considering the value 0.24 S/m), but the values are not stable. After that, the support of the nanotubes has been replaced, using a carbon fibre prepreg. The principal problem with this kind of acquisition is linked with the mechanical characteristics of the prepreg before curing. Moreover the curing process has squeezed the matrix making not easy the following measurements. The principal problem is linked with the clamping and with the fact that the samples do not offer a continuum field for the propagation of the current. To understand (at least) if there is a dependence from the temperature of the value of the conductivity, the samples have been tested during heating up and cooling down cycle: there is a dependence from the temperature of the value of the current (we can see it considering the abrupt decreasing of current after the abrupt cooling down).

2.3 Graphene (rGOH)

As for the MWCNT we studied the conductivity of a Reduced Hydrogenated Graphene Oxide (a coated Kapton film from Danubia NanoTech [7]) in different conditions starting from a Single Layer configuration. Each layer is 0.5cm*4cm. First of all, a single layer of rGOH has been analysed. Clearly, to define a conductivity is necessary to define the resistivity of the material. In this case is not simple because we should have the area of the cross section of the film. Graphene films exhibits a stable behaviour. The value of the current seems to depend weakly from the sample and clearly the difference is due to different geometric characteristics and imperfections. The law tesion/current is linear. At this point, we put the graphene layer inside a prepreg sandwich made up of 4 layers. We have noticed a weak growth of the current for a fixed level of voltage $(1V)$ from the previous test. This phenomenon could be explained considering that the prepreg has a better value of conductivity, so putting the film inside it we increase the global conductivity of the sample. At this point the samples have been cured under vacuum. In order to avoid the oxidation of the film, we waited the Tamb before removing the samples from the vacuum pump. After that we have tested the samples with the potentiostat at *Tamb*. The value of conductivity seems to be unchanged. The next step has been to measure the level of current for a fixed voltage during heating up. In Figure 2.3, the Temperature is measured in the oven, while the sensor measures inside the material. The delayed signal is therefore due to heating up. Moreover, to avoid the oxidation of the samples, they have been placed under vacuum. This has made the measurements quite unstable and complicated: first of all the action of the vacuum make worse the grip of the cable, then, since the film is very fragile, the action of the pup has destroyed most of the samples. For the survived ones we have realized a linear model where the samples exhibit a linear behaviour increasing temperature. Using that linear model we obtain a value of $dI/dT = 0.0001173$ with a Root Mean Squared Error: 0.000346. (according to the F-test we can apply the linear model; F-statistic vs. constant model: 739, p-value = 1.08e-34). Further tests should be done to have a more numerous selection of values of the dI/dT, but the principal future goal is to find a way to test the samples under vacuum without destroying the most of them!

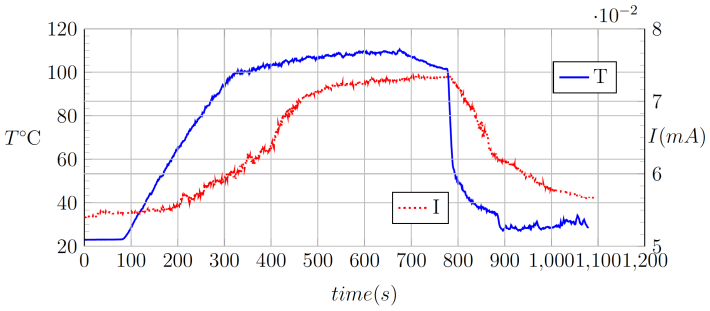

Figure 2. Sample and Measurements during Heating

3 CONCLUSION

Talking about the MWCNTs, the most of the results have been obtained for the case study of Metal Sheets with MWCNTs inside epoxy matrix. In this case there were enough data to realize and experimental linear model for the gradient of the specific conductivity with temperature. As concerns rGOH, also this time we could estimate a value for the $d\sigma/dT$, but probably the most interesting results is that to perform this kind of experiment a complete different set-up is needed in order to measure in a more easily way the current through the material. A solution could be the use of an hot press. Another important result is that to avoid the oxidation of the graphene film during heating and curing, the measurement of the conductivity must be realized in a vacuum package. On the whole, we can say that the linearity of the law $d\sigma/dT$ underlines the possibility of using the properties of these materials to create sensors, not only for strain (with the advantage of high Gauge Factors), but also for temperature.

ACKNOWLEDGEMENTS

The project was performed as an initials study within the Vinnova funded project Cosing. Linnea Selegrd and SAAB Aeronautics is acknowledged for fruitful discussions and supply of CNT. Viera Skakalov at Danubia Nanotech has kindly supported with knowledge and rGOH film.

REFERENCES

[1] Sumio Iijima and Toshinari Ichihashi. Single-shell carbon nanotubes of 1-nm diameter. 363(6430):603–605, Jun 1993.

[2] D. S. Bethune, C. H. Klang, M. S. de Vries, G. Gorman, R. Savoy, J. Vazquez, and R. Beyers. Cobalt-catalysed growth of carbon nanotubes with single-atomic-layer walls. 363(6430):605–607, Jun 1993.

[3] A Allaoui, S Bai, H.M Cheng, and J.B Bai. Mechanical and electrical properties of a mwnt/epoxy composite. *Composites Science and Technology*, 62(15):1993 – 1998, 2002.

[4] A. Moisala, Q. Li, I.A. Kinloch, and A.H. Windle. Thermal and electrical conductivity of single- and multi-walled carbon nanotube-epoxy composites. *Composites Science and Technology*, 66(10):1285 – 1288, 2006.

[5] Yuqiang Zeng, Tian Li, Yonggang Yao, Tangyuan Li, Liangbing Hu, and Amy Marconnet. Thermally conductive reduced graphene oxide thin films for extreme temperature sensors. *Advanced Functional Materials*, 29(27):1901388, 2019.

[6] Qingxia Liu, Huiling Tai, Zhen Yuan, Yujiu Zhou, Yuanjie Su, and Yadong Jiang. A high-performances flexible temperature sensor composed of polyethyleneimine/reduced graphene oxide bilayer for real-time monitoring. *Advanced Materials Technologies*, 4(3):1800594, 2019.

[7] https://www.danubiananotech.com.

Influence of tooth profile modifications on the dynamic behavior of a planetary gear set: experimental investigation and numerical validation for different amplitudes of tooth profile modifications

J. Neufond[1,2], E. Rigaud[1], J. Perret-Liaudet[1*] and A. Carbonelli[2]

[1]LTDS, Ecole Centrale de Lyon
36 Avenue Guy de Collongue, 69134 Écully, Ecully, FRANCE
Email: jessica.neufond@vibratec.fr, emmanuel.rigaud@ec-lyon.fr,
joel.perret-liaudet@ec-lyon.fr

[2]VIBRATEC
28 Chemin du Petit Bois, 69130, Ecully, FRANCE
Email: alexandre.carbonelli@vibratec.fr

ABSTRACT

The aim of this work is to perform an experimental and numerical investigation of the dynamic behavior of a planetary gear set. Measurements are performed using a specific test bench and are compared with numerical results obtained from an efficient computational scheme. Two similar planetary gear sets are considered in order to study the influence of tooth profile modifications on the static transmission error and on the dynamic behavior of the planetary gear set. The first sample consists in standard gears without tooth modifications, while in the second sample, sun gear and planets have with tip relief corrections. First, the internal parametric excitations, corresponding to the static transmission errors (STE) and the mesh stiffness fluctuations, are characterized. Then, the dynamic behavior is investigated. The comparisons between numerical results and measurements show that the computational scheme leads to satisfying results.

1 INTRODUCTION

Planetary gear sets provide high gear ratio in a compact package. They are widely used in automatic gearbox transmissions of hybrid vehicles, energy production systems such as wind turbines, home automation applications such as shutter and blind [1]. Compared to cylindrical gears with fixed and

parallel axes, predicting and controlling the whining noise emitted from a planetary gear set remains a difficult problem because of the coupling between the multiple gear meshes and the mobility of the planet axes. It is assumed that the main source of excitation corresponds to the static transmission error (STE) and the mesh stiffness fluctuations generated by multiple gear meshes [2-4]. The STE mainly results from tooth deflections, tooth surface modifications and manufacturing errors. Under operating conditions, they induce dynamic mesh forces transmitted to the housing through wheel bodies, shafts and bearings [5]. Housing vibratory state is directly related to the radiated noise [6]. Although several previous studies deal with the dynamic behavior of planetary gear sets [7-10], few experimental data are available in the literature, especially concerning the influence of tooth profile modifications on the dynamic behavior. This study presents the experimental investigation of the static transmission error and the housing vibratory state of planetary gear sets under various operating speeds. Measurements are compared with numerical results obtained from an efficient computation scheme [11, 12].

2 PRESENTATION OF THE PLANETARY GEAR SETS AND THE TEST BENCH

The experimental investigation of the dynamic behavior is performed using two samples of a planetary gear set developed for several industrial applications. It is designed with one stage, three planets and spur gears. The input is the sun gear and the output is the planets carrier, letting the ring gear fixed.

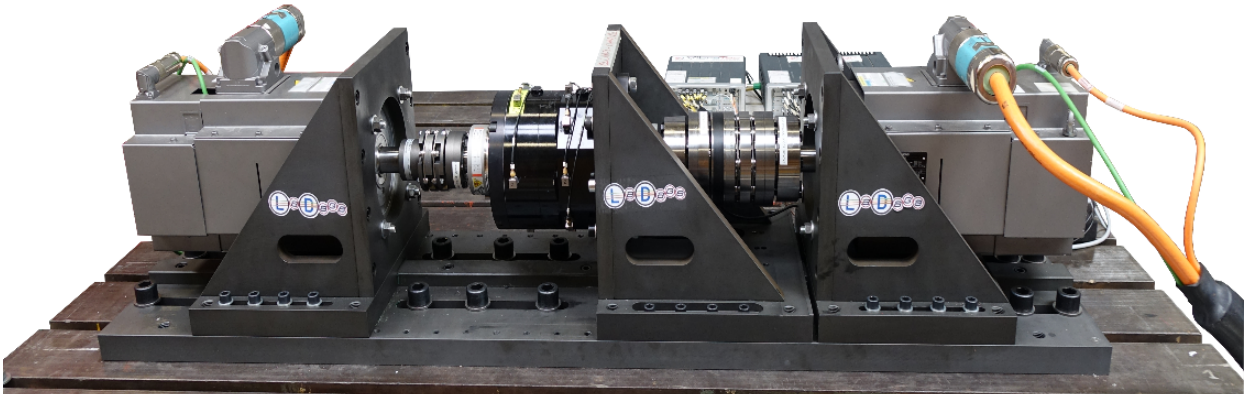

Figure 1. The test bench.

3 STATIC TRANSMISSION ERROR: CORRELATION BETWEEN MEASUREMENT AND NUMERICAL MODEL

The measurement of STE is usually performed for very low rotational speed, here at 60 rpm. The applied output torque is 50 Nm. This value is lower than the capacity of the planetary gear, but the motor characteristics do not allow long measurement with a higher torque. The overall STE fluctuations between the sun-gear and the carrier are deduced from the input and output instantaneous rotation speeds measured thanks to the optical encoders. The spectral contents at mesh frequency harmonics are extracted and the STE is rebuilt from those spectra.

Comparisons between time evolutions show a very good agreement between experiments and numerical results in terms of amplitude. This confirms the ability of the proposed method to accurately describe the transmission error. Nevertheless, comparisons between spectral contents show that the fourth first orders are correctly estimated for all configurations, except for the modified/counterclockwise. Higher order harmonics remain difficult to measure and to predict.

4 DYNAMIC RESPONSE

The dynamic response of the planetary gears set is computed for the four configurations previously presented. For each configuration, STE, taken as excitation source, is computed with the actual mean micro-geometry values extracted from gear metrology reports.
The dynamic response is computed using a method described in [6]. The computational scheme is summarized on Figure 2. First, simulations are compared to experimental results. Then, the different test cases are considered in order to evaluate the influence of tooth corrections on the housing vibratory state.
Comparison between simulations and measurement of the quadratic mean value of the acceleration in function of the input rotational speed. Differences can be explained by the discrepancies observed in the metrological reports between the left and right flanks of the gears teeth. Nevertheless, it is well known that the gear manufacturing tolerances have an important impact on the gearbox noise variability [13, 14].

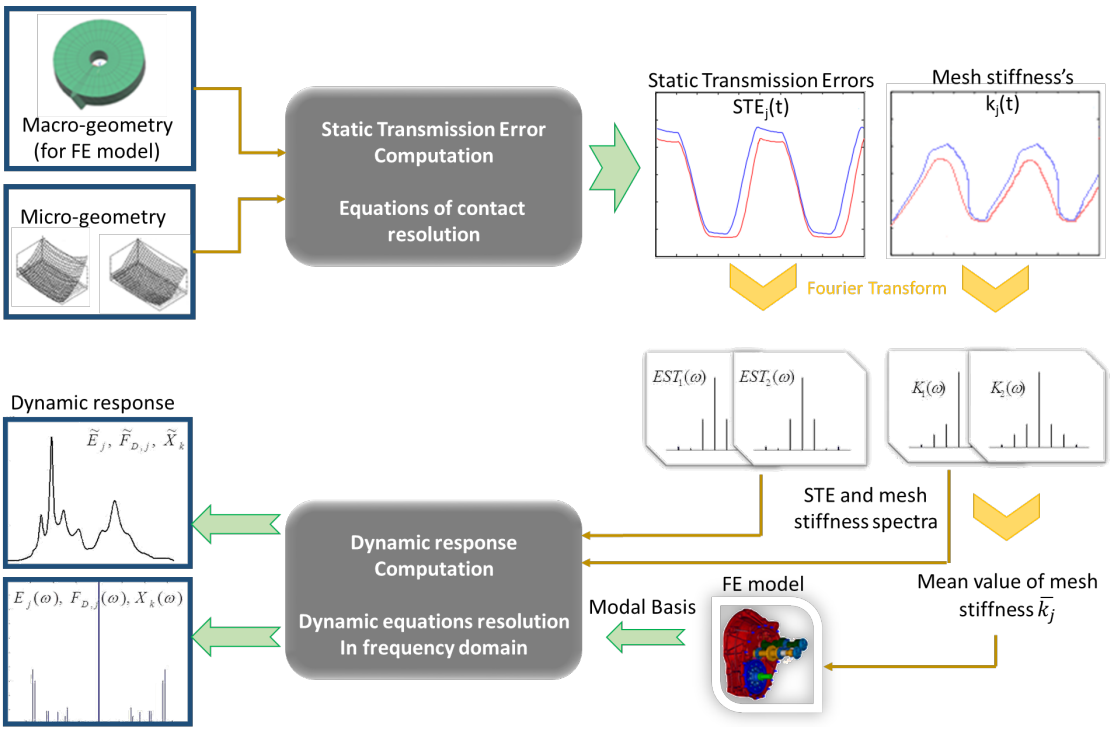

Figure 2: From STE to housing vibratory state, the complete computation scheme.

5 CONCLUSION AND FUTURE WORK

In this paper, the static transmission error and the dynamic behavior of a planetary set for a large range on input speed are investigated in actual context, both experimentally and numerically. Comparisons between numerical simulations and measurements show the ability of the proposed numerical model to compute the overall STE and to predict accurately the housing vibratory state, responsible of the whining noise. The order tracking of dynamic response shows a multi-harmonic behavior, mainly driven by internal parametric excitations. Regimes corresponding to main resonances are identified. Amplitudes of the overall STE and the evolution of the dynamic response in function of the input velocity are well predicted for most of harmonics and tested configurations. Investigation of several samples and configurations of the planetary gear set allows analysis of the influence of tooth profile modifications. Other test case are planned, which will provide an in-depth look at the planetary gear set behavior, in particular the fact of having voluntarily different corrections between planets.

6 ACKNOWLEDGMENTS

This work has been performed within the LabCom LADAGE (Laboratoire de dynamique des engrenages) funded by the French National Research Agency / ANR under the reference number ANR-14-LAB6-0003. The authors are also members of the LabEx CeLyA (Centre Lyonnais d'Acoustique) funded by the French Ministry of Research.

REFERENCES

[1] CG. Cooley, RG. Parker, A review of planetary and epicyclic gear: dynamic and vibration research, Applied Mechanics Reviews, 2014; 66(4): 060804.

[2] DB. Welbourn, Fundamental knowledge of gear noise – a survey. Proc Conf Noise Vibrat Engines Trans 1979; C177/79: 9–29.

[3] SL. Harris, Dynamic loads on the teeth of spur gears. Proc IMechE 1958; 172: 87–112.

[4] RW. Gregory, SL. Harris, RG. Munro, Dynamic behaviour of spur gears. Proc IMechE 1963; 178: 207–218.

[5] E. Rigaud, J. Sabot, Effect of elasticity of shafts, bearings, casing and couplings on the critical rotational speeds of a gearbox. VDI Berichte 1996; 1230: 833–845.

[6] A. Carbonelli, E. Rigaud, J. Perret-Liaudet, Vibro-acoustic analysis of geared systems – predicting and controlling the whining noise. Automotive NVH Technology, Fuchs A, Nijman E and Priebsch H-H (Eds), Springer briefs in applied sciences and technology. Springer International Publishing 2016, pp.63–79.

[7] G. Liu, RG. Parker, Dynamic Modeling and Analysis of Tooth Profile Modification for Multimesh Gear Vibration. ASME. J. Mech, 2008, 130(12):121402-121402-13.

[8] M. Inalpolat, A. Kahraman, Dynamic Modelling of Planetary Gears of Automatic Transmissions. Proceedings of the Institution of Mechanical Engineers, Part K: Journal of Multi-Body Dynamics, 222(3), 2018, 229–242.

[9] RG. Parker, V. Agashe, SM. Vijayakar, Dynamic Response of a Planetary Gear System Using a Finite Element/Contact Mechanics Model. ASME. J. Mech, 1999, 122(3):304-310.

[10] C. Yuksel, A. Kahraman, Dynamic tooth loads of planetary gear sets having tooth profile wear, Mechanism and Machine Theory, Volume 39, Issue 7, 2004, 695-715

[11] J. Perret-Liaudet, "An original method for computing the response of a parametrically excitated forced system," JSV, vol. 196, 1996, 165-177.

[12] J.Neufond, E. Denimal, E. Rigaud, J.Perret-Liaudet, A.Carbonelli, Whining noise computation of a planetary gear set induced by the multi-mesh excitations. Proc. Inst. Mech. Eng. C, 2019

[13] T. Nonaka, A. Kubo, S. Kato, T. Ohmori, Silent gear design for mass produced gears with scatters in tooth accuracy, ASME Proceedings of the International Power Transmission and Gearing Conference, Scottdale, USA, Vol. 2, 1992, 589-595.

[14] N. Driot, E. Rigaud, J. Sabot, J. Perret-Liaudet, Allocation of gear tolerances to minimize gearbox noise variability; Acustica united with Acta Acustica; 87, 67-76, 2001.

COMPARISON OF NUMERICAL MODELS FOR THE PREDICTION OF BLADDER TANK CRASHWORTHINESS

D. Cristillo[1], F. Di Caprio[1], C. Pezzella[2], C. Paciello[2], M. Belardo[1], L. Di Palma[1]

[1] CIRA (Italian Aerospace Research Centre) - Airframe Design & Dynamic Lab.
Via Maiorise, snc, 81043 - Capua (CE), ITALY
Email: d.cristillo@cira.it; f.dicaprio@cira.it; m.belardo@cira.it; l.dipalma@cira.it

[2] Step Sud Mare srl
Via Ex Aeroporto c/o Consorzio Il Sole, LOTTO X1, 80038 - Pomigliano d'Arco (NA)
Email: claudio.pezzella@stepsudmare.com; carmen.paciello@stepsudmare.com

ABSTRACT

Nowadays helicopters, thanks to its unique vertical take-off and landing properties, play significant roles in transportation, medical rescue, aerial detection, and so on. However, the possibility of an accident must be taken into account from the first design phases, trying to adopt all possible solutions to minimize the consequences due to possible crashes. In particular, approximately 15 % of the injuries and deaths in helicopter accidents are caused by fuel ignition on account of the fuel tank failure. In this context, a methodology to predict the tank behaviour during the crash, can be conceived. This paper provides a comparison between two numerical models, developed by means of different software: Abaqus and Ls-Dyna, and experimental test came from literature, in order to assets the capability in simulating this kind of events.

1 INTRODUCTION

Nowadays, helicopters are widely used in military and civil fields owing to its unique vertical take-off and landing properties, excellent hover performance and low-speed characteristics. It is becoming increasingly obvious that helicopters play significant roles in transportation, medical rescue, aerial detection, and so on. During the operative life of a generic aircraft, and therefore also of a helicopter, it is possible that it could incur into dangerous situations such like an emergency landing or worse scenarios. Even if several attempts have been made to improve helicopter crashworthiness and passenger safety level during the critical events, the crashes could generate

serious injuries and even the death of occupants. According to the statistics, approximately 15 % of the injuries and deaths in army and civilian helicopter accidents are caused by fuel ignition on account of the fuel tank failure [1]. Consequently, the crashworthiness is the crucial concern in the design of a helicopter fuel tank to improve the survivability of aircraft occupants and structures under crash situations [2]. Since the 1960s, the US army has issued the first military regulations (MILDTL-27422) that defines the performance requirements for helicopter fuel tanks to eliminate post-crash fire after an emergency landing [3]. As described in the MIL-DTL-27422, the drop impact test must be conducted to check the dynamic response of the fuel tank. Numerical models for the analysis of water sloshing in a fuel tank during crash was developed and verified by experimental results, which generates four different models to simulate the water inside the tank [4]. Luo et al. [5] analysed the crashworthiness of fuel tank for helicopter by utilizing the finite element method (FEM) for the purpose of validating energy-absorption capabilities of the textile layer and protection frame. Kim and Kim [6] numerically simulated crash behaviour of fuel cell group of rotorcraft based on the smoothed particle hydrodynamics (SPH) method by utilizing the commercial software LS-DYNA. In this paper two numerical models for the prediction of fuel tank crash was developed and verified by experimental results find in literature. Numerically the behaviour of fuel have been simulated by means of algorithm based on the smoothed particle hydrodynamics (SPH) method by utilizing two commercial software LS-DYNA and Abaqus.

2 EXPERIMENTAL TEST

In order to validate the numerical model, experimental data find in literature was used. A soft tank realized with one layer of nylon woven fabric composite material and 760 mm long, 760mm wide and 600 mm high and full of water (350 kg) was used as reference in this work [7]. In the drop test the tank falls freely and drops on a rigid surface, on which four pressure sensors are installed in order to record the time-history reaction force. The reference [7] reports two different experimental test which are performed with two different set of impact parameters: drop height equal to 15.2 and 19.8 m that correspond to an impact velocities equal to 17.3 and 19.7 m/s, respectively.

3 NUMERICAL MODEL

3.1 Finite element model

The experimental test is simulated by means of a FE model composed by three parts: the fuel tank, the ground and the fluid inside the fuel tank. In particular, the fuel tank is realized by using shell elements with a thickness of 2 mm, the ground is treated as a rigid body and hexahedral elements is used for the fluid.

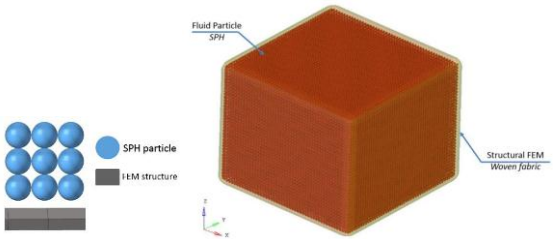

Figure 1 FE Model

3.2 Smooth Particle Hydrodynamics method (SPH)

The Smoothed Particle Hydrodynamics (SPH) are represented by three-dimensional elements with three degree of freedom and defined by their centre of mass. These elements have their own shape functions that depends on the connectivity of the particles. The interpolation distance between the particles, called smoothing length, furnish the location and gave information about the transmission among the different particles. In the SPH approach the water is simulated as particles with the same dimensions and distances without mass.

3.3 Water material model

The behaviour of the fluid material inside the fuel tank is regulated by the equation of state (EOS) relates pressure to a specific change rate of the material volume at a physical state. The Us-Up equation is chosen for the water formulation.

3.4 Tank material model

The fuel tank is composed by a crash-resistant layer made of textile. The mechanical characteristics of this material is find out by a uniaxial tensile tests of the woven material. It is tested that the density of the woven material is 1150 kg/m^3. The average thickness of the woven material is 2 mm. Stress–strain curves of the woven material is reported in Figure 2.

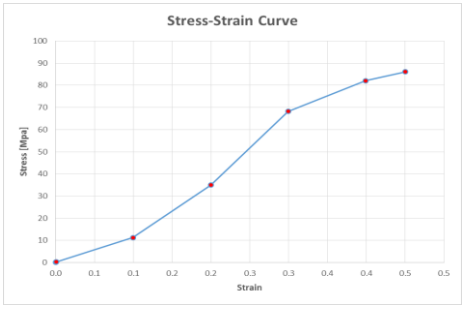

Figure 2 Stress–strain curves of the woven material

4 NUMERICAL RESULTS

The comparison, between Ls-Dyna and Abaqus, of deformation modes of the fuel tank is shown in Figure 3. The figure shows the deformation of the tank in six different time step. The images seems to put in evidence that the model realized with Ls-Dyna is more rigid than Abaqus model. In particular the frames at time step 4 and 5 show that tank made up with Abaqus is more sagged than the other.

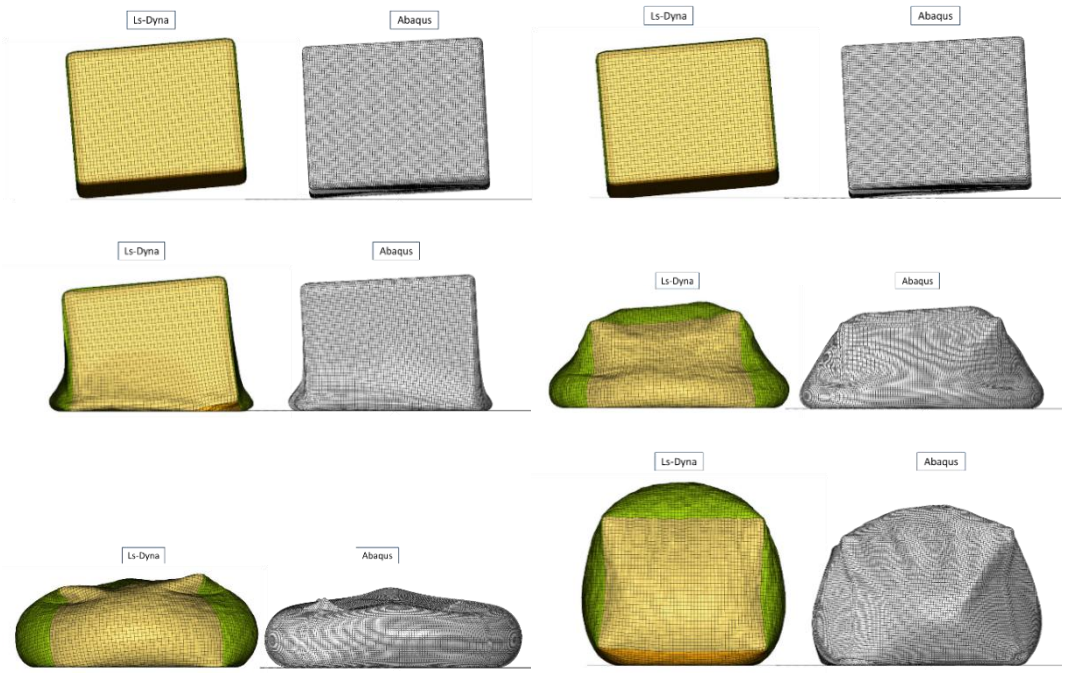

Figure 3 Comparison of deformation modes of the fuel tank between Ls-Dyna (on the left) and Abaqus (on the right)

Figure 4 shows the time histories of the reaction force on the rigid impact surface. It is possible to note that both codes are able to reproduce, with a good accuracy, the general trend of the dynamic event. The first two peaks represent the total tank sag on the soil, which lasts about 20 ms. After that in the numerical simulations the tank starts to rebound and therefore the reaction force

goes to zero within 20-30 ms. The figure shows that the peak of the resultant force at the impact instant is similar between the numerical and the reference values.

In particular, the experimental value is about 622 kN, instead the maximum force evaluated by Abaqus is 637 kN (+2.4 % respect experimental value), and the value obtained with Ls-Dyna is 607 kN (-2.4% respect experimental value). Furthermore, the second peak of force underline, how previously observed, that the Ls-Dyna model is more rigid than Abaqus one.

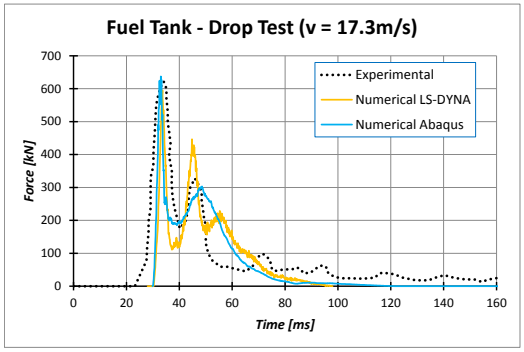

Figure 4: Impact force: Numerical and reference data

5 CONCLUSION

The present work provides a numerical investigation on the crashworthiness of bladder tank for aeronautical application. The test case assumed as reference represent the standard tank in according to the MIL-DTL-27422. In particular, two different commercial code was used to simulate the experimental test came from literature. For both code the same geometrical and FE models and the same material models were adopted. The obtained results highlighted that both code are able to simulate with a good accuracy the first parts of the experimental test. Actually the error, in terms of maximum reaction force is small that 3%. After the first peak, that both codes replicate very well, the results diverges a little bit. Ls-Dyna model seems to be stiffer than the Abaqus one, since the Ls-Dyna second peak is higher than the Abaqus one. Further, the response time are different and this aspect lead to suppose a slight stiffness in the Ls-Dyna model. Despite that, the numerical results are very good, especially considering the complexity of the analysed problem.

ACKNOWLEDGEMENTS

Grant Agreement number: 738078 — DEsign, development, manufacture, testing and Flight qualification of nExt geNeration fuel storage system with aDvanced intEgRated gauging and self-sealing capabilities (DEFENDER)

REFERENCES

[1] V. Giavotto, C. Caprile, G. Sala. The design of helicopter crashworthiness. Energy absorption of aircraft structures as an aspect of crashworthiness. Proceedings of the AGARD 66th meeting of the structures and material panel, pp 6.1–6.9, 1988

[2] JL Yang, Wu WH (2001) Study on the armed helicopter crashworthiness designs. Chin J Mech Eng 37(5):16

[3] Harris FD, Kasper EF, Iseler LE (2000) US civil rotorcraft accidents, 1963 through 1997. NASA STI Program, NASA/TM-2000-209597, USAAMCOM-TR-00-A-006

[4] Anghileri M, Castelletti LML, Tirelli M (2005) Fluid–structure interaction of water filled tanks during the impact with the ground. Int J Impact Eng 31(3):235–254

[5] Luo C, Liu H, Yang JL et al (2007) Simulation and analysis of crashworthiness of fuel tank for helicopters. Chin J Aeronaut 20(3):230–235

[6] Kim HG, Kim S (2014) Numerical simulation of crash impact test for fuel cell group of rotorcraft. Int J Crashworthiness 19(6):639–652

[7] Xianfeng Yang, Zhiqiang Zhang, Jialing Yang and Yuxin (2016) Sun Fluid–structure interaction analysis of the drop impact test for helicopter fuel tank

Design strategy of the wing of the Next Generation Civil Tilt-Rotor Technology Demonstrator

A. Marika Belardo[1], B. Jacopo Beretta [2], Aniello Daniele Marano[3], Gianluca Diodati[1], Nicola Paletta[2], Mario Graziano[4], Mariacarmela Capasso[4], Francesco Di Caprio[1], Luigi Di Palma[1]
[1]Italian Aerospace Research Centre (CIRA), Capua, IT
[2]IBK-Innovation GmbH, Hamburg, DE
[3]PhD student funded by CIRA at Department of Industrial Engineering – University of Naples Federico II, Naples, IT
[4]Step Sud Mare Srl, Pomigliano D'Arco, IT
Email: m.belardo@cira.it, jacopo.beretta@ibk-innovation.de, aniellodaniele.marano@unina.it, g.diodati@cira.it, nicola.paletta@ibk-innovation.de, mario.graziano@stepsudmare.com, mariacarmela.capasso@stepsudmare.com, f.dicaprio@cira.it, l.dipalma@cira.it.

ABSTRACT

The T-WING project is a Clean Sky 2 research project aimed at designing, manufacturing, qualifying and flight testing the new wing of the Next-Generation Civil Tiltrotor Technology Demonstrator (NGCTR-TD. Requirements, design strategy, methodology and main steps followed to achieve the composite wing design are presented. The main driving requirements have been expressed in terms of structural, dynamic, aeroelastic and functional requirements and wing preliminary loads. Based on the above-mentioned requirements, the first design loop is performed by targeting an optimal wing structure able to withstand preliminary design loads, and simultaneously with stiffness and inertia distributions leading to a configuration free from flutter within the flight envelope. The outcome from the first design loop is then used to build a global FEM, to be used for a multi-objective optimization performed in ALTAIR OptiStruct environment.

1 INTRODUCTION

Horizon 2020 Clean Sky 2 FRC IADP NextGenCTR will be dedicated to the design, construction and flying of an innovative Civil Tiltrotor technology demonstrator [1-3]. NGCTR's demonstration activities, led by Leonardo Helicopters (LH), will aim to validate its architecture, technologies/systems and operational concepts, with significant improvement with respect to the current state-of-the-art tiltrotors. The NGCTR-TD is characterized by a different concept for the tilting mechanism with respect to the upcoming LH civil tiltrotor platform: a fixed engine installation with a

split gearbox to provide the proprotor tilting mechanism, based on new capabilities in aerodynamic and structural analysis, design, and next-generation manufacturing and assembly principles. This will also allow important operational cost reduction to address the competitiveness of the architecture and solutions adopted. T-WING consortium is working on the composite wing of the NGCTR-TD planned to be flying in 2023. The task undertaken by the consortium is aimed at designing, manufacturing, qualification and flight-testing of the wing and moveable surfaces of the NGCTR-TD, whose design is based on the requirements defined in cooperation with LH, the Work Area Leader. Once the wing will be manufactured and qualified, it will be assembled to all the other components of the NGCTR-TD. The last step of the development consists of a flight test campaign which will lead to the validation of the flight loads used for the preliminary design of the wing. Among the main technological advances of the NGCTR-TD with respect to current tilt rotors technologies, the following characterize the new vehicle: a new high efficient wing in helicopter mode by means of a rotating outboard flaperon and a large morphing surface that reduces the wing area beneath the rotors during hovering; a highly integrated composite wing structure; a compact structural wing box, since almost half of the wing chord-length is dedicated to the large moveable surfaces.

Figure 1 NGCTR

2 STATE OF ART

The tiltrotor represents the overcoming of the helicopter's limitations for a fast and reliable point to point connection or intercity flights and in order to improve public mobility and access to air transportation. Indeed, the tiltrotor combines the maximum cruising speed, range, endurance and payload of the airplane with the vertical lift capabilities of a helicopter. Although many tiltrotor concepts have been developed, few have actually flown, namely the NASA's XV-3 and XV-15, the Bell's military tiltrotors V22 and V280 and, finally, the AW609, currently subjected to certification process for use in the civil sphere.

3 REQUIREMENTS

Being the tilt-rotor able to operate as both a helicopter and an aircraft, the airworthiness specifications are both taken from CS-25 and CS-29 Airworthiness Requirements, and from brand-new requirements introduced specifically for tilt-rotors [4]. The wing box architecture and rib spacing of the NGCTR-TD comes out mainly from the fuel capacity requirement. The available internal space is maximized to host fuel bladders, hydraulics, electrical and avionics equipment, the control surface actuators and the driveshaft connecting the gearboxes of the tilting mechanism. Once the wing will be connected to the fuselage several flight mechanics requirements to be satisfied. Dynamic requirements concern the limitations on the natural frequencies of the wing to grant no coupling between wing modes and FCS/ rotors modes [5]. In addition, in the preliminary design of a tiltrotor with the lowest possible weight, the wing structural design, in terms of skin and wing box components thicknesses, has to cope with strength, buckling and stiffness requirements, the latter mainly dictated by fundamental aeroelastic requirements. Once preliminary sizing has been achieved, Finite Elements Models (FEM) and Digital Mock Up can be set up to verify compliance with all the remaining requirements, such as wing preliminary loads, accessibility, assembly & integration and to assess manufacturability.

4 DESIGN STRATEGY

Based on the above-mentioned requirements, the design strategy is composed of two main phases (Fig. 2). The first phase (top of Fig 2) consists in a multi-objective optimization (M-OO) [6-

7], looped with aeroelastic analyses, mainly consisting of Matlab in-house codes (based on classical shear flow formulas in closed thin-walled sections and panel buckling formulas), that allow performing optimization runs in a very short time (compared with Finite Elements Analysis) with an acceptable degree of fidelity. The process aim is to find a set of feasible thickness and caps areas compliant with the strength and structural dynamics requirements, with the lowest possible mass:

- A first composite wing structure able to withstand preliminary design loads, and free from flutter within the flight envelope is obtained.
- The outcome from the previous step is then used to refine the model and compute more reliable flight loads and repeat aeroelastic analyses, returning further requirements to be fulfilled in terms of wing stiffness and inertia distributions.

The second phase (bottom of Fig 2) consists in the Finite Element modelling of the wing, to allow a multi-objective optimization within Altair OptiStruct environment. In particular the optimization is performed for the composite structures (skins and spars), in order to find the best solution - in terms of thickness - which minimizes the structural weight and is compliant with stiffness (flexural and torsional), strength & buckling requirements. The Finite Element model of the wing is made of mainly 2D and 1D Elements. The composites components subjected to the optimization are modelled with equivalent PSHELL. The optimization constraints are:

1. No buckling up to 80% of Limit Load on skin and spars;
2. Strength Margin of Safety > 0 at Ultimate Load on composite parts (max strain criterion);
3. Max allowed wing tip flexural displacements and torsion angle.

The algorithm is a gradient descent optimization. A total of no. 15 Loading conditions are considered: no. 12 load cases for strength and buckling plus no. 3 load cases for Flexural Out of Plane M_x, Torsional M_y and Flexural In Plane M_z.

The design variables of this optimization process are the thicknesses of the upper and lower skins and of the spars, all made of Carbon Fiber Reinforced Plastic. The outcome is a zonal optimization along the wingspan, as shown in figure 3. The optimized FEM will be used to compute new stiffness distributions and update structural aeroelastic stick beam model and repeat analyses. Moreover, this zonal optimization is the starting point of an engineered model and a detailed FEM, which will take into account also manufacturing constraints and it is beyond the scope of the present work.

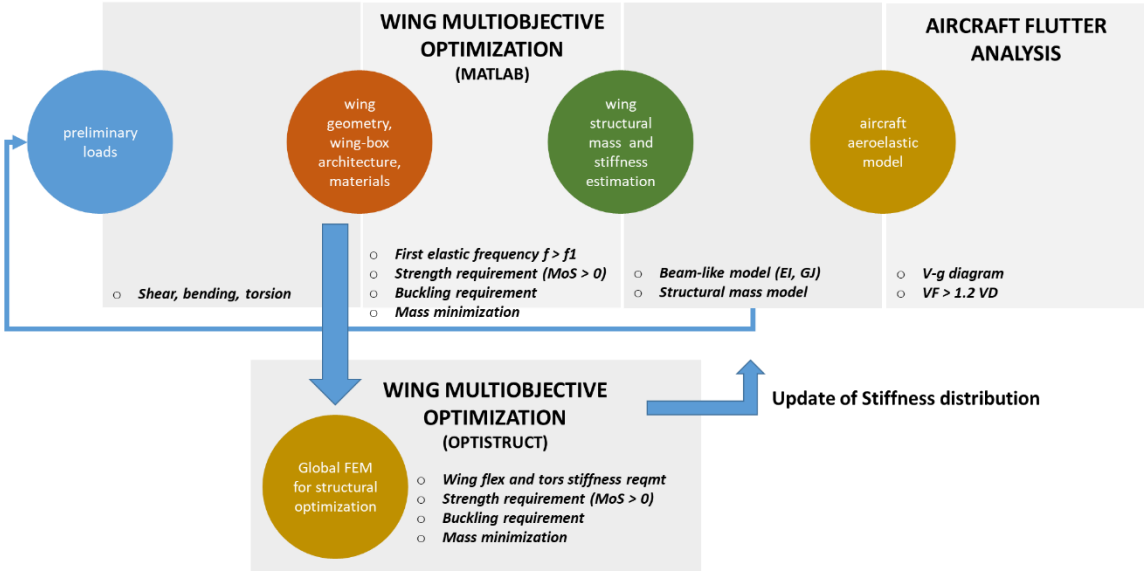

Figure 2. Design strategy flowchart

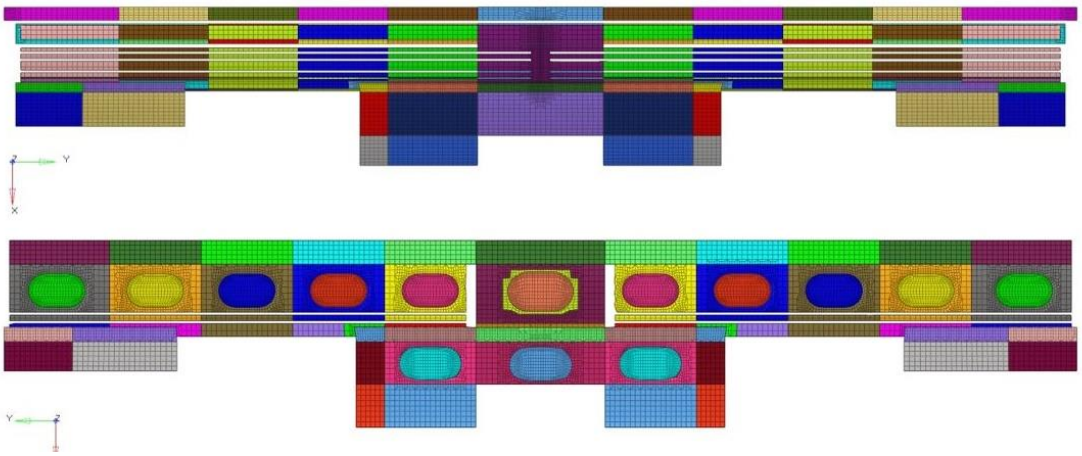

Figure 3. Design strategy flowchart

5 CONCLUDING REMARKS

In this paper the main steps followed to achieve the composite wing preliminary sizing of the NGCTR-TD tiltrotor have been presented. In particular the design strategy, aimed at finding a first optimal solution on terms of composite components thickness, is based on a two-level optimization: the first one performed with engineering models (not FEM), and the latter within OPTISTRUCT FEA environment.

ACKNOWLEDGEMENTS

This project has received funding from the Clean Sky 2 Joint Undertaking under the European Union's Horizon 2020 research and innovation programme under Grant Agreement No CS2-GAM-FRC-2014-2015 FRC GAM 2018 No. 807090.

REFERENCES

[1] CLEAN SKY 2 Joint Undertaking Third Amended Bi-Annual Work Plan and Budget 2018-2019, Annex to decision CS-GB-2019-04-09 Decision Third Amended and Budget 2018-19.

[2] Smith, D. E.; Wilkerson, J.; Montoro, G. J.; Coy, J.; and Zuk, J.: Technology Development for Runway Independent Aircraft. Proceedings of the American Helicopter Society 59th Annual Forum, Phoenix, AZ

[3] Larry A. Young, William W. Chung; Alfonso Paris; Dan Salvano; Ray Young; Huina Gao; Ken Wright; David Miller; Victor Cheng: A Study of Civil Tiltrotor Aircraft in NextGen Airspace

[4] Johnson, W.; Yamauchi, G.K.; and Watts, M.E.: Design and Technology Requirements for Civil Heavy Lift Rotorcraft. American Helicopter Society Vertical Lift Aircraft Design Conference, San Francisco, CA.

[5] Jiri Cecrdle: Whirl Flutter of Turboprop Aircraft Structures. Cambridge, UK, Woodhead Publishing

[6] Deb, K.: Multi-objective optimization using evolutionary algorithms. John Wiley & Sons

[7] Belardo M.; Beretta J.; Marano A. D.; Diodati G.; Paletta N.; Di Palma L.: On the preliminary structural design strategy of the wing of the Next Generation Civil Tilt-Rotor Technology Demonstrator. AERODays Bucharest, RO, 2019.

DYNAMIC CHARACTERIZATION OF POLYMERIC VIBRATION DAMPERS

M. Barbieri[1*], A. De Felice[1], F. Pellicano[1], S. Sorrentino[1] and A. Zippo[1]

[1]Department of Engineering Enzo Ferrari
University of Modena and Reggio Emilia, Modena, ITALY
Email: {mark, alessandro.defelice, francesco.pellicano,
silvio.sorrentino, antonio.zippo}@unimore.it

ABSTRACT

Polymeric dampers are used in many fields for vibration isolation. These devices are based upon a low stiffness and high damping connection between a vibrating support and the item to be fastened. Whenever the connection is assured by a polymeric element, it is mandatory to be aware that stiffness and damping change with the excitation frequency. The characterization of stiffness and damping of the polymeric element in terms of storage modulus and loss modulus is commonly carried out at low frequency by means of a Dynamic Mechanical Analysis (DMA), nonetheless this approach cannot be applied at higher frequency. In the present study, a novel experimental approach for estimating the frequency dependent storage modulus and loss modulus in a polymeric vibration damper is presented. The proposed method is based on a direct measurement of the energy loss in hysteretic cycles and it is suitable for simple implementation using common instruments for vibration measurement.

1 INTRODUCTION

Vibration control is a relevant design requirement for several industrial applications, often achieved by means of passive damping technologies involving viscoelastic materials. Among them, elastomeric vibration isolators are widely adopted, consisting of a low stiffness and high damping connection between a vibrating support and the item to be fastened. Due to the presence of polymeric elements, to characterize the dynamic behaviour of a damper, it is of paramount importance estimating stiffness and damping changes with excitation frequency and temperature [1,2,3].

Most commonly, experimental results presented in the literature deal with measurements of the viscoelastic properties of prismatic rubber elements [4] or beam–like specimens [5]. Although

being dealt with several papers, there is still a lack of well–designed experimental work dealing with the measurement of damping properties of polymeric vibration isolators. In this case the characterization is commonly carried out at low frequency by means of a Dynamic Mechanical Analysis (DMA), nonetheless this approach cannot be applied at higher frequency [6].

In the present study, the polymeric vibration damper is modelled as a single degree of freedom system, using a shaker as source of vibration. The viscoelastic properties of the system are described by its dynamic stiffness, a complex function of the frequency, whose real (storage modulus) and imaginary (loss modulus) parts are experimentally estimated. The proposed method is based on a direct measurement of the energy loss in hysteretic cycles, and it is suitable for simple implementation using common instruments for vibration measurement.

2 TESTING EQUIPMENT

Damping measurements are carried out on the specimen of polymeric vibration damper shown in Figure 1a. The test rig (Figure 1b) is composed of a large steel mass and a Bruel & Kjear 4808 electrodynamic shaker. Both the mass and the shaker are suspended with low stiffness supports. The shaker exerts a force on an aluminium disk which is connected to the large mass by means of the test specimen (*i.e.* the polymeric damper shown in Figure 1a). The instrumentation consists of three accelerometers and a dynamic load cell. Measured points are:
a_0: mono–axial accelerometer on the shaker;
a_1: mono–axial micro–accelerometer on the right side of the damper;
F_1: dynamic load cell on the right side of the damper;
a_2: mono–axial accelerometer on the steel mass.
The shaker is connected to the aluminium disk by means of a stinger, in order to avoid lateral loading of the load cell and of the test specimen.

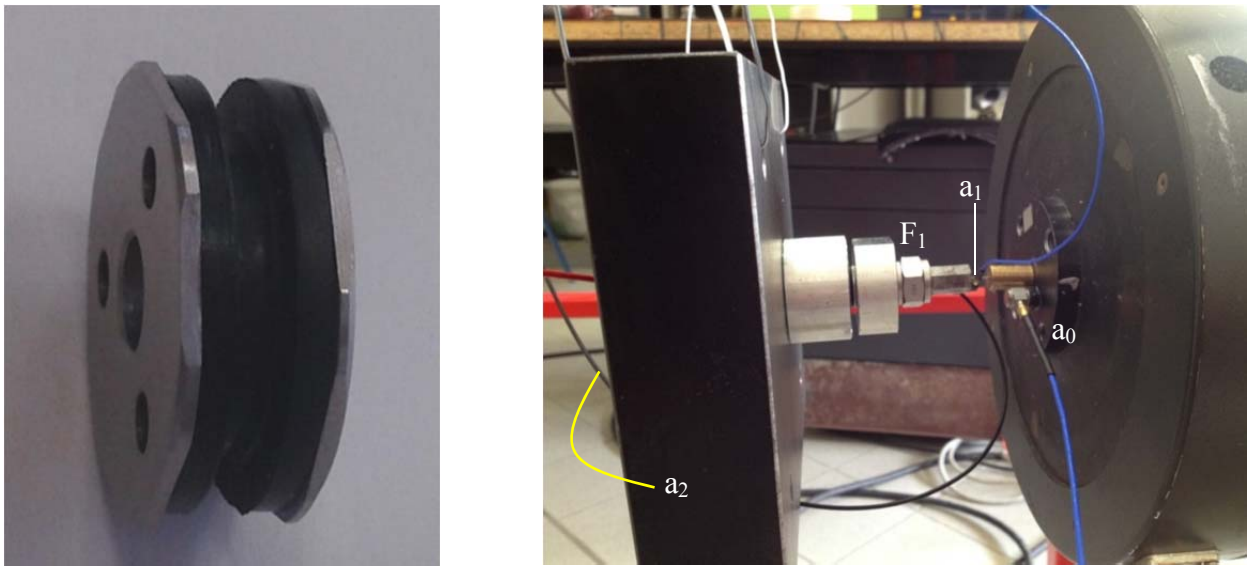

(a) (b)

Figure 1. Polymeric vibration damper (a) and electrodynamic shaker experimental setup (b).

3 EXPERIMENTAL RESULTS

In order to characterize the damping, a cyclic loading is applied to the polymeric damper by means of the shaker (Figure 1b), forces and accelerations are measured during 50 hysteresis loops. In the following, the characterization in terms of viscous damping and of complex modulus will be shown.

The excitation signal is a stepped sine with varying frequency from 150 to 1050 Hz

(logarithmically spaced). For each frequency, a sufficient amount of periods are neglected in order to avoid the transients then 50 periods are stored. The acceleration signal is integrated numerically in order to obtain the velocity; the relative velocity (v) is measured as the difference between mass velocity (v_2) and disk velocity (v_1) as well as the force F_1. Consequently, the work lost in a cycle can be estimated as:

$$\mathcal{W}_d' = \int_0^{\frac{2\pi}{\omega}} \mathrm{F}(t)\, \mathrm{v}(t)\, dt \tag{1}$$

and the value of the equivalent viscous damping is computed according to:

$$c_{eq} = \frac{\int_0^{\frac{2\pi}{\omega}} \mathrm{F}(t)\, \mathrm{v}(t)\, dt}{\int_0^{\frac{2\pi}{\omega}} \mathrm{v}^2(t)\, dt} \tag{2}$$

It is worthwhile noting that Equation 2 involves measured signals only; integrals are performed by Simpson's rule.

At low frequency there is an interaction between the stinger and the system, so that the response is nonlinear, and the proposed method is not reliable. Conversely, at frequencies over 500 Hz, the response is linear, and clean hysteresis curves can be obtained.

Thanks to performed measurements, it is possible to compute the frequency dependence of the real stiffness k and of the loss factor η, which are needed to characterize the polymeric damper. Figure 2a shows that real stiffness is increased from 500 Hz to 1000 Hz by 40 %. Three different runs are shown, which differ for the controlled variable and for the length of the stinger. The average error between run 1 and run 2 is 2%. The behaviour of the loss factor η vs. frequency is shown in Figure 2b. Above 500 Hz, the measured values are in agreement with the expected behaviour of a polymer where real stiffness is increasing. At 1000 Hz the loss factor is 0.26, which is equivalent to a dimensionless damping of 0.13.

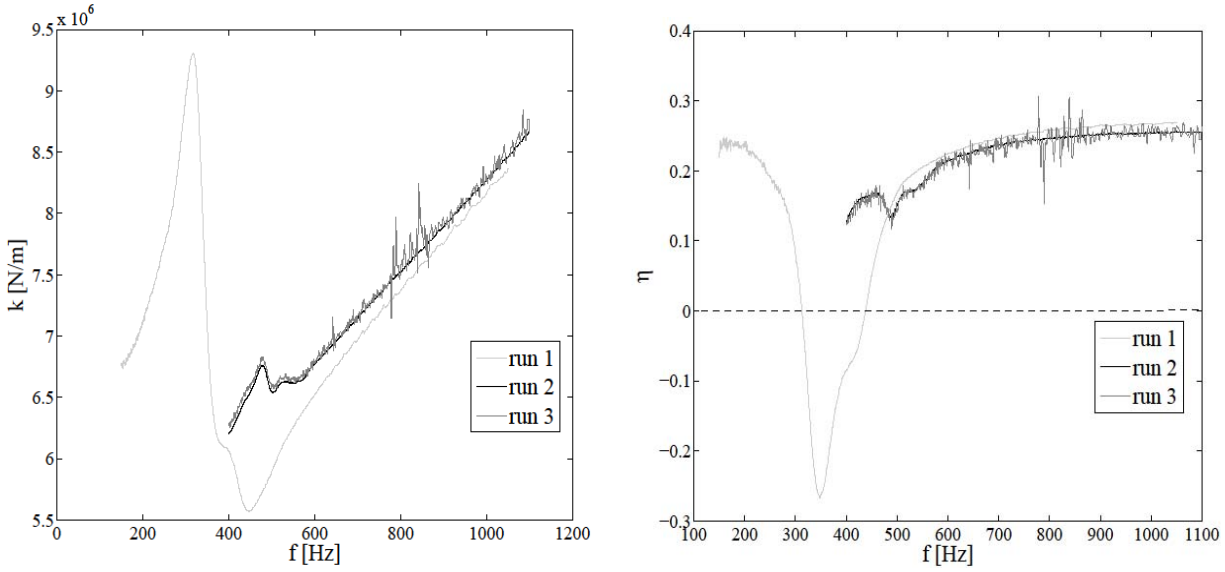

(a) (b)

Figure 2. Real (a) and Imaginary (b) parts of dynamic stiffness vs frequency.

Figure 3 shows a hysteresis loop on the force/displacement diagram. This plot is obtained by numerically integrating the measured accelerations twice. Such measurements are clean, and the 50 cycles are almost overlapping, therefore the whole procedure of measurement and data processing is robust and repeatable. This robustness is particularly relevant out of resonances, where the signal vs. noise ratio is especially unfavourable, making the difference between the proposed method and other

techniques presented in the literature, as for instance Ref. [4] where the accuracy of estimates out of resonances is claimed, but actually it is far from being accomplished.

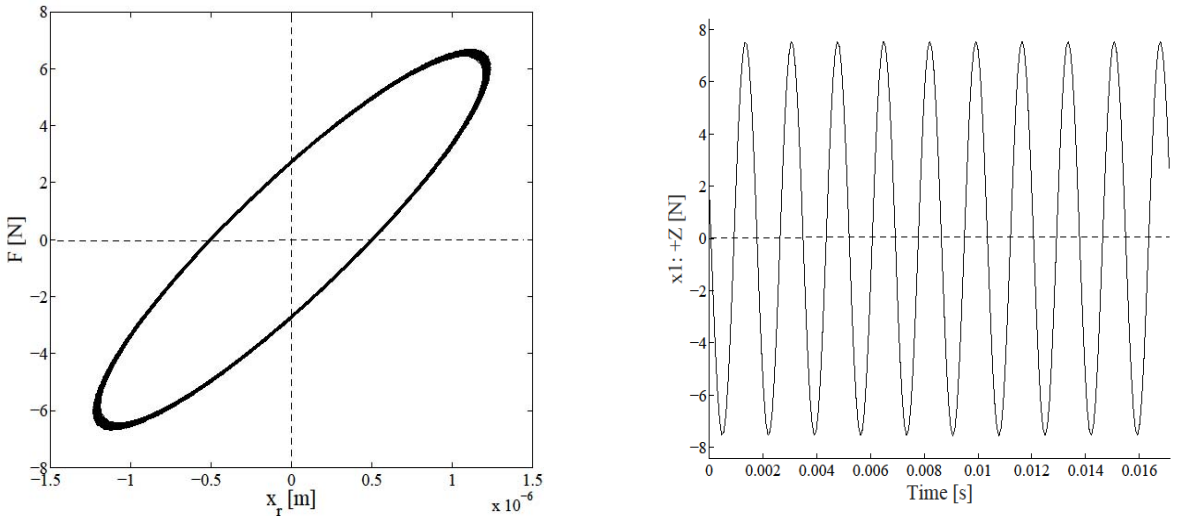

(a) (b)

Figure 3. Work lost per cycle at 1050 Hz (a) and related time history (b).

4 CONCLUDING REMARKS

In the present work a test rig for characterizing dynamic stiffness and damping of a polymeric damper is presented. While standard quasi–static procedures (DMA) provide information at low frequency, the current method is capable to provide data at frequencies in the range 500–1000 Hz, which are of high interest in the automotive field.

A great advantage of the proposed method is that it can be implemented using standard vibration testing equipment, such as a small shaker, mono–axial accelerometers and a dynamic load cell. Measured real stiffness and loss factor curves are in agreement with the literature, and therefore they can used to fit a rheological model of the polymeric material, which will be useful for modelling purposes.

REFERENCES

[1] C. Zener. *Elasticity and Anelasticity of Metals*, The University of Chicago Press, Chicago, 1948.

[2] A.S. Nowick, B.S. Berry. *Anelastic relaxation in crystalline solids*, Academic Press, New York – London, 1972.

[3] A.D. Nashif, D.I.G. Jones, J.P. Henderson. *Vibration Damping*, John Wiley, New York, 1985.

[4] D. Koblar, M. Boltežar. Evaluation of the frequency–dependent Young's modulus and damping factor of rubber from experiment and their implementation in finite element analysis. *Experimental Techniques*, online 11 November 2013.

[5] G.L. Ghiringhelli, M. Terraneo. Analytically driven experimental characterization of damping in viscoelastic materials. *Aerospace Science and Technology*. 40, 75-85, 2015.

[6] H. Abramovich, D. Govich, A. Grunwald. Damping measurements of laminated composite materials and aluminum using the hysteresis loop method. *Progress in Aerospace Sciences*. 78, 8-18, 2015.